

# Close Range Photogrammetry

Principles, techniques and applications

**Professor Dr Thomas Luhmann**

Institute for Applied Photogrammetry and Geoinformatics  
University for Applied Sciences, Oldenburg, Germany

**Dr Stuart Robson**

Senior Lecturer, Department of Geomatic Engineering  
University College London, UK

**Dr Stephen Kyle**

Consultant in Large Scale Metrology,  
Guernsey, Channel Islands, UK

**Professor Ian Harley**

Professor Emeritus, Department of Geomatic Engineering  
University College London, UK



**Whittles Publishing**

Published by  
**Whittles Publishing**,  
Dunbeath,  
Caithness KW6 6EG,  
Scotland, UK  
[www.whittlespublishing.com](http://www.whittlespublishing.com)

© 2011 T Luhmann, S Robson, S Kyle & I Harley

ISBN for CD 978-184995-057-2  
Print edition 978-1870325-50-9

*All rights reserved.  
No part of this publication may be reproduced,  
stored in a retrieval system, or transmitted,  
in any form or by any means, electronic,  
mechanical, recording or otherwise  
without prior permission of the publishers.*

# Preface

The capacity to make accurate three-dimensional measurements has always been fundamental to the physical sciences and is of increasing importance in manufacturing, engineering, biology, forensic investigation, medical science, architecture, archaeology and other fields. Many tools and techniques have been developed in many disciplines but each tends to be specialised and to be applicable only for objects within a limited range of dimensions. Photogrammetry transcends those limitations: it may be used equally for mapping from cameras in space and for measuring the microtopography of human skin. Photogrammetry has usually been regarded as one of the specialisms of geomatics (or surveying, to use a more familiar word) for the production of maps. Today, however, photogrammetry is readily available to engineers and many other professionals who wish to make accurate three-dimensional measurements of complex objects.

This book explains the application of photogrammetry to such tasks, and provides the mathematics, physics and photographic theory necessary for a good understanding of the techniques and is very closely based on Luhmann's *Nahbereichsphotogrammetrie* published in German by Wichmann in 2000 and, in a second edition, in 2003. That book stimulated a demand for a similar text in English. This book is addressed not only to photogrammetrists but also to both students and experts in optical three-dimensional metrology and three-dimensional image processing.

As well as giving a little history, we have attempted to describe the highest level of development of the subject at the time of publication. Technology changes extremely rapidly and the book is published at a time when analogue imaging and processing techniques are being replaced by fully digital methods. We believe, however, that analogue methods should be discussed here as they can help directly in realizing the potential of newer techniques. A good knowledge of conventional photography is essential, for example, for the optimal application of digital imaging systems.

We would like to thank Keith Whittles from Whittles Publishing for his support and especially for his belief that our work would be finished in a reasonable period of time. We would also like to thank all friends, colleagues and companies for their technical input and for material submitted for inclusion. Last but not least, we express our gratitude to our own families.

In a book by four authors, working part-time on such a large task and under the pressure of a deadline, readers will inevitably find discontinuities of style, some repetition and some errors. We hope that you will forgive such faults; we look forward to feedback especially concerning matters that should be corrected.

*Thomas Luhmann, Stuart Robson, Stephen Kyle, Ian Harley*



# Contents

<b>Abbreviations .....</b>	x
<b>Image sources .....</b>	xii
<b>1 Introduction .....</b>	1
1.1 Overview .....	1
1.2 Fundamental methods.....	2
1.2.1 The photogrammetric process .....	2
1.2.2 Aspects of photogrammetry .....	3
1.2.3 Image forming model .....	6
1.2.4 Photogrammetric systems.....	8
1.2.5 Photogrammetric products.....	11
1.3 Applications.....	13
1.4 Historical development.....	15
References and further reading .....	25
<b>2 Mathematical fundamentals .....</b>	31
2.1 Coordinate systems.....	31
2.1.1 Image and camera coordinate systems .....	31
2.1.2 Comparator coordinate system .....	32
2.1.3 Model coordinate system.....	32
2.1.4 Object coordinate system .....	33
2.1.5 3D instrument coordinate system .....	33
2.2 Coordinate transformations .....	34
2.2.1 Plane transformations .....	34
2.2.2 Spatial transformations .....	39
2.3 Adjustment techniques .....	52
2.3.1 The problem.....	52
2.3.2 Least-squares method (Gauss-Markov linear model) .....	55
2.3.3 Measures of quality .....	59
2.3.4 Error detection in practice .....	67
2.3.5 Computational aspects.....	70
2.4 Geometric elements .....	72
2.4.1 Analytical geometry in the plane .....	73
2.4.2 Analytical geometry in 3D space .....	82
2.4.3 Surfaces.....	90
2.4.4 Compliance with design .....	93
References .....	94

---

<b>3 Imaging technology .....</b>	97
3.1 Imaging concepts .....	97
3.1.1 Methods of image acquisition .....	97
3.1.2 Imaging configurations .....	98
3.2 Geometric fundamentals .....	100
3.2.1 Image scale and accuracy .....	100
3.2.2 Optical imaging .....	104
3.2.3 Interior orientation of a camera .....	114
3.2.4 Resolution .....	129
3.2.5 Fundamentals of sampling theory .....	132
3.3 Imaging systems .....	135
3.3.1 Analogue imaging systems .....	135
3.3.2 Digital imaging systems .....	147
3.3.3 Laser-based measuring systems .....	176
3.3.4 Other imaging systems .....	181
3.4 Targeting and illumination .....	183
3.4.1 Object targeting .....	183
3.4.2 Illumination techniques .....	190
References .....	195
<b>4 Analytical methods .....</b>	201
4.1 Overview .....	201
4.2 Orientation methods .....	202
4.2.1 Exterior orientation .....	202
4.2.2 Collinearity equations .....	204
4.2.3 Orientation of single images .....	206
4.2.4 Object position and orientation by inverse resection .....	214
4.2.5 Orientation of stereo image pairs .....	215
4.3 Bundle triangulation .....	229
4.3.1 General remarks .....	229
4.3.2 Mathematical model .....	234
4.3.3 Object coordinate system (definition of datum) .....	244
4.3.4 Generation of approximate values .....	251
4.3.5 Quality measures and analysis of results .....	260
4.3.6 Strategies for bundle adjustment .....	264
4.4 Object reconstruction .....	266
4.4.1 Single image processing .....	266
4.4.2 Stereoscopic processing .....	274
4.4.3 Multi-image processing .....	283
4.5 Line photogrammetry .....	293
4.5.1 Space resection using parallel object lines .....	293
4.5.2 Collinearity equations for straight lines .....	296
4.5.3 Relative orientation with straight lines .....	297

4.5.4	3D similarity transformation with straight lines .....	299
4.5.5	Bundle adjustment with straight lines .....	300
4.5.6	Bundle adjustment with geometric elements .....	301
4.6	Multi-media photogrammetry .....	302
4.6.1	Light refraction at media interfaces .....	302
4.6.2	Extended model of bundle triangulation .....	307
4.7	Panoramic photogrammetry .....	309
4.7.1	Cylindrical panoramic imaging model .....	309
4.7.2	Orientation of panoramic imagery .....	311
4.7.3	Epipolar geometry .....	313
4.7.4	Spatial intersection .....	315
	References .....	315
<b>5</b>	<b>Digital image processing .....</b>	<b>319</b>
5.1	Fundamentals .....	319
5.1.1	Image processing procedure .....	319
5.1.2	Pixel coordinate system .....	320
5.1.3	Handling image data .....	322
5.2	Image preprocessing .....	327
5.2.1	Point operations .....	327
5.2.2	Filter operations .....	333
5.2.3	Edge extraction .....	339
5.3	Geometric image transformation .....	350
5.3.1	Fundamentals of rectification .....	351
5.3.2	Grey value interpolation .....	352
5.3.3	3D visualisation .....	354
5.4	Digital processing of single images .....	361
5.4.1	Approximate values .....	361
5.4.2	Measurement of single point features .....	364
5.4.3	Contour following .....	376
5.5	Image matching and 3D object reconstruction .....	378
5.5.1	Overview .....	378
5.5.2	Feature-based matching procedures .....	380
5.5.3	Correspondence analysis based on epipolar geometry .....	385
5.5.4	Area-based multi-image matching .....	388
5.5.5	Matching methods with object models .....	392
	References .....	397
<b>6</b>	<b>Photogrammetric measuring systems .....</b>	<b>401</b>
6.1	Comparators .....	401
6.1.1	Design principles .....	401
6.1.2	Analogue image comparators .....	402
6.1.3	Digital image comparators .....	402

6.2	Single camera systems.....	404
6.2.1	Camera with hand-held probing device .....	404
6.2.2	Probing system with integrated camera .....	405
6.2.3	Camera system for robot calibration .....	406
6.2.4	High-speed 6 DOF system .....	407
6.3	Stereoscopic processing systems.....	407
6.3.1	Analytical stereo-instruments .....	407
6.3.2	Digital stereoprocessing systems.....	410
6.3.3	Stereovision systems.....	412
6.4	Multi-image measuring systems.....	413
6.4.1	Interactive processing systems .....	413
6.4.2	Mobile industrial point measuring systems.....	415
6.4.3	Stationary industrial on-line measuring systems.....	420
6.5	Systems for surface measurement .....	424
6.5.1	Active pattern projection .....	425
6.5.2	Passive pattern projection.....	431
6.6	Acceptance and re-verification of measuring systems.....	433
6.6.1	Definition of terms .....	433
6.6.2	Differentiation from coordinate measuring machines.....	435
6.6.3	Uncertainty of length measurement .....	436
	References .....	438
<b>7</b>	<b>Measurement concepts and solutions in practice .....</b>	<b>441</b>
7.1	Project planning.....	441
7.1.1	Planning criteria.....	441
7.1.2	Accuracy issues .....	442
7.1.3	Restrictions on imaging configuration .....	443
7.1.4	Computer-aided design of the imaging network .....	445
7.2	Camera calibration.....	448
7.2.1	Calibration methods.....	448
7.2.2	Imaging configurations.....	453
7.3	Dynamic photogrammetry.....	458
7.3.1	Relative movements between object and imaging system .....	458
7.3.2	Recording cinematic sequences.....	461
7.4	Close-range aerial imagery.....	465
	References .....	467
<b>8</b>	<b>Example applications .....</b>	<b>469</b>
8.1	Architecture and cultural heritage .....	469
8.1.1	Photogrammetric building records .....	469
8.1.2	3D models.....	472
8.1.3	Free-form surfaces .....	475
8.2	Engineering surveying and civil engineering.....	478

---

8.2.1	Measurement of deformations.....	478
8.2.2	Tunnel profile measurement.....	481
8.2.3	Deformation of concrete tanks .....	482
8.3	Industrial applications .....	484
8.3.1	Power stations and industrial plant.....	484
8.3.2	Aircraft and space industries .....	485
8.3.3	Car industry .....	487
8.3.4	Ship building industry .....	488
8.4	Forensic applications .....	489
8.5	Medicine .....	491
8.5.1	Surface measurement.....	491
8.5.2	On-line measuring systems.....	492
	References .....	494
<b>Index</b>	.....	497

## Abbreviations

ADC	analogue-to-digital converter
AGC	automatic gain control
ASCII	American Standard Code for Information Interchange
ASPRS	American Society for Photogrammetry and Remote Sensing
BRDF	bidirectional reflection distribution function
CAAD	computer aided architectural design
CAD	computer aided design
CAM	computer aided manufacturing
CCD	charge coupled device
CCIR	Comité consultatif international pour la radio (International Radio Consultative Committee)
CD-ROM	compact disk – read-only memory
CID	charge injection device
CIE	Commission Internationale de l'Éclairage (International Commission on Illumination)
CIPA	Comité International de Photogrammétrie Architecturale (International Committee for Architectural Photogrammetry)
CMM	coordinate measurement machine
CMOS	complementary metal oxide semi-conductor
CT	computer tomogram, tomography
CTF	contrast transfer function
DAGM	Deutsche Arbeitsgemeinschaft für Mustererkennung (German Association for Pattern Recognition)
DCT	discrete cosine transform
DGPF	Deutsche Gesellschaft für Photogrammetrie, Fernerkundung und Geoinformation (German Society for Photogrammetry, Remote Sensing and Geoinformation)
DGZfP	Deutsche Gesellschaft für Zerstörungsfreie Prüfung (German Society for Non-Destructive Testing)
DIN	Deutsches Institut für Normung (German institute for standardization)
DLT	direct linear transformation
DMD	digital mirror device
DOF	degree(s) of freedom
DRAM	dynamic random access memory
DSM	digital surface model
DTP	desktop publishing
DVD	digital versatile (video) disk
DXF	autocad data exchange format
EP	entrance pupil
E'P	exit pupil
EPS	encapsulated postscript
FFT	full frame transfer or fast Fourier transform
FMC	forward motion compensation
FOV	field of view
FPGA	field-programmable gate array
FT	frame transfer
GIF	graphic interchange format
GIS	geo(graphic) information system
GMA	Gesellschaft für Meß- und Automatisierungstechnik (Society for Metrology and Automation Technology)
GPS	global positioning system
HDTV	high definition television

IEEE	Institute of Electrical and Electronic Engineers
IFOV	instantaneous field of view
IHS	intensity, hue, saturation
IL	interline transfer
INS	inertial navigation system
ISO	International Organisation for Standardization
ISPRS	International Society for Photogrammetry and Remote Sensing
JPEG	Joint Photographic Expert Group
LAN	local area network
LCD	liquid crystal display
LED	light emitting diode
LoG	Laplacian of Gaussian
LSM	least squares matching
LUT	lookup table
LW/PH	line widths per picture height
LZW	Lempel-Ziv-Welch (compression)
MOS	metal oxide semiconductor
MPEG	Motion Picture Expert Group
MR	magnetic resonance
MTF	modulation transfer function
PCMCIA	Personal Computer Memory Card International Association
PLL	phase-locked loop or pixel-locked loop
PNG	portable network graphics
PSF	point spread function
REM	raster electron microscope
RGB	red, green, blue
RMS	root mean square
RMSE	root mean square error
RPV	remotely piloted vehicle
RV	resolution power
SCSI	small computer systems interface
SLR	single lens reflex (camera)
SNR	signal-to-noise ratio
SPIE	The International Society for Optical Engineering
TIFF	tagged image file format
TTL	through the lens
TV	television
USB	universal serial bus
VDI	Verband Deutscher Ingenieure (German Association of Engineers)
VLL	vertical line locus
VR	virtual reality
VRML	virtual reality modelling language

## Image sources

- ABW Automatisierung + Bildverarbeitung Dr. Wolf GmbH, Frickenhausen, Germany: 3.129cd  
AICON 3D Systems GmbH, Braunschweig, Germany: 3.76c, 3.109, 3.111, 3.117c, 6.8, 6.10, 6.21, 6.25, 6.26, 6.27, 6.46a, 8.27  
AXIOS 3D Services GmbH, Oldenburg, Germany: 8.37a  
BrainLAB AG, Heimstetten, Germany: 8.38  
Breuckmann GmbH, Meersburg, Germany: 6.34  
Carl Zeiss (ZI Imaging, Intergraph), Oberkochen, Jena, Germany: 1.25, 1.26, 1.27, 1.28, 3.12, 3.48, 3.96, 3.129ab, 6.2, 6.42, 6.43, 6.44, 8.11  
DaimlerChrysler, Forschungszentrum Ulm, Germany: 5.68  
Dalsa Inc., Waterloo, Ontario, Canada: 3.63a, 5.35a  
DMT Deutsche MontanTechnologie, German Mining Museum, Bochum, Germany: 7.22  
Dresden University of Technology, Forschungsgruppe 3D Display, Germany: 6.13b  
ESTEC, Noordwijk, Netherlands: 8.28  
Fachhochschule Bielefeld, Abt. Minden, Fachbereich Architektur und Bauingenieurwesen, Germany: 4.59  
Fachhochschule Osnabrück, Internet Site "Einführung in Multimedia", Germany: 3.60, 3.62  
Fokus GmbH Leipzig, Germany: 4.58  
Frank Data International NV, Netherlands: 8.8a  
Fraunhofer Institute for Applied Optics and Precision Engineering (IOF), Jena: 6.38, 6.39, Germany  
Fraunhofer Institute for Factory Operation and Automation (IFF), Magdeburg, Germany: 6.16  
GOM Gesellschaft mbH, Braunschweig, Germany: 6.36  
GSI Geodetic Services Inc., Melbourne, Florida, USA: 1.15, 1.32, 3.54, 3.55, 3.83, 3.84, 3.117b, 3.124b, 6.3, 8.24  
Hasselblad Svenska AB, Göteborg, Sweden: 3.52  
HDW Howaldtswerke Deutsche Werft, Kiel, Germany: 8.31  
Imetric SA, Porrentruy, Switzerland: 1.14, 1.19, 3.85, 6.20, 6.28, 7.10  
Institute of Applied Photogrammetry and Geoinformatics (IAPG), FH Oldenburg, Germany: 1.1, 1.12, 1.13, 1.17, 3.28, 3.29, 3.32, 3.68, 3.71, 3.73, 3.78, 3.87, 3.88, 3.89, 3.99, 3.117a, 3.119, 3.120, 4.10, 4.52, 4.56, 4.61, 5.2b, 5.11, 5.41, 5.53, 5.66, 6.14, 6.15, 7.6b, 7.20, 7.21, 8.4, 8.7, 8.12, 8.13, 8.20, 8.21  
Institute of Geodesy and Geoinformatics, Applied Photogrammetry and Cartography, TU Berlin, Germany: 1.23, 3.108  
Institute of Geodesy and Photogrammetry (IGP), ETH Zürich, Switzerland: 1.21, 4.75, 7.17, 8.5, 8.6  
Institute of Photogrammetry, University of Bundeswehr, Neubiberg, Germany: 7.18, 7.19  
Institute of Photogrammetry (IfP), University of Stuttgart, Germany: 8.9  
Institute of Photogrammetry and Geoinformatics (IPI), University of Hannover, Germany: 8.10, 8.14, 8.15, 8.16, 8.17  
Institute of Photogrammetry and Image Processing, TU Braunschweig, Germany: 1.18, 7.6a, 8.31, 8.32  
INVERS, Essen, Germany: 8.19, 8.22, 8.23  
Jenoptik Laser-Optik-Systeme GmbH, Jena, Germany: 3.86, 3.90, 3.91  
Kamera Werk Dresden, Germany: 3. 98  
Kodak AG, Stuttgart, Germany: 1.31  
Konica Corporation, Tokyo, Japan: 3.116a  
Leica Geosystems (Wild, Kern, LH Systems, Cyra), Heerbrugg, Switzerland: 3.49, 3.50, 3.105, 3.110, 3.112, 3.113, 4.68, 4.70, 4.73, 6.12, 6.14, 6.31  
Landeskriminalamt Nordrhein-Westfalen, Düsseldorf, Germany: 8.34  
Mapvision Ltd, Espoo, Finland: 1.30, 6.40  
Messbildstelle GmbH, Dresden, Germany: 8.3  
Metronor GmbH, Saarbrücken, Germany, Norway: 6.6, 6.24  
NASA, Jet Propulsion Laboratory, Pasadena, Ca., USA: 6.17  
Phocad Ingenieurgesellschaft mbH, Aachen, Germany: 1.33, 6.19

Physikalisch-Technische Bundesanstalt, Braunschweig, Germany: 6.46b  
Plus Orthopedics (Precision Instruments), Aarau, Switzerland: 8.37bc, 8.39  
Ricoh Corporation, San Bernardino, Ca., USA: 3.118b  
Rollei Fototechnic GmbH, Braunschweig, Germany: 1.16, 1.29, 3.13, 3.53, 3.56, 3.63b, 3.81, 3.82, 3.93,  
3.95, 3.128, 4.44, 6.5, 6.9, 6.18, 7.8, 8.33  
Sine Patterns LLC, Rochester, NY, USA: 3.34a  
Sony Deutschland GmbH, Köln, Germany: 3.76b  
Stadtpolizei Zürich, Switzerland: 8.34  
Transmap Corporation, Columbus, Ohio, USA: 8.8b  
University of Aalborg, Department of Development and Planning, Denmark: 4.59  
University of Melbourne, Department of Geomatics, Parkville, Australia: 4.42, 5.2, 8.25  
Volkswagen AG, Wolfsburg, Germany: 2.4, 6.45, 8.30  
Weinberger Deutschland GmbH, Erlangen, Germany: 3.103, 7.15  
Zoller and Fröhlich GmbH, Wangen im Allgäu, Germany: 3.105

# 1 Introduction

## 1.1 Overview

Chapter 1 provides an overview of the fundamentals of photogrammetry, with particular reference to close range measurement. After a brief discussion of the principal methods and systems, typical applications are presented. The chapter ends with a short historical review of close range photogrammetry.

Chapter 2 deals with mathematical basics. These include the definition of some important coordinate systems and the derivation of geometric transformations which are needed for a deeper understanding of topics presented later. In addition, the major aspects of least squares adjustment and statistics are summarised. Finally, a number of important geometrical elements used for object representation are discussed.

Chapter 3 is concerned with photogrammetric image acquisition for close range applications. Because of the wide variety of applications and instrumentation this chapter is extensive and wide-ranging. After an introduction to geometric basics and the principles of image acquisition, there follow discussions of analogue and digital imaging equipment as well as specialist areas of image recording. The chapter ends with a summary of targeting and illumination techniques.

Analytical methods of image orientation and object reconstruction are presented in Chapter 4. The emphasis here is on bundle triangulation. The chapter also presents methods for dealing with single, stereo and multiple image configurations based on measured image coordinates.

Chapter 5 brings together many of the relevant methods of digital photogrammetric image processing. In particular, those which are most useful to dimensional analysis and three dimensional object reconstruction are presented.

Photogrammetric measurement systems developed for close range are discussed in Chapter 6. They are classified into systems designed for single image, stereo image and multiple image processing. Interactive and automatic, mobile and stationary systems are considered, along with surface measurement systems utilising projected light patterns.

Chapter 7 discusses imaging configurations for, and solutions to, some critical close range tasks. After an introduction to network planning and optimisation the chapter concentrates on techniques for camera calibration, dynamic applications and aerial imaging from low flying heights.

Finally, Chapter 8 uses case studies and examples to demonstrate the potential for close range photogrammetry in fields such as architecture and heritage conservation, the construction industry, manufacturing industry and medicine.

## 1.2 Fundamental methods

### 1.2.1 The photogrammetric process

Photogrammetry encompasses methods of image measurement and interpretation in order to derive the shape and location of an object from one or more photographs of that object. In principle, photogrammetric methods can be applied in any situation where the object to be measured can be photographically recorded. The primary purpose of a photogrammetric measurement is the three dimensional reconstruction of an object in digital form (coordinates and derived geometric elements) or graphical form (images, drawings, maps). The photograph or image represents a store of information which can be re-accessed at any time.

Fig. 1.1 shows examples of photogrammetric images. The reduction of a three-dimensional object to a two-dimensional image implies a loss of information. Object areas which are not visible in the image cannot be reconstructed from it. This not only includes hidden parts of an object such as the rear of a building but also regions which can not be recognised due to lack of contrast or limiting size, for example individual bricks in a building façade. Whereas the position in space of each point on the object may be defined by three coordinates, there are only two coordinates available to define the position of its image. There are geometric changes caused by the shape of the object, the relative positioning of camera and object, perspective imaging and optical lens defects. Finally there are also radiometric (colour) changes since the reflected electromagnetic radiation recorded in the image is affected by the transmission media (air, glass) and the light-sensitive recording medium (film, electronic sensor).

For the reconstruction of an object from photographs or images it is therefore necessary to describe the optical process by which an image is created. This includes all elements which contribute to this process, such as light sources, properties of the surface of the object, the medium through which the light travels, sensor and camera technology, image processing, film development and further processing (Fig. 1.2).

Methods of image interpretation and measurement are then required which permit the image of an object point to be identified from its form, brightness or colour distribution. For every

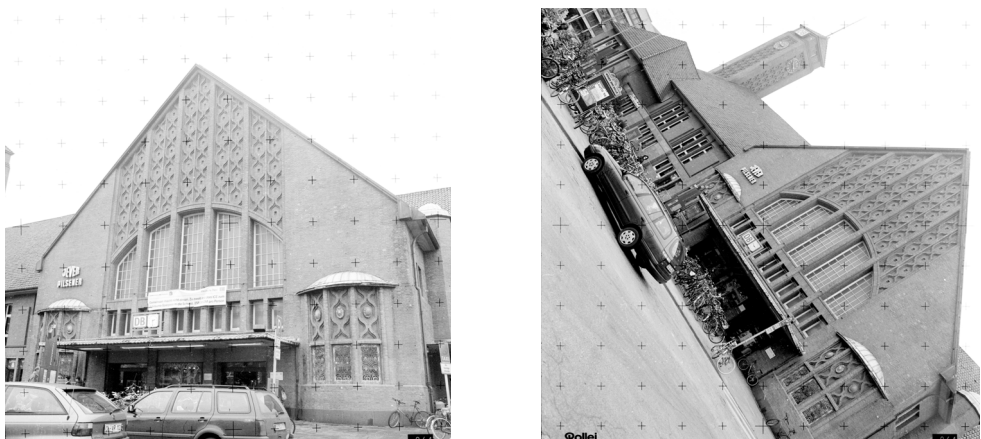


**Figure 1.1** Photogrammetric images

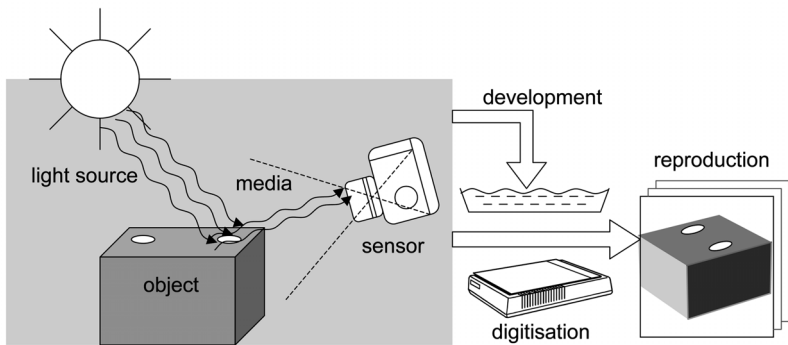


**Figure 1.2** From object to image

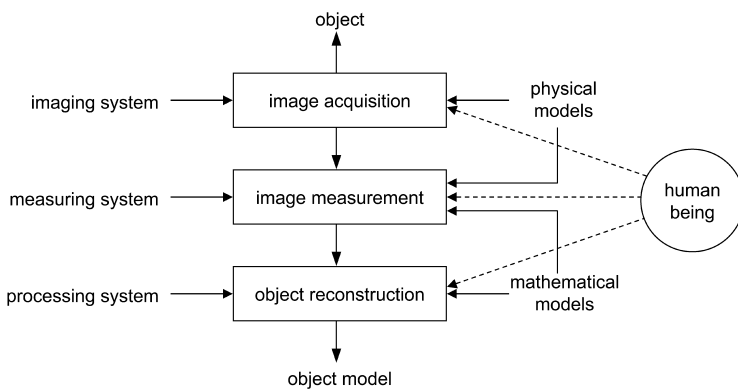


**Figure 1.3** The photogrammetric process: from object to model

image point, values in the form of radiometric data (intensity, grey value, colour value) and geometric data (position in image) can then be obtained. This requires measurement systems with the appropriate geometric and optical quality.

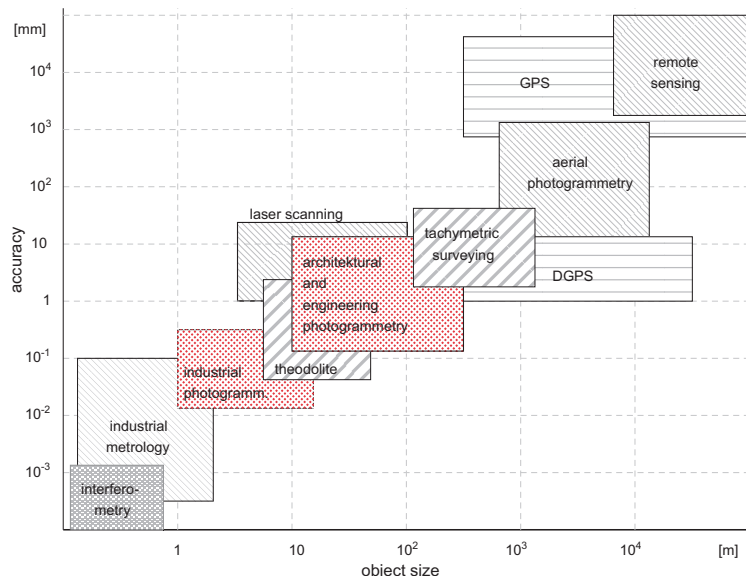
From these measurements and a mathematical transformation between image and object space, the object can finally be modelled.

Fig. 1.3 simplifies and summarises this sequence. The left hand side indicates the principal instrumentation used whilst the right hand side indicates the methods involved. Together with the physical and mathematical models, human knowledge, experience and skill play a significant role. They determine the extent to which the reconstructed model corresponds to the imaged object or fulfils the task objectives.

### 1.2.2 Aspects of photogrammetry

Because of its varied applications, close range photogrammetry has a strong interdisciplinary character. There are not only close connections with other measurement techniques but also with fundamental sciences such as mathematics, physics, information sciences or biology.

Close range photogrammetry has significant links with aspects of graphics and photographic science, for example computer graphics and computer vision, digital image processing, computer aided design (CAD), geographic information systems (GIS) and cartography.



**Figure 1.4** Relationship between object size and accuracy for different measurement methods<sup>1</sup>

Traditionally, there are also strong associations of close range photogrammetry with the techniques of surveying, particularly in the areas of adjustment methods and engineering surveying. With the increasing application of photogrammetry to industrial metrology and quality control, links have been created in other directions.

Fig. 1.4 gives an indication of the relationship between size of measured object, required measurement accuracy and relevant technology. Although there is no hard and fast definition, it may be said that close range photogrammetry applies to objects ranging from 1m to 200m in size, with accuracies under 0.1mm at the smaller end (manufacturing industry) and 1cm accuracy at the larger end (architecture and construction industry).

Optical methods using light as the information carrier lie at the heart of non-contact 3D measurement techniques. Measurement techniques using electromagnetic waves may be subdivided in the manner illustrated in Fig. 1.5. Techniques based on light waves are as follows:

- Triangulation techniques

Photogrammetry (single, stereo and multiple imaging), angle measuring systems (theodolites), indoor GPS, structured light (light section procedures, fringe projection, phase measurement, moiré topography), focusing methods, shadow methods, etc.

- Interferometry

Optically coherent time-of-flight measurement, holography, speckle interferometry, coherent radar

- Time-of-flight measurement

Distance measurement by optical modulation methods, pulse modulation, etc.

<sup>1</sup> Unsharp borders indicating typical fields of applications of measuring methods.

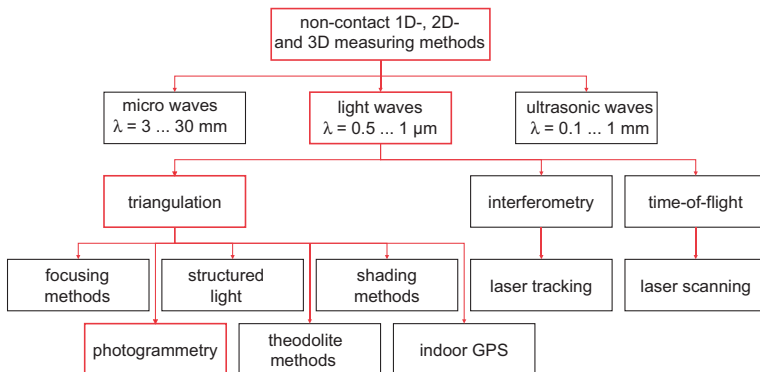


**Figure 1.5** Non-contact measuring methods

The clear structure of Fig. 1.5 is blurred in practice since multi-sensor and hybrid measurement systems utilise different principles in order to combine the advantages of each.

Photogrammetry can be categorised in a multiplicity of ways:

- By camera position and object distance
  - Satellite photogrammetry: processing of satellite images,  $h >$  ca. 200km
  - Aerial photogrammetry: processing of aerial photographs,  $h >$  ca. 300m
  - Terrestrial photogrammetry: measurements from a fixed terrestrial location
  - Close range photogrammetry: imaging distance  $h <$  ca. 300m
  - Macro photogrammetry: image scale  $> 1$  (microscope imaging)
- By number of measurement images
  - Single image photogrammetry: single image processing, mono-plotting, rectification, orthophotographs
  - Stereophotogrammetry: dual image processing, stereoscopic measurement
  - Multi-image photogrammetry:  $n$  images where  $n > 2$ , bundle triangulation
- By method of recording and processing
  - Plane table photogrammetry: graphical evaluation (until ca. 1930)
  - Analogue photogrammetry: analogue cameras, opto-mechanical measurement systems (until ca. 1980)
  - Analytical photogrammetry: analogue images, computer-controlled measurement
  - Digital photogrammetry: digital images, computer-controlled measurement
  - Videogrammetry: digital image acquisition and measurement
  - Panorama photogrammetry: panoramic imaging and processing
  - Line photogrammetry: analytical methods based on straight lines and polynomials
- By availability of measurement results
  - Real-time photogrammetry: recording and measurement completed within a specified time period particular to the application

- Off-line photogrammetry:  
sequential, digital image recording, separated in time or location from measurement
- On-line photogrammetry:  
simultaneous, multiple, digital image recording, immediate measurement
- By application or specialist area
  - Architectural photogrammetry: architecture, heritage conservation, archaeology
  - Engineering photogrammetry: general engineering (construction) applications
  - Industrial photogrammetry: industrial (manufacturing) applications
  - Forensic photogrammetry: applications to diverse legal problems
  - Biostereometrics: medical applications
  - Motography: recording moving target tracks
  - Multi-media photogrammetry: recording through media of different refractive indices
  - Shape from stereo: stereo image processing (computer vision)

### 1.2.3 Image forming model

Photogrammetry is a three-dimensional measurement technique which uses central projection imaging as its fundamental mathematical model (Fig. 1.6). Shape and position of an object are determined by reconstructing bundles of rays in which, for each camera, each image point  $P'$ , together with the corresponding perspective centre  $O'$ , defines the spatial direction of the ray to the corresponding object point  $P$ . Provided the imaging geometry within the camera and the location of the imaging system in object space are known, then every image ray can be defined in 3D object space.

From the intersection of at least two corresponding (homologous), spatially separated image rays, an object point can be located in three dimensions. In stereophotogrammetry two images are used to achieve this. In multi-image photogrammetry the number of images involved is, in principle, unlimited.

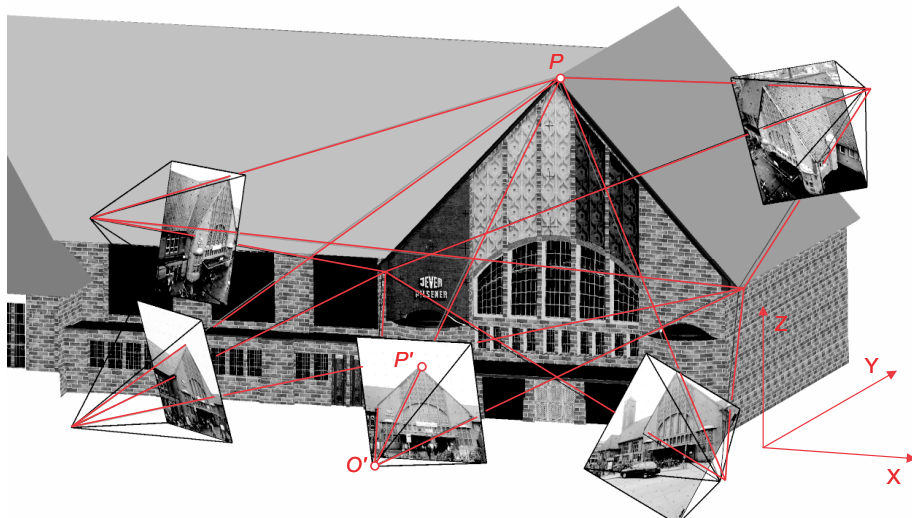


**Figure 1.6** Principle of photogrammetric measurement

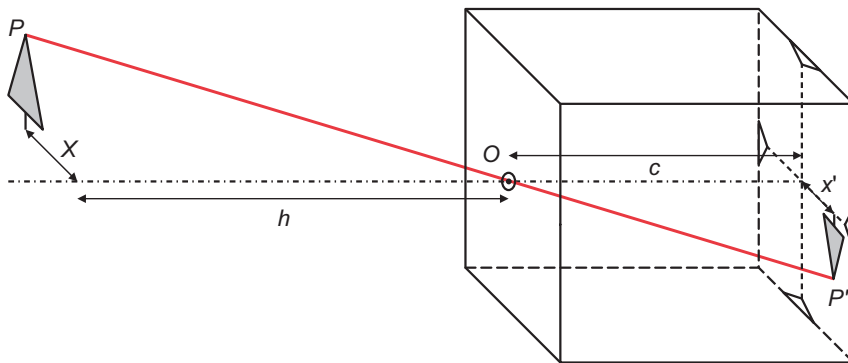


**Figure 1.7** Pinhole camera model

The interior orientation<sup>1</sup> parameters describe the internal geometric model of a camera. With the model of the pinhole camera as its basis (Fig. 1.7), the most important reference location is the perspective centre  $O$ , through which all image rays pass. The interior orientation defines the position of the perspective centre relative to a reference system fixed in the camera (image coordinate system), as well as departures from the ideal central projection (image distortion). The most important parameter of interior orientation is the principal distance,  $c$ , which defines the distance between image plane and perspective centre (see section 3.2.3).

A real and practical photogrammetric camera will differ from the pinhole camera model. The necessity of using a relatively complex objective lens, a camera housing which is not built for stability and an image recording surface which may be neither planar nor perpendicular to the optical axis of the lens gives rise to departures from the ideal imaging geometry. The interior orientation, which will include parameters defining these departures, must be determined by calibration for every camera.

A fundamental property of a photogrammetric image is the image scale or photo-scale. The photo-scale factor  $m$  defines the relationship between the object distance  $h$  and principal distance  $c$ . Alternatively it is the relationship between an object distance  $X$  in the object, in a direction parallel to the image plane, and the corresponding distance in image space  $x'$ :

$$m = \frac{h}{c} = \frac{X}{x'} \quad (1.1)$$

The photo-scale is in every case the deciding factor in resolving image details, as well as the photogrammetric measurement accuracy, since any measurement error in the image is multiplied in the object space by the scale factor (see section 3.2.1). Of course, when dealing with complex objects, the scale will vary throughout the image; one usually quotes a nominal or average value.

---

<sup>1</sup> In normal English, the orientation of an object implies direction or angular attitude. Photogrammetric usage, deriving from German, applies the word to groups of camera parameters. Exterior orientation parameters incorporate this angular meaning but extend it to include position. Interior orientation parameters, which include a distance, two coordinates and a number of polynomial coefficients, involve no angular values; the use of the terminology here underlines the connection between two very important, basic groups of parameters.

The exterior orientation parameters specify the spatial position and orientation of the camera in a global coordinate system. The exterior orientation is described by the coordinates of the perspective centre in the global system and three suitably defined angles expressing the rotation of the image coordinate system with respect to the global system (see section 4.2.1). The exterior orientation parameters are calculated indirectly, after measuring image coordinates of well identified object points with fixed and known global coordinates.

Every measured image point corresponds to a spatial direction from projection centre to object point. The length of the direction vector is initially unknown i.e. every object point lying on the line of this vector generates the same image point. In other words, although every three dimensional object point transforms to a unique image point for given orientation parameters, a unique reversal of the projection is not possible. The object point can be located on the image ray, and thereby absolutely determined in object space, only by intersecting the ray with an additional known geometric element such as a second spatial direction or an object plane.

Every image generates a spatial bundle of rays, defined by the imaged points and the perspective centre, in which the rays were all recorded at the same point in time. If all the bundles of rays from multiple images are intersected as described above, a dense network is created; for an appropriate imaging configuration, such a network has the potential for high geometric strength. Using the method of bundle triangulation any number of images (ray bundles) can be simultaneously oriented, together with the calculation of the associated three dimensional object point locations (Fig. 1.6, see section 4.3).

## 1.2.4 Photogrammetric systems

### 1.2.4.1 Analogue systems

Analogue photogrammetry (Fig. 1.8) is distinguished by different instrumentation components for data recording and for data processing as well as by a separation in location, time and personnel between the on-site recording of the object and the data evaluation in the laboratory or office. Preparatory work and targeting, additional (surveying) measurement and image recording with expensive analogue (film or plate) cameras take place on site. Photographic development takes place in a laboratory, so that direct, on-site control of image quality is not possible. Subsequently the photographs are measured using specialised instruments. The procedure involves firstly a determination of photo orientation followed by the actual processing of the photographic data.

The data obtained photogrammetrically are often further processed by users who do not wish to be involved in the actual measurement process since it requires complex photogrammetric knowledge, instrumentation and skills. The entire procedure, involving recording, measurement and further processing, is very time consuming using analogue systems, and many essential stages cannot be completed on site. Direct integration of analogue systems in procedures such as manufacturing processes is not possible.

### 1.2.4.2 Digital systems

The photogrammetric procedure has changed fundamentally with the development of digital imaging systems and processing (Fig. 1.9). By utilising appropriately targeted object points and digital on-line image recording, complex photogrammetric tasks can be executed within minutes on-site. A fully automatic analysis of the targeted points replaces the manual procedures for orientation and measurement. Special photogrammetric measuring instruments

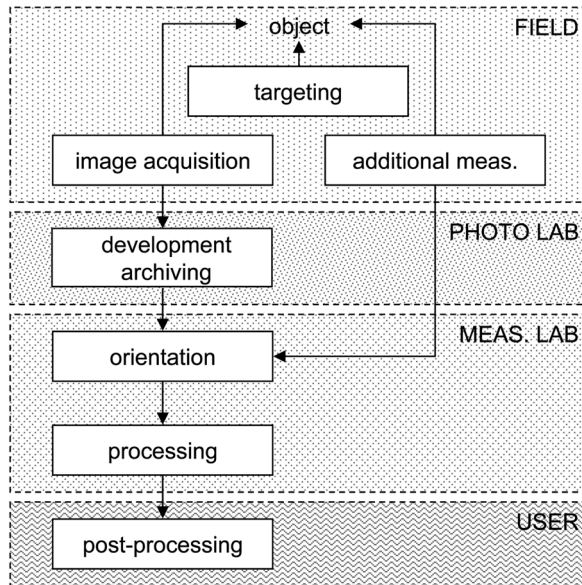


**Figure 1.8** Analogue photogrammetric system

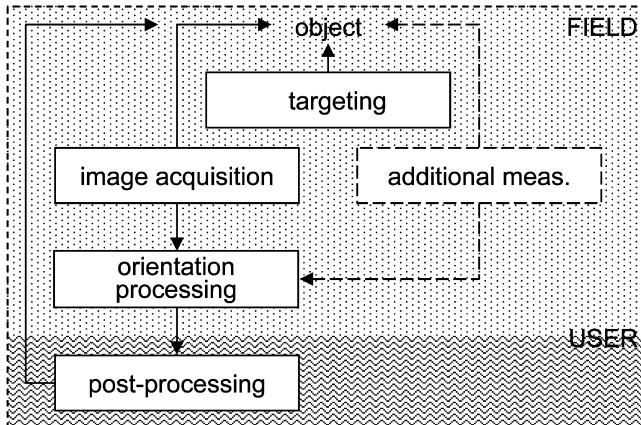


**Figure 1.9** Digital photogrammetric system

are no longer required and are replaced by standard computing equipment. The high degree of automation also enables non-specialist users to carry out the photogrammetric recording and data evaluation.

Digital systems, since they offer automation and short processing cycles, are essential to the application of photogrammetry in complex real-time applications such as, in particular, industrial metrology and robotics. Decisions can be made directly on the basis of feedback from the photogrammetric results. If the result is delivered within a certain process-specific time period, the term real-time photogrammetry is commonly used.

### 1.2.4.3 Recording and analysis procedures

Fig. 1.10 shows the principal procedures in close range photogrammetry which are briefly summarised in the following sections.

#### 1. RECORDING

##### a) Targeting:

Target selection and attachment to object features to improve automation and increase the accuracy of target measurement in the image

##### b) Determination of control points or scaling lengths:

Creation of a global object coordinate system by definition of reference (control) points and/or reference lengths (scales)

##### c) Image recording:

Analogue or digital image recording of the object with a photogrammetric system

#### 2. PRE-PROCESSING

##### a) Computation:

Calculation of reference point coordinates and/or distances from survey observations (e.g. using network adjustment)

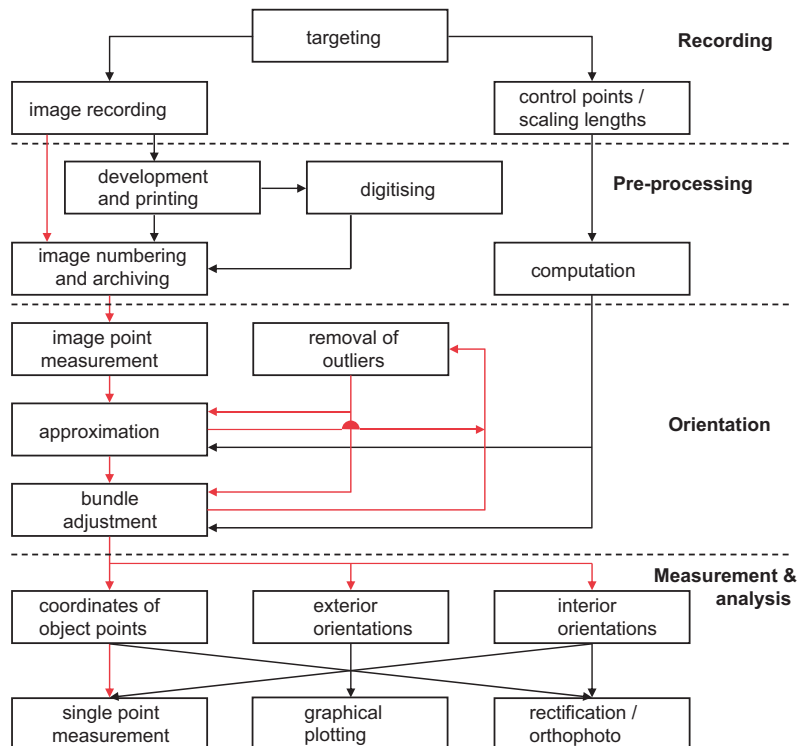


Figure 1.10 Recording and analysis procedures (red: can be automated in a digital system)

- b) Development and printing:  
Photographic laboratory work (developing film, making photographic prints)
- c) Digitising:  
Conversion of analogue photographs into digital images (scanning)
- d) Numbering and archiving:  
Assigning photo numbers to identify individual images and archiving or storing the photographs

### 3. ORIENTATION

- a) Measurement of image points:  
Identification and measurement of reference and scale points  
Identification and measurement of tie points (points observed in two or more images simply to strengthen the network)
- b) Approximation:  
Calculation of approximate (starting) values for unknown quantities to be calculated by the bundle adjustment
- c) Bundle adjustment:  
Adjustment program which simultaneously calculates parameters of both interior and exterior orientation as well as the object point coordinates which are required for subsequent analysis
- d) Removal of outliers:  
Detection and removal of gross errors which mainly arise during (manual) measurement of image points

### 4. MEASUREMENT AND ANALYSIS

- a) Single point measurement:  
Creation of three dimensional object point coordinates for further numerical processing
- b) Graphical plotting:  
Production of scaled maps or plans in analogue or digital form (e.g. hard copies for maps and electronic files for CAD models or GIS)
- c) Rectification/Orthophoto:  
Generation of transformed images or image mosaics which remove the effects of tilt relative to a reference plane (rectification) and/or remove the effects of perspective (orthophoto)

This sequence can, to a large extent, be automated (connections in red in Fig. 1.10). Provided that the object features are suitably marked and identified using coded targets, initial values can be calculated and measurement outliers (gross errors) removed by robust estimation methods.

Digital image recording and processing can provide a self-contained and fast data flow from capture to presentation of results, so that object dimensions are available directly on site. One distinguishes between off-line photogrammetry systems (one camera, measuring result available after processing of all acquired images), and on-line photogrammetry systems (minimum of two cameras simultaneously, measuring result immediately).

#### 1.2.5 Photogrammetric products

In general, photogrammetric systems supply three dimensional object coordinates derived from image measurements. From these, further elements and dimensions can be derived, for example

lines, distances, areas and surface definitions, as well as quality information such as comparisons against design and machine control data. The direct determination of geometric elements such as straight lines, planes and cylinders is also possible without explicit calculation of point coordinates. In addition the recorded image is an objective data store which documents the state of the object at the time of recording. The visual data can be provided as corrected camera images, orthophotos or graphical overlays (Fig. 1.11). Examples of graphical presentation are shown in Fig. 1.12 and Fig. 1.13.

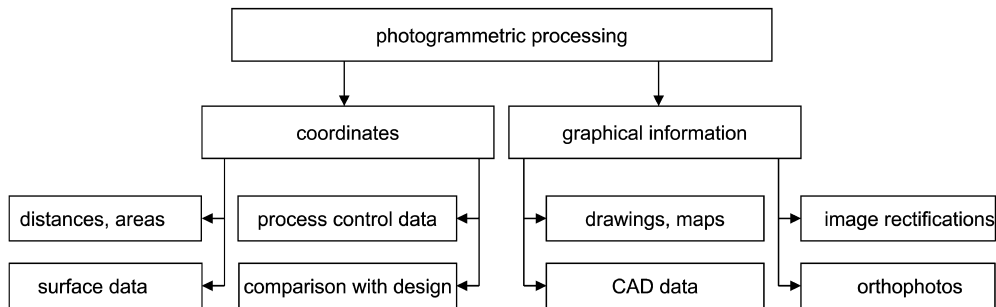


**Figure 1.11** Typical photogrammetric products

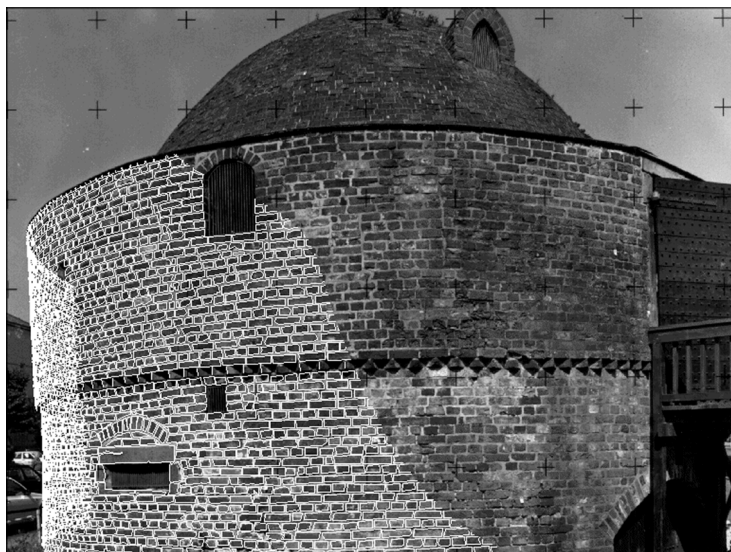


**Figure 1.12** Measurement image overlaid with part of the photogrammetrically derived CAD data

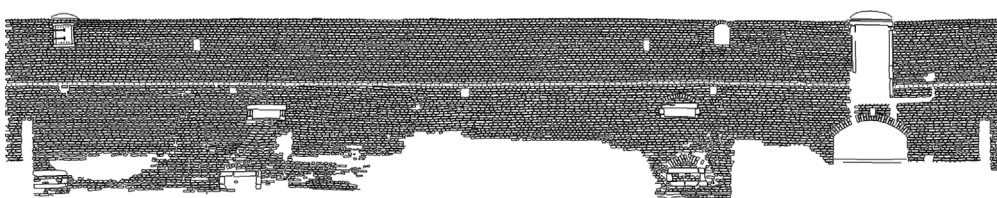


**Figure 1.13** Cylindrical projection of CAD data

## 1.3 Applications

Much shorter imaging ranges and alternative recording techniques differentiate close range photogrammetry from its aerial and satellite equivalents.

Writing in 1962 E. H. Thompson summarised the conditions under which photogrammetric methods of measurement would be useful:

“... first, when the object to be measured is inaccessible or difficult of access; second, when the object is not rigid and its instantaneous dimensions are required; third, when it is not certain that the measures will be required at all; fourth, when it is not certain, at the time of measurement, what measures are required; and fifth, when the object is very small ...”.

To these may be added three more: when the use of direct measurement would influence the measured object or would disturb a procedure going on around the object; when real-time results are required; and when the simultaneous recording and the measurement of a very large number of points is required.

The following applications (with examples) are among the most important in close range photogrammetry:

- Automotive, machine and shipbuilding industries
  - Inspection of tooling jigs
  - Reverse engineering of design models
  - Manufacturing control
  - Optical shape measurement
  - Recording and analysing car safety tests
  - Robot calibration



**Figure 1.14** Car building

- Aerospace industry
  - Measurement of parabolic antennae
  - Control of assembly
  - Inspection of tooling jigs
  - Space simulations

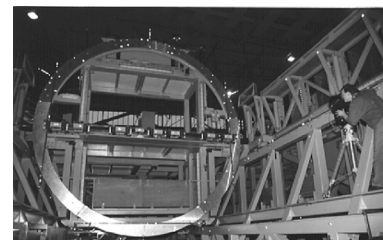


**Figure 1.15** Aircraft construction

- Architecture, heritage conservation, archaeology
  - Façade measurement
  - Historic building documentation
  - Deformation measurement
  - Reconstruction of damaged buildings
  - Mapping of excavation sites
  - 3D city models



**Figure 1.16** Building record

- Engineering
  - As-built measurement of process plants
  - Measurement of large civil engineering sites
  - Deformation measurements
  - Pipework and tunnel measurement
  - Mining
  - Evidence documentation



**Figure 1.17** Bridge measurement

- Medicine and physiology
  - Tooth measurement
  - Spinal deformation
  - Plastic surgery
  - Motion analysis and ergonomics
  - Microscopic analysis
  - Computer-assisted surgery

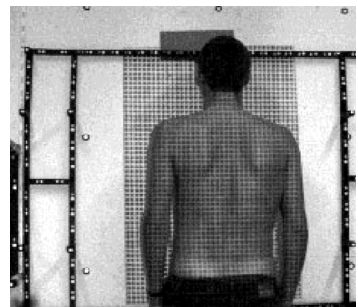


**Figure 1.18** Spinal analysis

- Forensic, including police work
  - Accident recording
  - Scene-of-crime measurement
  - Legal records
  - Measurement of persons



**Figure 1.19** Accident recording

- Information systems
  - Building information systems
  - Facility management
  - Production planning
  - Image databases

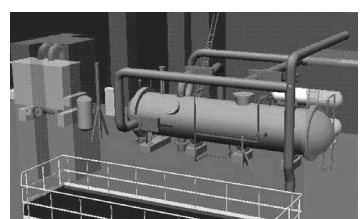


**Figure 1.20** Facility management system

- Natural sciences
  - Liquid flow measurement
  - Wave topography
  - Crystal growth
  - etc.

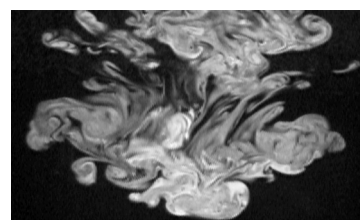


**Figure 1.21** Flow measurement

In general, similar methods of recording and analysis are used for all applications of close range photogrammetry.

- powerful analogue or digital recording systems
- freely chosen imaging configuration with almost unlimited numbers of photographs
- photo orientation based on the technique of bundle triangulation
- visual and digital analysis of the images
- presentation of results in the form of 3D coordinate files, CAD data, photographs or drawings

Industrial and engineering applications make special demands of the photogrammetric technique:

- limited recording time on site (no significant interruption of industrial processes)
- delivery of results for analysis after only a brief time
- high accuracy requirements
- proof of accuracy attained

## 1.4 Historical development

It comes as a surprise to many that the history of photogrammetry is almost as long as that of photography itself and that, for at least the first fifty years, the predominant application of photogrammetry was to close range, architectural measurement rather than to topographical mapping. Only a few years after the invention of photography during the 1830s and 1840s by Fox Talbot in England, by Niepce and Daguerre in France, the French military officer Laussedat began experiments in 1849 on the image of a façade of the Hotel des Invalides. Admittedly Laussedat was then using a camera lucida and did not obtain photographic equipment until 1852

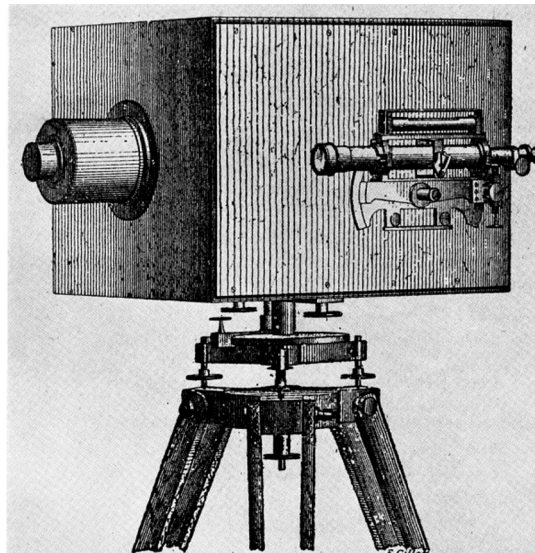


**Figure 1.22** One of the first photogrammetric cameras, by Brunner in 1859 (after von Gruber 1930)

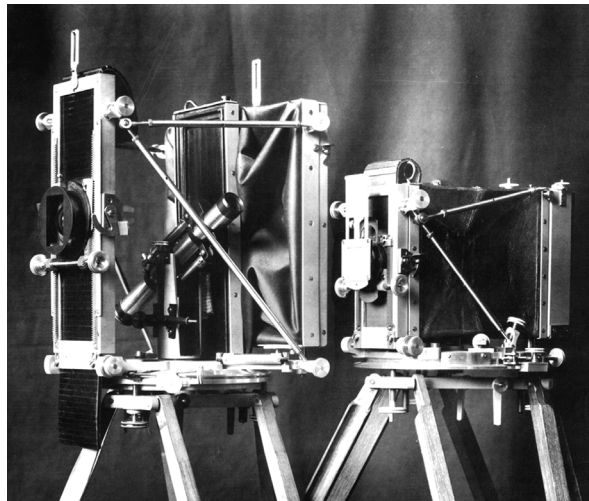


**Figure 1.23** Metric cameras by Meydenbauer (ca. 1890)  
left:  $30 \times 30 \text{ cm}^2$ , right:  $20 \times 20 \text{ cm}^2$  (after Albertz and Wiedemann 1997)

(Poivilliers 1961); he is usually described as the first photogrammetrist. In fact it was not a surveyor but an architect, the German Meydenbauer, who coined the word “photogrammetry”. As early as 1858 Meydenbauer used photographs to draw plans of the cathedral of Wetzlar and by 1865 he had constructed his “great photogrammeter” (Meydenbauer 1912), a forerunner of the phototheodolite.

Meydenbauer used photography in order to avoid the conventional, often dangerous, manual method of measuring façades. He developed his own photogrammetric cameras with image formats up to  $40 \text{ cm} \times 40 \text{ cm}$  (see Fig. 1.23), using glass plates to carry the emulsion. Between 1885 and 1909 on behalf of the state of Prussia, Meydenbauer compiled an archive of around 16 000 metric<sup>1</sup> images of the most important architectural monuments; it is still partly in existence today. The development of such archives has continued in many countries to this very day as insurance against damage or destruction of the cultural heritage (an example of Thompson’s third category: when it is not certain that the measures will be required at all, see section 1.3). Meydenbauer also developed graphical photogrammetric methods for the production of plans of building façades.

The phototheodolite, as its name suggests, represents a combination of camera and theodolite. The direct measurement of orientation angles leads to a simple photogrammetric orientation. A number of inventors, such as Porro and Paganini in Italy, in 1865 and 1884 respectively, and Koppe in Germany, 1896, developed such instruments (Fig. 1.24).

From terrestrial photographs, horizontal bundles of rays could be constructed; with two or more cameras a survey could be completed point by point using intersecting rays. By virtue of their regular and distinct features, architectural subjects lend themselves to this technique often

---

<sup>1</sup> A metric camera is defined as one with known and stable interior orientation.

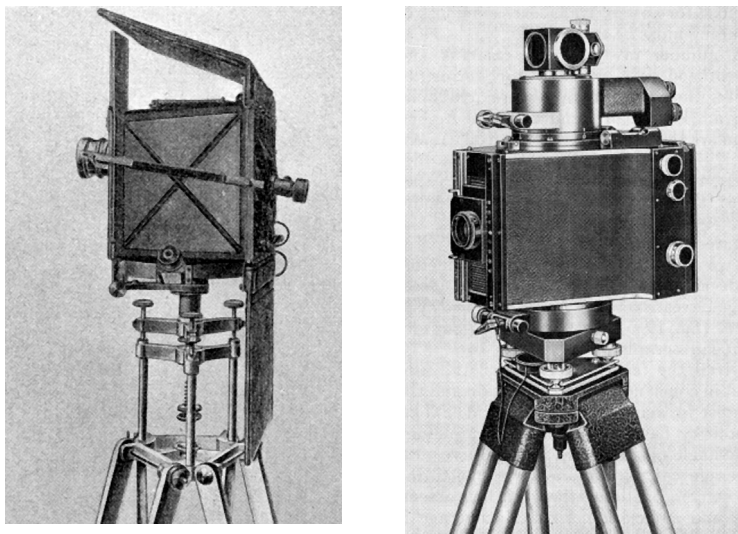


**Figure 1.24** Phototheodolite by Finsterwalder (1895) and Zeiss Jena 19/1318 (ca. 1904)

referred to as plane table photogrammetry. When using terrestrial pictures in mapping, by contrast, there was a major difficulty in identifying the same point on different photographs, especially when they were taken from widely separated camera stations; but a wide separation is desirable for accuracy. It is for these reasons that so much more architectural than topographic photogrammetry was performed during the 19<sup>th</sup> century. Nonetheless, a certain amount of topographic mapping took place during the last three decades of that century; most of this fell into Thompson's first category, "when the object to be measured is inaccessible or difficult of access" (see section 1.3), for example the mapping of the Alps by Paganini in 1884 and the mapping of vast areas of the Rockies in Canada by Deville (Thompson 1965). Jordan mapped the Dachel oasis in 1873 and Finsterwalder developed analytical solutions.

The development of stereoscopic measurement around the turn of the century was a momentous breakthrough in the history of photogrammetry. The stereoscope had already been invented between 1830 and 1832 (Wheatstone 1838) and Stolze had discovered the principle of the floating measuring mark in Germany in 1893 (Sander 1923). Two other scientists, Pulfrich in Germany and Fourcade in South Africa, working independently and almost simultaneously<sup>1</sup>, developed instruments for the practical application of Stolze's discovery (Meier 2002, Atkinson 2002). Their stereocomparators permitted simultaneous settings of identical measuring marks on the two photographs and the recording of image coordinates for use in subsequent numerical computations; points were fixed by numerical intersection and measurement was still made point by point (Fig. 1.25).

Photogrammetry was about to enter the era of analogue computation, a very foreign concept to surveyors with their long tradition of numerical computation: digital computation was too slow to allow the unbroken plotting of detail, in particular of contours, which stereoscopic

<sup>1</sup> Pulfrich's lecture in Hamburg announcing his invention was given on 23rd September 1901, while Fourcade delivered his paper in Cape Town nine days later on 2nd October 1901.

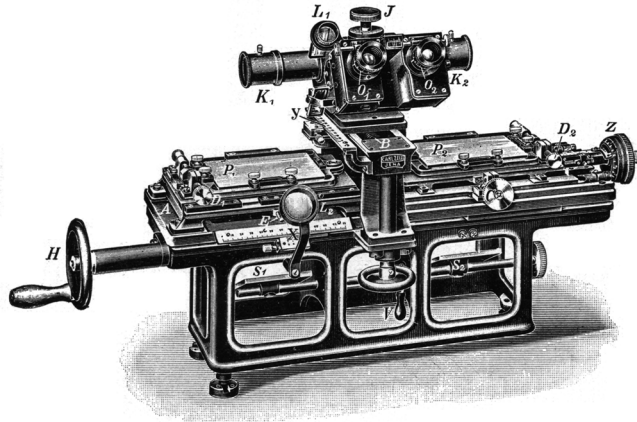


**Figure 1.25** Pulfrich's stereocomparator (Zeiss, 1901)

measurement seemed to offer so tantalisingly. Only analogue computation could extend the possibility of instantaneous feedback to the observer. If many surveyors regarded analogue computation as an aberration, then it became a remarkably successful one for a large part of the 20<sup>th</sup> century.

During the latter part of the 19<sup>th</sup> century and in several countries much effort and imagination was directed towards the invention of stereoplotting instruments, necessary for the accurate and continuous plotting of topography. In Germany, Hauck proposed such an apparatus. In Canada, Deville developed “the first automatic plotting instrument in the history of photogrammetry” (Thompson 1965). Deville’s instrument had several defects, but its design inspired several subsequent workers to overcome these, including both Pulfrich, one of the greatest contributors to photogrammetric instrumentation, and Santoni, perhaps the most prolific of photogrammetric inventors.

In Germany, conceivably the most active country in the early days of photogrammetry, Pulfrich’s methods were very successfully used in mapping. This inspired von Orel in Vienna to design an instrument for the “automatic” plotting of contours, leading ultimately to the Orel-Zeiss Stereoautograph which came into productive use in 1909. In England, F. V. Thompson was slightly before von Orel in the design and use of the Vivian Thompson Stereoplotter (Atkinson 1980, 2002); he went on to design the Vivian Thompson Stereoplanigraph (Thomson 1908) which was described by E. H. Thompson (Thompson 1974) as “the first design for a completely automatic and thoroughly rigorous photogrammetric plotting instrument”.

The rapid development of aviation which began shortly after this was another decisive influence on the course of photogrammetry. Not only is the Earth photographed vertically from above an almost ideal subject for the photogrammetric method, but also aircraft made almost all parts of the Earth accessible at high speed. In the first half of the 20<sup>th</sup> century these favourable circumstances allowed impressive development in photogrammetry, with tremendous economic benefit in air survey. On the other hand, while stereoscopy opened the way for the application of photogrammetry to the most complex surfaces such as might be found in close range work, the geometry in such cases was often far from ideal photogrammetrically and there was no corresponding economic advantage to promote its application.

Although there was considerable opposition from surveyors to the use of photographs and analogue instruments for mapping, the development of stereoscopic measuring instruments forged ahead remarkably in many countries during the period between the First World War and the early 1930s. Meanwhile, non-topographic use was sporadic as there were few suitable cameras and analogue plotters imposed severe restrictions on principal distance, image format and disposition and tilts of cameras. Instrumentally complex systems were being developed using optical projection (for example Multiplex), opto-mechanical principles (Zeiss Stereoplaniograph) and mechanical projection using space rods (for example Wild A5, Santoni Stereocartograph), designed for use with aerial photography. By 1930 the Stereoplaniograph C5 was in production, a sophisticated instrument able to use oblique and convergent photography—even if makeshift cameras had to be used at close range, experimenters at least had freedom in the orientation and placement of the cameras; this considerable advantage led to some noteworthy work.

As early as 1933 Wild stereometric cameras were being manufactured and were in use by Swiss police for the mapping of accident sites, using the Wild A4 Stereoautograph, a plotter especially designed for this purpose. Such stereometric cameras comprise two identical metric cameras fixed to a rigid base of known length and such that their axes are coplanar, perpendicular to the base and, usually, horizontal<sup>1</sup> (Fig. 3.2a, see section 4.4.2). Other manufacturers have also made stereometric cameras (Fig. 1.26) and associated plotters (Fig. 1.27); a great deal of close range work has been carried out with this type of equipment. Initially glass plates were used in metric cameras in order to provide a flat image surface without significant mechanical effort (see example in Fig. 1.28). From the 1950s film was increasingly used in metric cameras which were then equipped with a mechanical film-flattening device.



**Figure 1.26** Zeiss SMK 40 and SMK 120 stereometric cameras



**Figure 1.27** Zeiss Terragraph stereoplotter

<sup>1</sup> This is sometimes referred to as the ‘normal case’ of photogrammetry.



Figure 1.28 Zeiss TMK 6 metric camera

In the 1950s we were on the verge of the period of analytical photogrammetry. The expanding use of digital, electronic computers in that decade engendered widespread interest in the purely analytical or numerical approach to photogrammetry as against the prevailing analogue methods. While analogue computation is inflexible, in regard to both input parameters and output results, and its accuracy is limited by physical properties, a numerical method allows virtually unlimited accuracy of computation and its flexibility is bounded only by the mathematical model on which it is based. Above all, it permits over-determination which may improve precision, lead to the detection of gross errors and provide valuable statistical information about the measurements and the results. The first analytical applications were to photogrammetric triangulation. As numerical methods in photogrammetry improved, the above advantages, but above all their flexibility, were to prove invaluable at close range.

Subsequently stereoplotters were equipped with devices to record model coordinates for input to electronic computers. Arising from the pioneering ideas of Helava (Helava 1957), computers were incorporated in stereoplotters themselves, resulting in analytical stereoplotters with fully numerical reconstruction of the photogrammetric models. Bendix/OMI developed the first analytical plotter, the AP/C, in 1964; during the following two decades analytical stereoplotters were produced by the major instrument companies and others. While the adaptability of such instruments has been of advantage in close range photogrammetry (Masry and Faig 1977), triangulation programs with even greater flexibility were soon to be developed, as described below, which were more suited to the requirements of close range work.

Analytical photogrammetric triangulation is a method, using numerical data, of point determination involving the simultaneous orientation of all the photographs and taking all interrelations into account. Work on this line of development had appeared before WWII, long before the development of electronic computers. Analytical triangulation demanded instruments to measure photocordinates. The first stereocomparator designed specifically for use with aerial photographs was the Cambridge Stereocomparator designed in 1937 by E. H. Thompson (Arthur 1960). By 1955 there were five stereocomparators on the market (Harley 1963) and monocomparators designed for use with aerial photographs also appeared.

The bundle method of photogrammetric triangulation, more usually known as bundle adjustment, is of vital importance to close range photogrammetry. Seminal papers by Schmid (1956-57, 1958) and Brown (1958) laid the foundations for theoretically rigorous block adjustment. A number of bundle adjustment programs for air survey were developed and became commercially available, such as those by Ackermann *et al.* (1970) and Brown (1976). Programs designed specifically for close range work have appeared since the 1980s, such as STARS (Fraser and Brown 1986), BINGO (Kruck 1983), MOR (Wester-Ebbinghaus 1981) and CAP (Hinsken 1989).

The importance of bundle adjustment in close range photogrammetry can hardly be overstated. The method imposes no restrictions on the positions or the orientations of the cameras; nor is there any necessity to limit the imaging system to central projection. Of equal or greater importance, the parameters of interior orientation of all the cameras may be included as unknowns in the solution. Until the 1960s many experimenters appear to have given little attention to the calibration<sup>1</sup> of their cameras; this may well have been because the direct calibration of cameras focused for near objects is usually much more difficult than that of cameras focused for distant objects. At the same time, the inner orientation must usually be known more accurately than is necessary for vertical aerial photographs because the geometry of non-topographical work is frequently far from ideal. In applying the standard methods of calibration in the past, difficulties arose because of the finite distance of the targets, whether real objects or virtual images. While indirect, numerical methods to overcome this difficulty were suggested by Torlegård (1967) and others, bundle adjustment now frees us from this concern. For high precision work it is no longer necessary to use metric cameras which, while having the advantage of known and constant interior orientation, are usually cumbersome and expensive. Virtually any camera can now be used. Calibration via bundle adjustment is usually known as self-calibration (see section 4.3.2.4).

The use of traditional stereophotogrammetry at close ranges has declined. As an alternative to the use of comparators, multi-photo analysis systems which use a digitizing pad as a measuring device for photo enlargements (e.g. Rollei MR2, 1986) have been widely used for architectural and accident recording. Many special cameras have been developed; for example modified professional photographic cameras which have an inbuilt réseau (an array of engraved crosses on a glass plate which appear on each image) for photogrammetric use (Wester-Ebbinghaus 1981) (Fig. 1.29).



**Figure 1.29** Rolleiflex SLX (ca. 1980) semi-metric camera

---

<sup>1</sup> In photogrammetry, unlike computer vision, calibration refers only to interior orientation. Exterior orientation is not regarded as part of calibration.

Since the middle of the 1980s the use of opto-electronic image sensors has increased dramatically. Advanced computer technology enables the processing of digital images, particularly for automatic recognition and measurement of image features, including pattern correlation for determining object surfaces. Procedures in which both the image and its photogrammetric processing are digital are often referred to as digital photogrammetry. Initially standard video cameras were employed generating analogue video signals which could be digitised with resolutions up to  $780 \times 580$  picture elements (pixels) and processed in real time (real-time photogrammetry, videogrammetry). The first operational on-line multi-image systems became available in the late 1980s (e.g. Haggrén 1987, Fig. 1.30). Automated precision monocomparators, in combination with large format réseau cameras, were developed for high-precision, industrial applications (Fraser and Brown 1986, Luhmann and Wester-Ebbinghaus 1986). Analytical plotters were enhanced with video cameras to become analytical correlators, used for example in car body measurement (Zeiss Indusurf 1987). Closed procedures for simultaneous multi-image processing of grey level values and object data based on least squares methods were developed (e.g. Förstner 1982, Gruen 1985).

The limitations of video cameras in respect of their small image format and low resolution led to the development of scanning cameras which enabled the high resolution recording of static objects to around  $6000 \times 4500$  pixels. In parallel with this development, electronic theodolites were equipped with video cameras to enable the automatic recording of directions to targets (Kern SPACE).

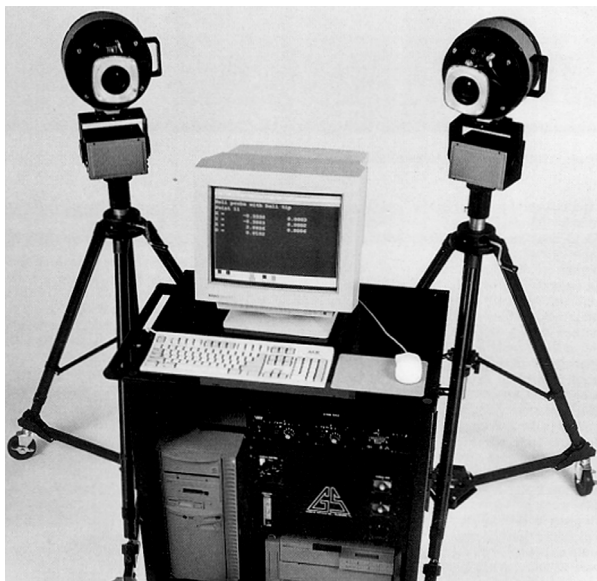
Digital cameras with high resolution, which can provide a digital image without analogue signal processing, have been available since the beginning of the 1990s. Resolutions range from about  $1000 \times 1000$  pixels (e.g. Kodak Megaplus) to over  $4000 \times 4000$  pixels. Easily portable still video cameras can store high resolution images directly in the camera (e.g. Kodak DCS 460, Fig. 1.31). They have led to a significant expansion of photogrammetric measurement technology, particularly in the industrial field. On-line photogrammetric systems (Fig. 1.32) are increasingly used, in addition to off-line systems, both as mobile systems and in stationary configurations. Coded targets allow the fully automatic identification and assignment of object



Figure 1.30 Mapvision: on-line multi-image system (1987)



**Figure 1.31** Still-video camera Kodak DCS 460 (1996)



**Figure 1.32** GSI VSTARS on-line industrial measurement system

features and orientation of the image sequences. Surface measurement of large objects is now possible with the development of pattern projection methods combined with photogrammetric techniques.

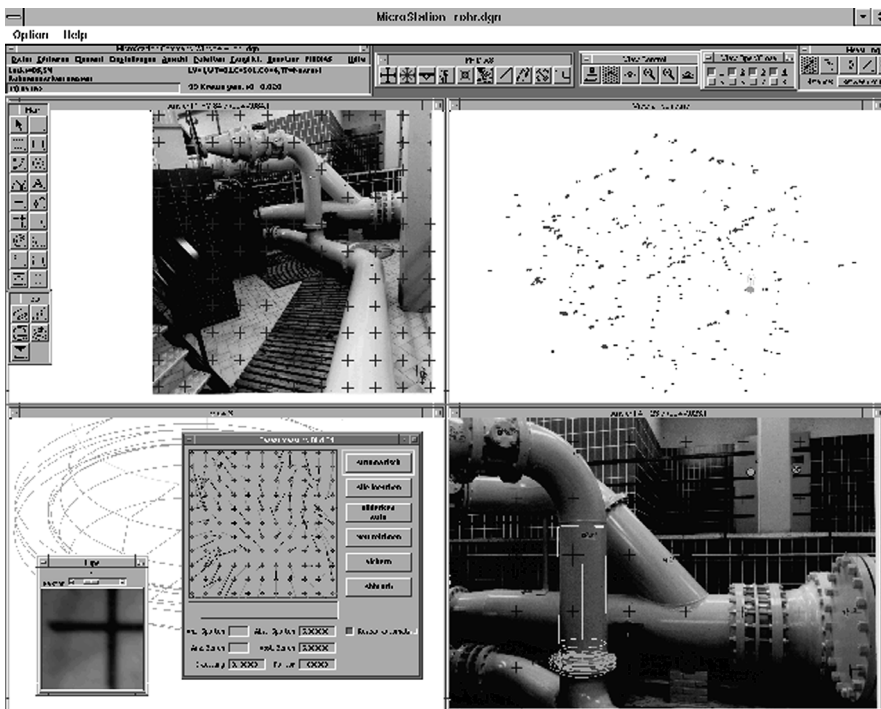


Figure 1.33 PHIDIAS-MS multi-image analysis system (1998)

Interactive digital stereo systems (e.g. Leica/Helava DSP, Zeiss PHODIS) have existed since around 1988 (Kern DSP-1) and are in 2005 increasingly replacing analytical plotters, but they are rarely employed for close range use. Interactive, graphical multi-image processing systems are of more importance here as they offer processing of freely chosen image configurations in a CAD environment (e.g. PHIDIAS from Phocad, Fig. 1.33). Easy-to-use low-cost software packages (e.g. PhotoModeler from EOS, ImageModeler from REALVIZ, iWitness from PhotoMetrix) provide object reconstruction and creation of virtual 3D models from digital images without the need for a deep understanding of photogrammetry.

A trend in close range photogrammetry is towards the integration or embedding of photogrammetric components in application-oriented hybrid systems. This includes links to such packages as 3D CAD systems, databases and information systems, quality analysis and control systems for production, navigation systems for autonomous robots and vehicles, 3D visualization systems, internet applications, 3D animations and virtual reality. Another trend is for methods from computer vision, such as projective geometry or pattern recognition, to be increasingly used for rapid solutions without high accuracy demands.

Close range photogrammetry is today a well established, universal 3D measuring technique, routinely applied in a wide range of interdisciplinary fields; there is every reason to expect its continued development long into the future.

Further reviews of the history of close range photogrammetry are available in Atkinson (1980), Atkinson (1996), Albertz and Wiedemann (1997), Grün (1994), Karara (1989), Brunner (1988) and von Gruber (1930) and von Gruber *et al.* (1932).

## References

- Ackermann, F., Ebner, H. and Klein, H. (1970) Ein Rechenprogramm für die Streifentriangulation mit unabhängigen Modellen. *Bildmessung und Luftbildwesen*, Heft 4/1970, pp. 206–217.
- Albertz, J. and Wiedemann, A. (ed.) (1997) *Architekturphotogrammetrie gestern-heute-morgen*. Technische Universität Berlin.
- Arthur, D. W. G. (1960) An automatic recording stereocomparator. *Photogrammetric Record* 3(16), 298–319.
- Atkinson, K. B. (1980) Vivian Thompson (1880–1917) not only an officer in the Royal Engineers. *Photogrammetric Record*, 10(55), 5–38.
- Atkinson, K. B. (ed.) (1996) *Close range photogrammetry and machine vision*. Whittles Publishing, Caithness, UK.
- Atkinson, K. B. (2002) Fourcade: The Centenary – Response to Professor H.-K. Meier. Correspondence, *Photogrammetric Record*, 17(99), 555–556.
- Brown, D. C. (1958) *A solution to the general problem of multiple station analytical stereotriangulation*. RCA Data Reduction Technical Report No. 43, Aberdeen 1958.
- Brown, D. C. (1976) The bundle adjustment – progress and prospects. *International Archives of Photogrammetry*, 21(3), ISP Congress, Helsinki, pp. 1–33.
- Brunner, K. (1988) Die Meßtischphotogrammetrie als Methode der topographischen Geländeaufnahme des ausgehenden 19. Jahrhunderts. *Zeitschrift für Photogrammetrie und Fernerkundung*, Heft 3/88, pp. 98–108.
- Förstner, W. (1982) On the geometric precision of digital correlation. *International Archives for Photogrammetry and Remote Sensing*, 26(3), 176–189.
- Fraser, C. S. and Brown, D. C. (1986) Industrial photogrammetry – new developments and recent applications. *Photogrammetric Record*, 12(68).
- von Gruber, O. (ed.) (1930) *Ferienkurs in Photogrammetrie*. Verlag Konrad Wittwer, Stuttgart.
- von Gruber, O. (ed.), McCaw, G. T. and Cazalet, F. A., (trans) (1932) *Photogrammetry, Collected Lectures and Essays*. Chapman & Hall, London.
- Gruen, A. (1985) Adaptive least squares correlation – a powerful image matching technique. *South African Journal of Photogrammetry, Remote Sensing and Cartography*, 14(3), pp. 175–187.
- Grün, A. (1994) Von Meydenbauer zur Megaplus – Die Architekturphotogrammetrie im Spiegel der technischen Entwicklung. *Zeitschrift für Photogrammetrie und Fernerkundung*, Heft 2/1994, pp. 41–56.
- Haggrén, H. (1987) Real-time photogrammetry as used for machine vision applications. *Canadian Surveyor*, 41(2), pp. 210–208.
- Harley, I. A. (1963) Some notes on stereocomparators. *Photogrammetric Record*, IV(21), 194–209.
- Helava, U. V. (1957) New principle for analytical plotters. *Photogrammetria*, 14, 89–96.
- Hinsken, L. (1989) CAP: Ein Programm zur kombinierten Bündelausgleichung auf Personalcomputern. *Zeitschrift für Photogrammetrie und Fernerkundung*, Heft 3/1989, pp. 92–95.
- Karara, H. M. (ed.) (1989) *Non-topographic photogrammetry*. 2nd ed., American Society for Photogrammetry and Remote Sensing.
- Kruck, E. (1983) *Lösung großer Gleichungssysteme für photogrammetrische Blockausgleichungen mit erweitertem funktionalem Modell*. Dissertation, Wiss. Arbeiten der Fachrichtung Vermessungswesen der Universität Hannover, Nr. 128.
- Luhmann, T. and Wester-Ebbinghaus, W. (1986) *Rolleimetric RS – A New System for Digital Image Processing*. Symposium ISPRS Commission II, Baltimore.
- Masry, S. E. and Faig, W. (1977) The Analytical Plotter in Close-Range Applications. *Photogrammetric Engineering and Remote Sensing*, January 1977.

- Meier, H.-K. (2002) Fourcade: The Centenary – Paper by L. P. Adams. Correspondence, *Photogrammetric Record*, **17**(99), 554–555.
- Meydenbauer, A. (1912) *Handbuch der Messbildkunst*. Knapp, Halle, 245p.
- Poivilliers, G. (1961) Address delivered at the opening of the Historical Exhibition, Ninth International Congress of Photogrammetry, London, 1960. *International Archives of Photogrammetry*, XIII, 1, 1961.
- Sander, W. (1923) Die stereoskopischen Messverfahren. *Zentralzeitung für Optik und Mechanik*, 44: 81–85, 96–100 and 110–114, Berlin.
- Schmid, H. (1956–57) An analytical treatment of the problem of triangulation by stereophotogrammetry. *Photogrammetria*, XIII, Nr. 2 and 3.
- Schmid, H. (1958) Eine allgemeine analytische Lösung für die Aufgabe der Photogrammetrie. *Bildmessung und Luftbildwesen*. 1958 Nr. 4 (103–113) and 1959 Nr. 1 (1–12).
- Thompson, E. H. (1962) Photogrammetry. *The Royal Engineers Journal*, **76**(4) 432–444. Reprinted in *Photogrammetry and surveying, a selection of papers by E. H. Thompson, 1910–1976*. Photogrammetric Society, London, 1977.
- Thompson, E. H. (1965) The Deville Memorial Lecture. *The Canadian Surveyor*, **19**(3) 262–272. Reprinted in *Photogrammetry and surveying, a selection of papers by E. H. Thompson, 1910–1976*. Photogrammetric Society, London, 1977.
- Thompson, E. H. (1974) The Vivian Thompson Stereo-Planigraph. *Photogrammetric Record*, **8**(43) 81–86.
- Thompson, V. F. (1908) Stereo-photo-surveying. *The Geographical Journal*, **31**: p. 534.
- Torlegård, K. (1967) *On the determination of interior orientation of close-up cameras under operational conditions using three-dimensional test objects*. Doctoral Thesis, Kungl. Tekniska Höskolan.
- Wester-Ebbinghaus, W. (1981) *Zur Verfahrensentwicklung in der Nahbereichsphotogrammetrie*. Dissertation, Bonn University.
- Wheatstone, C. (1838) Contribution to the physiology of vision – Part the first. On some remarkable, and hitherto unobserved, phenomena of binocular vision. *Philosophical Transactions of the Royal Society of London* for the year MDCCCXXXVIII, Part II, 371–94.

## Further reading

### Photogrammetry

- Adams, L. P. (2001) Fourcade: The centenary of a stereoscopic method of photogrammetric surveying. *Photogrammetric Record*, **17**(99), 225–242.
- Albertz, J. and Kreiling, W. (1989) *Photogrammetric guide*. 4th edition, Wichmann Verlag, Karlsruhe, Germany.
- Atkinson, K. B. (ed.) (1980) *Developments in close range photogrammetry-1*. Applied Science Publishers, London, UK.
- Deville, E. (1895) *Photographic Surveying*. Government Printing Bureau, Ottawa. p. 232.
- Deville, E. (1902) On the use of the Wheatstone Stereoscope in Photographic Surveying. *Transactions of the Royal Society of Canada*, Ottawa. **8**: 63–69.
- Fourcade, H. G. (1903) On a stereoscopic method of photographic surveying. *Transactions of the South African Philosophical Society*, **14**(1) 28–35. (Also published in 1902. *Nature*, **66** (1701) 139–141.)
- Kraus, K. (1997) *Photogrammetry, Volume 2, Advanced Methods and Applications*. With contributions by J. Jansa and H. Kager. Dümmler, Bonn.
- Kraus, K. (2000) *Photogrammetry, Volume 1, Fundamentals and Standard Processes*. With contributions by Peter Waldhäusl, translated by Peter Stewardson, Verlag H. Stam GmbH, Köln.

- Kraus, K. (2004) *Photogrammetrie, Band 1, Geometrische Informationen aus Photographien und Laserscaneraufnahmen*. Walter de Gruyter, Berlin, 516 p.
- Laussedat, A. (1898, 1901, 1903) *Recherches sur les instruments, les méthodes et le dessin topographiques*. Gauthier-Villars, Paris. (Vol. 1, 1898; Vol. 2 part 1, 1901; part 2 1903)
- McGlone, J. C. (ed.) (2004) *Manual of photogrammetry*. 5th edition, American Society for Photogrammetry and Remote Sensing.
- Mikhail, E. M., Bethel, J. S. and McGlone, J. C. (2001) *Introduction to Modern Photogrammetry*. John Wiley & Sons, New York.
- Pulfrich, C. (1902) Über neuere Anwendungen der Stereoskopie und über einen hierfür bestimmten Stereo-Komparator. *Zeitschrift für Instrumentenkunde*, 22(3):65–81.
- Schenk, T. (1999) *Digital Photogrammetry*, Vol. 1, TerraScience, Laurelville, USA.
- Thompson, M. M. (ed.) (1980) *Manual of Photogrammetry*. 4th edition, American Society for Photogrammetry and Remote Sensing.

### **Optics, camera and image acquisition**

- Born, M., Wolf, E. and Bhatia, A. B. (1999) *Principles of Optics*. Cambridge University Press, p. 986.
- Hecht, E. (2003) *Optics*. Addison Wesley.
- Holst, G. C. (1996) *CCD arrays, cameras and displays*. SPIE Press, JCD Publishing, USA.
- Inglis, A. F. and Luther, A. C. (1996) *Video engineering*. 2nd ed., McGraw-Hill, New York.
- Schwarze, R. (1997) Überblick und Vergleich aktueller Verfahren der optischen Form erfassung. GMA-Bericht 30, *Optische Form erfassung*, Langen, pp. 1-12.

### **Digital image processing, computer vision and pattern recognition**

- Demant, C., Streicher-Abel, B. and Waszkewitz, (1999) *Industrial image processing – Visual quality control in manufacturing*. Springer, p. 353.
- Gonzales, R. C. and Wintz, P. (1987) *Digital Image Processing*. 2nd edition, Addison Wesley, p. 503.
- Gonzales, R.C. and Woods, R.E. (2003) *Digital Image Processing*. Prentice Hall, p. 813.
- Graham, R. (1998) *Digital Imaging*. Whittles Publishing, Caithness, Scotland, UK.
- Haralick, R. M. and Shapiro, L. G. (1992) *Computer and robot vision*. Vol. I+II, Addison-Wesley, Reading, Ma., USA.
- Hartley, R. and Zisserman, A. (2000) *Multiple View Geometry*. Cambridge University Press, Cambridge, UK.
- Jähne, B., Haußecker, H. and Geißler, P. (1999) *Handbook of computer vision and applications; Vol. 1 Sensors and imaging; Vol. 2 Signal processing and pattern recognition; Vol. 3 Systems and applications*. Academic Press.
- Marr, D. (1982) *Vision*. Freeman, San Francisco.
- Parker, J. R. (1996) *Algorithms for Image Processing and Computer Vision*. John Wiley & Sons Inc, p. 432.
- Rosenfeld, A. and Kak, A. C. (1982) *Digital Picture Processing*, 2nd edition, Academic Press.
- Russ, J. C. (2002) *The Image Processing Handbook*. CRC Press, p. 752.

### **3D computer graphics**

- Foley, J. D., VanDam, A. and Feiner, S. K. (1995) *Computer Graphics*. Addison-Wesley Professional, p.1200.
- Laszlo, M. J. (1996) *Computational Geometry and Computer Graphics in C++*, Prentice-Hall, Upper Saddle River, NJ, p. 266.

- Shirley, P. (2002) *Fundamentals of Computer Graphics*. A K Peters, pp. 500.  
Watt, A. (1999) *3D Computer Graphics*. Addison Wesley Publishing, pp. 592.

### Least squares adjustment and statistics

- Cross, P. A. (1990) *Working Paper No. 6, Advanced least squares applied to position-fixing*. Department of Land Surveying, Polytechnic (now University) of East London p. 205.  
Mikhail, E. M. (1976) *Observations and least squares*. IEP, New York, p. 497.  
Mikhail, E. M. and Gracie, G. (1981) *Analysis & Adjustment of Survey Measurements*. Van Nostrand Reinhold Company, p. 368.  
Wolf, P. R. and Ghilani, C.D. (1997) *Adjustment Computations: Statistics and Least Squares in Surveying and GIS (Surveying & Boundary Control)*, John Wiley & Sons.

### Applications

- Fryer, J. G., Mitchell, H. L. and Chandler, J. H. (2006) *Applications of 3D measurement from images*. Whittles Publishing, Caithness, Scotland, UK.  
Harley, I. A. (1967) The non-topographical uses of photogrammetry. *The Australian Surveyor*, 21(7) 237–263.  
Luhmann, T. (ed.) (2002) *Nahbereichsphotogrammetrie in der Praxis*. Wichmann, Heidelberg, 318 p.  
Santoni, E. (1966) *Instruments and photogrammetric devices for survey of close-up subject with particular stress to that of car bodies and their components photographed at various distances*. Inedito. Reprinted in Selected Works, Ermenegildo Santoni, Scritti Scelti 1925–1968. Società Italiana di Fotogrammetria e Topografia, Firenze, 1971.

### Standards and guidelines

- DIN 1319: *Fundamentals of metrology*. Beuth, Berlin.  
DIN 18716: *Photogrammetry and remote sensing*. Beuth, Berlin.  
DIN 18709: *Concepts, abbreviations and symbols in surveying*. Beuth, Berlin.  
GUM (1993) *ISO guide to the expression of uncertainty in measurement (GUM)*.  
ISO 10360: *Geometrical Product Specifications (GPS) - Acceptance and reverification tests for coordinate measuring machines (CMM)*. Beuth, Berlin.  
VDI/VDE 2617: *Accuracy of coordinate measuring machines; characteristics and their checking*. VDI/VDE guide line, Part 1–6, Beuth, Berlin.  
VDI/VDE 2634: Optical 3D measuring systems. VDI/VDE guide line, Beuth, Berlin.

### Organisations, conferences and working groups

- ISPRS (International Society for Photogrammetry and Remote Sensing):  
Commission III: Theory and Algorithms  
Commission V: Close range Techniques and Machine Vision  
Publications: International Archives of Photogrammetry and Remote Sensing; ISPRS Journal of Photogrammetry and Remote Sensing  
[www.isprs.org](http://www.isprs.org)
- ASPRS (The American Society for Photogrammetry and Remote Sensing):  
Publication: Photogrammetric Engineering and Remote Sensing  
[www.asprs.org](http://www.asprs.org)

The Remote Sensing and Photogrammetry Society:

Publication: The Photogrammetric Record

[www.rspsoc.org](http://www.rspsoc.org)

DGPF (Deutsche Gesellschaft für Photogrammetrie und Fernerkundung): Publications:

Bildmessung und Luftbildwesen (to 1989), Zeitschrift für Photo-grammetrie und Fernerkundung (to 1997), Photogrammetrie-Fernerkundung-Geoinformation (since 1997); Publikationen der DGPF (proceedings of the annual symposia) [www.dgpf.de](http://www.dgpf.de)

CIPA (Comité International de Photogrammétrie Architecturale):

Publications and conference proceedings.

<http://cipa.icomos.org/>

CMCS (Coordinate Metrology Systems Conference)

Publications and conference proceedings.

[www.cmsc.org](http://www.cmsc.org)

SPIE (The International Society for Optical Engineering):

Publications and conference proceedings.

[www.spie.org](http://www.spie.org)

VDI/VDE-GMA (VDI/VDE-Gesellschaft für Mess- und Automatisierungstechnik):

Publications: technical guide lines, conference proceedings.

[www.vdi.de](http://www.vdi.de)



## 2 Mathematical fundamentals

This chapter presents mathematical fundamentals which are essential for a deeper understanding of close-range photogrammetry. After defining some common coordinate systems, the most important plane and spatial coordinate transformations are summarised. The basic theory of least-squares adjustment then follows and the chapter concludes with an introduction to homogeneous coordinates and graphical projections.

### 2.1 Coordinate systems

#### 2.1.1 Image and camera coordinate systems

The image coordinate system defines a two-dimensional image-based reference system of rectangular Cartesian coordinates,  $x'y'$ . Its physical relationship to the camera is defined by reference points, either fiducial marks or a reseau, which are projected onto the acquired image (see section 3.2.3.4). For a digital imaging system, the sensor matrix defines the image coordinate system. Usually the origin of the image or frame coordinates is located at the image centre.

The relationship between the plane image and the camera, regarded as a spatial object, can be established when the image coordinate system is extended by the  $z'$  axis normal to the image plane. This axis coincides approximately with the optical axis. The origin of this 3D camera coordinate system is located at the perspective centre  $O'$ . The image position  $B_1$  corresponds to a location in the physically acquired image, which is the image negative. For a number of mathematical calculations it is easier to use the corresponding image position  $B_2$ , in the equivalent positive image (see Fig. 2.1). Here the vector of image coordinates  $\mathbf{x}'$  points in the same direction as the vector to the object point  $P$ . In this case the principal distance must be defined as a negative value leading to the image vector  $\mathbf{x}'$ :

$$\mathbf{x}' = \begin{bmatrix} x' \\ y' \\ z' \end{bmatrix} = \begin{bmatrix} x' \\ y' \\ -c \end{bmatrix} \quad (2.1)$$

Thus the image vector  $\mathbf{x}'$  describes the projection ray, with respect to the image coordinate system, from the image point to the object point. The spatial position of the perspective centre in the image coordinate system is given by the parameters of *interior orientation* (see section 3.2.3).

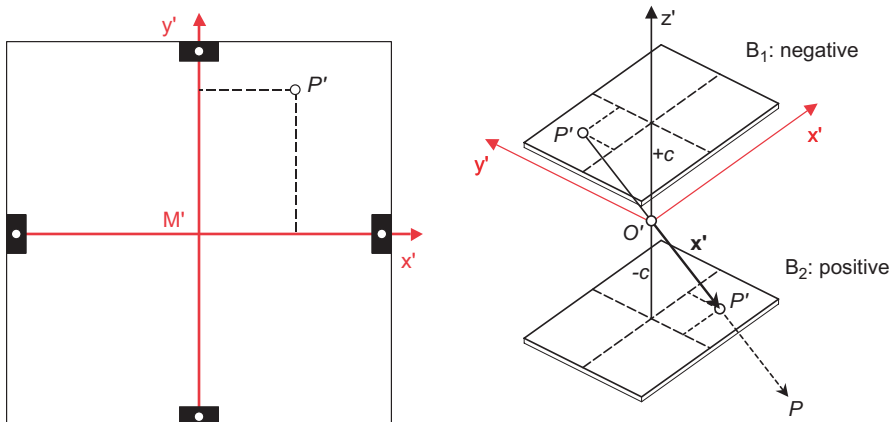


Figure 2.1 Image and camera coordinate system

### 2.1.2 Comparator coordinate system

The comparator coordinate system,  $x^*y^*$ , defines the coordinate system of an image measuring device that delivers length measurements in machine coordinates. The transformation of  $x^*y^*$  into image coordinates  $x'y'$  is usually performed by an affine transformation using fiducial or reseau marks as common points (see section 2.2.1.2).

### 2.1.3 Model coordinate system

The spatial Cartesian model coordinate system xyz is used to describe the relative position and orientation of two or more images (image coordinate systems). Normally its origin is at the perspective centre of one of the images. In addition the model coordinate system may be parallel to the related image coordinate system (see section 4.2.5.3).

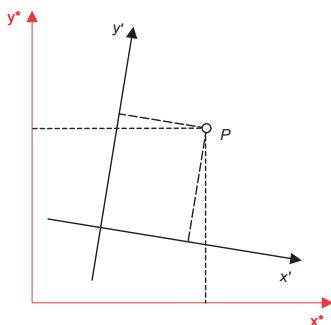


Figure 2.2 Comparator coordinate system

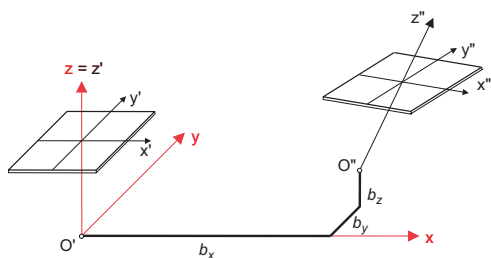


Figure 2.3 Model coordinate system

## 2.1.4 Object coordinate system

The term object coordinate system, also known as the world coordinate system, is here used for every spatial Cartesian coordinate system XYZ that is defined by reference points on the object. For example, national geodetic coordinate systems (X=easting, Y=northing, Z=altitude, origin at the equator) are defined by geodetically measured reference points.<sup>1</sup> Another example is the local object or workpiece coordinate system of a car body that is defined by the constructional axes (X=longitudinal car axis, Y=front axle, Z=height, origin at centre of front axle).

## 2.1.5 3D instrument coordinate system

A special case of three-dimensional coordinate system is an arbitrarily oriented one used by a 3D measuring-machine. This is not directly related to any superior system or particular object but if, for instance, just one reference scale is given (Fig. 2.5), then it is still possible to measure spatial object coordinates.

The definition of origin, axes and scale of a coordinate system is also known as the (geodetic) datum.

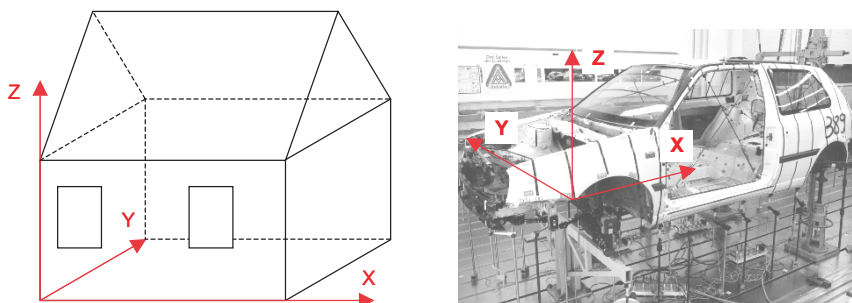


**Figure 2.4** Object coordinate systems

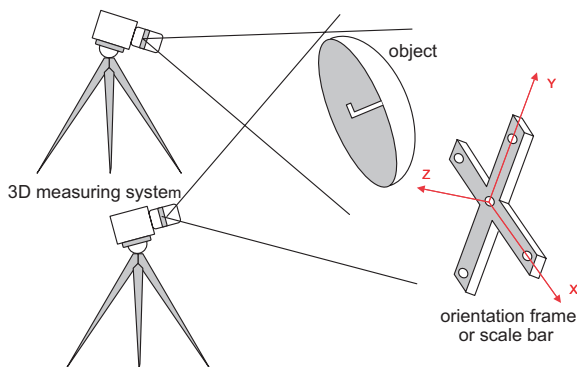


**Figure 2.5** 3D instrument coordinate system

<sup>1</sup> National systems of geodetic coordinates which use the geoid as a reference surface, are equivalent to a Cartesian coordinate system only over small areas.

## 2.2 Coordinate transformations

### 2.2.1 Plane transformations

#### 2.2.1.1 Similarity transformation

The plane similarity transformation is used for the mapping of two plane Cartesian coordinate systems. Generally a 4-parameter transformation is employed which defines two translations, one rotation and a scaling factor between the two systems. Angles and distance proportions are maintained.

Given a point  $P$  in the  $xy$  source system, the  $XY$  coordinates in the target system are:

$$\begin{aligned} X &= a_0 + a_1 x - b_1 y \\ Y &= b_0 + b_1 x + a_1 y \end{aligned} \quad (2.2)$$

or

$$\begin{aligned} X &= a_0 + m(x \cos \alpha - y \sin \alpha) \\ Y &= b_0 + m(x \sin \alpha + y \cos \alpha) \end{aligned} \quad (2.3)$$

Here  $a_0$  and  $b_0$  define the translation of the origin,  $\alpha$  is the rotation angle and  $m$  is the global scaling factor. In order to determine the four coefficients, a minimum of two identical points is required in both systems. With more than two identical points the transformation parameters can be calculated by an over-determined least-squares adjustment.

In matrix notation (2.2) is expressed as:

$$\mathbf{X} = \mathbf{A}\mathbf{x} + \mathbf{a}$$

$$\begin{bmatrix} X \\ Y \end{bmatrix} = \begin{bmatrix} a_1 & -b_1 \\ b_1 & a_1 \end{bmatrix} \begin{bmatrix} x \\ y \end{bmatrix} + \begin{bmatrix} a_0 \\ b_0 \end{bmatrix}$$

or in non-linear form with  $a_0 = X_0$  and  $b_0 = Y_0$

$$\mathbf{X} = m\mathbf{R}\mathbf{x} + \mathbf{X}_0$$

$$\begin{bmatrix} X \\ Y \end{bmatrix} = m \begin{bmatrix} \cos \alpha & -\sin \alpha \\ \sin \alpha & \cos \alpha \end{bmatrix} \begin{bmatrix} x \\ y \end{bmatrix} + \begin{bmatrix} X_0 \\ Y_0 \end{bmatrix} \quad (2.4)$$

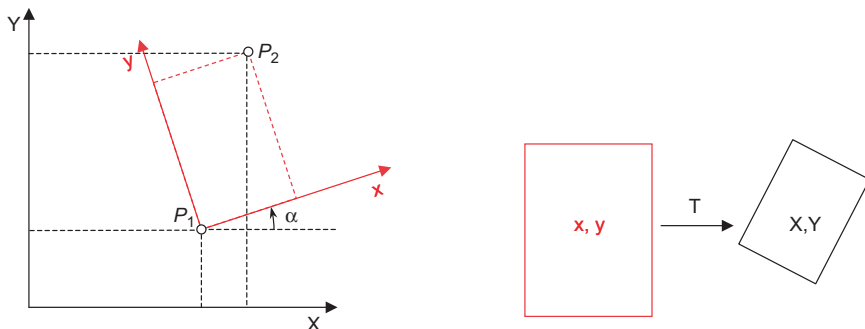


Figure 2.6 Plane similarity transformation

$\mathbf{R}$  is the rotation matrix corresponding to rotation angle  $\alpha$ . This is an orthogonal matrix having orthonormal column (or row) vectors and it has the properties:

$$\mathbf{R}^{-1} = \mathbf{R}^T \quad \text{and} \quad \mathbf{R}^T \mathbf{R} = \mathbf{I}$$

For the reverse transformation of coordinates from the target system into the source system, the transformation equations (2.4) are re-arranged as follows:

$$\begin{aligned} \mathbf{x} &= \frac{1}{m} \mathbf{R}^{-1} (\mathbf{X} - \mathbf{X}_0) \\ \begin{bmatrix} x \\ y \end{bmatrix} &= \frac{1}{m} \begin{bmatrix} \cos \alpha & \sin \alpha \\ -\sin \alpha & \cos \alpha \end{bmatrix} \begin{bmatrix} X - X_0 \\ Y - Y_0 \end{bmatrix} \end{aligned} \quad (2.5)$$

### 2.2.1.2 Affine transformation

The plane affine transformation is also used for the mapping of two plane coordinate systems. This 6-parameter transformation defines two displacements, one rotation, one shearing angle between the axes and two separate scaling factors.

For a point  $P$  in the source system, the XY coordinates in the target system are given by:

$$\begin{aligned} X &= a_0 + a_1 x + a_2 y \\ Y &= b_0 + b_1 x + b_2 y \end{aligned} \quad (2.6)$$

or in non-linear form with  $a_0 = X_0$  and  $b_0 = Y_0$

$$\begin{aligned} X &= X_0 + m_X x \cos \alpha - m_Y y \sin(\alpha + \beta) \\ Y &= Y_0 + m_X x \sin \alpha + m_Y y \cos(\alpha + \beta) \end{aligned} \quad (2.7)$$

The parameters  $a_0$  and  $b_0$  ( $X_0$  and  $Y_0$ ) define the displacement of the origin,  $\alpha$  is the rotation angle,  $\beta$  is the shearing angle between the axes and  $m_X, m_Y$  are the scaling factors for  $x$  and  $y$ . In order to determine the six coefficients a minimum of three identical points is required in both systems. With more than three identical points the transformation parameters can be calculated by over-determined least-squares adjustment.

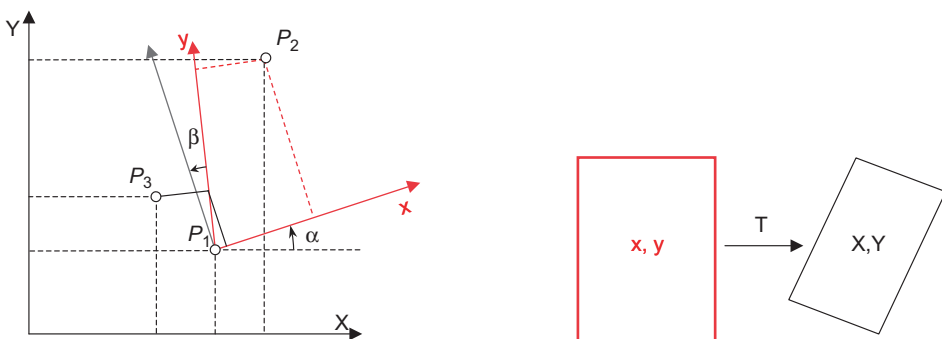


Figure 2.7 Plane affine transformation

In matrix notation the affine transformation can be written as:

$$\mathbf{X} = \mathbf{Ax} + \mathbf{a}$$

$$\begin{bmatrix} X \\ Y \end{bmatrix} = \begin{bmatrix} a_1 & a_2 \\ b_1 & b_2 \end{bmatrix} \begin{bmatrix} x \\ y \end{bmatrix} + \begin{bmatrix} a_0 \\ b_0 \end{bmatrix}$$

or

(2.8)

$$\begin{bmatrix} X \\ Y \end{bmatrix} = \begin{bmatrix} m_X \cos \alpha & -m_Y \sin(\alpha + \beta) \\ m_X \sin \alpha & m_Y \cos(\alpha + \beta) \end{bmatrix} \begin{bmatrix} x \\ y \end{bmatrix} + \begin{bmatrix} X_0 \\ Y_0 \end{bmatrix}$$

$\mathbf{A}$  is the affine transformation matrix. For lightly rotated and sheared systems the parameter  $a_1$  corresponds to the scaling factor  $m_X$  and the parameter  $b_2$  to the scaling factor  $m_Y$ .

### 2.2.1.3 Polynomial transformation

Non-linear deformations can be described by polynomials of degree  $n$ .

In general, the transformation model can be written as:

$$\begin{aligned} X &= \sum_{j=0}^n \sum_{i=0}^j a_{ji} x^{j-i} y^i \\ Y &= \sum_{j=0}^n \sum_{i=0}^j b_{ji} x^{j-i} y^i \end{aligned} \quad (2.9)$$

where  $n$  = degree of polynomial.

A polynomial of  $n=2$  is given by:

$$X = a_{00} + a_{10}x + a_{11}y + a_{20}x^2 + a_{21}xy + a_{22}y^2$$

$$Y = b_{00} + b_{10}x + b_{11}y + b_{20}x^2 + b_{21}xy + b_{22}y^2$$

The polynomial of  $n=1$  is identical to the affine transformation (2.6). In general, the number of coefficients required to define a polynomial transformation of degree  $n$  is:

$$u = (n+1)(n+2)$$

In order to determine the  $u$  coefficients, a minimum of  $u/2$  identical points is required in both systems.

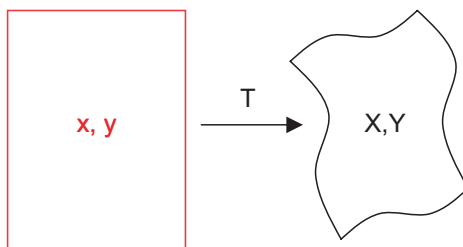


Figure 2.8 Plane polynomial transformation

### 2.2.1.4 Bilinear transformation

The bilinear transformation is similar to the affine transformation but extended by a mixed term:

$$\begin{aligned} X &= a_0 + a_1x + a_2y + a_3xy \\ Y &= b_0 + b_1x + b_2y + b_3xy \end{aligned} \quad (2.10)$$

In order to determine the eight coefficients, a minimum of four identical points is required.

The bilinear transformation can be used in the unconstrained transformation and interpolation of quadrilaterals (Fig. 2.9), for example in reseau grids or digital surface models.

For the transformation of a quadrangle with line length  $\Delta$ , the coefficients can be calculated as follows:

$$\begin{bmatrix} a_0 \\ a_1 \\ a_2 \\ a_3 \end{bmatrix} = \mathbf{A} \begin{bmatrix} x_1 \\ x_2 \\ x_3 \\ x_4 \end{bmatrix} \quad \text{and} \quad \begin{bmatrix} b_0 \\ b_1 \\ b_2 \\ b_3 \end{bmatrix} = \mathbf{A} \begin{bmatrix} y_1 \\ y_2 \\ y_3 \\ y_4 \end{bmatrix} \quad (2.11)$$

where  $\mathbf{A} = \begin{bmatrix} 1 & 0 & 0 & 0 \\ -1/\Delta & 1/\Delta & 0 & 0 \\ -1/\Delta & 0 & 1/\Delta & 0 \\ 1/\Delta^2 & -1/\Delta^2 & -1/\Delta^2 & 1/\Delta^2 \end{bmatrix}$

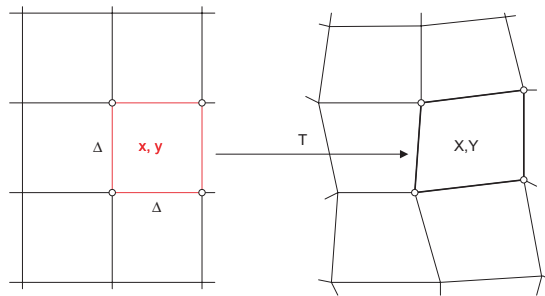


Figure 2.9 Bilinear transformation

### 2.2.1.5 Projective transformation

The projective transformation maps two plane coordinate systems using a central projection. All projection rays are straight lines through the perspective centre.

The transformation model is:

$$\begin{aligned} X &= \frac{a_0 + a_1x + a_2y}{1 + c_1x + c_2y} \\ Y &= \frac{b_0 + b_1x + b_2y}{1 + c_1x + c_2y} \end{aligned} \quad (2.12)$$

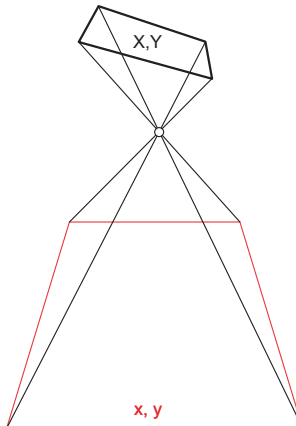


Figure 2.10 Plane projective transformation

The system of equations (2.12) is not linear. By multiplying by the denominator and rearranging, the following linear form can be derived. This is suitable as an observation equation in an adjustment procedure (see Fig. 2.10).

$$\begin{aligned} a_0 + a_1x + a_2y - X - c_1xX - c_2yX &= 0 \\ b_0 + b_1x + b_2y - Y - c_1xY - c_2yY &= 0 \end{aligned} \quad (2.13)$$

In order to determine the eight coefficients, four identical points are required where no three may lay on a common straight line. With more than four points the system of equations can be solved by adjustment (see calculation scheme in section 4.4.1.1). For the derivation of (2.12) the spatial similarity transformation can be used (see section 2.2.2.2).

The plane projective transformation preserves rectilinear properties and intersection points of straight lines. In contrast, angles, length and area proportions are not invariant. An additional

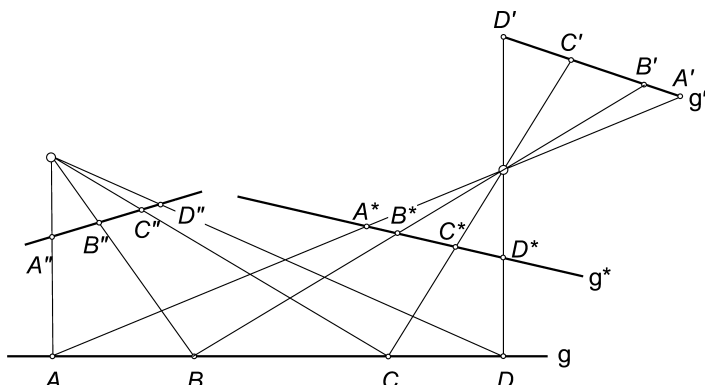


Figure 2.11 Cross ratios

invariant property of the central projection is the cross ratios of distances between points on a straight line. They are defined as follows:

$$\lambda = \frac{AD}{BD} \div \frac{AC}{BC} = \frac{A^*D^*}{B^*D^*} \div \frac{A^*C^*}{B^*C^*} = \frac{A'D'}{B'D'} \div \frac{A'C'}{B'C'} = \frac{A''D''}{B''D''} \div \frac{A''C''}{B''C''} \quad (2.14)$$

The cross ratios apply to all straight lines that intersect a bundle of perspective rays in an arbitrary position (Fig. 2.11).

The plane projective transformation is applied to single image analysis, e.g. for rectification or coordinate measurement in single images (see section 4.4.1).

## 2.2.2 Spatial transformations

### 2.2.2.1 Spatial rotations

#### *Rotation matrix using trigonometric functions*

For plane transformations, rotations take effect about a single point. In contrast, spatial rotations are performed successively about the three axes of a spatial coordinate system. Consider a point  $P$  in the source system xyz which is rotated with respect to the target system XYZ. Using trigonometric functions, individual rotations about the three axes of the target system are defined as follows:

#### 1. Rotation about Z axis

A Z axis rotation is conventionally designated by angle  $\kappa$ . This is positive in an anticlockwise direction when viewed down the positive Z axis towards the origin. From equation (2.4), this results in the following point coordinates in the target system XYZ:

$$X = x \cos \kappa - y \sin \kappa \quad \text{or} \quad \mathbf{X} = \mathbf{R}_\kappa \mathbf{x} \quad (2.15)$$

$$Y = x \sin \kappa + y \cos \kappa$$

$$Z = z$$

$$\begin{bmatrix} X \\ Y \\ Z \end{bmatrix} = \begin{bmatrix} \cos \kappa & -\sin \kappa & 0 \\ \sin \kappa & \cos \kappa & 0 \\ 0 & 0 & 1 \end{bmatrix} \begin{bmatrix} x \\ y \\ z \end{bmatrix}$$

#### 2. Rotation about Y axis

The corresponding rotation about the Y axis is designated by rotation angle  $\varphi$ . This results in the following XYZ target point coordinates:

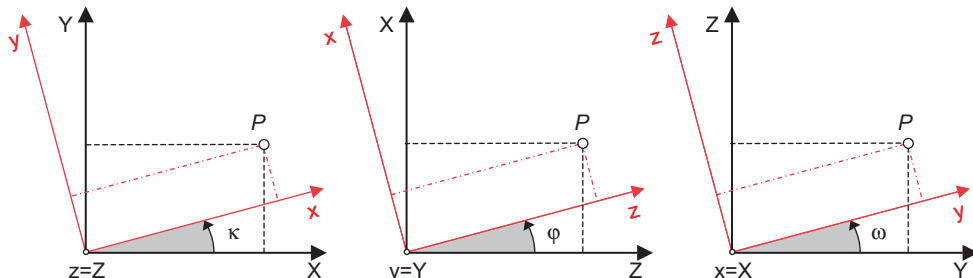


Figure 2.12 Definition of spatial rotation angles

$$\begin{aligned} X &= x \cos \varphi + z \sin \varphi & \text{or} & \quad \mathbf{X} = \mathbf{R}_\varphi \mathbf{x} \\ Y &= y \\ Z &= -x \sin \varphi + z \cos \varphi \end{aligned} \quad (2.16)$$

$$\left[ \begin{array}{c} X \\ Y \\ Z \end{array} \right] = \left[ \begin{array}{ccc} \cos \varphi & 0 & \sin \varphi \\ 0 & 1 & 0 \\ -\sin \varphi & 0 & \cos \varphi \end{array} \right] \left[ \begin{array}{c} x \\ y \\ z \end{array} \right]$$

### 3. Rotation about X axis

Finally, the X axis rotation is designated by angle  $\omega$  which results in XYZ values:

$$\begin{aligned} X &= x & \text{or} & \quad \mathbf{X} = \mathbf{R}_\omega \mathbf{x} \\ Y &= y \cos \omega - z \sin \omega \\ Z &= y \sin \omega + z \cos \omega \end{aligned} \quad (2.17)$$

$$\left[ \begin{array}{c} X \\ Y \\ Z \end{array} \right] = \left[ \begin{array}{ccc} 1 & 0 & 0 \\ 0 & \cos \omega & -\sin \omega \\ 0 & \sin \omega & \cos \omega \end{array} \right] \left[ \begin{array}{c} x \\ y \\ z \end{array} \right]$$

The complete rotation  $\mathbf{R}$  of a spatial coordinate transformation can be defined by the successive application of 3 individual rotations, as defined above. Only certain combinations of these 3 rotations are possible and these may be applied about either the fixed axial directions of the target system or the moving axes of the source system. If a general rotation is defined about moving axes in the order  $\omega \varphi \kappa$ , then the complete rotation is given by:

$$\mathbf{X} = \mathbf{Rx} \quad (2.18)$$

where

$$\mathbf{R} = \mathbf{R}_\omega \mathbf{R}_\varphi \mathbf{R}_\kappa \quad (2.19)$$

and

$$\begin{aligned} \mathbf{R} &= \begin{bmatrix} r_{11} & r_{12} & r_{13} \\ r_{21} & r_{22} & r_{23} \\ r_{31} & r_{32} & r_{33} \end{bmatrix} \\ &= \begin{bmatrix} \cos \varphi \cos \kappa & -\cos \varphi \sin \kappa & \sin \varphi \\ \cos \omega \sin \kappa + \sin \omega \sin \varphi \cos \kappa & \cos \omega \cos \kappa - \sin \omega \sin \varphi \sin \kappa & -\sin \omega \cos \varphi \\ \sin \omega \sin \kappa - \cos \omega \sin \varphi \cos \kappa & \sin \omega \cos \kappa + \cos \omega \sin \varphi \sin \kappa & \cos \omega \cos \varphi \end{bmatrix} \end{aligned}$$

If the rotation is alternatively defined about fixed axes in the order  $\omega \varphi \kappa$ , then the rotation matrix is given by:

$$\mathbf{R}^* = \mathbf{R}_\kappa \mathbf{R}_\varphi \mathbf{R}_\omega \quad (2.20)$$

This is mathematically equivalent to applying the same rotations about moving axes but in the reverse order.

Rotation matrices are orthogonal with the property that the inverse matrix equals the transpose:

$$\mathbf{R}^{-1} = \mathbf{R}^T \quad \text{and} \quad \mathbf{RR}^T = \mathbf{I}$$

From equation (2.17) the inverse transformation which generates the coordinates of a point  $P$  in the rotated system  $xyz$  from its  $XYZ$  values is therefore given by:

$$\mathbf{x} = \mathbf{R}^T \mathbf{X} \quad (2.21)$$

where

$$\mathbf{R}^T = \mathbf{R}_k^T \mathbf{R}_\phi^T \mathbf{R}_\omega^T \quad (2.22)$$

Note that in this inverse transformation, the individually inverted rotation matrices are multiplied in the reverse order.

From the matrix coefficients  $r_{11} \dots r_{33}$  in equation (2.19), the individual rotation angles can be calculated as follows:

$$\begin{aligned} \sin \varphi &= r_{13} \\ \tan \omega &= -\frac{r_{23}}{r_{33}} \\ \tan \kappa &= -\frac{r_{12}}{r_{11}} \end{aligned} \quad (2.23)$$

Equation (2.23) shows that the determination of  $\varphi$  is ambiguous due to solutions for  $\sin \varphi$  in two quadrants. In addition, there is no unique solution for the rotation angles if the second rotation ( $\varphi$  in this case) is equal to  $90^\circ$  or  $270^\circ$ . (Cosine  $\varphi$  in  $r_{11}$  and  $r_{33}$  then causes division by zero).

A simple solution to this ambiguity problem is to alter the order of rotation. In the case that the secondary rotation is close to  $90^\circ$ , the primary and secondary rotations can be exchanged, leading to the new order  $\varphi \omega \kappa$ . This procedure is used in close-range photogrammetry when the viewing direction of the camera is approximately horizontal (see Fig. 2.13 and also section 4.2.1.2). The resulting rotation matrix is then given by:

$$\mathbf{R}_{\varphi\omega\kappa} = \mathbf{R}_\varphi \mathbf{R}_\omega \mathbf{R}_\kappa \quad (2.24)$$

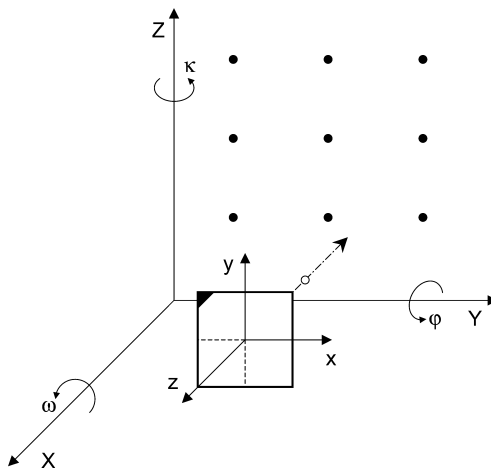


**Figure 2.13** Image configuration where  $\omega = 0^\circ$ ,  $\varphi = 90^\circ$  and  $\kappa = 90^\circ$

where

$$\mathbf{R}_{\phi\omega\kappa} = \begin{bmatrix} r_{11} & r_{12} & r_{13} \\ r_{21} & r_{22} & r_{23} \\ r_{31} & r_{32} & r_{33} \end{bmatrix}$$

$$= \begin{bmatrix} \cos \varphi \cos \kappa + \sin \varphi \sin \omega \sin \kappa & -\cos \varphi \sin \kappa + \sin \varphi \sin \omega \cos \kappa & \sin \varphi \cos \omega \\ \cos \omega \sin \kappa & \cos \omega \cos \kappa & -\sin \omega \\ -\sin \varphi \cos \kappa + \cos \varphi \sin \omega \sin \kappa & \sin \varphi \sin \kappa + \cos \varphi \sin \omega \cos \kappa & \cos \varphi \cos \omega \end{bmatrix}$$

### Example 2.1:

Referring to Fig. 2.13 an image configuration is shown where the primary rotation  $\omega = 0^\circ$ , the secondary rotation  $\varphi = 90^\circ$  and the tertiary rotation  $\kappa = 90^\circ$ . In this case the rotation matrix  $\mathbf{R}_{\omega\varphi\kappa}$  reduces to

$$\mathbf{R}_{\omega\varphi\kappa} = \begin{bmatrix} 0 & 0 & 1 \\ 1 & 0 & 0 \\ 0 & 1 & 0 \end{bmatrix}$$

This rotation matrix represents an exchange of coordinate axes. The first row describes the transformation of the X axis. Its x, y and z elements are respectively 0, 0 and 1, indicating a transformation of X to z. Correspondingly, the second row shows Y transforming to x and the third row transforms Z to y.

The exchange of rotation orders is not a suitable solution for arbitrarily oriented images (see Figs. 3.3 and 4.25). Firstly, the rotation angles of images freely located in 3D space are not easy to visualise. Secondly, ambiguities cannot be avoided, which leads to singularities when calculating orientations.

### *Rotation matrix using algebraic functions*

The ambiguities for trigonometric functions (above) can be avoided when a rotation matrix with algebraic functions is used. The three independent rotations are described by four algebraic parameters (quaternions)  $a...d$  (Hinsken 1987, Hartley and Zisserman 2000).

$$\mathbf{R}^T = \begin{bmatrix} d^2 + a^2 - b^2 - c^2 & 2(ab - cd) & 2(ac + bd) \\ 2(ab + cd) & d^2 - a^2 + b^2 - c^2 & 2(bc - ad) \\ 2(ac - bd) & 2(bc + ad) & d^2 - a^2 - b^2 + c^2 \end{bmatrix} \quad (2.25)$$

Implicitly, this rotation matrix contains a common scaling factor:

$$m = a^2 + b^2 + c^2 + d^2 \quad (2.26)$$

Using the constraint  $m = 1$ , an orthogonal rotation matrix with three independent parameters is obtained.

The geometric interpretation of this rotation matrix is not easy. However, using the rotation matrix of equation (2.19), the transformation of the four coefficients into standard rotation angles can be performed as follows:

$$\begin{aligned}
 \cos \varphi \sin \kappa &= 2(dc - ab) \\
 \cos \varphi \cos \kappa &= d^2 + a^2 - b^2 - c^2 \\
 \cos \varphi \sin \omega &= 2(da - bc) \\
 \cos \varphi \cos \omega &= d^2 - a^2 - b^2 + c^2 \\
 \sin \varphi &= 2(ac + bd)
 \end{aligned} \tag{2.27}$$

In summary, a rotation matrix with algebraic functions offers the following benefits:

- no use of trigonometric functions
- simplified computation of the design matrix and faster convergence in adjustment systems
- no singularities
- faster computation by avoiding power series for internal trigonometric calculations

#### *Rotation matrix with direction cosines*

The spatial rotation matrix can be regarded as a matrix of direction cosines of the angles between the original and the rotated coordinate axes. The unit vectors  $\mathbf{i}$ ,  $\mathbf{j}$ ,  $\mathbf{k}$  are defined in the direction of the rotated axes (Fig. 2.14).

$$\mathbf{R} = \begin{bmatrix} \cos(xX) & \cos(yX) & \cos(zX) \\ \cos(xY) & \cos(yY) & \cos(zY) \\ \cos(xZ) & \cos(yZ) & \cos(zZ) \end{bmatrix} = [\mathbf{i} \ \mathbf{j} \ \mathbf{k}] \tag{2.28}$$

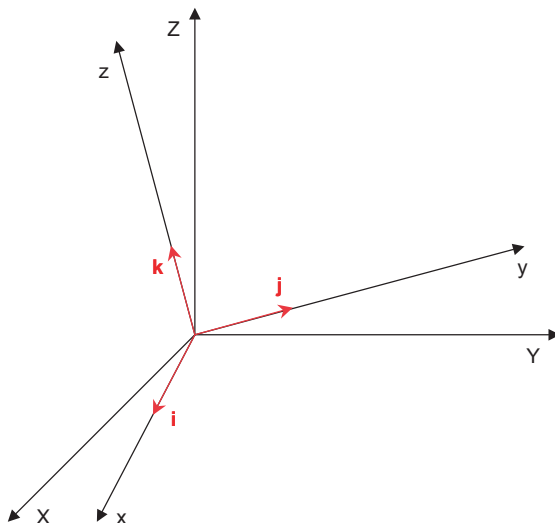


Figure 2.14 Direction cosines

*Differential rotation matrix for small rotations*

For differential rotations, the rotation matrix (2.19) reduces to

$$\mathbf{dR} = \begin{bmatrix} 1 & -d\kappa & d\varphi \\ d\kappa & 1 & -d\omega \\ -d\varphi & d\omega & 1 \end{bmatrix} \quad (2.29)$$

*Comparison of coefficients*

The spatial rotation defined in

$$\mathbf{X} = \mathbf{Rx}$$

depends on the nine coefficients  $r_{11} \dots r_{33}$  of  $\mathbf{R}$ . See, for example, the rotation order  $\omega \varphi \kappa$  about rotated axes which defines  $\mathbf{R}$  in equation (2.20). If the identical transformation result is to be achieved by a rotation matrix  $\mathbf{R}'$  using a different rotation order, the coefficients of  $\mathbf{R}'$  must be equal to those of  $\mathbf{R}$ :

$$\mathbf{R} = \mathbf{R}'$$

If the rotation angles  $\omega' \varphi' \kappa'$  of rotation matrix  $\mathbf{R}'$  are to be calculated from the explicitly given angles  $\omega \varphi \kappa$  of  $\mathbf{R}$ , this can be achieved by a comparison of matrix coefficients and a subsequent reverse calculation of the trigonometric functions.

**Example 2.2:**

Given the rotation matrix of (2.19) defined by angles  $\omega = 35$  gon,  $\varphi = 60$  gon,  $\kappa = 30$  gon, determine the rotation angles  $\omega' \varphi' \kappa'$  belonging to the equivalent rotation matrix  $\mathbf{R}'$  defined by (2.24):

- Evaluate the coefficients  $r_{11} \dots r_{33}$  of  $\mathbf{R}$  by multiplying out the individual rotation matrices in the order  $\mathbf{R} = \mathbf{R}_\omega \mathbf{R}_\varphi \mathbf{R}_\kappa$ , substituting the given values of  $\omega \varphi \kappa$ :

$$\mathbf{R} = \begin{bmatrix} 0.523720 & -0.266849 & 0.809017 \\ 0.763728 & 0.567802 & -0.307117 \\ -0.377407 & 0.778712 & 0.501169 \end{bmatrix}$$

- Write the coefficients  $r'_{11} \dots r'_{33}$  of  $\mathbf{R}'$  in trigonometric form by multiplying the individual rotation matrices in the order  $\mathbf{R}' = \mathbf{R}_\varphi \mathbf{R}_\omega \mathbf{R}_\kappa$ . Assign to each coefficient the values from  $\mathbf{R}$ , i.e.  $r'_{11} = r_{11}$ ,  $r'_{12} = r_{12}$ , and so on.
- Calculate the rotation angles  $\omega' \varphi' \kappa'$  of  $\mathbf{R}'$  by solving the trigonometric equations:  
 $\omega' = 19.873$  gon       $\varphi' = 64.692$  gon       $\kappa' = 59.301$  gon

**2.2.2.2 Spatial similarity transformation***Mathematical model*

The spatial similarity transformation is used for the shape-invariant mapping of a three-dimensional Cartesian coordinate system xyz into a corresponding target system XYZ. Both systems can be arbitrarily rotated, shifted and scaled with respect to each other. It is important to note that the rectangularity of the coordinate axes is preserved. This transformation is therefore a special case of the general affine transformation which requires 3 scaling factors and 3 additional shearing parameters for each coordinate axis—a total of 12 parameters.

The spatial similarity transformation, also known as a 3D Helmert transformation, is defined by 7 parameters: 3 translations to the origin of the xyz system (vector  $\mathbf{X}_0$  defined by  $X_0, Y_0, Z_0$ ), 3 rotation angles  $\omega, \varphi, \kappa$  about the axes XYZ (implied by orthogonal rotation matrix  $\mathbf{R}$ ) and one scaling factor  $m$ . The 6 parameters for translation and rotation correspond to the parameters of exterior orientation (see section 4.2.1). The transformation function for a point  $P(xyz)$ , defined by vector  $\mathbf{x}$ , is given by:

$$\mathbf{X} = \mathbf{X}_0 + m\mathbf{Rx} \quad (2.30)$$

or

$$\begin{bmatrix} X \\ Y \\ Z \end{bmatrix} = \begin{bmatrix} X_0 \\ Y_0 \\ Z_0 \end{bmatrix} + m \begin{bmatrix} r_{11} & r_{12} & r_{13} \\ r_{21} & r_{22} & r_{23} \\ r_{31} & r_{32} & r_{33} \end{bmatrix} \begin{bmatrix} x \\ y \\ z \end{bmatrix}$$

In order to determine the seven parameters, a minimum of seven observations is required. These observations can be derived from the coordinate components of at least three spatially distributed reference points (control points). They must contain at least 2 X, 2 Y and 3 Z components<sup>1</sup> and they must not lie on a common straight line in object space.

The spatial similarity transformation is of fundamental importance to photogrammetry for two reasons. Firstly, it is functionally equivalent to the central projection in 3D space, which is used to derive the collinearity equations. These are the fundamental equations of analytical photogrammetry (see section 4.2.2). Secondly, it is used for the transformation of local 3D coordinates (e.g. model coordinates, 3D measuring machine coordinates) into an arbitrary superior system (e.g. object or world coordinate system), for instance in the case of absolute orientation (see section 4.2.5.4) or bundle adjustment (see section 4.3).

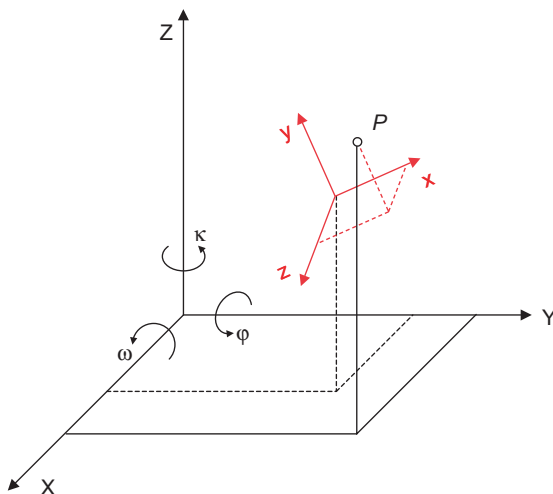


**Figure 2.15** Spatial similarity transformation

<sup>1</sup> It is assumed that the viewing direction is approximately parallel to the Z axis. For other image orientations, appropriately positioned control points are required.

There are simplified solutions for a transformation between two systems that are approximately parallel (e.g. Kraus 1997, Albertz and Kreiling 1989). In the general case both source and target system have an arbitrary relative orientation, i.e. any possible translation and rotation may occur. The calculation of transformation parameters then requires linearisation of the system of equations defined by the similarity transformation (2.30). Sufficient initial values are also required in order to determine the unknown parameters (see the following).

The system of equations is normally over-determined and the solution is performed by least-squares adjustment (see section 2.3). This derives an optimal fit between both coordinate systems. According to equation (2.30) every reference point defined in both systems generates up to three equations:

$$\begin{aligned} X &= X_0 + m(r_{11}x + r_{12}y + r_{13}z) \\ Y &= Y_0 + m(r_{21}x + r_{22}y + r_{23}z) \\ Z &= Z_0 + m(r_{31}x + r_{32}y + r_{33}z) \end{aligned} \quad (2.31)$$

By linearising the equations at approximate parameter values, corresponding correction equations are built up. Any reference point with defined X, Y and Z coordinates (full reference point) provides three observation equations. Correspondingly, reference points with fewer coordinate components generate fewer observation equations but they can still be used for parameter estimation. Thus a transformation involving 3 full reference points already provides 2 redundant observations. The 3-2-1 method (see section 4.3.3.2) used in industrial metrology, is based on 6 observations, does not derive a scale change, and therefore results in zero redundancy.

#### Approximate values

In order to calculate approximate values of the translation and rotation parameters of the similarity transformation, an intermediate coordinate system is formed. This is derived from 3 XYZ reference points  $P_1, P_2, P_3$  as indicated by system uvw (Fig. 2.16). The purpose at this

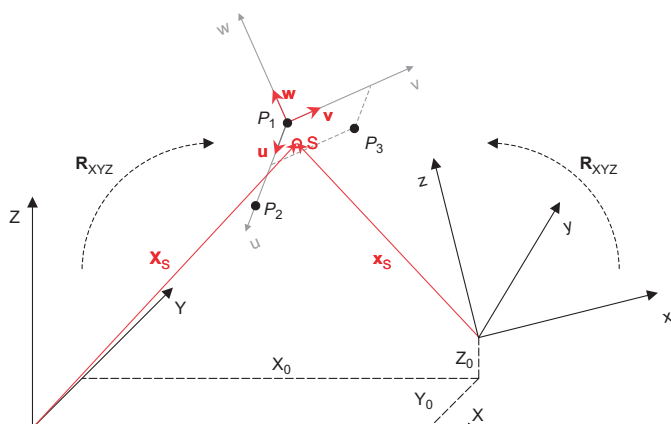


**Figure 2.16** Calculation of approximate values for 3D similarity transformation

stage is to calculate the parameters which transform the reference points from intermediate system uvw to coordinate systems XYZ and xyz.

$$\begin{aligned}\mathbf{P}_{XYZ} &= \mathbf{R}_{u \rightarrow X} \mathbf{P}_{uvw} + \mathbf{T}_{u \rightarrow X} \\ \mathbf{P}_{xyz} &= \mathbf{R}_{u \rightarrow x} \mathbf{P}_{uvw} + \mathbf{T}_{u \rightarrow x}\end{aligned}\quad (2.32)$$

Solving both equations for  $\mathbf{P}_{uvw}$  and re-arranging:

$$\mathbf{R}_{u \rightarrow X}^T (\mathbf{P}_{XYZ} - \mathbf{T}_{u \rightarrow X}) = \mathbf{R}_{u \rightarrow x}^T (\mathbf{P}_{xyz} - \mathbf{T}_{u \rightarrow x})$$

and finally for the coordinates of a point in system XYZ:

$$\begin{aligned}\mathbf{P}_{XYZ} &= \mathbf{R}_{u \rightarrow X} \mathbf{R}_{u \rightarrow x}^T \mathbf{P}_{xyz} + \mathbf{T}_{u \rightarrow X} - \mathbf{R}_{u \rightarrow X} \mathbf{R}_{u \rightarrow x}^T \mathbf{T}_{u \rightarrow x} \\ &= \mathbf{R}_{x \rightarrow X}^0 \mathbf{P}_{xyz} + (\mathbf{T}_{u \rightarrow X} - \mathbf{R}_{x \rightarrow X}^0 \mathbf{T}_{u \rightarrow x})\end{aligned}\quad (2.33)$$

Here matrices  $\mathbf{R}_{u \rightarrow X}$  and  $\mathbf{R}_{u \rightarrow x}$  describe the rotation of each system under analysis with respect to the intermediate system. The  $\mathbf{T}$  vectors describe the corresponding translations. The expression in brackets describes the translation between systems XYZ and xyz:

$$\mathbf{X}_{x \rightarrow X}^0 = \mathbf{T}_{u \rightarrow X} - \mathbf{R}_{x \rightarrow X}^0 \mathbf{T}_{u \rightarrow x} \quad (2.34)$$

To calculate the required parameters, the u axis of the intermediate system is constructed through  $P_1$  and  $P_2$  and the uv plane through  $P_3$  (corresponds to the 3-2-1 method). From the local vectors defined by the reference points  $\mathbf{P}_i(X_i, Y_i, Z_i)$ ,  $i = 1 \dots 3$ , normalized direction vectors are calculated as follows:

$$\begin{aligned}\mathbf{U} &= \frac{\mathbf{P}_2 - \mathbf{P}_1}{|\mathbf{P}_2 - \mathbf{P}_1|} & \mathbf{u} &= \frac{\mathbf{p}_2 - \mathbf{p}_1}{|\mathbf{p}_2 - \mathbf{p}_1|} \\ \mathbf{W} &= \frac{\mathbf{U} \times (\mathbf{P}_3 - \mathbf{P}_1)}{|\mathbf{U} \times (\mathbf{P}_3 - \mathbf{P}_1)|} & \mathbf{w} &= \frac{\mathbf{u} \times (\mathbf{p}_3 - \mathbf{p}_1)}{|\mathbf{u} \times (\mathbf{p}_3 - \mathbf{p}_1)|} \\ \mathbf{V} &= \mathbf{W} \times \mathbf{U} & \mathbf{v} &= \mathbf{w} \times \mathbf{u}\end{aligned}\quad (2.35)$$

Vector  $\mathbf{u}$  is a unit vector on the u axis,  $\mathbf{w}$  is perpendicular to the uv plane and  $\mathbf{v}$  is perpendicular to  $\mathbf{u}$  and  $\mathbf{w}$ . These 3 vectors directly define the rotation matrix from uvw to XYZ (see eq. 2.28):

$$\mathbf{R}_{u \rightarrow X} = [\mathbf{U} \ \mathbf{V} \ \mathbf{W}] \quad \mathbf{R}_{u \rightarrow x} = [\mathbf{u} \ \mathbf{v} \ \mathbf{w}] \quad (2.36)$$

In the same way rotation matrix  $\mathbf{R}_{xyz}$  is defined by the reference point coordinates in system xyz. The approximate rotation matrix from the xyz to the XYZ system is obtained from successive application of the above two matrices as follows:

$$\mathbf{R}_{x \rightarrow X}^0 = \mathbf{R}_{u \rightarrow X} \mathbf{R}_{u \rightarrow x}^T \quad (2.37)$$

Using the centroid of the reference points in both coordinate systems, approximate values for the translation parameters of the similarity transformation can be calculated:

$$\mathbf{x}_S = \begin{bmatrix} X_S \\ Y_S \\ Z_S \end{bmatrix} \quad : \text{centroid in XYZ system}$$

$$\mathbf{x}_S = \begin{bmatrix} x_S \\ y_S \\ z_S \end{bmatrix} \quad : \text{centroid in xyz system} \quad (2.38)$$

According to equation (2.34) the translation can then be calculated:

$$\mathbf{X}_{x \rightarrow X}^0 = \mathbf{X}_S - \mathbf{R}_{x \rightarrow X}^0 \mathbf{x}_S \quad (2.39)$$

### 2.2.2.3 Graphical transformations

#### *Homogeneous coordinates*

Graphical transformations are transformations and projections used in computer graphics and projective geometry. In this field homogeneous coordinates are often used to form these functions.

$$\mathbf{x}_h = \begin{bmatrix} x_h \\ y_h \\ z_h \\ w \end{bmatrix} \quad (2.40)$$

These include the important special case  $w = 1$  for Cartesian coordinates  $x, y, z$ :

$$\mathbf{x} = \begin{bmatrix} x_h/w \\ y_h/w \\ z_h/w \\ w/w \end{bmatrix} = \begin{bmatrix} x \\ y \\ z \\ 1 \end{bmatrix} \quad (2.41)$$

Using homogeneous coordinates, all coordinate transformations and translations, as well as axonometric and central projections, can be formulated in a unified way in any combination. They are therefore perfectly suited to calculations in computer graphics and CAD systems.

#### *General transformations*

The general linear transformation of homogeneous coordinates is given by:

$$\mathbf{X} = \mathbf{T}\mathbf{x} \quad (2.42)$$

where  $\mathbf{T}$  is the transformation or projection matrix

$$\mathbf{T} = \left[ \begin{array}{ccc|c} a_{11} & a_{12} & a_{13} & a_{14} \\ a_{21} & a_{22} & a_{23} & a_{24} \\ \hline a_{31} & a_{32} & a_{33} & a_{34} \\ \hline a_{41} & a_{42} & a_{43} & a_{44} \end{array} \right] = \left[ \begin{array}{c|c} \mathbf{T}_{11} & \mathbf{T}_{12} \\ \hline 3,3 & 1,3 \\ \hline \mathbf{T}_{21} & \mathbf{T}_{22} \\ \hline 3,1 & 1,1 \end{array} \right] \quad (2.43)$$

This transformation always results in a new homogeneous coordinate vector. The four submatrices contain information as follows:

$\mathbf{T}_{11}$  : scaling, reflection in a line, rotation

$\mathbf{T}_{12}$  : translation

$\mathbf{T}_{21}$  : perspective

$\mathbf{T}_{22}$  : homogeneous scaling (factor  $w$ )

Scaling or reflection about a line is performed by the factors  $s_X, s_Y, s_Z$

$$\mathbf{T}_S = \begin{bmatrix} s_X & 0 & 0 & | & 0 \\ 0 & s_Y & 0 & | & 0 \\ 0 & 0 & s_Z & | & 0 \\ \hline 0 & 0 & 0 & | & 1 \end{bmatrix} \quad : \text{scaling, reflection in a line} \quad (2.44)$$

A spatial rotation results if  $\mathbf{T}_{12}$  is replaced by the rotation matrix derived in section 2.2.2.1:

$$\mathbf{T}_R = \begin{bmatrix} r_{11} & r_{12} & r_{13} & | & 0 \\ r_{21} & r_{22} & r_{23} & | & 0 \\ r_{31} & r_{32} & r_{33} & | & 0 \\ \hline 0 & 0 & 0 & | & 1 \end{bmatrix} \quad : \text{spatial rotation} \quad (2.45)$$

Translation by a vector  $x_T, y_T, z_T$  is performed by the projection matrix

$$\mathbf{T}_T = \begin{bmatrix} 1 & 0 & 0 & | & x_T \\ 0 & 1 & 0 & | & y_T \\ 0 & 0 & 1 & | & z_T \\ \hline 0 & 0 & 0 & | & 1 \end{bmatrix} \quad : \text{translation} \quad (2.46)$$

Combined transformations  $\mathbf{T}_1, \mathbf{T}_2$  etc can be created by sequential multiplication of single projection matrices as follows:

$$\mathbf{X} = \mathbf{T}\mathbf{x} = \mathbf{T}_n \dots \mathbf{T}_2 \mathbf{T}_1 \mathbf{x} \quad (2.47)$$

In general, the multiplication order may not be changed because the projections are not necessarily commutative.

The reverse transformation is given by:

$$\mathbf{x} = \mathbf{T}^{-1}\mathbf{X} = \mathbf{T}_1^{-1}\mathbf{T}_2^{-1} \dots \mathbf{T}_n^{-1}\mathbf{X} \quad (2.48)$$

This inversion is only possible if the projection matrix is not singular, as is the normal case for the transformation of one 3D system onto another. However, if the vector  $\mathbf{x}$  is projected onto a plane, the projection matrix becomes singular. The original coordinates cannot then be calculated from the transformed plane coordinates  $\mathbf{X}$ .

Using homogenous coordinates, the spatial similarity transformation of equation (2.30) is given by:

$$\begin{aligned}
 \mathbf{X} &= \mathbf{T}_T \mathbf{T}_S \mathbf{T}_R \mathbf{x} \\
 \begin{bmatrix} X \\ Y \\ Z \\ 1 \end{bmatrix} &= \begin{bmatrix} 1 & 0 & 0 & X_0 \\ 0 & 1 & 0 & Y_0 \\ 0 & 0 & 1 & Z_0 \\ 0 & 0 & 0 & 1 \end{bmatrix} \begin{bmatrix} m & 0 & 0 & 0 \\ 0 & m & 0 & 0 \\ 0 & 0 & m & 0 \\ 0 & 0 & 0 & 1 \end{bmatrix} \begin{bmatrix} r_{11} & r_{12} & r_{13} & 0 \\ r_{21} & r_{22} & r_{23} & 0 \\ r_{31} & r_{32} & r_{33} & 0 \\ 0 & 0 & 0 & 1 \end{bmatrix} \begin{bmatrix} x \\ y \\ z \\ 1 \end{bmatrix} \quad (2.49) \\
 &= \begin{bmatrix} mr_{11} & mr_{12} & mr_{13} & X_0 \\ mr_{21} & mr_{22} & mr_{23} & Y_0 \\ mr_{31} & mr_{32} & mr_{33} & Z_0 \\ 0 & 0 & 0 & 1 \end{bmatrix} \begin{bmatrix} x \\ y \\ z \\ 1 \end{bmatrix}
 \end{aligned}$$

### Projections

For the projection of a 3D object into an image or plotting plane, it is common to distinguish between axonometric and perspective transformations.

For axonometric projections the object is projected onto the desired plane using a parallel projection. An example is the isometric projection widely used in CAD technology. The projection matrix for the isometric projection (Fig. 2.17) is given by:

$$\mathbf{T}_I = \begin{bmatrix} -\cos(30^\circ) & \cos(30^\circ) & 0 & 0 \\ -\sin(30^\circ) & -\sin(30^\circ) & 1 & 0 \\ 0 & 0 & 0 & 0 \\ 0 & 0 & 0 & 1 \end{bmatrix} \quad : \text{isometry} \quad (2.50)$$

where the transformed Z coordinate is discarded in the visualisation.

The central projection is modelled firstly for the following special case. The projection plane is oriented normal to the viewing direction Z with the distance  $c$  to the perspective centre. Referring to Fig. 2.18, the following ratios can be derived<sup>1</sup>.

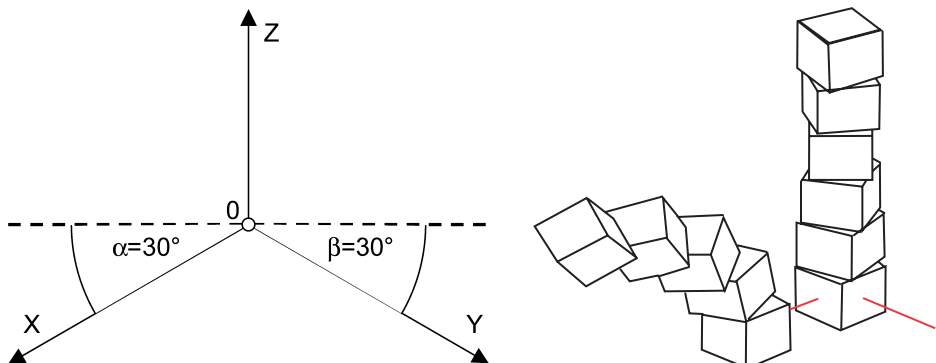


Figure 2.17 Isometric projection

<sup>1</sup> Here the usual notations for image coordinates  $x'$ ,  $y'$ , and  $c$  are used.

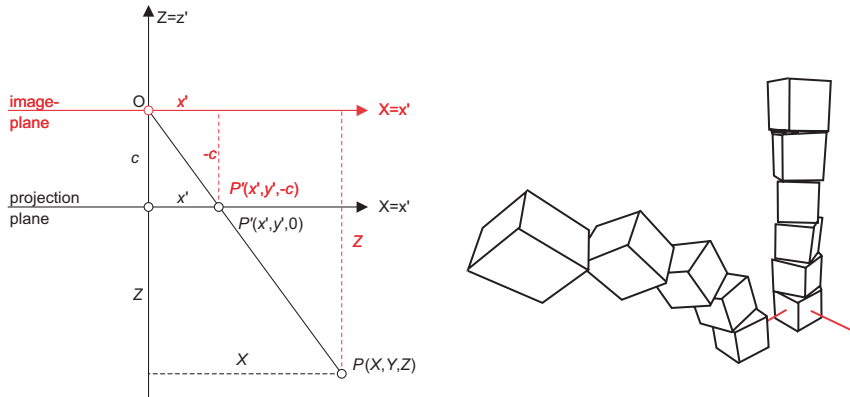


Figure 2.18 Central projection

$$\frac{x'}{X} = \frac{y'}{Y} = \frac{c}{Z+c} \quad (2.51)$$

and further rearranged to give  $x'$  and  $y'$ :

$$x' = \frac{X}{\frac{Z}{c} + 1} \quad y' = \frac{Y}{\frac{Z}{c} + 1} \quad (2.52)$$

If the perspective centre (focal length  $c$ ) moves to infinity, the denominator becomes 1 and the central projection changes to a parallel projection. Without affecting validity, the image coordinate system can then be shifted to the perspective centre (red position in Fig. 2.18), which leads to projection equations:

$$x' = \frac{-c}{Z} X = \frac{1}{m} X \quad y' = \frac{-c}{Z} Y = \frac{1}{m} Y \quad (2.53)$$

In matrix form, the transformation (2.53) is given by:

$$\begin{aligned} \bar{\mathbf{x}} &= \mathbf{T}_Z \mathbf{X} \\ \begin{bmatrix} \bar{x} \\ \bar{y} \\ \bar{z} \\ w \end{bmatrix} &= \begin{bmatrix} 1 & 0 & 0 & | 0 \\ 0 & 1 & 0 & | 0 \\ 0 & 0 & 1 & | 0 \\ 0 & 0 & -1/c & | 0 \end{bmatrix} \begin{bmatrix} X \\ Y \\ Z \\ 1 \end{bmatrix} = \begin{bmatrix} X \\ Y \\ Z \\ -Z/c \end{bmatrix} \end{aligned} \quad (2.54)$$

and for the resulting homogenous coordinates after division by  $m = -Z/c$ :

$$\begin{aligned} \mathbf{x}' &= \mathbf{T}_S^{-1} \bar{\mathbf{x}} \\ \begin{bmatrix} x' \\ y' \\ z' \\ 1 \end{bmatrix} &= \begin{bmatrix} -c/Z & 0 & 0 & | 0 \\ 0 & -c/Z & 0 & | 0 \\ 0 & 0 & -c/Z & | 0 \\ 0 & 0 & 1/Z & | 0 \end{bmatrix} \begin{bmatrix} \bar{x} \\ \bar{y} \\ \bar{z} \\ w \end{bmatrix} = \begin{bmatrix} -cX/Z \\ -cY/Z \\ -c \\ 1 \end{bmatrix} = \begin{bmatrix} X/m \\ Y/m \\ -c \\ 1 \end{bmatrix} \end{aligned} \quad (2.55)$$

It is obvious that rows 3 and 4 of the transformation matrix  $\mathbf{T}_s$  are linearly dependent and the matrix cannot be inverted. It is therefore not possible to calculate 3D object coordinates from 2D image coordinates in this case.

If the above  $H$  mentioned special case is extended to an arbitrary exterior orientation of the image plane (position and orientation in space), the transformation of object coordinates into image coordinates can be performed by the following matrix operation with respect to equation (2.49):

$$\mathbf{x}' = \mathbf{T}_S^{-1} \mathbf{T}_Z \mathbf{T}_R^{-1} \mathbf{T}_T^{-1} \mathbf{X}$$

$$\begin{bmatrix} x' \\ y' \\ z' \\ 1 \end{bmatrix} = \begin{bmatrix} \frac{r_{11}}{m} & \frac{r_{21}}{m} & \frac{r_{31}}{m} & \frac{-(r_{11}X_0 + r_{21}Y_0 + r_{31}Z_0)}{m} \\ \frac{r_{12}}{m} & \frac{r_{22}}{m} & \frac{r_{32}}{m} & \frac{-(r_{12}X_0 + r_{22}Y_0 + r_{32}Z_0)}{m} \\ \frac{r_{13}}{m} & \frac{r_{23}}{m} & \frac{r_{33}}{m} & \frac{-(r_{13}X_0 + r_{23}Y_0 + r_{33}Z_0)}{m} \\ -\frac{r_{13}}{cm} & -\frac{r_{23}}{cm} & -\frac{r_{33}}{cm} & \frac{r_{11}X_0 + r_{21}Y_0 + r_{31}Z_0}{cm} \end{bmatrix} \begin{bmatrix} X \\ Y \\ Z \\ 1 \end{bmatrix} \quad (2.56)$$

## 2.3 Adjustment techniques

### 2.3.1 The problem

This section provides a summary of some important techniques for the computation of over-determined, non-linear systems of equations by adjustment methods. These are essential for the understanding of numerous photogrammetric calculations. In general, the task is to determine a number of unknown parameters from a number of observed (measured) values which have a functional relationship to each other. If more observations are available than required for the determination of the unknowns, there is normally no unique solution and the unknown parameters are estimated according to functional and stochastic models. Readers should review specialist literature for a detailed discussion of adjustment methods (e.g. Wolf and Ghilani 1997, Cross 1990, Mikhail 1976, Mikhail and Gracie 1981).

#### 2.3.1.1 Functional model

A number of observations  $n$  (measured values) form an observation vector  $\mathbf{L}$ :

$$\mathbf{L} = (L_1, L_2, \dots, L_n)^T \quad : \text{observation vector} \quad (2.57)$$

Since the elements of the observation vector are measured data they are regarded as having small random error effects but are free of systematic defects. This may also be called the random vector  $\mathbf{L}$ .

A number  $u$  of unknown parameters must be determined. These form the vector of unknowns  $\mathbf{X}$ , also called the parameter vector.

$$\mathbf{X} = (X_1, X_2, \dots, X_u)^T \quad : \text{vector of unknowns} \quad (2.58)$$

The number of observations is assumed to be greater than the number of unknowns.

$$n > u$$

The functional model describes the relation between the “true” observation values  $\tilde{\mathbf{L}}$  and the “true” values of the unknowns  $\tilde{\mathbf{X}}$ . This relationship is expressed by the vector of functions  $\varphi$  of the unknowns:

$$\tilde{\mathbf{L}} = \varphi(\tilde{\mathbf{X}}) = \begin{bmatrix} \varphi_1(\tilde{\mathbf{X}}) \\ \varphi_2(\tilde{\mathbf{X}}) \\ \vdots \\ \varphi_n(\tilde{\mathbf{X}}) \end{bmatrix} \quad : \text{functional model} \quad (2.59)$$

Since the true values are normally not known, the observation vector  $\tilde{\mathbf{L}}$  is replaced by the measured observations  $\mathbf{L}$  and associated small residuum  $\mathbf{v}$ . Similarly, the vector of unknowns is replaced by the estimated (adjusted) unknowns  $\hat{\mathbf{X}}$ . As a result, the following non-linear correction equations are obtained:

$$\hat{\mathbf{L}} = \mathbf{L} + \mathbf{v} = \varphi(\hat{\mathbf{X}}) \quad (2.60)$$

If approximate values  $\mathbf{X}^0$  of the unknowns are available, the vector of unknowns can be expressed as the following sum:

$$\hat{\mathbf{X}} = \mathbf{X}^0 + \hat{\mathbf{x}} \quad (2.61)$$

i.e. only the small unknown values must be determined.

From the values in  $\mathbf{X}^0$ , approximate values of the observations can then be calculated using the functional model:

$$\mathbf{L}^0 = \varphi(\mathbf{X}^0) \quad (2.62)$$

In this way reduced observations (observed minus computed) are obtained:

$$\mathbf{l} = \mathbf{L} - \mathbf{L}^0 \quad (2.63)$$

For sufficiently small values of  $\hat{\mathbf{x}}$ , the correction equations can be expanded into a Taylor series around the approximate values  $\mathbf{X}^0$ , ignoring terms after the first:

$$\begin{aligned} \mathbf{L} + \mathbf{v} &= \varphi(\mathbf{X}^0) + \left( \frac{\partial \varphi_1(\mathbf{X})}{\partial \mathbf{X}_1} \right)_0 (\hat{\mathbf{X}} - \mathbf{X}^0) \\ &= \mathbf{L}^0 + \left( \frac{\partial \varphi_1(\mathbf{X})}{\partial \mathbf{X}_1} \right)_0 \hat{\mathbf{x}} \end{aligned} \quad (2.64)$$

After introduction of the Jacobian matrix  $\mathbf{A}$ , also known as the design, model or coefficient matrix:

$$\mathbf{A} = \left( \frac{\partial \varphi(\mathbf{X})}{\partial \mathbf{X}} \right)_0 = \begin{bmatrix} \left( \frac{\partial \varphi_1(\mathbf{X})}{\partial \mathbf{X}_1} \right)_0 & \left( \frac{\partial \varphi_1(\mathbf{X})}{\partial \mathbf{X}_2} \right)_0 & \dots & \left( \frac{\partial \varphi_1(\mathbf{X})}{\partial \mathbf{X}_u} \right)_0 \\ \left( \frac{\partial \varphi_2(\mathbf{X})}{\partial \mathbf{X}_1} \right)_0 & \left( \frac{\partial \varphi_2(\mathbf{X})}{\partial \mathbf{X}_2} \right)_0 & \dots & \left( \frac{\partial \varphi_2(\mathbf{X})}{\partial \mathbf{X}_u} \right)_0 \\ \vdots & \vdots & \ddots & \vdots \\ \left( \frac{\partial \varphi_n(\mathbf{X})}{\partial \mathbf{X}_1} \right)_0 & \left( \frac{\partial \varphi_n(\mathbf{X})}{\partial \mathbf{X}_2} \right)_0 & \dots & \left( \frac{\partial \varphi_n(\mathbf{X})}{\partial \mathbf{X}_u} \right)_0 \end{bmatrix} \quad (2.65)$$

the linearized correction equations are obtained:

$$\hat{\mathbf{I}}_{n,1} = \mathbf{1}_{n,1} + \mathbf{v}_{n,1} = \mathbf{A}_{n,n} \hat{\mathbf{x}}_{n,u,1} \quad (2.66)$$

The Jacobian matrix  $\mathbf{A}$  consists of differential quotients which describe the functional relation between the parameters and which are calculated from approximate values. The vector of unknowns contains the estimated parameters and  $\mathbf{I}$  is the vector of reduced observations. A computation scheme is given in section 2.3.2.2.

### 2.3.1.2 Stochastic model

The stochastic properties of the unknowns  $\mathbf{L}$  are defined by the covariance matrix  $\mathbf{K}_{ll}$

$$\mathbf{K}_{ll} = \begin{bmatrix} \sigma_1^2 & \rho_{12}\sigma_1\sigma_2 & \cdots & \rho_{1n}\sigma_1\sigma_n \\ \rho_{21}\sigma_2\sigma_1 & \sigma_2^2 & \cdots & \rho_{2n}\sigma_2\sigma_n \\ \vdots & \vdots & \ddots & \vdots \\ \rho_{n1}\sigma_n\sigma_1 & \cdots & \sigma_n^2 & \end{bmatrix} \quad (2.67)$$

where  $\sigma_i$ : standard deviation of observation  $L_i$ ,  $i = 1..n$

$\rho_{ij}$ : correlation coefficient between  $L_i$  and  $L_j$ ,  $i \neq j$

Introducing the multiplication factor  $\sigma_0^2$ , the cofactor matrix  $\mathbf{Q}_{ll}$  of observations is obtained:

$$\mathbf{Q}_{ll} = \frac{1}{\sigma_0^2} \mathbf{K}_{ll} = \mathbf{P}^{-1} \quad (2.68)$$

where  $\mathbf{P}_{ll}$  is the weight matrix.

The covariance matrix is the only component containing information about the accuracy of the functional model in the adjustment process. It is therefore called the stochastic model (see section 2.3.3.1) In the case of independent observations, the correlation coefficients become zero and the covariance matrix is reduced to a diagonal matrix. This is the standard case for many adjustment problems where either independent observations are given, or no significant knowledge about correlations between observations is available.

The weight matrix  $\mathbf{P}$  then becomes:

$$\mathbf{P}_{ll} = \begin{bmatrix} \frac{\sigma_0^2}{\sigma_1^2} & & & \\ & \frac{\sigma_0^2}{\sigma_2^2} & & \\ & & \ddots & \\ & & & \frac{\sigma_0^2}{\sigma_n^2} \end{bmatrix} = \begin{bmatrix} p_1 & & & \\ & p_2 & & \\ & & \ddots & \\ & & & p_n \end{bmatrix} \quad (2.69)$$

In this case an observation  $L_i$  with standard deviation  $\sigma_i = \sigma_0$  has weight

$$p_i = \frac{\sigma_0^2}{\sigma_i^2} = 1$$

and  $\mathbf{P}$  becomes the identity matrix  $\mathbf{I}$ .  $\sigma_0$  is the true value of the standard deviation of unit weight (standard deviation of an observation with weight = 1). It can be regarded as a multiplication constant. Refer to sections 2.3.2.1 and 2.3.3.1 for a definition of this parameter.

Usually the true standard deviation  $\sigma$  is not known in practical applications and the empirical standard deviation  $s$  is used instead. Here  $s$  denotes the standard deviation *a priori*, while  $\hat{s}$  represents the standard deviation *a posteriori* (adjusted standard deviation). The empirical standard deviation is only meaningful in cases of significant redundancy.

### 2.3.2 Least-squares method (Gauss-Markov linear model)

The Gauss-Markov adjustment model is based on the idea that the unknown parameters are estimated with maximum probability. Assuming a data set with an infinite number of measured values and normally distributed errors (non-centrality parameter  $\Delta = 0$ , i.e. no systematic errors), the following condition for the residuals results:

$$\mathbf{v}^T \mathbf{P} \mathbf{v} \rightarrow \min! \quad (2.70)$$

For independent observations it reduces to

$$\sum_{i=1}^n p_i v_i^2 = [p \mathbf{v} \mathbf{v}] \rightarrow \min! \quad (2.71)$$

It is known as a least-squares adjustment or minimisation using the L2 norm. The Gauss-Markov model ensures that unknown parameters are estimated unbiased and with minimum variance.

#### 2.3.2.1 Adjustment of direct observations

Consider a number of direct measurements of a single unknown value e.g. from repeated measurements. The functional model is then reduced to the extent that the required quantity is simply the mean of the observations.

For observations with individual accuracy the corresponding weights are estimated from the *a priori* standard deviations of the original observations  $s_i$  and of unit weight  $s_0$ :

$$p_i = \frac{s_0^2}{s_i^2} \quad : \text{weight of observation } i \quad (2.72)$$

The weight  $p_i$  can also be derived from the number of repeated measurements if multiple values for specific observations are available. In the case of uniform accuracies the weight is simplified to  $p_i = 1$ .

The estimated unknown is obtained by the geometric (weighted) average:

$$\hat{x} = \frac{p_1 l_1 + p_2 l_2 + \dots + p_n l_n}{p_1 + p_2 + \dots + p_n} = \frac{\sum_{i=1}^n p_i l_i}{\sum_{i=1}^n p_i} \quad (2.73)$$

The residuum of an observation  $i$  gives:

$$v_i = \hat{x} - l_i \quad (2.74)$$

After adjustment the *a posteriori* standard deviation of unit weight is given by

$$\hat{s}_0 = \sqrt{\frac{[p_{vv}]}{n-1}} = \sqrt{\frac{\sum p v^2}{n-1}} \quad (2.75)$$

The *a posteriori* standard deviation of the original observation  $i$  is given by

$$\hat{s}_i = \frac{\hat{s}_0}{\sqrt{p_i}} \quad (2.76)$$

The standard deviation of the average value is, in this case, equal to the standard deviation of the adjusted observations:

$$\hat{s}_{\bar{x}} = \frac{\hat{s}_0}{\sqrt{[p]}} \quad (2.77)$$

### 2.3.2.2 General least squares adjustment

Let the following linearised functions define an adjustment problem:

$$\begin{matrix} \hat{\mathbf{l}} \\ n,1 \end{matrix} = \begin{matrix} \mathbf{l} \\ n,1 \end{matrix} + \mathbf{v} = \mathbf{A} \begin{matrix} \hat{\mathbf{x}} \\ n,u \\ u,1 \end{matrix} \quad : \text{functional model}$$

$$\mathbf{Q}_{ll} = \frac{1}{s_0^2} \mathbf{K}_{ll} = \mathbf{P}^{-1} \quad : \text{stochastic model}$$

with  $n$  observations and  $u$  unknowns,  $n > u$ . To set up the weight matrix  $\mathbf{P}$ , the *a priori* standard deviations of observations  $s_i$  and the *a priori* standard deviation of unit weight  $s_0$  are required. They could, for example, be derived from the empirically known accuracy of a measuring device:

$$p_i = \frac{s_0^2}{s_i^2} \quad : \text{weight of observation } i$$

After generation of initial values, setting up of the Jacobian matrix  $\mathbf{A}$ , and calculation of reduced observations  $\mathbf{l}$ , the following computation scheme may be used in order to calculate the vector of unknowns (Pelzer 1985):

- 1)  $\begin{matrix} \mathbf{P} \\ n,n \end{matrix} = \mathbf{Q}_{ll}^{-1} \quad : \text{weight matrix}$
- 2)  $\begin{matrix} \mathbf{N} \hat{\mathbf{x}} - \mathbf{n} = \mathbf{0} \\ u,u \ u,1 \end{matrix} \quad : \text{normal equations} \quad (2.78)$

where

$$\begin{matrix} \mathbf{N} = \mathbf{A}^T \mathbf{P} \mathbf{A} \\ u,u \ u,n \ n,n,u \end{matrix} \quad : \text{matrix of normal equations}$$

$$\begin{matrix} \mathbf{n} = \mathbf{A}^T \mathbf{P} \mathbf{l} \\ u,1 \ u,n \ n,n,1 \end{matrix} \quad : \text{absolute term}$$

$$3) \quad \underset{u,u}{\mathbf{Q}} = \underset{u,u}{\mathbf{N}^{-1}} \quad : \text{solving the normal equations} \quad (2.79)$$

$$\begin{aligned} \hat{\mathbf{x}}_{u,1} &= \underset{u,u}{\mathbf{Q}} \underset{u,1}{\mathbf{n}} \\ &= (\mathbf{A}^T \underset{u,n}{\mathbf{P}} \underset{n,n,u}{\mathbf{A}})^{-1} \underset{u,n}{\mathbf{A}^T} \underset{n,n,n}{\mathbf{P}} \underset{n,1}{\mathbf{l}} \end{aligned} \quad : \text{where } \mathbf{Q} \text{ is the cofactor matrix of unknowns}$$

$$4) \quad \underset{n,1}{\mathbf{v}} = \underset{n,n,u}{\mathbf{A}} \underset{u,1}{\hat{\mathbf{x}}} - \underset{n,1}{\mathbf{l}} \quad : \text{residuals} \quad (2.80)$$

$$5) \quad \hat{\mathbf{l}}_{n,1} = \underset{n,1}{\mathbf{l}} + \underset{n,1}{\mathbf{v}} \quad : \text{adjusted observations}$$

$$\hat{\mathbf{L}}_{n,1} = \underset{n,1}{\mathbf{L}} + \underset{n,1}{\mathbf{v}}$$

$$6) \quad \hat{\mathbf{X}}_{u,1} = \hat{\mathbf{X}}_{u,1}^0 + \hat{\mathbf{x}}_{u,1} \quad : \text{vector of unknowns}$$

$$7) \quad \hat{s}_0 = \sqrt{\frac{\mathbf{v}^T \mathbf{P} \mathbf{v}}{n-u}} \quad : \text{standard deviation } a \text{ posteriori}$$

$$8) \quad \underset{u,u}{\mathbf{K}} = \hat{s}_0^2 \underset{u,u}{\mathbf{Q}} \quad : \text{variance-covariance matrix}$$

$$9) \quad \hat{\mathbf{L}}_{n,1}^! = \varphi(\hat{\mathbf{X}}_{n,1}) \quad : \text{final computing test}$$

The adjustment system must be solved iteratively if only coarse approximate values are given for non-linear problems (e.g. bundle adjustment – see section 4.3). In this case the corrected approximate values in iteration  $k$  of step (6) are used as new starting values for the linearised functional model of next iteration  $k+1$ , until the sum of added corrections for the unknowns is less than a given threshold.

$$\mathbf{X}_{k+1}^0 = \mathbf{X}_k^0 + \hat{\mathbf{x}}_k$$

In order to solve the normal system of equations (2) in step (3), the Jacobian matrix  $\mathbf{A}$  has to be of full column rank.

$$\underset{n,u}{r} = \text{rank}(\mathbf{A}) = u$$

This requirement means that the included observations allow a unique solution for the vector of unknowns and that the inverse of the normal equation matrix  $\mathbf{N}$  exists. For adjustment problems where some observations are missing for a unique solution, a rank defect  $d$  is detected:

$$d = u - r \quad : \text{rank defect} \quad (2.81)$$

This problem occurs, for example, in the adjustment of points in coordinate systems which are not uniquely defined by known reference points, or other suitable observations (datum defect).

The resulting singular system of normal equations can be solved with the help of the Moore-Penrose inverse (see section 4.3.3.3) or by including suitable constraints.

### 2.3.2.3 Conditional least squares adjustment

The above method of general least squares adjustment is based on a set of observation equations that model the measured observations as a function of the unknowns. An extended adjustment model results when additional constraints are incorporated between the unknowns. This method may be called the conditional least squares adjustment. The following cases are examples of such constraints between unknowns (see section 4.3.2.3):

- Coordinates of a number of adjusted object points must be located on a common geometric element e.g. a straight line, plane or cylinder.
- Two adjusted object points must have a fixed separation resulting, for example, from a high accuracy distance measurement between them.

The correction equations derived earlier are then extended by a number  $r'$  of non-linear constraints:

$$\Psi(\tilde{\mathbf{X}}) = \begin{bmatrix} \Psi_1(\tilde{\mathbf{X}}) \\ \Psi_2(\tilde{\mathbf{X}}) \\ \vdots \\ \Psi_{r'}(\tilde{\mathbf{X}}) \end{bmatrix} = \mathbf{0} \quad : \text{constraints} \quad (2.82)$$

Using approximate values, these constraint equations are linearized in an analogous way to the observation equations:

$$\mathbf{B}_{r',u} = \left( \frac{\partial \Psi(\mathbf{X})}{\partial \mathbf{X}} \right)_0 \quad : \text{linearised constraint equations} \quad (2.83)$$

Inconsistencies  $\mathbf{w}$  result from the use of approximate values instead of expected values for the unknowns:

$$\mathbf{B}\hat{\mathbf{x}} = -\mathbf{w} \quad : \text{vector of inconsistencies} \quad (2.84)$$

The linearised functional model reduces to:

$$\begin{aligned} \mathbf{A}\hat{\mathbf{x}} - \mathbf{v} &= \mathbf{w} \quad : \text{vector of inconsistencies} \\ \mathbf{B}\hat{\mathbf{x}} + \mathbf{w} &= \mathbf{0} \end{aligned} \quad (2.85)$$

The Gauss-Markov model (2.70) must be extended as follows:

$$\mathbf{v}^T \mathbf{P} \mathbf{v} + 2\mathbf{k}(\mathbf{B}\hat{\mathbf{x}} + \mathbf{w}) \rightarrow \min \quad (2.86)$$

which leads to the following extended normal system of equations (e.g. Wolf 1975):

$$\begin{bmatrix} \mathbf{A}^T \mathbf{P} \mathbf{A} & | & \mathbf{B}^T \\ \hline \mathbf{B} & | & \mathbf{0} \end{bmatrix} \begin{bmatrix} \hat{\mathbf{x}} \\ \mathbf{k} \end{bmatrix} + \begin{bmatrix} -\mathbf{A}^T \mathbf{P} \mathbf{I} \\ \mathbf{w} \end{bmatrix} = \mathbf{0} \quad : \text{normal equations}$$

$$\bar{\mathbf{N}} \quad \bar{\mathbf{x}} + \bar{\mathbf{n}} = \mathbf{0} \quad (2.87)$$

Here  $\mathbf{k}$  is the vector of Lagrangian multipliers. The numerical values of  $\mathbf{k}$  are not normally of interest, although the condition that  $\mathbf{A}^T \mathbf{P} \mathbf{v} + \mathbf{B}^T \mathbf{k} = 0$  can be tested for validity. Only the first  $u$  elements of the solution vector  $\tilde{\mathbf{x}}$  are therefore important.

The *a posteriori* standard deviation is then given by:

$$\hat{s}_0 = \sqrt{\frac{[p_{vv}]}{n-u+r'}} = \sqrt{\frac{p v^2}{n-u+r'}} \quad (2.88)$$

The redundancy  $f$  (degrees of freedom defined by the number of excess observations) changes to  $f = n-u+r'$ . Additional constraints can therefore increase redundancy or they can effectively compensate for missing observations which lead to a rank defect (see also free net adjustment, section 4.3.3.3).

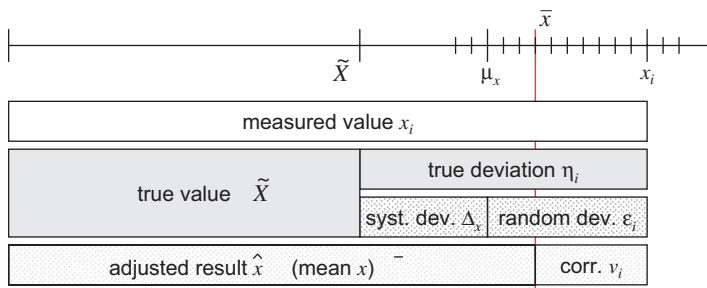
### 2.3.3 Measures of quality

Fig. 2.19 illustrates the relationship between the true value  $\tilde{X}$ , the expected value  $\mu_x$ , the mean or adjusted value  $\hat{x}$  and the single observation  $x_i$ . True value and expected value can differ due to systematic errors  $\Delta_x$ . The true deviation  $\eta_i$  is the sum of a systematic component  $\Delta_x$  and a random component  $\epsilon_i$ .

Since true value and expected value are unknown with a finite number of measurements, quality assessment of measured values is based on their residuals  $v_i$ . The quality values discussed below are based on statistical measures. Depending on application, the quality of a measured value (e.g. fit between cylinder and bore) must potentially be assessed by taking into account relevant associated conditions (see section 2.4.4).

#### 2.3.3.1 Precision and accuracy

The accuracy of observations and adjusted unknowns are of prime interest when analysing quality in an adjustment procedure. The calculated stochastic values provide information about the quality of the functional model with respect to the input data. This criterion is referred to as precision since it describes an internal quality of the adjustment process. In contrast, the term accuracy should only be used if a comparison to reference data of higher accuracy is performed. However, in practice accuracy is widely used as a general term for quality.



**Figure 2.19** True, stochastic and systematic deviation and correction (residuum)  
(after Möser *et al.* 2000)

*Standard deviation*

Using the cofactor matrix  $\mathbf{Q}$  or the covariance matrix  $\mathbf{K}$  (see equation 2.79), the standard deviations of unknowns can be obtained:

$$\mathbf{Q}_{\hat{x}\hat{x}} = \mathbf{Q} = \begin{bmatrix} q_{11} & q_{12} & \cdots & q_{1u} \\ q_{21} & q_{22} & \cdots & q_{2u} \\ \vdots & \vdots & \ddots & \vdots \\ q_{u1} & q_{u2} & \cdots & q_{uu} \end{bmatrix} \quad : \text{cofactor matrix of unknowns} \quad (2.89)$$

The cofactor matrix of adjusted observations is derived by

$$\mathbf{Q}_{\tilde{x}\tilde{x}} = \mathbf{A} \mathbf{Q} \mathbf{A}^T \quad : \text{cofactor matrix of adjusted observations} \quad (2.90)$$

The empirical standard deviation of unit weight is given by:

$$\hat{s}_0 = \sqrt{\frac{\mathbf{v}^T \mathbf{P} \mathbf{v}}{n-u}} \quad (2.91)$$

with redundancy:  $r = n-u$

If the *a posteriori* standard deviation diverges from the *a priori* standard deviation  $s_0$ , two possible sources of error are indicated. Firstly, the stochastic model may be set up incorrectly, although it should be noted that  $s_0$  does not affect the numerical values of the adjusted unknowns. Secondly, the functional model may be insufficient. For example, unmodelled systematic errors, or observations with gross errors, will affect the values of the unknowns.

According to (2.68) and (2.89) the standard deviation of a single unknown  $x_j$  is given by

$$\hat{s}_j = \hat{s}_0 \sqrt{q_{jj}} \quad (2.92)$$

where  $q_{jj}$  are the elements of the principal diagonal of matrix  $\mathbf{Q}$ .

*Root mean square*

In many cases adjustment results are reported as root mean square errors instead of the above defined standard deviation. The RMS value (root mean square) is the square root of the mean squared difference between  $n$  given nominal values  $X_{\text{nom}}$  and corresponding adjusted observations  $X_{\text{obs}}$

$$RMS = \sqrt{\frac{\sum (X_{\text{nom}} - X_{\text{obs}})^2}{n}} \quad (2.93)$$

In contrast, the RMSE value (root mean square error) indicates the RMS error of adjusted observations with respect to the mean of adjusted observations:

$$RMSE = \sqrt{\frac{\sum (X_i - \bar{X})^2}{n}} \quad (2.94)$$

It should be noted that RMS and RMSE are often not exactly defined or separated in practice. For appropriately large  $n$ , the RMSE is equal to the empirical standard deviation.

### Span

The span  $R$  denotes the maximum separation between two observations of a set of measurements.

$$R = X_{\max} - X_{\min} \quad (2.95)$$

The span is not unbiased as the observations may contain errors. However, it is important in metrology since, for manufacturing purposes, it may be necessary that all measured values lie within particular limits (tolerances). Hence, the span implicitly describes a confidence interval of 100% probability (see section 2.3.3.2). The span can also be defined as the difference between the minimum and maximum residuals in a data set.

### 2.3.3.2 Confidence interval

It is generally assumed that the observations in an adjustment process have a normal (Gaussian) random error distribution. Given a normally distributed random variable  $l$  with expected value  $\mu$  and standard deviation  $\sigma$ , the probability density function is given by:

$$f(x) = \frac{1}{\sigma\sqrt{2\pi}} \exp\left(-\frac{1}{2} \frac{(x-\mu)^2}{\sigma^2}\right) \quad (2.96)$$

The error of the random variable is defined by:

$$\varepsilon = l - \mu \quad : \text{random error} \quad (2.97)$$

This is valid for a normally distributed sample with an infinite number of sample points and an expected value defined as:

$$\mu = E\{x\} = \tilde{x} \quad : \text{expected value (true value)} \quad (2.98)$$

Fig. 2.20 shows the probability density function of the normalized Gaussian distribution ( $\mu = 0$ ,  $\sigma = 1$ ) and, for comparison, the systematically shifted distribution corresponding to the non-centrality parameter  $\Delta = 1^1$ . The area underneath the curve, between specified limits on the horizontal axis, corresponds to the probability that the error of a random variable lies between these limits. The total area under the curve = 1 and the probability limits are usually defined as a symmetrical factor of the standard deviation.

$$P\{-k\sigma < \varepsilon < k\sigma\}$$

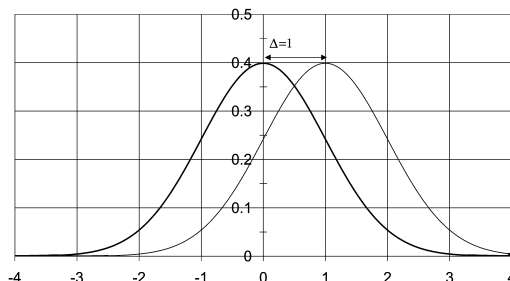


**Figure 2.20** Standardised Gaussian distribution

<sup>1</sup> In the following it is assumed that no systematic deviations exist, hence  $\Delta=0$ .

**Table 2.1** Probability of error  $|\varepsilon| < k\sigma$  at different degrees of freedom

Gaussian distribution		Student distribution			
$k$	$P$ $f=\infty$	$P$ $f=2$	$P$ $f=5$	$P$ $f=10$	$P$ $f=20$
1	68.3%	57.7%	63.7%	65.9%	67.1%
2	95.4%	81.6%	89.8%	92.7%	94.1%
3	99.7%	90.5%	97.0%	98.7%	99.3%

Table 2.1 shows that, in the case of an infinitely large data set (degrees of freedom  $f = \infty$ ), the probability is 68.3% that all deviations are within a single standard deviation of the true value ( $k = 1$ ). The probability rises to 95.4% for 2 standard deviations ( $k = 1.96$  for  $P = 95\%$ ). Lastly, only 0.3% of all errors lie outside limits defined by 3 standard deviations.

In the case of large but finite data sets, the Gaussian distribution is replaced by the t-distribution (Student distribution). The probability  $P$  that a deviation is larger than a given factor  $k$  of the standard deviation, increases with increasing degrees of freedom. For very large degrees of freedom the t-distribution becomes equivalent to the Gaussian distribution.

For real (finite) data sets, only estimates  $\hat{x}$  and  $\hat{s}$  of the true values  $\mu$  and  $\sigma$  can be computed. However, an interval between two limiting values  $C_u$  and  $C_o$  can be defined, within which  $\hat{x}$  is determined with probability  $P$  (Fig. 2.21). This confidence interval is given by

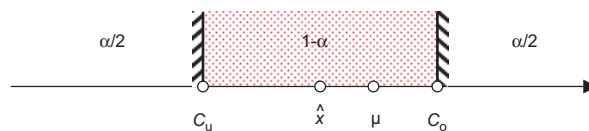
$$\begin{aligned} P\{C_u \leq \hat{x} \leq C_o\} &= 1 - \alpha \\ P\{\hat{x} < C_u\} &= \frac{\alpha}{2} \end{aligned} \quad (2.99)$$

with confidence level  $1 - \alpha$ .

The confidence limits for empirical estimate  $\hat{x}$  with a given empirical standard deviation are defined as:

$$\begin{aligned} C_u &= \hat{x} - t_{f,1-\alpha/2} s_{\hat{x}} \\ C_o &= \hat{x} + t_{f,1-\alpha/2} s_{\hat{x}} \end{aligned} \quad (2.100)$$

Here  $t$  is a quantile of the t-distribution. For example,  $t_{5, 0.975} = 2.57$  corresponds to a confidence level of 95% ( $\alpha = 0.05$ ) and  $f = 5$  degrees of freedom. The confidence interval therefore increases with a finite number of excess measurements i.e. the confidence that estimate  $\hat{x}$  lies between defined limits is reduced. Fig. 2.22 shows the limiting curves of confidence intervals for different degrees of freedom and different confidence levels.

**Figure 2.21** Confidence interval

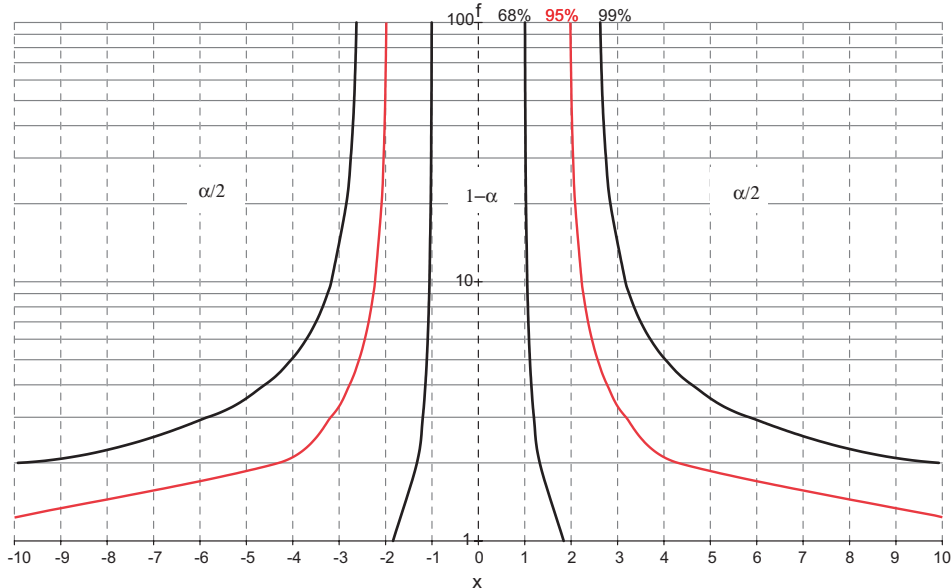


**Figure 2.22** Confidence intervals with different t-distributions

### 2.3.3.3 Correlations

In addition to standard deviations, dependencies between adjusted parameters can also be investigated in order to assess the quality of an adjustment result. They govern the coefficient of determination (the square of the correlation coefficient) and hence the adequacy of the functional model and geometric configuration of the observations.

According to (2.67) the covariance matrix provides the correlations between single parameters:

$$\mathbf{K}_{\hat{x}\hat{x}} = \hat{s}_0^2 \mathbf{Q}_{\hat{x}\hat{x}} = \begin{bmatrix} \hat{s}_1^2 & \rho_{12}\hat{s}_1\hat{s}_2 & \cdots & \rho_{1u}\hat{s}_1\hat{s}_u \\ \rho_{21}\hat{s}_2\hat{s}_1 & \hat{s}_2^2 & \cdots & \rho_{2u}\hat{s}_2\hat{s}_u \\ \vdots & \vdots & \ddots & \vdots \\ \rho_{u1}\hat{s}_1\hat{s}_u & \rho_{u2}\hat{s}_1\hat{s}_2 & \cdots & \hat{s}_u^2 \end{bmatrix} \quad (2.101)$$

The correlation coefficient  $\rho_{ij}$  between two unknowns  $i$  and  $j$  is defined by<sup>1</sup>:

$$\rho_{ij} = \frac{\hat{s}_{ij}}{\hat{s}_i\hat{s}_j} \quad -1 \leq \rho_{ij} \leq +1 \quad (2.102)$$

Higher correlation coefficients indicate linear dependencies between parameters. They should be avoided particularly because the inversion of the normal equation matrix, and hence the adjustment solution, can then become numerically unstable.

<sup>1</sup> Here the notation  $\rho$  is used for the empirical correlation coefficient in order to avoid confusion with the redundancy number.

### 2.3.3.4 Reliability

The reliability of an adjustment process indicates the potential to control the consistency of the observations and the adjustment model. It depends on the number of excess observations (total redundancy) and the geometric configuration (configuration of images). Reliability gives a measure of how well gross errors (outliers) can be detected in the set of observations.

Essential information about reliability can be derived from the cofactor matrix of residuals:

$$\mathbf{Q}_{vv} = \mathbf{Q}_{ll} - \mathbf{A}\mathbf{Q}\mathbf{A}^T \quad : \text{cofactor matrix of residuals} \quad (2.103)$$

The total redundancy in an adjustment is given by

$$r = n - u = \text{trace}(\mathbf{Q}_{vv}\mathbf{P}) = \sum r_i \quad (2.104)$$

where  $r_i$  are the elements of the principal diagonal of the redundancy matrix  $\mathbf{R} = \mathbf{Q}_{vv}\mathbf{P}$ .

$$\mathbf{R} = \mathbf{Q}_{vv}\mathbf{P} = \begin{bmatrix} r_{11} & & & \\ & r_{22} & & \\ & & \ddots & \\ & & & r_{nn} \end{bmatrix} \quad : \text{redundancy matrix} \quad (2.105)$$

$r_i$  is denoted as the redundancy number of an observation  $l_i$  with respect to the total redundancy  $r$  where

$$0 \leq r_i \leq 1$$

The redundancy number of an observation indicates the relative part of an observation which is significantly used for the estimation of the unknowns ( $1-r_i$ ), or which is not used ( $r_i$ ). Small redundancy numbers correspond to weak configurations which are hard to control, whilst high redundancy numbers enable a significant control of observations. If an observation has a redundancy number  $r_i = 0$ , it cannot be controlled by other observations. Hence, a gross error in this observation cannot be detected but it has a direct influence on the estimation of unknowns. If an observation has a very high redundancy number (0.8 to 1), it is very well controlled by other observations. When optimising an adjustment, such observations can initially be eliminated without a significant effect on the adjustment result.

The relation between residuals and observations is defined by:

$$\mathbf{v} = \mathbf{A}\hat{\mathbf{x}} - \mathbf{l} = \mathbf{R}\mathbf{l} \quad (2.106)$$

Hence, for gross (systematic) observation errors  $\Delta\mathbf{l}$ :

$$\Delta\mathbf{v} = -\mathbf{R}\Delta\mathbf{l} \quad (2.107)$$

Equation (2.107) does permit the detection of gross errors to be quantified because gross errors do not have correspondingly large residuals when redundancy numbers are small. A normalised residuum according to Baarda (1968) is therefore used:

$$w_i = \frac{v_i}{\hat{s}_{v_i}} \quad (2.108)$$

The standard deviation of a residual is given either by the cofactor matrix or redundancy numbers as follows:

$$\hat{s}_{v_i} = \hat{s}_0 \sqrt{(\mathbf{Q}_{vv})_{ii}} = \hat{s}_l \sqrt{(\mathbf{Q}_{vv}\mathbf{P})_{ii}} = \hat{s}_l \sqrt{r_i} \quad (2.109)$$

Here it is obvious that a redundancy number of  $r_i = 0$  leads to an indeterminate value of  $w_i$  and no error detection is then possible. The normalised residuals are normally distributed with expectation 0 and standard deviation 1. To detect a gross error they are compared with a threshold  $k$ :

$$|w_i| \begin{cases} > k: \text{gross error} \\ \leq k: \text{no gross error} \end{cases} \quad (2.110)$$

In order to compute the threshold value  $k$ , a statistical test is used where the value  $\delta_0$  (non-centrality parameter) is defined (Ackermann *et al.* 1980):

$$\delta_0 = \delta_0(\alpha, \beta)$$

where  $\alpha$  : probability of identifying an error-free value as a gross error  
(significance level)

$\beta$  : probability of identifying a defective value as a gross error  
(power of test)

This test establishes a null hypothesis which states that only randomly distributed errors may occur and the expected value of the normalised residuals must therefore be zero.

$$E\{w_0\} = 0 \quad (2.111)$$

The probability of a false decision is equal to  $\alpha$  (type 1 error). This is the decision that residuals  $w_i$  lie outside the range  $\pm k$  and are therefore excluded. Here  $k$  denotes a quantile of the t-distribution.

If a systematically disturbed gross error occurs, the expected value of the corresponding normalised residuum is not equal to zero and has standard deviation 1:

$$E\{w_a\} \neq 0 \quad (2.112)$$

Given the alternative hypothesis that only observations where  $|w_i| > k$  are identified as gross errors, a possible number of outliers still remain in the data set. The probability of this false decision (type 2 error) is  $1-\alpha$  (Fig. 2.23).

Using equations (2.107) and (2.108) a lower expected value can be defined for a gross error that can be detected significantly with power of test,  $\beta$ .

$$E\{\Delta l_a\} = \frac{\delta_0}{\sqrt{r_i}} s_{l_i} = \delta'_0 s_{l_i} \quad (2.113)$$

The following term is normalised with respect to  $\hat{s}_{l_i}$ :

$$\delta'_{0,i} = \frac{E\{\Delta l_a\}}{s_{l_i}} = \frac{\delta_0}{\sqrt{r_i}} \quad (2.114)$$

It serves as a measure of internal reliability of an adjustment system. It defines the factor by which a gross observation error  $\Delta l_a$  must be larger than  $\hat{s}_{l_i}$  in order to be detected with probability  $\beta$ .<sup>1</sup>

---

<sup>1</sup> Kraus (1997) denotes the expected value  $E\{\Delta l_a\}$  as IZ-value (internal reliability).

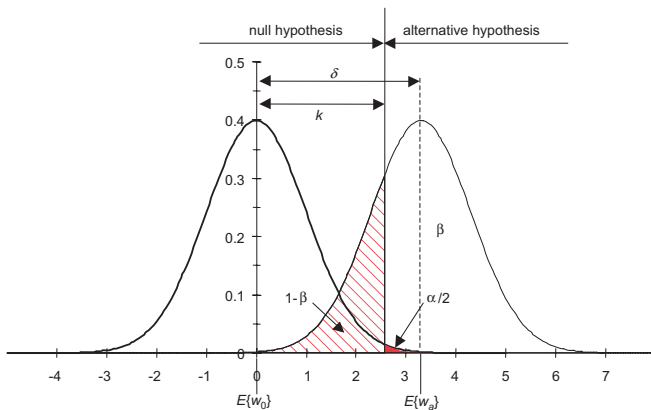


**Figure 2.23** Probability densities for null and alternative hypotheses

**Table 2.2** Test statistics and internal reliability for different significance numbers and power of test

	$\alpha = 5\%$ $\beta = 75\%$	$\alpha = 1\%$ $\beta = 93\%$	$\alpha = 0.1\%$ $\beta = 80\%$
$k$	1.96	2.56	3.29
$\delta'_0$	3.9	4.0	4.1

Table 2.2 shows some test statistics resulting from a chosen significance level  $\alpha$  and power of test  $\beta$ . The selected probabilities lead to similar measures of the internal reliability. It becomes clear that with increasing significance level (i.e. decreasing confidence level) the power of test is reduced and is therefore less effective.

In general a value of  $\delta'_0 = 4$  is appropriate for photogrammetric bundle adjustment (see section 4.3). It is also an appropriate value for the decision threshold  $k$  in inequality (2.110). In order to use this standard value for bundle adjustments, a high redundancy is required. Equation (2.114) clearly shows that the test value depends on the *a posteriori* standard deviation of a single observation and hence is a function of the standard deviation of unit weight  $\hat{s}_0$ . Smaller gross errors can therefore only be detected when  $\hat{s}_0$  becomes sufficiently small after iteration that its value is of the order of the precision of the observations (measurement precision).

In order to design a measuring project, the internal reliability can be calculated prior to knowledge of actual observations (measurement values) because the necessary information can be obtained from the Jacobian matrix  $\mathbf{A}$  and the (assumed) *a priori* accuracy values for the observations (see section 7.1.4.1).

During or after an iterative adjustment the internal reliability is used as criterion for the automated elimination of gross data errors.

The external reliability indicates the influence of defective observations on the estimated unknowns. For this purpose, the vector of internal reliability values, defined as in equation (2.113), is used in the system of equations (2.79). For each unknown it is possible to compute a total number of  $n$  values of external reliability, each dependent on an observation.

### 2.3.4 Error detection in practice

It is difficult to avoid gross data errors (outliers) in real projects. In photogrammetric applications they typically occur as a result of faulty measurements, errors in point identification, or mistakes in image numbering. Gross errors must be eliminated from the data set because they affect all estimated unknowns and standard deviations, leading to a significantly distorted adjustment result.

The residuals calculated in the adjustment should not be used directly for the detection of outliers. Residuals not only result from errors in the set of observations but also from errors in the geometric model i.e. a functional model of the adjustment which is incomplete. Model and data errors can both be present and their effects may overlap.

Most approaches for detection and elimination of gross errors are based on the assumption that only very few outliers exist, and in extreme cases only one. The method of least-squares adjustment described above is an optimal method which disperses the observation errors over all observations in the data set and where larger deviations affect the unknowns more than smaller. Where gross errors are present this results in a smearing effect. The ability to recognize a gross error is therefore limited, especially if several such outliers occur at the same time. Where there is an unfavourable geometric configuration of unknowns and number of outliers, even error-free observations may be identified as having gross errors. It is therefore critically important to eliminate only those observations that can be identified without doubt as errors. The elimination of outliers should always be associated with an analysis of the entire measurement task.

#### 2.3.4.1 Error detection without adjustment

If an adjustment process does not converge it may be reasonable to check the consistency of the original observations with respect to their initial values. Here the “residuals”, as defined by:

$$\mathbf{v} = \mathbf{L} - \mathbf{L}^0 \quad (2.115)$$

may indicate large discrepancies between measurement data and initial values, for example due to mistakes in point or image identification. However, a discrepancy here may simply be due to bad initial values and not necessarily to faulty measurements.

#### 2.3.4.2 Data snooping

Data snooping (Baarda 1968) is a method of error detection based on the value of internal reliability derived in section 2.3.3.2. It is based on the assumption that only one gross error exists in the data set.

After each iteration of the adjustment the observation is eliminated which, on the basis of the decision function (2.110), corresponds to the largest normalised residual  $w_i$ . The complete adjustment procedure is set up again and the computation repeated until no gross errors remain in the set of observations.

In cases where several large residuals  $w_i$  exist, and where their geometric configuration ensures they are independent of each other, it is possible to detect more than one outlier simultaneously. However, one should still check carefully those observations which are suspected as gross errors.

#### 2.3.4.3 Variance component estimation

The internal reliability value used in data snooping is a function of the standard deviation of the adjusted observations. These are derived from the covariance matrix by multiplication with the

standard deviation of unit weight  $\hat{s}_0$ . Since  $\hat{s}_0$  is a global value influenced by all residuals, it is really only useful for observations of equal accuracy. Data sets with different types of observations, or different levels of accuracy, should therefore be divided into separate groups with homogeneous accuracy.

In order to set up the weight matrix  $\mathbf{P}$ , each separate observation group  $g$  is assigned its own *a priori* variance:

$$s_{0,g}^2 \quad : \text{a priori variance of unit weight}$$

This variance, for example, can be derived from the existing known accuracy of a measuring device used for that specific observation group.

After computing the adjustment, the *a posteriori* variance can be determined:

$$\hat{s}_{0,g}^2 = \frac{\mathbf{v}_g^T \mathbf{P}_g \mathbf{v}_g}{r_g} \quad : \text{a posteriori variance of unit weight}$$

where  $r_g = \sum (r_i)_g$  (2.116)

Using the *a posteriori* variance of unit weight, it is possible to adjust the *a priori* weights in succeeding adjustments until the following condition is achieved:

$$Q_g = \frac{\hat{s}_{0,g}}{s_{0,g}} = 1 \quad (2.117)$$

Subsequently, the normal data snooping method can be used.

Taking equation (2.68) into account, the variance of unit weight can be used to calculate the variance of a complete observation group.

#### 2.3.4.4 Robust estimation with weighting functions

The comments above indicate that the residuals resulting from an adjustment process are not directly suitable for the detection of one or more gross errors. Different approaches have therefore been developed for defining the weights  $p_i$  as a function of the residuals in successive iterations. If the weighting function is designed such that the influence of a gross error is reduced as the error becomes larger, then it is referred to as robust estimation (robust adjustment). One possible approach is given by the following function (Klein 1984):

$$p'_i = p_i \frac{1}{1 + (a | v_i |)^b} \quad (2.118)$$

For  $v_i = 0$  it reduces to  $p'_i = 1$  and for  $v_i = \infty$  it reduces to  $p'_i = 0$ . The parameters  $a$  and  $b$  form the curve of a bell-shaped weighting function. With

$$a_i = \frac{\sqrt{p_i}}{\sqrt{r_i s_0 k}} = \frac{1}{s_{v_i} k} \quad (2.119)$$

the parameter  $a$  is controlled by the redundancy number of an observation. Definition of parameters  $b$  and  $k$  is done empirically. With a correct choice of parameters, the quotient  $Q$  (see preceding section) converges to 1.

Kruck (1995) proposes a weighting function that is also based on redundancy numbers:

$$p'_i = p_i \frac{\tan\left(\frac{1-r_m}{c}\right)}{\tan\left(\frac{1-r_i}{c}\right)} \quad (2.120)$$

The constant  $c$  is defined empirically,  $r_m$  is referred to as the average redundancy or constraint density:

$$r_m = \frac{n-u}{n} \quad (2.121)$$

The weights become constant values when the stability  $r_i = r_m$  is reached (balanced observations). Kruck (1995) gives an example in the case of relative orientation, known to be sensitive to gross errors, where this procedure reliably detects a large gross error.

Procedures for robust estimation are primarily designed to reduce the effect of so-called leverage points. Leverage points in the sense of adjustment are those observations which have a significant geometric meaning but only small redundancy numbers. Gross errors at leverage points affect the complete result but are barely detectable. Using balanced weights, leverage points and observations with gross errors are temporarily assigned the same redundancy numbers as every other observation. As a result they can be detected more reliably. After elimination of all defective observations, a final least-squares adjustment is calculated using the original weights.

#### 2.3.4.5 Robust estimation according to L1-norm

In recent times more attention has been paid to the principle of adjustment according to the L1 norm, especially for gross error detection in weak geometric configurations. For example, it is used to calculate approximate orientation values using data sets containing gross errors (e.g. Kampmann 1986, Fellbaum 1996).

The L1 approach is based on the minimisation of the absolute values of the residuals, whilst the L2 approach (least squares) minimises the sum of squares of the residuals:

$$\text{L1 norm: } \sum |v| \rightarrow \min \quad (2.122)$$

$$\text{L2 norm: } \sum v^2 \rightarrow \min$$

The solution of the system of equations using the L1 approach is a task in linear optimisation. It is much more difficult to handle than the L2 approach in terms of mathematics, error theory and computation algorithms. One solution is given by the Simplex algorithm known from linear programming.

The L1 approach is also suitable for balancing weights according to equation (2.121). Fellbaum and Godding (1995) also report on an example of relative orientation where several gross errors can be detected simultaneously. In theory it is possible with the L1-norm to process data sets with up to 50% gross errors. The reason is that the L1 solution uses the median value whereas the L2 solution is based on the arithmetic mean which has a smearing effect.

After error elimination based on the L1-norm, the final adjustment should be calculated according to the least-squares approach.

## 2.3.5 Computational aspects

### 2.3.5.1 Linearisation

In order to linearise the functional model at initial values two methods are available:

- exact calculation of the first derivative
- numerical differentiation

Exact calculation of the differential coefficient

$$\left( \frac{\partial \varphi(X)}{\partial X} \right)_0$$

may require considerably more manual programming effort for complex functions such as those expressed by rotation matrices.

In contrast, numerical differentiation is based on small changes to the initial values of unknowns in order to calculate their effects on the observations:

$$\begin{aligned} L_{+\Delta x}^0 &= \varphi(X^0 + \Delta X) \\ L_{-\Delta x}^0 &= \varphi(X^0 - \Delta X) \end{aligned} \quad (2.123)$$

The difference quotients are then:

$$\frac{\Delta \varphi(X)}{\Delta X} = \frac{L_{+\Delta x}^0 - L_{-\Delta x}^0}{2\Delta X} \approx \frac{\partial \varphi(X)}{\partial X} \quad (2.124)$$

In a computer program the function  $\varphi$  can be entered directly, for example in a separate routine. The set up of the Jacobian matrix  $\mathbf{A}$  and subsequent adjustment procedure can then be programmed independently of the functional model. Only the increment  $\Delta X$  need be adjusted if necessary.

Compared with numerical differentiation, the exact calculation of differential quotients leads to faster convergence. If suitable initial values are available, then after a number of iterations both adjustment results are, for practical purposes, identical.

### 2.3.5.2 Normal systems of equations

In order to solve solely for the solution vector  $\hat{x}$ , efficient decomposition algorithms can be used which do not require the inverse of the normal equation matrix  $\mathbf{N}$ , for example the Gaussian algorithm. However, for many photogrammetric and geodetic calculations a quality analysis based on the covariance matrix is required and so the inverse of  $\mathbf{N}$  must be computed. The dimension of the normal system of equations based on (2.78) is  $u \times u$  elements. For photogrammetric bundle adjustments, the number of unknowns  $u$  can easily range from a few hundred up to a few thousand. Often a direct inversion of the normal equation matrix is not possible or else consumes too much computation time.

Usually the matrix  $\mathbf{N}$  is factorised according to Cholesky. Using the triangular rearrangement

$$\mathbf{C}^T \mathbf{C} = \mathbf{N} \quad (2.125)$$

inserted into equation (2.78)

$$\mathbf{C}^T \mathbf{C} \hat{x} = \mathbf{n} \quad (2.126)$$

and the substitution

$$\mathbf{C}\hat{\mathbf{x}} = \mathbf{g} \quad (2.127)$$

the equation becomes

$$\mathbf{C}^T \mathbf{g} = \mathbf{n} \quad (2.128)$$

For the computation of  $\mathbf{g}$ , and subsequently  $\hat{\mathbf{x}}$ , only a diagonal matrix must be inverted.

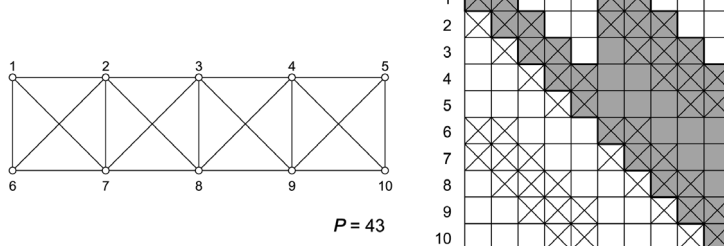
### 2.3.5.3 Sparse matrix techniques and optimisation

The computational effort to solve the normal system of equations is mainly a function of the dimensions of matrix  $\mathbf{C}$ . Since matrix  $\mathbf{N}$  can consist of numerous zero elements relating to unknowns which are not connected by an observation, then these elements are also present in  $\mathbf{C}$ .

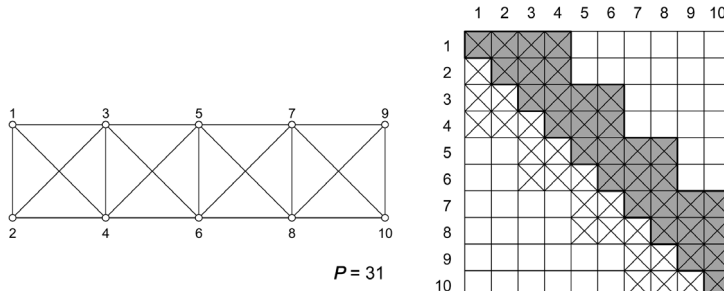
Sparse techniques provide efficient use of RAM. Instead of a full matrix, a profile is stored which, for each column of a matrix, only records elements from the first non-zero value up to the principal diagonal, together with a corresponding index value.

Fig. 2.24 shows an example of a network of observations and the corresponding structure of the normal equation matrix. The crosses indicate connections between unknowns while the blank fields have zero values. For example, point 2 is connected to points 1, 3, 6, 7 and 8.

In this example the size of the profile to be stored i.e. the number of stored matrix elements, amounts to  $P = 43$ . In order to reduce the profile size without modifying the functional relationships, the point order can be sorted (Banker's algorithm), leading to the result of Fig. 2.25. The profile size in this case has been reduced to  $P = 31$ .



**Figure 2.24** Order of point numbers without optimisation (after Kruck 1983)



**Figure 2.25** Order of point numbers after optimisation (after Kruck 1983)

Since the resulting computational effort for matrix inversion is a quadratic function of the profile size, optimisation is of major importance for solving large systems of equations. For further information see Kruck (1983) and Hinsken (1987).

## 2.4 Geometric elements

The geometric reconstruction of a measured object is the major goal of a photogrammetric process. For this reason a short summary of geometric elements and their mathematical definition is given in this section. It distinguishes between planar elements, spatial elements and surface descriptions that are the basic result of a photogrammetric measurement. For a detailed description of the methods of analytical geometry, the reader should refer to specialist literature relating to geometry and 3D computer graphics e.g. Foley *et al.* (1995), Watt (1999), Shirley (2002).

Except in very few cases, photogrammetric methods are based on measurement of discrete object points. Geometric elements such as straight lines, planes, cylinders etc. are normally calculated in a post-processing step using the measured 3D points. For over-determined solutions, least-squares fitting methods are used. Computed geometric elements can then either be combined or intersected in order to create additional geometric elements such as the intersection line between two planes. Alternatively, specific dimensions can be derived from them, such as the distance between two points (Fig. 2.26).

In addition to the determination of regular geometric shapes, the determination and visualisation of arbitrary three dimensional surfaces (free-form surfaces) is of increasing importance. This requires a basic knowledge of different ways to represent 3D surfaces, involving point grids, triangulation, analytical curves etc.

Many of these calculations are embedded in state-of-the-art 3D CAD systems or programs for geometric quality analysis. CAD and photogrammetric systems are therefore often combined. However, geometric elements may also be directly employed in photogrammetric calculations e.g. as conditions for the location of object points (see section 4.3.2.3). In addition, some evaluation techniques enable the direct calculation of geometric 3D elements without the use of discrete points (e.g. contour method, section 4.4.3.2).

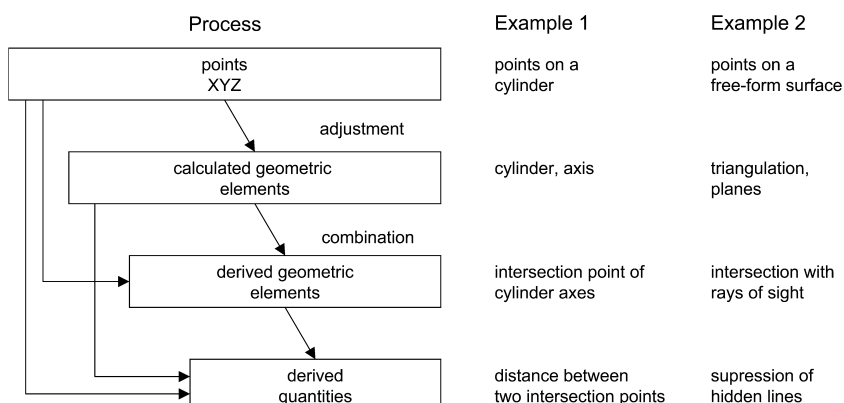


**Figure 2.26** Calculation progress for geometric elements

## 2.4.1 Analytical geometry in the plane

### 2.4.1.1 Straight line

#### Parametric form

The straight line  $g$  between two points  $P_1$  and  $P_2$  (Fig. 2.27) is to be determined. For all points  $P(x,y)$  belonging to  $g$ , the proportional relationship

$$\frac{y - y_1}{x - x_1} = \frac{y_2 - y_1}{x_2 - x_1} \quad (2.129)$$

leads to the parametric form of the straight line:

$$\begin{aligned} \mathbf{x} &= \mathbf{x}_1 + t(\mathbf{x}_2 - \mathbf{x}_1) \\ \begin{bmatrix} x \\ y \end{bmatrix} &= \begin{bmatrix} x_1 \\ y_1 \end{bmatrix} + t \begin{bmatrix} x_2 - x_1 \\ y_2 - y_1 \end{bmatrix} \end{aligned} \quad (2.130)$$

Point  $P_1(x_1, y_1)$  is defined at  $t = 0$  and point  $P_2(x_2, y_2)$  at  $t = 1$ .

The distance  $d$  of a point  $Q(x, y)$  from the straight line is defined by:

$$d = \frac{(y_2 - y_1)(x - x_1) - (x_2 - x_1)(y - y_1)}{\sqrt{(x_2 - x_1)^2 + (y_2 - y_1)^2}} \quad (2.131)$$

#### Analytical form

The analytical form of a straight line

$$Ax + By + C = 0 \quad (2.132)$$

leads to the following relations (Fig. 2.27):

$$y = mx + c$$

where

$$m = \tan \alpha = -\frac{A}{B} = \frac{y_2 - y_1}{x_2 - x_1} \quad : \text{slope} \quad (2.133)$$

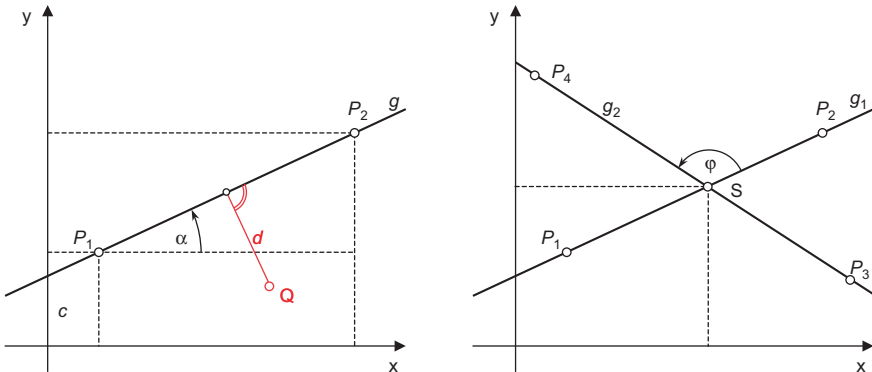


Figure 2.27 Definition of straight lines

$$c = -\frac{C}{B} \quad : \text{intersection point on y axis}$$

The distance  $d$  to point  $Q(x, y)$  is given by:

$$d = \frac{Ax + By + C}{\sqrt{A^2 + B^2}} \quad (2.134)$$

### *Intersection of two straight lines*

Given two straight lines  $g_1$  and  $g_2$ , their point of intersection  $S$  is derived from (2.132) as:

$$\begin{aligned} x_S &= \frac{B_1 C_2 - B_2 C_1}{A_1 B_2 - A_2 B_1} \\ y_S &= \frac{C_1 A_2 - C_2 A_1}{A_1 B_2 - A_2 B_1} \end{aligned} \quad (2.135)$$

From (2.130) two equations for parameters  $t_1$  and  $t_2$  are obtained:

$$\begin{aligned} (x_2 - x_1)t_1 + (x_3 - x_4)t_2 &= x_3 - x_1 \\ (y_2 - y_1)t_1 + (y_3 - y_4)t_2 &= y_3 - y_1 \end{aligned} \quad (2.136)$$

The point of intersection is obtained by substituting  $t_1$  or  $t_2$  into the original straight line equations:

$$\begin{aligned} \mathbf{x}_S &= \mathbf{x}_1 + t_1(\mathbf{x}_2 - \mathbf{x}_1) = \mathbf{x}_3 + t_2(\mathbf{x}_4 - \mathbf{x}_3) \\ \begin{bmatrix} x_S \\ y_S \end{bmatrix} &= \begin{bmatrix} x_1 \\ y_1 \end{bmatrix} + t_1 \begin{bmatrix} x_2 - x_1 \\ y_2 - y_1 \end{bmatrix} = \begin{bmatrix} x_3 \\ y_3 \end{bmatrix} + t_2 \begin{bmatrix} x_4 - x_3 \\ y_4 - y_3 \end{bmatrix} \end{aligned} \quad (2.137)$$

The angle between both lines is given by:

$$\tan \varphi = \frac{A_1 B_2 - A_2 B_1}{A_1 A_2 - B_1 B_2} = \frac{m_2 - m_1}{m_1 m_2 + 1} \quad (2.138)$$

If both lines are defined by their direction vectors

$$\mathbf{a} = \mathbf{x}_2 - \mathbf{x}_1 \quad \text{and} \quad \mathbf{b} = \mathbf{x}_4 - \mathbf{x}_3$$

then the angle between them can be found from the scalar product of both vectors:

$$\cos \varphi = \frac{\mathbf{a} \cdot \mathbf{b}}{|\mathbf{a}| |\mathbf{b}|} = \frac{\mathbf{a}^T \mathbf{b}}{|\mathbf{a}| |\mathbf{b}|} \quad (2.139)$$

The scalar product is zero if the lines are mutually perpendicular.

### *Regression line*

The generalised regression line which is a best-fit to a set of points is the straight line which minimises the sum of squared distances  $d_i$  of all points  $P_i$  (Fig. 2.28). For  $n$  point coordinates with equal accuracy in the x and y directions the criterion is expressed as:

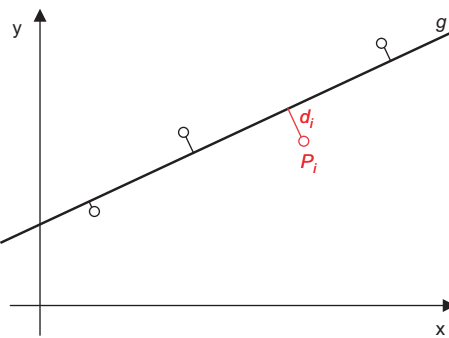


**Figure 2.28** Regression line

$$d_1^2 + d_2^2 + \dots + d_n^2 = \sum_{i=1}^n d_i^2 \rightarrow \min \quad (2.140)$$

The regression line passes through the centroid of the points

$$x_0 = \frac{1}{n} \sum_{i=1}^n x_i \quad \text{and} \quad y_0 = \frac{1}{n} \sum_{i=1}^n y_i \quad (2.141)$$

One point on the straight line is therefore already given. The direction of the line is defined by

$$\tan 2\varphi = \frac{2 \sum (x_i - x_0)(y_i - y_0)}{\sum (y_i - y_0)^2 - (x_i - x_0)^2} \quad (2.142)$$

Alternatively, the direction of the line can be expressed by the direction vector  $(a, b)$  which is equal to the eigenvector of the maximum eigenvalue of matrix  $\mathbf{B}$  (Wolf 1975, Forbes 1989):

$$\mathbf{B} = \mathbf{A}^T \mathbf{A}$$

where  $\mathbf{A} = \begin{bmatrix} x_1 - x_0 & y_1 - y_0 \\ \vdots & \vdots \\ x_n - x_0 & y_n - y_0 \end{bmatrix}$

$$(2.143)$$

Without restriction, the optimisation principle based on minimum quadratic distances according to equation (2.140) can be applied to regression lines in space as well as other best-fit elements.

#### 2.4.1.2 Circle

From the generalised equation for second order curves (conic sections)

$$Ax^2 + 2Bxy + Cy^2 + 2Dx + 2Ey + F = 0 \quad (2.144)$$

The special cases of circle and ellipse are of major interest in close-range photogrammetry.

A circle is given by  $B = 0$ ,  $A = C$  and  $D^2 + E^2 - AF > 0$ . Then equation (2.144) can be rewritten as:

$$x^2 + y^2 + 2mx + 2ny + q = 0 \quad (2.145)$$

For a circle with centre  $(x_C, y_C)$  and radius  $r$  we get

$$(x - x_C)^2 + (y - y_C)^2 = r^2 \quad (2.146)$$

where

$$r = \sqrt{m^2 + n^2 - q} \quad x_C = -m \quad y_C = -n$$

The distance of any point  $P_i(x_i, y_i)$  from the circumference is given by:

$$\begin{aligned} d_i &= r_i - r \\ &= \sqrt{(x_i - x_C)^2 + (y_i - y_C)^2} - r \end{aligned} \quad (2.147)$$

The linear equation (2.145) can easily be used to calculate a best-fit circle. In order to determine the three unknown parameters of a circle, a minimum of three points is required. For a point  $P_i$  on the circumference, the linear observation equation is

$$\varphi_i(m, n, q) = x_i^2 + y_i^2 + 2mx_i + 2ny_i + q = 0 \quad (2.148)$$

The non-linear equation (2.147) can also be used as observation equation. The best-fit circle is obtained by least-squares minimisation of all point distances  $d_i$ . With initial approximate values for the centre coordinates and radius, the design matrix  $\mathbf{A}$  consists of the differential quotients

$$\frac{\partial \varphi_i}{\partial m} = 2x_i \quad \frac{\partial \varphi_i}{\partial n} = 2y_i \quad \frac{\partial \varphi_i}{\partial q} = 1 \quad (2.149)$$

The solution is iterative until the unknowns no longer change appreciably.

### 2.4.1.3 Ellipse

A non-rotated ellipse is defined by setting the conditions  $B = 0$  and  $\text{sign}A = \text{sign}C$  in equation (2.144). Calculation of the five remaining parameters requires a minimum of five points on the circumference of the ellipse. One possible calculation scheme for a best-fit ellipse is now presented, given  $n$  points on the ellipse,  $P_i(x, y)$ ,  $i = 1 \dots n$ .

In the first instance the approximate centre of the ellipse is estimated by the centroid of the ellipse points:

$$x_0 = \frac{1}{n} \sum_{i=1}^n x_i \quad y_0 = \frac{1}{n} \sum_{i=1}^n y_i \quad (2.150)$$

The parameters to be determined are the translations  $\Delta x$ ,  $\Delta y$  of the centre, the semiaxes  $a$ ,  $b$  and the rotation  $\alpha$  of the ellipse. The relation between the rotated and translated system uv and the xy system is given by a coordinate transformation (see Fig. 2.29):

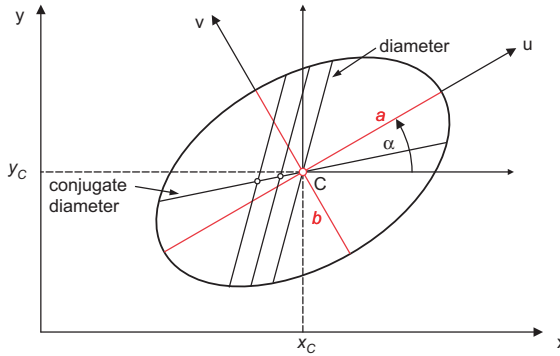


Figure 2.29 Geometry of an ellipse

$$\begin{aligned}x &= x_0 + \Delta x \\&= x_0 + u \cos \alpha - v \sin \alpha \\y &= y_0 + \Delta y \\&= y_0 + u \sin \alpha + v \cos \alpha\end{aligned}\tag{2.151}$$

Inserting the coordinate displacements  $\Delta x$ ,  $\Delta y$  into equation (2.144), multiplication and rearrangement gives:

$$\begin{aligned}&u^2(A \cos^2 \alpha + B \cos \alpha \sin \alpha + C \sin^2 \alpha) \\&+ uv(B \cos^2 \alpha - B \sin^2 \alpha + 2C \cos \alpha \sin \alpha - 2A \cos \alpha \sin \alpha) \\&+ v^2(A \sin^2 \alpha - B \cos \alpha \sin \alpha + C \cos^2 \alpha) \\&+ u(D \cos \alpha + E \sin \alpha) \\&+ v(E \cos \alpha - D \sin \alpha) \\&+ F = 0\end{aligned}\tag{2.152}$$

In simplified form, the conic section in the uv system is given by:

$$A'u^2 + B'uv + C'v^2 + D'u + E'v + F' = 0\tag{2.153}$$

This form describes an ellipse whose axes are now parallel to the uv axes. The condition  $B' = 0$  is also fulfilled. By applying trigonometric formulae to this condition, the rotation angle  $\alpha$  is given by:

$$\tan 2\alpha = \frac{B}{A - C}\tag{2.154}$$

For a circle where  $A = C$  (see above), the rotation angle cannot be determined.

The semiaxes are given by

$$\begin{aligned}a &= \sqrt{\frac{C'D'^2 + A'E'^2 - A'C'F'}{A'^2 C'}} \\b &= \sqrt{\frac{C'D'^2 + A'E'^2 - A'C'F'}{A'C'^2}}\end{aligned}\tag{2.155}$$

The coordinate shifts to the origin of the uv-system (centroid) can be calculated from:

$$\begin{aligned} A'\Delta u^2 + D'\Delta u &= 0 & C'\Delta v^2 + E'\Delta v &= 0 \\ \Rightarrow \Delta u &= -\frac{D'}{A'} & \Rightarrow \Delta v &= -\frac{E'}{C'} \end{aligned} \quad (2.156)$$

Hence, the centre of the ellipse in the original system xy is given by

$$\begin{aligned} x_C &= x_0 + \Delta u \cos \alpha - \Delta v \sin \alpha \\ y_C &= y_0 + \Delta u \sin \alpha + \Delta v \cos \alpha \end{aligned} \quad (2.157)$$

Equation (2.144) is linear and can be used as observation equation for a point  $P_i$ :

$$\varphi_i(A, B, C, D, E) = -1 \quad (2.158)$$

The differential quotients for a point  $P_i(x, y)$  in the design matrix are computed by:

$$\frac{\partial \varphi_i}{\partial A} = x_i^2 \quad \frac{\partial \varphi_i}{\partial B} = x_i y_i \quad \frac{\partial \varphi_i}{\partial C} = y_i^2 \quad \frac{\partial \varphi_i}{\partial D} = x_i \quad \frac{\partial \varphi_i}{\partial E} = y_i \quad (2.159)$$

The adjusted parameters can be used to compute the rotation angle according to equation (2.154). Substituting the angle in equation (2.152) determines the ellipse parameters in the uv system. Finally the ellipse centre is calculated from equation (2.157).

An alternative method for the determination of the ellipse centre is based on the geometry of ellipse diameters. Ellipse diameters are chords that are bisected by the ellipse centre. A conjugate diameter is defined by the straight line through the mid point of all chords which are parallel to a given diameter. A given diameter and its conjugate intersect at the ellipse centre (see Fig. 2.29).

The determination of ellipse parameters, in particular the centre coordinates, is an important part of the measurement of circular targets which are projected as ellipses in the central perspective image (see section 5.4.2.5). As a good approximation, the ellipse centre corresponds to the centre of the circular target (see section 3.4.1.1 for restrictions).

#### 2.4.1.4 Curves

Consider the requirement that a polynomial with  $k + 1$  points  $P_i(x_i, y_i)$ ,  $i = 0 \dots k$ , be described by a closed curve. If the curve should pass through the vertices of a polygon, the process is referred to as interpolation. If the curve should be an optimal fit to the polygon, it is referred to as approximation. Curves in general are usually defined by polynomials whose order and curvature properties can be varied with respect to the application.

Comprehensive overviews about approximation and interpolation using polynomials are given, for example, in textbooks about computer graphics e.g. Foley *et al.* (1995), Watt (1999), Shirley (2002). An easily read description of these methods is given by Grieger (1992).

##### *Polynomials*

A polynomial of degree n is a function of the form:

$$Q(x) = a_n x^n + a_{n-1} x^{n-1} + \dots + a_1 x^1 + a_0 \quad (2.160)$$

that is defined by  $n+1$  coefficients.

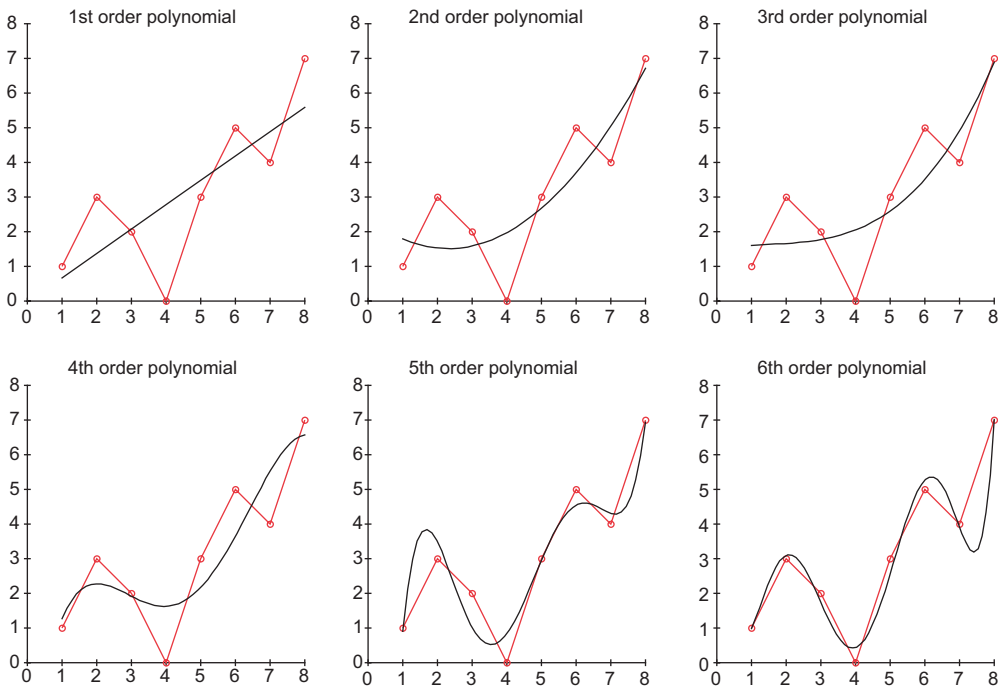


**Figure 2.30** Polygon with 8 data points and polynomial interpolations of different order

All points in a data set are used to determine the polynomial coefficients, if necessary by least-squares adjustment. For over-determined solutions, the polynomial does not normally pass through the vertices of the polygon defined by the points. In particular it does not intersect the end points. Polynomials of higher degree quickly tend to oscillate between the points (Fig. 2.30).

A more natural curve shape is obtained if the polygon is approximated by piecewise polynomials. A piecewise polynomial  $Q(x)$  is a set of  $k$  polynomials  $q_i(t)$ , each of order  $n$ , and  $k+1$  nodes<sup>1</sup>  $x_0, \dots, x_k$ , with:

$$Q(x) = \{q_i(t)\} \quad (2.161)$$

for  $x_i \leq t \leq x_{i+1}$  and  $i = 0, \dots, k-1$

Using additional constraints it is possible to generate an approximation curve that is both continuous and smooth. All methods which follow generate a curve that passes through the end points of the polygon and which can be differentiated  $n-1$  times at all points. Approximations based on cubic splines ( $n=3$ ) are of major importance for they provide suitable smoothness with a minimum polynomial degree.

### Splines

Splines are used to interpolate between the points of a polygon i.e. the curve passes through all the points. For this purpose basic B-spline functions of degree  $n$  and order  $m = n+1$  are suitable.

<sup>1</sup> Nodes are the given points defining a curve i.e. the vertices of a polygon.

They are recursively defined for a set of nodes  $x_0, x_1, \dots x_{k-1}$ :

$$B_{i,0}(t) = \begin{cases} 1 & \text{for } x_i \leq t \leq x_{i+1} \\ 0 & \text{otherwise} \end{cases}$$

$$B_{i,n}(t) = \frac{t - x_i}{x_{i+n} - x_i} B_{i,n-1}(t) + \frac{x_{i+n+1} - t}{x_{i+n+1} - x_{i+1}} B_{i+1,n-1}(t) \quad (2.162)$$

for  $x_i \leq t \leq x_{i+n+1}$ .

Optimal smoothness at the data points is required for spline interpolation i.e. continuous derivatives up to the order  $n-1$  should exist. This criterion is fulfilled by the following linear combination of  $k+1$  nodes:

$$S_n(t) = \sum_{i=0}^{n+k-1} a_i B_{i,n}(t) \quad (2.163)$$

For the frequently used cubic spline function ( $n = 3$ )

$$S_3(t) = \sum_{i=0}^{k+2} a_i B_{i,3}(t) \quad (2.164)$$

a number  $k+3$  of coefficients  $a_i$  have to be determined by a corresponding number of equations. Here  $k+1$  equations are provided by the data points and the remaining two equations defined by additional constraints. For example, for natural splines these are:

$$\begin{aligned} S_3''(x_0) &= 0 \\ S_3''(x_n) &= 0 \end{aligned} \quad (2.165)$$

Fig. 2.31a shows a polygon approximated by a cubic spline. The resulting curve continuously passes through the vertices (nodes). Splines are therefore most effective when the vertices are free of position errors i.e. no smoothing is desired. However, the shape of the entire curve is affected if only one point changes.

### B-Splines

For many technical applications it is more feasible to approximate a given polygon by a curve with the following properties:

- analytical function is simple to formulate
- can be easily extended to higher dimensions, especially for the surface approximations
- smoothness at vertices is easy to control
- variation of a node has only a local effect on the shape of the curve

The requirements are almost met by B-spline approximations which are a combination of basic functions (2.162) for each point to be interpolated  $P(t)$ :

$$P(t) = \begin{cases} x(t) = \sum_{i=0}^k x_i B_{i,n}(t) & 0 \leq t \leq k-n+1 \\ y(t) = \sum_{i=0}^k y_i B_{i,n}(t) & \end{cases} \quad (2.166)$$

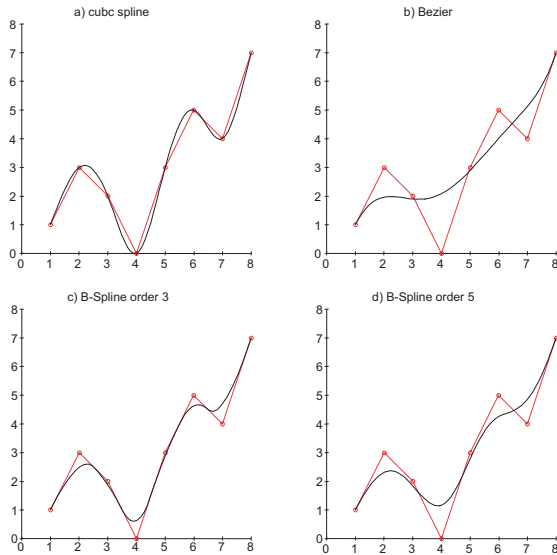


**Figure 2.31** Spline interpolation and Bezier and B-spline approximation

It is obvious that the spline basic functions are directly weighted by the coordinates of the vertices instead of the computed coefficients. The smoothness of the curve is controlled by the order  $m = n + 1$ , whereby the curve becomes smoother with increasing order. Fig. 2.31c and d show B-spline approximations of order  $m = 3$  and  $m = 5$ . In addition the computed curve always lies inside the envelope of the polygon, in contrast to normal spline or polynomial interpolation. Moreover, the approach can be extended directly to three-dimensional polygons (surface elements).

#### Bezier approximation

The Bezier approximation has been developed by the car industry. Here a given polygon is approximated by a curve that has optimal smoothness but does not pass through the vertices. The approximation

$$P(t) = \begin{cases} x(t) = \sum_{i=0}^k x_i BE_{i,k}(t) \\ y(t) = \sum_{i=0}^k y_i BE_{i,k}(t) \end{cases} \quad 0 \leq t \leq 1 \quad (2.167)$$

is similar to the B-spline approximation but is based on the Bernstein polynomials

$$BE_{i,k}(t) = \frac{k!}{i!(k-i)!} t^i (1-t)^{k-i} \quad 0 \leq t \leq 1 \quad (2.168)$$

All points in the polygon data set are used for the computation of the curve. The approach can be extended directly to three-dimensional polygons (see section 2.4.3.2).

Fig. 2.31b shows the curve which results from Bezier approximation of a polygon. The continuous curve does not pass through the vertices, but shows an averaged shape. Bezier

curves are therefore very suitable for applications where the data points are not free of error and smoothing is required.

## 2.4.2 Analytical geometry in 3D space

### 2.4.2.1 Straight line

The form of a straight line in 3D space can be derived directly from the straight line in 2D space. Thus a straight line between two points  $P_1(x_1, y_1, z_1)$  and  $P_2(x_2, y_2, z_2)$  is given by the proportional relationships:

$$\frac{x - x_1}{x_2 - x_1} = \frac{y - y_1}{y_2 - y_1} = \frac{z - z_1}{z_2 - z_1} \quad (2.169)$$

and in parametric form:

$$\begin{aligned} \mathbf{x} &= \mathbf{x}_1 + t(\mathbf{x}_2 - \mathbf{x}_1) \\ \begin{bmatrix} x \\ y \\ z \end{bmatrix} &= \begin{bmatrix} x_1 \\ y_1 \\ z_1 \end{bmatrix} + t \begin{bmatrix} x_2 - x_1 \\ y_2 - y_1 \\ z_2 - z_1 \end{bmatrix} \\ &= \begin{bmatrix} x_0 \\ y_0 \\ z_0 \end{bmatrix} + t \begin{bmatrix} a \\ b \\ c \end{bmatrix} \end{aligned} \quad (2.170)$$

Here  $P_0(x_0, y_0, z_0)$  is any point on the line. The direction cosines are defined by

$$\begin{aligned} \cos \alpha &= \frac{x_2 - x_1}{d} = a \\ \cos \beta &= \frac{y_2 - y_1}{d} = b \quad \text{where } d = \sqrt{(x_2 - x_1)^2 + (y_2 - y_1)^2 + (z_2 - z_1)^2} \\ \cos \gamma &= \frac{z_2 - z_1}{d} = c \end{aligned} \quad (2.171)$$

At first glance it looks as though there are 6 independent parameters for a straight line in 3D space. Taking into account the condition

$$a^2 + b^2 + c^2 = 1$$

there are only two direction parameters that are linearly independent. In addition, the coordinate  $z_0$  of a point on the straight line can be derived from the corresponding  $x_0$  and  $y_0$  coordinates. Hence, 4 independent parameters remain in order to describe a straight line in space:

$$\begin{aligned} 1. \text{ direction vector: } & (a, b, 1) \\ 2. \text{ point on the line: } & z_0 = -ax_0 - by_0 \end{aligned} \quad (2.172)$$

For numerical reasons, these two criteria are only valid for straight lines which are approximately vertical (parallel to the z axis). Arbitrarily oriented straight lines must therefore first be transformed into a vertical direction (see also section 2.4.2.3).

#### *Intersection of two straight lines*

The intersection point of two straight lines in space only exists if both lines lie in a common plane, otherwise the lines are skew. In this case the shortest distance  $e$  between them is defined

along a direction which is perpendicular to both. For two lines  $g_i$ ,  $i=1, 2$ , each defined by a point  $P_i(x_i, y_i, z_i)$  and direction cosine  $a_i, b_i, c_i$  the shortest distance  $e$  is given by:

$$e = \frac{\pm \begin{vmatrix} x_1 - x_2 & y_1 - y_2 & z_1 - z_2 \\ a_1 & b_1 & c_1 \\ a_2 & b_2 & c_2 \end{vmatrix}}{\sqrt{a^2 + b^2 + c^2}} \quad (2.173)$$

where

$$a = \begin{vmatrix} a_1 & b_1 \\ a_2 & b_2 \end{vmatrix} \quad b = \begin{vmatrix} b_1 & c_1 \\ b_2 & c_2 \end{vmatrix} \quad c = \begin{vmatrix} c_1 & a_1 \\ c_2 & a_2 \end{vmatrix}$$

For consistency, the point of intersection  $S$  is then defined at half this distance  $e/2$  between both lines (Fig. 2.32). Using the factors

$$\lambda = -\frac{\begin{vmatrix} x_1 - x_2 & y_1 - y_2 & z_1 - z_2 \\ a & b & c \\ a_2 & b_2 & c_2 \end{vmatrix}}{\begin{vmatrix} a_1 & b_1 & c_1 \\ a_2 & b_2 & c_2 \\ a & b & c \end{vmatrix}} \quad \mu = -\frac{\begin{vmatrix} x_1 - x_2 & y_1 - y_2 & z_1 - z_2 \\ a & b & c \\ a_1 & b_1 & c_1 \end{vmatrix}}{\begin{vmatrix} a_1 & b_1 & c_1 \\ a_2 & b_2 & c_2 \\ a & b & c \end{vmatrix}}$$

the spatial coordinates of points  $S_1$  and  $S_2$  at the ends of the perpendicular reduce to

$$\begin{aligned} x_{S1} &= x_1 + \lambda a_1 & x_{S2} &= x_2 + \mu a_2 \\ y_{S1} &= y_1 + \lambda b_1 & y_{S2} &= y_2 + \mu b_2 \\ z_{S1} &= z_1 + \lambda c_1 & z_{S2} &= z_2 + \mu c_2 \end{aligned}$$

and hence the point of intersection  $S$ :

$$x_S = \frac{x_{S1} + x_{S2}}{2} \quad y_S = \frac{y_{S1} + y_{S2}}{2} \quad z_S = \frac{z_{S1} + z_{S2}}{2} \quad (2.174)$$

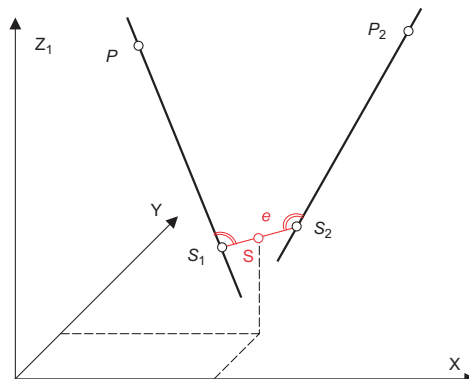


Figure 2.32 Intersection of two spatial straight lines

The intersection angle  $\varphi$  between both lines is given by:

$$\cos \varphi = a_1 a_2 + b_1 b_2 + c_1 c_2 \quad (2.175)$$

The intersection of two straight lines in space is used for spatial intersection in stereo photogrammetry (see section 4.4.2.2). Here the distance  $e$  provides a quality measure for the intersection.

#### *Straight line regression in space*

The calculation of a best-fit straight line in space can be derived directly from the algorithm presented in section 2.4.1.1. The distance of a point  $P_i(x_i, y_i, z_i)$  from the straight line defined by the point  $P_0(x_0, y_0, z_0)$  and the direction cosine  $a, b, c$  is given by:

$$d_i = \sqrt{u_i^2 + v_i^2 + w_i^2} \quad (2.176)$$

where

$$u_i = c(y_i - y_0) - b(z_i - z_0)$$

$$v_i = a(z_i - z_0) - c(x_i - x_0)$$

$$w_i = b(x_i - x_0) - a(y_i - y_0)$$

The fitted line passes through  $P_0$ , the centroid of all points on the line. As in the two-dimensional case, the spatial direction of the line is defined by the eigenvector which corresponds to the largest eigenvalue of the matrix  $\mathbf{B}$ :

$$\mathbf{B} = \mathbf{A}^T \mathbf{A}$$

$$\text{where } \mathbf{A} = \begin{bmatrix} x_1 - x_0 & y_1 - y_0 & z_1 - z_0 \\ \vdots & \vdots & \vdots \\ x_n - x_0 & y_n - y_0 & z_n - z_0 \end{bmatrix} \quad (2.177)$$

#### **2.4.2.2 Plane**

##### *Parameters*

A plane in space is defined by  $n \geq 3$  points which must not lie on a common straight line. The analytical form of a plane is given by:

$$Ax + By + Cz + D = 0 \quad (2.178)$$

A plane in 3D space is therefore analogous to a straight line in 2D (see equation 2.132 for comparison). The vector  $\mathbf{n}(A, B, C)$  is defined as a vector normal to the plane with direction cosines

$$\begin{aligned} \cos \alpha &= \frac{A}{\sqrt{A^2 + B^2 + C^2}} = a \\ \cos \beta &= \frac{B}{\sqrt{A^2 + B^2 + C^2}} = b \\ \cos \gamma &= \frac{C}{\sqrt{A^2 + B^2 + C^2}} = c \end{aligned} \quad (2.179)$$

Given a point  $P_0(x_0, y_0, z_0)$  on the plane with normal vector having direction cosines  $(a, b, c)$ , then all points  $(x, y, z)$  on the plane are defined by the following equation:

$$a(x - x_0) + b(y - y_0) + c(z - z_0) = 0 \quad (2.180)$$

Given a plane that is formed by 3 points  $P_1, P_2, P_3$ , any other point  $P$  on the plane meets the condition (Fig. 2.33):

$$\begin{vmatrix} x - x_1 & y - y_1 & z - z_1 \\ x_2 - x_1 & y_2 - y_1 & z_2 - z_1 \\ x_3 - x_1 & y_3 - y_1 & z_3 - z_1 \end{vmatrix} = 0 \quad (2.181)$$

This determinant corresponds to the volume of a parallelepiped defined by its three vectors. It can be taken as a definition of the coplanarity condition used in relative orientation (see section 4.2.5.3).

The distance of a point  $Q(x, y, z)$  from the plane is given by (see equation (2.180) for comparison):

$$d = a(x - x_0) + b(y - y_0) + c(z - z_0) \quad (2.182)$$

#### *Intersection of line and plane*

Given a straight line defined by point  $(x_G, y_G, z_G)$  and direction cosines  $(a_G, b_G, c_G)$

$$\begin{bmatrix} x \\ y \\ z \end{bmatrix} = \begin{bmatrix} x_G \\ y_G \\ z_G \end{bmatrix} + t \begin{bmatrix} a_G \\ b_G \\ c_G \end{bmatrix} \quad (2.183)$$

and a plane defined by point  $(x_E, y_E, z_E)$  and direction cosines  $(a_E, b_E, c_E)$ :

$$a_E(x - x_E) + b_E(y - y_E) + c_E(z - z_E) = 0 \quad (2.184)$$

Substituting in equation (2.184) for the variable point from equation (2.183), the solution for line parameter  $t$  is:

$$t = \frac{a_E(x_E - x_G) + b_E(y_E - y_G) + c_E(z_E - z_G)}{a_E a_G + b_E b_G + c_E c_G} \quad (2.185)$$

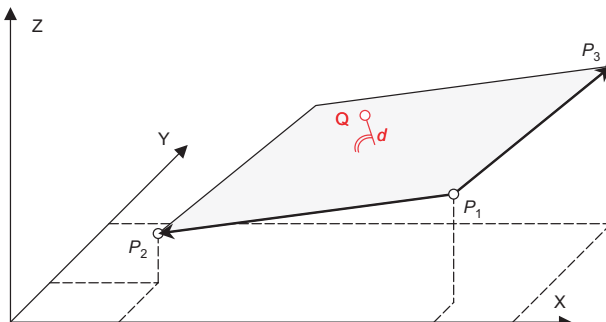


Figure 2.33 Definition of a plane in space

The denominator becomes zero if the line is parallel to the plane. The coordinates of the point of intersection are obtained if the solution for  $t$  is substituted in equation (2.183).

As an example, the intersection of line and plane is used in photogrammetry for single image analysis in conjunction with object planes (see section 4.4.1.2).

### *Intersection of two planes*

The intersection line of two non-parallel planes has a direction vector  $\mathbf{a}(a, b, c)$  which is perpendicular to the vectors  $\mathbf{n}_1$  and  $\mathbf{n}_2$  normal to the planes:

$$\mathbf{n}_1 \cdot \mathbf{a} = 0 \quad \text{and} \quad \mathbf{n}_2 \cdot \mathbf{a} = 0 \quad (2.186)$$

The length of the direction vector  $\mathbf{a}$  may be set to an arbitrary value, for example defined by  $c = 1$ . The two remaining parameters can then be calculated using equations (2.186).

A point  $\mathbf{x}_0$  on the line of intersection is defined by where it intersects a principal coordinate plane e.g. the xy-plane. The intersection line is then given in parametric form:

$$\mathbf{x} = \mathbf{x}_0 + t\mathbf{a}$$

### *Best-fit plane*

In analogy with best-fitting lines, the best-fit plane is calculated by minimising the distances  $d_i$  in equation (2.182). The adjusted plane that fits  $n$  points is defined by the centroid  $P_0$  of the points and the direction cosines of the normal vector. The matrix  $\mathbf{A}$ , used for the computation of eigenvalues, is identical to the matrix given in equation (2.177). However, here the direction cosines correspond to the eigenvector with the minimum eigenvalue.

#### **2.4.2.3 Rotationally symmetric shapes**

The measurement of rotationally symmetric shapes is of major importance, especially in industrial metrology. They have the common property that they can be described by a single reference axis (straight line in space) and one or more shape parameters (see Table 2.3).

**Table 2.3** 3D rotationally symmetric shapes (selection)

shape	parameters	number of points
3D circle	centre point $x_0, y_0, z_0$ normal vector $l, m, n$ radius $r$	$\geq 3$
cylinder	axis point $x_0, y_0, z_0$ direction vector $l, m, n$ radius $r$	$\geq 5$
paraboloid	summit of curve $x_0, y_0, z_0$ direction vector $l, m, n$ focal length $p/2$	$\geq 6$

These shapes (cylinder, 3D circle and paraboloid) are often used in practical applications of close-range photogrammetry and are explained below in more detail. For the analysis of other rotationally symmetric shapes (sphere, ellipsoid, cone etc.) the reader is directed to further references (e.g. Hunt 1988, Stroud 2001).

### Cylinder

A cylinder (Fig. 2.34) is defined by

- one point  $(x_0, y_0, z_0)$  on the axis of the cylinder
- the direction vector  $(a, b, c)$  of the axis
- the radius  $r$ .

With reference to equation (2.172), a cylinder whose axis is approximately vertical is defined by 5 independent parameters. A minimum of 5 observations are therefore required to compute the parameters i.e. a minimum of 5 points on the cylinder surface are necessary.

The distance of a point from the cylinder surface is given by:

$$d_i = r_i - r$$

where

$$r_i = \frac{\sqrt{u_i^2 + v_i^2 + w_i^2}}{\sqrt{a^2 + b^2 + c^2}} \quad (2.187)$$

and

$$u_i = c(y_i - y_0) - b(z_i - z_0)$$

$$v_i = a(z_i - z_0) - c(x_i - x_0)$$

$$w_i = b(x_i - x_0) - a(y_i - y_0)$$

In the special case where  $x_0 = y_0 = a = b = 0$  the above relations simplify to

$$r_i = \sqrt{x_i^2 + y_i^2}$$

The differential coefficients required to set up the design matrix  $\mathbf{A}$  are given by:

$$\begin{aligned} \frac{\partial d_i}{\partial x_0} &= -\frac{x_i}{r_i} & \frac{\partial d_i}{\partial y_0} &= -\frac{y_i}{r_i} & \frac{\partial d_i}{\partial r} &= -1 \\ \frac{\partial d_i}{\partial a} &= -\frac{x_i z_i}{r_i} & \frac{\partial d_i}{\partial b} &= -\frac{y_i z_i}{r_i} \end{aligned} \quad (2.188)$$

The following procedure provides one possible algorithm for the computation of a best-fit cylinder with given initial values of  $(x_0, y_0, z_0)$ ,  $(a, b, c)$  and  $r$ :

1. Translate the data points  $P_i$  onto a local origin near the axis
2. Rotate the axis into an approximate vertical (z) direction with rotation matrix  $\mathbf{R}(a, b, c)$ :  
Steps 1 and 2 temporarily transform an arbitrarily oriented cylinder into a local system<sup>1</sup> x'y'z' where the transformed cylinder is oriented vertically and the axis passes through the origin (see Fig. 2.34)
3. Set up and solve the normal system of equations using (2.188)
4. Correct the unknowns and reverse the transformation back into the original coordinate system:

Steps 1–4 are repeated until the unknowns do not change appreciably.

An example of the use of cylinders in close-range photogrammetry is in process plant (pipeline) modelling. Note that discrete 3D points on the cylinder surface are not necessarily

---

<sup>1</sup> Exceptionally the notation x'y'z' is used. This is normally reserved for image coordinates.

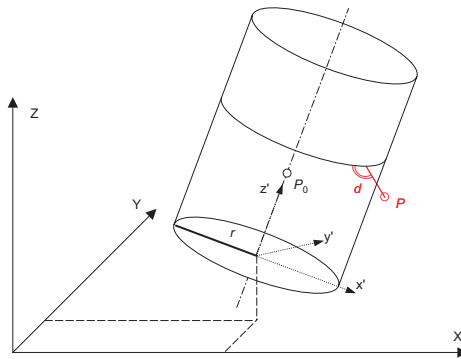


Figure 2.34 Definition of a cylinder

required and a cylinder can also be determined by photogrammetric measurement of its edges in an image (see section 4.4.3.2).

#### *Circle in 3D space*

A 3D circle is a circle located in an arbitrarily oriented plane in space (Fig. 2.35). It is defined by

- the centre  $(x_0, y_0, z_0)$ ,
- direction cosines  $(a, b, c)$  of the normal vector to the plane
- the radius  $r$ .

With regard to (2.172), a 3D circle in an approximately horizontal (xy) plane is defined by 6 independent parameters. A minimum number of 6 observations is therefore required to compute the parameters. These can be provided by 3 points on the circumference.

Analogously to the best-fit cylinder, a distance can be defined from a fitted point in space to the circle circumference. Here the point not only has a radial distance to the circle but also a perpendicular distance to the plane. The distance is given by

$$d_i^2 = e_i^2 + f_i^2 \quad (2.189)$$

Here  $e_i$  is the radial distance analogous to the definition in (2.147) and  $f_i$  is the distance from the plane according to (2.182). In order to calculate a best-fit circle both components must be minimised.

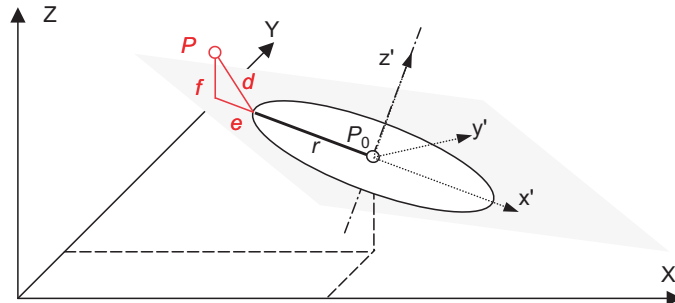


Figure 2.35 Definition of a 3D circle

$$\sum_{i=1}^n d_i^2 = \sum_{i=1}^n e_i^2 + \sum_{i=1}^n f_i^2 \quad (2.190)$$

Defining  $c = 1$  as in (2.172), there are 6 remaining parameters  $x_0, y_0, z_0, a, b$  and  $r$ . For the special case  $x_0 = y_0 = z_0 = a = b = 0$  the differential coefficients of the design matrix are:

$$\begin{aligned} \frac{\partial e_i}{\partial x_0} &= -\frac{x_i}{r_i} & \frac{\partial e_i}{\partial a} &= -\frac{x_i z_i}{r_i} \\ \frac{\partial e_i}{\partial y_0} &= -\frac{y_i}{r_i} & \frac{\partial e_i}{\partial b} &= -\frac{y_i z_i}{r_i} \\ \frac{\partial e_i}{\partial z_0} &= -\frac{z_i}{r_i} & \frac{\partial e_i}{\partial r} &= -1 \\ \frac{\partial f_i}{\partial x_0} &= 0 & \frac{\partial f_i}{\partial a} &= x_i \\ \frac{\partial f_i}{\partial y_0} &= 0 & \frac{\partial f_i}{\partial b} &= y_i \\ \frac{\partial f_i}{\partial z_0} &= -1 & \frac{\partial f_i}{\partial r} &= 0 \end{aligned} \quad (2.191)$$

The parameters are determined iteratively in the way described for a best-fit cylinder.

As in the case of the cylinder, discrete points on the circumference of the 3D circle are not necessarily required and its parameters can also be determined by direct measurement of the circle edges (see section 4.4.3.2).

### Paraboloid

A paraboloid (Fig. 2.36) is defined by

- the vertex  $P_0$
- the direction cosines  $(a, b, c)$  of its axis
- the offset distance  $p/2$  to the focus  $F$ .

A minimum of 6 points on the surface of the paraboloid is required to determine the parameters.

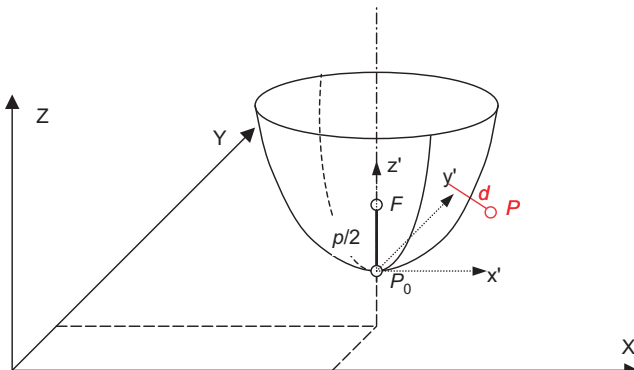


**Figure 2.36** Definition of a rotational paraboloid

In a local coordinate system  $x'y'z$ , the equation of the paraboloid is given by

$$z' = \frac{x'^2 + y'^2}{r^2} \quad (2.192)$$

and the offset distance  $p/2$  to the focal point  $F$ :

$$\frac{p}{2} = \frac{r^2}{4} \quad (2.193)$$

Paraboloids have application in the measurement of parabolic antennas.

### 2.4.3 Surfaces

Objects with surfaces which cannot be described by the above geometric elements are, in the first instance, usually represented by a reasonably dense distribution of 3D surface points. From these 3D point clouds, triangular mesh generation can create digital surface models of a more suitable and higher density. Analytical functions can also be used in a similar way to polynomials (see section 2.4.1.4) in order to approximate the shape of the surface (Kraus 1997).

Surfaces which can be defined as a function  $Z = f(X, Y)$  are known as 2½D surfaces. Here every point on a horizontal XY plane is related to exactly one unique height value Z. Terrain models and simple component surfaces are examples of 2½D surfaces (Fig. 2.37). In contrast, objects with holes and occlusions have true 3D surfaces where a point on the surface is defined by a function  $Z = f(X, Y, Z)$ . A sculpture or cup with a handle are examples for such 3D bodies (Fig. 2.38).

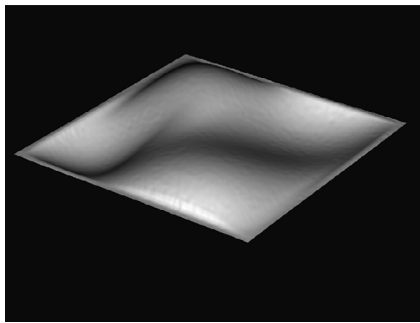
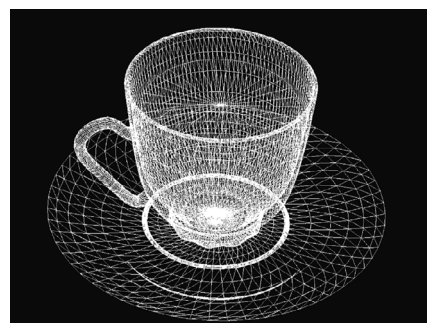
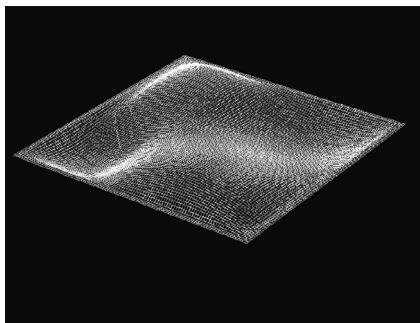


**Figure 2.37** Example of a 2½D surface

**Figure 2.38** Example of a 3D surface

### 2.4.3.1 Digital surface model

A 3D point cloud represents a digital surface model (DSM) if its point density (grid spacing) is sufficient for describing changes in surface shape. The point distribution can have a regular structure (e.g.  $\Delta X = \Delta Y = \text{const.}$ ) or an irregular spacing. Object edges (breaklines) can be represented by special point codes or by additional vector-based data such as polygons.

#### *Triangulation*

The simplest way to generate a closed surface from the point cloud is by triangulation (Fig. 2.39), where every three adjacent 3D points combine to form a triangular surface element. Delaunay triangulation offers an appropriate method of creating such a triangular mesh. This identifies groups of three neighbouring points whose maximum inscribed circle does not include any other surface point.

Each triangle can be defined as a plane in space using equation (2.180) and the result is a polyhedron representation or wire model of the surface.

There is normally no topological relation between the 3D points. Differential area elements must be established between adjacent points in order to generate a topologically closed surface which enables further processing as a surface description.

As part of the triangulation a hierarchical structure should be set up for the topology which enables simple and non-ambiguous access to the elements 3D point, line and polygon. This can, for example, be provided by a tree structure which ensures that corner points and lines (connections between points) are stored only once within the object representation (Fig. 2.40).

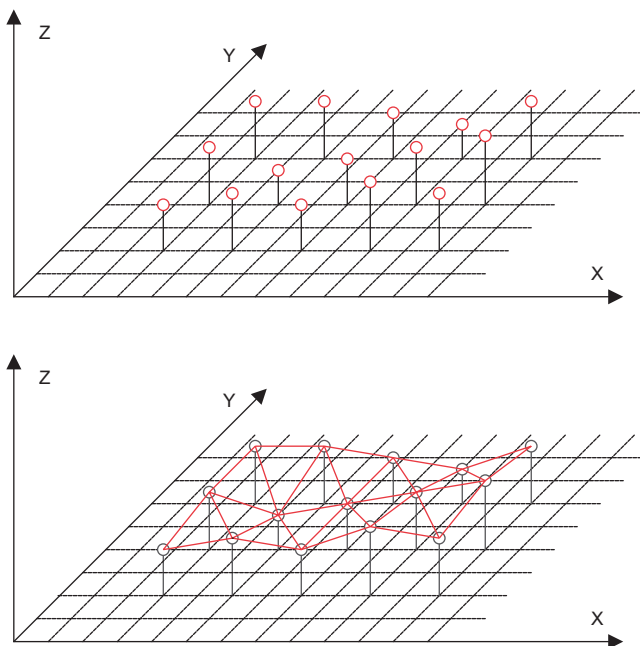


**Figure 2.39** Triangulation of a 3D point cloud

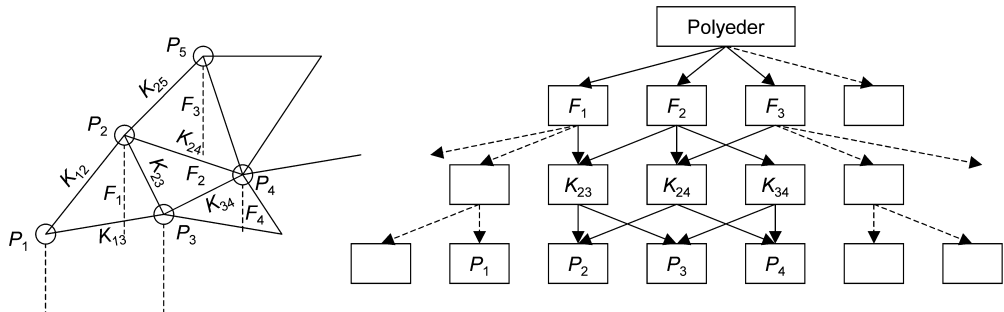


**Figure 2.40** Tree-structure for representation of a polyhedron of triangular surface elements  $F$ , triangle edges  $K$  and 3D points  $P$

The approximation of a surface by small planar surface elements has the advantage that it is easy to perform further calculations of, say, normal vectors or intersections with a straight line. These are required, for example, in visualisation using ray tracing techniques (see section 5.3.3.1). If triangular elements rather than polygons are used for surface descriptions then the planarity of surface elements is guaranteed.

### Interpolation

Additional points can easily be interpolated within a given triangular element. For a tilted plane defined in a local coordinate system  $x'y'z'$ , with origin located in one of the vertices of the triangle (Fig. 2.41), then the equation for the plane is given by

$$z = a_0 + a_1x' + a_2y' \quad (2.194)$$

The coefficients can be calculated as follows (Kraus 1997):

$$\begin{bmatrix} a_0 \\ a_1 \\ a_2 \end{bmatrix} = \frac{1}{x'_2y'_3 - x'_3y'_2} \begin{bmatrix} x'_2y'_3 - x'_3y'_2 & 0 & 0 \\ y'_2 - y'_3 & y'_3 & -y'_2 \\ x'_3 - x'_2 & -x'_3 & x'_2 \end{bmatrix} \begin{bmatrix} z_1 \\ z_2 \\ z_3 \end{bmatrix} \quad (2.195)$$

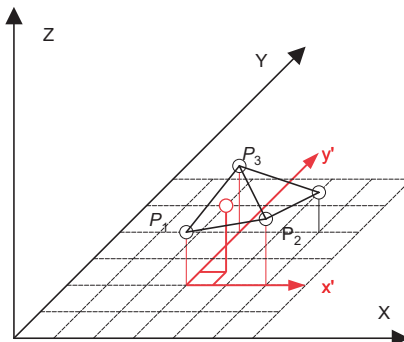


**Figure 2.41** Interpolation within a triangular mesh

For meshes consisting of four points, additional points can be calculated by bilinear interpolation according to equation (2.10).

#### 2.4.3.2 B-spline and Bezier surfaces

Three-dimensional surfaces can be represented directly by a general form of the B-spline used for curves in a plane (see section 2.4.1.4). Given a three-dimensional net of  $m+1 \times n+1$  nodes (surface model, see Fig. 2.39), a B-spline surface approximation gives:

$$Q(s,t) = \begin{cases} x(s,t) = \sum_{i=0}^m \sum_{j=0}^n x_{ij} B_{i,\alpha}(s) B_{j,\beta}(t) \\ y(s,t) = \sum_{i=0}^m \sum_{j=0}^n y_{ij} B_{i,\alpha}(s) B_{j,\beta}(t) \\ z(s,t) = \sum_{i=0}^m \sum_{j=0}^n z_{ij} B_{i,\alpha}(s) B_{j,\beta}(t) \end{cases} \quad (2.196)$$

where

$$0 \leq s \leq m - \alpha + 1 \quad \text{and} \quad 0 \leq t \leq n - \beta + 1$$

The result is a quadratic approximation when  $\alpha = \beta = 2$  and a cubic spline approximation when  $\alpha = \beta = 3$ . The determination of the basic functions  $B$  is equivalent to the two-dimensional case.

In an analogous way, Bezier approximations can be generated for 3D elements. They are mainly used for the construction of industrial free-form surfaces, for example in the automotive industry for the representation of car body surfaces.

#### 2.4.4 Compliance with design

In industrial dimensional metrology, the measurement of geometric elements is normally related to a component's functionality i.e. the measurement result is used to analyse how well the measured object meets its design function. The elements discussed above, which are a best-fit according to least-squares (L2 approach), may be used only in cases when the measured point coordinates have random, normally distributed errors. Non-systematic errors in the production of components might not be detected due to the smearing effect of the L2 approach. Depending on the function of a component, additional geometric descriptions are required (see Table 2.4).

**Table 2.4** Approximation criteria for standard form elements  
(selection, after Weckenmann 1993)

element	L2 approach	minimum zone	tangential constraint	minimum circumscribed	maximum inscribed
point	•			•	
line	•	•	•		
circle	•	•		•	•
plane	•	•	•		
sphere	•	•		•	•
cylinder	•	•		•	•
cone	•	•		•	•

The minimum zone element meets the condition that the maximum deviation between component surface and calculated element is a minimum. The minimum circumscribed element is the calculated element that includes all measured points within a minimum area. The maximum inscribed element is the maximum size of the element that excludes all measured points (Weckenmann 1993, Heinrichowski 1989).

Fig. 2.42 shows different estimations of a circle applied to a measured drill hole. If the drill hole is used for a cylindrical shaft, the circular shape must fulfil the minimum circumscribed condition whilst the maximum inscribed condition must be met by the shaft.

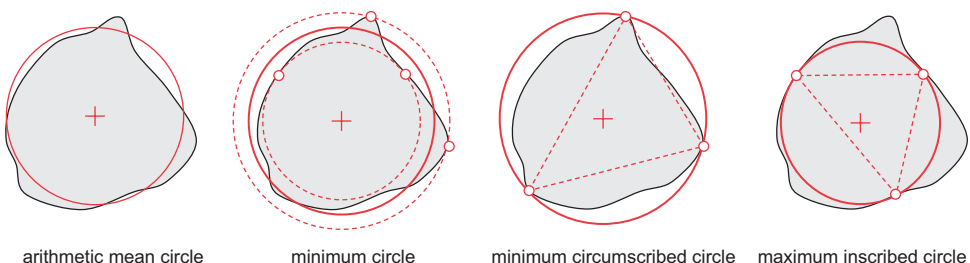


**Figure 2.42** Different estimations of a circle applied to a drill hole (after Weckenmann 1993)

## References

- Ackermann, F., Förstner, W., Klein, H., Schrot, R., and van Mierlo, J. (1980) *Große Datenfehler und die Zuverlässigkeit der photogrammetrischen Punktbestimmung*. Seminar, Universität Stuttgart.
- Albertz, J. and Kreiling, W. (1989) *Photogrammetric guide*. 4th edition, Wichmann Verlag, Karlsruhe, Germany.
- Baarda, W. (1968) *A testing procedure for use in geodetic networks*. Niederländische Geodätische Kommission, New Series 2, Nr. 5, Delft.
- Cross, P. A. (1990) *Working Paper No. 6, Advanced least squares applied to position-fixing*. Department of Land Surveying, Polytechnic (now University) of East London, pp. 205.
- Fellbaum, M. (1996) *Robuste Bildorientierung in der Nahbereichsphotogrammetrie*. Dissertation, Technische Universität Clausthal, Geodätische Schriftenreihe der Technischen Universität Braunschweig, Nr. 13.
- Fellbaum, M. and Godding, R. (1995) *Economic Solutions in Photogrammetry through a Combination of Digital Systems and Modern Estimation Techniques*. In Gruen/Kahmen (ed.) *Optical 3D Measurement Techniques III*, Wichmann Verlag, Karlsruhe, pp. 362–372.
- Foley, J. D., VanDam, A. and Feiner, S. K. (1995) *Computer Graphics*. Addison-Wesley Professional, p. 1200.
- Forbes, A. B. (1989) *Least-squares best-fit geometric elements*. National Physical Laboratory, Report DITC 140/89, Teddington, United Kingdom.
- Grieger, I. (1992) *Graphische Datenverarbeitung*. Springer Verlag, Berlin.
- Hartley, R. and Zisserman, A. (2000) *Multiple View Geometry*. Cambridge University Press, Cambridge, UK.
- Heinrichowski, M. (1989) *Normgerechte und funktionsorientierte Auswerteverfahren für punktweise erfaßte Standardormelemente*. Dissertation, Universität der Bundeswehr Hamburg.
- Hinsken, L. (1987) *Algorithmen zur Beschaffung von Näherungswerten für die Orientierung von beliebig im Raum angeordneten Strahlenbündeln*. Deutsche Geodätische Kommission, Reihe C, Nr. 333.
- Hunt, R. A. (1988) *Calculus with Analytic Geometry*. Harper & Row, New York. p. 1080.

- Kampmann, G. (1986) *Robuster Ausreißertest mit Hilfe der L1-Norm-Methode*. Allgemeine Vermessungs-Nachrichten, 93, pp. 139–147.
- Klein, H. (1984) *Automatische Elimination grober Datenfehler im erweiterten Blockausgleichungsprogramm PAT-M*. Bildmessung und Luftbildwesen, Heft 6/1984, pp. 273–280.
- Kraus, K. (1997) *Photogrammetry, Volume 2, Advanced Methods and Applications*. With Contributions by J. Jansa and H. Kager. Dümmler, Bonn.
- Kruck, E. (1983) *Lösung großer Gleichungssysteme für photogrammetrische Blockausgleichungen mit erweitertem funktionalem Modell*. Dissertation, Wiss. Arbeiten der Fachrichtung Vermessungswesen der Universität Hannover, Nr. 128.
- Kruck, E. (1995) Balanced least squares adjustment for relative orientation. In Gruen/Kahmen (ed.) *Optical 3D Measurement Techniques III*. Wichmann Verlag, Heidelberg, pp. 486–495.
- Mikhail, E. M. (1976) *Observations and least squares*. IEP, New York, p. 497.
- Mikhail, E. M. and Gracie, G. (1981) *Analysis & Adjustment of Survey Measurements*. Van Nostrand Reinhold Company, p. 368.
- Möser, M., Müller, G., Schlemmer, H. and Werner, H. (2000) Handbuch für Ingenieurgeodäsie, Band 1, Grundlagen. Wichmann, Heidelberg.
- Pelzer, H. (ed.) (1985) *Geodätische Netze in Landes- und Ingenieurvermessung II*. Verlag Konrad Wittwer, Stuttgart.
- Shirley, P. (2002) *Fundamentals of Computer Graphics*. A K Peters, p. 500.
- Stroud, K. A. (2001) *Engineering Mathematics*. Industrial Press; 5th Bk & Cdr edition, p. 1236.
- Watt, A. (1999) *3D Computer Graphics*. Addison Wesley Publishing, pp. 592.
- Weckenmann, A. (1993) Auswerteverfahren und Antaststrategien in der Koordinatenmeßtechnik. In Neumann (ed.) *Koordinatenmeßtechnik – Neue Aspekte und Anwendungen*. Expert Verlag, Ehning, pp. 133–169.
- Wolf, H. (1975) *Ausgleichsrechnung – Formeln zur praktischen Anwendung*. Ferd. Dümmler Verlag, Bonn.
- Wolf, P. R. and Ghilani, C. D. (1997) *Adjustment Computations: Statistics and Least Squares in Surveying and GIS (Surveying & Boundary Control)*, John Wiley & Sons.



# 3 Imaging technology

Photogrammetric imaging technologies for close-range measurement purposes impact upon all processes from the preparation of the measuring object prior to imaging, through image acquisition, to subsequent analysis of the image content. In this chapter common imaging concepts are introduced, the mathematical and physical imaging model is described and available analogue, digital and hybrid image recording systems are presented and compared. The chapter finishes by discussing some signalisation and illumination techniques which are used in many practical engineering applications.

## 3.1 Imaging concepts

### 3.1.1 Methods of image acquisition

The basic steps necessary for photogrammetric imaging are illustrated in Fig. 3.1 with analogue imaging on the left hand side and digital recording on the right hand side.

Despite rapid recent advances in digital technologies, analogue imaging and processing systems have maintained advantages in terms of excellent information capacity of film materials and the highly refined and proven camera technology available. Visual image compilation is based on the skills and experiences of the human operator. The key disadvantage of the analogue process is the time delay incurred for chemical processing and drying of the

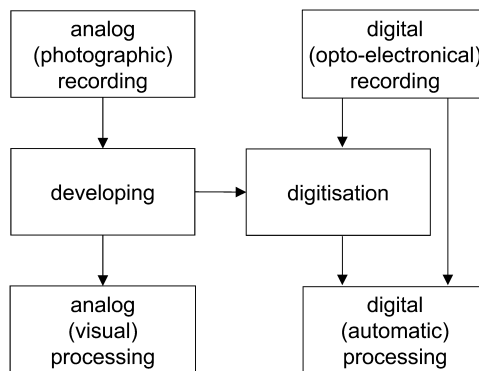


**Figure 3.1** Imaging and processing concepts

photographic material before the image can be viewed. A secondary limitation is that the photographic image is not as geometrically stable as its digital counterpart resulting in lower image measurement accuracies.

The purely digital approach, as shown on the right hand side, is able to provide image data directly from the sensor. However, given the level of current technology, digital recording is not yet able to provide the large area imaging sensors necessary for equivalent performance. The key advantage of the digital approach is that automated image measurement and analysis can be used for efficient photogrammetric processing of the images, higher image measuring accuracies and simultaneous display of image and graphics. In addition, a continuous and conceivably real time data flow from image acquisition to the presentation of results is possible.

Scanning, the digitisation of analogue images using an appropriately designed image scanner, yields a hybrid interim solution that combines the advantages of the photographic image technology with those of digital image processing. As a disadvantage, the extra digitisation step is time-consuming with the resampling process resulting in a loss of image quality over the photographic original.

### 3.1.2 Imaging configurations

In photogrammetry, imaging configuration is referred to as the arrangement of camera stations and viewing directions for object measurement. Usually in photogrammetry, the following imaging configurations are distinguished:

- single image acquisition
- stereo image acquisition
- multi-image acquisition

#### 3.1.2.1 Single image acquisition

Three-dimensional reconstruction of an object from a single image is only possible if additional geometric information about the object is available. Single image processing is typically applied for rectifications (of plane object surfaces, see section 4.4.1.1) and orthophotos (by integrating a digital surface model, see section 4.4.1.2), and plane object measurements (after previous definition of an object plane, see section 4.4.1.2). The achievable accuracy of object measurement depends primarily on the image scale (see section 3.2.1) and the ability to distinguish those features which are to be measured within the image.

Single image photogrammetry can be applied, for example, to the reconstruction of planar building façades or to the measurement of planar engineering work pieces.

#### 3.1.2.2 Stereo image acquisition

Stereo imagery is typically acquired where a visual or automated stereoscopic image compilation process is to be used. Visual processing requires near parallel viewing directions similar to the normal case (Fig. 3.2a) as the human visual system can only process images comfortably within a limited angle of convergence. For digital stereo image processing (stereo image matching is covered in section 5.5), the prerequisites of human vision can be ignored with the result that more convergent image pairs can be used (Fig. 3.2b). Shifted cameras (Fig. 3.2c) provide parallel viewing directions but different scales for both images. Provided points of detail to be measured are visible in both images. Such differences in image scale can be accommodated through differential zooming in the viewing optics, or mathematically through the use of an appropriate scale factor.

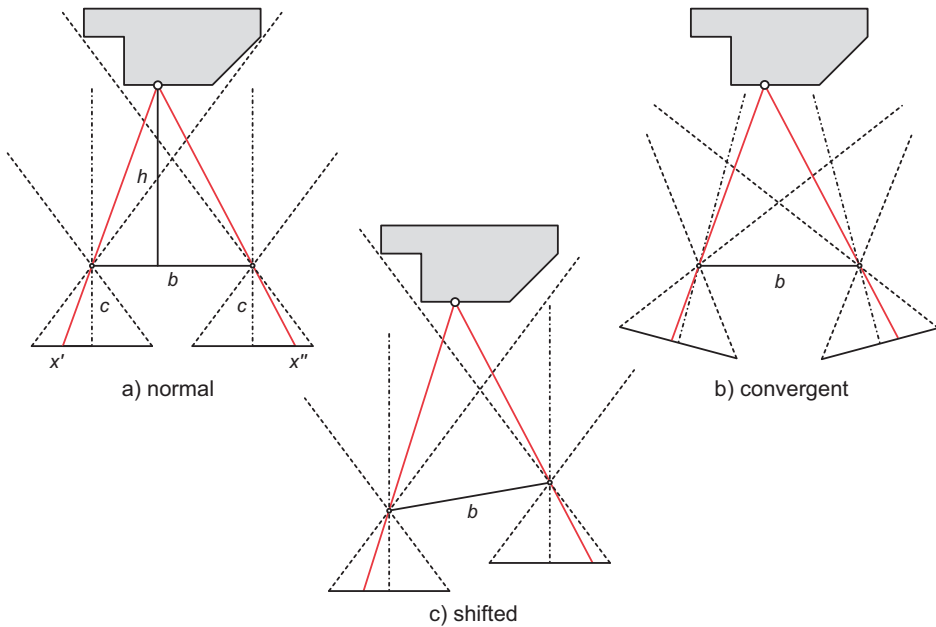


**Figure 3.2** Stereo image configurations

In the simplest case, three-dimensional object reconstruction using image pairs is based on the measurement of image parallaxes  $px' = x' - x''$  (Fig. 3.2a) that can be transformed directly into a distance measure  $h$  in the viewing direction (see section 4.4.2.2). More generally image coordinates  $(x'y', x''y'')$  of homologous (corresponding) image points can be measured in order to calculate 3D coordinates by spatial intersection (see section 4.4.2.2). The accuracy of the computed object coordinates in the viewing direction will generally differ from those parallel to the image plane. Differences in accuracy are a function of the intersecting angle between homologous image rays defined by the height-to-base ratio  $h/b$ .

Stereo imagery is most important for the measurement of non-signalised object surfaces that can be registered by the visual setting of an optical floating mark (see section 4.4.2.1). Special stereometric cameras have been developed for stereophotogrammetry (see section 3.3.1.3). An example application in industry is the measurement of free-form surfaces where one camera can be replaced by an orientated pattern projector (see section 6.5.1).

### 3.1.2.3 Multi-image acquisition

Multi-image configurations (Fig. 3.3) are not restricted with respect to the selection of camera stations and viewing directions. In principle, the object is acquired by an unlimited number of images from locations chosen to enable sufficient intersecting angles of bundles of rays in object space.

Object coordinates are determined by multi-image triangulation (bundle adjustment, see section 4.3, or spatial intersection, see section 4.4.3.1). If a sufficient number and configuration of image rays (at least 3–4 images per object point) are provided, uniform object accuracies in all coordinates can be obtained (see section 3.2.1.2).

In close-range photogrammetry multi-image configurations are the most common case. They are required in all situations where a larger number of different viewing locations are

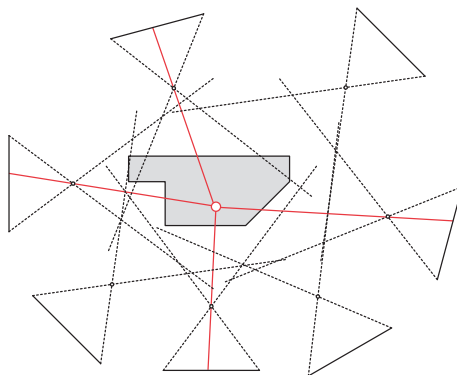


**Figure 3.3** Multi-image acquisition (all-around configuration)

necessary due to the object structure (e.g. occlusions, measurement of both interior and the exterior surfaces) or to maintain specified accuracy requirements. Images can be arranged strip- or block-wise (Fig. 4.28) or as all-around configurations (Fig. 4.30) but, in principle, without any restrictions (Fig. 1.6, Fig. 8.2).

Where sufficient geometric configuration is present, multi-image configurations enable the simultaneous calibration of the camera(s) by self calibrating bundle adjustment procedures (see section 4.3.2.4).

## 3.2 Geometric fundamentals

### 3.2.1 Image scale and accuracy

Image scale and achievable accuracy are the basic criteria of photogrammetric imaging and will dominate the choice of camera system and imaging configuration.

#### 3.2.1.1 Image scale

The image scale number  $m$  is defined by the ratio of object distance  $h$  to the principal distance  $c$  (lens focal length with the addition of an extension in order to achieve sharp focus) of the camera system used. It may also be given as the ratio of a distance in object space  $X$  to the corresponding distance in image space  $x'$ :

$$m = \frac{h}{c} = \frac{X}{x'} = \frac{1}{M} \quad (3.1)$$

In order to achieve sufficient accuracy and detectability of fine detail in the scene, the image scale  $M$  has to be defined appropriately with respect to the available imaging system and the exterior environmental conditions. Fig. 3.4 illustrates the relationship of object distance, principal distance and image format on the resulting image scale.

Using a camera with a smaller image format from the same taking location, the imaged object area is reduced since the image scale and principal distance remain constant (Fig. 3.4a). In contrast, a larger image scale can be achieved if the object distance is reduced for the same image format (Fig. 3.4b).

For a shorter object distance (Fig. 3.4b), or a longer principal distance (Fig. 3.4c), a larger image scale will result with a commensurately reduced imaged object area i.e. the number of images necessary for complete coverage of the object will increase.

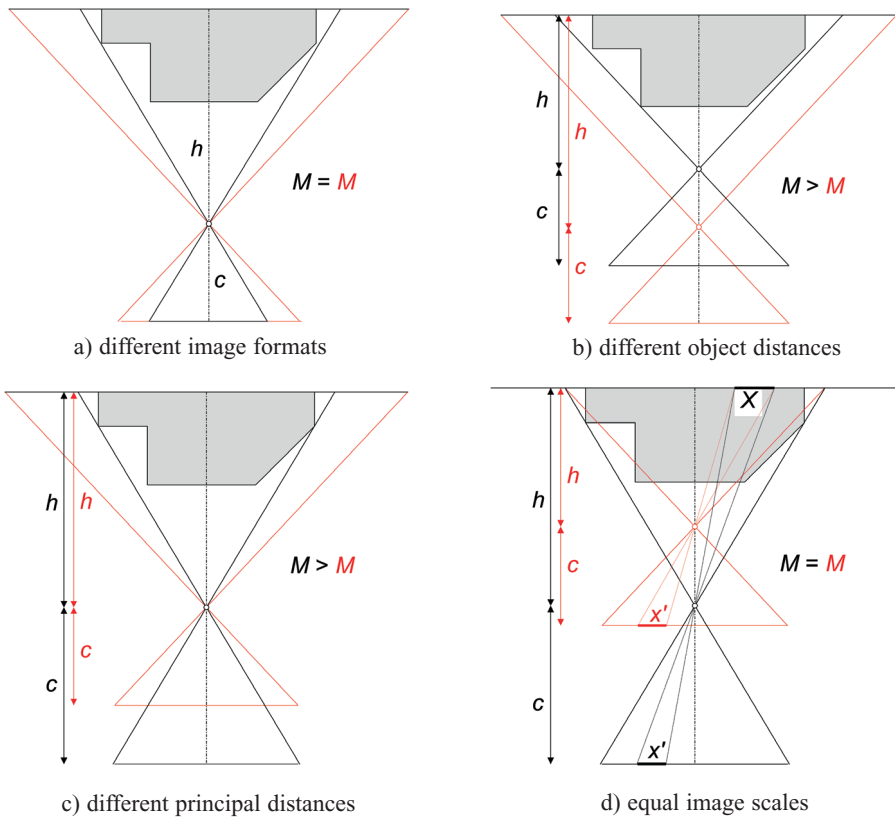


**Figure 3.4** Dependency of image scale on image format, focal length and object distance

Fig. 3.4d shows that equal image scales can be obtained by different imaging configurations. With respect to image scale it can be concluded that the selection of imaging system and camera stations is often a compromise between contrary requirements. Note however that any change in the position of the camera with respect to the object will result in a different perspective view of the object. Conversely, changing the focal length of the lens, or altering the camera format dimensions, whilst maintaining the camera position, will not alter the perspective.

### Example 3.1:

Given a camera with image format  $s' = 60$  mm and a principal distance of  $c = 40$  mm (wide angle), compute the object distance  $h$ , where an object size of 7.5 m is imaged over the full format.

Solution:

$$1. \text{ image scale number: } m = \frac{X}{x'} = \frac{7500}{60} = 125 \quad (M=1:125)$$

$$2. \text{ object distance: } h = mc = 125 \times 40 = 5000 \text{ mm} = 5 \text{ m}$$

An image consists of a uniform scale only in the case of a strict normal viewing direction with respect to a strict plane object. For small deviations from the normal an average image scale number related to an average object distance can be used for further estimations. In practical imaging configurations large deviations in image scale result mainly from

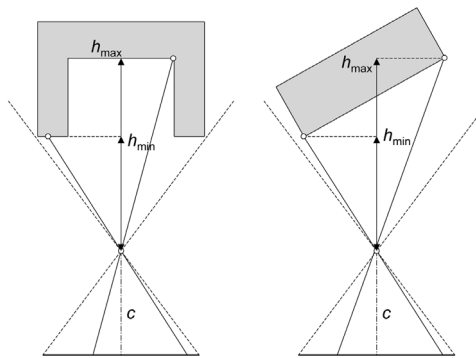


Figure 3.5 Different image scales

- large spatial depth of the object and/or
- extreme convergent images of a plane object.

For these cases (see Fig. 3.5) minimum and maximum image scales have to be used for project planning and accuracy estimations.

### 3.2.1.2 Accuracy estimation

The achievable accuracy<sup>1</sup> in object space of a photogrammetric measurement requires assessment against an independent external standard, but the precision of the derived coordinates can be estimated approximately according to Fig. 3.6.

Differentiation of equation (3.1) shows that the uncertainty of an image measurement  $dx'$  can be transferred into object space by the image scale number  $m$ :

$$dX = m dx' \quad (3.2)$$

Applying the law of error propagation the standard deviation (mean error) yields:

$$s_X = ms_{x'} \quad (3.3)$$

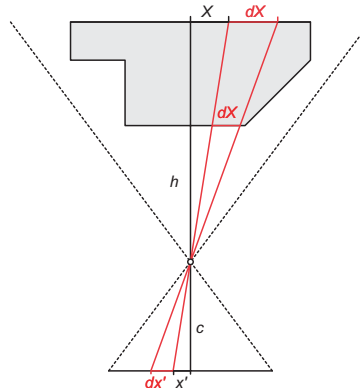


Figure 3.6 Single image acquisition

<sup>1</sup> Here the term accuracy is used as a general quality criteria. See section 2.3.3.1 for a definition of accuracy, precision and reliability.

In many cases a relative precision, rather than an absolute value, that is related to the maximum object dimension  $S$ , or the maximum image format  $s'$  is calculated:

$$\frac{s_X}{S} = \frac{s_{x'}}{s'} \quad (3.4)$$

Equation (3.4) shows that a larger image format yields better measurement precision.

### Example 3.2:

Consider an object with  $S = 7.5$  m photographed at an image scale of  $m = 125$ . What is the necessary image measuring accuracy  $s_{x'}$ , if an object precision of  $s_X = 0.5$  mm is to be achieved.

Solution:

1. from (3.3):  $s_{x'} = \frac{s_X}{m} = \frac{0.5}{125} = 0.004 \text{ mm} = 4 \mu\text{m}$

2. relative accuracy:  $\frac{s_X}{S} = 1 : 15000 = 0.007\%$

In the first instance, the achievable object precision according to (3.3) indicates the relationship between scale and resulting photogrammetric precision. Furthermore it is a function of the imaging geometry (number of images, intersecting geometry of rays in space) and the identification capability of the measured image locations. Consequently, presenting relative precisions is only useful if the measuring object, imaging configuration, processing methods and accuracy verification test are sufficiently described.

Equation (3.3) must be extended by a design factor  $q$  that provides an appropriate weighting of the imaging configuration:

$$s_X = qms_{x'} \quad (3.5)$$

Fraser (1996) calculates the design factor by a parameter  $q_D$  that is related to the intersecting geometry of the imaging configuration, and the mean number of target images  $k$  per photo:

$$q = \frac{q_D}{\sqrt{k}} \quad (3.6)$$

For the default practical case  $k = 1$  can be assumed.

Schlögelhofer (1989) proposes a design factor that consists of additional factors for orientation of the object coordinate system (datum), intersection quality, deformations (spatial configuration of bundles) and control elements (accuracy of reference points):

$$q = (1 + l)(o + vp) \quad (3.7)$$

where  $l$ : datum orientation accuracy (zero for reference points with superior accuracy)

$o$ : intersecting quality (similar to  $q_D$ )

$v$ : deformation factor (values of 0.5–4 depending on the bundle configuration)

$p$ : control elements factor (0 = dense net of reference points, 2 = weak network)

For sufficiently well determined reference points ( $l = 0$ ) equation (3.7) can be simplified to:

$$q = o + vp \quad (3.8)$$

The factors  $o$ ,  $v$  and  $p$  vary for each imaging configuration. Alternatively, they can be calculated by simulation or modelling (see section 7.1.4).

Practical values for the design factor  $q$  vary between 0.4–0.8 for excellent imaging configurations (e.g. all-around configuration, see Fig. 3.3) up to 1.5–3.0 and even worse for weak stereo configurations (see Fig. 3.2).

If the object is signalised (e.g. by circular high-contrast retro targets) and imaged by an all-around configuration, equation (3.5) provides a useful approximation for all three coordinate axes, such that  $q = 0.7$  can be achieved. In cases where the object cannot be recorded from all sides, accuracies aligned with the viewing direction can be expected to significantly differ from the other axes. As an example, the achievable precision in the viewing direction  $Z$  for a normal stereo pair (see section 4.4.2.2) can be estimated by:

$$s_Z = \frac{h^2}{bc} s_{px'} = m \frac{h}{b} s_{px'} \quad (3.9)$$

Here  $b$  defines the distance between both camera stations (stereo base) and  $s_{px'}$  the image measurement precision of the x-parallax; base  $b$  and principal distance  $c$  are assumed to be free of error. Viewing direction measurement precision depends on the image scale ( $h/c$ ) and on the intersecting geometry, defined by the height-to-base ratio ( $h/b$ ).

### Example 3.3:

Consider a stereo image pair at an image scale of  $M = 1:125$ , an object distance of  $h = 5$  m and a base length of  $b = 1.2$  m. Compute the achievable precision in the  $XY$ -direction (parallel to the image plane) and in the  $Z$ -direction (viewing direction) respectively, given a parallax measurement precision of  $s_{px'} = 4 \mu\text{m}$  (assume  $s_{px'} = s_{x'} = s_{y'}$ ).

Solution:

$$1. \text{ Precision in } Z: s_Z = m \frac{h}{b} s_{px'} = 125 \times \frac{5}{1.2} \times 0.004 = 2.1 \text{ mm}$$

$$2. \text{ Precision in } XY \text{ where } q_{XY} = 1: s_X = s_Y = ms_{x'} = 125 \times 0.004 = 0.5 \text{ mm}$$

$$3. \text{ Design factor from equation (3.5): } q_Z = \frac{s_Z}{ms_{x'}} = 4.2$$

The example shows that the precision in the viewing direction is reduced by a factor of 4.

## 3.2.2 Optical imaging

### 3.2.2.1 Geometric optics

The optical imaging model for thin lenses is illustrated in Fig. 3.7. The well-known lens equations can be derived from the displayed proportions (e.g. Schröder 1990, Ray 1994, Born *et al.* 1999, Hecht 2003):

$$\frac{1}{a'} - \frac{1}{a} = \frac{1}{f'} \quad (3.10)$$

$$zz' = -f'^2 \quad (3.11)$$

where

$a$ : object distance

$a'$ : image distance  $\approx$  principal distance  $c$

$f, f'$ : external and internal focal length

$z, z'$ : focal object distance and image distance  
 $H_1, H_2$ : external and internal principal planes

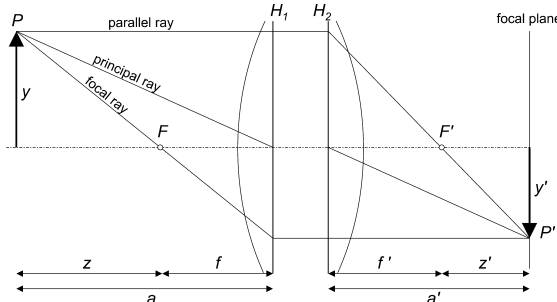


Figure 3.7 Geometrical construction for a typical thin lens system

In addition the imaging scale is given in analogy to (3.1)<sup>1</sup>:

$$\beta' = \frac{y'}{y} = \frac{a'}{a} = -\frac{z'}{f'} = 1 : m \quad (3.12)$$

An object point  $P$  is focused at distance  $a'$  from the internal principal plane  $H_2$ . For an object point at infinity distance  $a' = f'$ .

### 3.2.2.2 Refraction and reflection

The refractive index  $n$  is defined as the ratio of the velocities of light propagation through two different media (frequency is invariant):

$$n = \frac{c_1}{c_2} \quad : \text{refractive index} \quad (3.13)$$

In order to define material related refractive indices,  $c_1$  is assigned to the velocity of propagation in a vacuum or in air:

$$n = \frac{c_{\text{air}}}{c} \quad (3.14)$$

The refractive index of pure water has been determined to be  $n = 1.33$  whilst for glass the value varies between 1.45 and 1.95 depending on the material constituents of the glass. In general homogeneous and isotropic media are assumed. A ray of light passing from a low density media to a more dense media is refracted towards the axis of incidence at the media interface  $T$ , as denoted by Snell's law (Fig. 3.8).

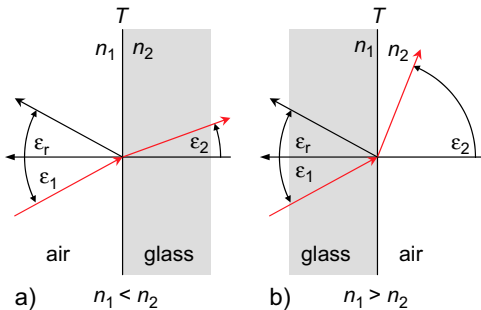
$$n_1 \sin \varepsilon_1 = n_2 \sin \varepsilon_2 \quad : \text{Snell's law of refraction} \quad (3.15)$$

The law can also be expressed as a function of the tangent:

$$\frac{\tan \varepsilon_1}{\tan \varepsilon_2} = \sqrt{n^2 + (n^2 - 1) \tan^2 \varepsilon_1} \quad (3.16)$$

where  $n = \frac{n_2}{n_1}$  and  $n_2 > n_1$

<sup>1</sup> In optics  $\beta'$  is used instead of  $M$ .

**Figure 3.8** Refraction and reflection (after Schröder 1990)

For the case of reflection it holds that  $n_2 = -n_1$  and the law of reflection follows:

$$\varepsilon_r = -\varepsilon_1 \quad : \text{law of reflection} \quad (3.17)$$

The velocity of propagation of light depends on the wavelength. The resulting change of refraction and reflection is denoted as dispersion.

### 3.2.2.3 Diffraction

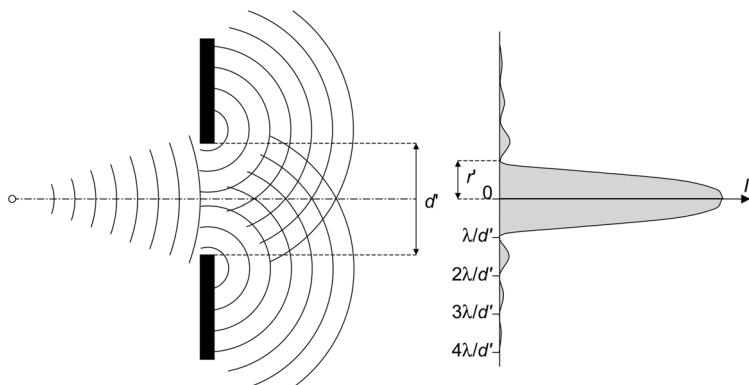
Diffraction occurs if the straight propagation of spherical wave fronts of light are disturbed e.g. by passing through a slit diaphragm (linear aperture). Instead of the ideal point-shape projection, the resultant is a diffraction disk that exhibits an intensity pattern defined by interference lines (Fig. 3.9).

The intensity  $I$  observed for a phase angle  $\varphi$  yields:

$$I(\varphi) = \frac{\sin x}{x} = \text{sinc}(x) \quad (3.18)$$

where

$$x = \frac{\pi d' \sin \varphi}{\lambda}$$

**Figure 3.9** Diffraction for a slit aperture

$d'$ : slit width

$\lambda$ : wavelength

$\varphi$ : phase angle

The intensity becomes a minimum for the values

$$\sin \varphi_n = n \frac{\lambda}{d'} \quad n = 1, 2, \dots \quad (3.19)$$

Hence, the radius  $r'$  of the first interfering ring ( $n = 1$ ) at the image plane is given by:

$$r' = \frac{\lambda}{d'} f' = \lambda k \quad (3.20)$$

where

$f'$ : focal length

$$k = \frac{f'}{d'} : \text{f-number}$$

Diffraction occurs not only for limiting bundles at apertures or lens barrels but also for (regular) grid structures as they exist for the arrangement of sensor elements of imaging sensors (see section 3.2.5.2). In conjunction with deviations of the lens equation (3.10), (defocusing) diffraction yields the point spread function (PSF). This wavelength depending effect is described by the contrast or modulation transfer function (see sections 3.2.4 and 3.2.5).

### 3.2.2.4 Perspective centre and distortion

Mathematically, the perspective centre is defined by the point of central perspective that is the point through which all straight lines from all image rays pass. In contrast for the optical projection of a compound objective both an external and an internal perspective centre can be defined. Each is defined by the intersection point of the optical axis with the entrance pupil EP and the exit pupil E'P respectively. The position and size of the entrance and exit pupils are defined by the lens design and the limiting bundle of the lens aperture (Fig. 3.10). Hence, the position of the perspective centre depends on the chosen aperture.

In the ideal case of Fig. 3.7 the angle of incidence  $\tau$  is equal to the exit angle  $\tau'$ , and the principal distance  $c$  is equal to the image distance  $a'$ . As the position of entrance pupil and exit pupil do not usually coincide with the principal planes, an incident ray enters according

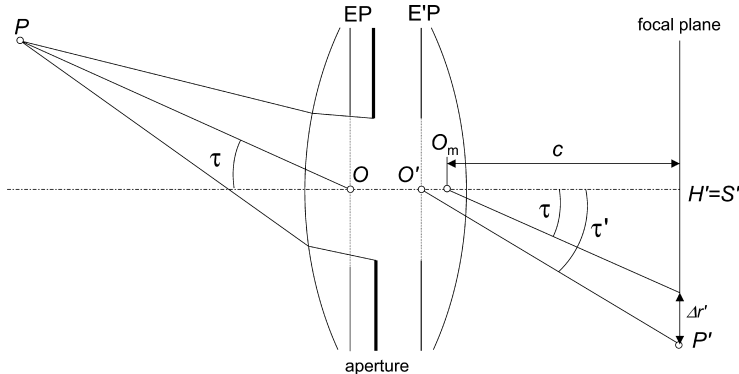


Figure 3.10 Perspective centre and principal distance (after Kraus 2000)

to angle  $\tau$ , and exits according to a different angle  $\tau'$ . This effect is radially symmetric with a point of symmetry  $S'$ . With respect to the nominal position an image point  $P'$  is shifted according to an amount  $\Delta r'$ , that is referred to as radial-symmetric distortion (see also Fig. 3.21 and Fig. 3.22).

$$\Delta r' = r' - c \tan \tau \quad (3.21)$$

This equation shows that the magnitude of radial distortion is a function not only of radius but also of the principal distance.

The point of autocollimation  $H'$  is defined as the intersecting point of the optical axis of the lens  $OO'$  and the image plane. In order to minimise the effect of distortion for standard lenses, the mathematical perspective centre  $O_m$  (used for photogrammetric calculations) is defined such that the nadir is located in  $H'$ , with the result that the difference between the angles  $\tau$  and  $\tau'$  becomes a minimum. If the optical axis is not normal with respect to the image plane,  $O_m$  is not positioned on the optical axis (Fig. 3.11).  $H'$  is then denoted as the principal point and the photogrammetric reference axis is defined by the straight line  $O_m H'$ . In object space it is given by the parallel ray passing  $O^1$ . The image radius  $r'$  of an image point and the effect of radial-symmetric distortion  $\Delta r'$  are defined with respect to the principal point  $H'$  (see section 3.2.3.1).

In practice, each lens generates distortion. The above described radial-symmetric distortion can be reduced to quantities  $\Delta r' < 4 \mu\text{m}$  for symmetrically designed high-quality lenses (Fig. 3.12). In contrast, asymmetric lens designs yield significantly larger distortion values,

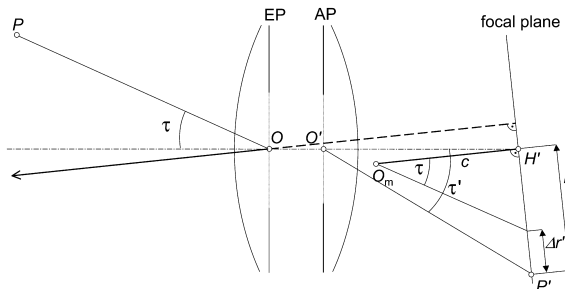


**Figure 3.11** On the definition of the principal point for tilted image plane (after Kraus 2000)

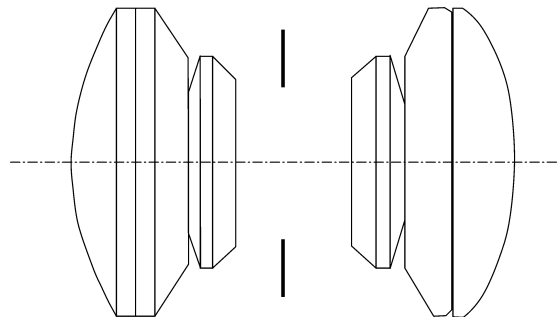


**Figure 3.12** Example of a symmetric lens design  
(Lametar 8/f = 200 for Zeiss UMK,  $\Delta r'_{\max} = \pm 4 \mu\text{m}$  at  $r' < 90 \text{ mm}$ )

<sup>1</sup> Usually the notions  $O$  or  $O'$  are used although when  $O_m$  is meant.

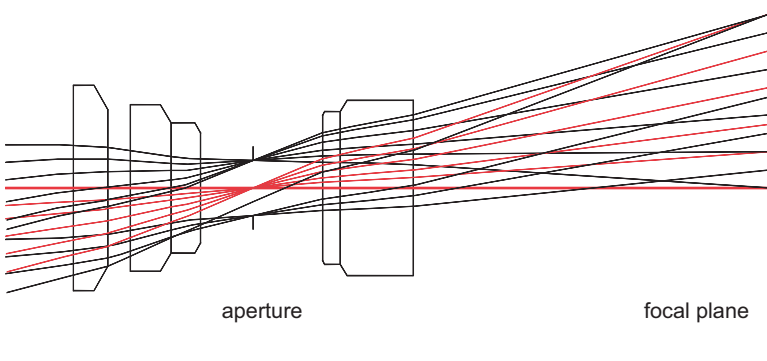


**Figure 3.13** Path of light for an asymmetric lens  
(Sonnar 4/f = 150 for Rollei 6008,  $\Delta r' = \pm 85 \mu\text{m}$  at  $r' = 33 \text{ mm}$ ,  $\Delta r' = \pm 13 \mu\text{m}$  at  $r' = 10 \text{ mm}$ )

especially for the corner areas of the image. As an example, Fig. 3.13 illustrates the path of light inside an asymmetric telephoto lens (see Fig. 3.20 to Fig. 3.22).

In contrast, tangential and asymmetric distortion are attributable to decentring and tilt of individual lens elements within the objective (Fig. 3.24 shows the effect in image space). For good quality lenses tangential distortions are usually 10 times smaller than radial-symmetric distortion and thus can be neglected for many photogrammetric purposes. However, the increasingly used simple video lenses have been shown to exhibit significantly larger tangential and asymmetric distortion values. Distortions in the range of more than  $30 \mu\text{m}$  are possible and are attributable to the low cost of these lenses combined with the small size of their individual elements.

### 3.2.2.5 Focusing

In practical optical imaging a projected point is sharply observed by the human eye, under normal viewing conditions, if the diameter of the circle of confusion  $u'$  does not exceed a diameter of  $20 \mu\text{m}$  for photographic systems and about 1 pixel for digital imaging sensors. Hence not only the object point  $P$  focused in distance  $a$  is sharply defined but all points between  $P_1$  and  $P_2$  appear sharp (Fig. 3.14).

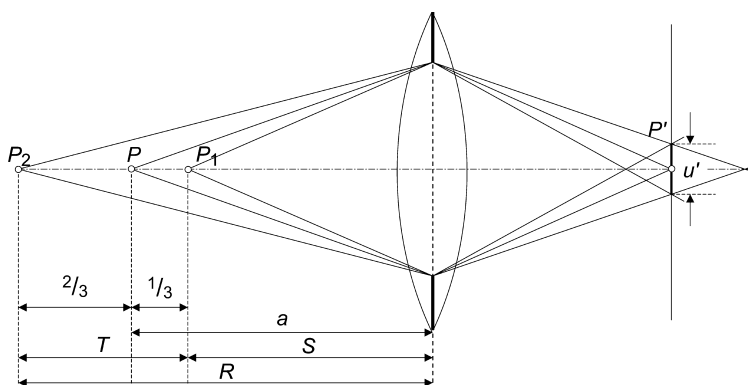


**Figure 3.14** Focusing and depth of field

The distance to the nearest and the furthest sharply defined object point can be calculated as follows:

$$R = \frac{a}{1+K} \quad S = \frac{a}{1-K} \quad (3.22)$$

where

$$K = \frac{k(a-f)u'}{f^2}$$

and

$k$ : f-number

$f$ : focal length

$a$ : focused object distance

By re-arranging equation (3.22) the diameter of the defocusing circle  $u'$  can be calculated:

$$u' = \frac{S-R}{S+R} \frac{f^2}{k(a-f)} \quad (3.23)$$

The depth of field is defined by

$$T = S - R = \frac{2u'k(1+\beta')}{\beta'^2 - \left(\frac{u'k}{f}\right)^2} \quad (3.24)$$

Hence, for a given circle of confusion diameter, depth of field depends on the f-number of the lens  $k$  and the imaging scale  $\beta'$ . The depth of field will increase if the aperture is reduced, the object distance enlarged, or if the focal length is reduced through the use of a wider angle lens. Fig. 3.15 shows the non-linear curve of the resulting depth of field at different scale numbers and apertures.

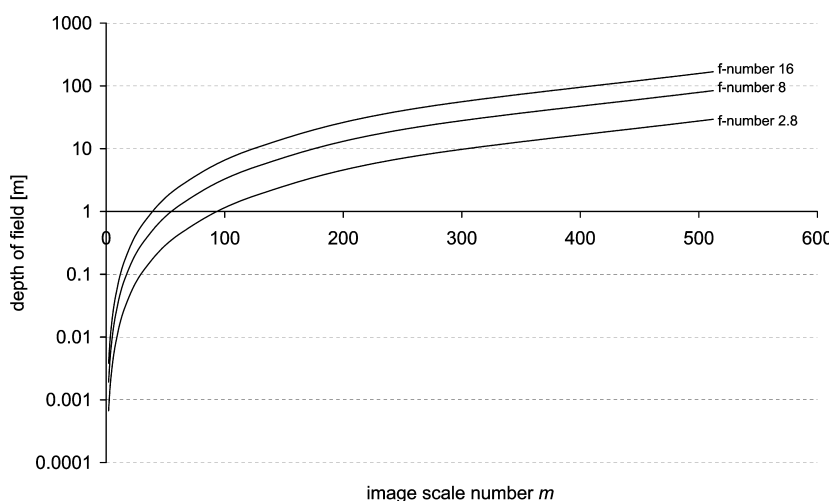


Figure 3.15 Depth of field as a function of image scale number

For large object distances equation (3.24) can be simplified to

$$t = \frac{2u'k}{\beta'^2} \quad (3.25)$$

When imaging objects at infinity, depth of field can be optimised if the lens is not focused at infinity but to the hyperfocal distance  $b$ . Then the depth of field ranges between the nearest acceptably sharp point  $R$  to  $\infty$ .

$$b = \frac{f^2}{u'k} \quad (3.26)$$

#### Example 3.4:

Consider a photograph of an object at distance  $a = 5$  m and image scale number  $m = 125$  respectively  $\beta' = 0.008$ . The depth of focus for each aperture  $k = 2.8$  and  $k = 11$  is required.

Solution:

$$\text{1. for } k = 2.8 \quad t = \frac{2u'k}{\beta'^2} = \frac{2 \times 2 \times 10^{-5} \times 2.8}{0.008^2} \\ = 1.8 \text{ m}$$

$$\text{2. for } k = 11 \quad t = 6.9 \text{ m}$$

Sufficient depth of field has to be considered especially carefully for convergent imagery, where there is variation in scale across the image, and when imaging objects with large depth variations. Depth of field can become extremely small for large image scales (small  $m$ ), for example those achieved at very close ranges.

It is worth noting that under many circumstances a slight defocusing of the image can be tolerated if signalised centric targets are used for image measurement. In the visual case, the human eye can centre a symmetrical measuring mark over a blurred circle and in the automated case, the optical centroid remains unchanged for digital image measurement if the image is defocused.

#### 3.2.2.6 Light fall-off and vignetting

For conventional lenses, the luminous intensity  $E$  effective at the imaging plane, where the light sensitive material is located, is reduced with increasing field angle  $\Omega$  according to the  $\cos^4$  law:

$$E(\Omega) = E \cos^4 \Omega \quad (3.27)$$

Hence the image gets darker towards its periphery. The effect is particularly observable for wide and super wide angle lenses where it may be necessary to use a concentrically graduated neutral density filter in the optical system to reduce the image intensity at the centre of the field of view. Fish eye lenses avoid the  $\cos^4$  law through the use of different projections which reduce the fall off in illumination at the expense of image distortions. The  $\cos^4$  reduction in image intensity can be amplified if vignetting, caused by physical obstructions due to mounting parts of the lens, is taken into account (Robson *et al.* 1999).

### 3.2.2.7 Lenses

#### *Relative aperture and f-number*

The light gathering capacity of a lens is measured by the relative aperture as the ratio of the iris diameter  $d'$  of the entrance pupil to the focal length  $f$  (Fig. 3.16):

$$\text{relative aperture} = \frac{d'}{f} \quad (3.28)$$

For a lens with an entrance pupil of  $d' = 20$  mm and a focal length of  $f = 80$  mm the relative aperture yields 1:4.

The f-number  $k$  is given by the reciprocal of relative aperture:

$$k = \frac{f}{d'} \quad (3.29)$$

A higher f-number corresponds to a smaller relative aperture i.e. the light gathering capacity is reduced. Changes in f-number follow a progression whereby the area of aperture (hence the amount of gathered light) changes by a factor of 2 from step to step. The f-number also alters the depth of field (see section 3.2.2.5).

**Table 3.1** Standard f-number sequence

1	1.4	2	2.8	4	5.6	8	11	16	22	...
---	-----	---	-----	---	-----	---	----	----	----	-----

#### *Viewing angle and format angle*

The field of view  $2\alpha'$  of a lens is defined by its focal length and the diameter of the entrance pupil (Fig. 3.16):

$$\tan \alpha' = \frac{d'}{2f} \quad (3.30)$$

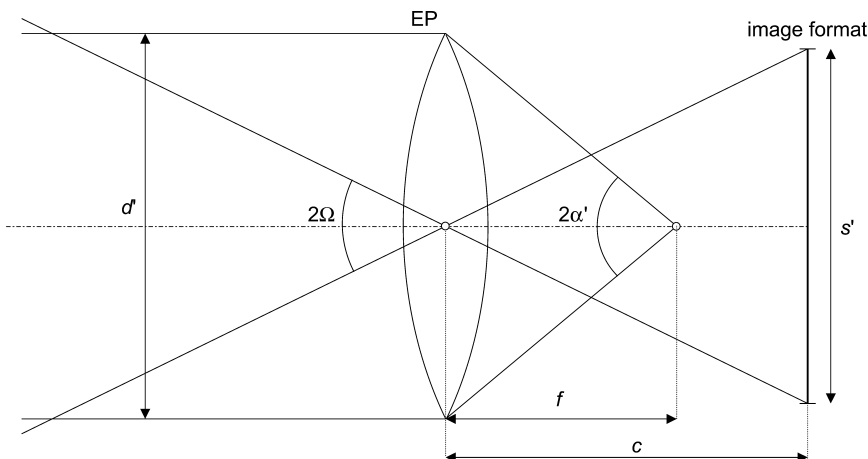


**Figure 3.16** Field of view and format angle

In contrast, the format angle (field angle)  $2\Omega$  is given by the maximum usable image angle with respect to the diagonal of a given image format  $s'$  and the principal distance  $c$ :

$$\tan \Omega = \frac{s'}{2c} \quad (3.31)$$

Format angle is a convenient method of distinguishing between different basic lens types (Table 3.2). As a rule of thumb the focal length of a normal lens is approximately equal to the diagonal of the image format. Small image formats (found in video cameras and low cost digital cameras) require short focal lengths in order to produce wide angles of view.

**Table 3.2** Resulting focal lengths for typical lens types and image formats

lens type	format-angle	video [8 × 6 mm <sup>2</sup> ]	small format [36 × 24 mm <sup>2</sup> ]	medium format [60 × 60 mm <sup>2</sup> ]	large format [230 × 230 mm <sup>2</sup> ]
image diagonal	$2\Omega$	10 mm	43 mm	84 mm	325 mm
tele lens (small angle)	15 – 25°	> 22 mm	> 90 mm	> 190 mm	610 mm
normal lens (default)	40 – 70°	7 – 13 mm (8 mm)	40 – 60 mm (50 mm)	70 – 115 mm (80 mm)	280 – 440 mm (300 mm)
wide angle	70 – 100°	4 – 7 mm	18 – 35 mm	35 – 60 mm	135 – 230 mm
fish-eye	>100°	<4 mm	<18 mm	<35 mm	<135 mm

### Zoom lenses

Zoom or vario lenses enable a varying focal length to be produced from a single lens system. Designs may also permit constant focusing and maintenance of the same relative aperture as focal length is changed. Fig. 3.17 illustrates the principle of a zoom lens where moving a central lens group gives a change in focal length whilst motion of a second group of lenses provides focus compensation.

According to section 3.2.2.4, a change in focal length yields a new interior orientation. Due to the zoom lens construction, will not only the spatial position of the perspective centre be altered but parameters of radial and decentring distortion will also change. Whilst zoom lenses can be calibrated photogrammetrically, off-the-shelf designs cannot be assumed to provide high mechanical stability. Thus while they provide great flexibility, they are seldom used in practice for accurate work.

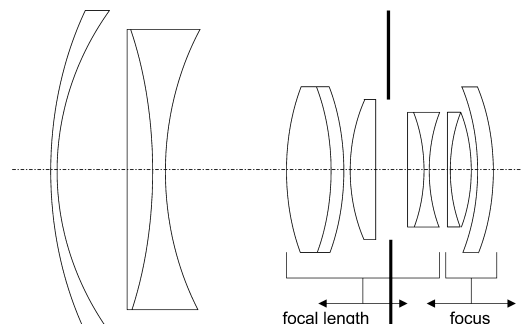


**Figure 3.17** Principle of a vario lens (after Marchesi 1985)

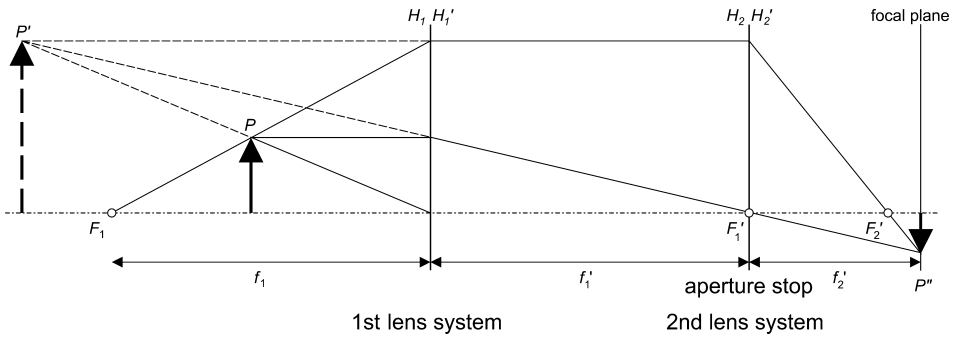


Figure 3.18 Two-stage telecentric lens (after Schmidt 1993)

### Telecentric lenses

Telecentric lenses are designed such that all object points are imaged with equal image scales regardless of their distance. A two-stage telecentric lens consists of two lens groups where the object-orientated principal plane of the second (right) system coincides with the focal plane of the first (left) system (Fig. 3.18). The aperture stop is also positioned at this location. An object point  $P$  located within one focal length of the first system is virtually projected into  $P'$ . The second system projects  $P'$  sharply into the image plane at  $P''$ . Since all points in object space lie on a parallel axis (hence distance-independent), light rays are projected through identical principal rays, thus they are imaged at the same position in the focal plane.

The limitation of the bundle of rays yields a limited size of the object given either by the maximum diameter of the aperture-stop or the lens. Telecentric lenses are mainly used for imaging of small objects ( $\varnothing < 100$  mm) in the field of two-dimensional optical metrology. The imaging model does not follow central projection but can be modelled as a parallel projection.

### 3.2.3 Interior orientation of a camera

#### 3.2.3.1 Parameters of interior orientation

A camera can be modelled as a spatial system that consists of a planar imaging area (film or electronic sensor) and the lens with its perspective centre. The parameters of interior orientation of a camera define the spatial position of the perspective centre, the principal distance and the location of the principal point. They also encompass deviations from the principle of central perspective to include radial and tangential distortion and often image affinity and orthogonality.

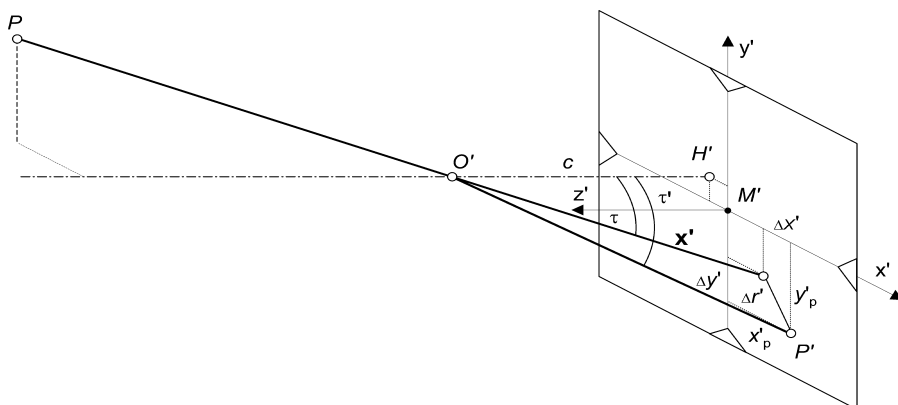


Figure 3.19 Interior orientation

Fig. 3.19 illustrates the schematic imaging process of a photogrammetric camera. Position and distance of the perspective centre and deviations from the central perspective model are described with respect to the image coordinate system as it is defined by means of reference or fiducial points (film based system) or the pixel array (electronic system). The origin of the image coordinate system is located in the image plane. For the following analytical calculations the origin of the image coordinate system is shifted to coincide with the perspective centre according to Fig. 2.1.

Hence, the parameters of interior orientation are (see section 3.2.2.4):

- principal point  $H'$ :

Nadir of the perspective centre with image coordinates  $(x'_0, y'_0)$ , for standard cameras approximately equal to the centre of the image:  $H' \approx M'$

- principal distance  $c$ :

Normal distance to the perspective centre from the image plane in the negative  $z'$  direction; approximately equal to the focal length of the lens when focused at infinity:  $c \approx f'$

- parameters of functions describing imaging errors:

Functions or parameters that describe deviations from the central perspective model are dominated by the effect of radial-symmetric distortion  $\Delta r'$

If these parameters are known, the (error-free) imaging vector  $\mathbf{x}'$  can be defined with respect to the perspective centre (hence, the principal point):

$$\mathbf{x}' = \begin{bmatrix} x' \\ y' \\ z' \end{bmatrix} = \begin{bmatrix} x'_p - x'_0 - \Delta x' \\ y'_p - y'_0 - \Delta y' \\ -c \end{bmatrix} \quad (3.32)$$

where

$x'_p, y'_p$ : measured coordinates of image point  $P'$

$x'_0, y'_0$ : coordinates of the principal point  $H'$

$\Delta x', \Delta y'$ : axis-related correction values for imaging errors

The parameters of interior orientation are determined by camera calibration (see section 3.2.3.7).

### 3.2.3.2 Functions describing imaging errors

#### Correction functions

Deviations from the ideal central perspective model, attributable to imaging errors, are expressed in the form of correction functions  $\Delta x', \Delta y'$  to the measured image coordinates. According to section 3.2.2.4, distortion is related to the principal point i.e. in the first instance, measured image coordinates  $x'_p, y'_p$  are corrected by a shift of the principal point  $x'_0, y'_0$ :

$$\begin{aligned} x^\circ &= x'_p - x'_0 && : \text{image coordinates related to the principal point} \\ y^\circ &= y'_p - y'_0 \end{aligned}$$

where

$$r' = \sqrt{x^\circ 2 + y^\circ 2} \quad : \text{image radius, distance from the principal point}$$

Hence, the image coordinates  $x^\circ, y^\circ$  are corrected by:

$$\begin{aligned} x' &= x^\circ - \Delta x' && : \text{corrected image coordinates} \\ y' &= y^\circ - \Delta y' \end{aligned}$$

Strictly speaking, the values  $x^\circ, y^\circ$  are only approximations since the corrections  $\Delta x', \Delta y'$  must be calculated using the final image coordinates  $x', y'$ . Consequently, correction values must be applied iteratively (see section 3.2.3.3).

Key deviations from the ideal central perspective are generated by the following physical effects:

### 1. Radial distortion

Radial (symmetric) distortion constitutes the major imaging error for most camera systems. It is attributable to variations in refraction at each individual component lens within the objective. It is a function not only of the lens design used but also of the chosen focusing distance, and of the object distance at a constant focus<sup>1</sup>. Fig. 3.20 shows the effect of radial distortion as a function of the image radius of an imaged point. In the example, the distortion increases with distance from the principal point. For standard lenses it can reach more than 100  $\mu\text{m}$  in the image corners.

The distortion curve is usually modelled with a polynomial series (Seidel series) with distortion parameters  $K_1$  to  $K_n$  (Brown 1971):

$$\Delta r'_{\text{rad}} = K_1 r'^3 + K_2 r'^5 + K_3 r'^7 + \dots \quad (3.33)$$

For most lens types the series can be truncated after the second or third term without any significant loss of accuracy. Then the image coordinates are corrected proportionally:

$$\Delta x'_{\text{rad}} = x' \frac{\Delta r'_{\text{rad}}}{r'} \quad \Delta y'_{\text{rad}} = y' \frac{\Delta r'_{\text{rad}}}{r'} \quad (3.34)$$

The distortion parameters defined in equation (3.33) are numerically correlated with image scale or principal distance. In order to avoid these correlations a linear part of the distortion function is separated. This is equivalent to a rotation of the distortion curve into the direction of the  $r'$  axis, thus yielding to a second zero-crossing (Fig. 3.21).

$$\Delta r'_{\text{rad}} = K_0 r' + K_1 r'^3 + K_2 r'^5 + K_3 r'^7 \quad (3.35)$$

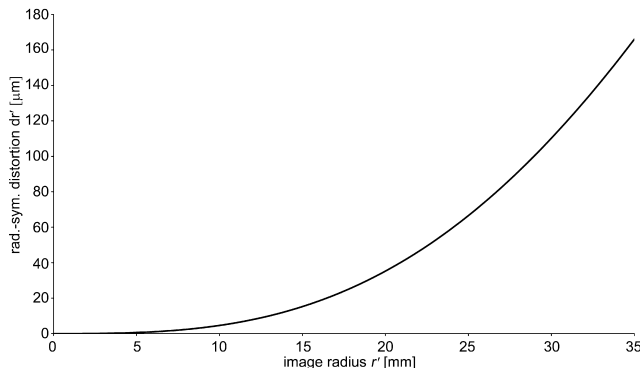
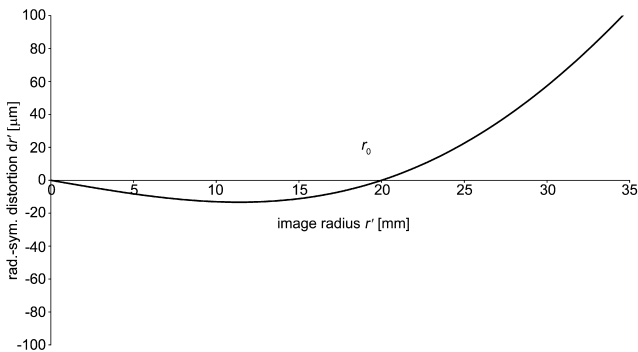


Figure 3.20 Radial-symmetric distortion (Rollei Sonnar 4/150)

<sup>1</sup> The distance-dependent effect is usually considered only for highest accuracy specifications (see section 3.2.3.2).



**Figure 3.21** Typical balanced lens distortion curve (Rollei Sonnar 4/150)

Alternatively a polynomial of the following type is used<sup>1</sup>:

$$\Delta r'_{\text{rad}} = A_1 r'(r'^2 - r_0^2) + A_2 r'(r'^4 - r_0^4) + A_3 r'(r'^6 - r_0^6) \quad (3.36)$$

By simple rearrangement of (3.36) it can be shown that the same effect is yielded as with equation (3.35):

$$\Delta r'_{\text{rad}} = A_1 r'^3 + A_2 r'^5 + A_3 r'^7 - r'(A_1 r_0^2 + A_2 r_0^4 + A_3 r_0^6) \quad (3.37)$$

Here the term in brackets is a constant analogue to  $K_0$ . However  $r_0$  cannot be chosen arbitrarily as there is a dependency on the parameters  $A_1, A_2, A_3$ . In practice,  $r_0$  should be chosen such that minimal and maximal distortion values are more or less equal with respect to the complete image format (balanced radial distortion, Fryer 1996). Usually  $r_0$  is set to approximately 2/3 of the maximum image radius.

Fig. 3.21 shows a typical curve of radial-symmetric distortion according to equation (3.36) and Fig. 3.22 displays the corresponding two-dimensional effect with respect to the image format. Balanced radial lens distortion is only necessary when the distortion correction is to be applied using analogue methods, for example by using specially shaped cams within the

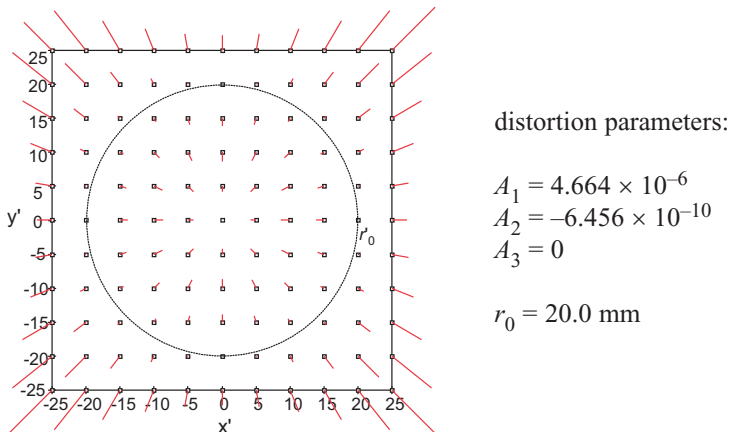


**Figure 3.22** Effect of radial-symmetric distortion (data from Table 3.3)

<sup>1</sup> Additional correction functions are discussed on page 120.

mechanical space rod assembly.  $r_0$  is not commonly used in the calibration of digital systems since during digital data processing the correction is purely numerical rather than mechanical.

Often a table of correction values for radial-symmetric distortion is derived from camera calibration for subsequent use by a real time processing system to interpolate correction values for image coordinates (Table 3.3).

**Table 3.3** Correction data for distortion (see Fig. 3.21, Fig. 3.22)

$r'$ (mm)	$\Delta r'$ (mm)	$r'$ (mm)	$\Delta r'$ (mm)	$r'$ (mm)	$\Delta r'$ (mm)
0	0.0000	10	-0.0132	22	0.0076
1	-0.0018	11	-0.0129	23	0.0121
2	-0.0035	12	-0.0122	24	0.0170
3	-0.0052	13	-0.0112	25	0.0225
4	-0.0068	14	-0.0098	26	0.0285
5	-0.0082	15	-0.0080	27	0.0350
6	-0.0096	16	-0.0057	28	0.0419
7	-0.0107	17	-0.0031	29	0.0494
8	-0.0117	18	-0.0057	30	0.0574
9	-0.0125	19	-0.0031	31	0.0658
10	-0.0130	20	0.0000	32	0.0748
11	-0.0133	21	0.0035	33	0.0842

## 2. Tangential distortion

Radial-asymmetric distortion, often called tangential or decentring distortion (Fig. 3.23), is mainly caused by decentring and misalignment of individual lens elements within the objective. It can be compensated for by the following function (Brown 1971):

$$\begin{aligned}\Delta x'_{\tan} &= B_1(r'^2 + 2x'^2) + 2B_2x'y' \\ \Delta y'_{\tan} &= B_2(r'^2 + 2y'^2) + 2B_1x'y'\end{aligned}\quad (3.38)$$

Compared to the radial-symmetric part, radial-asymmetric distortion shows much smaller quantities for most quality lenses. Hence, it is often determined for high accuracy specifications only. If low cost lenses are used, as is often the case for video and surveillance camera systems, significant tangential distortion can be present.

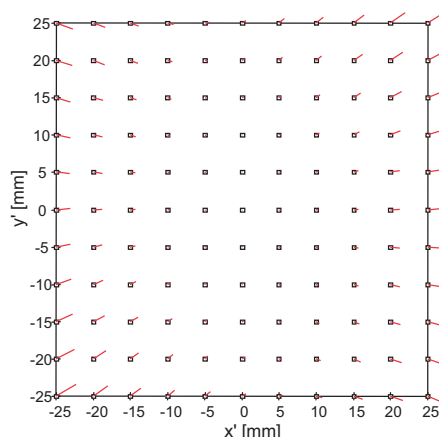
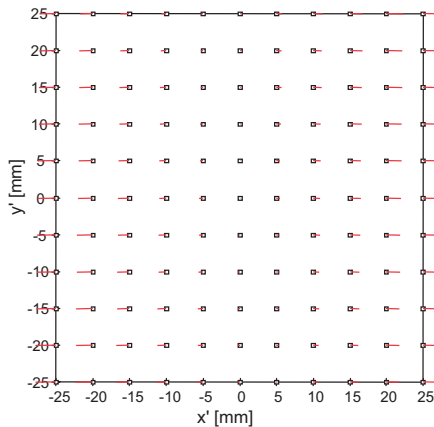


**Figure 3.23** Effect of radial-asymmetric and tangential distortion

### 3. Affinity and shear

Affinity and shear are used to describe deviations of the image coordinate system with respect to orthogonality and uniform scale of the coordinate axes (Fig. 3.24). For analogue cameras these effects can be compensated for by means of an affine transformation based upon measurements of fiducial marks or a réseau. Digital imaging systems can produce these characteristics if the sensor has light sensitive elements that are rectangular rather than square. Affinity and shear also exist for video images that are transferred in analogue form before being digitised by a frame grabber. The following function can be used to provide an appropriate correction:

$$\begin{aligned}\Delta x'_{\text{aff}} &= C_1 x' + C_2 y' \\ \Delta y'_{\text{aff}} &= 0\end{aligned}\quad (3.39)$$



### 4. Total correction

The individual terms used to model the imaging errors of most typical photogrammetric imaging systems can be summarised as follows:

$$\begin{aligned}\Delta x' &= \Delta x'_{\text{rad}} + \Delta x'_{\tan} + \Delta x'_{\text{aff}} \\ \Delta y' &= \Delta y'_{\text{rad}} + \Delta y'_{\tan} + \Delta y'_{\text{aff}}\end{aligned}\quad (3.40)$$

#### *Additional parameter sets*

There are many cases in photogrammetric literature where sets of additional parameters are included in the mathematical modelling process. Such sets are often designed to accommodate systematic effects identifiable in the image residuals, but which are not directly attributable to physical mechanisms.

An approach by Brown (1976) has been developed specifically for large format analogue aerial cameras:

$$\begin{aligned}\Delta x'_{\text{Brown}} &= D_1 x' + D_2 y' + D_3 x' y' + D_4 y'^2 + D_5 x'^2 y' + D_6 x' y'^2 + D_7 x'^2 y'^2 \\ &\quad + [E_1(x'^2 - y'^2) + E_2 x'^2 y'^2 + E_3(x'^4 - y'^4)] \frac{x'}{c} \\ &\quad + [E_4(x'^2 + y'^2) + E_5(x'^2 + y'^2)^2 + E_6(x'^2 + y'^2)^3] x' + E_7 + E_9 \frac{x'}{c} \\ \Delta y'_{\text{Brown}} &= D_8 x' y' + D_9 x'^2 + D_{10} x'^2 y' + D_{11} x' y'^2 + D_{12} x'^2 y'^2 \\ &\quad + [E_1(x'^2 - y'^2) + E_2 x'^2 y'^2 + E_3(x'^4 - y'^4)] \frac{y'}{c} \\ &\quad + [E_4(x'^2 + y'^2) + E_5(x'^2 + y'^2)^2 + E_6(x'^2 + y'^2)^3] y' + E_8 + E_9 \frac{y'}{c}\end{aligned}\quad (3.41)$$

**Example 3.5:**

A calibration of a Kodak DCS420 digital camera gives the following correction parameter set:

$$\begin{array}{lll} A_1 = -4.185 \times 10^{-4} & A_2 = 6.823 \times 10^{-7} & A_3 = 9.825 \times 10^{-9} \\ B_1 = -6.019 \times 10^{-6} & B_2 = -9.843 \times 10^{-6} & \\ C_1 = -2.472 \times 10^{-4} & C_2 = -9.193 \times 10^{-5} & r'_0 = 6 \text{ mm} \end{array}$$

Compute the effects of individual distortion terms for two image points, the first located in the centre of the image and the second in one corner:

	$x'_1$	$y'_1$	$x'_2$	$y'_2$	
$x', y'$	1.500	1.500	7.000	4.500	mm
$A_1, A_2, A_3$	17.8	17.8	-61.1	-39.3	$\mu\text{m}$
$B_1, B_2$	-0.1	-0.1	-1.6	-1.5	$\mu\text{m}$
$C_1, C_2$	-0.5	0.0	-2.1	0.0	$\mu\text{m}$
total	17.2	17.7	-64.8	-40.7	$\mu\text{m}$

This example demonstrates that the effect of radial distortion dominates. However, if the accuracy potential of this camera of about  $0.2 \mu\text{m}$  (1/50th pixel) is to be reached, the other image errors have also to be considered.

In addition to parameters for modelling deformations in the image plane ( $D_1$  to  $D_{12}$ ) terms for the compensation of film or sensor unflatness are included ( $E_1$  to  $E_6$ ) that are formulated as a function of the radial distance or of the tangent of the imaging angle ( $x'/c$  or  $y'/c$ ) respectively. However, the approach is more difficult to interpret geometrically, and it can easily be over-parameterised (linear dependency of individual parameters). Parameter sets of similar complexity are used by Jacobsen (1982) and Kruck (1983). For self-calibrating bundle adjustment, individual parameters should be tested for their significance and correlation with respect to each other. Any parameters which fail such tests should be eliminated on a weakest first basis.

Beyer (1992) has recommended the following parameter set for digital imaging systems:

$$\begin{aligned} \Delta x'_{\text{Beyer}} &= \Delta x'_0 - \frac{x'}{c} \Delta c + K_1 x' r'^2 + K_2 x' r'^4 + K_3 x' r'^6 \\ &\quad + P_1(r'^2 + 2x'^2) + 2P_2 x' y' - C_1 x' + C_2 y' \\ \Delta y'_{\text{Beyer}} &= \Delta y'_0 - \frac{y'}{c} \Delta c + K_1 y' r'^2 + K_2 y' r'^4 + K_3 y' r'^6 \\ &\quad + 2P_1 x' y' + P_2(r'^2 + 2y'^2) + C_2 x' \end{aligned} \tag{3.42}$$

Here the parameters  $K$  describe radial-symmetric distortion,  $P$  describe radial-asymmetric and tangential distortion and  $C$  models affinity and shear. The parameters  $\Delta x'_0$ ,  $\Delta y'_0$  and  $\Delta c$  are used for small corrections to the spatial position of the perspective centre. Together with the factors  $x'/c$  and/or  $y'/c$  they show a similar effect as introduction of  $r_0$  in equation (3.36).

In computer vision the parameters of interior orientation are typically expressed by a calibration matrix  $\mathbf{K}$  which consists of five degrees of freedom (principal distance  $c$ , principal point  $x'_0, y'_0$ , shear  $s$  and scale variation of axes  $m$ ).

$$\mathbf{K} = \begin{bmatrix} c & s & x'_0 \\ 0 & (1+m)c & y'_0 \\ 0 & 0 & 1 \end{bmatrix} \quad (3.43)$$

$\mathbf{K}$  is part of a general  $3 \times 4$ -projection matrix for the transformation from object space into image space by terms of homogeneous coordinates (see section 2.2.2.3). In this method lens distortion cannot directly be integrated and must be modelled by a position-dependent correction matrix  $\mathbf{dK}(x', y')$  (Hartley and Zisserman 2000, Mugnier *et al.* 2004).

#### Correction of distance-dependant distortion

Strictly speaking, the above mentioned approaches for the correction of lens distortion are valid only for points of an object plane parallel to the image plane that is focused, according to the lens equation (3.10), at a distance  $a'$  which is equivalent to  $c$  with respect to the interior perspective centre (Fraser and Shortis 1992, Dold 1997). Imaging rays of points outside this object plane pass through the lens along a different optical path, hence are subject to different distortion effects. As an example, Fig. 3.25 shows the distortion curves of object points in different image scales (object distances).

This effect can be considered by the introduction of a distance-dependent correction term. Fryer and Brown (1986) describe the definition of a scaling factor:

$$\gamma_{SS'} = \frac{c_{S'}}{c_S} = \frac{S'}{S'} \frac{(S - c)}{(S' - c)} \quad (3.44)$$

where  $c_s$ : principal distance (image distance) of object distance  $S$   
 $c_{s'}$ : principal distance (image distance) of object distance  $S'$

For a given set of distortion parameters  $K_{1s'}, K_{2s'}, K_{3s'}$  for an object plane at distance  $S'$  according to equation (3.35), the correction of radial distortion for object points at a focused distance  $S$  can be calculated as follows:

$$\Delta r'_{SS'} = \gamma_{SS'}^2 K_{1S'} r'^3 + \gamma_{SS'}^4 K_{2S'} r'^5 + \gamma_{SS'}^6 K_{3S'} r'^7 \quad (3.45)$$

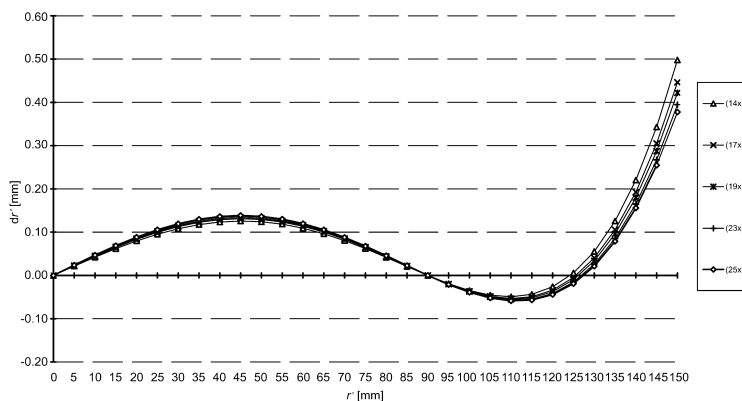


Figure 3.25 Lens distortion curves for different image scales (after Dold 1997)

This model is suited for high-precision measurements made at large scales ( $m < 30$ ) and lenses with relatively small distortion values. As the distance-dependent distortion effect increases with image scale (decreasing object distance), Fraser and Shortis (1992) propose the introduction of an empirically estimated correction factor  $g_{ss'}$ , that can be determined for each individual lens:

$$\Delta r'_{SS'} = \Delta r'_S + g_{SS'}(\Delta r'_{S'} - \Delta r'_S) \quad (3.46)$$

Radial and tangential distortion can also be formulated as a function of the focused distance  $S$ :

$$\begin{aligned} \Delta x'_S &= \left(1 - \frac{c}{S}\right) \left[ P_1(r'^2 + 2x') + 2P_2x'y' \right] \\ \Delta y'_S &= \left(1 - \frac{c}{S}\right) \left[ P_2(r'^2 + 2y') + 2P_1x'y' \right] \end{aligned} \quad (3.47)$$

Dold (1997) proposes the following set of parameters for the correction of distance-dependent distortion that can be estimated, in contrast to the above mentioned approaches, completely within a self-calibrating bundle adjustment. However, it should be noted that incorporation of such corrections within a self-calibration require very strong networks that contain many images taken at each distance setting in order to provide a robust and reliable parameter set.

$$r'_{dist} = \frac{1}{Z^*} \left[ D_1 r'(r'^2 - r_0^2) + D_2 r'(r'^4 - r_0^4) + D_3 r'(r'^6 - r_0^6) \right] \quad (3.48)$$

where  $Z^*$  = denominator of collinearity equations (4.10)

$\approx S$  (object distance)

Extension of equation (3.40) leads to the following total correction of imaging errors:

$$\begin{aligned} \Delta x' &= \Delta x'_{rad} + \Delta x'_{tan} + \Delta x'_{aff} + \Delta x'_{dist} \\ \Delta y' &= \Delta y'_{rad} + \Delta y'_{tan} + \Delta y'_{aff} + \Delta y'_{dist} \end{aligned} \quad (3.49)$$

Usually distance-dependent distortion does not exceed more than 1  $\mu\text{m}$  at the edge of the image. Hence, it must only be considered for high-accuracy measurement tasks where sub-micron image measuring accuracies will be achieved. This is most relevant for large-scale industrial applications with analogue large-format cameras, but also for high-resolution digital cameras that provide an accuracy potential of better than 0.5  $\mu\text{m}$ . The effect will be most prevalent where there is a large range of depth over the object or objects to be recorded.

### 3.2.3.3 Iterative correction of imaging errors

Measured image points can be corrected *a priori* if the parameters of interior orientation are known. Example cases are the calculation of object coordinates by space intersection, or the resampling of distortion-free images. Often misunderstandings occur for the sequence and sign of image error corrections. For a unique definition it is necessary to know the source of distortion values and details about the implementation of the used program, which is often not available in practice.

The correction model described in equation (3.32) is based on the assumption that the error corrections are calculated by self-calibrating bundle adjustment. In the collinearity model (4.8), points in the object space are given and their associated image coordinates are calculated. Existing distortion values are then added to these image coordinates.

$$\begin{aligned}x' &= f(X, Y, Z, X_0, Y_0, Z_0, \omega, \phi, \kappa, c, x'_0) + \Delta x'(x', y') \\y' &= f(X, Y, Z, X_0, Y_0, Z_0, \omega, \phi, \kappa, c, y'_0) + \Delta y'(x', y')\end{aligned}\quad (3.50)$$

The corrections to be applied depend on the current values of image coordinates. Thus a correct calculation is only possible after a sufficient number of iterations. After adjustment correction parameters based on adjusted object coordinates and orientation parameters are computed with error-free image coordinates. Consequently, these correction values are only directly applicable to image coordinates for those calculations that lead from object space to image space.

The opposite case occurs if image coordinates are measured in a distorted image. Here, distortion correction must be applied iteratively. The iterative process utilises the corrected image position of each particular iteration as the starting point for the following correction value calculation. The process is continued until the computed correction is insignificant.

Where lenses with large distortions are used, the requirement for recursive image coordinate correction, as displayed in Fig. 3.26, is of major importance. Table 3.4 summarises the effect of iterative correction of image coordinates for typical camera systems. It becomes obvious that significant errors can occur for cameras with larger image formats and higher distortion values (DCS 645M: 13.4 μm, DCS 460: 30 μm). In contrast, for the other examples a non-iterative correction can be used (Rollei 6008: 0.8 μm, CCD-Kamera JAI: 0.2 μm). In practice it is always better to default to iterative correction since the additional computation time is generally insignificant. Typically 4 iterations are required.

**Table 3.4** Effect of iterative distortion correction for typical camera systems

camera	Rollei 6008	Kodak ProBack DCS 645M	Kodak DCS 460	JAI
lens	f=150 mm	f=35 mm	f=15 mm	f=8 mm
c	150.5566	-35.6657	14.4988	-8.2364
x'_0	0.023	-0.0870	0.1618	0.2477
y'_0	0.014	0.4020	-0.1199	0.0839
A <sub>1</sub>	4.664E-06	-9.0439E-05	-4.5020E-04	-1.9016E-03
A <sub>2</sub>	-6.456E-10	6.3340E-08	1.7260E-06	3.1632E-05
A <sub>3</sub>	0	-1.5294E-11	-4.0890E-10	0
B <sub>1</sub>	0	2.5979E-06	-1.4670E-06	-2.6175E-05
B <sub>2</sub>	0	-7.2654E-07	-6.6260E-06	-7.3739E-05
C <sub>1</sub>	0	1.0836E-04	-2.5300E-04	9.8413E-03
C <sub>2</sub>	0	1.0964E-05	-1.6130E-04	-7.2607E-06
image coordinate x'	25.000	18.000	13.000	3.200
image coordinate y'	25.000	18.000	9.000	2.400
total effect	0.0767	-0.2641	0.2229	-0.0211
iterative correction	-0.0008	-0.0134	-0.0304	-0.0002

### 3.2.3.4 Physical definition of the image coordinate system

The image coordinate system must not only be defined physically with respect to the camera body, but must also be reconstructable within the image. Three common methods are found in photogrammetric imaging systems (Fig. 3.27):

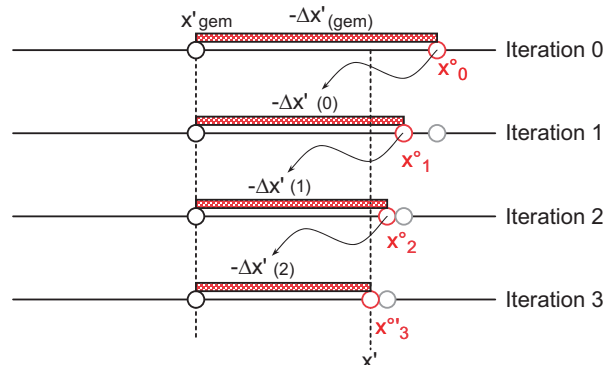


**Fig. 3.26** Recursive distortion correction of image coordinates

### 1. Fiducial marks

The image coordinate system is defined by at least four unique fiducial marks each of which has calibrated nominal coordinates. During exposure the fiducial marks are either imaged in contact with, or projected onto the image. Fiducial marks are typically found in classical metric film cameras and are used in association with a mechanically flattened image plane (examples in Fig. 3.28).

### 2. Réseau

A réseau consists of a thin plane glass plate with a grid of calibrated reference points (réseau crosses) etched onto it. The plate is mounted directly in front of, and in contact with the film (sensor), and projected onto the image at exposure (example in Fig. 3.29). Deviations of planarity

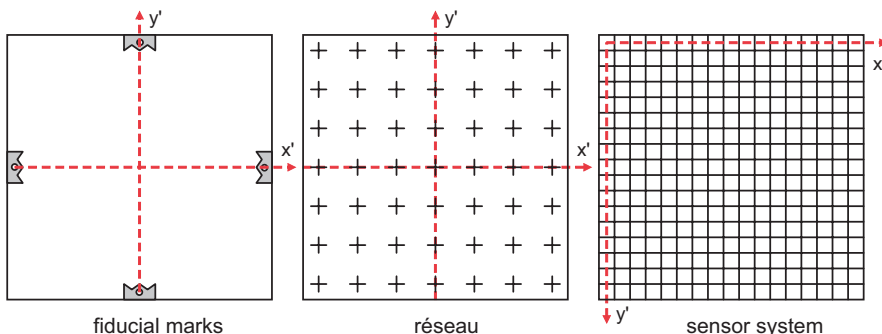


**Figure 3.27** Image coordinate systems



**Figure 3.28** Two different fiducial marks designs



**Figure 3.29** Réseau crosses projected onto a film

or film deformations can later be compensated numerically by the imaged réseau. As a variant a réseau can also be realised by a back-projection of grid-wise distributed reference points.

### 3. Sensor coordinate system

Artificial reference points for the definition of the image coordinate system are not necessary for digital cameras if a unique relationship between digital image and opto-electronic image sensor is provided. This is true for fixed mounted matrix sensors (CCD and CMOS arrays) and direct digital read-out of the image information. Usually the origin of these systems is defined in the upper left corner, hence a left-handed coordinate system results.

#### 3.2.3.5 Transformations for interior orientation

Using image reference points (fiducial marks) a transformation between the image coordinate system and the machine coordinate system of the image measuring device can be determined. Position and rotation of the image with respect to the measuring system can be compensated by a similarity transformation according to (2.2).

Further effects resulting differently in x and y direction like film and paper shrinking, or sheering of coordinate axes can be compensated by an affine transformation according to (2.6).

For réseau images grid-wise affine or bilinear (2.10) transformations are preferred. In the case of irregular réseau grids or invisible réseau points (e.g. non-measurable crosses in Fig. 3.29 right), a synthetic point grid can be generated based on the finite element method. Subsequently, the actual grid-wise transformation of measured image points is performed (Kotowski and Weber 1984).

After an initial global affine transformation of all measured  $s$  réseau points, residuals of réseau points as well as deviations  $\Delta x_k, \Delta y_k$  at points of a calculated interpolation grid of  $m \times n$  grid points can be ascertained (Fig. 3.30). These deviations are used as observations for correction equations of bilinear form:

$$\begin{aligned} v(\Delta x)_k &= (1 - \Delta x_k)(1 - \Delta y_k)\Delta x_{i,j} + \Delta x_k(1 - \Delta y_k)\Delta x_{i+1,j} \\ &\quad + (1 - \Delta x_k)\Delta y_k\Delta x_{i,j+1} + \Delta x_k\Delta y_k\Delta x_{i+1,j+1} - \Delta x_k \end{aligned} \quad (3.51)$$

where  $k = 1, \dots, s$

In addition the second derivatives are minimised i.e. the interpolation grid consists of minimal curvatures at the edges of adjacent points:

$$v(\Delta x)_{x,x_{i,j}} = \Delta x_{i-1,j} - 2\Delta x_{i,j} + \Delta x_{i+1,j} - 0 \quad (3.52)$$

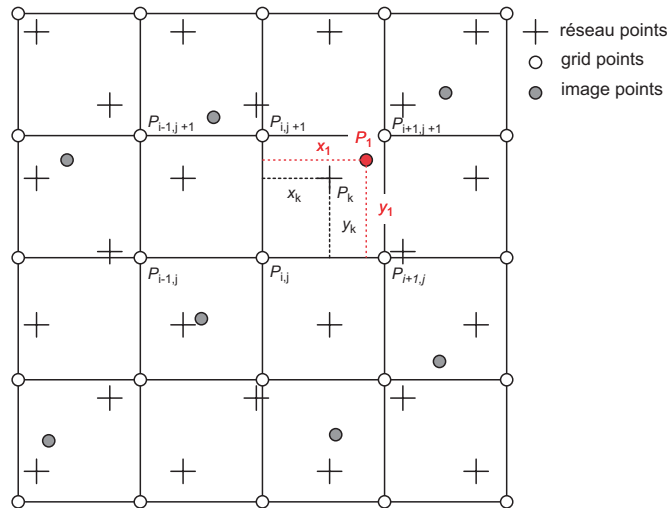


**Figure 3.30** Réseau points and image points inside a regular interpolation grid  
(after Kotowski and Weber 1984)

where  $i = 2, \dots, m-1$   
where  $j = 1, \dots, n$

The equivalent procedure is applied for the y-direction. The complete system of correction equations is solved by least-squares adjustment. Here observations of grid points as well as second derivatives can be weighted individually in order to control the smoothness of the interpolated grid.

The above mentioned réseaux transformation can also be solved with finite element interpolation. This process allows for the image-wise compensation of film deformations. A similar approach can be used to describe the unflatness of digital imaging sensors. In such a case it can be applied either constantly for a specific sensor or for a complete image series (Tecklenburg *et al.* 2001).

The transformation between imaging sensor and measuring device can be omitted for digital imaging systems if a direct digital data transfer between sensor and image processing system is provided. In such a case the pixels constituting the digital image are identical to the sensor elements. For many image processing systems a memory orientated left-handed pixel coordinate system is used. It is possible to transform pixel coordinates into metric coordinates by applying scaling factors derived from manufacturer-supplied pixel dimensions.

### 3.2.3.6 Metric and semi-metric cameras

The expression metric camera is used for photogrammetric cameras with stable optical-mechanical design. For these cameras the parameters of interior orientation can be calibrated in the factory (laboratory) which are assumed to be constant over a long period of time. Usually metric cameras consist of a fixed mounted fix-focus lens with minimal distortion. In addition, a mechanically flattened image plane (pressure or vacuum systems) are provided, hence four fiducial marks are sufficient for the definition of the image coordinate system (Fig. 3.31a). The instrumental accuracy of analogue metric cameras ranges between ca. 2 and 10  $\mu\text{m}$ .

A semi-metric camera meets the above metric camera requirements only with respect to a plane image surface and a plane image coordinate system. These specifications are fulfilled by a réseau for photographic cameras, and the physical surface of the imaging sensor for digital cameras.

For a semi-metric camera (Fig. 3.31b) the spatial position of the principal point is only given approximately with respect to the image coordinate system. It is not assumed to be constant over a longer period of time. This effect can result from the inclusion of interchangeable and focusable lenses, or for an unstable mounting of the lens or imaging sensor, for example. Fig. 3.32 illustrates this effect for a series of 90 images acquired with a Fuji FinePix S1 Pro digital camera. The observed variations can only be handled by image-variant camera calibration.

Cameras without a suitable photogrammetric reference system and/or without a planar image surface are referred to as amateur or non-metric cameras. These can be used for photogrammetric purposes, but only when no other photogrammetric imaging system is available. With such systems, uncontrolled changes in interior orientation are likely to occur on an image by image basis, resulting in a significant loss of accuracy when compared to metric or semi-metric cameras.

Technical details of metric and semi-metric cameras are presented in section 3.3.1.3 and 3.3.1.4.

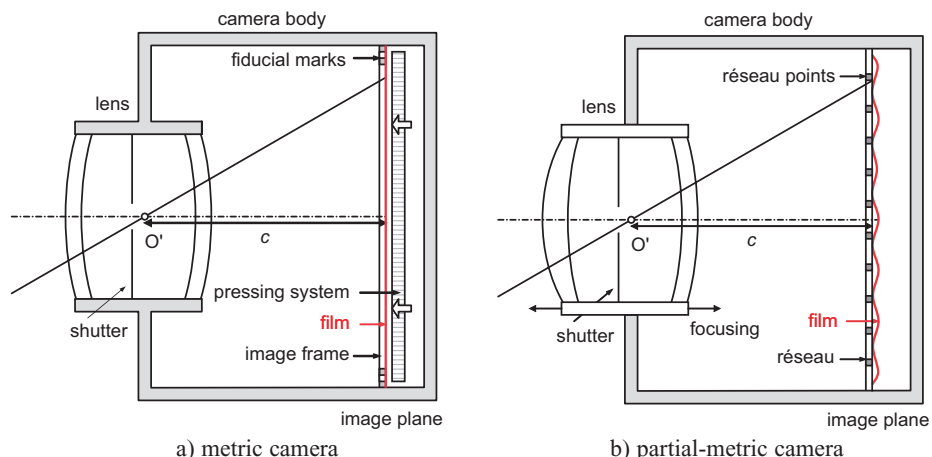


**Figure 3.31** Principle of metric and semi-metric camera

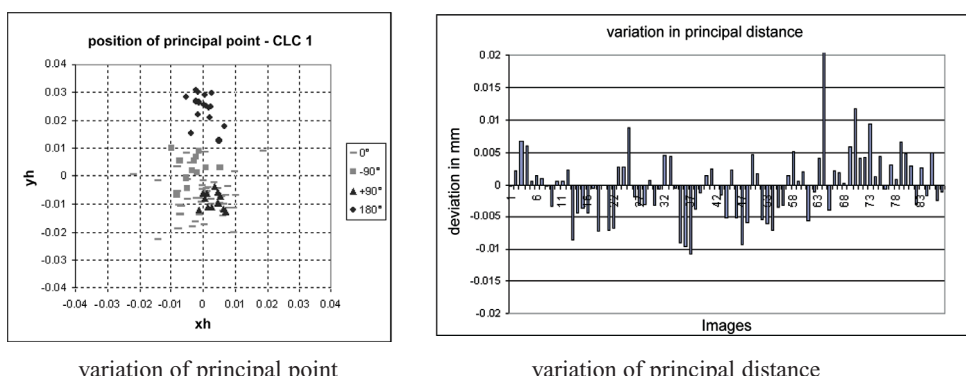


**Figure 3.32** Variation of the perspective centre position over a series of images (Fuji S1 Pro)

### 3.2.3.7 Determination of the interior orientation (calibration)

In photogrammetry, the determination of the parameters of interior orientation is usually referred to as calibration. State-of-the-art close-range techniques employ analytical calibration methods to derive the parameters of the chosen camera model indirectly from photogrammetric image coordinate observations. For this purpose, the imaging function is extended by the inclusion of additional parameters that model the position of the perspective centre and image distortion effects.

Usually calibration parameters are estimated by bundle adjustment (simultaneous calibration, section 4.3.2.4). Depending on available object information (reference points, distances, constraints) suitable imaging configurations must be chosen (see section 7.2).

The necessity for the periodic calibration of a camera is a question of the accuracy specifications, the mechanical construction of the camera and environmental conditions during field work. Consequently the time and form of the most appropriate calibration may vary; see Table 3.5

**Table 3.5** How calibration methods vary with objectives and references systems

type of calibration	imaging system	method of calibration	reference	assumption
one-time factory	metric	factory or laboratory (see section 7.2.1.1)	calibrated test instruments (e.g. goniometer or comparators)	camera parameters are valid for the life of the camera
long-term (e.g. annual) checks	metric	laboratory or test field	calibrated test instruments, reference points, scale bars, plumb lines	camera parameters are valid for a long period of time
immediately before object measurement	partial-metric, metric	test field calibration, self calibration (see section 7.2.1.2)	reference points, distances on test field, use of straight lines	camera parameters do not alter until the time of measurement
integrated into object reconstruction	partial-metric, metric	self-calibration, on-the-job calibration (see section 7.2.1.4)	reference points, distances on object, use of straight lines	constant interior orientation over the period of image acquisition
of each individual image	partial-metric	self-calibration with variable interior orientation (see section 4.3.2.4)	reference points, distances on object, use of straight lines rule	parameters relating to camera stability e.g. constant distortion values

For the default case the parameters of interior orientation are assumed to be constant for the period of image acquisition. However, especially in close-range applications, it may happen that lenses or lens focus has to be changed for an image series, and/or mechanical or thermal influences occur. Each alteration of the camera geometry will result in a change of interior orientation, hence an individual set of parameters must be computed for each camera configuration used.

From a camera calibration standpoint the difference between metric and semi-metric cameras become largely irrelevant as the stability of interior orientation depends on the required

accuracy. Consequently, even metric cameras are calibrated on-the-job if required by the measuring task. As an example, partial-metric digital cameras can be calibrated in advance if they are used with special multi-camera systems (on-line systems).

### 3.2.4 Resolution

#### 3.2.4.1 Geometric resolving power

The geometric resolving power of a film or an imaging system defines its capability to distinguish between a number of black and white lines pairs with equal spacing, width and contrast in the resulting image. It is therefore a measure of the information content of an image. The resolving power  $RP$  is measured visually as the number of line pairs per millimetre (Lp/mm). Alternatively the terms lines per millimetre (L/mm) or dots per inch (dpi) may be used<sup>1</sup>. Such terms describe the ability of the imaging system to distinguish imaged details, with the interest usually being in the maximum distinguishable spatial frequency attainable (Fig. 3.33, see also section 3.2.5.1).

$$F = \frac{1}{\Delta X} \quad f = \frac{1}{\Delta x'} \quad (3.53)$$

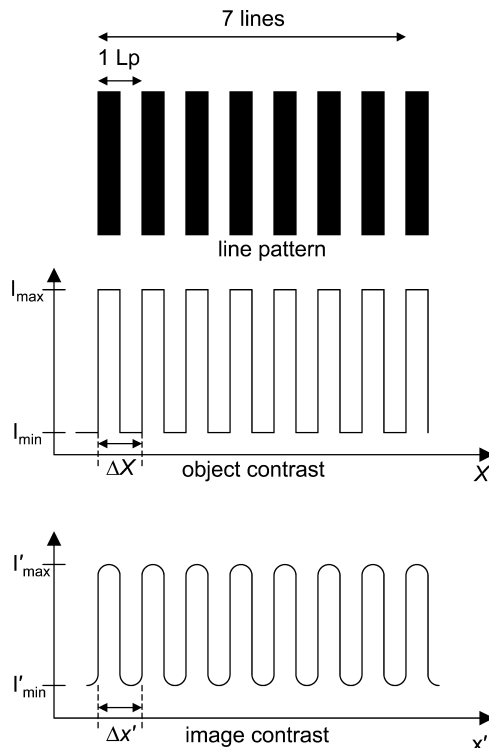


**Figure 3.33** Line pattern and contrast transfer

<sup>1</sup> With the unit L/mm only black lines are counted, with Lp/mm black and white lines (pairs) are counted, i.e. the notions are comparable since a black line is only visible if bordered by white lines.

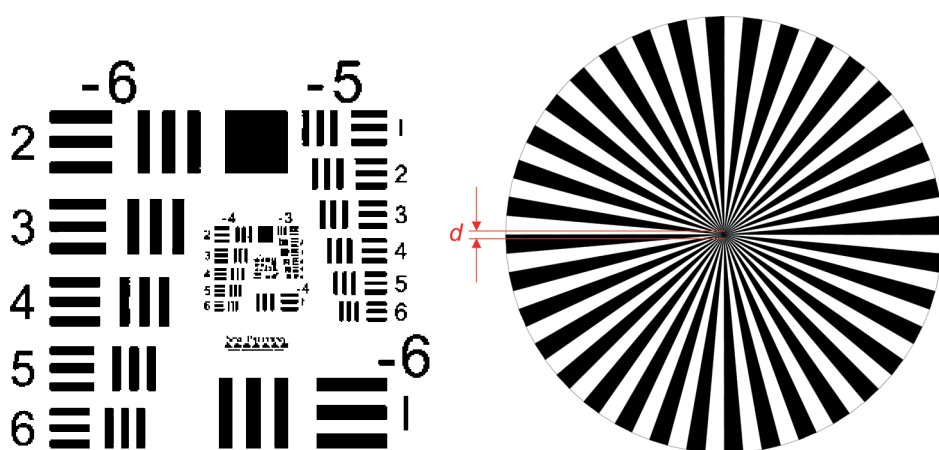


**Figure 3.34** Test chart and Siemens star for the measurement of resolving power

The spatial frequencies  $F$  in object space with respect to  $f$  in image space are the reciprocals of the corresponding line spacings  $\Delta X$  in object space with respect to  $\Delta x'$  in image space.

Resolving power can be measured by imaging a test pattern whose different spatial frequencies are known (Fig. 3.34). For the example, the Siemens star figure consisting of 72 sectors (36 sector pairs) allows the maximum resolving power of the imaging system to be determined in Lp/mm by observation of the number of sectors related to the perimeter of the inner circle that are just distinguishable.

$$AV = \frac{36}{\pi d} \quad (3.54)$$

#### Example 3.6:

A Siemens star is printed with a diameter of the non-resolved circle of about 0.5 mm (looking glass). Thus the print resolution of this book page can be computed as follows:

1. Resolving power:  $RP = \frac{36}{\pi \times 0.5} \approx 23 \text{ L/mm}$
2. Line size:  $x' = 1/RP = 0.044 \text{ mm}$
3. Transformation in dpi:  $RP = \frac{25 \times 4}{x'} = 582 \text{ dpi} \approx 600 \text{ dpi}$

The minimum resolved structure size in object space (structure resolution)  $\Delta X$  is calculated by image scale and resolving power as follows:

$$\Delta X = m \Delta x' = m \frac{1}{RP} \quad (3.55)$$

The resolving power of modern film materials ranges between 40 and 250 L/mm. Specialised photographic emulsions for printing purposes and holography offer up to 3000 Lp/mm. Black-and-white films have higher resolving powers than colour films due to the simpler nature of their micro image structure. The applicability of resolving power to opto-electronic sensors is discussed in section 3.3.2.2.

### 3.2.4.2 Contrast and modulation transfer function

The actual resolving power of a film or a complete imaging system depends on the contrast i.e. for decreasing contrast signal transfer performance is reduced. Such a reduction in contrast affects higher spatial frequencies first. A contrast-independent formulation of the resolving power is given by the contrast transfer function (CTF).

The object contrast  $K$  and the imaged contrast  $K'$  are functions of the minimal and maximal intensities  $I$  of the fringe pattern (Fig. 3.33):

$$K(f) = \frac{I_{\max} - I_{\min}}{I_{\max} + I_{\min}} \quad K'(f) = \frac{I'_{\max} - I'_{\min}}{I'_{\max} + I'_{\min}} \quad (3.56)$$

Hence the contrast transfer  $CT$  of a spatial frequency  $f$  follows:

$$CT(f) = \frac{K'(f)}{K(f)} \quad (3.57)$$

For most imaging systems contrast transfer varies between 0 and 1.<sup>1</sup> The contrast transfer function (CTF) defines the transfer characteristic as a function of the spatial frequency  $f$  (Fig. 3.35). Here the resolving power RP can be defined by the spatial frequency that is related to a given minimum value of the CTF (e.g. 30% or 50%). Alternatively RP can be determined as the intersection point of an application-dependent threshold function of a receiver or observer that cannot resolve higher spatial frequencies. Usually a perception limiting function, that describes the contrast-dependent resolving power of the human eye with optical magnification, is used as the threshold function. An instrumental threshold function (RETAS, resolving threshold of application system) can also be used e.g. if the required resolution for a printing post-processing of an image is to be determined (Bähr 1992).

If the rectangular function of Fig. 3.33 is replaced by a sine wave of the spatial signal, the contrast transfer function is denoted as the modulation transfer function (MTF) for the analogue image acquisition process.

For an optical system an individual MTF can be defined for each system component (atmosphere, lens, developing, scanning etc.). The total system MTF is given by multiplying the individual MTFs (Fig. 3.36):

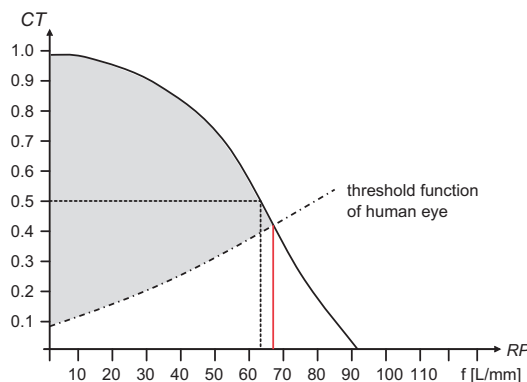


**Figure 3.35** Contrast transfer function (CTF)

<sup>1</sup> Systems are available that enhance image micro contrast to deliver a CTF greater than 1 e.g. digital edge enhancement or photographic adjacency effects.

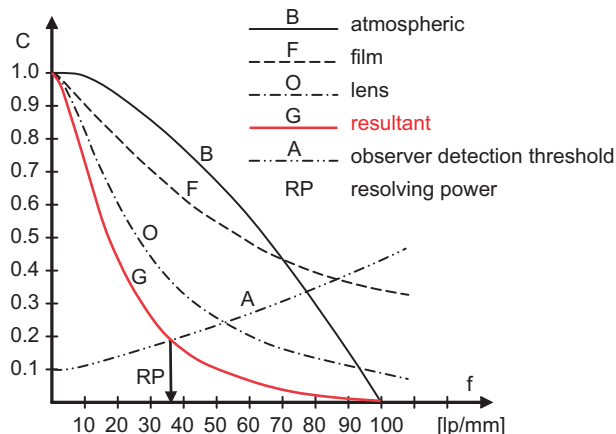


**Figure 3.36** Resulting total MTF (after Konecny and Lehmann 1984)

$$MTF_{\text{total}} = MTF_{\text{atmosphere}} \times MTF_{\text{lens}} \times MTF_{\text{sensor}} \times \dots \times MTF_n \quad (3.58)$$

As a result, the transfer capability of an optical system is predominantly limited by the weakest component. With the MTF of each component known, it is possible to identify limiting components and optimise the imaging system in order to achieve a desired performance.

### 3.2.5 Fundamentals of sampling theory

#### 3.2.5.1 Sampling theorem

A continuous analogue signal is converted into a discrete signal by sampling. The amplitude of the sampled signal can then be transferred into digital values by a process known as quantisation.

If sampling is performed under the assumption of a regular arrangement of detector or sensor elements of spacing  $\Delta x_s$ , then the sampling frequency  $f_A$  can be expressed as:

$$f_A = \frac{1}{\Delta x_s} \quad (3.59)$$

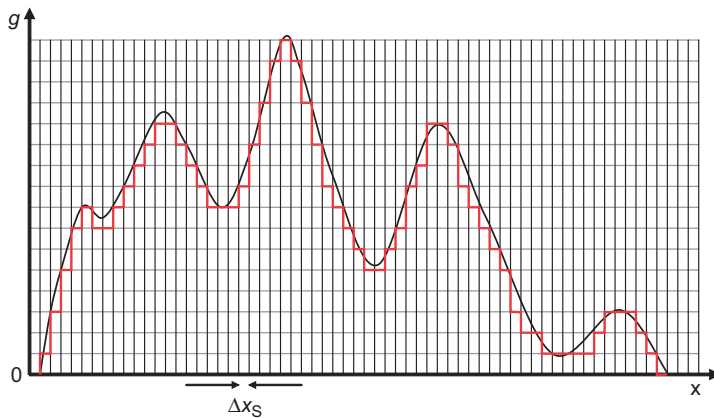


**Figure 3.37** Sampling and quantisation

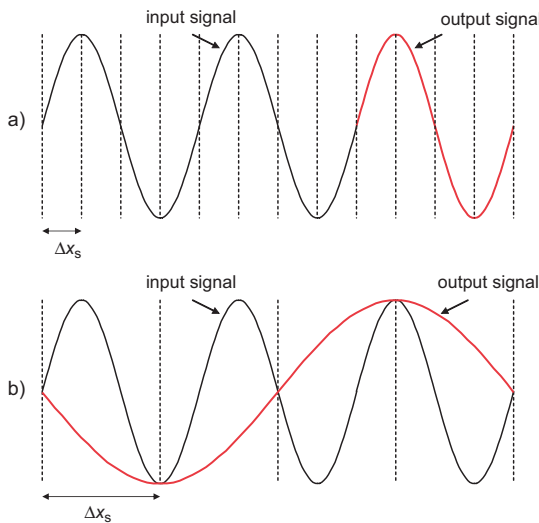


**Figure 3.38** (a) Nyquist sampling (b) and undersampling/aliasing

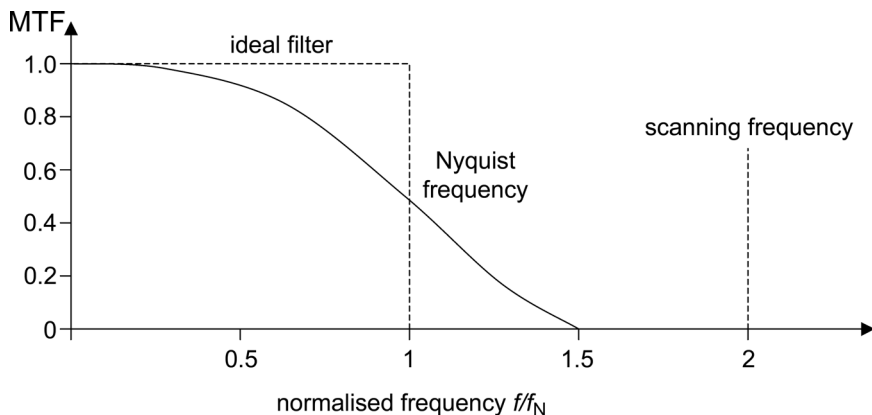


**Figure 3.39** MTF as a function of the normalised frequency

According to Shannon's sampling theorem the Nyquist frequency  $f_N$  defines the highest spatial frequency that can be reconstructed by  $f_A$  without loss of information:

$$f_N = \frac{1}{2} f_A = \frac{1}{2\Delta x_s} \quad : \text{Nyquist frequency} \quad (3.60)$$

Spatial frequencies  $f$  higher than the Nyquist frequency are undersampled, and they are displayed as lower frequencies (aliasing) (see Fig. 3.38).

The transfer characteristic of the sampling system can be described with the modulation transfer function (MTF). With respect to a normalised frequency  $f / f_N$  the MTF falls off significantly above 1 (=Nyquist frequency). If the aliasing effects (Fig. 3.38) are to be avoided, the system must consist of a band-pass filter (anti-aliasing filter) that, in the ideal case, cuts off all frequencies above the Nyquist frequency (Fig. 3.39).

### 3.2.5.2 Detector characteristics

The scanning device consists of one or several detectors (sensor elements) of limited size with constant spacing with respect to each other. It is important to realise that, because of the need to place a variety of electronic devices in the sensing plane, not all of the area of each detector element is likely to be light sensitive. Sampling and transfer characteristics are therefore a function of both the size of the light-sensitive detector area (aperture size  $\Delta x_D$ ) and of the detector spacing (pixel spacing  $\Delta x_s$ ).

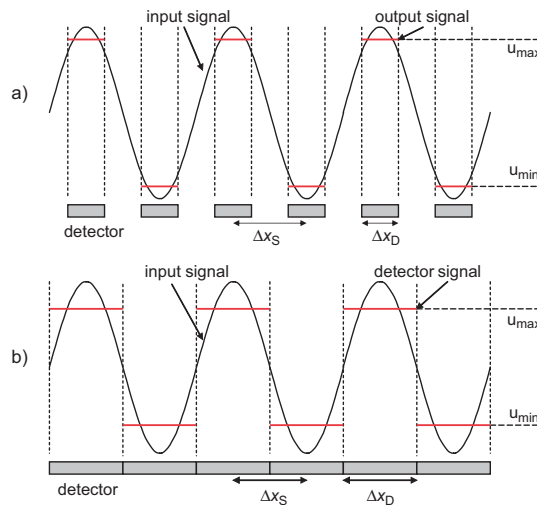
In contrast to the scanning scheme of Fig. 3.38 real sampling integrates with respect to the detector area.

Fig. 3.40a displays the scanning output of a detector signal of a sensor with light sensitive regions of size  $\Delta x_D$  and sensor element gaps that result in a detector spacing of  $\Delta x_s = 2\Delta x_D$  (e.g. interline-transfer sensor, Fig. 3.66). In contrast Fig. 3.40b shows the sampling result with light sensitive regions without gaps  $\Delta x_s = \Delta x_D$  (e.g. frame-transfer sensor, Fig. 3.65). For the latter case the detector signal is higher (greater light sensitivity), however, dynamic range ( $u_{\max} - u_{\min}$ ) and hence modulations are reduced.

The MTF of a detector scanning system is given by:

$$MTF_{Detector} = \frac{\sin(\pi\Delta x_D f)}{\pi\Delta x_D f} = \text{sinc}(\pi\Delta x_D f) \quad (3.61)$$

The sinc function was already introduced for diffraction at aperture slits; see section 3.2.2.3. The function shows that a point signal (Dirac pulse) also generates an output at adjacent detector elements. In theory this is true even for elements at an infinite distance from the pulse. In combination with possible defocusing of the image, the point spread function PSF means that sharp intensity changes (attributable to edges for example), lead to more or less smoothed grey level profiles. Consequently both MTF and PSF can be reconstructed from an analysis of edge profiles.



**Figure 3.40** Detector signals:

- a) light sensitive size equal to half detector spacing and b) light sensitive size equal to detector spacing

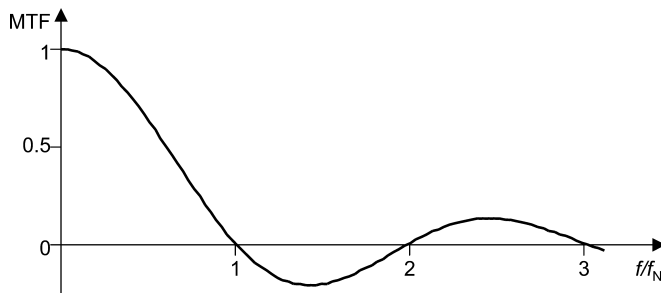


**Figure 3.41** MTF of a detector system

The MTF becomes zero for  $f = k / \Delta x_D$  where  $k = 1, 2, \dots, n$ . The first zero-crossing ( $k = 1$ ) is given by the frequency

$$f_0 = \frac{1}{\Delta x_D} \quad (3.62)$$

The first zero crossing point can be regarded as a natural resolution limit, however with zero contrast. Fig. 3.41 shows a typical MTF of a detector system. Negative values correspond to reverse contrast i.e. periodic black fringes are imaged as white patterns, and vice versa. Usually the MTF is shown up to the first zero-crossing only.

Further overviews on sampling theory and transfer characteristics are given by: Holst (1996), Inglis and Luther (1996), Lenz and Fritsch (1990).

### 3.3 Imaging systems

#### 3.3.1 Analogue imaging systems

Analogue imaging systems are based on light-sensitive photographic emulsions used as film or, in special cases, as glass plates. While this section is intended to provide sufficient information for a basic understanding of key photographic fundamentals necessary for photogrammetric understanding, those specifically interested in photography are directed towards standard texts on the subject such as Arnold *et al.* (1971), Jacobson and Jacobson (1980), Jacobson *et al.* (1983) or Langford (1982, 1983).

##### 3.3.1.1 Photographic fundamentals

###### Film layers

Fig. 3.42 illustrates the schematic design of a modern black-and-white film. Based on a 100–200  $\mu\text{m}$  thick film base layer (e.g. cellulose triacetate or polyethylene terephthalate) there are one or more emulsion layers consisting of light-sensitive silver-halide grains. The emulsion layers are approximately 5–20  $\mu\text{m}$  thick with individual silver-halide grains having a size of ca. 0.2–2  $\mu\text{m}$ . At a basic level it can be assumed that light sensitivity is proportional to grain density. Hence, increasing light-sensitivity will generate higher granularity of the film emulsion and therefore shorter camera shutter times at the expense of reduced image quality. By using several emulsion layers containing grains of different properties, and even by varying the grain shape, the overall light sensitivity can be improved while minimising grain noise (see Fig. 3.42).

Colour films consist of three emulsion layers. Each is sensitive to one of the additive colours of the visible spectrum (red, green, blue) and, in addition to light sensitive silver bromide grains,

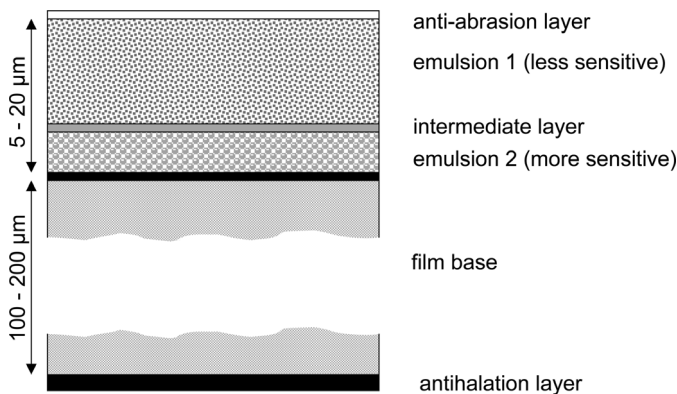


**Figure 3.42** Schematic design of film layers (b/w film)

include complex compounds called colour couplers. During the chemical development process colour dye particles are attached to the molecules in proportion to the incident light intensity of the corresponding colour channel. When the developed film (colour reversal film) is viewed under white light the true colours of the photographed object are visible according to the subtractive colour mode (yellow, magenta, cyan).

#### *The photographic process*

On exposure to light, energy is trapped at sites on the silver halide grains called sensitivity specks. The metallic silver produced by this mechanism is termed the latent image. The number of silver halide grains with latent image depends on the exposure, hence duration and intensity of the incident light. The latent image is unstable and invisible to the naked eye and must be chemically processed to render it both visible and permanent.

The following are the key chemical processes:

#### 1. Development:

Development is a reduction reaction involving electron transfer from the developing agent to the exposed silver halide producing metallic silver. It is selective in that it acts faster on exposed grains, probably being catalysed by the metallic silver produced. The degree of development is a function of developer type, time and temperature. The unexposed silver halides remain unchanged, and are thus still sensitive to light.

#### 2. Fixing:

After an intermediate stop bath, which is used to arrest development, the film is processed in a fixing bath. Here the unexposed silver halide molecules are extracted so that the film is no longer light sensitive. Finally the film is washed and dried. As a result a permanent negative of the photographed object is achieved.

The optical density (darkness) of the resultant image is a function of film sensitivity and exposure; this area of photographic science is termed sensitometry. The degree of density is defined by the optical density  $D$  as the logarithmic reciprocal of the transparency  $T$ :

$$D = \log \frac{1}{T} \quad (3.63)$$

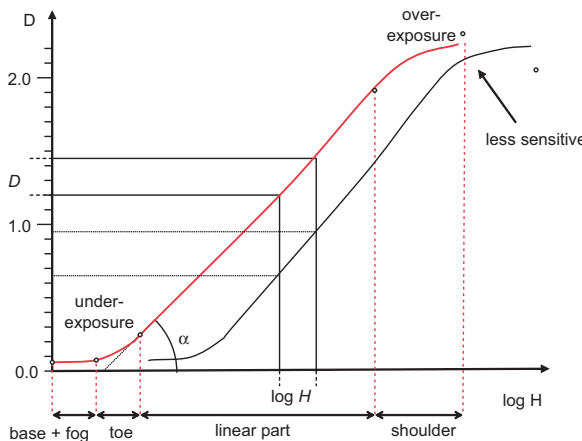


Figure 3.43 Characteristic curves

The logarithm is introduced to agree with the response of the human visual system where equal density intervals are interpreted with equidistant brightness. Most common photographic films provide a density range between 0 and 3.

For an average scene, the exposure  $H$  given to the film depends on the illuminance at the image plane  $E$  [lux] and exposure time  $t$  [s]:

$$H = Et \quad (3.64)$$

The relationship between exposure and image density is described by the photographic characteristic curve (Fig. 3.43). Its major portion is a straight line where the film can be exposed normally i.e. equal exposure intervals lead to equal density intervals. The non-linear parts of the curve are referred to as "the toe" (left) and "the shoulder" (right). Exposure outside of the linear section will result in either too dark an image (over exposure) or too light an image (under exposure).

The slope of the straight line portion is defined by its gradient  $\gamma$ :

$$\gamma = \tan\alpha = \frac{\Delta D}{\Delta \log H} \quad (3.65)$$

Photographic systems with a gamma value of 1 are described as being of normal contrast. Alternatives are higher contrast materials, such as Kodak Technical Pan, which provide steeper gradients ( $\gamma > 1$ ), and low contrast systems providing lower gradients ( $\gamma < 1$ ). While predominantly a property of the photographic emulsion, minor adjustments to the gamma value can be made during development.

### Sensitivity

The light sensitivity of a photographic emulsion is defined by the exposure required under laboratory conditions to yield a density of 0.1  $D$  above the film base plus fog level (see Fig. 3.43). Film sensitivity is given by the DIN or ASA series:

Table 3.6 Film sensitivity values

DIN	...	15	18	21	24	27	30	...
ASA	...	25	50	100	200	400	800	...

According to ISO standards ISO 1974, film sensitivity at 100 ASA which is equivalent to 21 DIN is denoted as ISO 100/21°. Each step in the ISO series represents a doubling in sensitivity i.e. half of the exposure is required. Hence the set of film sensitivities produced by manufacturers are in sympathy with f-number and exposure time increments available in standard camera systems (both provide steps of 2 or 1/2 respectively).

The spectral sensitivity of general purpose photographic films is adapted to the human eye. While non-sensitised and orthochromatic films are only sensitive to blue or green light respectively, panchromatic films cover the complete visible range ( $400 \text{ nm} \leq \lambda \leq 700 \text{ nm}$ ). In addition, infra-red sensitive films are of special importance in aerial photogrammetry, while they do not play an important role for close-range applications. Fig. 3.72 shows the sensitivity of different films and imaging sensors.

### 3.3.1.2 Analogue camera technology

#### *Camera types*

Three major camera designs can be identified among the wide variety of camera systems that are available to the photographer:

- View finder camera

The view finder camera uses a viewing lens that is separated from the actual camera taking lens. Such camera designs are generally very light in weight as the optical systems and image formats are compact. However, direct observation of the image is not possible for focusing, depth of field control or lens interchange. More importantly for close range work, the difference in content between the viewfinder image and the taking image give rise to spatial parallax errors. Image coverage corrections can be made in the form of masks, but it is not possible to fully correct the difference in perspective.

- Single lens reflex camera

For the single lens reflex (SLR) camera viewing is directly through the taking lens whereby a plane mirror deflects the path of rays into a view finder ocular (Fig. 3.44). Before exposure the mirror is flipped out of the optical path. Single lens reflex cameras with a simple box viewfinder (often equipped with a magnifier) consist of a ground glass focusing screen where the image can be viewed from above. The focus screen image appears upside down and reversed (mirrored horizontally). The principle is applied for many medium-format cameras (for example in Fig. 3.53).

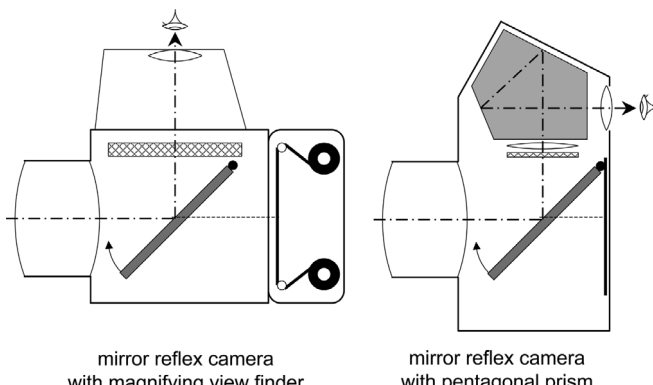
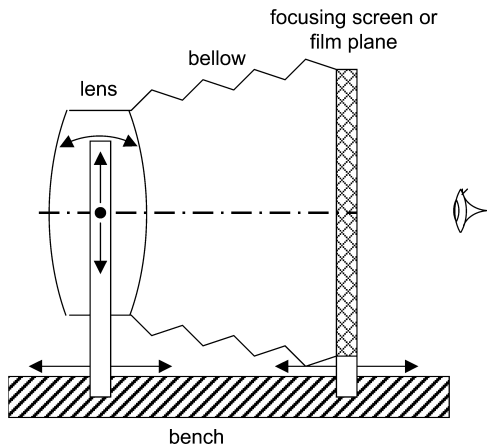


Figure 3.44 Mirror reflex cameras (after Marchesi 1985)



**Figure 3.45** Studio camera

Single lens reflex cameras with pentagonal prism viewfinders provide an upright unrevised view of the scene. In this case the optical path following the focusing screen is deflected by a pentagonal prism that compensates for the mirror effect. Prism view finders are often provided as optional extras for attachment to cameras with simple viewfinder systems.

When an opto-electronic imaging sensor is used instead of the photographic film, camera designers have an extra option in that the view finder can be replaced with an LCD display so that the acquired image can be observed without any optical deflections (see section 3.3.2, Fig. 3.81).

- Studio camera

Studio cameras allow for the individual translation and rotation of lens and film planes. By tilting the lens, special focus settings can be enabled i.e. according to Scheimpflug's condition which maximises depth of field in a particular plane. When the lens is shifted the perspective imaging properties are changed e.g. to avoid convergent lines for vertical architectural pictures. Studio cameras represent the ultimate in photographic quality by virtue of their large image sizes (5" x 7" and 10" x 8" being common). Due to their bulky nature and relatively cumbersome deployment they are typically used in professional studio applications or for landscape and architectural work. In photogrammetry the principles of rotation of the image and film plane are used in analogue rectifiers (e.g. the Zeiss SEG V).

#### *Shutter*

The shutter is used to open the optical path for the duration of time necessary for correct exposure. For conventional camera systems two basic types are used: the focal plane shutter and the interlens or leaf shutter.

The majority of 35 mm single lens reflex cameras use a focal plane shutter that is mounted directly in front of the film plane. For exposure a small slit moves across the film format (Fig. 3.46). Variation in the size of the slit allows a variety of short duration shutter settings. Focal plane shutters are easy to design and provide shutter times of less than 1/4000 s. If the camera moves parallel to the shutter movement (e.g. for photos from a driving vehicle), spatially displaced imaging positions occur i.e. for each differential exposure interval the image has a different exterior orientation.

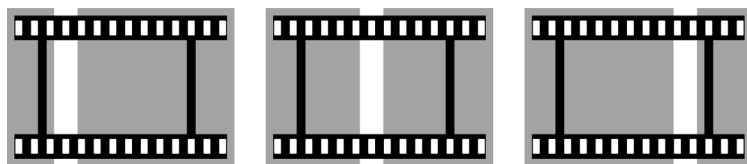


Figure 3.46 Principle of the focal plane shutter

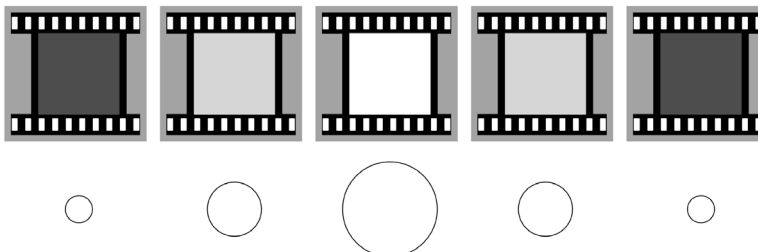


Figure 3.47 Principle of the interlens shutter

Interlens shutters are typically mounted between the lens elements close to the aperture stop within the lens, and so each lens must have its own shutter. Mechanically sprung blades are used to open the shutter radially (Fig. 3.47). In the figure the diameter of each circle shows the diameter of the shutter as it opens and closes and the tone in the image shows the level of light reaching the image plane. In practice the opening and closing of the shutter can be regarded as instantaneous, meaning that the complete image is exposed simultaneously with the same projection even if the camera platform moves. Interlens shutters require much more mechanical effort since the individual elements must be sprung open and then closed. As a consequence shortest shutter times are restricted to about 1/500 s. In photogrammetry, they are usually encountered in low cost viewfinder cameras and in professional medium and large format cameras.

### 3.3.1.3 Camera designs suitable for photogrammetry

#### *Metric cameras*

Metric cameras (see section 3.2.3.6) are purpose designed and built for photogrammetric use and were widely available between the 1920s and 1980s since an *a posteriori* calibration of the camera was practically impossible at that time. Such cameras are designed to very high specifications and require precision engineering technologies. Typical metric designs include flattening of the film plane (using either glass plates as the emulsion carrier, by a pressing or a vacuum device) and distortion-free high-quality lenses. The resulting advantages of close conformance to the perspective projection and known interior orientation from such systems are offset to some extent by their high cost and generally inconvenient handling due to the basic level of photographic control typically included (Atkinson 1989). Many of the benefits of modern professional cameras such as interchangeable lenses, mirror reflex viewing, automatic exposure, motorized film transport and low weight are not usually provided by metric cameras.

Typical technical features of metric cameras are:

- constant principal distance due to fixed mounted fix-focus lens
- distortion-free lens,  $\Delta r' < 4 \mu\text{m}$

- image plane perpendicular to the optical axis
- principal point = centre point of image format
- planar image surface using glass plates or mechanical film flattening
- large image format
- optional add-on devices for geodetic measurement of reference points (see Fig. 3.49)



**Figure 3.48** Metric camera  
Zeiss UMK 1318



**Figure 3.49** Metric camera  
Wild P31



**Figure 3.50** Metric camera  
Wild P32

In practice analogue metric cameras are only used now if the image quality associated with a large image format is required for a specific task, camera self-calibration is not possible or where the presence of (many) réseau points in the image is undesirable.

The Zeiss UMK 1318 (Fig. 3.48) belongs to the very few analogue metric cameras still used in practice, testament to its rugged design and exceptional image quality. It is characterised by the large image format of 130 mm × 180 mm, and the use of either glass plates with a pressure plate or film based materials through the use of a dedicated motorised vacuum flattening film magazines. The camera was available (it is no longer manufactured) with high-quality lenses of 100 mm, 200 mm, and 300 mm principal distance which exhibited maximum distortions of 2–10 µm. A super wide 64 mm lens version was also produced. The camera is capable of providing an instrumental image accuracy of ca. 2 µm, if the parameters of interior orientation are determined by self-calibration. This corresponds to a relative accuracy of about 1:100,000 with respect to the image diagonal.

Table 3.7 summarises technical data of analogue metric cameras (see also Fig. 3.49, Fig. 3.50, and Fig. 1.27).

**Table 3.7** Technical data of analogue metric cameras (selection)

supplier	type	image format [mm]	lenses [mm]	imaging distance[m]	weight [kg]
Zeiss	UMK	130 × 180	64, 100, 200, 300	1.4 – infinity	10 – 12
Zeiss	TMK	80 × 100	60, 120	10	13
Wild	P32	60 × 80	64	3.3	3
Wild	P31	83 × 117	45, 100, 200	1.5, 6.6, 18	6
Wild	C 40 / C 120	60 × 80	64	2.5, 10	10 – 13
Zeiss	SMK 40/120	80 × 100	60	2.5, 5	20

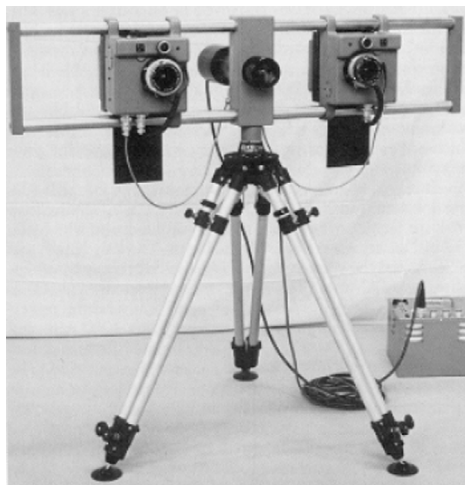


**Figure 3.51** Stereometric camera Kelsh K-460

#### *Stereometric cameras*

Stereometric cameras consist of two identical metric cameras mounted on a stable mechanical base bar. Their exposure can be synchronised. In the past they were of major importance e.g. in architectural photogrammetry or for accident recording. The images are acquired according to the normal case of stereophotogrammetry (Fig. 4.60), and can be processed in simple analogue plotting instruments (example in Fig. 1.27). For the last twenty years systems such as the stereometric camera Zeiss SMK 40/120 (Fig. 1.26) or Kelsh K-460 (variable base 24–92 cm, Fig. 3.51) were sometimes used for engineering applications e.g. for the measurement of car body surfaces (Fig. 6.42).

#### **3.3.1.4 Semi-metric cameras**

##### *Réseau principle*

Semi-metric cameras employ a planar sheet of glass onto which is etched a regular grid of calibrated reference points (réseau plate). The film is pushed into contact with the réseau plate at exposure so that images of the crosses are projected onto the film. The measured location of each cross can then be numerically compared to its calibrated location in order to correct for in



**Figure 3.52** Medium-format camera Hasselblad MK70

plane and out of plane film deformations (see section 3.2.3.4). Fig. 3.52 shows a semi-metric Hasselblad MK70 camera which was the first commercially available system where a professional photographic camera was modified to a photogrammetric camera by using a réseau.

An alternative method is provided by a grid of illuminated targets which are back projected through the film base. While réseau cameras belong to the class of semi-metric cameras since the réseau is typically introduced as a modification to a standard photographic cameras, purpose built back projected réseau cameras, such as the CRC1 (Fig. 3.55, see section 3.2.3.5) can be regarded as being metric.

A weakness of the réseau system is that when the réseau points are not imaged with sufficient contrast, for example in areas of deep shadow, the acquired images réseau data cannot be reliably measured and therefore image correction becomes impossible. However, using a separate pre-exposure of the réseau a better contrast of the réseau points can be achieved. For this purpose the shutter is opened, and a diffuse light source is used for pre-exposure e.g. by looking into the diffuse sky or by an additional light source temporarily mounted in front of the lens. After pre-exposure the film is not transported but exposed by the actual (low contrast) measuring object.

Nowadays<sup>1</sup> réseau cameras are available with various different image formats (see Table 3.8). Semi-metric cameras based on professional 35 mm or medium-format camera systems offer convenient handling and have a large range of different lenses and accessories. 35 mm-cameras with 24 mm × 36 mm image format, using réseau plates consisting of 5 × 7 crosses, provide a geometric accuracy that is sufficient for most architectural applications. For applications where the imaged réseau crosses disturb the viewing or image measurement requirements, the small image format also allows for a number of réseau points located at the border of the image. Examples for 35-mm réseau cameras are given by the Rollei 3003 metric or adaptations of the

**Table 3.8** Technical data of analogue réseau cameras (selection)

supplier	type	image format [mm]	lenses [mm]	réseau spacing [mm]	weight [kg]
Geodesign	Nikon, Geometric	36 × 24	28, 35, 50	5	< 1
Rollei	3003 metric	36 × 24	15 – 135	5	1.3
Leica	R5	36 × 24	18 – 135	5	1.2
Rollei	6006/6008 metric	55 × 55	40 – 500	2, 5, 25	2.0
Hasselblad	MK70	55 × 55	60, 100	10	2.0
Hasselblad	MKW	55 × 55	38	5	1.8
Pentax	PAMS 645 P	50 × 40	35 – 200	20, 25	1.4
Linhof	Metrica 45	105 × 127	90, 150	2.5, 10	7.5
Rollei	R_metrica	102 × 126	75, 150	2	9.5
GSI	CRC-2	115 × 115	65, 90, 120	25	9
GSI	CRC-1	230 × 230	120, 240	50	20
Rollei	LFC	230 × 230	165, 210	2	20

<sup>1</sup> It is obvious that réseau cameras will be completely replaced by digital cameras in the very near future due to the incremental advances in digital image quality.

35 mm Nikon F-series SLR cameras. In principle every analogue camera can be modified by a réseau. Relative accuracies in the range of ca. 1:5,000 – 1:10,000 can be achieved.

In contrast, medium-format réseau cameras with an image format of 60 mm × 60 mm up to 90 mm × 60 mm provide relative accuracies between 1:10,000 and 1:50,000. The best-known medium-format cameras are the Rollei 6006 metric (Fig. 3.53) and its successor 6008 metric (Fig. 3.128), which are further developments of the Rollei SLX (Fig. 1.29) (Wester-Ebbinghaus 1980 and 1983). Since it is representative of many similar systems the Rollei 6006/6008 metric is described in more detail.

The camera is a single lens reflex design with a focusing screen view finder (see Fig. 3.44). The shaft view finder can be replaced by a pentagonal prism. Off-the-shelf roll-film is used for the separate film magazine that usually accepts films for 12 images (with optional special magazines with up to 70 images). Motorised film transport can be used for image series of up to 2.5 images per second. Exposure is measured using an integral mode through the lens (TTL) metering system which can be used in either a manual or automatic mode. Additional system accessories such as infra-red remote control, synchronisation of several cameras, ring flash, Polaroid back and so on are available.

Various lenses are available for the Rollei 6006/6008 system. For photogrammetric purposes, usually high-quality Zeiss lenses with focal lengths 40 mm (Distagon, wide-angle), 60 mm (Distagon, near wide-angle), 80 mm (Planar, normal angle) and 150 mm (Sonnar, tele-lens) are used. All lenses are equipped with an electronically controlled interlens shutter. Lenses are attached to the camera body by a bayonet mount. Focusing is restricted to pre-defined mechanical distance settings.

The integrated réseau consists, by default, of  $11 \times 11$  crosses with 5 mm spacing. Optionally a reduced réseau with  $3 \times 3$  crosses at 25 mm spacing is available. For industrial applications, where higher accuracy is required, a réseau of 2 mm spacing is offered.

The camera is calibrated in the factory using a test field calibration (see section 7.2.1.2). The calibration report shows *a priori* values of interior orientation (for different distance settings), that can be used for applications which are not suited to self calibration. The image coordinates of the réseau points are calibrated with an accuracy of 1 µm, whereby deviations from integer nominal values (réseau spacing 5 mm) are less than 2 µm. Principal distance and principal point



**Figure 3.53** Medium-format camera Rollei 6006 metric



Figure 3.54 Medium-format camera GSI CRC-2



Figure 3.55 Large format camera GSI CRC-1



Figure 3.56 Large format camera Rollei LFC

are given with an *a priori* accuracy of ca. 10–20 µm. Since the user can change lenses, higher *a priori* accuracies are not reasonable. The accuracy potential of the camera is about ca. 1–2 µm, achievable with sufficiently configured self-calibration.

The higher accuracies required by certain applications can be achieved using camera systems with image formats between 115 mm × 115 mm (Fig. 3.54) up to aerial format 230 mm × 230 mm (Fig. 3.55, Fig. 3.56). Cameras in the lower large format serve as a compromise between medium format and aerial format, where higher accuracies can be combined with easier handling. However, system costs are much higher than for real medium format cameras. Cameras with image formats up to 115 mm × 115 mm provide relative accuracies of ca. 1:50,000 up to 1:100,000.

Two camera systems in aerial format ( $230\text{ mm} \times 230\text{ mm}$ ) have been built for specialist industrial applications. The GSI CRC-1 camera (Fig. 3.55) consists of a mechanical film flattening vacuum back that is equipped with a back-projected grid-like arrangement of circular illuminated targets located behind the film. By measurement of both the position and diameter of the targets in plane and out of plane, film deformations can be numerically corrected. The camera was designed to be used with 120 mm (large wide-angle) and 240 mm (near wide-angle) focal length lenses. A purpose built rotating camera mount is available to acquire images that are rolled around the optical axis. When targeted object points (retro-reflective points) are used, images are measured with a purpose built digital precision comparator (Fig. 6.3) and a suitable image configuration is given. Relative object accuracies of 1:200,000 and better can be achieved. The camera system was designed for, and is used predominantly in, the aerospace industry (Fraser and Brown 1986).

A system of similar capabilities is offered by Rollei LFC (Large Format Camera) (Fig. 3.56). This camera design included a réseau of 2 mm spacing, which given the aerial survey film format, produces  $11500 \times 11500$  réseau points. Measurement of these can only be done automatically. Using the réseau-scanners Rollei RS1-C (Fig. 6.5) a single réseau mesh can be measured digitally. This system has also been applied to high accuracy industrial measurement applications (Dold 1997).

### 3.3.1.5 Non-metric cameras

Every type of conventional camera that does not provide any additional aids for the definition of the interior orientation is referred to as a non-metric camera. In special cases images taken by such cameras have been processed for photogrammetric purposes e.g. for the evaluation of accidents or for the reconstruction of historical buildings (e.g. from old post cards).

The key problem of non-metric images is the missing photogrammetric image coordinate system. Normally unique reference points, related to the principal point, do not exist and even image corners often cannot be reconstructed. A suitable analytical method for image orientation is given by the Direct Linear Transformation (DLT, see section 4.2.3.2), that does not require an image coordinate system. Fig. 3.57 shows an example of an image where neither fiducial marks nor camera-fixed image corners are visible.



**Figure 3.57** Example of an image taken by a non-metric camera (historical picture of the Worms cathedral)

### 3.3.2 Digital imaging systems

#### 3.3.2.1 System components

Digital imaging systems use opto-electronic sensors for image acquisition instead of photographic emulsions. They directly provide an electronic image that can be digitised by suitable electronic components and transferred to a local processor or host computer for measurement and analysis. Hence the term digital imaging system summarises all system components involved in the generation of a digital image (Fig. 3.58).

The electro-magnetic radiation (light) emitted or reflected by the object is imaged by a sensor as a function of time (exposure time, integration time) and space (line-wise or area-based). After signal enhancement and processing an analogue image signal, in the form of an electric voltage proportional to the amount of light falling on the sensor, is produced. At a second stage this signal is sampled by means of an analogue to digital converter in order to produce a digital image consisting of a series of discrete numerical values for each light sensitive cell or pixel in the image. This digital image can then be used for further processing such as discrete point measurement, or edge detection.

As far as digital photogrammetry is concerned, where geometrically quantifiable images are required, the development of digital imaging technology is closely related to the technology of CCD image sensors (charge coupled devices). They were invented at the beginning of the 1970s (Boyle and Smith 1970), and can recently be found in many imaging applications. Overviews on CCD sensors and video technology are given by e.g. Holst (1996), Inglis and Luther (1996) and Shortis and Beyer (1996). Recently CMOS technologies for opto-electronic imaging sensors are gaining in importance (see section 3.3.2.2).

In photogrammetric practice the following imaging systems can be distinguished:

- Video cameras

Small-format cameras delivering an analogue or digital video signal in real-time (25–30 frames per second) according to video and TV standards. By default the number of pixels amounts to ca.  $780 \times 580$  pixels, and up to  $1900 \times 1100$  pixels for newer high definition TV developments.

- High-resolution digital cameras

Cameras with digital output delivering high-resolution images usually between  $1000 \times 1000$  and  $4000 \times 4000$  pixels (valid 2005). Image frequencies of between 30 frames per second to several seconds per image can be achieved.

- Scanning cameras

Imaging systems that extend pixel resolution or image format by sequential scanning by means of a moving image sensor. Based on different principles, pixel numbers between ca.

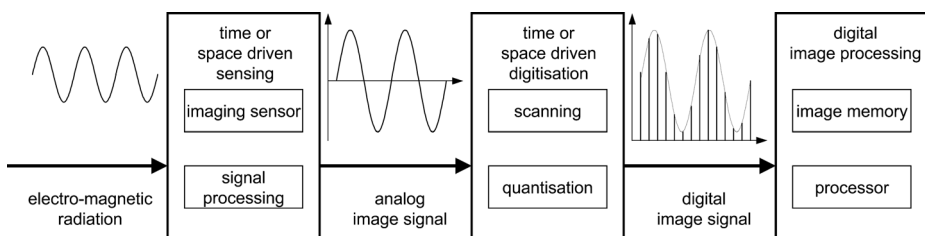
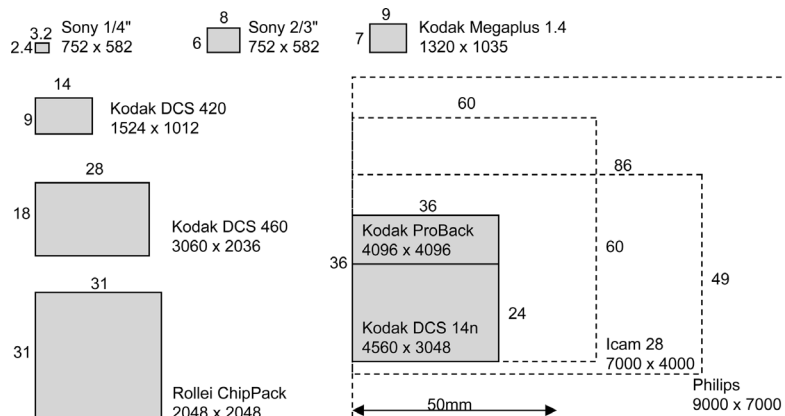


Figure 3.58 Digital imaging system



**Figure 3.59** Image formats of recent CCD cameras and matrix sensors

3000 × 2300 pixels and ca. 20,000 × 20,000 pixels can be obtained. These systems can only be used for stationary imaging conditions.

The development during the last two decades have led to growing numbers of sensor elements and larger image formats for CCD and CMOS sensors. Fig. 3.59 displays typical formats of imaging sensors (valid 2005).

### 3.3.2.2 Opto-electronic imaging sensors

#### *Sensor principle*

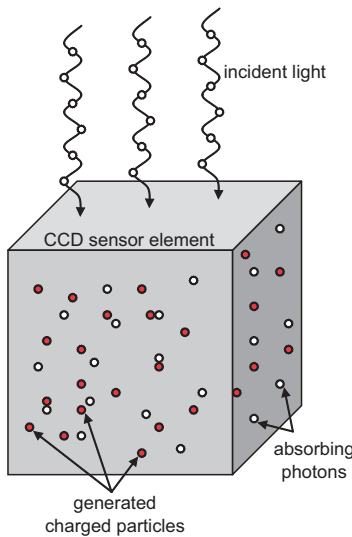
For photogrammetric imaging systems solid state sensors are used exclusively. Cameras with analogue picture tubes have no significance in photogrammetry due to large geometric distortions. Solid state imaging sensors consist of a large number of light-sensitive detector elements that are arranged on semi-conductor modules either line-wise or matrix-wise (line or matrix sensor). Each detector element (sensor element) generates an electric charge that is proportional to the amount of incident illumination falling on it. The sensor is arranged such that the charge at each individual element can be read out, processed and digitised.

Fig. 3.60 illustrates the principle of a single sensor element. Incident light, in the form of photons, is absorbed in a semi-conducting layer generating pairs of electron holes (charged particles). The ability of a sensor element to create a number  $n_E$  of charged particles from a number of  $n_p$  imitated photons is expressed by the external quantum efficiency  $\eta_{ext}$ . The quantum efficiency depends on the sensor material and wavelength of the incident light.

$$\eta_{ext} = \frac{n_E}{n_p} \quad (3.66)$$

The negative charged particles are attracted by a positive electrode. Charges are accumulated in proportion to the amount of incident light until saturation or overflow of charge is achieved. The positive electric field of the electrode is generated by a potential well that gathers the negative charged particles. For CCD sensors the detector elements are built on MOS-capacitors (metal-oxide semiconductor).

Sensor elements can be arranged as lines or as matrices. Fig. 3.61 shows the simplified layout of a CCD line sensor. Each active sensor element is directly connected to a serial read-out register



**Figure 3.60** Transformation of photons into charged particles

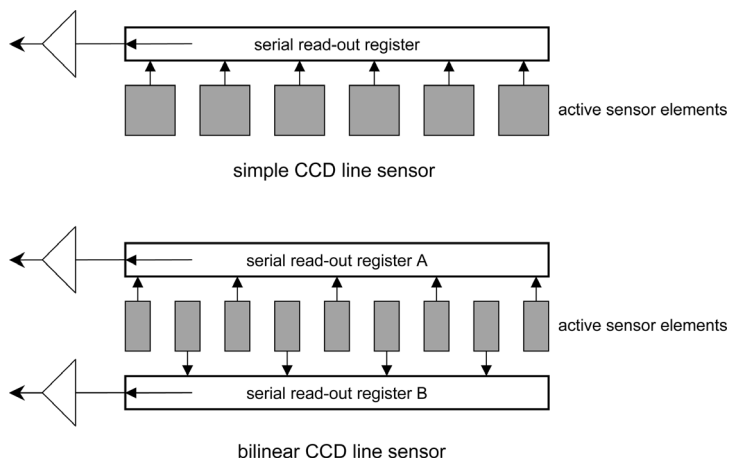


**Figure 3.61** Principle of simple and bilinear CCD line sensors

that is used to output the generated charge. In contrast, bilinear arranged CCD lines provide doubled resolution if the sensor elements are coupled in an alternating manner with two read-out registers.

The core problem for such sensor arrangements is the transportation of the charge stored in the sensor element to an output. Fig. 3.62 illustrates a typical solution for a line-wise arrangement of sensor elements. The cumulated charge of electrode 1 cannot discharge at time  $t_1$ , since there is no voltage potential on the next electrode. At time  $t_2$  the voltage of electrode 2 is set equal to the voltage of electrode 1 (equal potential) forcing a portion of the charge under electrode 1 to flow to electrode 2. At time  $t_3$  the voltages of electrode 1 and 3 have a low value i.e. the complete charge is shifted under electrode 2, hence one electrode width to the right.

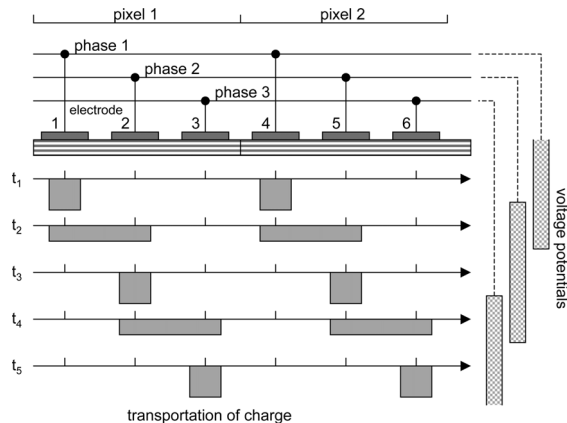


**Figure 3.62** Principle of CCD charge transportation (bucket brigade device)

This process is continued until the charge reaches the read-out register at the end of a line. There the charges are detected and transformed into electric voltage signals. The process is usually denoted as CCD principle, or bucket brigade device.

CCD line sensors can consist of more than 12,000 sensor elements. Given a sensor spacing of ca. 4 µm to 20 µm the length of line sensors can be more than 100 mm. Line sensors are used for a wide variety of different technical purposes such as line cameras, fax machines, photo scanners or digital copiers.

#### *Matrix sensors*

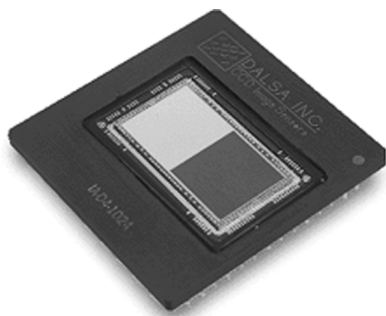
Photogrammetric image acquisition in close-range is usually performed by matrix sensors (examples in Fig. 3.63). In comparison to line sensors, the layout of matrix sensors is more complicated since the read-out process must be accomplished in two dimensions.

Three major principles can be distinguished for CCD matrix sensors that differ in sensor layout and read-out process:

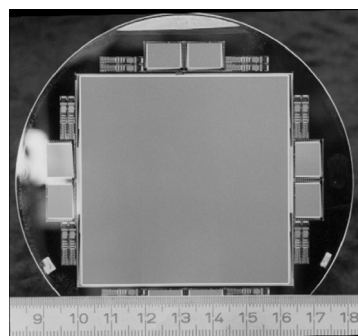
- frame transfer
- full-frame transfer
- interline transfer

Frame-transfer sensors (FT) consist of a light-sensitive sensor zone and an equally sized opaque storage zone (Fig. 3.63a), each built in vertical CCD bucket brigades. After exposure, charge is moved vertically from the sensor zone into the storage zone. From there they are rapidly shifted line by line into the read-out register (Fig. 3.64). Charge transfer from the sensing to the storage zone can be carried out very rapidly, allowing high frame rates to be achieved since the sensor zone can be exposed while the image is written out of the camera from the storage zone. Because the storage zone is not light-sensitive the electronic design of the sensor requires practically no gap between single sensor elements.

A simpler variation is given by the full-frame transfer sensor (FFT, Fig. 3.63b). It consists of a sensor zone only from where charges are directly transferred into the read-out register (Fig. 3.65). During read-out the sensor zone may not be exposed. In contrast to FT sensors, FFT sensors show higher vertical smearing effects since longer transfer times are required. The simpler layout



a) Frame-transfer sensor with imaging zone and storage zone (Dalsa)



b) Silicon wafer of a full-frame sensor with  $4096 \times 4096$  elements

Figure 3.63 CCD matrix sensors

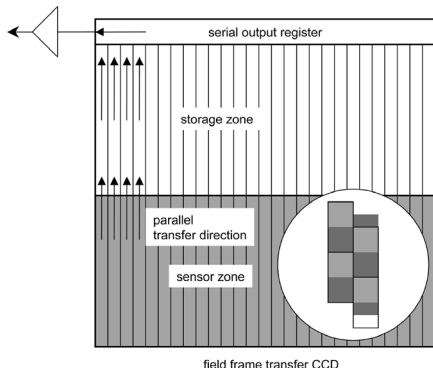


Figure 3.64 Principle of a frame-transfer sensor

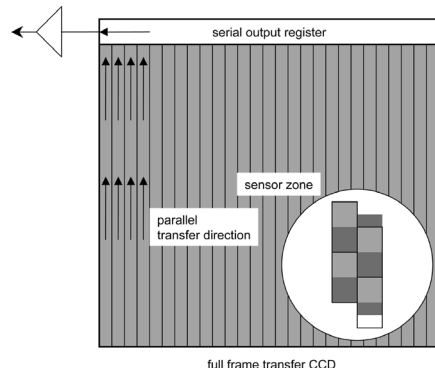
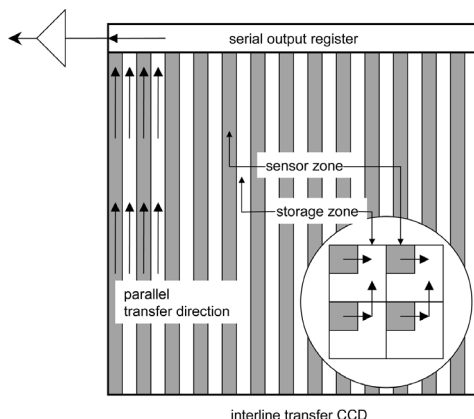


Figure 3.65 Principle of a full-frame transfer sensor

enables very large sensor areas<sup>1</sup> with very small sensor elements ( $6\text{--}9 \mu\text{m}$  size). Such layouts are used for high-resolution digital cameras with typically more than  $1000 \times 1000$  sensor elements (manufacturers include Thomson, Kodak, Fairchild, and Dalsa). Often the number of FFT sensor elements is based on integer powers of 2 ( $512 \times 512$ ,  $1024 \times 1024$ ,  $4096 \times 4096$ ).

In contrast, interline-transfer sensors (IL) have a completely different layout. The light-sensitive sensor elements (photo diodes) are separately arranged with a gap between their adjacent elements of the size of one detector. In the first instance, charged particles are shifted into the right transfer column. Subsequently, they are transferred in a vertical, optically opaque CCD bucket brigade towards the read-out register (Fig. 3.66). The light-sensitive area of the detector covers only ca. 25% of the total sensor area (ca. 90 to 100% for FT sensors) i.e. IL sensors are less light-sensitive. IL-sensors with standard pixel numbers of about  $780 \times 580$  pixels are mainly used for CCD-video and TV cameras (especially colour cameras) e.g. manufactured by Sony or Pulnix. High-resolution IL sensors have up to  $1900 \times 1000$  pixels.

<sup>1</sup> The production of very large CCD sensors is limited mainly by logistical restrictions (production numbers, quality) rather than technological restrictions.



**Figure 3.66** Principle of an interline-transfer sensor

Current sensor designs typically employ microlens arrays in order to increase the fill factor of each pixel. A microlens array consists of a series of lens elements, each of which is designed to collect the light falling on a region approximating to the area of a single pixel and to direct that light to the smaller light sensitive region of the pixel (Fig. 3.67, Fig. 3.68). While microlenses significantly enhance pixel fill factor, they typically retain the limitation of only being able to receive light over a  $\pm 30$  degree range of angles. This performance can limit the use of such arrays for extreme wide angle recording unless special optics are used.

#### *CMOS imaging sensors*

CMOS technology (complementary metal oxide semi-conductor) is a widely used technique for the design of computer processors and memory chips. Recently CMOS is increasingly applied

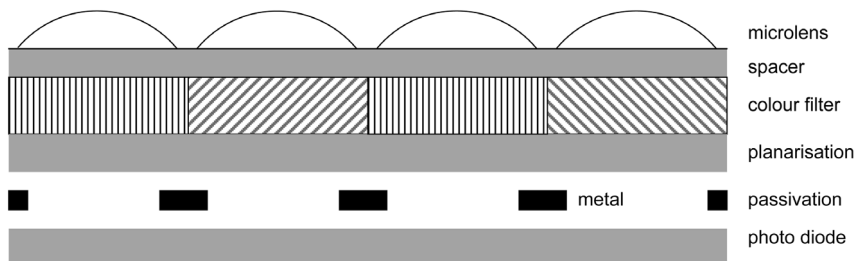


**Figure 3.67** Example layout of a microlens structure

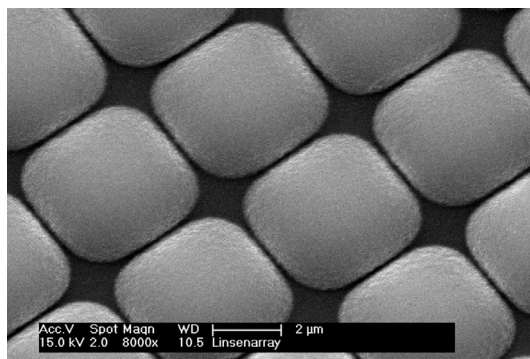


**Figure 3.68** Microlens array (raster electron microscope, 8000  $\times$  magnification)

for opto-electronic imaging sensors, since it provides significant advantages with respect to CCD technology:

- only 1/10 to 1/3 of power consumption compared to CCD sensors
- lower manufacturing costs
- direct addressable sensor elements; acquisition of arbitrary image windows
- high image frequencies with more than 1000 frames per second
- CMOS sensors can be adapted with on-chip processing devices e.g. for sensor control or image processing
- high dynamic range and low image noise

CMOS imaging sensors are already available with  $4000 \times 4000$  sensor elements. They can be designed with multiple sensor layers, each sensitised to a selected spectral band (see section 3.3.2.7).

In contrast to CCD sensor elements (MOS capacitors) CMOS detectors are based on photo diodes or transistor elements. The charge generated by the incident light is directly processed by an integrated amplifier and digitiser unit that is directly attached to the pixel element. Hence, sequential charge transfer is not applied. As a consequence, single sensor elements can be operated or processed, and higher robustness against blooming and transfer losses is achieved (Hauschild 1999, Yadid-Pecht and Etienne-Cummings 2004). Fig. 3.69 illustrates the principle layout of a CMOS matrix sensor.

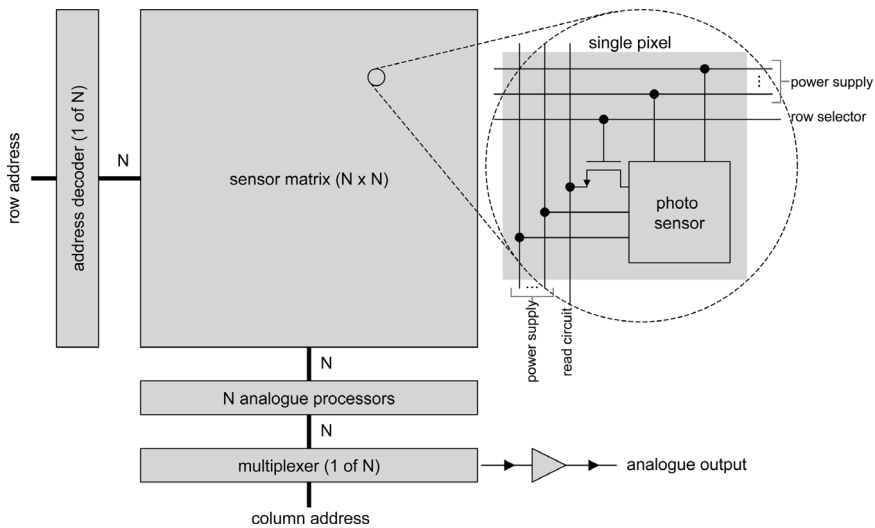


**Figure 3.69** Architecture of a simple 2D CMOS sensor (after Hauschild, 1999)

### *Resolving power*

The theoretical resolving power of monochrome CCD sensors is limited by two factors<sup>1</sup> (Lenz and Fritsch 1990):

- detector spacing  $\Delta x_s$  (distance between sensor elements) and scanning theorem (Nyquist frequency  $f_N$ )
- detector size  $\Delta x_d$  (aperture size) and MTF (limiting frequency  $f_0$ )

<sup>1</sup> The resolution of colour sensors further depends on the colour acquisition mode, see section 3.3.2.8

According to section 3.2.5.2, different theoretical resolution limits can be achieved for FT, FFT and IL sensors due to different arrangement of sensor elements. Furthermore, for all types, image quality can differ in both x and y directions where rectangular, rather than square, light sensitive regions have been used (Table 3.9).

**Table 3.9** Resolving power of different CCD sensors

		FT Valvo NXA	FFT Kodak	IL Sony
detector spacing in x	$\Delta x_{sx}$ [ $\mu\text{m}$ ]	10.0	9.0	11.0
detector spacing in y	$\Delta x_{sy}$ [ $\mu\text{m}$ ]	15.6	9.0	11.0
detector size in x	$\Delta x_{dx}$ [ $\mu\text{m}$ ]	10.0	9.0	5.5
detector size in y	$\Delta x_{dy}$ [ $\mu\text{m}$ ]	15.6	9.0	5.5
Nyquist-frequency in x	$f_{Nx}$ [lp/mm]	50	55	45
Nyquist- frequency in y	$f_{Ny}$ [lp/mm]	32	55	45
theoretical resolution in x	$f_{0x}$ [lp/mm]	100	111	180
theoretical resolution in y	$f_{0y}$ [lp/mm]	64	111	180

For FFT sensors or progressive-scan sensors (no interlaced mode) with square detector elements, equal resolving power can be expected in both horizontal and vertical directions.

IL sensors have approximately the same detector spacing as FT sensors, however each pixel is split into a light-sensitive detector and a shift register. Hence, the resulting theoretical resolving power is four times higher than the Nyquist frequency, and about two times higher than for FT and FFT sensors.

In practice, theoretical resolving power cannot be achieved unless the sampling interval is small enough to push the Nyquist frequency up beyond the effective resolution limit (cut-off) for that MTF. Normally the best that can be achieved is a full-fill system, for example the Kodak FFT in Table 3.9, where the Nyquist frequency is about half the theoretical resolution. In practical systems, frequencies higher than the Nyquist frequency are filtered out in order to avoid aliasing and micro lenses are used in order to provide pixel fill factors close to unity. Micro scanning systems (section 3.3.2.5) are able to achieve closer to theoretical resolving power since they subsample by moving the detector in fractions of a pixel between images.

In comparison to photographic emulsions, recent opto-electronic sensors have equal or even better resolutions but, at the same time, usually much smaller image formats. A comparable resolution is achieved with sensor element sizes of about  $7 \mu\text{m}$  or less.

In the digital photographic industry alternative image quality measures are currently in use. The value MTF50 defines the spatial frequency in lp/mm where the MTF is equal to 50%. With line widths per picture height (LW/PH) digital cameras are classified as a function of line width instead of line pairs. LW/PH is equal to  $2 \times \text{lp/mm} \times (\text{picture height in mm})$ . The term cycles or line pairs per pixel (c/p or lp/p) is used to give an indicator of the performance of a pixel.

#### *Geometric accuracy*

The geometric accuracy of matrix sensors is mainly influenced by the precision of the sensor elements position. Due to the lithographic manufacturing process of semi-conductors CCD matrix sensors have regular detector positions of better than  $0.1\text{--}0.2 \mu\text{m}$ , corresponding to 1/60

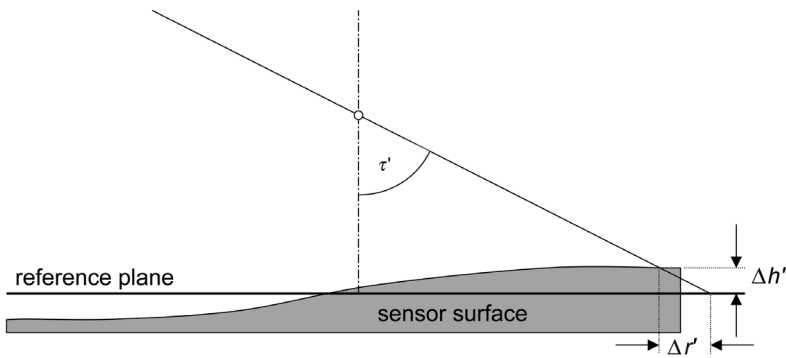


Figure 3.70 Lateral displacement for an unflat sensor surface

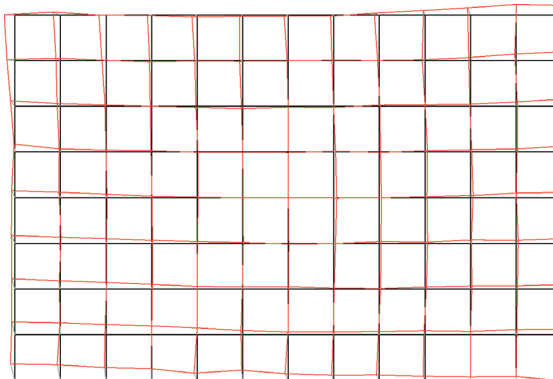


Figure 3.71 Sensor deformations (red) after finite element calibration (Kodak DCS460)

to 1/100 of the size of a sensor element. This does not mean that the resulting image can be evaluated by this accuracy. Several electronic processing steps are performed between image acquisition and digital storing that may degrade image geometry and contrast (Shortis and Beyer 1996, Lenz 1992, Dähler 1987).

An additional effect is given by the possible unflatness of the sensor surface. For sensor areas of  $1500 \times 1000$  pixels unflatness of up to  $10 \mu\text{m}$  has been demonstrated (Shortis and Beyer 1996). Depending on the viewing angle a vertical height difference of a sensor element yields a proportional lateral dislocation in the image (Fig. 3.70). If a non-systematic unflatness of the sensor surface occurs, usual approaches for the correction of distortion (additional parameters) fail. A suitable correction model based on finite elements has been shown by Tecklenburg *et al.* (2001). Fig. 3.71 shows deformations of an imaging sensor computed by this approach.

#### *Radiometric properties*

Light falling onto a CCD sensor is either reflected from the sensor surface, absorbed within the semi-conducting layer, or transmitted if high-energy photons are present. Absorption happens if the wavelength of light is shorter than the minimum wavelength  $\lambda_g$  of the radiated material. According to

$$\lambda_g = \frac{hc_0}{E_g} \quad (3.67)$$

where  $c_0$ : velocity of propagation =  $3 \times 10^8$  m/s  
 $h$ : Planck's quantum of action =  $6.62 \times 10^{-34}$  Js  
 $E_g$ : energy between conduction and valence band

Silicon used in the manufacture of CCD sensors has an energy of  $E_g$  of 1.12 eV, thus a minimum wavelength of  $\lambda_g = 1097$  nm, hence in near infra-red. In comparison to film layers and the human eye, CCD sensors show a significantly wider spectral sensitivity (Fig. 3.72). Optionally infra-red absorbing filters can be attached to the sensor in order to restrict incident radiation to visible wavelengths.

For very bright areas in the scene (hot spots) the sensor may be subject to saturation or overflow effects where the imaged signal flows into adjacent pixels. Such effects are caused by movement of charged particles into neighbouring sensor elements (blooming), and by continuous charge integration during the read-out process (smear). In photogrammetric applications these effects can be observed for brightly illuminated retro-reflective targets resulting in an incorrect determination of the target centre. Blooming and smear can also occur within images of natural scenes where large variations in lighting and contrast are present (example in Fig. 3.73).

Independent of the image-forming incident light, thermal effects in the semi-conducting layer can generate small portions of charge yielding a background noise to the sensor signal. This background noise is referred to as dark current since it occurs independently of any image illumination and can be observed in total darkness.

Artificial cooling of the sensor can reduce background noise i.e. the radiometric dynamic range is improved. Cooling down by 5–10°C yields to a noise reduction by a factor of 2. Artificially cooled sensors are typically applied for applications with low light intensity and long integration times (e.g. imaging sensors for astronomy).

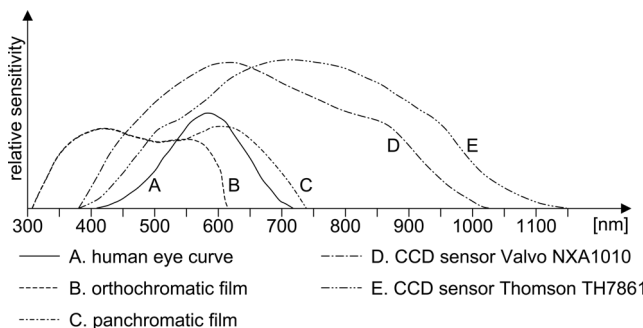


Figure 3.72 Spectral sensitivity

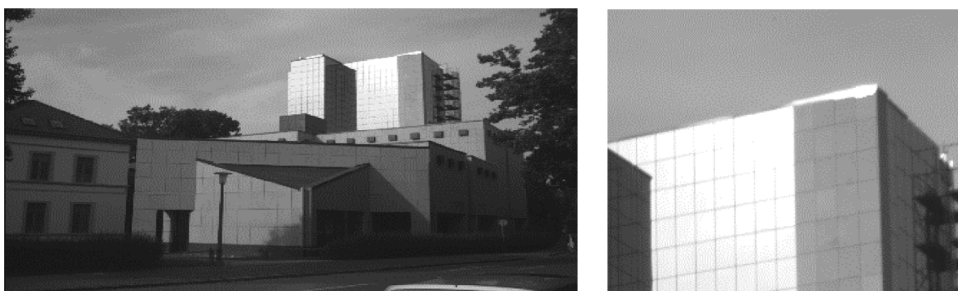


Figure 3.73 Blooming effect for an architectural image (camera: Kodak DCS420)

The radiometric dynamic range is defined by the signal-to-noise ratio (SNR):

$$SNR = \frac{S}{\sigma_S} = 20 \log \frac{S}{\sigma_S} [\text{dB}] \quad (3.68)$$

$S$  denotes the maximum signal amplitude and  $\sigma_S$  denotes the system noise, caused by photon shot noise, dark current and circuit noise. For CCD matrix sensors a SNR of about 1:1000 corresponding to 60 dB is typical. If an additional noise for the subsequent A/D conversion is assumed, the CCD sensor signal should be digitised with at least 10–12 bits per pixel.

### 3.3.2.3 CCD video cameras

#### Video standards

The term CCD video cameras can be used to describe all cameras that deliver an image signal according to standardised video signals. These standards are based on the specifications for analogue image transfer for video and TV technology.

Standard video formats require image signals with an aspect ratio of 4:3. CCIR (Europe) and RS-170 (America, Asia) are the two standards in use world-wide, whose specifications only differ slightly (see Table 3.10). For the CCIR format a video signal is based on 25 frames per second generated in interlaced scanning mode (50 full-frame images per second). A single frame consists of the odd or even image lines, respectively. A full frame has 625 lines.

Each individual line is led by a line synchronisation signal (horizontal sync), each image (frame) commences with an image synchronisation signal (vertical sync). The time period of a single frame is  $1/25 \text{ s} = 40 \text{ ms}$  i.e. a single line requires  $40 \text{ ms} / 625 = 64 \mu\text{s}$ . Some of the image lines contain no image information, thus 576 active image lines remain. Subtracting the time for synchronisation signals, each active image lines spans  $52 \mu\text{s}$ . For an assumed number of 744 image points per line the time for one image point (pixel) results to 69 ns.

CCD video cameras are equipped with a matrix sensor that can be read out within a video cycle (25–30 images per second). They can differ concerning usable image format and number of sensor elements. With respect to physical sensor size, definitions developed for former vidicon tube type cameras are still in use today with sensor format dimensions classified in sizes between  $1/4''$  (inch) and  $1''$ .

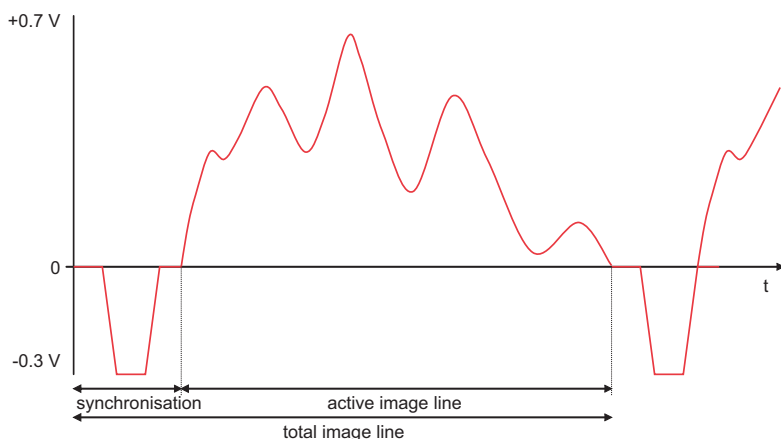


Figure 3.74 Design of an analogue video signal

**Table 3.10** Specifications of video standards

	CCIR	RS-170	remarks
full frame frequency	25 Hz	30 Hz	
single frame frequency	50 Hz	60 Hz	
number of image lines	625	525	
active image lines	576	480	
time of an image line	64 µs	63.5 µs	
frequency of an image line	15.6 kHz	15.7 kHz	
time of an active line	52 µs	52.5 µs	only image information
image points per line	744	752	no standard
time of an image point	69 ns	70 ns	
frequency of an image point	14.5 MHz	14.5 MHz	≈ pixel-clock frequency

The number of sensor lines in a CCD video camera are scaled to the video standard. Usually between 480 and 580 lines are used whereby each line consists of approximately 600 to 780 sensor elements. According to the image formats, displayed in Table 3.11, the size of a single sensor element (pixel) varies between 4 µm (1/4" cameras) and 15 µm (2/3" cameras). Cameras with square pixels and cameras with rectangular pixels are possible. For video cameras recent tendencies towards higher resolution and larger area sensors can be observed.

**Table 3.11** Typical image formats of video cameras

format (typical) [mm]	diagonal (image tube) [inch]	diagonal CCD-sensor [mm]	sensor elements (typical)	size of a sensor element [µm]	example
3.2 × 2.4	1/4	4.0	752 × 582	4.2 × 4.2	Sony DXC-LS1P
4.8 × 3.6	1/3	6.0	752 × 582	7.4 × 7.4	Pulnix TMC-63M
6.4 × 4.8	1/2	8.0	768 × 494	8.4 × 9.8	Pulnix TM-7
8.8 × 6.6	2/3	11.0	768 × 593	11.0 × 11.0	Sony XC-77
9.1 × 6.9	2/3	11.4	1300 × 1030	6.7 × 6.7	Pulnix TM-1300
9.1 × 9.1	1	12.7	1024 × 1024	9.0 × 9.0	Pulnix TM-1001
12.0 × 12.0	1	16.0	1024 × 1024	12.0 × 12.0	Dalsa CA-D4
14.0 × 8.0	1	16.1	1920 × 1035	7.3 × 7.6	Sony XCH-1125

Standard CCD video cameras are designed to be compatible with video standards by reading pixel data out of the sensor in interlaced mode. In contrast the sensor image of so-called progressive scan cameras (also denoted as slow scan cameras) are read out in full-frame mode i.e. the complete image is exposed at one and the same time. Relative movements (also vibrations) between camera and object no longer lead to blurring effects for the resulting video image (Fig. 3.75). In addition to providing a standard video output these cameras require a separate interface in order to access the progressive scan signal.

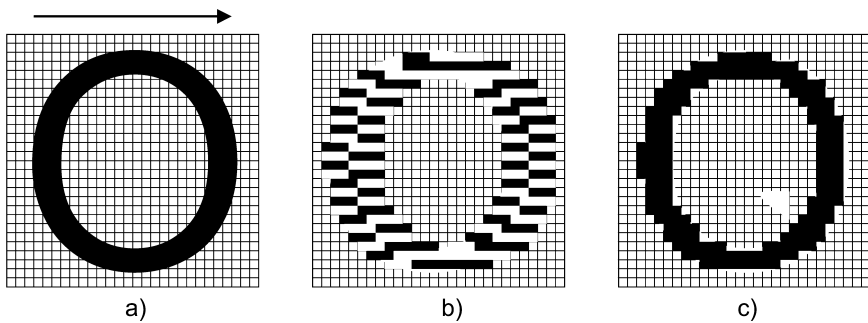


**Figure 3.75** (a) Recording and resulting image of a moving object by (b) an interlaced and (c) a progressive-scan system



**Figure 3.76** Examples of CCD video cameras

Due to the numerous applications of CCD video cameras, especially for commercial video market and general surveillance tasks, the choice of video cameras is immense. Home-video and TV-cameras, especially camcorders, are often based on mass produced IL sensors. FT sensors are often used in technical applications since, by virtue of larger fill factors, they provide higher light sensitivity compared to IL sensors. Micro-head cameras can have very small body dimensions (e.g. a 17 mm camera head diameter is readily available Fig. 3.76).

#### *Components of a CCD video camera*

In general, CCD video cameras are not designed for high-precision geometric measurement tasks. The optical-mechanical arrangement of the imaging sensor, camera body, filters and lens will often not meet the dimensional stability requirements demanded by photogrammetric measurement needs. In addition, the image signal is processed internally in many cases resulting in a loss of the precise geometric relationship between imaging sensor and resulting image.

Fig. 3.77 displays the schematic layout of a CCD video camera. The imaging sensor is embedded in a ceramic housing and covered by a thin glass plate in order to make it mechanically robust. Often a diffuser is mounted in front as a low-pass filter to compensate for aliasing effects. In some cases, a matrix of semi-cylindrical lenses (microlenses) are used instead, one lens per pixel. An optional infra-red cut-off filter can be included to absorb wavelengths longer than 700 nm.

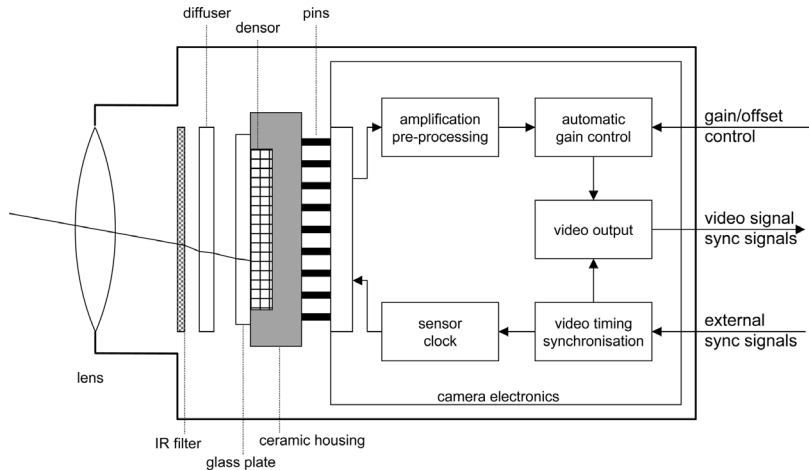


**Figure 3.77** Schematic layout of a CCD video camera (after Shortis and Beyer 1996)

Usually a C-mount or CS mount lens adapter with screw thread is used. For off-the-shelf cameras it cannot be assumed that the individual optical components making up the lens are sufficiently well aligned to the optical axis, nor have a homogeneity that meets photogrammetric requirements. In addition, many video lenses have large radial and tangential image distortions that must be modelled (optical distortions of 10's of pixels being common).

After sensor read-out the image signal is amplified and pre-processed. Subsequently its contrast and brightness may be automatically adjusted through the use of an automatic gain control whereby the analogue signal is amplified to the maximum amplitude. The level of amplification is controlled by the brightest and the darkest locations in the image. For technical cameras gain control can be controlled externally (Fig. 3.78). Since automatic gain control is a post-processing step, loss of geometric quality and undesired brightness changes cannot be excluded. In addition and most noticeably under poor lighting conditions, gain controls can increase image noise. Automatic gain control should be switched off if sufficient and constant illumination conditions are available.

Both image sensor and video signal require high-frequent synchronisation signals that are delivered by a pulse generator (sensor clock). Synchronisation can also be controlled by an

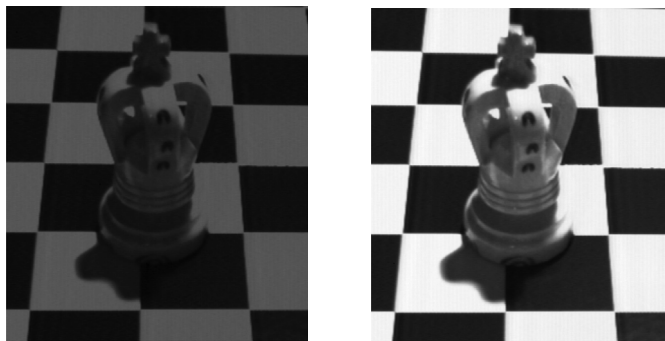


**Figure 3.78** Video image without (left) and with (right) automatic gain control at constant illumination

external signal e.g. for the synchronised image acquisition of several cameras, or for the synchronisation of a video frame grabber for the precise digitisation of a video signal (see below).

In addition to standard cameras, high-resolution video cameras are available that are designed for HDTV (high definition television) applications. With ca. 1100 lines and ca. 1900 pixels per line they enable image acquisition with an aspect ratio of 16:9. It should be noted however that HDTV is currently not fully standardised (Goldschmidt and Peipe 1994, Inglis and Luther 1996).

#### *Digitisation of analogue video signals*

In order to provide an output stream of digital images, the analogue video signal must be digitised by an analogue to digital converter (ADC) which is synchronised to the video frame cycle rate of the sensor (e.g. 25 frames per second). Frame Grabbers are additional computer integrated hardware devices connected via a data transfer bus system which contain an ADC and associated timing electronics. The digitised video image can either be displayed in real-time either on the graphical user-interface of the computer, or transferred to computer memory or a digital recording device such as a digital tape.

Fig. 3.79 shows the simplified layout of a frame grabber for the digitisation of a monochrome video signal. Using a video multiplexer the system can switch between different video sources. By means of PLL synchronisation (phase locked loop) horizontal synchronisation pulses are extracted from the video signal in order to correctly drive the analogue-to-digital converter (ADC). After the detection of the beginning of a line the ADC scans the analogue signal at a pre-defined scanning frequency to deliver 8-bit grey values by default. The grey values are stored line by line in image memory after they have passed an input lookup-table (LUT) where they are optionally transformed e.g. converted into a negative image (see section 5.2.1.2). For image display, the image memory content passes through an output LUT before being converted into an analogue video image. Digital access to image data, lookup tables and other data processing functions of the frame grabber are enabled through a computer interface.

The geometry of the digitised video image is affected by the scanning process. The start of an image line is detected by an electronic synchronisation process called a Pixel Lock Loop (PLL) which contributes a potential uncertainty of about 0.1 pixels. This uncertainty is referred to as line jitter. Variations of the scanning frequency lead to deviations within an image line

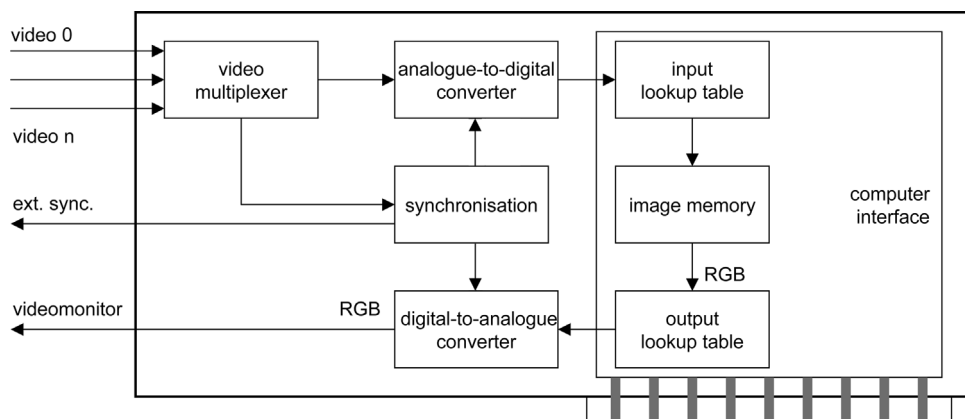


**Figure 3.79** Schematic layout of a frame grabber

called pixel jitter. Usually the scanning frequency is generated internally in the frame grabber rather than using the signal driving the sensor, hence it may not be identical to the pixel frequency of the CCD sensor. According to Table 3.10 the pixel frequency is ca. 14.5 MHz depending on the imaging sensor. If the scanning frequency is different the resulting pixel size along a line (x) will alter:

$$s'_x = s_x \frac{n_X}{n_C} = \frac{s_x n_X}{f_A t_X} \quad (3.69)$$

where  $s'_x$ : scanned horizontal pixel size  
 $s_x$ : horizontal size of a CCD sensor element  
 $n_X$ : number of CCD elements per line  
 $n_C$ : number of scanned pixels per line  
 $f_A$ : scanning frequency  
 $t_X$ : active time of an image line (52 µs for CCIR)

As a result the digitised pixel size can differ in x and y directions. For photogrammetric applications this effect must be compensated for by introducing an affinity parameter into the model of interior orientation (see section 3.2.3.2). Thus photogrammetric video-based measuring systems have to be calibrated together with the actual used frame grabber.

### Example 3.7:

Consider a CCD video camera with  $604 \times 576$  sensor elements and an image format of  $6.0 \text{ mm} \times 4.5 \text{ mm}$  (size of sensor elements:  $10.0 \mu\text{m} \times 7.8 \mu\text{m}$ ). The connected frame grabber enables a scanning rate of 10 MHz (size of image memory  $512 \times 512$  pixels). What is the resulting size of a digitised pixel and the required scanning frequency to generate square pixels?

Solution:

$$1. \text{ Scanned pixels per line: } n_C = f_A \times t_X = 10 \text{ MHz} \times 52 \mu\text{s} = 520$$

With an image memory size of 512 pixels per line 8 pixels are erased from each line.

$$2. \text{ Scanned pixel size: } s'_x = \frac{s_x \times n_X}{n_C} = \frac{10 \mu\text{m} \times 604}{520} = 11.6 \mu\text{m}$$

Hence the scanned pixel size differs from the original size of the sensor element.

$$3. \text{ Pixel aspect ratio: } m = \frac{s'_x}{s'_y} = \frac{11.6 \mu\text{m}}{7.8 \mu\text{m}} = 1.4 \approx 3:2$$

$$4. \text{ Scanning frequency: } f_A = \frac{s_x n_X}{s'_x t_X} = \frac{10 \mu\text{m} \times 604}{7.8 \mu\text{m} \times 52 \mu\text{s}} = 14.89 \text{ MHz}$$

For a scanning frequency of 14.89 MHz the scanned horizontal pixel size is equal to the vertical size of a sensor element that remains unchanged with scanning.

If a video camera is synchronised by a trigger from the frame grabber (or vice versa), accuracies of about 0.05 pixels (ca.  $0.5 \mu\text{m}$ ) in the image plane can be achieved under practical conditions. An additional accuracy improvement can be obtained if the video scanning is controlled by a pixel-synchronous pulse of the camera (pixel clock). Today video cameras with

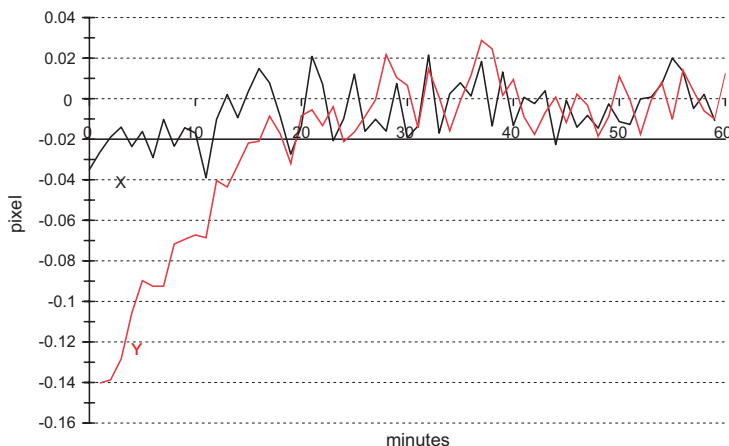


**Figure 3.80** Drift of measured sensor coordinates during warm-up

internal digital output exist where analogue to digital conversion is performed inside the camera, consequently the timing signals at the sensor can be identical to those at the A/D converter.

Video cameras require a warm up period of up to 2 hours. During warm up, image coordinate displacements of several tenths of a pixel have been shown to occur (Beyer 1992). Fig. 3.80 shows an example of sensor drift measured under controlled laboratory conditions. The figure shows coordinate differences extracted from five images of a warm up time series. For the x direction only small shifts can be observed that are below the measuring uncertainty of ca.  $\pm 0.02$  pixel after 10 minutes. In contrast, in they direction a drift of ca. 0.15 pixel can be observed within the first 20 minutes. Part of this effect is caused by temperature increases on mechanical components, but electronic devices inside the camera also contribute as they warm up.

For TV-camcorders, development trends are towards digital video cameras where image sequences are stored digitally (with for example MPEG audio and video compression) instead of an analogue video tape (Fig. 3.76). In addition, digital video cameras with direct computer interfaces (e.g. USB, Firewire, CameraLink) are available that do not require a separate frame grabber.

In photogrammetry, CCD video cameras are generally used in specialised real-time applications with relative accuracies of the order of 1:5,000 to 1:15,000.

### 3.3.2.4 High-resolution digital cameras

After developments at the end of the 1980s (e.g. Kodak Megaplus,  $1320 \times 1035$  pixels), a growing number of high-resolution imaging sensors have become available at reasonable price. In this field, developments for consumer, orientated digital photography are the driving force in that they offer numerous imaging systems for amateur users, and high-resolution monochrome and colour cameras for the professional photographer.

High-resolution digital cameras such as still-video cameras, scanning cameras, digital camera backs or specialised metric cameras are readily available for photogrammetric practice. In combination with established photographic camera technologies they provide powerful and user-friendly systems. Data transfer is either performed off-line by means of an internal storage device (e.g. PCMCIA-disk, SmartMedia, CompactFlash, MicroDrive), or on-line with a connected computer. In addition imaging systems with integrated processors exist where a variety of image processing functions are performed directly inside the camera.

Table 3.12 shows a selection of high-resolution digital cameras. Due to the rapid technological progress in this area the table only indicates a recent view (valid 2005) without claiming completeness or long-term availability in the market.

**Table 3.12** Selection of digital imaging systems

supplier	type	format [mm]	number of pixels	pixel size [μm]	type	year <sup>1)</sup>
Kodak	Megaplus-1.4	9 × 7	1320 × 1035	7 × 7	CCD	1986
Kodak	Megaplus-4.2i	18 × 18	2029 × 2044	9 × 9	CCD	1992
Kodak	DCS 200	14 × 9	1536 × 1042	9 × 9	CCD	1992
Kodak	Megaplus-6.3i	28 × 18	3070 × 2048	9 × 9	CCD	1995
Kodak	DCS 460	28 × 18	3060 × 2036	9 × 9	CCD	1995
GSI	INCA 4.2	18 × 18	2029 × 2044	9 × 9	CCD	1997
Rollei	ChipPack	31 × 31	2048 × 2048	15 × 15	CCD	1997
Imetric	ICam 6	37 × 25	3072 × 2048	12 × 12	CCD	1998
Kodak	Megaplus 16.8i	37 × 37	4096 × 4096	9 × 9	CCD	1998
Imetric	ICam 28	86 × 49	7168 × 4096	12 × 12	CCD	1998
Rollei	d7/d30 metric <sup>5</sup>	9 × 7	2552 × 1920	3.5 × 3.5	CCD	1999
Rollei	db44 metric	37 × 37	4080 × 4076	9 × 9	CCD	1999
GSI	INCA 6.3	28 × 18	3060 × 2036	9 × 9	CCD	2001
Kodak	ProBack 645M	37 × 37	4096 × 4096	9 × 9	CCD	2002
Kodak	DCS Pro 14n / c	36 × 24	4560 × 3048	8 × 8	CMOS	2003
Nikon	D100	24 × 16	3008 × 2000	8 × 8	CMOS	2004
Sigma	SD 10	21 × 14	2268 × 1512	9 × 9	CMOS, Foveon	2004
Fuji	S3 Pro	23 × 15.5	4256 × 2848	5.5 × 5.5	CMOS	2004
GSI	INCA 3	31.5 × 21	3500 × 2350	9 × 9	CCD	2004
Jenoptik	Eyelike emotion <sup>22</sup>	48 × 36	5344 × 4000	9 × 9	CCD	2004
Canon	D1 S (Mk II)	36 × 24	4992 × 3328	7 × 7	CMOS	2005
Phase One	P 45	41 × 37	7216 × 5412	6.8 × 6.8	CCD	2005
Rollei	RSC	52 × 52	4500 × 4500	11 × 11	réseau-scan	1988
Kontron	ProgRes 3012	9 × 7	4608 × 3480	2 × 2	micro-scan	1990
Zeiss	UMK HighScan	166 × 120	15414 × 11040	11 × 11	4 CCDs, macro-scan	1994
RJM	JenScan	9 × 7	4488 × 3072	2 × 2	micro-scan	1996
KWD	Rotascan Noblex	360°, 60	42379 × 8600	7 × 7	panorama-scan	1999
Jenoptik	Eyelike ProgRes	29 × 29	6144 × 6144	5 × 5	micro-scan	1999
Rollei	Gamma S12	56 × 56	3500 × 3500	16 × 16	line-scan	2000
KST	Eyescan M2	360°, 60	54000 × 10200	7 × 7	panorama-scan	2000

1) year of first appearance (partly estimated)

In general, digital cameras with matrix sensors are referred to as still-video cameras if a number of single shots can be stored directly inside the camera. Simple digital viewer cameras with up to ca.  $3500 \times 2500$  pixels are increasingly used in the amateur photo market. For instance, solid-state memory devices data storage (flash memory) or micro hard disks, capable of storing several gigabytes of image data, are used for data storage. Cameras of this type can be used for accurate photogrammetric measurement tasks if auto-focus is disabled and zooming is limited in order to facilitate self calibration (example in Fig. 3.81).

High-resolution still-video cameras based on small-format single lens reflex cameras provide the mainstay for much digital photogrammetric work. A matrix sensor is positioned in the image plane and a storage device is integrated inside the camera. These systems have been available since the early 1990s. As an example, Fig. 1.31 shows a Kodak/Nikon DCS 460 still-video camera. This camera was a development of the Kodak DCS200 and DCS420 ( $1524 \times 1012$  pixels) cameras but delivered an image of  $3060 \times 2036$  pixels. Based on a  $9 \mu\text{m}$  pixel size, the sensor format of  $28 \text{ mm} \times 18 \text{ mm}$ , was much closer to the photographic  $35 \text{ mm}$ -camera format ( $36 \text{ mm} \times 24 \text{ mm}$ ) than other systems available at that time. Consequently, small-format wide angle lenses could be used without significant restrictions whereby the format angle must be related to the effective image format (extension of focal length). A memory space of 6 MB (monochrome) or 18 MB (colour) without image compression is required per image, but with memory cards and compatible micro hard disk drives available in capacities of the order of 2 GB local image storage is no longer a key issue. Alternatively, instead of internal image storage, camera control and image transfer can be operated via an SCSI interface to a host computer.

The camera consists of a Kodak matrix sensor of high geometric quality. Normally the sensor is spring mounted to the back of the camera body without a stable connection to the lens. Since mechanical movements cannot be avoided during a longer image series the calibration of the camera must consider image-variant parameters or the definition of multiple cameras for the image set is necessary (see section 4.3.2.4). Under practical conditions an accuracy of about 0.2 to  $0.5 \mu\text{m}$  ( $1/50$ – $1/20$  pixel) can be achieved with the DCS460 if the camera is handled with care, precisely measured targets are used and object reconstruction is performed by bundle adjustment with self-calibration. This is equivalent to a relative accuracy of the order of 1:100,000 (Peipe 1995b). The mentioned restrictions are also valid for modern digital cameras that are equipped with CMOS sensors in full  $35 \text{ mm}$ -format (e.g. Kodak DCS Pro 14n with  $4660 \times 3048$  pixels, Nikon D2X with  $4288 \times 2848$  pixels).

The major advantage of still-video systems is the quick and handy image acquisition and the possibility to transfer images directly into a laptop computer. Thus image quality can be evaluated and varied while recording an image network, or photogrammetric processing can



Figure 3.81 Still-video camera Rollei d7 metric<sup>5</sup>

be performed immediately. Still-video cameras are used both for photogrammetric off-line systems (one camera, sequential image recording, separated image processing and object reconstruction), and for on-line systems (two or more cameras, simultaneous image recording, immediate image processing and object reconstruction).

Digital camera backs are available for medium format film cameras that use interchangeable film magazines. One of the first of this kind was the Rollei ChipPack ( $2048 \times 2048$  pixel), digital camera back operated with a Rollei 6008 body (Fig. 3.82, Godding and Woytowicz 1995).

Purpose built photogrammetric digital metric cameras<sup>1</sup> are available that guarantee high geometric stability due to their opto-mechanical design. For example, the GSI/Leica INCA 6.3 ( $3060 \times 2036$  pixel) metric camera, which is based on a Kodak Megaplus digital camera, also has an integrated processor for image processing (Fig. 3.83). The processor not only allows image data to be compressed, but it can also be used for detection and measurement of targeted points, thus only image coordinates need be transferred to a host computer for standard applications with retro-targets. The accuracy potential of the INCA 6.3 is of the order of 1:100,000 (Brown and Dold 1995). The next generation INCA 3 camera (Fig. 3.84) provides  $3500 \times 2350$  pixels, an integrated Pentium 3 processor and wireless LAN capabilities.

The Imetric ICam 6 ( $3072 \times 2048$  pixels) and ICam 28 ( $7168 \times 4096$  pixels) metric cameras are equipped with integrated computers for automatic point measurement and 3D calculations (Fig. 3.87). The systems offer high data rates (64 MB/s for ICam 6) and high radiometric resolution (up to 16 bit per pixel) (Beyer 1998). Up to 56 MB of data per single image can be recorded using an ICam 28.

Digital cameras with  $4000 \times 4000$  pixels or more are available from several manufacturers. Digital camera backs available from Kodak, Jenoptik (Fig. 3.86) or PhaseOne can be mounted to different medium format bodies forming high-resolution imaging systems that can be successfully applied to photogrammetric applications.

Fig. 3.87 shows the Kodak DCS ProBack 645M with 35 mm lens combined with a Mamiya body. The camera consists of an independent power supply and image storing device, hence it



**Figure 3.82** Digital camera Rollei 6008 / ChipPack



**Figure 3.83** Digital metric camera  
DSI/ Leica INCA 6.3

<sup>1</sup> Here the term metric camera is used for a camera specially designed for measuring.



**Figure 3.84** Digital metric camera GSI/ INCA 3



**Figure 3.85** Digital metric cameras Imetric ICam 6/28 with their CCD sensors



**Figure 3.86** Digital camera back JenOptik Eyelike emotion<sup>22</sup>



**Figure 3.87** Digital camera Kodak DCS ProBack 645M

is suitable for hand-held shots. A measurement accuracy of about 1:150,000 can be achieved if the weak stability of the sensor back is modelled by image-variant parameters of interior orientation (Jantos *et al.* 2002). Fig. 3.88 shows a reduced picture acquired with the camera (originally in colour), Fig. 3.89 shows a corresponding window of this image at its original resolution.



**Figure 3.88** Reduced image recorded by a Kodak DCS ProBack 645M

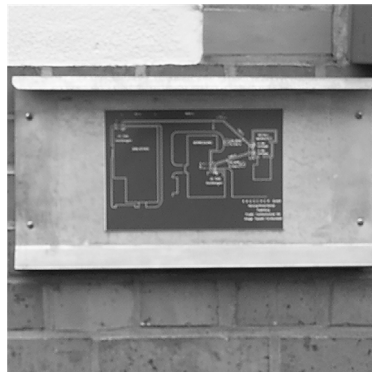


**Figure 3.89** Original window taken from the image of Fig. 3.88

### 3.3.2.5 Scanning cameras

Since the resolution of digital cameras was a limiting factor a few years ago, scanning cameras were developed in order to increase pixel resolution by sequential scanning of an object or scene (see also Table 3.12). Two basic scanning principles can be distinguished: micro scanning and macro-scanning. However, such systems can only deliver high quality images if there is no relative movement between camera and object.

#### *Micro-scanning*

In the case of micro-scanning cameras piezo elements are used to translate an interline-transfer matrix sensor horizontally and vertically, in fractions of the sensor element size (micro-scan factor) (Fig. 3.90). A high resolution output image is created by alternating the storage of single images. The final image has a geometric resolution that is increased by the micro-scan factor in both directions (Lenz and Fritsch 1990). From a photogrammetric standpoint, the micro-scanning principle results in a reduction of effective pixel size while maintaining the usable image format of the camera.

Cameras based on this principle are the RJM JenScan (4608 × 3072 pixels), Kontron ProgRes 3012 (4608 × 3480 pixels) and Jenoptik Eyelike (6144 × 6144 pixels, Fig. 3.91). Even higher resolutions can be achieved if micro-scanning is combined with the principle of macro-scanning (see below).

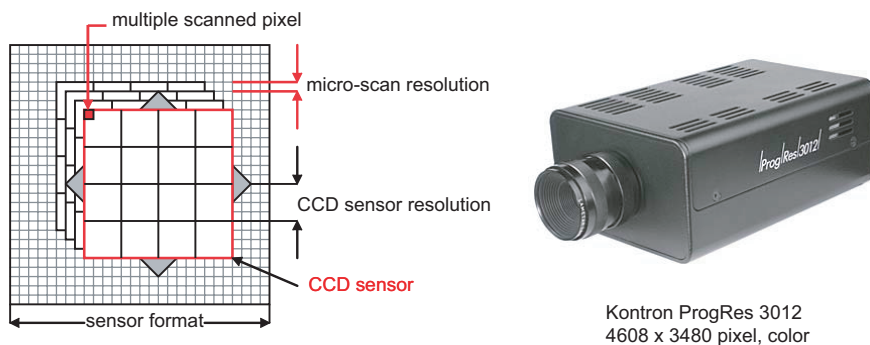


Figure. 3.90 Principle and example of a micro-scanning camera



Figure 3.91 Jenoptik Eyelike

### *Macro-scanning*

Macro-scanning systems work with a CCD line sensor or CCD matrix sensor that is shifted in wider steps over a larger image format. The position of single partial images is either determined optical-numerically or mechanically. Finally all partial images can be combined to produce a complete large-format image.

Fig. 3.92 illustrates the principle of a line-scanning camera. A single CCD line sensor is moved vertically across the total format of the camera by means of a mechanical guiding device. The resolution of the line-scanning camera is defined by the arrangement of sensor elements in the horizontal direction and by the step resolution of the mechanical guiding device in the vertical direction.

Line-scanning camera backs are offered for normal medium-format cameras (up to  $4'' \times 5''$  format) that can be used instead of a film magazine. To provide an example the Rollei ScanPack ( $5850 \times 5000$  pixels) and Rollei Gamma S12 ( $3500 \times 3500$  pixels) scanning modules are mentioned here (Fig. 3.93). Due to their limited mechanical guiding accuracy these systems are usually not applied for photogrammetry, but are used mainly for professional still-photography.

An example of optical-numerical sensor orientation is given by the Réseau-Scanning Camera Rollei RSC (Wester-Ebbinghaus 1989, Riechmann 1990, see Fig. 3.94 and Fig. 3.95). It consists of a CCD matrix sensor with  $750 \times 580$  elements that delivers an analogue video signal. The resultant mosaic image format has dimensions  $52 \text{ mm} \times 52 \text{ mm}$  with a

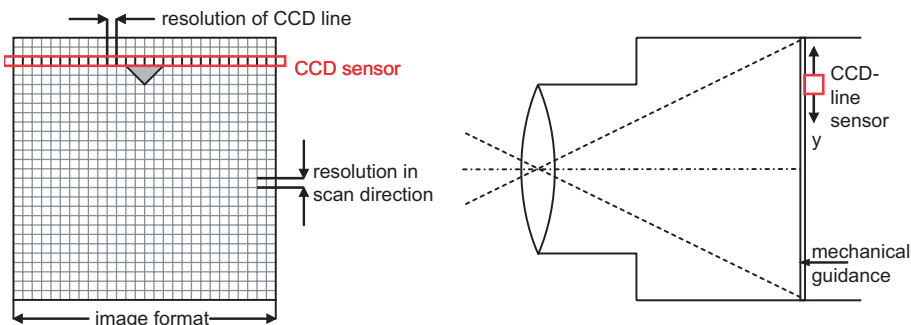


Figure 3.92 Principle of a line-scanning camera

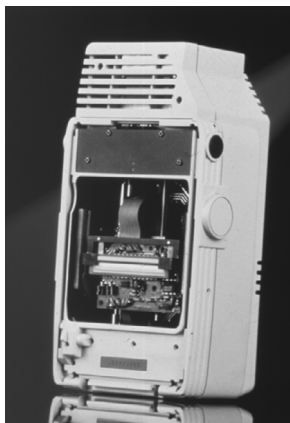


Figure 3.93 Line-scanning camera Rollei 6008 / ScanPack and Rollei Gamma S12

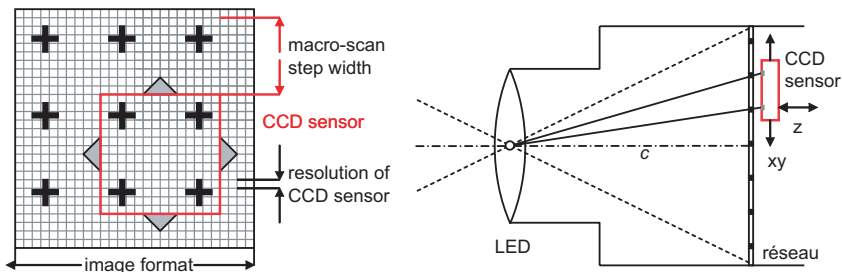


Figure 3.94 Principle of the réseau-scanning camera

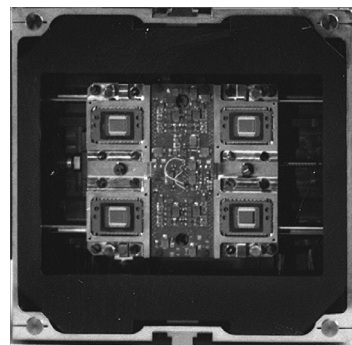
Figure 3.95 Réseau-scanning camera  
Rollei RSC

Figure 3.96 Scanning unit of the macro-scan camera Zeiss UMK HighScan

corresponding resolution of  $4500 \times 4500$  pixels. A réseau equipped glass plate with 2 mm mesh width is mounted in front of the sensor, so that  $4 \times 3$  réseau points are imaged at each sensor position. Which crosses are recorded on the sensor at each instant can be determined using the less accurate stepper motor information. Automatic measurement of réseau points and their subsequent transformation onto the nominal coordinates of the réseau leads to a numerically calculated sensor position without requiring a high level of mechanical stability.

In order to generate sharp and high-contrast images the réseau is illuminated by an LED that is mounted into the lens. Hence, sensor orientation requires a second image that only displays the réseau points while the object is hidden by the closed shutter. Subsequently the LED is turned off and the shutter is opened so that the réseau is almost invisible and the object can be imaged. In addition to a movement in the xy direction the sensor can also be moved in z-direction parallel to the optical axis. The camera is designed such that the projected images of the LED allow not only the réseau locations to be determined but also accounts for changes in lens distortion with varying object distance. Thus the system permits focusing without the need to redetermine interior orientation. This design has been demonstrated to deliver a target image measurement accuracy potential of the order of  $1 \mu\text{m}$ . As an example, the camera is used for robot calibration, whereby only the interesting image areas are scanned and processed on-line.

Based on the Zeiss UMK (Fig. 3.48) large format metric camera, the Zeiss UMK HighScan records an image format of  $120 \text{ mm} \times 166 \text{ mm}$  on a step by step basis by means of four parallel arranged matrix sensors (Fig. 3.96, Kludas 1995). The resulting image consists of ca.  $15,000 \times 11,000$  pixels. The accuracy of the mechanical guiding device is about  $5 \mu\text{m}$ . The camera has been applied to specific applications of high-resolution digital stereo imaging, where it has been used in combination with a fringe projector (see Fig. 6.43).

By combination of micro scanning with macro-scanning the image resolution of a digital camera can be increased arbitrarily. The MARC camera is a colour imaging system with a selectable resolution of up to  $20,000 \times 20,000$  pixels requiring a memory space per image of up to 1.7 GB (Lenz *et al.* 1994). The camera is designed for high-quality recording and archiving of paintings.

### 3.3.2.6 Panoramic cameras

Digital panoramic cameras with a scanning CCD line form a special case of the macro-scan technique. A vertically mounted sensor line is rotated about a vertical axis where it images the surrounding object area (rotating line scanner). The mathematical projection model is a parallel projection in the horizontal direction, while it is still a central perspective projection in the vertical direction. The resulting image consists of a cylindrical projection surface.

An eccentricity vector  $e$  between the perspective centre and the rotation axis must be determined by camera calibration. For photogrammetric processing of panoramic images, the mathematical model is extended for the  $x'$  direction whereby the image coordinate  $x'$  (column position in image) is defined as a function of the rotation angle  $\alpha$  and the eccentricity vector see Fig. 3.97 (Lisowski and Wiedemann 1999, Schneider and Maas 2003). A number of systems are available on the market e.g. the panorama camera Rotascan-Noblex (max.  $42,379 \times 8,600$  pixels) or the KST EyeScan-M3 metric (Fig. 3.98, max.  $54,000 \times 10,200$  pixels). Most cameras provide  $360^\circ$  images and can also produce smaller user definable sections.

Panoramic images can also be generated from single frame images if the individual images have a sufficient overlap. A geometrically exact stitching of such panoramas can only be performed if the single images are acquired around a common rotation axis, and if the interior orientation parameters are known (example image in Fig. 3.99).

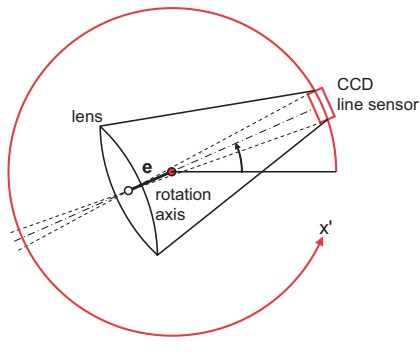


**Figure 3.97** Principle of a panorama-scanning camera

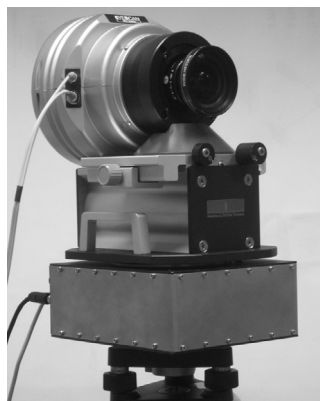


**Figure 3.98** Digital panorama camera  
KST EyeScan M3



**Figure 3.99** Digital panorama image created by stitching to a cylindrical geometry

Several spatially distributed panoramas can be used for photogrammetric methods such as bundle triangulation or space intersection if they are based on cylinder coordinates (Chapman and Deacon 1997, Schneider and Maas 2003, Luhmann and Tecklenburg 2002). Mathematical models are presented in section 4.7.

### 3.3.2.7 Colour cameras

In order to create true colour images, incident light must be separated into three spectral bands, typically, red, green and blue. Separation can be performed by four common methods summarised in Table 3.13.

**Table 3.13** Features of colour separating methods

	3-chip camera	RGB filter	mosaic mask	true colour sensor
number of sensors	3	1	1	1
number of images	1	3	1	1
number of video signals	3	1	1	1
dynamic scenes	yes	no	yes	yes
resolution	full	full	half	full
colour convergency	adjustment	yes	low-pass filter	yes

- Parallel or 3-chip method

A prism system is used to simultaneously project incident light onto three similar CCD sensors. Each sensor is located behind a different colour filter so that each registers the intensity of only one colour channel (Fig. 3.100). Full sensor resolution is obtained, however exact alignment is required in order to avoid colour shifts. The camera delivers three separated analogue video signals that have to be digitised in parallel. The principle is used for professional colour cameras, most of which are used either in TV studios or by mobile film crews.

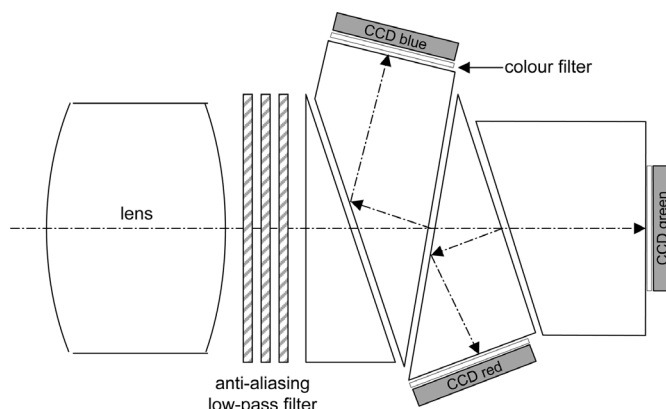


**Figure 3.100** Optical schematic of a 3-CCD or 3-chip camera

- Time-multiplex method

Colour separation is performed by sequential recording using a single sensor whereby for each image a fundamental (red, green or blue) colour filter is introduced into the optical system. Full sensor resolution is preserved, but dynamic scenes cannot be imaged. This method can be applied to both matrix sensor and scanning cameras. The camera delivers only one video signal which must be sampled temporally in order to generate a digital RGB combination from the single colour bands.

- Space-multiplex- or colour-mask methods

A filter mask is mounted in front of the CCD matrix sensor that makes individual sensor elements sensitive to only one fundamental colour. Strip or mosaic masks are used with the preferred pattern being the Bayer pattern mosaic mask shown below. In comparison to the above mentioned methods, geometric resolution will decrease since inputs from surrounding filtered sensor elements are sampled to compute the value of each colour pixel in the output image (Fig. 3.101). The principle allows for the recording of moving objects. Its cost effectiveness means that it is used for practically all amateur digital and video camera systems.

- True colour sensor

Foveon manufactures a CMOS-based high-resolution 1-chip true colour sensor consisting of three layers that are each sensitive to one fundamental colour. In this case the property of silicon that light of different wavelengths show different penetration depths is used.

Hence, this sensor provides the full resolution of a usual CMOS sensor with true-colour registration capability (Lyon and Hubel 2002).

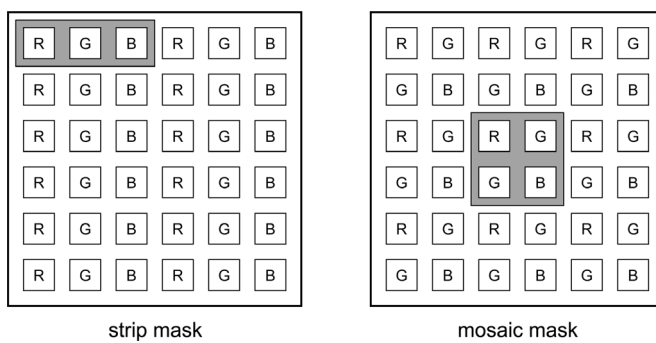


**Figure 3.101** Strip and mosaic masks

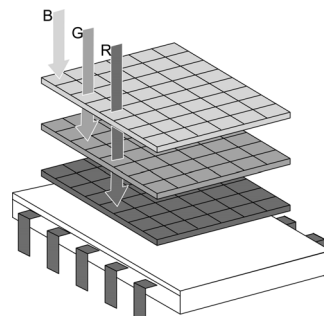


**Figure 3.102** Principle layout of the Foveon X3 RGB sensor

Digital colour cameras are increasingly applied in close-range photogrammetry since the widely used consumer cameras are equipped with colour sensors by default. Digital colour images are most important in those fields where realistic texture mapping is desired.

### 3.3.2.8 High-speed cameras

High-speed cameras provide the recording of fast dynamic scenes with image frequencies much higher than for standard video cameras. Today high-speed cameras exist that can record more than 1000 images per second at resolutions of the order of  $1500 \times 1000$  pixels. They are mainly used for the monitoring of dynamic production processes, but also for the analysis of moving objects in industry, medicine and research (Fig. 3.103).

In general these imaging systems can be characterised as follows:

- Progressive-scan CCD-sensor

Progressive-scan sensors have the ability to read out image data on a line by line basis. While removed from television standards, this method minimises image displacements due to subject movements which can occur during interline sampling (Fig. 3.75). This sensor type can also allow the number of lines in the output image to be reduced in order to increase image data rates.

- CMOS sensors

As an alternative to progressive-scan sensors CMOS imaging sensors are available that provide exposure times of a few microseconds due to an electronic shutter that is integrated

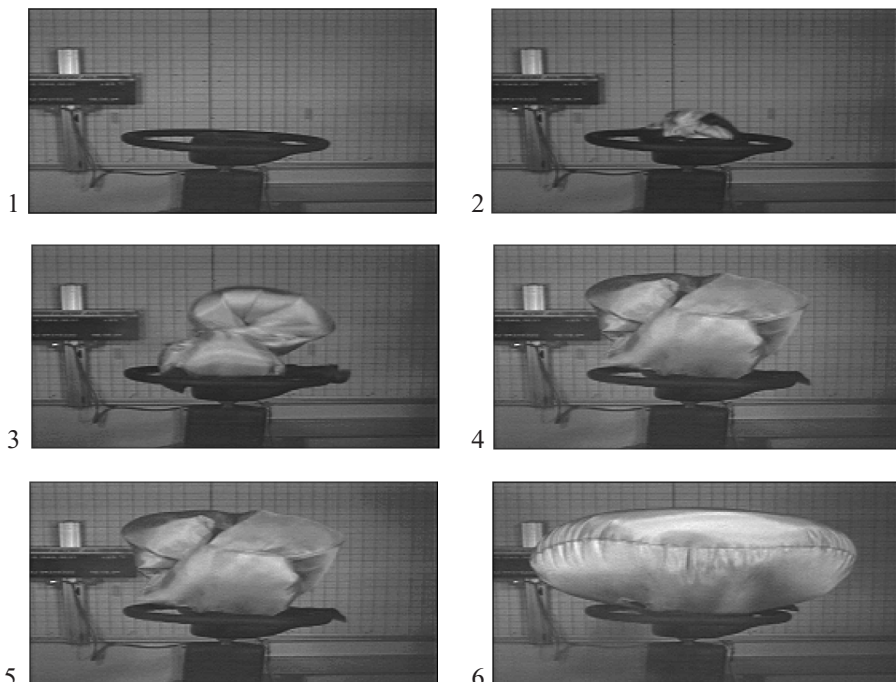


**Figure 3.103** Subset of an image sequence (Weinberger SpeedCam)

in the sensor. These sensors facilitate direct addressing of individual pixels, but have the disadvantage of increased image noise when compared to CCD sensors.

- Electronic shutter

Electronic shutters control the integration time of the imaging sensor with exposure times of  $50\text{ }\mu\text{s}$ .

- Solid-state image memory

Solid-state image memory modules are used for the immediate storing of the image sequence either in the camera or very close to the camera unit. The maximum number of images and the maximum recording period depend on the image memory capacity and the (selectable) sensor resolution.

- Analogue or digital image output

The image sequence stored in memory can be read out either as an analogue standard video signal, or as a digital image series.

- External trigger signals

External trigger signals allow the camera to be synchronised with an external event and serve to control the image acquisition process e.g. depending on a machine production cycle.

- Recording of additional information

Storing of additional information (image number, data rate etc.) allows for subsequent image sequence analysis.

- Onboard processing

CMOS sensors combined with specialised FPGA processors are able to process incoming images in real-time. Hence timely unlimited image sequences can be recorded (for an example see section 6.2.4).

High-speed cameras are offered by different suppliers. Representative among others, Fig. 3.103 shows a subset of an image sequence recorded by the Weinberger SpeedCam ( $256 \times 128$  pixel, 1000 images per second) camera. A number of current systems are able to record  $1500 \times 1000$  pixels at 1000 images per second and up to 100,000 images per second at reduced resolutions. Such cameras rely on local high speed memory buffers and gigabit Ethernet connections.

### 3.3.2.9 Future prospects

Digital imaging sensors are accepted in close-range photogrammetric practice and have replaced analogue photographic image recording in many fields. Recent state-of-the-art (2005) enables the routine manufacturing of imaging sensors of up to  $7000 \times 4000$  pixels, and special sensors with higher resolution (up to  $9000 \times 7000$  pixels) are in development or are already used in astronomy and medicine. The huge market of professional digital photography is leading to cost reductions mainly in the area of 6, 7 and 8 megapixel sensors. While these are excellent for many purposes, work is needed to determine the effect of their internal colour reconstruction algorithms on photogrammetric measurement accuracy. Imaging sensors of higher resolution can be expected to become available for industrial and technical applications, however at much lower production rates and therefore proportionately higher cost. CMOS cameras are replacing standard CCD technology for most mainstream applications due to their lower cost. However better image quality, inherent in the CCD design, can be expected to keep this type of

sensor as the choice for applications where image quality is of importance. So-called intelligent cameras consisting of an integrated processor used for internal image processing tasks are entering the market and allow control or measurement tasks to be carried out directly at image acquisition time within the camera.

Scanning cameras are currently only used for those applications where extremely high resolutions (in colour) are required at non-critical recording times and stationary objects e.g. for the digital archiving of paintings and the recording of historic sites and monuments.

The high accuracy potential of matrix sensors better than  $0.1 \mu\text{m}$  in image space demands for a more detailed model for interior orientation. Inhomogeneities of the sensor surface, minimal variations of optical distortion and unknown electronic processing steps have to be considered in future if the desired accuracy levels are to be achieved.

### 3.3.3 Laser-based measuring systems

Laser-based measuring systems are discussed here as photogrammetry and laser-scanning are competing increasingly in practice and more significantly offer real advantages when used in combination for a wide range of applications. In the broad sense both methods can be classified as optical measurement methods.

#### 3.3.3.1 3D laser-scanner

3D laser-scanning describes the three-dimensional measurement of the surface of an object through the analysis of the reflected light from a laser beam which is scanned over the object surface. Polar coordinates, with an origin at the scanning system are described by angle and range measurements. If the reflected intensity is also registered, an object image is recorded where each measured 3D point is associated with an intensity value, based upon the reflectance of the object surface at the wavelength of the laser light. In the first instance, laser-scanners were developed for airborne applications whereby a laser scan of the ground from an aircraft could be used to produce a digital terrain model. They are increasingly used in close-range applications, which range from the recording of building interiors to the measurement of complex structures.

Systems recently available on the market differ mainly in terms of physical principle, measuring frequency, measuring accuracy, range of operation, beam diameter and costs. So-called camera-view scanners observe a restricted sector of a semi-sphere, while 360° or panoramic scanners allow for an all-around measurement from one station. Overviews on current laser scanning technology and associated commercial products are given by Marshall (2004), Deumlich and Staiger (2002) and Runne *et al.* (2001).

Fig. 3.104 shows the schematic layout of a laser-scanner with two galvanometer deflection mirrors and phase-difference measurement of two modulated signals. Phase-difference measurement enables high measuring frequencies ( $> 2.5 \times 10^9$  points per second).

Most commercially available laser-scanners systems utilise range detection by time-of-flight measurement. Time-of-flight or pulse measurement is less sensitive with respect to object surface variations, thus it is generally preferred for general purpose surface measurements. Achievable measurement rates are about two orders of magnitude slower than for phase difference measurement. Figs. 3.105 to Fig. 3.107 show two typical instruments, Table 3.14 summarises their technical data.

If the registered data ( $X$ ,  $Y$ ,  $Z$ , Intensity) is stored in a matrix, two data sets can be derived: a range image where the value assigned to each pixel is proportional to the range of the object

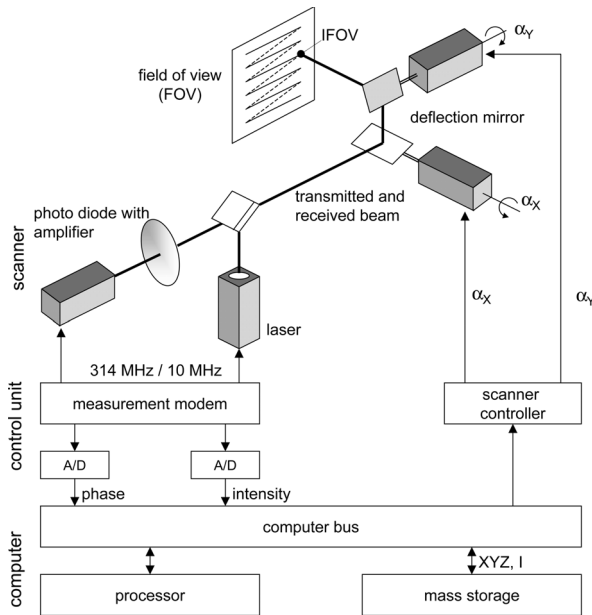


**Figure 3.104** Principle of laser-scanning (after Wehr 1998)



**Figure 3.105** Laser-scanner  
Zoller & Fröhlich Imager 5003



**Figure 3.106** Laser-scanner Leica  
CYRAX 2500



**Figure 3.107** Laser-scanner  
Riegl LMS Z360i

**Table 3.14** Examples of laser scanning systems with technical data drawn from company product information

	Zoller & Fröhlich Imager 5003	Riegl LMS Z360i	Leica CYRAX 2500
type of instrument	panoramic view	panoramic view	camera view
range detection	phase difference	time-of-flight	time-of-flight
laser			
wavelength	780 nm	near infrared	532 nm
power	23 mW (class 3R)	class 1	1 mW (class 3R)
beam diameter	3-4 mm at 10 m	7mm (0.25 mrad)	6 mm at 50 m
resolution	3.5 mm at 10 m	0.4 mm at 10 m	0.1 mm at 10 m
field of view			
distance	0.4 to 25.2 m	2 to 200 m	1.5 to 100 m
horizontally	360°	360°	40°
vertically	270°	90°	40°
max. data rate (points/s)	625,000	24,000	-277
accuracy			
range	±3 mm + 2 mm/m	±5 mm	±4 mm
angle	±0.01°	±0.01°	±3.4°
coordinates	±5 mm/25 m		±6 mm/50
weight	13 kg + 3 kg (socket)	13 kg	20.5 kg
specialties	registration of intensity values	registration of intensity values, integrated high-resolution camera	registration of intensity values, integrated video camera

surface from the scanner (Fig. 3.108a), and secondly an intensity image where the value assigned to each pixel is a function of the strength of the return signal from the surface of the object (Fig. 3.108b). The intensity image appears similar to a photographic image, however it only records reflection values for the wavelength of the implemented laser.

The most important capability of a general purpose laser-scanning system is the fast three-dimensional measurement of a (large) object surface with high point density. A typical range based scanning system is able to provide an accuracy of a 3D coordinate of the order of 3–10 mm for a 10 m distance. In addition to angle and range measurement the accuracy is also dependent on the stability of the instrument station (e.g. tripod).

Laser-scanners can be combined with a digital camera that observes a similar field of view (Fig. 3.107). If the digital image is calibrated and orientated with respect to the laser-scanner, image and range data can be processed simultaneously. In 3D mono-plotting mode (visual) point identification can be performed in the image while the corresponding 3D coordinates are interpolated from the 3D point cloud (Beraldin 2004, El-Hakim *et al.* 1988, Studnicka *et al.* 2003, Benning *et al.* 2004).

Since they produce point measurements based upon the reflection of a laser beam from a surface, 3D laser-scanners can record large numbers of points without any targeting requirement. In a similar manner to photogrammetry, laser-scanning is a line of sight process so complex objects have to be recorded from several instrument stations such that each individual point cloud can be transformed into a common coordinate system by means of identical points or surface matching procedures. In common with other area based scanning methods, a major

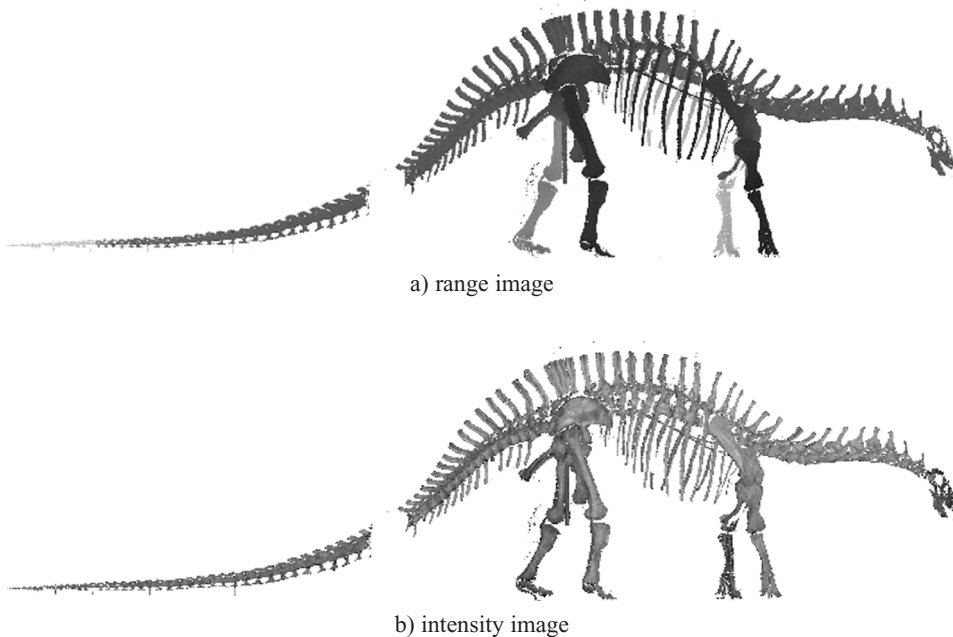


**Figure 3.108** 3D registration of a dinosaur skeleton by laser-scanning (after Wiedemann and Wehr 1998)

drawback is unstructured data acquisition (see section 6.5.1). Usually measured point clouds must be thinned out and structured either manually or with automatic numeric search procedures in order to prepare the data for further processing by an end user. Additionally acquired image data can also be useful for registration of point clouds taken from multiple stations (Wendt 2004).

### 3.3.3.2 Laser trackers

Laser trackers measure the 3D coordinates of a corner cube that is positioned so as to represent a single point in the object space. Range is determined by interferometry and angle is measured by state of the art angle encoders. Servo drives integrated into the systems facilitate continuous tracking of points. Laser trackers are predominantly used for the measurement of strategic points on large free-form manufactured objects, as large scale deflection gauges or to enable the dynamic registration of moving objects.

Laser trackers consist of high-precision angle encoders and interferometric range measurement opto-electronics to yield accuracies of better than 0.1 mm at object distances of the order 15–20 m for measured 3D coordinates. There are systems available with both relative and absolute range measurement. Since a laser beam can also be reflected by a reflector ball or a prism, these systems work with touch probe tools (Fig. 3.109).

Laser tracker vendors include Leica Geosystems, Faro and API. Fig. 3.110 and Fig. 3.111 show typical examples of these systems. Leica Geosystems offer the combination of a laser tracker with a photogrammetric camera system (Dold 2002). According to the manufacturer the technology enables not only the real-time measurement of a position (X, Y, Z) but also the orientation parameters (3 angles) of moving objects (6 DOF). As examples touch probes or a hand-held surface scanner can be combined with the laser tracker (Fig. 3.112).

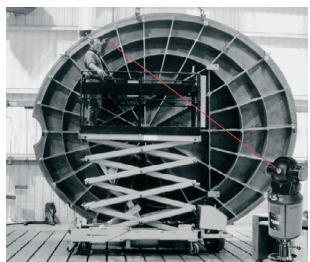


**Figure 3.109** Reflector ball  
(above) and object  
measurement (below)



**Figure 3.110** Laser tracker  
Leica LTD 800



**Figure 3.111** Laser tracker  
Faro



**Figure 3.112** Laser tracker Leica LT 800 combined with a digital camera (T-Cam) for measurement of position and orientation of a hand probe (T-Probe)

### 3.3.3.3 Laser radar

The laser-radar system Leica LR200 (Fig. 3.113) (now Metris) is similar in design to a laser tracker, but range measurement is performed by absolute phase measurement with continuously altered modulation frequency. The system operates without a reflector since a reflected signal of only ca.  $1 \times 10^{-12}$  of the transmitted signal power is required for range measurement. Hence nearly specular or polished surfaces can be measured. The angle of view for measurement of optically diffused surfaces can range up to  $85^\circ$  with respect to the surface normal. For the basic



**Figure 3.113** Laser radar system Leica LR200

instrument design, typical measurement accuracy is reported to be of the order of 0.1 mm at a distance of 10 m (Dold 2002).

### 3.3.4 Other imaging systems

#### 3.3.4.1 Video-theodolite

Video-theodolites are based on a conventional electronic theodolite with a digital video camera integrated into the optical path. While electronic angular read-out is used for acquiring horizontal and vertical directions, the video image can be digitised and processed to enable automatic target detection and point measurement. These instruments are similar in principle to the photo-theodolite (see Fig. 1.24).

Fig. 3.114 illustrates the design of the Leica TM 3000 V video-theodolite. The telescope image is projected onto a digital sensor by means of a beam splitter. The use of a beam splitter

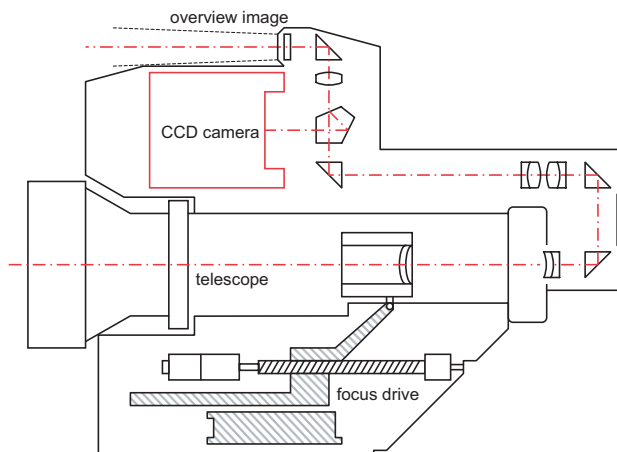


**Figure 3.114** Schematic diagram of the Leica TM 3000 V video-theodolite

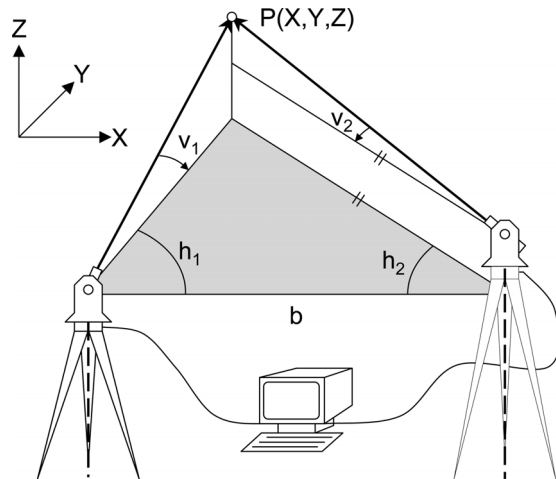


**Figure 3.115** Theodolite measuring system

means that a visual observation is still possible. An optical coupling device serves as the switching between a telescope image and a wide-angle overview image. Target coordinates are measured inside a digitised camera image. These measurements can be corrected for horizontal and vertical angles if a suitable camera calibration is available. Angular accuracies of about 0.15 mgon can be achieved if retro-reflective targets are used as signalised objects (see section 3.4.1.1).

If the video-theodolite is equipped with servo-motors for driving its vertical and horizontal axes and its focus as shown for the TM 3000 V, *a priori* known target points can be imaged and measured automatically. An integrated range finder allows for 3D measurements in polar mode with only one sensor. Alternatively, a system can be configured using a pair of video-theodolites. In such a case, three-dimensional object points can be determined by spatial intersection of measured angles (Fig. 3.115, Staiger 1992, Kyle 1993).

### 3.3.4.2 Cameras with position finders

For the registration of complex objects, for example large industrial plants, engineering objects or 3D city models, it might be useful to compute approximate on-site information on the exterior orientation of any images used for analysis. One principle possibility is the combination of a camera with an absolute position finder e.g. an inertial or GPS system<sup>1</sup>.

GPS-based position finding requires signals to be received from at least four GPS satellites that must be arranged in a suitable geometric constellation. Thus the method can only be applied in outdoor environments. The current generation of GPS receivers are able to deliver a position accuracy of 10–100 m, whilst more sophisticated solutions based on DGPS (Differential GPS) provide accuracies in the cm-range. Fig. 3.116 shows the example of an analogue camera equipped with a GPS receiver and a compass for azimuth measurement. In such a case, coordinate information can be superimposed onto the image, but fully digital solutions can easily be realized.

<sup>1</sup> Refer to specialised literature for further information about GPS and inertial systems e.g. Schlemmer (1996).



Figure 3.116 Cameras with GPS receiver

Inertial systems or units (INS, INU) measure the current position by a continuous integration of accelerations that occur due to the movement of the imaging system from an initial known position. Inertial systems are complex devices that are relatively sensitive to mechanical shocks. Field-proven camera and inertial system combinations are at the research and development stage for close-range applications. In the field of mobile mapping, digital camera or video systems are already combined with GPS and INS (Kahmen *et al.* 2002, see section 8.1.1.2).

## 3.4 Targeting and illumination

### 3.4.1 Object targeting

In many applications, locations to be measured on an object need to be signalled with artificial targets, for example:

- natural object points that cannot be identified sufficiently,
- providing uniquely defined points for comparable measurements,
- geodetic measurement of control points,
- automatic point identification and measurement,
- accuracy improvement.

The physical size and type of target to be used depends on the chosen imaging configuration (camera stations and viewing directions, image scale, resolution) and illumination (light source, lighting direction).

#### 3.4.1.1 Circular targets

Due to their radial-symmetric design, circular targets are well suited for photogrammetric use with the centre of the target representing the actual 3D point to be measured. Determination of the target centre is rotation-invariant and, over a wide range of image magnifications, also scale-invariant. Circular targets are useful not only for manual, interactive measurements, but also for automated digital point detection and measurement.

For analogue images the centre of circular targets can be determined by centering a symmetrical circular- or point-shaped floating mark. For digital imagery the target centre can be calculated by centroid methods, correlation with a reference pattern, or by analytical determination of circle or ellipse centre (see section 5.4.2).

*Retro-reflective targets*

Retro-reflective targets (retro-targets) are widely used in practice, particularly in industrial applications. They consist of a retro-reflective material that is either covered by a black surround (mask) according to the target pattern, or is stamped in an equivalent form from the raw material. The retro-reflective material consists either of a dense arrangement of small reflective balls ( $\varnothing \approx 80 \mu\text{m}$ ), or an array of microprisms (Clarke 1994). Usually retro-targets are circular in shape, however they can be manufactured in any size and shape (examples in Fig. 3.117). In order to achieve high contrast target images retro-reflective targets must be illuminated from the viewing direction of the camera (e.g. by a ring flash, see Fig. 3.128).

The microscopic balls or prisms of a retro-target are attached to a supporting material. Incident light is reflected internally within each ball to return parallel to its incident path. Optionally the material may have a plastic coat to allow the surface to function under wet conditions, but at the expense of reduced light return. For masked targets balls can partly be occluded at the edge of the target, so that the desired centre is optically dislocated laterally. The shift depends on the viewing direction and gives rise to a 3D target location which is above the physical centre of the target if a triangulation method is applied (Fig. 3.118). The opposite effect occurs for stamped targets leading to a triangulated 3D point below physical target level. Both effects can result in a shift of about 50  $\mu\text{m}$  and should be corrected by the point determination software (Dold 1997).

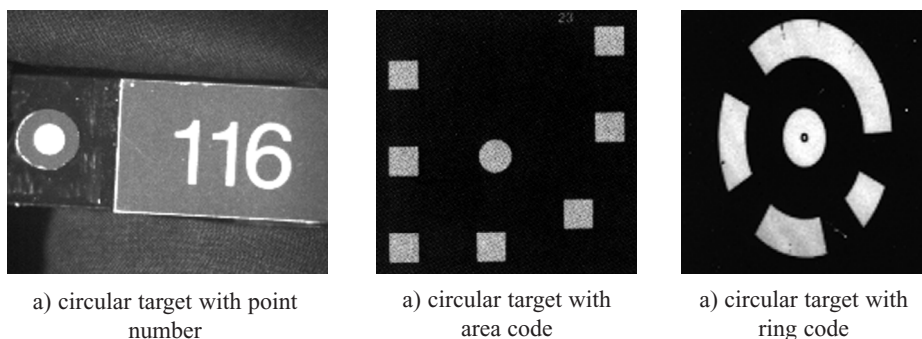


**Figure 3.117** Examples of retro-reflective targets

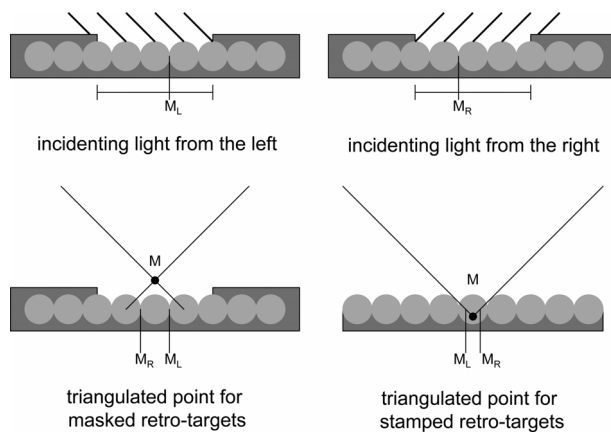


**Figure 3.118** Position of virtual centre retro-targets (after Dold 1997)

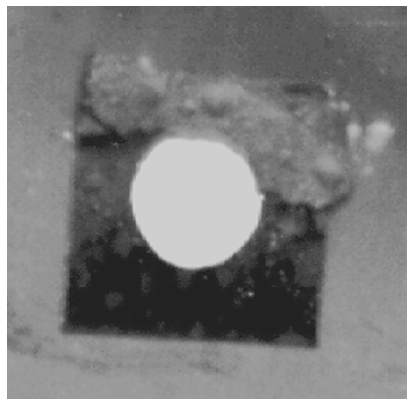


Figure 3.119 Degraded retro-target

Retro-reflective target materials are sensitive to surface dirt (dust, oil) and mechanical stress (abrasion). In both cases reflectivity is affected as well as the point contour so that a degradation in 3D measurement quality will result. Fig. 3.119 shows an example of a degraded retro-target. In such cases the plastic coated versions may be more appropriate, since the ability to wipe those clean can more than offset their reduced light output and viewing angle.

Further drawbacks of retro-targets include:

- relatively high costs per target, particularly for large or coded targets (section 3.4.1.2), due to the manufacturing process
- limitations in target dimensions and therefore target density which can be adhered to the object surface
- self-adhesive targets can generally only be used once, requiring a new set of targets for each object to be measured.

#### *Other targets*

The above-mentioned drawbacks of retro-reflective targets require alternative materials or targeting techniques for a number of applications.

Circular plastic targets with a centric target point are suitable for a long-term targeting of outdoor objects (e.g. buildings, bridges) that are also useful for geodetic measurements. They can be produced in almost any size. Self-adhesive paper marks can be used for temporary targeting of tie points where no long-term reproducibility is required. In this way arbitrary patterns and additional information can be provided at minimal cost. Since paper prints are not retro-reflective, image contrast and target detectability strongly depend on the acquisition of high quality photography and the abilities of the feature extraction algorithm selected for subsequent processing.

Luminous targets are more complex. They are used in those applications where no artificial illumination is possible or where a recording or measurement process is controlled by switching illuminated targets on or off. Luminous targets can be equipped with a LED (light emitting diode) that is mounted behind a semi-transparent plastic cover. These targets provide optimal contrast and sharp edges (Fig. 3.120). As examples, LEDs are applied for manual probes in on-line measuring systems (e.g. Petterson 1992, Fig. 3.124) or for motography (see section 7.3.2.2).

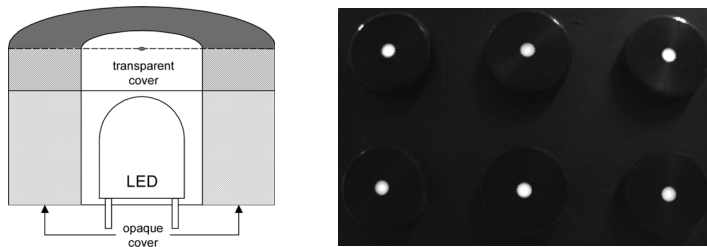


Figure 3.120 Possible construction of a luminous target

#### *Target diameter and eccentricity of the centre*

In order for accurate measurements to be made, the diameter of the circular target images needs to be suited to the target detection and measurement process to be used. For analogue measurement systems diameters of the order of 100–150% of the floating mark diameter are appropriate. For digital processing systems it is generally accepted that target images should be at least 5 pixels in diameter. Besides practical side conditions (e.g. maximum permitted size for pasting an object) the maximum usable target diameter is also a function of the maximum allowed eccentricity between the true position of the projected circle centre and the centre of the imaged elliptical target.

According to Fig. 3.121 a central-perspective projection of a circular target yields an elliptical shape in the image. Usually the centre of the target is determined by the centre of the image ellipse (see section 5.4.2). Strictly speaking there is an eccentricity  $e$  between the calculated ellipse centre and the actual target centre to be determined. The degree of eccentricity depends on the size of the target, viewing direction, lateral offset to the optical axis and image scale. It can be estimated as follows:

$$e = r_m - \frac{c}{2} \left( \frac{\frac{R_m + \frac{d}{2} \sin(90 - \alpha)}{Z_m - \frac{d}{2} \cos(90 - \alpha)}}{\frac{R_m - \frac{d}{2} \sin(90 - \alpha)}{Z_m + \frac{d}{2} \cos(90 - \alpha)}} + \right) \quad (3.70)$$

where  $e$ : eccentricity of projection

$d$ : target diameter in object space

$r_m$ : image radius of projected target

$\alpha$ : viewing direction = angle between image plane and target plane

$R_m$ : lateral offset of target to optical axis

$Z_m$ : object distance to target

$c$ : principal distance

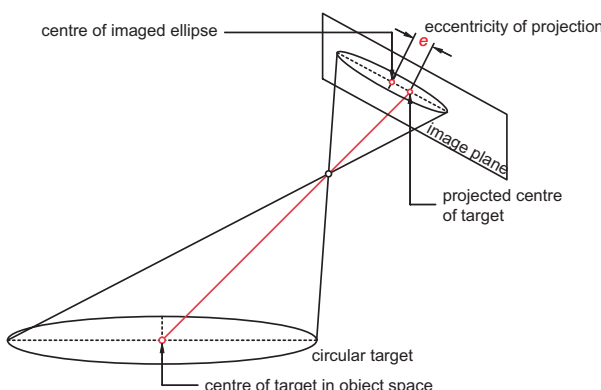


Figure 3.121 Eccentricity of a projected circular target (after Dold 1997)

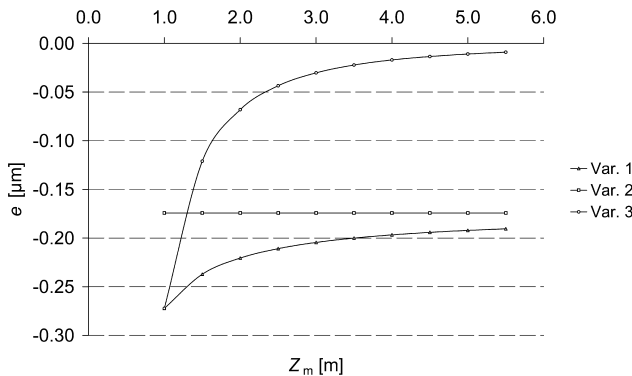


Figure 3.122 Eccentricity of projection vs object distance

where  $r_m = 35$  mm (medium format)

$c = 40$  mm (wide angle)

$\alpha = 60^\circ$  (maximum effect)

- var.1: variable target diameter in object space with  $d' = d / m = 170\text{--}200 \mu\text{m}$  (17–20 pixels at 10  $\mu\text{m}$ )
- var.2: variable target diameter in object space = constant target diameter in image space with  $d' = 160 \mu\text{m}$  (16 pixel)
- var. 3: constant target diameter in object space = variable target diameter in image space with  $d' = 36\text{--}200 \mu\text{m}$  (4–20 pixel)

### Example 3.8:

Fig. 3.122 shows the result of eccentricity in three variants. In the example, when a medium-format camera (image radius  $r_m = 35$  mm) with a wide-angle lens ( $c = 40$  mm) is used object distances to the target vary between 1 m and 6 m. The angle between image plane and target plane amounts to  $60^\circ$ , giving maximum eccentricity. The three variants differ with respect to the selected target diameter.

For the first variant targets are used where their physical diameter is increased in proportion to their distance from the camera (object distance) to yield image diameters between 170  $\mu\text{m}$  and 200  $\mu\text{m}$ . For a pixel size of 10  $\mu\text{m}$  this is equivalent to ca. 17–20 pixel diameter. The maximum resulting eccentricity is 0.27  $\mu\text{m}$ , decreasing with increasing object distance.

For variant 2 the target image diameter remains constant at 160  $\mu\text{m}$ , independent of the object distance. The resulting eccentricity is constant at 0.17  $\mu\text{m}$ .

For variant 3, equal target sizes ( $d = 5$  mm) are used for all object distances resulting in target image diameters between 36  $\mu\text{m}$  and 200  $\mu\text{m}$  (4–20 pixel). The maximum resulting eccentricity is 0.27  $\mu\text{m}$ .

As a matter of fact, small targets and large object distance yield negligible eccentricities (less than 0.5  $\mu\text{m}$ ). For larger image scales, large image formats (e.g. aerial film), large viewing angles and high accuracy specifications, eccentricity becomes significant and must be corrected (Ahn *et al.* 1997, Dold 1997).

The effect of eccentricity is extremely complex for the multi-photo convergent image configurations that characterise most high accuracy photogrammetric measurements. It is assumed that the effect is compensated by the parameters of interior and exterior orientation if

they are estimated using self-calibration techniques. For high-precision applications ( $<0.5\text{ }\mu\text{m}$  in image space) it is recommended that small targets are used, however the targets, or level of ring flash illumination for retro-targets, must be capable of providing target image diameters of the order of 5–10 pixels in image space if suitable measuring accuracies are to be achieved.

Eccentricity does not matter if the target centre is calculated as the centre of a circle in 3D space as it can be solved by the edge algorithm (section 4.4.3.2) or bundle adjustment with geometric 3D elements (Kager 1981, section 4.5.6).

### 3.4.1.2 Coded targets

Targets, encoded with individual point identification numbers can be used to automate point identification. The point codes are arranged in lines, rings or regions around the central target point (Fig. 3.117b and c, Fig. 3.123). Codes with more than several hundred point identification numbers can be designed (Niederöst and Maas 1996, Schneider 1996, Ahn and Schultes 1997, Shortis *et al.* 2003).

Coded targets should meet the following requirements:

- invariance with respect to position, rotation and size
- invariance with respect to perspective or affine distortion
- robust decoding with error detection (even with partial occlusions)
- precise defined and identifiable centre
- sufficient number of different point identification numbers
- perceptibility of the point pattern in arbitrary orientated images
- fast processing times for pattern recognition
- minimum pattern size
- low production costs

The point identification number is decoded by image analysis of the number and configuration of code patterns. The pattern displayed in Fig. 3.123 (upper row) is based on barcode-techniques where the code can be reconstructed from a series of black and white marks (bit series). The number of coded characters is limited by the number of bits of the barcode. The patterns

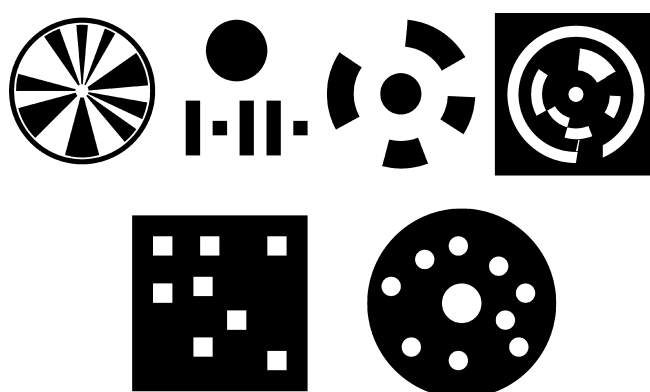


**Figure 3.123** Selection of coded targets.  
Upper row: barcode patterns; lower row: coordinate patterns

displayed in Fig. 3.123 (lower row) consist of additional points arranged in a local coordinate system where the target identification number is a function of the local distribution of points. For decoding, the planar area pattern is transformed to the nominal reference coordinate system of the pattern i.e. the local position of each point yields its encoded point number.

Alphanumeric point numbers can be detected by means of optical character recognition. However, the computational effort is higher, and the reliability is lower due to the sensitivity of the technique to localised image quality (Caesar and Michaelis 1997).

### 3.4.1.3 Eccentric targeting

Eccentric targeting tools, suitable for hidden object areas that cannot be observed by a camera, are also available. With reference to Fig. 3.124 the actual (eccentric) point to measure  $P$  will be determined indirectly by the 3D coordinates of a number of auxiliary points  $Q_i$  that are fixed in a local configuration. These points can either be arranged in linear form (2–3 points) or spatially ( $\geq 3$  points) with given 3D reference coordinates in a local coordinate system. The points  $Q$  can be either retro-reflective targets (passive targeting), or luminous LEDs (active targets). Manually guided hand probes are used in many areas of industrial measurement and must be observed by at least two cameras simultaneously, with a new image pair being taken for each point measured with the probe. Such a system is often termed an on-line system.

In order to measure drilling holes or work piece edges, specially designed mechanical adapters are used to provide a fixed relationship between a number of measurable targets and the actual point or edge to be measured. In this case, production accuracy of the adapter has a direct affect on the resulting accuracy of the indirectly measured object point.

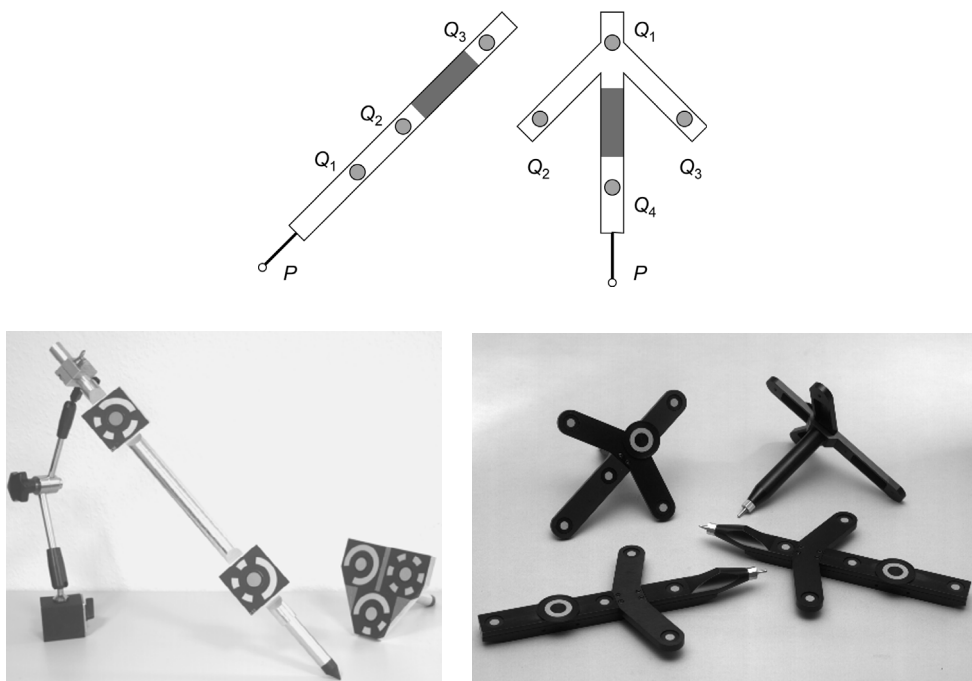


**Figure 3.124** Principle of eccentric probing and examples of tools

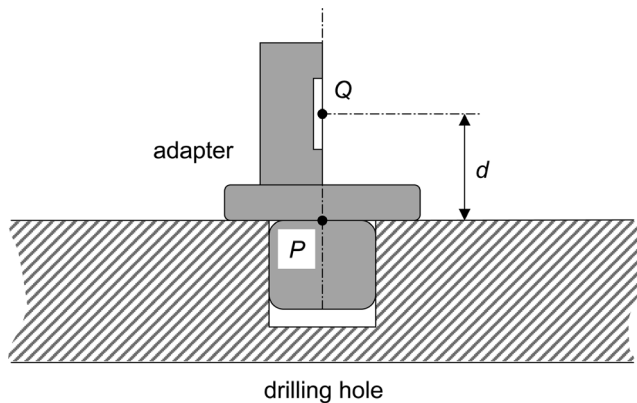


**Figure 3.125** Principle of a drilling hole adapter

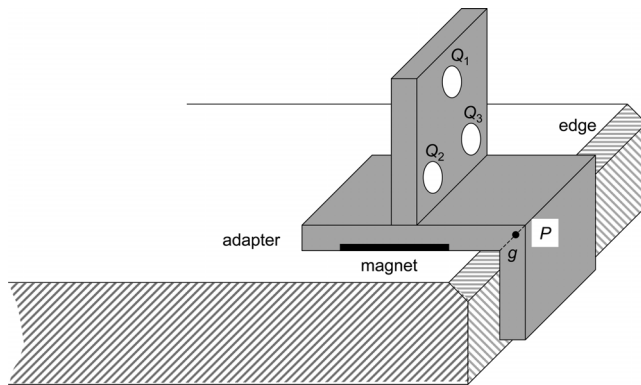


**Figure 3.126** Principle of an edge adapter

Fig. 3.125 shows the principle of an adapter for indirect measurement of the position of drilling holes. The optically measurable target is mounted such that the measured point  $Q$  is located in the drilling axis with a known distance (offset)  $d$  to the desired drilling hole point  $P$ .

The edge adapter displayed in Fig. 3.126 consists of three target points  $Q_i$ , whose local relation to the inner straight line  $g$  resp. an edge point  $P$  is known. Such adapters can be equipped with magnets for rapid mounting on metallic surfaces. If one or several auxiliary points  $Q$  are formed by coded targets, the photogrammetric system can identify the adapter type, hence the virtual point  $P$  can be calculated automatically. However, multiple-point adapters with coded targets require significantly more visible space, thus adapter size increases.

### 3.4.2 Illumination techniques

#### 3.4.2.1 Electronic flash

Electronic flash systems can be attached and synchronised to almost all modern photographic and many digital camera systems. While the electronic flash output may occur in 1/70,000 s or less, the camera shutter is usually synchronised to the flash unit at shutter speeds of up to 1/30 s to 1/250 s. Electronic flash performance is characterised by the guide number  $Z$ . Guide number describes the ability of the flash to enable a sufficient object illumination for a given object

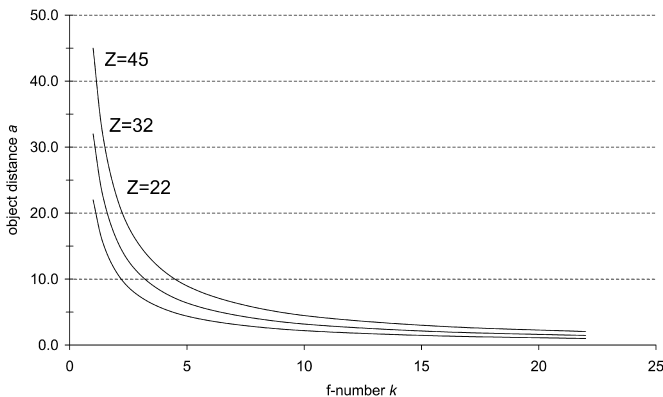


Figure 3.127 Usable object distances for different guide numbers and f-numbers

distance  $a$  in metres and a given f-number  $k$  (Fig. 3.127). Higher guide numbers indicate greater light output (Marchesi 1985).

$$a = \frac{Z}{k} \quad (3.71)$$

Ring-flashes consisting of a lens-concentric electronic flash tube are of special importance for photogrammetry (see Fig. 3.128). They are used for illuminating objects marked with retro-reflective targets. Their light output, concentric and close to the lens axis direction, ensures optimal retro-reflective target image contrast. It is important to note that electronic flash units with automatic exposure options utilise light measurement systems that are calibrated for general purpose photography. Correctly illuminated retro targets do not require as much light output and it is generally necessary to use manual controls in order to obtain consistent image quality. When illumination is controlled effectively, it is possible to adjust the exposure parameters such that only reflecting target images appear in the final image (example in Fig. 7.8). Such a situation is ideal for rapid automated target detection and measurement.

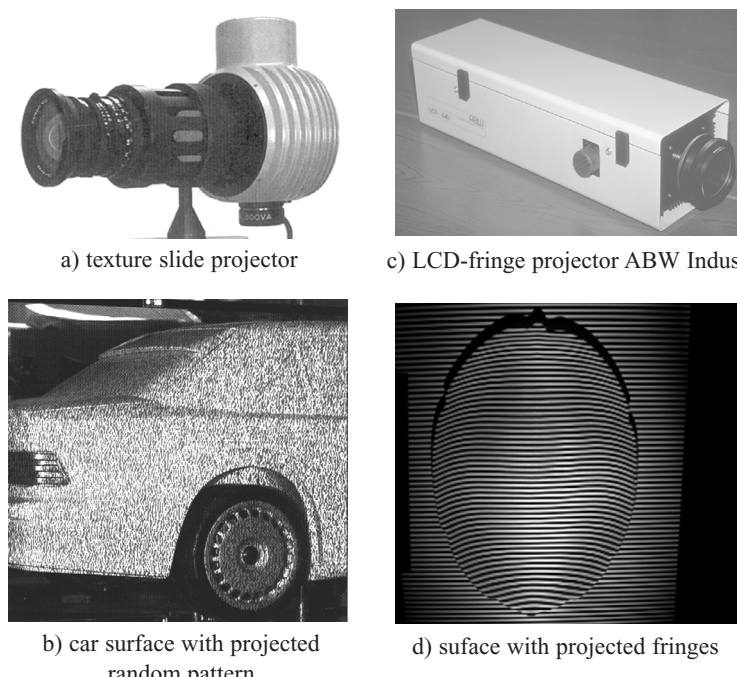


Figure 3.128 Semi-metric camera Rollei 6008 with ring-flash and roll unit

### 3.4.2.2 Projectors

Arbitrary light patterns can be projected onto object surfaces by means of slide projectors or computer-controlled LCD projectors (liquid crystal display). These devices are typically used if the object does not provide sufficient natural texture, or if the projected image is designed so as to form part of the surface reconstruction algorithm. Fig. 3.129 shows examples of projectors used for industrial photogrammetry.

LCD fringe projectors have increased in importance since they are suited to the projection of line patterns for subsequent surface measurement by structured light methods (see section 6.5.1). A reflector-condenser optical system illuminates a CCD array where the programmed line pattern is projected through a lens onto the object surface (Fig. 3.130). LCD-based video projectors or beamers are used to project video and computer images with arbitrary patterns and in colour. Current projectors have resolutions of up to  $1280 \times 1280$  lines (Wolf 1999).



**Figure 3.129** Projection of artificial surface structures

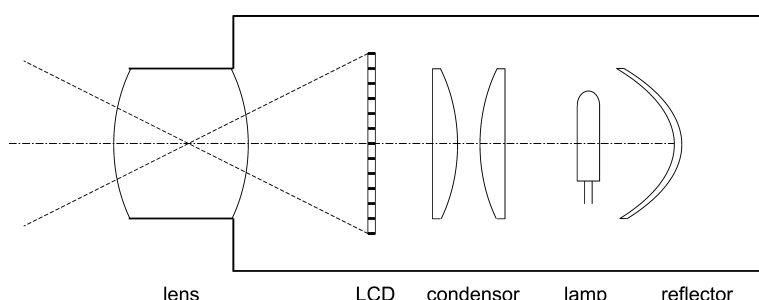


**Figure 3.130** Design principle of a LCD-fringe projector

Higher light output and image contrast can be achieved with micro-mirror chips (Digital Mirror Device, DMD). Movable micro-mirrors of about  $16 \mu\text{m}$  size are attached to a semiconductor. They can be controlled digitally in order to reflect or absorb incident light. Micro-mirror chips are available with  $1280 \times 1024$  points or more and circuit times of 20 ms. They can be applied as projectors, and as monitors as well.

If a projector is calibrated and orientated it can be treated as a camera in the photogrammetric process. In such a situation, the position of a projector point within the slide or LCD/DMD plane is analogous to an image coordinate measurement and the collinearity equations can be used to compute its direction. This approach is used for LCD/DMD projectors integrated into structured light systems for optical 3D metrology (Strutz 1993, Michaelis 1997).

### 3.4.2.3 Laser

Laser projectors can be used for structuring an object surface e.g. with point or line-shaped patterns. In contrast to other light sources, high illumination powers can be achieved even for eye safe laser classes (up to Class 2).

Laser projectors can be classified into three groups:

- Point projection

A single laser point is projected onto the object, for example with a laser pointer. The resulting point pattern is not a perfect circle. Deviations between projecting axis and surface normal give rise to an elliptical structure. Interference, caused by speckle effects, generates an inhomogeneous intensity distribution within the laser point area that is view dependent, so that the optical centroid does not correlate with the geometric centre (Fig. 3.131). For these reasons laser point projection is seldom used for photogrammetric applications.

- 1D line projection

Laser lines can be projected by means of a cylindrical lens mounted in front of the laser source (Fig. 3.134). Projected lines are used for triangulation with line section methods.

- 2D laser patterns can be created by special front lenses or diffraction gratings mounted in front of the laser source (Fig. 3.133).

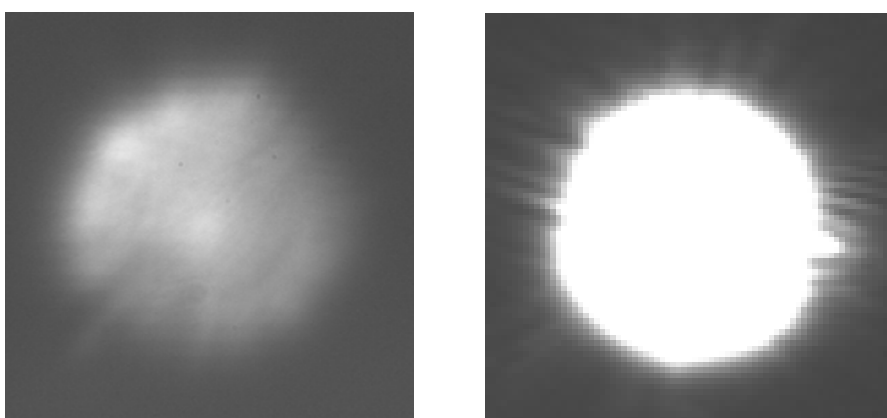


**Figure 3.131** Magnified image of laser points

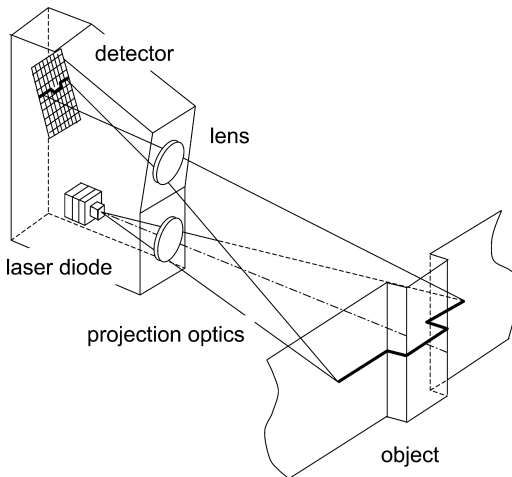


**Figure 3.132** Principle of light-section method (after Schwarte 1997)

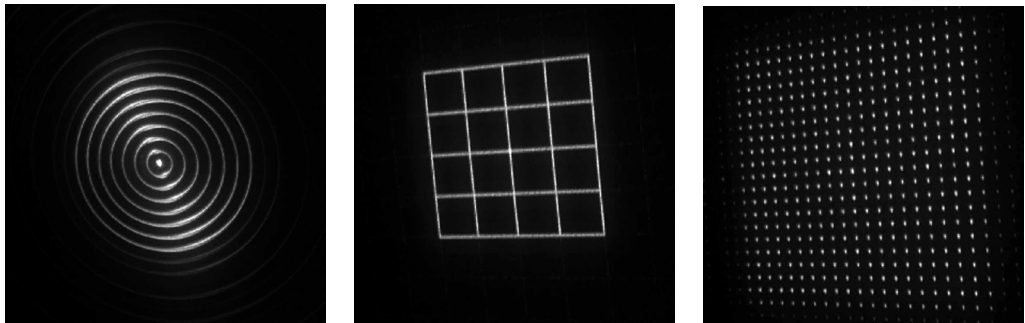


**Figure 3.133** Laser projection of two-dimensional patterns by front lenses

Arbitrary patterns can be generated by fast 2D laser scanners. A laser beam is projected over two movable galvanometer mirrors that are rotating with high frequencies (up to 15 MHz) (principle in Fig. 3.104 without range detection). If the projection frequency is higher than the integration time of the camera (or the human eye), a continuous two-dimensional pattern is visible in the image.

#### 3.4.2.4 Direct lighting

Direct lighting techniques are of major importance since the measurement of particular object areas, for example edges, can be enhanced by the controlled generation of shadows. This is applicable e.g. in the illumination of object edges that are to be measured by image edge detection without any further targeting (see section 4.4.3.2). Under such situations the physical object edge and the optical image edge must be identical.

Depending on the relative position of object surface and camera, direct lighting must be chosen such that the (upper) adjacent surface of the object edge is reflecting light into the viewing direction of the camera, while the other (collateral) surface is shadowed, or light is not reflected into the camera (Fig. 3.134). Contrast characteristics and image edge structure depend on the reflection properties of the two surfaces, and on the physical object edge shape. For example a right angle edge can be expected to give better results than a curved or bevelled edge.

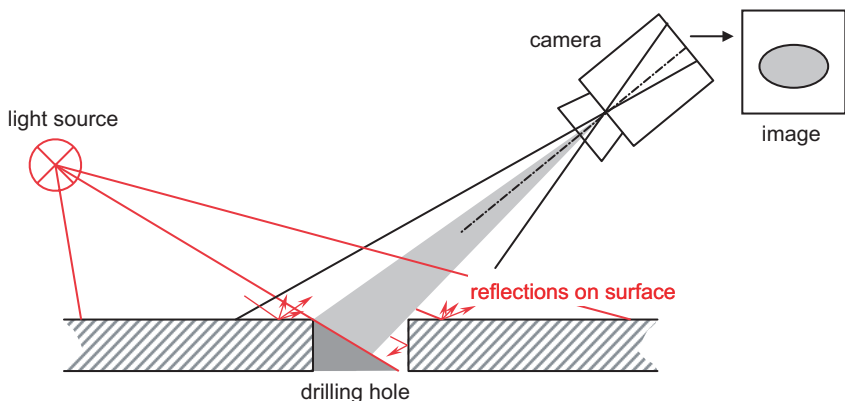
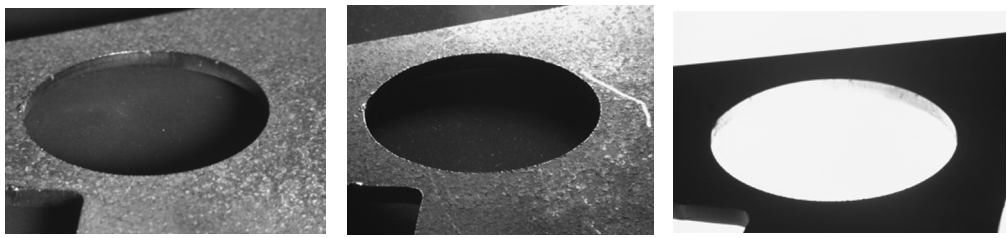


**Figure 3.134** Directed lighting for edge measurement



a) directory from the camera

b) according to Fig 3.134

c) diffuse from below

**Figure 3.135** Illumination of a metal workpiece drilling hole

Fig. 3.135 shows the influence of different illumination types for the projection of object edges on a metal workpiece. Illumination from the viewing direction of the camera (a) yields an insufficient image of the edge. If light is incident from the opposite direction (b), the edge of the drilling hole is correctly located in the object surface. With the geometry given in this figure, a diffuse illumination source located below the drilling hole (c) will also yield an appropriate edge image.

## References

- Ahn, S. J. and Kotowski, R. (1997) Geometric Image Measurement Errors of Circular Object Targets. In Gruen/Kahmen (ed.) *Optical 3-D Measurement Techniques IV*, Wichmann, Heidelberg, pp. 463–471.
- Ahn, S. J. and Schultes, M. (1997) A new circular coded target for the automation of photogrammetric 3-D surface measurements. In Gruen/Kahmen (ed.) *Optical 3-D Measurement Techniques IV*. Wichmann Verlag, Heidelberg, pp. 225–234.
- Arnold, C. R., Rolls, P. J. and Stewart, J. C. J. (1971) *Applied Photography*, Focal Press, London, p. 510.
- Atkinson, K. B. (1989) Instrumentation for non-topographic photogrammetry. In Karara (ed.) *Non-Topographic Photogrammetry*. 2nd Edition, American Society for Photogrammetry and Remote Sensing, pp. 15–35.
- Bähr, H.-P. (1992) Appropriate pixel size for orthophotography. *International Archives of Photogrammetry and Remote Sensing*, **29**(1), Washington.

- Beralidin, J.-A. (2004) Integration of Laser Scanning and Close-Range Photogrammetry – The Last Decade and Beyond. XXth Congress. International Society for Photogrammetry and Remote Sensing. Istanbul, Turkey, July 12–23, 2004. Commission VII, pp. 972–983.
- Benning, W., Becker, R. and Effkemann, C. (2004) Extraktion von Ecken, Kanten und Profilen aus Laserscannerdaten, gestützt durch photogrammetrische Aufnahmen. In Luhmann (ed.) *Photogrammetrie-Laserscanning-Optische 3D-Messtechnik*, Oldenburger 3D-Tage 2004, Wichmann, Heidelberg, pp. 213–220.
- Beyer, H. (1998) *Next generation metrology cameras and machine control*. ISPRS Commission V Symposium, Hakodate, Japan.
- Beyer, H. (1992) *Geometric and radiometric analysis of a CCD-camera based photogrammetric close-range system*. Mitteilungen Nr. 51, Institut für Geodäsie und Photogrammetrie, ETH Zürich.
- Born, M., Wolf, E. and Bhatia, A. B. (1999) *Principles of Optics*. Cambridge University Press, p. 986.
- Boyle, W. S. and Smith, G. E. (1970) Charge coupled semiconductor devices. *Bell Systems Technical Journal*, **49** pp. 587–593.
- Brown, D. C. (1971) Close-range camera calibration. *Photogrammetric Engineering*, **37**(8), pp. 855–866.
- Brown, D. C. (1976) The bundle adjustment – progress and perspectives. *International Archives of Photogrammetry*, **21**(3), ISP Congress, Helsinki, pp. 1–33.
- Brown, J. and Dold, J. (1995) V-STARS – A system for digital industrial photogrammetry. In Gruen/Kahmen (ed.) *Optical 3-D Measurement Techniques III*. Wichmann Verlag, Heidelberg, pp. 12–21.
- Caesar, T. and Michaelis, M. (1997) *Ein neues Verfahren zur robusten Erkennung textcodierter Marken*. Zeitschrift für Photogrammetrie und Fernerkundung, Heft 5-6/1997, pp. 150–157.
- Chapman, D. and Deacon, A. (1997) The role of spatially indexed image archives for “As-Built” modelling of large process plant facilities. In Gruen/Kahmen (ed.) *Optical 3-D Measurement Techniques IV*. Wichmann Verlag, Heidelberg; pp. 475–482.
- Clarke, T. A. (1994) *An analysis of the properties of targets used in digital close range photogrammetric measurement*, Videometrics III. SPIE Vol. 2350. Boston. pp. 251–262.
- Dähler, J. (1987) *Problems in digital image acquisition with CCD cameras*. Fast Processing of Photogrammetric Data, Interlaken, pp. 48–59.
- Deumlich, F. and Staiger, R. (2002) *Instrumentenkunde der Vermessungstechnik*. 9. Auflage, Wichmann Verlag, Heidelberg.
- Dold, J. (1997) *Ein hybrides photogrammetrisches Industriemeßsystem höchster Genauigkeit und seine Überprüfung*. Dissertation, Heft 54, Schriftenreihe Studiengang Vermessungswesen, Universität der Bundeswehr, München.
- Dold, J. (2002) *3D non-contact metrology for antenna manufacturing and testing*. Proceedings 25th ESA Antenna Workshop on Satellite Antenna Technology, ESTEC, Nordwijk, Niederlande.
- El-Hakim, S. F., Brenner, C. and Roth, G. (1998) A Multi-Sensor Approach to Creating Accurate Virtual Environments, ISPRS Journal of Photogrammetry and Remote Sensing, **53**(6), 379–391.
- Fraser, C. S. (1996a) Network design. In Atkinson (ed.) *Close Range Photogrammetry and Machine Vision*. Whittles Publishing, Caithness, UK, pp. 256–281.
- Fraser, C. S. and Brown, D. C. (1986) Industrial Photogrammetry – New Developments and Recent Applications. *The Photogrammetric Record*, **12**(68).
- Fraser, C. S. and Shortis, M. (1992) Variation of distortion within the photographic field. *Photogrammetric Engineering and Remote Sensing*, **58**(6), pp. 851–855.
- Fryer, J. G. (1996) Camera calibration. In Atkinson (ed.) *Close Range Photogrammetry and Machine Vision*. Whittles Publishing, Caithness, UK, pp. 156–179.
- Fryer, J. G. and Brown, D. C. (1986) Lens distortion for close-range photogrammetry. *Photogrammetric Engineering & Remote Sensing*, **52**(1), pp. 51–58.
- Godding, R. and Woytowicz, D. (1995) A new digital high-resolution recording system. ISPRS Intercommission Workshop *From Pixels to Sequences*, Zürich, pp. 31–35.
- Goldschmidt, R. and Peipe, J. (1994) Investigation of a HDTV Camera for Photogrammetric Application. *Int. Archives of Photogrammetry and Remote Sensing*, **30**(1), pp. 122–124.

- Hartley, R. and Zisserman, A. (2000) *Multiple View Geometry*. Cambridge University Press, Cambridge, UK.
- Hauschild, R. (1999) *Integrierte CMOS-Kamerasysteme für die zweidimensionale Bildsensorik*. Dissertation, Universität Duisburg.
- Hecht, E. (2003) *Optics*. Addison Wesley.
- Holst, G. C. (1996) *CCD arrays, cameras and displays*. SPIE Press, JCD Publishing, USA.
- Inglis, A. F. and Luther, A. C. (1996) *Video engineering*. 2nd ed., McGraw-Hill, New York.
- ISO (1974). *Speed of sensitised photographic emulsions*. International Standards Organisation, 6.
- Jacobsen, K. (1982) Selection of additional parameters by program. ISPRS Comm. III, Helsinki, *Int. Archives of Photogrammetry and Remote Sensing*, **24-3**, pp. 266–275.
- Jacobson, K. I. and Jacobson, R. E. (1980) *Developing*. 18th Edition, Focal Press, New York, p. 422.
- Jacobson, R. E., Ray, S. F., Attridge, G. G. and Axford, N. B. (1983) *The Manual of Photography*. 7th Edition, Focal Press, London, p. 628.
- Jantos, R., Luhmann, T., Peipe, J. and Schneider, C.-T. (2002) *Photogrammetric performance evaluation of the Kodak DCS Pro Back*. ISPRS Symposium Comm. V, Korfu.
- Kager, H. (1981) *Bündeltriangulation mit indirekt beobachteten Kreiszentren*. Geowissenschaftliche Mitteilungen der Studienrichtung Vermessungswesen der TU Wien, Heft 19, pp. 37.
- Kahmen, H., Niemeier, W. and Retscher, G. (ed.) (2002) *Geodesy for Geotechnical and Structural Engineering II*. Institut für Geodäsie und Geophysik, Technische Universität Wien, ISBN 3-9501492-1-X.
- Kludas, T. (1995) *Three-dimensional surface reconstruction with the Zeiss photogrammetric industrial measurement system InduSURF Digital* (in German). Publikationen der DGPF, Band 3, Dresden 1994, pp. 127–133.
- Konecny, G. and Lehmann, G. (1984) *Photogrammetrie*. Verlag Walter de Gruyter, Berlin.
- Kotowski, R. and Weber, B. (1984) *A procedure for on-line correction of systematic errors*. 15th ISPRS Congress, Rio de Janeiro, Commission III, Vol. XXV, part 3a, pp. 553–560.
- Kraus, K. (2000) *Photogrammetry, Volume 1, Fundamentals and Standard Processes*. With contributions by Peter Waldhäusl, translated by Peter Stewardson, Verlag H. Stam GmbH, Köln.
- Kruck, E. (1983) *Lösung großer Gleichungssysteme für photogrammetrische Blockausgleichungen mit erweitertem funktionalen Modell*. Dissertation, Universität Hannover.
- Kyle, S. (1993) Dimensional reference for robot calibration. *Optical 3D Measurement Techniques II* (Eds. Grün/Kahmen) Wichman Verlag, Karlsruhe.
- Langford, M. J. (1982) *Basic Photography*. 4th Edition, Focal Press, London, p. 397.
- (1983) *Advanced Photography*. 4th Edition, Focal Press, London, p. 355.
- Lenz, R. (1992) Gewinnung von Bilddaten mit CCD-Flächensensoren. In Welsch et al. (ed.). *Geodätische Meßverfahren im Maschinenbau*. Schriftenreihe DVW, 1/1992, Wittwer Verlag, Stuttgart, pp. 149–163.
- Lenz, R. and Fritsch, D. (1990) On the Accuracy of Videometry with CCD-Sensors. *International Journal Photogrammetry and Remote Sensing (IJPRS)*, 45, pp. 90–110.
- Lenz, R., Beutlhauser, R. and Lenz, U. (1994) A microscan/macroscan 3×12 bit digital color CCD camera with programmable resolution up to 20992 × 20480 picture elements. *International Archives of Photogrammetry and Remote Sensing*, **30**(5), Melbourne, pp. 225–230.
- Lisowski, W. and Wiedemann, A. (1999) *Auswertung von Bilddaten eines Rotationszeilen-scanners*. Publikationen der DGPF, Band 7, München 1998.
- Luhmann, T. and Tecklenburg, W. (2002) *Bundle Orientation and 3-D Object Reconstruction from Multiple-Station Panoramic Imagery*. ISPRS Symposium Comm. V, Korfu, 2002.
- Lyon, R. and Hubel, P. (2002) *Eyeing the Camera: Into the Next Century*. IS&T/TSID 10th Color Imaging Conference Proceedings, Scottsdale, Az., USA, pp. 349–355.
- Marchesi, J. J. (1985) *Photokollegium 1-5*. Verlag Photographie, Schaffhausen.
- Marshall, G. F. (2004) *Handbook of Optical and Laser Scanning*. 1st Edition, CRC Press.
- Michaelis, M. (1997) *3D-Objekterfassung mit Photogrammetrie und Streifenprojektion*. Publikation der DGPF, Band 5, Oldenburg 1996, pp. 167–173.

- Mugnier, C. J., Förstner, W., Wrobel, B., Paderes, F. and Munji, R. (2004) *The mathematics of photogrammetry*. In McGlone et al. (ed.) *Manual of Photogrammetry*, pp. 181–316.
- Niederöst, M. and Maas, H.-G. (1997) *Entwurf und Erkennung von codierten Zielmarken*. Publikation der DGPF, Band 5, Oldenburg 1996, pp. 55–62.
- Peipe, J. (1995b) Photogrammetric investigation of a  $3000 \times 2000$  pixel high-resolution still-video camera. ISPRS Intercommission Workshop *From Pixels to Sequences*, Zürich, pp. 36–39.
- Petterson, A. (1992) Metrology Norway System – an on-line industrial photogrammetry system. *International Archives of Photogrammetry and Remote Sensing*, **29**(5), Washington, pp. 43–49.
- Ray, S. F. (1994) *Applied photographic optics*. Second edition, Focal Press, Oxford. p. 586.
- Riechmann, W. (1990) *The reseau-scanning camera – conception and first measurement results*. ISPRS Symposium Commission V, Zürich.
- Robson, S., Shortis, M. R. and Ray, S. F. (1999) *Vision metrology with super wide angle and fisheye optics*. *Videometrics VI*, SPIE Volume 3641:pp. 199–206.
- Runne, H., Niemeier, W. and Kern, F. (2001) Application of Laser Scanners to Determine the Geometry of Buildings. In: Grün/Kahmen (ed.) *Optical 3D-Measurement Techniques V*, Vienna, pp. 41–48.
- Schlemmer, H. (1996) *Grundlagen der Sensorik*. Wichmann Verlag, Heidelberg.
- Schlögelhofer, F. (1989) *Qualitäts- und Wirtschaftlichkeitsmodelle für die Ingenieurphotogrammetrie*. Dissertation, Geowissenschaftliche Mitteilungen, Nr. 32, Technische Universität Wien.
- Schmidt, F. (1993) 2D-Industriemeßtechnik mit CCD-Sensoren. *Zeitschrift für Photogrammetrie und Fernerkundung*, Heft 2/1993, pp. 62–70.
- Schneider, C.-T. (1996) DPA Win – A PC based digital photogrammetric station for fast and flexible on-site measurement. *International Archives of Photogrammetry and Remote Sensing*, **31**(B5), pp. 530–533.
- Schneider, D. and Maas, H.-G. (2003) Geometric Modelling and Calibration of a High Resolution Panoramic Camera. In Grün/Kahmen (eds.) *Optical 3-D Measurement Techniques VI*. Vol. II, Institute of Geodesy and Photogrammetry, ETH Zürich, pp. 122–129.
- Schröder, G. (1990) *Technische Optik*. Kamprath Reihe, Vogel Verlag, Würzburg.
- Schwarte, R. (1997) *Überblick und Vergleich aktueller Verfahren der optischen Form erfassung*. GMA-Bericht 30, *Optische Form erfassung*, Langen, pp. 1–12.
- Shortis, M. R. and Beyer, H. A. (1996) Sensor technology for digital photogrammetry and machine vision. In Atkinson (ed.) *Close Range Photogrammetry and Machine Vision*, Whittles Publishing, Caithness, UK, pp. 106–155.
- Shortis, M. R., Seager, J. W., Robson, S. and Harvey, E. S (2003) Automatic recognition of coded targets based on a Hough transform and segment matching. *Videometrics VII*, SPIE Vol, 5013, pp. 202–208
- Staiger, R. (1992) Automatische und dynamische Koordinatenmessung mit mobilen Sensorsystemen. In Welsch et al. (ed.) *Geodätische Meßverfahren im Maschinenbau*. Schriftenreihe DVW, 1/1992, Wittwer Verlag, Stuttgart, pp. 81–96.
- Strutz, T. (1993) *Ein genaues aktives Bildtriangulationsverfahren zur Oberflächen-vermessung*. Dissertation, Fakultät für Maschinenbau, Universität Magdeburg.
- Studnicka, N., Riegl, J. and Ullrich, A. (2003) Zusammenführung und Bearbeitung von Laserscanndaten und hochauflösenden digitalen Bildern eines hybriden 3D-Laser-Sensorsystems. In Luhmann (ed.) *Photogrammetrie-Laserscanning-Optische 3D-Messtechnik*, Oldenburger 3D-Tage 2004, Wichmann, Heidelberg, pp. 183–190.
- Tecklenburg, W., Luhmann, T. and Hastedt, H. (2001) Camera Modelling with Image-variant Parameters and Finite Elements. In Grün/Kahmen (ed.) *Optical 3-D Measurement Techniques V*, Wichmann Verlag, Heidelberg.
- Wehr, A. (1998) Scannertechniken zur dimensionellen Oberflächenbestimmung. 44. DVW-Seminar *Hybride Vermessungssysteme*, Schriftenreihe des DVW, Band 29, pp. 125–148.
- Wendt, A. (2004) On the automation of the registration of point clouds using the Metropolis algorithm. *International Archives of the Photogrammetry, Remote Sensing and Spatial Information Science*, **35**(3).

- Wester-Ebbinghaus, W. (1980) Aerial photography by radio controlled model helicopter. *The Photogrammetric Record*, X(55).
- Wester-Ebbinghaus, W. (1983) *Ein photogrammetrisches System für Sonderanwendungen*. Bildmessung und Luftbildwesen Heft 3/1983, pp. 118–128.
- Wester-Ebbinghaus, W. (1989) Das Réseau im photogrammetrischen Bildraum. *Zeitschrift für Photogrammetrie und Fernerkundung*, Heft 3/1989, pp. 3–10.
- Wiedemann, A. and Wehr, A. (1998) *Vermessung von Dinosaurierskeletten mit Stereophotogrammetrie und Laserscanner*. Publikationen der DGPF, Band 6, Frankfurt 1997, pp. 301–308.
- Wolf, H. (1999) *Systematische Zusammenstellung der Projektionstechniken zur strukturierten Beleuchtung*. 6. ABW-Workshop zur 3D-Bildverarbeitung, Technische Akademie Esslingen.
- Yadid-Pecht, O. and Etienne-Cummings R. (2004) CMOS Imagers: From Phototransduction to Image Processing. 1st Edition, Springer.



## 4 Analytical methods

### 4.1 Overview

This chapter deals with the analytical methods which are essential for the calculation of image orientation parameters and object information (coordinates and geometric elements). The methods are based on measured image coordinates derived from both analogue image measurement and digital image processing.

Due to their differing importance in practical use, the analytical methods of calculation are classified according to the number of images involved. It is common to all methods that the relationship between image information and object geometry is established by the parameters of interior and exterior orientation. Procedures usually occur in the following stages:

- provision of object information (reference points, distances, geometric elements)
- measurement of image points for orientation (image coordinates)
- calculation of orientation parameters (interior and exterior orientation)
- object reconstruction from oriented images (new points, geometric elements)

Depending on method and application, these stages are performed either sequentially, simultaneously or iteratively in a number of processing passes.

Fig. 4.1 is a simplified illustration of the typical methods for determination of orientation parameters (exterior only) and for the reconstruction of 3D object geometry (new points, geometric elements). Both procedures are based on measured image coordinates and known object information. It is obvious that 3D point determination for object reconstruction cannot be performed without the parameters of exterior orientation i.e. position and orientation of an image in space.

If orientation data and coordinates of reference points or measured object points are available, further object reconstruction can be performed according to one or more of the following methods:

- Numerical generation of points and geometric elements: Using images of known orientation for the determination of additional object coordinates and geometric elements by, for example, spatial intersection
- Graphical object reconstruction: Extraction of graphical and geometric information to create maps, drawings or CAD models
- Rectification or orthophoto production: Transformation of the measurement imagery into image-based products using arbitrary projections

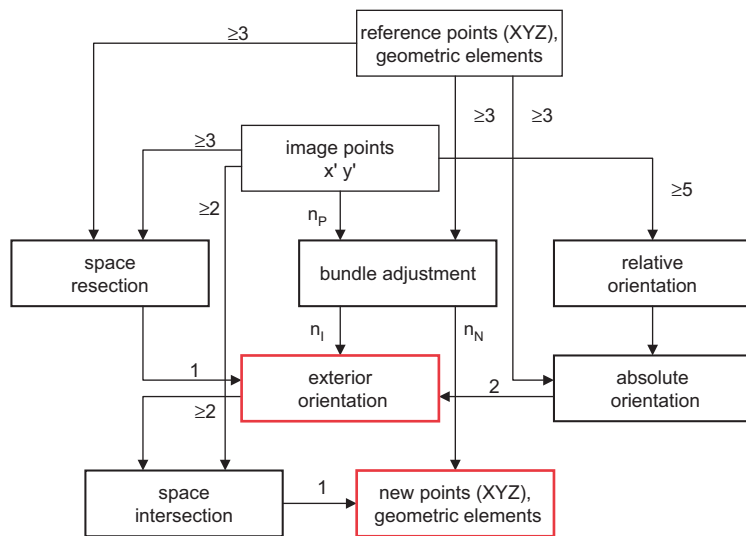


**Figure 4.1** Methods and data flow for orientation and point determination

With regard to the number of images involved, the following methods can be identified:

- Single image analysis (see section 4.4.1): Analysis of single images which take into account additional geometric information and constraints in object space (straight lines, planes, surface models etc.)
- Stereoscopic processing(see section 4.4.2): Visual or digital processing of image pairs based on the principles of stereoscopic image viewing and analysis
- Multi-image processing (see sections 4.3 and 4.4.3): Simultaneous evaluation of an unlimited number of images of an object

In addition to traditional methods using discrete points, analytical processing of higher geometric elements (straight line, plane, cylinder etc.) is being increasingly employed. Line photogrammetry for example (see section 4.5) uses orientation procedures and 3D object reconstruction which are based on straight lines in the object or image space.

Comprehensive overviews of analytical methods for orientation and object reconstruction are given in standard books on photogrammetry (e.g. Kraus 2000, Albertz and Kreiling 1989), and also in some recent text books on computer vision (e.g. Wrobel 1999, Haralick and Shapiro 1992, Klette *et al.* 1996, Hartley and Zisserman 2000).

## 4.2 Orientation methods

### 4.2.1 Exterior orientation

#### 4.2.1.1 Standard case

The exterior orientation consists of six parameters which describe the spatial position and orientation of the camera coordinate system with respect to the global object coordinate system (Fig. 4.2). The standard case in aerial photography of a horizontal image plane is also used as the basic model in close-range photogrammetry. Terrestrial photogrammetry is covered in the next section as a special case.

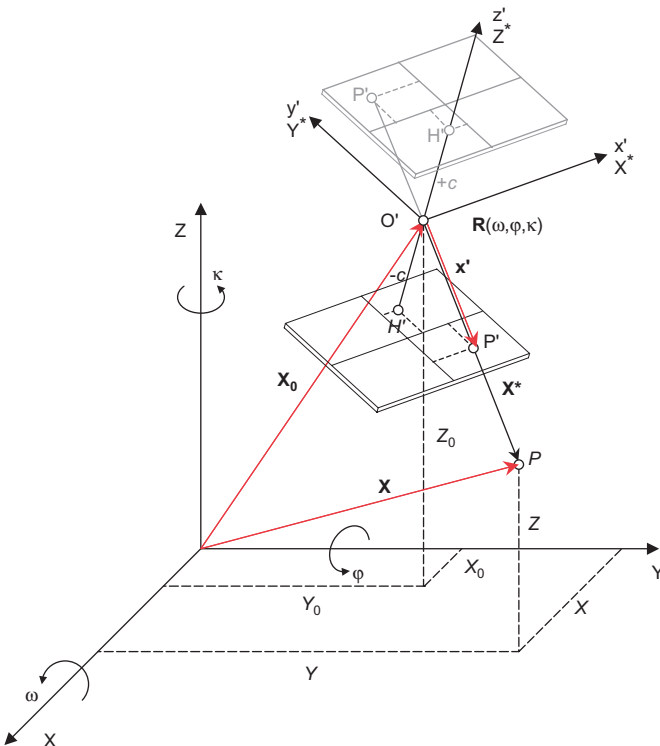


**Figure 4.2** Exterior orientation and projective imaging

The camera coordinate system has its origin at the perspective centre of the image (see section 2.1.1). It is further defined by reference features fixed in the camera (fiducial marks, reseau, sensor system). It can therefore be reconstructed from the image and related to an image measuring device (comparator). In photogrammetry this procedure is often known as reconstruction of interior orientation or simply interior orientation.

The spatial position of the image coordinate system is defined by the vector  $\mathbf{X}_0$  from the origin to the perspective centre  $O'$ . The orthogonal rotation matrix  $\mathbf{R}$  defines the angular orientation in space. It is the resultant of three independent rotations  $\omega$ ,  $\varphi$ ,  $\kappa$  about the coordinate axes  $X$ ,  $Y$ ,  $Z$  (see section 2.2.2.1).

$$\mathbf{X}_0 = \begin{bmatrix} X_0 \\ Y_0 \\ Z_0 \end{bmatrix} \quad : \text{position of perspective centre} \quad (4.1)$$

$$\mathbf{R} = \mathbf{R}_\omega \mathbf{R}_\varphi \mathbf{R}_\kappa$$

$$\mathbf{R} = \begin{bmatrix} r_{11} & r_{12} & r_{13} \\ r_{21} & r_{22} & r_{23} \\ r_{31} & r_{32} & r_{33} \end{bmatrix} \quad : \text{rotation matrix} \quad (4.2)$$

The elements of the rotation matrix  $r_{ij}$  can be defined either as trigonometric functions of the three rotation angles or as functions of four algebraic variables (see section 2.2.2.1).

With given parameters of exterior orientation, the direction from the perspective centre  $O'$  to the image point  $P'$  (image vector  $\mathbf{x}'$ ) can be transformed into an absolutely oriented spatial ray from the perspective centre to the object point  $P$ .

#### 4.2.1.2 Special case of terrestrial photogrammetry

For the special case of conventional terrestrial photogrammetry the camera axis is approximately horizontal. In order to avoid singularities in trigonometric functions, the rotation sequence must either be re-ordered (see section 2.2.2.1) or the image coordinate system must be defined by axes  $x'$  and  $z'$  (instead of  $x'$  and  $y'$ , see section 2.1.1). In this case image acquisition systems which provide angle measurements e.g. video theodolites, can use rotation angles  $\omega$  (tilt about horizontal axis),  $\kappa$  (roll around optical axis) and  $\varphi$  or  $\alpha$  (azimuth) instead of the standard sequence  $\omega$ ,  $\varphi$ ,  $\kappa$  (Fig. 4.3). It must be remembered that here survey angles are positive clockwise.

The modified rotation order  $\varphi$ ,  $\omega$ ,  $\kappa$  leads to the rotation matrix:

$$\mathbf{R}_{\text{terr.}} = \begin{bmatrix} r_{11} & r_{12} & r_{13} \\ r_{21} & r_{22} & r_{23} \\ r_{31} & r_{32} & r_{33} \end{bmatrix} \quad (4.3)$$

$$= \begin{bmatrix} \cos \varphi \cos \kappa - \sin \varphi \sin \omega \sin \kappa & -\sin \varphi \cos \omega & \cos \varphi \sin \kappa + \sin \varphi \sin \omega \cos \kappa \\ \sin \varphi \cos \kappa + \cos \varphi \sin \omega \sin \kappa & \cos \varphi \cos \omega & \sin \varphi \sin \kappa - \cos \varphi \sin \omega \cos \kappa \\ -\cos \omega \sin \kappa & \sin \omega & \cos \omega \cos \kappa \end{bmatrix}$$

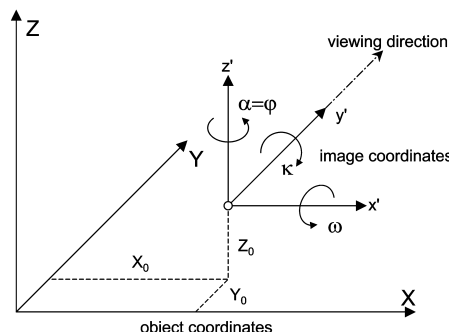


Figure 4.3 Exterior orientation for terrestrial photogrammetry

#### 4.2.2 Collinearity equations

The central projection in space is at the heart of many photogrammetric calculations. Thus the coordinates of an object point  $P$  can be derived from the position vector to the perspective centre  $\mathbf{X}_0$  and the vector from the perspective centre to the object point  $\mathbf{X}^*$  (Fig. 4.2):

$$\mathbf{X} = \mathbf{X}_0 + \mathbf{X}^* \quad (4.4)$$

The vector  $\mathbf{X}^*$  is given in the object coordinate system. The image vector  $\mathbf{x}'$  may be transformed into object space by rotation matrix  $\mathbf{R}$  and a scaling factor  $m$ . Then, since it is in the same direction as  $\mathbf{X}^*$ :

$$\mathbf{X}^* = m \mathbf{R} \mathbf{x}' \quad (4.5)$$

Hence, the projection of an image point into a corresponding object point is given by:<sup>1</sup>

$$\mathbf{X} = \mathbf{X}_0 + m\mathbf{R}\mathbf{x}'$$

$$\begin{bmatrix} X \\ Y \\ Z \end{bmatrix} = \begin{bmatrix} X_0 \\ Y_0 \\ Z_0 \end{bmatrix} + m \begin{bmatrix} r_{11} & r_{12} & r_{13} \\ r_{21} & r_{22} & r_{23} \\ r_{31} & r_{32} & r_{33} \end{bmatrix} \begin{bmatrix} x' \\ y' \\ z' \end{bmatrix} \quad (4.6)$$

The scale factor  $m$  is an unknown value which varies for each object point. If only one image is available then only the direction to an object point  $P$  can be determined but not its absolute position in space. The 3D coordinates of  $P$  can only be computed if this spatial direction intersects another geometrically known element (e.g. intersection with a second ray from another image or intersection with a given surface in space).

By inverting equation (4.6), adding the principal point  $H'$  ( $x'_0, y'_0$ ) and introducing correction terms  $\Delta\mathbf{x}'$  (image distortion parameters), the image coordinates are given by:

$$\mathbf{x}' - \mathbf{x}'_0 - \Delta\mathbf{x}' = \frac{1}{m} \mathbf{R}^{-1} (\mathbf{X} - \mathbf{X}_0)$$

$$\begin{bmatrix} x' - x'_0 - \Delta x' \\ y' - y'_0 - \Delta y' \\ z' \end{bmatrix} = \frac{1}{m} \begin{bmatrix} r_{11} & r_{21} & r_{31} \\ r_{12} & r_{22} & r_{32} \\ r_{13} & r_{23} & r_{33} \end{bmatrix} \begin{bmatrix} X - X_0 \\ Y - Y_0 \\ Z - Z_0 \end{bmatrix} \quad (4.7)$$

Note that the inverse rotation matrix is equal to its transpose. By dividing the first and second equations by the third equation, the unknown scaling factor  $m$  is eliminated and the collinearity equations follow:

$$x' = x'_0 + z' \frac{r_{11}(X - X_0) + r_{21}(Y - Y_0) + r_{31}(Z - Z_0)}{r_{13}(X - X_0) + r_{23}(Y - Y_0) + r_{33}(Z - Z_0)} + \Delta x'$$

$$y' = y'_0 + z' \frac{r_{12}(X - X_0) + r_{22}(Y - Y_0) + r_{32}(Z - Z_0)}{r_{13}(X - X_0) + r_{23}(Y - Y_0) + r_{33}(Z - Z_0)} + \Delta y' \quad (4.8)$$

These equations describe the transformation of object coordinates ( $X, Y, Z$ ) into corresponding image coordinates ( $x', y'$ ) as functions of the interior orientation parameters ( $x'_0, y'_0, c, \Delta x', \Delta y'$ ) and exterior orientation parameters ( $X_0, Y_0, Z_0, \omega, \varphi, \kappa$ ) of one image.

An alternative form is given if the object coordinate system is transformed (translation and rotation) by shift to the perspective centre and orientation parallel to the image coordinate system. Within the local coordinate system which results, object coordinates are denoted by  $X^*$ ,  $Y^*$ ,  $Z^*$  (see Fig. 4.2). After multiplication by image scale  $1/m$  and correction for principal point shift and image deformations, the collinearity equations for image coordinates follow:

$$\begin{bmatrix} X^* \\ Y^* \\ Z^* \end{bmatrix} = \mathbf{R}^{-1} \begin{bmatrix} X - X_0 \\ Y - Y_0 \\ Z - Z_0 \end{bmatrix} \quad : \text{spatial translation and rotation} \quad (4.9)$$

<sup>1</sup> In equations (4.6)  $z'$  appears where, on the basis of Fig. 4.2, one would expect to see  $-c$ . For reasons of generality in order to extend the algebra to certain types of imaging systems such as panorama cameras, the value  $z'$  appears in equations throughout.

$$\begin{bmatrix} x' \\ y' \end{bmatrix} = \frac{z'}{Z^*} \begin{bmatrix} X^* \\ Y^* \end{bmatrix} + \begin{bmatrix} x'_0 \\ y'_0 \end{bmatrix} + \begin{bmatrix} \Delta x' \\ \Delta y' \end{bmatrix} \quad : \text{projection into image plane} \quad (4.10)$$

$$m = \frac{Z^*}{z'}$$

The collinearity equations demonstrate clearly that each object point is projected into a unique image point, if it is not occluded by other object points. The formulas effectively describe image generation inside a camera by the geometry of a central projection.

The equations (4.8) form the fundamental equations of analytical photogrammetry. It is important to note that, since the observed measurements stand alone on the left-hand side, these equations are suitable for direct use as observation equations in an over-determined least-squares adjustment (see section 2.3.2). For example, the collinearity equations are used to set up the equation system for spatial intersection (section 4.4.3.1), space resection (section 4.2.3.1) and bundle triangulation (section 4.3). Additionally, they offer the mathematical basis for the generation of orthophotos and the principle of analytical stereo plotting systems (see section 6.3.1).

### 4.2.3 Orientation of single images

Orientation of single images is taken to mean, in the first instance, the process of calculating the parameters of exterior orientation. Since direct determination, for example by angle or distance measurement, is not usually possible, methods of indirect orientation are employed. These make use of XYZ reference points whose image coordinates may be measured in the image. Common calculation procedures can be divided into two groups:

1. Calculation of exterior orientation based on collinearity equations:

The method of space resection provides a non-linear solution that requires a minimum of three XYZ reference points in object space and approximate values for the unknown orientation parameters (see also section 4.2.3.1).

2. Calculation of exterior orientation based on projective relations:

The most popular method in this group is the Direct Linear Transformation (DLT). It requires a minimum of five XYZ reference points, but provides a direct solution without the need for approximate values (see also section 4.2.3.2).

#### 4.2.3.1 Space resection

##### *Resection with known interior orientation*

Space resection is used to compute the exterior orientation of a single image. The procedure requires known XYZ coordinates of at least three object points  $P_i$  which do not lie on a common straight line. The bundle of rays through the perspective centre from the reference points can fit the corresponding points in image plane  $P'_i$  in only one unique position and orientation of the image (Fig. 4.4).<sup>1</sup>

Using the measured image coordinates of the reference points, and with known parameters of interior orientation, the following system of correction equations can be derived from the collinearity equations (4.8):

$$\begin{aligned} x' + vx' &= F(X_0, Y_0, Z_0, \omega, \varphi, \kappa, x'_0, z', \Delta x', X, Y, Z) \\ y' + vy' &= F(X_0, Y_0, Z_0, \omega, \varphi, \kappa, y'_0, z', \Delta y', X, Y, Z) \end{aligned} \quad (4.11)$$

<sup>1</sup> Strictly speaking, alternative solutions exist with only three reference points but these can be avoided if at least one more reference point is added (further information in next section).

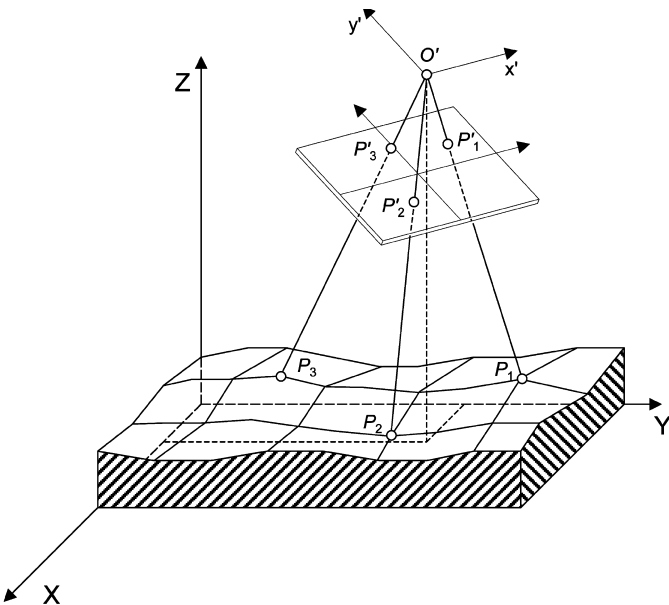


Figure 4.4 Space resection

Function  $F$  is a representation of equations (4.8) in which the underlined values are introduced as unknowns. This system can be linearised at approximate values by Taylor series expansion and solved by least-squares adjustment.

Each of the measured image points provides two linearised correction equations (Albertz and Kreiling 1989):

$$\begin{aligned}
 vx'_i &= \left( \frac{\partial x'}{\partial X_0} \right)^0 dX_0 + \left( \frac{\partial x'}{\partial Y_0} \right)^0 dY_0 + \left( \frac{\partial x'}{\partial Z_0} \right)^0 dZ_0 \\
 &\quad + \left( \frac{\partial x'}{\partial \omega} \right)^0 d\omega + \left( \frac{\partial x'}{\partial \varphi} \right)^0 d\varphi + \left( \frac{\partial x'}{\partial \kappa} \right)^0 d\kappa - (x'_i - x'^0_i) \\
 vy'_i &= \left( \frac{\partial y'}{\partial X_0} \right)^0 dX_0 + \left( \frac{\partial y'}{\partial Y_0} \right)^0 dY_0 + \left( \frac{\partial y'}{\partial Z_0} \right)^0 dZ_0 \\
 &\quad + \left( \frac{\partial y'}{\partial \omega} \right)^0 d\omega + \left( \frac{\partial y'}{\partial \varphi} \right)^0 d\varphi + \left( \frac{\partial y'}{\partial \kappa} \right)^0 d\kappa - (y'_i - y'^0_i)
 \end{aligned} \tag{4.12}$$

Here  $x'_i$  and  $y'_i$  are the measured image coordinates and  $x'^0_i$  and  $y'^0_i$  are the image coordinates which correspond to the approximate orientation parameters.

Simplification of the collinearity equations (4.8), by substituting  $k_X$  and  $k_Y$  for the numerators and  $N$  for the denominator, leads to

$$\begin{aligned}
 x' &= x'_0 + z' \frac{k_X}{N} + \Delta x' \\
 y' &= y'_0 + z' \frac{k_Y}{N} + \Delta y'
 \end{aligned} \tag{4.13}$$

from which the differential coefficients of (4.12) are given by:

$$\begin{aligned}\frac{\partial x'}{\partial X_0} &= \frac{z'}{N^2} (r_{13}k_X - r_{11}N) \\ \frac{\partial x'}{\partial Y_0} &= \frac{z'}{N^2} (r_{23}k_X - r_{21}N) \\ \frac{\partial x'}{\partial Z_0} &= \frac{z'}{N^2} (r_{33}k_X - r_{31}N) \\ \frac{\partial x'}{\partial \omega} &= \frac{z'}{N} \left\{ \frac{k_X}{N} [r_{33}(Y - Y_0) - r_{23}(Z - Z_0)] - r_{31}(Y - Y_0) + r_{21}(Z - Z_0) \right\} \\ \frac{\partial x'}{\partial \varphi} &= \frac{z'}{N} \left\{ \frac{k_X}{N} [k_Y \sin \kappa - k_X \cos \kappa] - N \cos \kappa \right\} \\ \frac{\partial x'}{\partial \kappa} &= \frac{z'}{N} k_Y\end{aligned}\tag{4.14a}$$

$$\begin{aligned}\frac{\partial y'}{\partial X_0} &= \frac{z'}{N^2} (r_{13}k_Y - r_{12}N) \\ \frac{\partial y'}{\partial Y_0} &= \frac{z'}{N^2} (r_{23}k_Y - r_{22}N) \\ \frac{\partial y'}{\partial Z_0} &= \frac{z'}{N^2} (r_{33}k_Y - r_{32}N) \\ \frac{\partial y'}{\partial \omega} &= \frac{z'}{N} \left\{ \frac{k_Y}{N} [r_{33}(Y - Y_0) - r_{23}(Z - Z_0)] - r_{32}(Y - Y_0) + r_{22}(Z - Z_0) \right\} \\ \frac{\partial y'}{\partial \varphi} &= \frac{z'}{N} \left\{ \frac{k_Y}{N} [k_X \cos \kappa + k_Y \sin \kappa] + N \sin \kappa \right\} \\ \frac{\partial y'}{\partial \kappa} &= -\frac{z'}{N} k_X\end{aligned}\tag{4.14b}$$

The coefficients  $r_{ij}$  can be derived from the rotation matrix  $\mathbf{R}$  according to (2.19).

#### *Resection with unknown interior orientation*

For images from cameras with unknown parameters of interior orientation (e.g. amateur cameras) the number of unknown parameters, ignoring distortion in the first instance, increases by 3 ( $c, x'_0, y'_0$ ) to a total of 9. Two more reference points, providing 4 additional image observation equations, are required for the solution (a minimum of 5 reference points in total).

If all reference points lie approximately on a plane then the normal system of equations for the resection is singular, since the problem can be solved by an 8-parameter projective transformation between image and object planes (2.12). However, if one of the unknown parameters, such as the principal distance, is fixed to an arbitrary value a unique solution can be computed.

If a suitable spatial distribution of object points is available, the space resection approach can be used to calibrate the parameters of interior orientation  $c, x'_0, y'_0, \Delta x', \Delta y'$  from only one image. The number of elements to be determined increases to a total of 11 if the parameters  $A_1$  and  $A_2$  for radially symmetric distortion are introduced (6 for exterior and 5 for interior orientation). In this case a minimum of 6 spatially distributed XYZ reference points are required.

### *Approximate values for resection*

In some situations approximate values for the unknown parameters of exterior orientation can be readily determined by one of the following methods.

- Approximate values by direct measurement

Approximate orientation values can possibly be measured on site, for example by survey methods. The camera position can often be determined by simple means such as estimation off a site plan. Even rotation angles can be estimated sufficiently well in simple configurations, for example without oblique or rolled views.

- Approximate values from free-hand sketches

With some software packages it is possible to manually digitise a simple free-hand sketch, drawn on site, which shows camera positions and observation directions. The digitised sketch can be transformed into the global coordinate system by reference points, thus providing approximate values of the orientation parameters.

- Small image rotations

If the coordinate axes of the image system are approximately parallel to the object coordinate system, initial rotation angles can be approximated by the value zero. The parameters for translation  $X_0$  and  $Y_0$  can be estimated from the centroid of the reference points; the object distance ( $Z - Z_0$ ) can be determined from the principal distance and approximately known image scale.

### *Resection with minimum object information*

In the general case of arbitrary position and orientation of an image, approximate values can no longer be easily estimated but must be computed. This can be performed according to the following scheme (Hunt 1984, Kyle 1990, Wrobel 1999). An algebraic, rather than a geometric, solution is given by Smith (1965). Haralick *et al.* (1994) gives additional direct solutions for space resection.

Given a minimum of three XYZ reference points, the position of the perspective centre  $O'$  is first determined. As shown in Fig. 4.5 a tetrahedron can be formed by the perspective centre and the three object points. From the simple properties of triangles, the angles  $\alpha$ ,  $\beta$ ,  $\gamma$  of the tetrahedrons  $O'P'_1P'_2P'_3$  and  $O'P_1P_2P_3$  can be calculated from the measured image coordinates of  $P'_1$ ,  $P'_2$  and  $P'_3$  and the principal distance  $c$ . However, the side lengths of the tetrahedron,  $d_i$ ,  $i = 1 \dots 3$ , remain unknown at this stage.

If each of the tetrahedron sides is rotated into the plane of the three object points, the configuration of Fig. 4.6 is obtained. Taking as an example the triangle formed by object points  $P_1$ ,  $P_2$  and the required perspective centre  $O'$ , it is obvious that a circle  $K_1$  can be constructed from known distance  $s_{12}$  and angle  $\alpha$  calculated previously, and that  $O'$  lies on this circle. Similarly, circle  $K_2$  can be constructed from  $s_{23}$  and circle  $K_3$  from  $s_{13}$ . Three spheres may be formed by rotating the circles about their corresponding chords  $P_1P_2$ ,  $P_2P_3$ , and  $P_3P_1$ . Intersection of these spheres provides the spatial position of  $O'$ .

Rather than computing the intersection of these spheres, the following iterative search strategy estimates the unknown side lengths of the tetrahedron and from these the perspective centre can be more simply calculated as described below. The search is made as follows. Starting near  $P_1$  in circle  $K_1$ , a test point  $R$  is stepped around the circle and distances  $d_{R1}$  and  $d_{R2}$  calculated at test positions. Distance  $d_{R1}$  is an estimate of side length  $d_1$  and  $d_{R2}$  an estimate of side length  $d_2$ . Distance  $d_{R2}$  is transferred into circle  $K_2$  where a corresponding value  $d_{R3}$  can be calculated from angle  $\beta$  and the known distance  $s_{23}$ . Finally  $d_{R3}$  is transferred into circle  $K_3$  where, in a similar way, distance  $d_1$  is again estimated as value  $d'_{R1}$ . At the end of the loop a difference  $\Delta d_1 = d_{R1} - d'_{R1}$  results. If  $R$  is stepped further around the circle until it approaches  $P_2$ ,

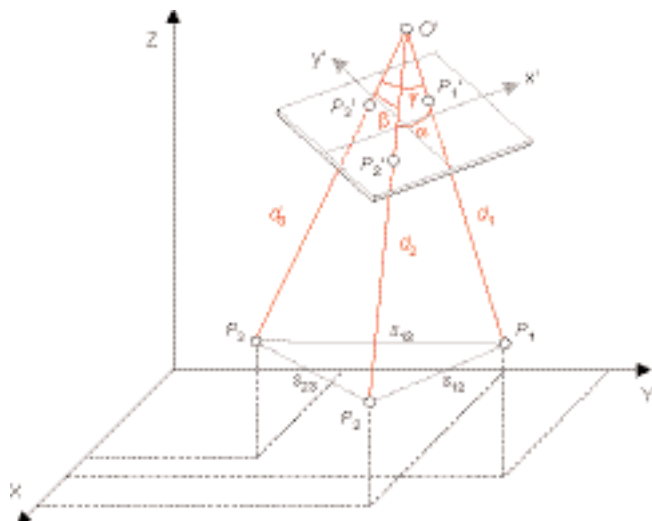


Figure 4.5 Tetrahedron for space resection

the sign of the difference at some position will change. At this position sufficiently good approximate values for the side lengths  $d_i$  are available.

When transferred into circle  $K_2$ ,  $d_{R2}$  in general creates two possible positions for  $O'$  and therefore two possible values of distance  $d_{R3}$ . When transferred into circle  $K_3$  each value of  $d_{R3}$  generates two possible positions for  $O'$  which therefore leads to a total number of four possible solutions for the position of the perspective centre. To ensure that all possible solutions are investigated, and correct solutions with  $\Delta d_1 = 0$  are found, the circles must be searched in order of increasing size, starting with the smallest.

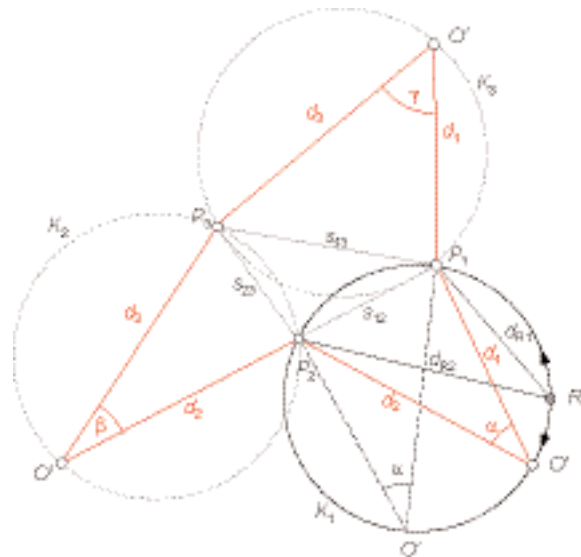
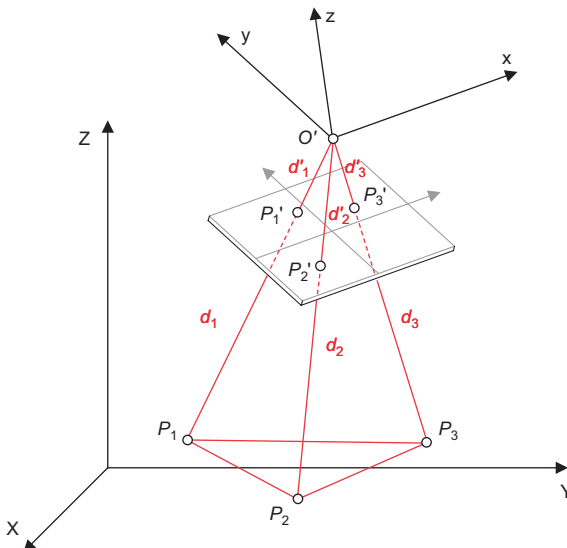


Figure 4.6 Approximate values for space resection



**Figure 4.7** Similarity transformation for space resection

Now the rotation and translation of the image coordinate system with respect to the object coordinate system can be determined. Using the side lengths estimated above for one of the solutions, the coordinates of reference points  $P_i, i = 1 \dots 3$ , are calculated in the camera coordinate system xyz, with origin  $O'$ , which coincides with the image coordinate system  $x'y'z'$  (Fig. 4.7):

$$\mathbf{x}_i = \frac{d_i}{d'_i} \mathbf{x}'_i \quad \text{where } d' = \sqrt{x'^2 + y'^2 + z'^2} \quad (4.15)$$

$$x_i = d_i \frac{x'_i}{d'} \quad y_i = d_i \frac{y'_i}{d'} \quad z_i = d_i \frac{z'_i}{d'}$$

Approximate values for the rotation parameters can then be derived by a spatial similarity transformation i.e. absolute orientation (see sections 2.2.2.2 and 4.2.5.4), since the coordinates of  $P_1, P_2, P_3$  are known in both the xyz and the XYZ systems.

$$\mathbf{X}_i = \mathbf{X}_0 + m \mathbf{R} \mathbf{x}_i \quad \text{for } i = 1, 2, 3 \quad (4.16)$$

Since the distances  $P_i P_{i+1}$  are the same in both systems the scale factor  $m$  will be unity. The rotation matrix  $\mathbf{R}$  rotates the xyz coordinate system parallel to the XYZ system. Finally the required translation  $\mathbf{X}_0$  may be found using the xyz coordinates  $\mathbf{x}_i$  of a reference point  $P_i$  and rotated by  $\mathbf{R}$ . For example, using  $P_1$ :

$$\mathbf{X}_0 = \mathbf{X}_1 - \mathbf{R} \mathbf{x}_1 \quad (4.17)$$

For the reasons given above, the spatial position of  $O'$  and the corresponding rotation matrix are not unique. The ambiguity can be resolved by use of a fourth reference point. Its transformed coordinates, found from equation (4.17), may be compared with the reference coordinates. A good match indicates the correct solution.

Amongst other applications, space resection is used to compute initial orientation values from approximate object point coordinates (see section 4.3.4.1).

### Quality measures

In addition to the accuracy of image coordinate measurement, the quality of the resection depends on the number and distribution of reference points. Measured image points should ideally fill the image format. If all the reference points are located on or close to a common straight line, the normal system of equations becomes singular or numerically weak. Similarly there is no solution if object points and perspective centre are all located on the same danger surface such as a cylinder (see also section 4.2.5.3).

As in other adjustment problems the *a posteriori* standard deviation of unit weight  $s_0$  can be used as a quality criterion for the resection. It represents the internal accuracy of the observations, in this case the measured image coordinates. In addition the standard deviations of the estimated orientation parameters can be analysed. They can be derived from the covariance matrix and hence depend on  $s_0$ .

#### 4.2.3.2 Direct Linear Transformation (DLT)

Using Direct Linear Transformation (DLT) it is possible, by solving a linear system of equations, to determine the orientation of an image without the need for approximate initial values (Abdel-Aziz and Karara 1971). The method is based on the collinearity equations, extended by an affine transformation of the image coordinates. No image coordinate system fixed in the camera is required.

The transformation equation of the DLT is given by:

$$\begin{aligned} x &= \frac{L_1 X + L_2 Y + L_3 Z + L_4}{L_9 X + L_{10} Y + L_{11} Z + 1} \\ y &= \frac{L_5 X + L_6 Y + L_7 Z + L_8}{L_9 X + L_{10} Y + L_{11} Z + 1} \end{aligned} \quad (4.18)$$

Here  $x$  and  $y$  are the measured comparator or image coordinates and  $X, Y, Z$  are the 3D coordinates of the reference points. The coefficients  $L_1$  to  $L_{11}$  are the DLT parameters to be estimated and from these the parameters of interior orientation (3) and exterior orientation (6) can be derived. Overviews are provided by McGlone *et al.* (1989) and Mikhail *et al.* (2001). The two remaining elements describe shearing and scaling of the affine transformation. By re-arrangement of equations (4.18) the following linear system is obtained:

$$\begin{aligned} L_1 X + L_2 Y + L_3 Z + L_4 - x L_9 X - x L_{10} Y - x L_{11} Z - x &= 0 \\ L_5 X + L_6 Y + L_7 Z + L_8 - y L_9 X - y L_{10} Y - y L_{11} Z - y &= 0 \end{aligned} \quad (4.19)$$

In order to solve this system of equations for  $n$  reference points ( $n \geq 6$ ) according to the usual model  $\mathbf{v} = \mathbf{A}\hat{\mathbf{x}} - \mathbf{l}$  the design matrix  $\mathbf{A}$  is set up as follows:

$$\mathbf{A}_{n,u} = \begin{bmatrix} X_1 & Y_1 & Z_1 & 1 & 0 & 0 & 0 & 0 & -x_1 X_1 & -x_1 Y_1 & -x_1 Z_1 \\ 0 & 0 & 0 & 0 & X_1 & Y_1 & Z_1 & 1 & -y_1 X_1 & -y_1 Y_1 & -y_1 Z_1 \\ X_2 & Y_2 & Z_2 & 1 & 0 & 0 & 0 & 0 & -x_2 X_2 & -x_2 Y_2 & -x_2 Z_2 \\ 0 & 0 & 0 & 0 & X_2 & Y_2 & Z_2 & 1 & -y_2 X_2 & -y_2 Y_2 & -y_2 Z_2 \\ \vdots & \vdots \\ X_n & Y_n & Z_n & 1 & 0 & 0 & 0 & 0 & -x_n X_n & -x_n Y_n & -x_n Z_n \\ 0 & 0 & 0 & 0 & X_n & Y_n & Z_n & 1 & -y_n X_n & -y_n Y_n & -y_n Z_n \end{bmatrix} \quad (4.20)$$

Determination of the 11 DLT parameters requires a minimum of 6 reference points. Since equations (4.20) are linear in the unknowns  $L_i$  no approximate values of the unknown parameters are required. Because of the affine transformation applied to the measured image coordinates, there is no need for an image coordinate system defined by reference points fixed in the camera, such as fiducial marks. Instead it is possible to make direct use of measured comparator coordinates and, in general, coordinates from an arbitrary image measuring device with non-orthogonal axes and different axial scale factors e.g. pixel coordinates. Images from non-metric cameras which have no image coordinate system or have an unknown interior orientation can therefore be evaluated by this method.

Because of its robust linear form, the DLT is also used for the calculation of approximate exterior orientation parameters prior to a bundle adjustment. The more familiar orientation parameters can be derived from the DLT parameters as follows:

With

$$L = \frac{-1}{\sqrt{L_9^2 + L_{10}^2 + L_{11}^2}}$$

the parameters of interior orientation are obtained as follows:

$$\begin{aligned} x'_0 &= L^2(L_1L_9 + L_2L_{10} + L_3L_{11}) && : \text{coordinates of principal point} \\ y'_0 &= L^2(L_5L_9 + L_6L_{10} + L_7L_{11}) \\ c_x &= \sqrt{L^2(L_1^2 + L_2^2 + L_3^2) - x'^2_0} && (4.21) \\ c_y &= \sqrt{L^2(L_5^2 + L_6^2 + L_7^2) - y'^2_0} && : \text{principal distance (different scales in } x \text{ and } y) \end{aligned}$$

The parameters of exterior orientation, as defined by the elements of rotation matrix  $\mathbf{R}$ , are given by

$$\begin{aligned} r_{11} &= \frac{L(x'_0L_9 - L_1)}{c_x} & r_{12} &= \frac{L(y'_0L_9 - L_5)}{c_y} & r_{13} &= LL_9 \\ r_{21} &= \frac{L(x'_0L_{10} - L_2)}{c_x} & r_{22} &= \frac{L(y'_0L_{10} - L_6)}{c_y} & r_{23} &= LL_{10} \\ r_{31} &= \frac{L(x'_0L_{11} - L_3)}{c_x} & r_{32} &= \frac{L(y'_0L_{11} - L_7)}{c_y} & r_{33} &= LL_{11} \end{aligned} \quad (4.22)$$

The position of the perspective centre is given by

$$\begin{bmatrix} X_0 \\ Y_0 \\ Z_0 \end{bmatrix} = - \begin{bmatrix} L_1 & L_2 & L_3 \\ L_5 & L_6 & L_7 \\ L_9 & L_{10} & L_{11} \end{bmatrix}^{-1} \begin{bmatrix} L_4 \\ L_8 \\ 1 \end{bmatrix} \quad (4.23)$$

To avoid possible numerical uncertainties, the elements of the rotation matrix must be normalised to an orthonormal matrix. The individual rotation angles can be further derived according to equation (2.23), with due regard to the ambiguities indicated. The DLT model can be extended by correction terms for radially symmetric distortion.

Together with the benefits of the DLT mentioned above there are some drawbacks. If the parameters of interior orientation are known, the DLT has an excess of parameters. In addition,

singular or weakly conditioned systems of equations arise if all reference points are located on a common plane, or if the denominator in equations (4.18) is close to zero. Measurement errors in the image coordinates and errors in reference point coordinates cannot be detected by the DLT and this results in false parameters. Finally the minimum number of 6 reference points cannot always be provided in real applications.

By the aid of projective geometry and homogeneous coordinates, a direct solution can also be found. This approach determines a  $3 \times 4$  projection matrix  $\mathbf{P}$ , again with 11 independent parameters (Hartley and Zisserman 2000, Förstner and Wrobel 2004, Mugnier *et al.* 2004).

#### 4.2.4 Object position and orientation by inverse resection

##### 4.2.4.1 Position and orientation of an object with respect to a camera

An inverse space resection enables the determination of the spatial position and orientation of an object with respect to the camera coordinate system. The procedure is sometimes known as the 6 DOF (degrees of freedom) calculation for the target object.

Based on the parameters of exterior orientation described in equations (4.1) and (4.2) the relationship between coordinates of a point,  $\mathbf{X}$  in the object system and  $\mathbf{x}^*$  in the camera system (see Fig. 4.2), is given by:

$$\mathbf{X} = \mathbf{X}_0 + \mathbf{R}\mathbf{x}^* \quad (4.24)$$

Rearranging (4.24) gives:

$$\mathbf{x}^* = \mathbf{R}^{-1}(\mathbf{X} - \mathbf{X}_0) \quad (4.25)$$

where  $\mathbf{x}^*$  gives the coordinates with respect to the camera system of a point on the object.

If the camera remains still during an imaging sequence, the spatial motion of a body can be fully determined by repeated inverse space resections.

##### 4.2.4.2 Position and orientation of one object relative to another

The spatial relationship between two objects can also be calculated by space resection, provided that both objects appear in the same image. In this case a reference object is required with its own local coordinate system, XYZ, in which the position and orientation of a second object is to be determined. This second object, here referred to as the locator, has a separate coordinate system, xyz. Two space resections are calculated using control points given in each of these two coordinate systems:

$$\mathbf{X} = \mathbf{X}_0 + \mathbf{R}_R \mathbf{x}^* \quad : \text{resection on reference points} \quad (4.26)$$

$$\mathbf{x} = \mathbf{x}_0 + \mathbf{R}_L \mathbf{x}^* \quad : \text{resection on locator points} \quad (4.27)$$

Rearranging (4.27) gives:

$$\mathbf{x}^* = \mathbf{R}_L^{-1}(\mathbf{x} - \mathbf{x}_0) \quad (4.28)$$

Substituting for  $\mathbf{x}^*$  in (4.26) from (4.28):

$$\begin{aligned} \mathbf{X} &= \mathbf{X}_0 + \mathbf{R}_R (\mathbf{R}_L^{-1}(\mathbf{x} - \mathbf{x}_0)) \\ &= \mathbf{X}_0 + \mathbf{R}_R \mathbf{R}_L^{-1}(\mathbf{x} - \mathbf{x}_0) \\ \mathbf{X} &= \mathbf{X}_0 + \mathbf{R}(\mathbf{x} - \mathbf{x}_0) \end{aligned} \quad (4.29)$$

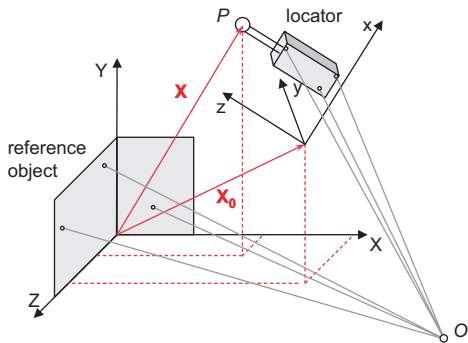


**Figure 4.8** 6 DOF relation between two objects and a camera

in which

- x:** position of a locator point  $P$  (e.g. a probing tip, see Fig. 4.8) within its xyz system
- X:** position of the same point  $P$  in the XYZ reference system (which is the result required)
- $x_0, X_0$ :** coordinates of the projection centre within locator xyz and reference XYZ systems respectively
- $R_L, R_R$ :** rotation matrices of camera axes with respect to locator xyz and reference XYZ systems respectively
- R:** rotation matrix of the locator xyz axes with respect to the XYZ axes

#### 4.2.5 Orientation of stereo image pairs

The orientation of a stereo pair provides exterior orientation parameters of both images (Fig. 4.9). In principle this task can be solved separately for each image by space resection (see section 4.2.3.1) but three-dimensional reference points (full reference points) are then required for each photo (see Fig. 4.4). The reference points can be identical or different for each image.

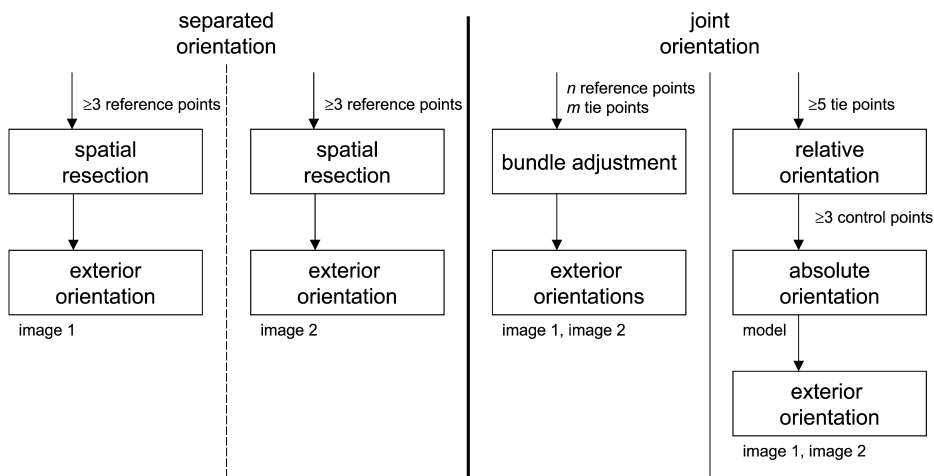


**Figure 4.9** Orientation methods for stereo images

In this procedure the geometric relationship between the two images in a stereo model is not used.

Fig. 4.10 shows a typical stereo pair where both images cover the object with an overlap of at least 50% (a standard overlap is 60%, see also Fig. 3.2a). This feature can be employed in the orientation of both images.

The one-step solution employs the principle of bundle triangulation (Fig. 4.23) for the special case of two images. Here the orientation elements of both images are determined simultaneously in one step using the image coordinates of the reference points and additional tie points (see section 4.2.5.1).

The traditional two-step solution of this problem works as follows. In the first step the correspondence between the images, and the coordinates of model points, are determined in a local coordinate system (relative orientation). In the second step the transformation into the global object coordinate system is performed using reference points (absolute orientation).

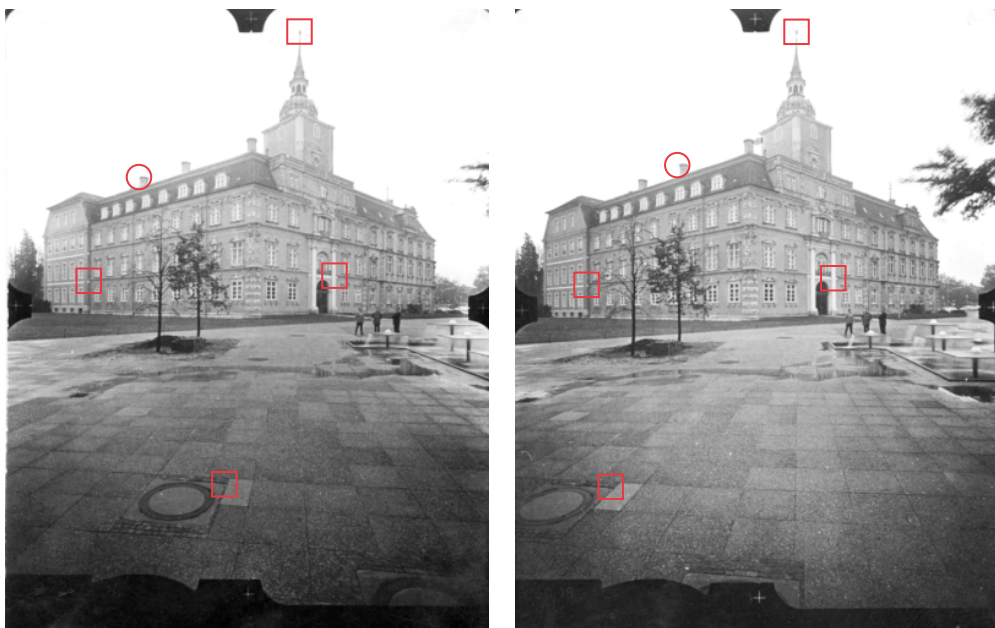


**Figure 4.10** Tie points in a stereo model  
□ : correctly matched points; ○ : incorrectly matched points

#### 4.2.5.1 Tie points

Tie points are identified as homologous points in the images i.e. they represent the same object point. They assist in the geometric connection between two or more images and need not be reference points. They must be selected to cover a sufficient area in image and object space in order to provide a robust connection between the images.

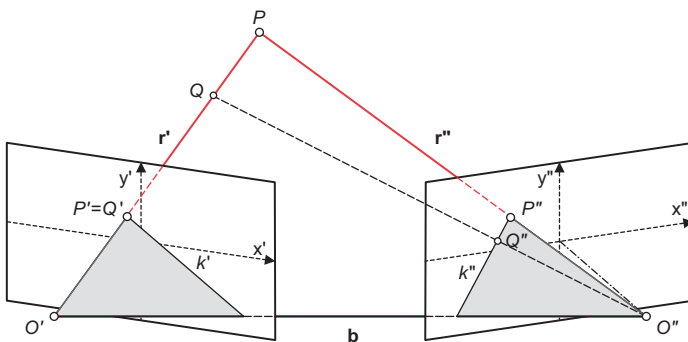
Homologous points can be identified visually, either by stereoscopic viewing or by monoscopic measurement of single images. Non-targeted object points can be identified more reliably by stereoscopic viewing. Correspondence between homologous points can also be performed by digital stereo image matching (see section 5.5.3). Here similarities in grey level patterns are compared in order to match corresponding points (image correlation).

Normally there is no orientation information available during the tie point measurement stage and so there are few controls to prevent false measurements. In larger photogrammetric projects, gross errors (blunders) are therefore almost always present in the observations due to errors in measurement or identification. Fig. 4.10 shows an example of four correct tie points and one incorrect.

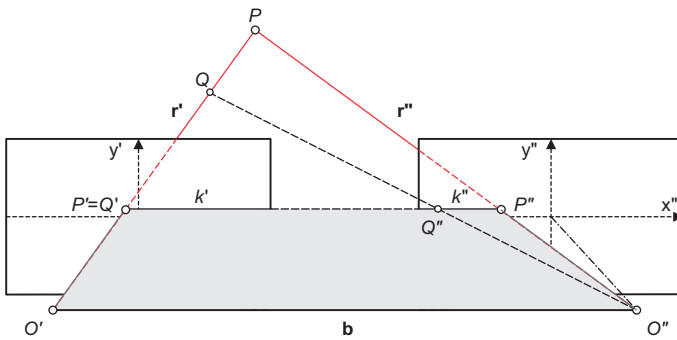
#### 4.2.5.2 Epipolar geometry

Fig. 4.11 shows the geometry of a stereo pair imaging any object point  $P$ . The base  $\mathbf{b}$ , and the projected rays  $\mathbf{r}'$  and  $\mathbf{r}''$  from each perspective centre to the object point, define an epipolar plane, sometimes called a basal plane. This plane intersects the image planes along lines  $k'$  and  $k''$ , which are known as epipolar lines. In the case of convergent images the epipolar lines are convergent. In the special case of normal stereophotogrammetry, the epipolar lines are parallel to the  $x'$  direction (Fig. 4.12, see also section 4.4.2.2).

The importance of epipolar geometry lies in the fact that, assuming an error-free ray intersection, an image point  $P''$  in the right image, corresponding to  $P'$  in the left image, must lie on the epipolar plane and hence on the epipolar line  $k''$ . Thus the search space for matching corresponding points can be significantly reduced. Assuming an additional object point  $Q$  lying on ray  $O'P$  it is obvious that the difference in distance (depth) between  $Q$  and  $P$  results in a parallax along the epipolar line  $k''$ . In the normal case of stereo photogrammetry the parallax is purely in the  $x'$  direction (x-parallax or horizontal parallax).



**Figure 4.11** Epipolar plane for convergent images



**Figure 4.12** Epipolar plane for normal case of stereo photogrammetry

If the orientation parameters are known, the position of the epipolar line  $k''$  corresponding to  $P'$  (or vice versa) can be calculated. Given an arbitrary image point  $P'$ , and with projection equations (4.6), two points  $P$  and  $Q$  on the ray  $r'$  can be calculated for two different arbitrary values of scaling factor  $m$ . The XYZ coordinates of points  $P$  and  $Q$  can subsequently be projected into the right image using the collinearity equations (4.8). The epipolar line  $k''$  is then defined by the straight line containing image points  $P''$  and  $Q''$ .

The epipolar lines can also be calculated from the parameters of relative orientation which are derived below (see following section).

#### 4.2.5.3 Relative orientation

Relative orientation describes the translation and rotation of one image with respect to its stereo partner in a common local model coordinate system. It is the first stage in the two-step orientation of a stereo image pair (see Fig. 4.9).

The numerical method of relative orientation can be easily developed for the following case. A local three-dimensional model coordinate system xyz is located in the perspective centre of the first (left) image and oriented parallel to its image coordinate system (Fig. 4.13). The parameters of exterior orientation of the left image with respect to the model coordinate system are therefore already given:

$$\begin{aligned}x_{01} &= 0 & \omega_1 &= 0 \\y_{01} &= 0 & \varphi_1 &= 0 \\z_{01} &= 0 & \kappa_1 &= 0\end{aligned}\tag{4.30}$$

Now the second (right) image is oriented in the model coordinate system by 3 translations and 3 rotations:

$$\begin{aligned}x_{02} &= bx & \omega_2 & \\y_{02} &= by & \varphi_2 & \\z_{02} &= bz & \kappa_2 &\end{aligned}\tag{4.31}$$

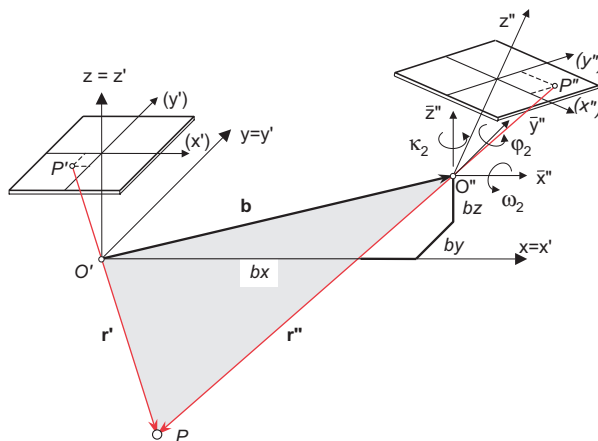


**Figure 4.13** Model coordinate system and relative orientation (left image fixed)

The base space vector  $\mathbf{b}$  between the perspective centres  $O'$  and  $O''$  is defined by the base components  $bx$ ,  $by$  and  $bz$ . It is stated in the following section that the condition for correct relative orientation is that all pairs of homologous rays must be coplanar with the base. Suppose that the right hand perspective centre is displaced along the base line towards  $O'$  and that the image is not rotated. It is clear that the homologous rays of Fig. 4.13 will still be coplanar with the base and that they will intersect in a point lying on the line between  $O'$  and  $P'$ . Consideration of similar triangles shows that the scale of the model will be directly proportional to the length of the base. That is to say, the model coordinate system can be scaled by an arbitrary factor depending on our choice of base length. One of the base components is therefore set to a constant value, commonly

$$bx = 1$$

Five independent elements  $by$ ,  $bz$  and  $\omega_2$ ,  $\varphi_2$ ,  $\kappa_2$  therefore remain for the definition of the relative orientation.

For an alternative formulation of the relative orientation, the x axis of the model coordinate system is defined by the stereo base and the origin of the system is located in the left hand perspective centre. The parameters of exterior orientation in the model coordinate system are then given by:

$$\begin{array}{ll} x_{01} = 0 & \omega_1 \\ y_{01} = 0 & \varphi_1 \\ z_{01} = 0 & \kappa_1 \end{array}$$

$$\begin{array}{ll} x_{02} = bx & \omega_2 = 0 \\ y_{02} = 0 & \varphi_2 \\ z_{02} = 0 & \kappa_2 \end{array}$$

The five elements to be determined are here expressed by five independent rotation angles  $\omega_1$ ,  $\varphi_1$ ,  $\kappa_1$  and  $\omega_2$ ,  $\varphi_2$ ,  $\kappa_2$ . Instead of  $\omega_1$  (rotation about x axis) or  $\omega_2$  a differential  $\omega$  rotation may be used as an alternative. The scale is again set to an arbitrary value, normally with  $bx = 1$ .

#### *Coplanarity constraint*

The computational solution of relative orientation utilises the condition that an object point  $P$  and the two perspective centres  $O'$  and  $O''$  must lie in a plane (coplanarity constraint). This is the epipolar plane defined by vectors  $\mathbf{b}$ ,  $\mathbf{r}'$  and  $\mathbf{r}''$ , which also contains the image points  $P'$  and  $P''$ .

The coplanarity constraint is only fulfilled if rays  $\mathbf{r}'$  and  $\mathbf{r}''$  strictly intersect in object point  $P$  i.e. if the positions of image points  $P'$  and  $P''$ , as well as the orientation parameters, are free of error. For each pair of homologous image points one coplanarity constraint equation can be derived. Consequently, in order to calculate the five unknown orientation parameters, a minimum of five homologous points (tie points) with measured image coordinates is required. The constraint is equivalent to the minimisation of y-parallaxes at all observed points  $P$ . The term y-parallax is defined by equation (4.39).

The coplanarity constraint can be expressed using the scalar triple product of the three vectors. They lie in a plane if the volume of the parallelepiped that they define is zero:

$$(\mathbf{b} \times \mathbf{r}') \cdot \mathbf{r}'' = 0 \quad (4.32)$$

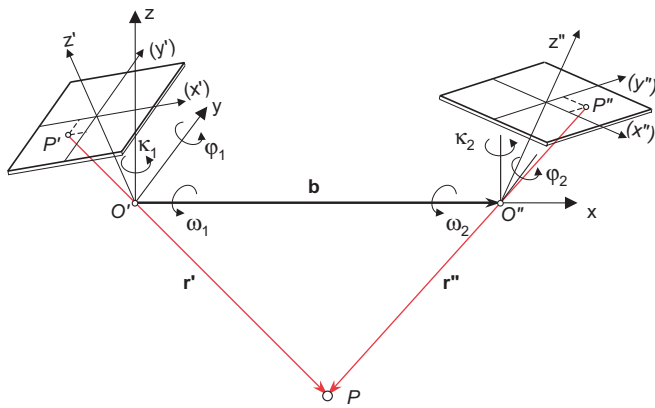


**Figure 4.14** Model coordinate system with base defining the x axis

Alternatively, equation (4.32) can be expressed by the determinant of the following matrix. The base vector  $\mathbf{b}$  is given by the three base components, the image vector  $\mathbf{r}'$  is given by the image coordinates in the left image and the image vector  $\mathbf{r}''$  is given by the image coordinates of the right image, transformed by the relative rotation parameters.

$$\Delta = \begin{vmatrix} 1 & x' & \bar{x}'' \\ by & y' & \bar{y}'' \\ bz & z' & \bar{z}'' \end{vmatrix} = 0 \quad (4.33)$$

$$\mathbf{b} \quad \mathbf{r}' \quad \mathbf{r}''$$

where  $\begin{bmatrix} \bar{x}'' \\ \bar{y}'' \\ \bar{z}'' \end{bmatrix} = \begin{bmatrix} a_{11} & a_{12} & a_{13} \\ a_{21} & a_{22} & a_{23} \\ a_{31} & a_{32} & a_{33} \end{bmatrix} \begin{bmatrix} x'' \\ y'' \\ z'' \end{bmatrix}$

$$\mathbf{r}'' = \mathbf{Ax}''$$

Here  $\mathbf{A}$  is the rotation matrix of the right hand image, so that the coefficients  $a_{11}, a_{12} \dots$  are functions of the rotation angles  $\omega_2, \varphi_2, \kappa_2$ . Different principal distances for both images may be introduced as  $z' = -c_1$  and  $z'' = -c_2$ . For each measured tie point  $P_i$  one observation equation can be established using equation (4.33). An elegant discussion of the problem of relative orientation is given in (Thompson 1959).

#### Calculation

The calculation of the five elements of relative orientation follows the principle of least-squares adjustment (see section 2.3.2.2). Based on the coplanarity condition the following correction equation can be set up for each tie point:

$$v_\Delta = \frac{\partial \Delta}{\partial by} dy + \frac{\partial \Delta}{\partial bz} dz + \frac{\partial \Delta}{\partial \omega_2} d\omega_2 + \frac{\partial \Delta}{\partial \varphi_2} d\varphi_2 + \frac{\partial \Delta}{\partial \kappa_2} d\kappa_2 + \Delta^0 \quad (4.34)$$

In the case of approximately parallel viewing directions, the initial values required for linearisation are as follows:

$$by^0 = bz^0 = \omega_2^0 = \varphi_2^0 = \kappa_2^0 = 0 \quad (4.35)$$

$\Delta^0$  is the volume of the parallelepiped calculated from the initial values. The difference coefficients can again easily be computed using the following determinants (computation scheme according to Albertz and Kreiling 1989):

$$\begin{aligned} \frac{\partial \Delta}{\partial by} &= \begin{vmatrix} 0 & x' & \bar{x}'' \\ 1 & y' & \bar{y}'' \\ 0 & z' & \bar{z}'' \end{vmatrix} \quad \frac{\partial \Delta}{\partial bz} = \begin{vmatrix} 0 & x' & \bar{x}'' \\ 0 & y' & \bar{y}'' \\ 1 & z' & \bar{z}'' \end{vmatrix} \\ \frac{\partial \Delta}{\partial \omega_2} &= \begin{vmatrix} 1 & x' & 0 \\ by & y' & -\bar{z}'' \\ bz & z' & \bar{y}'' \end{vmatrix} \quad \frac{\partial \Delta}{\partial \varphi_2} = \begin{vmatrix} 1 & x' & -\bar{y}'' \sin \omega_2 + \bar{z}'' \cos \omega_2 \\ by & y' & \bar{x}'' \sin \omega_2 \\ bz & z' & -\bar{x}'' \cos \omega_2 \end{vmatrix} \\ \frac{\partial \Delta}{\partial \kappa_2} &= \begin{vmatrix} 1 & x' & -\bar{y}'' \cos \omega_2 \cos \varphi_2 - \bar{z}'' \sin \omega_2 \cos \varphi_2 \\ by & y' & \bar{x}'' \cos \omega_2 \cos \varphi_2 - \bar{z}'' \sin \varphi_2 \\ bz & z' & \bar{x}'' \sin \omega_2 \cos \varphi_2 + \bar{y}'' \sin \varphi_2 \end{vmatrix} \end{aligned} \quad (4.36)$$

The approximate values are iteratively improved by the adjusted corrections until there is no significant change.

Here the standard deviation of unit weight  $s_0$  provides little information about achieved accuracy because the volumes of the parallelepipeds are used as observations instead of the measured image coordinates. Residuals of the estimated orientation elements result in skew intersection of the rays  $\mathbf{r}'$  and  $\mathbf{r}''$ , thus generating y-parallaxes in model space. It is therefore advantageous to analyse the quality of relative orientation using the computed model coordinates.

#### Model coordinates

The relationship between image and model coordinates can be expressed by the following ratios:

$$\begin{aligned} \frac{x}{x'} = \frac{y}{y'} = \frac{z}{z'} = \lambda &\quad : \text{scale factor of left image for a particular point} \\ \frac{x-bx}{\bar{x}''} = \frac{y-by}{\bar{y}''} = \frac{z-bz}{\bar{z}''} = \mu &\quad : \text{scale factor for right image for the same point} \end{aligned} \quad (4.37)$$

Elimination of model coordinates gives the scale factors as:

$$\lambda = \frac{bx\bar{z}'' - bz\bar{x}''}{x'\bar{z}'' - z'\bar{x}''} \quad \mu = \frac{bxz' - bzx'}{x'\bar{z}'' - z'\bar{x}''} \quad (4.38)$$

and hence the model coordinates

$$x = \lambda x' \quad z = \lambda z' \quad (4.39)$$

$$y_1 = \lambda y' \quad y_2 = by + \mu \bar{y}''$$

$$y = \frac{y_1 + y_2}{2} \quad py = y_2 - y_1$$

Due to uncertainties in measurement there are two solutions for the model coordinates in the  $y$  direction i.e. corresponding rays are skew and do not exactly intersect, which results in  $y$ -parallax  $py$ .

Additional arbitrary homologous image points can be measured in the relatively oriented model, and transformed into model coordinates  $xyz$  using equations (4.39). They describe a three-dimensional object surface, correctly shaped, but at an arbitrarily defined scale resulting from our arbitrary choice,  $bx = 1$ . The transformation of model coordinates into a global object coordinate system at true scale is performed by absolute orientation (see section 4.2.5.4). The set of formulas (4.39) describe a special case of spatial intersection (see also sections 4.4.2.2, 4.4.3.1).

#### *Calculation of epipolar lines*

The equation of the epipolar line  $k''$  in the right-hand image is given in parametric form as:

$$\mathbf{k}'' = \mathbf{p}'' + t(\mathbf{q}'' - \mathbf{p}'') \quad (4.40)$$

Here  $\mathbf{k}''$  is the locus of points on the straight line through image points  $\mathbf{p}''$  and  $\mathbf{q}''$ , which correspond to the arbitrary model points  $P$  and  $Q$  lying on the ray  $\mathbf{r}'$  (Fig. 4.11). If the parameters of relative orientation (exterior orientation of both images in the model coordinate system) are inserted into the collinearity equations (4.8), the image coordinates in the right-hand image are obtained:

$$\begin{aligned} x''_i &= z'' \frac{r_{11}(x_i - bx) + r_{21}(y_i - by) + r_{31}(z_i - bz)}{r_{13}(x_i - bx) + r_{23}(y_i - by) + r_{33}(z_i - bz)} \\ y''_i &= z'' \frac{r_{12}(x_i - bx) + r_{22}(y_i - by) + r_{32}(z_i - bz)}{r_{13}(x_i - bx) + r_{23}(y_i - by) + r_{33}(z_i - bz)} \end{aligned} \quad (4.41)$$

Here  $r_{ij}$  are the elements of the rotation matrix of  $\omega_2$ ,  $\varphi_2$ ,  $\kappa_2$ . The perspective centre  $O'$  can be used in place of point  $P$

$$\begin{aligned} x_P &= 0 \\ P : \quad y_p &= 0 \\ z_p &= 0 \end{aligned}$$

Point  $Q$  is given by multiplication of the image vector  $\mathbf{x}'$  by an arbitrary scaling factor  $\lambda$ .

$$\begin{aligned} x_Q &= -\lambda x' \\ Q : \quad y_Q &= -\lambda y' \\ z_Q &= -\lambda z' \end{aligned}$$

By inserting the model coordinates into equations (4.41) the image coordinates of points  $\mathbf{p}''$  and  $\mathbf{q}''$  are obtained and hence the straight line equation of the epipolar line. Due to unavoidable measurement errors, the search for point  $P''$ , the homologous point to  $P'$ , should not be done along straight line  $k''$  but within a narrow band either side of this line.

#### *Calculation of normalised images*

Digitised convergent stereo images can be rectified in order to correspond to the normal case of stereo photogrammetry. Stereopairs which have been normalised in this way are also referred to as epipolar stereopairs. After rectification they are suitable for ocular stereo viewing. In addition

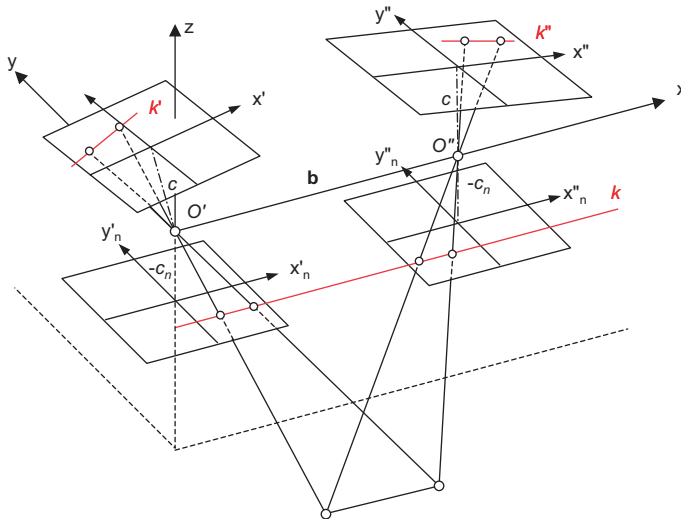


**Figure 4.15** On the geometry of normalised images

the epipolar lines are parallel to the  $x'$  direction, enabling simplified algorithms for stereo image matching to be applied (see section 5.5.3.1).

Fig. 4.15 illustrates the spatial position of normalised images with respect to the stereo model. With given exterior orientations for both images (e.g. in model coordinate system xyz), three-dimensional image coordinates  $x'_n, y'_n, -c_n$  in the normalised images can be transformed using equation (4.8) into the image coordinates  $x', y'$  of the original image (and analogously for the second image). Rectification is performed when, for all points in the images, the grey level of the original image  $g'(x', y')$  is copied to position  $x'_n, y'_n$  in the normalised image (see section 5.3).

#### *Quality of relative orientation*

The existence of y-parallax  $py$  (defined in 4.39) at a point in the model indicates failure of homologous rays to intersect at that point. The y-parallaxes, considered over the whole model, may be used as a measure of the quality of relative orientation; y-parallax at photo scale gives a normalised figure.

If the y-parallax at a point  $i$  in the model is  $py_i$ , then the y-parallax at photo scale may be taken as

$$py_{ip} = \frac{z'}{z_i} py_i \quad (4.42)$$

Assuming that  $by$  and  $bz$  are small compared to  $bx$ , the following expression gives a measure of the quality of the relative orientation:

$$s_{py_p} = \frac{1}{n} \sqrt{\sum_{i=1}^n py_{ip}^2} \quad (4.43)$$

The intersection angle  $\alpha$  of homologous image rays is the angle between the two spatial vectors  $\mathbf{r}'$  and  $\mathbf{r}''$  where:

$$\cos \alpha = \frac{\mathbf{r}'^T \mathbf{r}''}{|\mathbf{r}'||\mathbf{r}''|} \quad (4.44)$$

Taking all  $n$  tie points into account, the mean intersection angle can be calculated:

$$\bar{\alpha} = \frac{1}{n} \sum_n \alpha \quad (4.45)$$

The mean intersection angle approximately describes the ratio of the stereo base  $b$  to the mean object distance  $h$ . Not only will the computation of the relative orientation be optimum but also the accuracy of point determination in the model will be optimum when rays intersect at or near right angles (Fig. 4.16):

$$\tan \frac{\bar{\alpha}}{2} \approx \frac{b}{2h} \quad (4.46)$$

The quality of relative orientation depends on the following criteria:

- Accuracy of image coordinates

The accuracy of image coordinates depends partly on the measuring accuracy of the instrument and partly on the ability to identify matching points in both images. Image patches with poor structure can be matched less accurately than areas with a significant grey level structure, regardless of the image processing method (visual interpretation or digital image matching).

- Number and distribution of tie points in model space

Tie points should be chosen in model space to ensure a robust geometric link between both images. A point distribution as recommended by von Gruber is particularly suitable. This has a tie point in each corner of the model space and one in the middle of each long side. This distribution is strictly possible only in the normal case (Fig. 4.17).

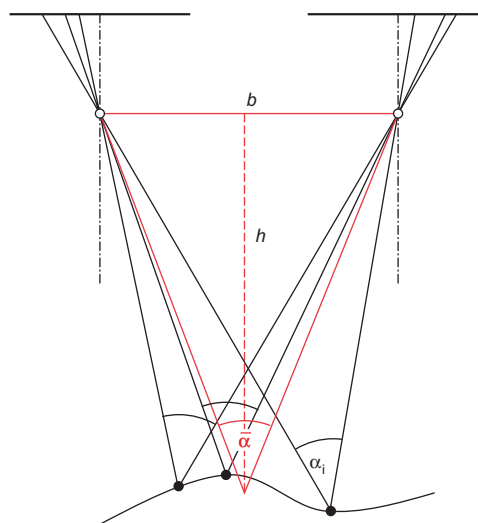
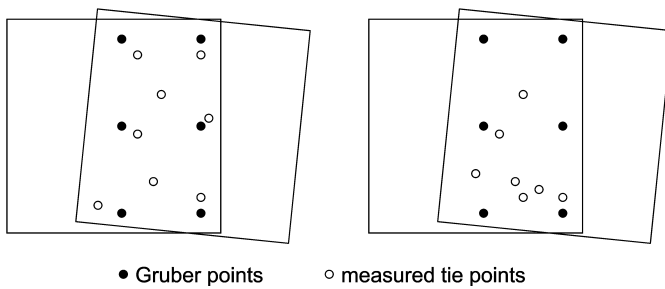


Figure 4.16 Mean intersecting angle



**Figure 4.17** Good and bad distribution of tie points in model space

If object structure, for example containing large homogeneous areas, does not allow an optimum distribution of homologous points, then uncontrollable model errors may occur in the regions not covered. If all tie points lie on a common straight line, the resulting normal system of equations becomes singular.

To properly control the relative orientation, at least 8–10 well distributed tie points should be measured.

- Base-to-height ratio

If the base of the stereo model is small relative to object distance (height) then ray intersection angles are poor. The parameters of relative orientation are then determined with greater uncertainty. As mentioned above, an optimal configuration is achieved with intersection angles of around 90 degrees.

- Distribution of tie points in object space

There are a few exceptional cases where singular or weakly conditioned normal equations occur, even though there is a good point distribution in model space. Amongst other cases this applies to the danger cylinder, where the object points used as tie points and the perspective centres of both images lie on a common cylindrical surface (Fig. 4.18). This effect can also occur where object surfaces have small curvatures and the imaging lens has a long focal length. The same problem exists for the space resection, if the image to be oriented is also located on a danger surface (Thompson 1966).

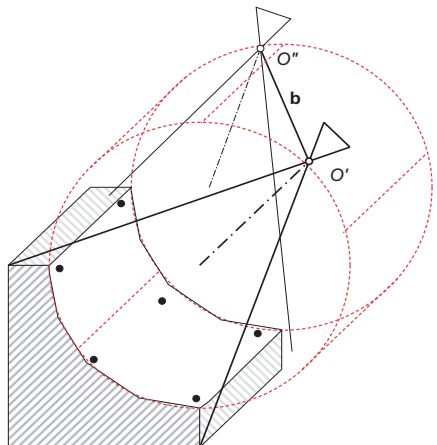


**Figure 4.18** Danger cylinder above a curved surface

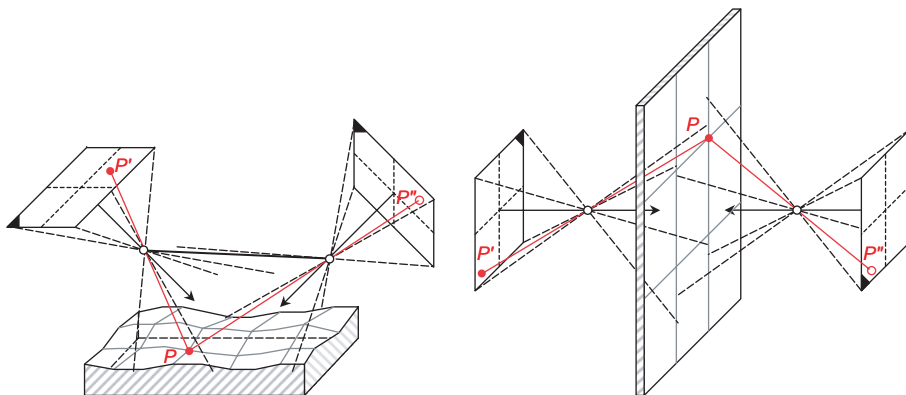


**Figure 4.19** Convergent image pair configurations

#### *Special cases of relative orientation*

The method of relative orientation is widely used for traditional stereo image analysis on analytical stereo instruments. These applications typically have parallel imaging directions which permit stereoscopic viewing (as shown in Fig. 4.13). The orientation elements are then relatively small so that initial values for the iterative adjustment can be zero.

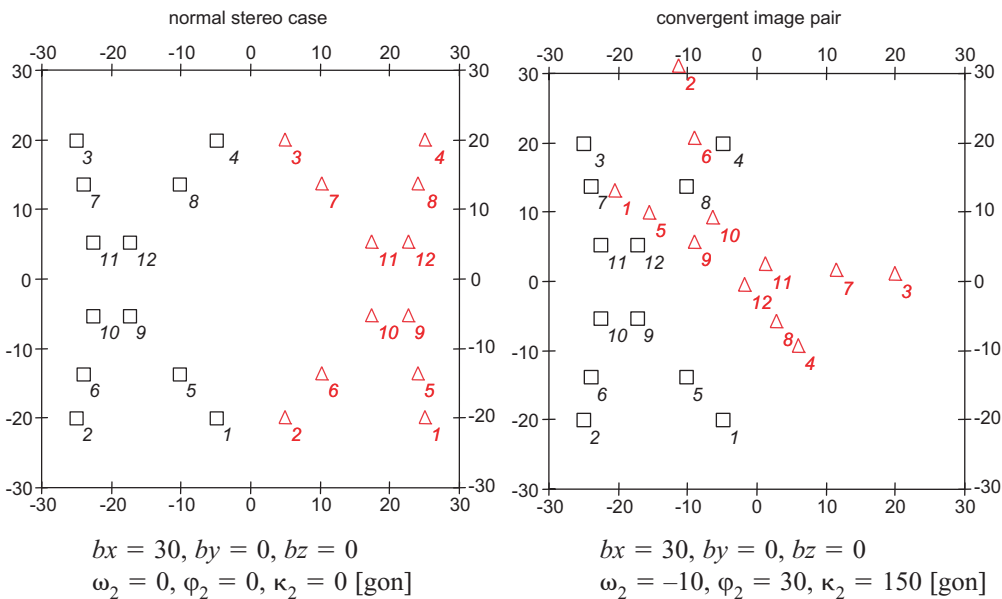
Close-range photogrammetry, in contrast, often involves arbitrary convergent multi-image configurations. For this case relative orientation is not used as the actual orientation method but only as one step in the calculation of approximate values for the subsequent bundle adjustment (see section 4.3.4.1). Here the image pairs may have orientation values that differ significantly from those of the normal case (examples in Fig. 4.19).

Fig. 4.20 shows the distribution in image space of 12 homologous points in a stereo pair, in which the right hand image has significant tilts with respect to the left hand image.

It is not possible to define approximate values for the relative orientation of arbitrarily oriented images according to equation (4.35). Instead the methods of spatial similarity transformation (see section 2.2.2.2) or space resection (see section 4.2.3.1) can be applied. For these methods tie points require 3D object coordinates which may be calculated by transforming image coordinates in both images by an approximate scale factor.

In multi-image applications it is possible that two or more images are exposed at the same point but with different orientations. It is also possible that images are located behind one another on the same viewing axis. In these and similar cases both images cover a common model space which does not provide distinct intersections at object points (Fig. 4.21). The calculation of relative orientation then leads to poor results or fails completely. Such images can, of course, be included with others in a multi-image bundle adjustment.

A further special case occurs for relative orientation using images of strictly planar surfaces. This happens often in close-range applications, for example in the measurement of flat façades or building interiors. In this case only 4 tie points are required because both bundles of rays can be related to each other by an affine transformation with 8 parameters. In order to solve the adjustment problem, the planarity of the object surface can be handled by an additional constraint equation. This constraint can replace one of the required coplanarity conditions so that only four tie points are necessary.



**Figure 4.20** Image point distribution for different orientations  
△ right image, □ left image

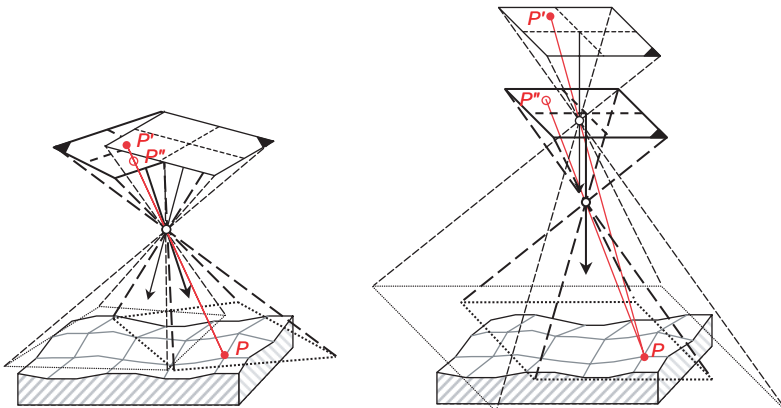


**Figure 4.21** Overlapping image pairs with insufficient spatial ray intersections

#### 4.2.5.4 Absolute orientation

##### Mathematical model

Absolute orientation describes the transformation of the local model coordinate system xyz, resulting from a relative orientation with arbitrary position, rotation and scale, into the object coordinate system XYZ via reference points. Reference points are object points measured in the model coordinate system which have one or more known coordinate components in object space (e.g. XYZ, XY only or Z only). The reference points can be identical to the tie points already used for relative orientation, or they can be measured subsequently as model points in the relatively oriented model.

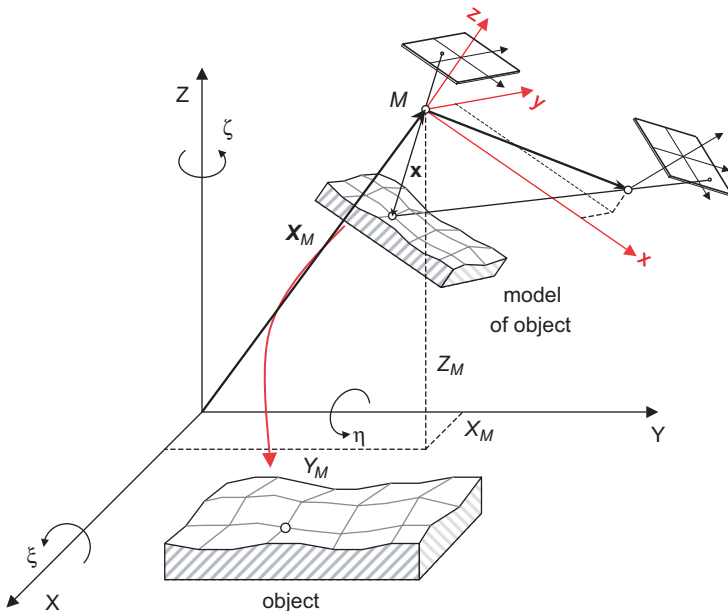


Figure 4.22 Absolute orientation

Absolute orientation consists of a spatial similarity transformation with three translations, three rotations and one scaling factor as described in equation (2.30) (see section 2.2.2.2). In order to solve the system of equations a minimum of seven suitable point elements are required, for example taken from three spatially distributed XYZ reference points.

Fig. 4.22 illustrates the transformation of the model coordinate system xyz with origin at  $M$ , into the object coordinate system, XYZ. The coordinates of  $M$  in the XYZ system are  $\mathbf{X}_M$ . The rotation matrix  $\mathbf{R}$  is a function of the three rotation angles  $\xi, \eta, \zeta$  about the axes XYZ. The transformation for a model point with coordinates xyz (vector  $\mathbf{x}$ ) is given by:

$$\begin{aligned}\mathbf{X} &= \phi(X_M, Y_M, Z_M, m, \xi, \eta, \zeta, x, y, z) \\ &= \mathbf{X}_M + m\mathbf{Rx}\end{aligned}\quad (4.47)$$

or

$$\begin{bmatrix} X \\ Y \\ Z \end{bmatrix} = \begin{bmatrix} X_M \\ Y_M \\ Z_M \end{bmatrix} + m \begin{bmatrix} r_{11} & r_{12} & r_{13} \\ r_{21} & r_{22} & r_{23} \\ r_{31} & r_{32} & r_{33} \end{bmatrix} \begin{bmatrix} x \\ y \\ z \end{bmatrix}$$

where  $m$  is a scalar.

Equations (4.47) are non-linear and will be solved in the usual way; if there is redundancy the solution will be based on a least-squares adjustment (see section 2.3.2.2) in which each coordinate component of a reference point provides one linearised correction equation.

#### *Definition of the datum*

In many close-range applications, 3D reference points (full reference points) are available. Each reference point therefore provides three correction equations. In aerial photogrammetry it is

possible that some reference points have only known plan position (XY) and others only height (Z), resulting in a reduced set of correction equations. In order to solve the absolute orientation, at least 2 X coordinates, 2 Y coordinates and 3 Z coordinates must be available (see also section 4.3.3.2).

The reference points should be well distributed over the object space to be transformed. If all reference points lie on or near a common straight line, a singular or weak system of equations results.

#### *Calculation of exterior orientations*

From the parameters of relative and absolute orientation for an image pair, the exterior orientation parameters of each image can be calculated.

The position of the perspective centre  $\mathbf{X}_{0_i}$  of an image  $i$  is derived from the origin of the model coordinate system  $\mathbf{X}_M$  and the transformed components of the base  $\mathbf{b}$ :

$$\mathbf{X}_{0_i} = \mathbf{X}_M + m\mathbf{R}_{\xi\eta\zeta}\mathbf{b}_i \quad (4.48)$$

For the left hand image ( $i = 1$ ) the base components are zero; hence  $\mathbf{X}_{0_1} = \mathbf{X}_M$ .

In order to calculate the rotation matrix of image  $i$ ,  $\mathbf{R}_{i_{\omega\varphi\kappa}}$ , with respect to the object system, the rotation matrix  $\mathbf{A}_{\omega_i\varphi_i\kappa_i}$  of the relative orientation is pre-multiplied by the rotation matrix of  $\mathbf{R}_{\xi\eta\zeta}$  the absolute orientation:

$$\mathbf{R}_{i_{\omega\varphi\kappa}} = \mathbf{R}_{\xi\eta\zeta}\mathbf{A}_{\omega_i\varphi_i\kappa_i} \quad (4.49)$$

After absolute orientation, object coordinates are available for the model points. As an alternative, therefore, the parameters of exterior orientation can also be determined by space resection using the transformed model coordinates in object space.

## 4.3 Bundle triangulation

### 4.3.1 General remarks

#### 4.3.1.1 Objectives

Bundle triangulation (bundle block adjustment, multi-image triangulation, multi-image orientation) is a method for the simultaneous numerical fit of an unlimited number of spatially distributed images (bundles of rays). It makes use of photogrammetric observations (measured image points), survey observations and an object coordinate system (Fig. 4.23). Using tie points, single images are merged into a global model in which the object surface can be reconstructed in three dimensions. The connection to a global object coordinate system can be provided by a minimum number of reference points so that larger areas without reference points can be bridged by multi-image sub-sets. The most important geometric constraint is that all corresponding (homologous) image rays should intersect in their corresponding object point with minimum inconsistency.

In an over-determined system of equations, an adjustment technique estimates 3D object coordinates, image orientation parameters and any additional model parameters, together with related statistical information about accuracy and reliability. Since all observed (measured) values, and all unknown parameters of a photogrammetric project are taken into account within one simultaneous calculation, the bundle triangulation is the most powerful and accurate method of image orientation and point determination in photogrammetry.

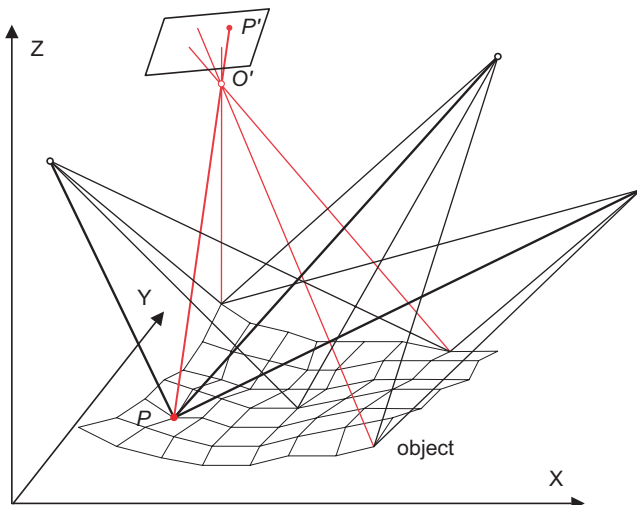


**Figure 4.23** Multi-image triangulation

#### 4.3.1.2 Development

The potential power and accuracy of analytical photogrammetry had been recognised by surveyors long before the arrival of electronic computers; for example, in the years immediately before WWII the Ordnance Survey of Great Britain began to develop methods of computation for air survey based on image coordinates measured in the Cambridge Stereocomparator (Shewell 1953). In the 1950s many mapping organisations were experimenting with the new automatic computers; Tewinkel (1958) was able to publish a paper on the “future of analytical aerial triangulation”. But it was the ballistic missile industry which gave the impetus for the development of bundle triangulation, today the dominant technique for triangulation in close range photogrammetry (Schmid 1955, 1958, 1959).

Bundle triangulation can be understood as the generalised form of space resection with inclusion of additional unknowns for further images and object points (new points). The practical problems in bundle triangulation do not lie in the mathematical formulation but in the following areas:

- solution of large systems of normal equations (up to a few thousand unknowns)
- generation of approximate values for the unknowns
- detection and elimination of gross data errors

The development of practical bundle adjustments is closely related to increases in computing power. Programs for aerial photogrammetry have largely been developed independently of those for close-range applications.

The triangulation of aerial images is characterised mainly by

- predominant use of regular strip arrangements of images (Fig. 4.24)
- advantageous structure of normal system of equations
- easier generation of approximate values (e.g. rotations approximately zero)
- large numbers of images and object points
- use of only one calibrated metric camera.

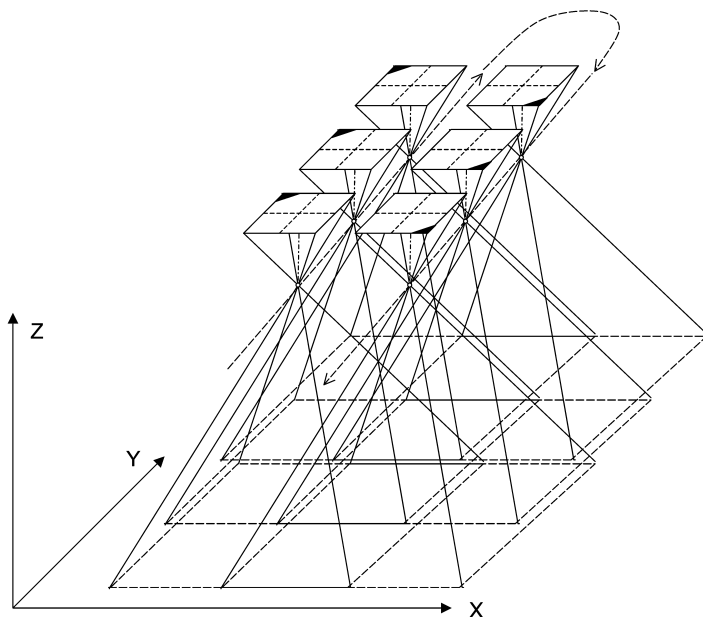


**Figure 4.24** Image configuration for aerial photogrammetry

In contrast, most close-range photogrammetry is characterised by:

- irregularly arranged, arbitrary and often unfavourable image configurations (Fig. 4.25)
- more complex structure of normal system of equations
- arbitrarily oriented object coordinate systems
- combined adjustment of survey observations and conditions
- (several) imaging systems to be calibrated simultaneously

Since the early 1980s the bundle adjustment has been accepted in all areas of photogrammetry. As a result of diverse requirements and applications there are many different bundle adjustment packages on the market. As examples, for aerial applications there are

- PAT-B (PAT-M) (University of Hanover, Germany) (Ackermann *et al.* 1970)
- BLUH (University of Stuttgart, Germany) (Jacobsen 1982)
- ORIMA (Leica Geosystems, Switzerland)

and for close-range photogrammetry

- BINGO (GIP, Germany) (Kruck 1983)
- STARS (GSI, USA) (Fraser and Brown 1986)
- CAP ( $K^2$  Photogrammetry, Germany) (Hinsken 1989)
- ORIENT (Technical University of Vienna, Austria) (Kager 1989)
- PHIDIAS/BUN (PHOCAD, Germany) (Benning and Schwermann 1997)
- AX.ORI (AXIOS 3D, Germany) (Hemken and Luhmann 2002)

Particularly since its introduction for close-range use (Brown 1976), the method of bundle adjustment has considerably widened the application area as a result of its ability to handle almost arbitrary image configurations with few restrictions on the image acquisition systems.

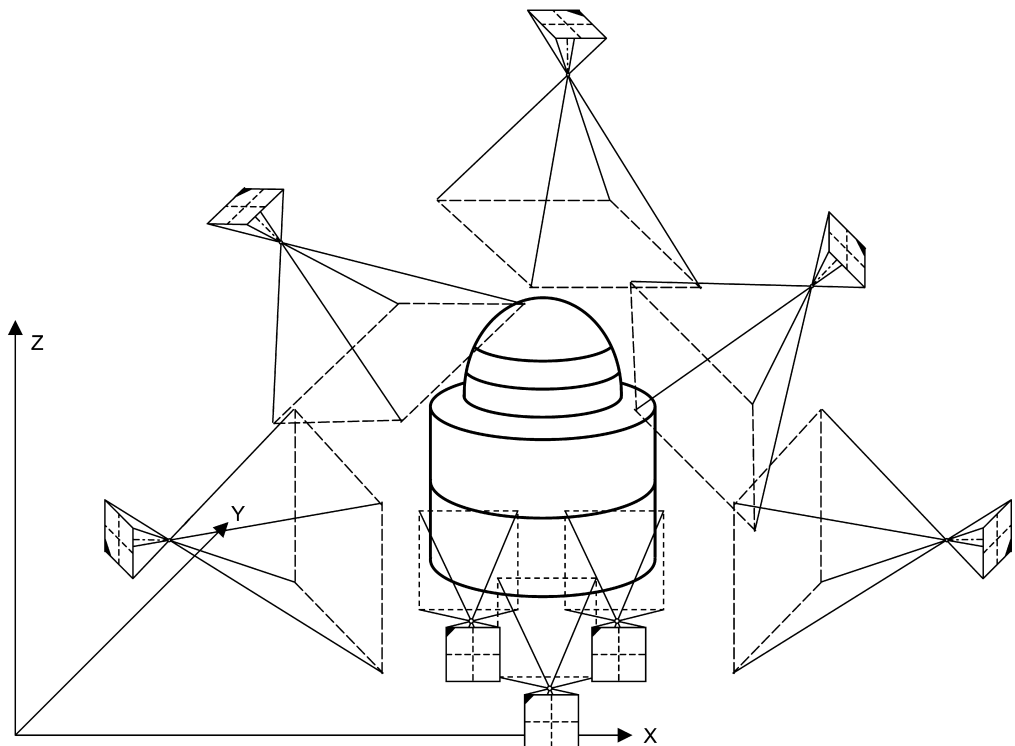


**Figure 4.25** Arbitrary close-range image configuration

#### 4.3.1.3 Data flow

Fig. 4.26 shows the principle data flow for a bundle adjustment process. Input data for bundle adjustment are typically photogrammetric image coordinates generated by manual or automatic (digital) image measuring systems. Each measured image point is stored together with a unique point identifier and the corresponding image number (Fig. 4.27). This is sufficient to reconstruct the three-dimensional shape of the object surface, as represented by the measured object points.

Additional information in the object space (e.g. measured distances, angles, points, straight lines, planes) can also be taken into account. They provide the definition of an absolute scale and the position and orientation of the object coordinate system (datum definition). This information is entered into the system as, for example, reference point files or additional observations (e.g. constraints between object points, see section 4.3.2.3).

In order to linearise the functional model, approximate values must be generated. For simpler image configurations they can be extracted from planning data or project sketches. The generation of approximate values for more complex configurations (larger number of images, arbitrary orientations) is performed by iterative calculation methods (see section 4.3.4).

The principal results of bundle adjustment are the estimated 3D coordinates of the object points. They are given in an object coordinate system defined by reference points or free net adjustment (see section 4.3.3.3).

In addition, the exterior orientation parameters of all images are estimated. These can be further used, for example, in analytical plotters or for subsequent spatial intersections computed

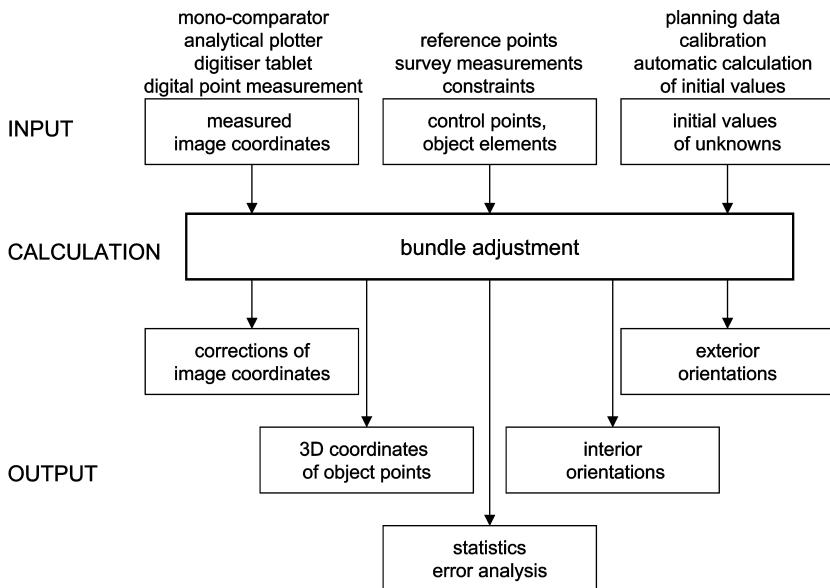


Figure 4.26 Data flow for bundle adjustment process

outside the bundle adjustment. The interior orientation parameters are estimated if the cameras are calibrated simultaneously within the adjustment.

In order to analyse the quality of the bundle adjustment, it is possible to calculate image coordinate residuals (corrections), standard deviations of object points and orientation data, correlations between parameters and reliability numbers for the detection of gross errors.

71	2	0.1160	16.9870	0.0017	0.0017	1	1
71	3	-13.1730	16.9660	0.0017	0.0017	1	1
71	5	-14.9590	-12.9070	0.0017	0.0017	1	1
71	6	0.0480	-12.9780	0.0017	0.0017	1	1
71	7	15.0780	-12.9560	0.0017	0.0017	1	1
71	8	14.1720	2.9660	0.0017	0.0017	1	1
71	9	0.7820	3.8060	0.0017	0.0017	1	1
71	10	-19.2630	-6.3410	0.0017	0.0017	1	1
72	2	10.9920	12.6640	0.0017	0.0017	1	1
72	3	1.6690	21.3820	0.0017	0.0017	1	1
72	5	-20.9080	2.6880	0.0017	0.0017	1	1
72	6	-11.8780	-7.6560	0.0017	0.0017	1	1
72	7	-1.9050	-18.9510	0.0017	0.0017	1	1
72	8	10.1100	-7.3660	0.0017	0.0017	1	1
72	9	0.9680	3.1290	0.0017	0.0017	1	1
72	10	-19.0800	9.7620	0.0017	0.0017	1	1
98	1	-0.0790	2.8960	0.0017	0.0017	1	1
98	2	-8.9560	0.6350	0.0017	0.0017	1	1
98	3	-20.5460	-2.3040	0.0017	0.0017	1	1
98	4	-12.3520	-7.4400	0.0017	0.0017	1	1
98	5	0.4360	-15.4010	0.0017	0.0017	1	1
98	6	13.2960	-8.6670	0.0017	0.0017	1	1
98	7	21.9810	-4.0580	0.0017	0.0017	1	1
98	8	9.2680	-0.0460	0.0017	0.0017	1	1
98	9	0.2590	-1.9800	0.0017	0.0017	1	1
98	10	-10.3580	-12.7920	0.0017	0.0017	1	1

Figure 4.27 Example of an image coordinate file  
with image number, point number, x', y', sx', sy', code1, code2

### 4.3.2 Mathematical model

#### 4.3.2.1 Adjustment model

The mathematical model of the bundle adjustment is based on the collinearity equations (see section 4.2.2).

$$\begin{aligned} x' &= x'_0 + z' \frac{r_{11}(X - X_0) + r_{21}(Y - Y_0) + r_{31}(Z - Z_0)}{r_{13}(X - X_0) + r_{23}(Y - Y_0) + r_{33}(Z - Z_0)} + \Delta x' \\ y' &= y'_0 + z' \frac{r_{12}(X - X_0) + r_{22}(Y - Y_0) + r_{32}(Z - Z_0)}{r_{13}(X - X_0) + r_{23}(Y - Y_0) + r_{33}(Z - Z_0)} + \Delta y' \end{aligned} \quad (4.50)$$

The structure of these equations allows the direct formulation of primary observed values (image coordinates) as functions of all unknown parameters in the photogrammetric imaging process. The collinearity equations, linearised at approximate values, can therefore be used directly as observation equations for a least-squares adjustment according to the Gauss-Markov model.

It is principally the image coordinates of homologous points which are used as observations<sup>1</sup>. The following unknowns are iteratively determined as functions of these observations:

- three-dimensional object coordinates for each new point  $i$  ( $u_p$ , 3 unknowns each)
- exterior orientation of each image  $j$  ( $u_p$ , 6 unknowns each)
- interior orientation of each camera  $k$  ( $u_C$ , 0 or  $\geq 3$  unknowns each)

The bundle adjustment therefore represents an extended form of the space resection (see section 4.2.3.1, equation (4.11)):

$$\begin{aligned} x'_i + vx'_i &= F(X_{0j}, Y_{0j}, Z_{0j}, \omega_j, \varphi_j, \kappa_j, x'_{0k}, y'_{0k}, c_k, \Delta x'_k, X_i, Y_i, Z_i) \\ y'_i + vy'_i &= F(X_{0j}, Y_{0j}, Z_{0j}, \omega_j, \varphi_j, \kappa_j, x'_{0k}, y'_{0k}, c_k, \Delta y'_k, X_i, Y_i, Z_i) \end{aligned} \quad (4.51)$$

where       $i$ : point index  
                $j$ : image index  
                $k$ : camera index

The non-linear equations (4.50) are linearised using a Taylor series expansion with approximate values for all unknowns inside the brackets in (4.51). Here the differential coefficients, already derived in formulas (4.14), are extended by the derivatives with respect to object coordinates:

$$\begin{aligned} \frac{\partial x'}{\partial X} &= -\frac{z'}{N^2} (r_{13}k_X - r_{11}N) & \frac{\partial y'}{\partial X} &= -\frac{z'}{N^2} (r_{13}k_Y - r_{12}N) \\ \frac{\partial x'}{\partial Y} &= -\frac{z'}{N^2} (r_{23}k_X - r_{21}N) & \frac{\partial y'}{\partial Y} &= -\frac{z'}{N^2} (r_{23}k_Y - r_{22}N) \\ \frac{\partial x'}{\partial Z} &= -\frac{z'}{N^2} (r_{33}k_X - r_{31}N) & \frac{\partial y'}{\partial Z} &= -\frac{z'}{N^2} (r_{33}k_Y - r_{32}N) \end{aligned} \quad (4.52)$$

<sup>1</sup> Additional observations such as object point coordinates, distances or directions are introduced in section 4.3.2.3.

If the interior orientation parameters are introduced as unknowns, the following differential coefficients are added:

$$\begin{aligned}\frac{\partial x'}{\partial x'_0} &= 1 & \frac{\partial y'}{\partial y'_0} &= 1 \\ \frac{\partial x'}{\partial c} &= -\frac{k_X}{N} & \frac{\partial y'}{\partial c} &= -\frac{k_Y}{N}\end{aligned}\quad (4.53)$$

Derivatives with respect to additional parameters of distortion are introduced in a similar way (see section 3.2.3.1). If linearisation is done numerically (see section 2.3.5.1), the projection equations and selected distortion model can be programmed directly into the source code and a rigorous differentiation is not required.

In standard form, the linearised model is given by

$$\mathbf{I}_{n,1} + \mathbf{v}_{n,1} = \mathbf{A}_{n,u u,1} \hat{\mathbf{x}}_{u,1}$$

and the corresponding system of normal equations is

$$\mathbf{N}_{u,u u,1} \hat{\mathbf{x}}_{u,1} + \mathbf{n}_{u,1} = \mathbf{0}_{u,1} \quad (4.54)$$

where

$$\mathbf{N}_{u,u} = \mathbf{A}_{u,n}^T \mathbf{P}_{n,n n,u} \mathbf{A}_{n,n n,u}$$

$$\mathbf{n}_{u,1} = \mathbf{A}_{u,n}^T \mathbf{P}_{n,n n,1} \mathbf{l}_{n,1}$$

The solution vector and its covariance matrix are estimated in an iterative adjustment:

$$\hat{\mathbf{x}}_{u,1} = \mathbf{Q}_{u,u u,1} \mathbf{n}_{u,1} = (\mathbf{A}_{u,n}^T \mathbf{P}_{n,n n,u} \mathbf{A}_{n,n n,u})^{-1} \mathbf{A}_{u,n}^T \mathbf{P}_{n,n n,1} \mathbf{l}_{n,1} \quad (4.55)$$

where

$$\mathbf{Q}_{u,u} = \mathbf{N}_{u,u}^{-1} \quad : \text{cofactor matrix}$$

$$\mathbf{K}_{u,u} = s_0^2 \mathbf{Q}_{u,u} \quad : \text{variance-covariance matrix}$$

#### 4.3.2.2 Normal equations

The number of unknowns in the adjustment system can be calculated as follows:

$$u = u_I n_{images} + u_P n_{points} + u_C n_{cameras} (+u_{datum})$$

where

$$u_I = 6, u_P = 3 \text{ and } u_C = 0 \dots \geq 3 \text{ (see above)}$$

In addition to the unknown orientation parameters and point coordinates, up to seven parameters are still required for datum definition. However, these can be eliminated by use of reference points or appropriate condition equations (datum defect, see section 4.3.3.1). Table 4.1 gives examples of the number of observations and unknowns for different image configurations.

**Table 4.1** Number of unknowns and observations for different image configurations

	Example 1 aerial setup (Fig. 4.28)	$u$	$u_{total}$	Example 2 closed loop set-up (Fig. 4.30)	$u$	$u_{total}$	Example 3 test field calibration (Fig. 7.12f)	$u$	$u_{total}$
$n_{images}$	8	6	48	16	6	96	8	6	48
$n_{points}$	14	3	42	25	3	75	13+6	3	57
$n_{ref. pts.}$	6	0	0	0	0	0	3 distances	0	0
$n_{cameras}$	1	0	0	1	5	5	1	7	7
$u_{datum}$	0		0	7		(7)	6		(6)
$u_{total}$			90	176	112				
$n_{obs}$			110			384			304
$r = n - u$			20			208			192

Example 1 represents a regular arrangement for aerial photogrammetry or the measurement of plane building façades (Fig. 4.28). The number of unknowns is  $u = 90$  if 8 images and 14 new points are assumed. The datum is defined by 6 reference points. For image acquisition a metric camera with known interior orientation is used.<sup>1</sup>

The connection matrix in Fig. 4.28 shows which point is measured in which image. The numbering of object points by measurement strip produces the typical diagonal structure of connections, which is also seen in the structure of the Jacobian matrix  $\mathbf{A}$  and the resulting normal equations (Fig. 4.29). In order to solve the normal equations, the order of observations can be further optimised by suitable sorting algorithms (see section 2.3.5.1).

On average each object point is measured in 2.8 images. Each measured image point provides 2 observations. Hence, with a total number of  $n = 110$  observations and a total redundancy number of  $r = n - u = 110 - 90 = 20$ , redundancy in the adjustment system is relatively weak.

Example 2 shows a typical closed loop image configuration for an object formed from a cylinder and hemisphere (Fig. 4.30). The object is recorded in two image acquisition sets which have a relative vertical shift (bottom set images 1 – 8, top set images 9 – 16). The object point on top of the dome appears in all images. As there are no reference points available, the datum defect of 7 is eliminated by a free net adjustment (see section 4.3.3.3). A non-metric camera is used so 5 parameters of interior orientation must be simultaneously calibrated. A total of 176 unknowns must therefore be estimated.

The corresponding connection matrix (Fig. 4.31) shows an average of 7.7 images for each object point. The redundancy is therefore much higher than in example 1 (aerial or façade arrangement). With 384 measured image coordinates, the total redundancy is  $r = 384 - 176 = 208$ .

However, the extent to which the adjustment system can be calculated, and the quality of the results, are less a question of total redundancy than the geometric configuration of the system.

<sup>1</sup> For a clearer illustration a reduced number of object points is used in this example.

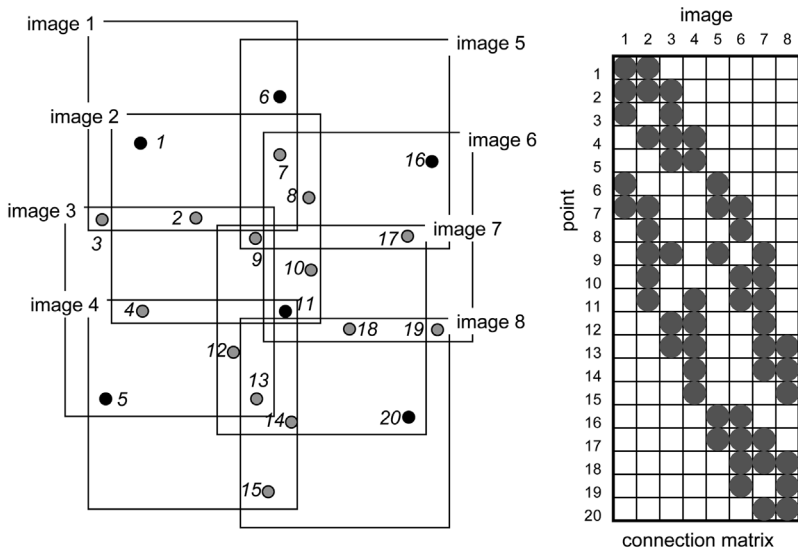


**Figure 4.28** Example 1: aerial or façade arrangement

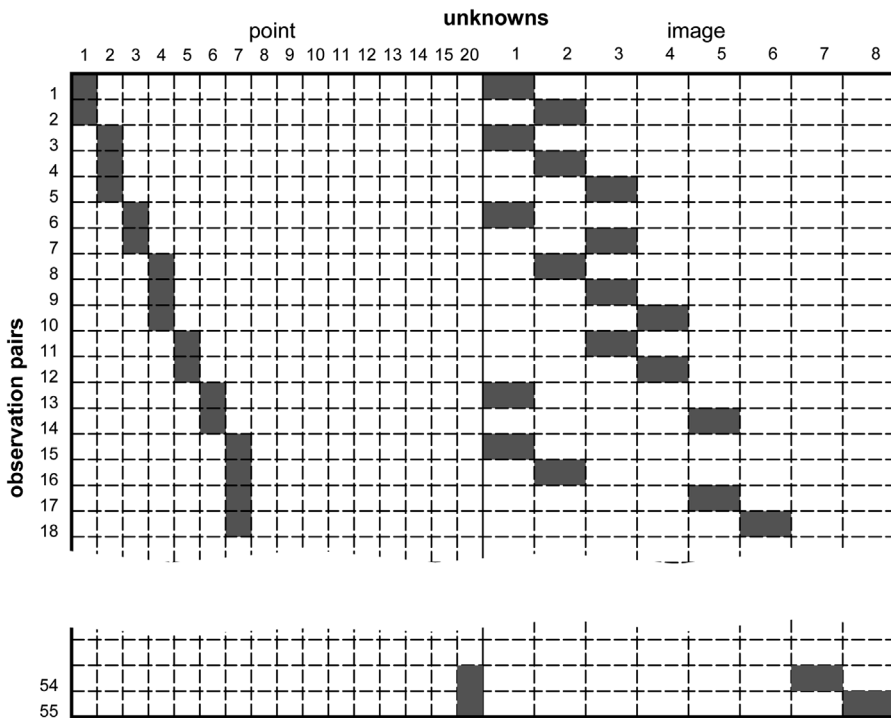


**Figure 4.29** Structure of design matrix A according to example 1 (Fig. 4.28)

Consider the arrangement of example 1 (Fig. 4.28) which allows for the determination of plane coordinates (parallel to the image plane) to an acceptable accuracy while a different point accuracy, which varies as a function of the base-to-height ratio, applies along the viewing direction

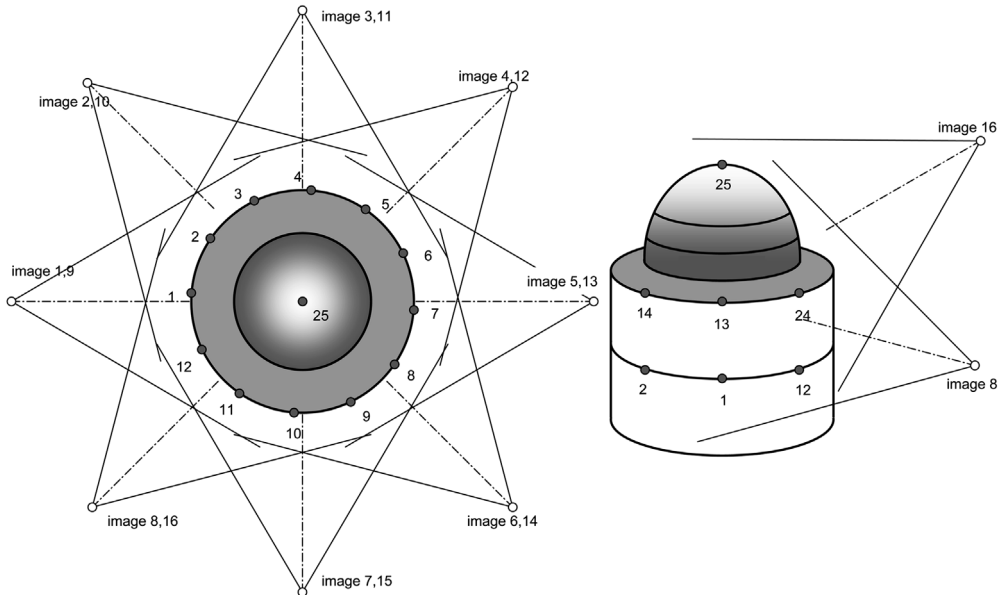


Figure 4.30 Example 2: closed loop configuration

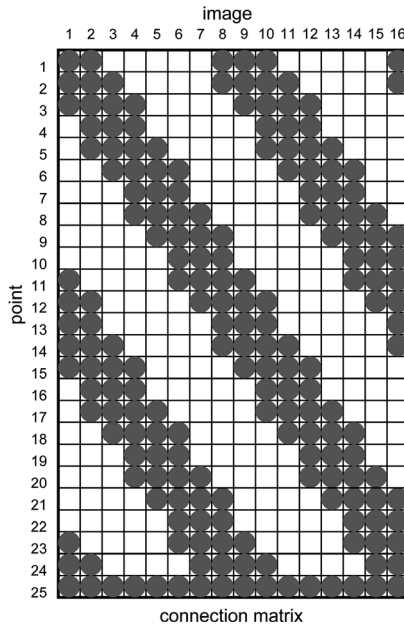


Figure 4.31 Connection matrix of example 2 (Fig. 4.30)

(see section 3.2.1). It is not practicable to perform a camera calibration with this set-up. In contrast, the arrangement of example 2 (Fig. 4.30) represents a very stable geometry which can provide not only self-calibration but also a high and homogenous point accuracy in all three coordinate axes.

Finally example 3 in Table 4.1 refers to an arrangement for test field calibration according to Fig. 7.12f (see section 7.2.2.2). If the test field, in this case with 13 points and 3 distances

(6 points), is completely covered by each of the 8 images, a total number of  $u = 112$  unknowns and  $n = 304$  observations results. Even with this simple set-up a high redundancy and stable geometric configuration are both achieved.

#### 4.3.2.3 Combined adjustment of photogrammetric and survey observations

The system of equations in (4.50) describes the original model of bundle triangulation by defining the image coordinates  $x', y'$  (observations) as a function of the unknowns, specifically of the object coordinates  $X, Y, Z$ . Additional information about the object or additional non-photogrammetric measurements are not considered in (4.50).

An extended model for the bundle adjustment takes additional (survey) observations into account as, for example, measured distances, directions or angles. Other constraints on the object can also be integrated, such as known points, coordinate differences, straight lines, planes or surfaces having rotational symmetry (Fig. 4.32).

All additional observations can be weighted according to their accuracy or importance and therefore have a rigorous stochastic treatment in the adjustment process (Kruck 1983, Wester-Ebbinghaus 1985).

##### *Coordinates, coordinate differences and distances*

It is particularly easy to introduce observed coordinates, coordinate differences or distances. The following observation equations result from the introduction of

object coordinates:

$$\begin{aligned} X &= X \\ Y &= Y \\ Z &= Z \end{aligned} \tag{4.56}$$

coordinate differences:

$$\begin{aligned} \Delta X &= X_2 - X_1 \\ \Delta Y &= Y_2 - Y_1 \\ \Delta Z &= Z_2 - Z_1 \end{aligned} \tag{4.57}$$

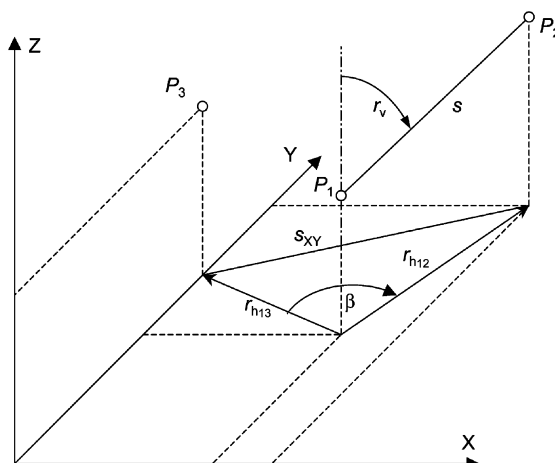


Figure 4.32 Some survey observations

slope distances:

$$s = \sqrt{(X_2 - X_1)^2 + (Y_2 - Y_1)^2 + (Z_2 - Z_1)^2} \quad (4.58)$$

distances in XY plane:

$$s_{XY} = \sqrt{(X_2 - X_1)^2 + (Y_2 - Y_1)^2} \quad (4.59)$$

distances in XZ plane:

$$s_{XZ} = \sqrt{(X_2 - X_1)^2 + (Z_2 - Z_1)^2} \quad (4.60)$$

distances in YZ plane:

$$s_{YZ} = \sqrt{(Y_2 - Y_1)^2 + (Z_2 - Z_1)^2} \quad (4.61)$$

### *Exterior orientations*

Known position or orientation data of a camera can be taken into account by the following additional observation equations:

exterior orientation:

$$\begin{array}{ll} X_0 = X_0 & \omega = \omega \\ Y_0 = Y_0 & \varphi = \varphi \\ Z_0 = Z_0 & \kappa = \kappa \end{array} \quad (4.62)$$

Normally the exterior orientation cannot be measured directly. Older metric cameras (see section 3.3.1.3) may be combined with surveying instruments. In this case surveyed angles (azimuth, elevation) can be introduced as rotation angles of exterior orientation; the rotation matrix must be properly defined (see section 4.2.1.2). In addition, exterior orientation parameters may be known from previous calculations and so can be processed with a corresponding weight.

### *Directions and angles*

Survey directions and angles, for example observed by theodolite, can be introduced as follows, under the condition that the horizontal plane corresponds to the XY plane and the theodolite's vertical axis corresponds to the Z axis (Fig. 4.32):

horizontal direction:

$$r_h = \arctan\left(\frac{X_2 - X_1}{Y_2 - Y_1}\right) \quad (4.63)$$

horizontal angle:

$$\beta = \arctan\left(\frac{X_3 - X_1}{Y_3 - Y_1}\right) - \arctan\left(\frac{X_2 - X_1}{Y_2 - Y_1}\right) \quad (4.64)$$

vertical angle:

$$r_v = \arctan\left(\frac{Z_2 - Z_1}{\sqrt{(X_2 - X_1)^2 + (Y_2 - Y_1)^2 + (Z_2 - Z_1)^2}}\right) \quad (4.65)$$

This can be extended to complete sets of surveyed directions (several measured horizontal directions from one station). With the above observation types pure 3D survey nets can also be adjusted.

#### *Auxiliary coordinate systems*

The introduction of auxiliary coordinate systems is a very elegant way of formulating additional information in object space (Wester-Ebbinghaus 1985). An auxiliary coordinate system  $\bar{X}, \bar{Y}, \bar{Z}$  is a 3D coordinate system arbitrarily oriented in space and used to define additional observations or constraints. For example, this can be local reference point configurations with a defined relation to each other or local geometric elements (e.g. rotationally symmetric shapes).

The auxiliary coordinate system can be transformed into the object coordinate system  $X, Y, Z$  using a spatial similarity transformation (see section 2.2.2.2):

$$\bar{\mathbf{X}} = \bar{\mathbf{X}}_0 + \bar{m} \mathbf{R}_{\bar{\omega}\bar{\varphi}\bar{\kappa}} (\mathbf{X} - \mathbf{X}_0) \quad (4.66)$$

or

$$\begin{bmatrix} \bar{X} \\ \bar{Y} \\ \bar{Z} \end{bmatrix} = \begin{bmatrix} \bar{X}_0 \\ \bar{Y}_0 \\ \bar{Z}_0 \end{bmatrix} + \bar{m} \begin{bmatrix} r_{11} & r_{12} & r_{13} \\ r_{21} & r_{22} & r_{23} \\ r_{31} & r_{32} & r_{33} \end{bmatrix} \begin{bmatrix} X - X_0 \\ Y - Y_0 \\ Z - Z_0 \end{bmatrix}$$

where

$\bar{X}, \bar{Y}, \bar{Z}$  : spatial coordinates in local system

$X_0, Y_0, Z_0$  : centroid of point cloud in  $X, Y, Z$  system  
(constant coordinate values in the adjustment process)

$\bar{X}_0, \bar{Y}_0, \bar{Z}_0$  : origin of system  $X, Y, Z$  with respect to system  $\bar{X}, \bar{Y}, \bar{Z}$

$\mathbf{R}_{\bar{\omega}\bar{\varphi}\bar{\kappa}}$  : rotation matrix transforming  $X, Y, Z$  parallel to  $\bar{X}, \bar{Y}, \bar{Z}$

$\bar{m}$  : scaling factor between both systems

The seven transformation parameters must be introduced as unknowns in the adjustment; hence approximate values must be provided. It is now possible to define functional relationships between object points within the auxiliary coordinate system. They can be expressed by parameters  $B_i$ , which can be transformed into the object coordinate system using equation (4.66). Parameters  $B_i$  can describe simple geometric conditions and also object surfaces of higher order.

$$f(X, Y, Z, \bar{\omega}, \bar{\varphi}, \bar{\kappa}, \bar{X}_0, \bar{Y}_0, \bar{Z}_0, \bar{m}, B_i) = g(\bar{X}, \bar{Y}, \bar{Z}, B_i) = C \quad (4.67)$$

$C$  is a constant or the result of constraint equation, expressed as function  $f$  in the object coordinate system or as function  $g$  in the auxiliary coordinate system. An arbitrary object plane is therefore defined by

$$\bar{X} = C \quad (4.68)$$

A straight line in the auxiliary coordinate system is defined by

$$\bar{X} = C, \quad \bar{Y} = C \quad (4.69)$$

A rotational solid is given by

$$\bar{X}^2 + \bar{Y}^2 + h(\bar{Z}, B_i) = C \quad (4.70)$$

The function  $h$  defines the shape of the solid in the direction of the rotational axis e.g. for a circular cylinder with radius  $r$

$$h(\bar{Z}, B_i) = 0 \quad \text{and} \quad C = r^2 \quad (4.71)$$

or for a sphere with radius  $r$ :

$$h(\bar{Z}, B_i) = \bar{Z}^2 \quad \text{and} \quad C = r^2 \quad (4.72)$$

#### *Applications of additional observations*

With the aid of the additional observations above, the adjustment system can be influenced in the following ways:

- Weak image configurations can be stabilised by introducing additional object information.
- Surveyed or other measured object data, and photogrammetric observations, can be adjusted in one step e.g. in order to minimise net strains (inconsistencies between object points) or to handle measurement data from different sources in a balanced way.
- Unlimited numbers of known distances (scales) between new points can be observed and processed according to their accuracy.
- Single object points can be forced onto an object surface by geometric conditions, e.g. points on a cylindrical surface (pipe line)<sup>1</sup>.
- Information about exterior orientation provided by instruments such as inertial navigation units (INU), GPS location or gyroscopes, can support the adjustment process. Mechanically defined conditions, such as the movement of a camera along a straight line or circle, can also be added as additional observations. This applies equally to geometric constraints between the orientation parameters of different cameras e.g. for stereo cameras or camera/projector arrangements.
- Additional information which is introduced with an unrealistic weight can negatively affect adjustment result. This point is particularly important in practice and demands a careful choice of weights and analysis of results.

#### **4.3.2.4 Adjustment of additional parameters**

##### *Self-calibration*

Functions for the correction of imaging errors are referred to as additional parameter functions. Functional models which describe real optical characteristics of image acquisition systems (parameters of interior orientation) have been summarised in section 3.2.3. When these parameters are determined within the bundle adjustment, the procedure is known as self-calibration.

The linearised model of the adjustment is extended by differential coefficients for camera constant and principal point, as given in equation (4.53). Again, approximate values of the

---

<sup>1</sup> Conditions include both weak constraints defined by additional observations with standard deviations, as well as fixed constraints which force an exact condition.

additional unknowns must be provided, although the following initial values are usually sufficient:

principal distance:	$c \approx f$ (focal length)
principal point:	$x'_0 \approx y'_0 \approx 0$
radial (symmetric) distortion:	$A_1 \approx A_2 \approx 0$
tangential (asymmetric) distortion:	$B_1 \approx B_2 \approx 0$
affinity and shear:	$C_1 \approx C_2 \approx 0$

The ability to determine single parameters depends, on one hand, on the modelling of the physical projection. Parameter sets based on faulty physical assumptions can lead to weakly conditioned systems of equations, over-parameterised systems or high correlations between parameters. On the other hand, interior orientation parameters can only be reliably calculated if image configuration and distribution of object points are well chosen. Section 7.2.2 summarises suitable image configurations for self-calibration.

The parameters of interior orientation can additionally be handled as observed values with a corresponding weight. The observation equations in this case are given by:

$$\begin{aligned} c &= c & A_1 &= A_1 \\ x'_0 &= x'_0, & A_2 &= A_2 \\ y'_0 &= y'_0 & etc. \end{aligned} \tag{4.73}$$

If additional parameters are introduced, the structure of the normal system of equations changes significantly. While the design matrix illustrated in Fig. 4.29 shows a distinctive diagonal structure with a large number of zero elements, the normal equation matrix of adjustment systems with additional parameters contains larger areas with non-zero elements. Each measured image coordinate is functionally connected with the unknowns of interior orientation, hence the right hand side of the matrix is completely filled.

In order to invert the resulting normal equation matrices, much more storage and computing power is required. Sparse matrix techniques have been successfully applied in practice for the efficient use of computing resources (see section 2.3.5).

#### Calibration with variable interior orientation

The models normally used for interior orientation assume constant camera parameters during the period of image acquisition. If the camera geometry changes over this period, for example due to refocusing or a change of lens, a ‘new’ camera with its own parameters must be assigned to the related images. The simultaneous determination of more than one group of parameters requires an image configuration appropriate for the calibration of each camera (see section 7.2.2).

If stable camera parameters cannot be guaranteed for longer periods, the interior orientation must be calibrated individually for each image. Maas (1999) presents an approach to image-variant calibration that provides corrections for a shift of the perspective centre (camera constant and principal point coordinates) but otherwise assumes stable distortion parameters for all images. For this purpose the image-variant parameters are introduced as observed unknowns with approximate values and *a priori* standard deviations which correspond to the expected shift of the perspective centre. The numerical stability of the adjustment is maintained provided there is a suitable number of object points each with an appropriate number of image rays. Depending on image configuration and current state of the camera, applications using still video cameras

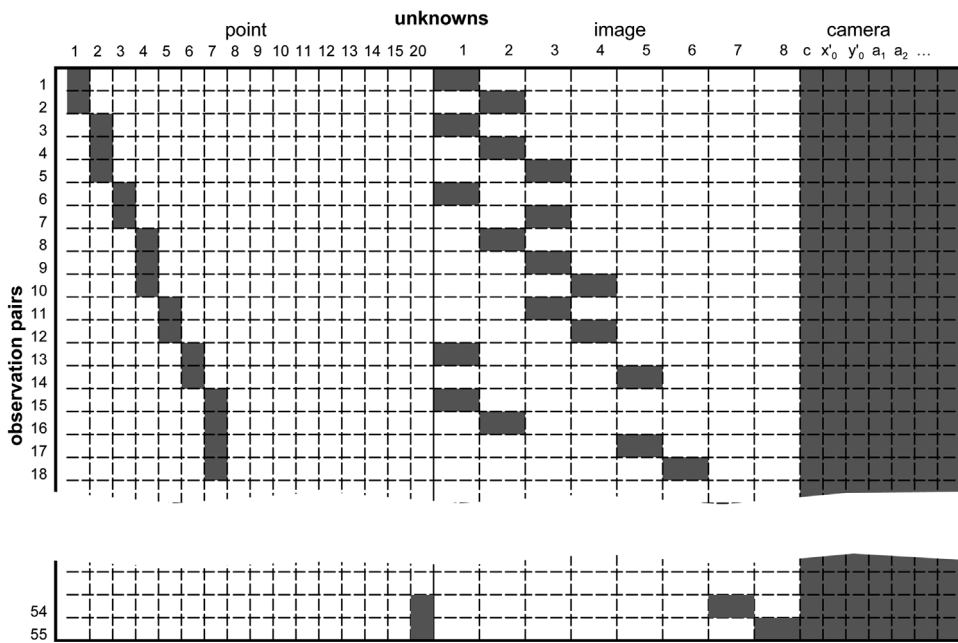


**Figure 4.33** Structure of design matrix A, extended by additional unknowns for the interior orientation of a camera (compare Fig. 4.29)

report an accuracy increase by a factor of 2 to 4 compared with cases in which image-variant parameters are not used (see section 3.3.2.4).<sup>1</sup>

### 4.3.3 Object coordinate system (definition of datum)

#### 4.3.3.1 Rank and datum defect

A network composed of purely photogrammetric observations leads to a singular system of normal equations because, although the shape of the network can be determined, its absolute position and orientation in space cannot be determined. The resulting system of equations has a rank defect

$$d = u - r \quad (4.74)$$

where

$u$ : number of unknowns

$r$ : rank(A)

The rank defect is caused by a datum defect in the observed network which, for a three-dimensional network, can be removed by defining 7 additional elements:

3 translations

3 rotations

1 scaling factor

If at least one known distance is observed then the datum defect is reduced by 1. The information is introduced as an additional distance observation according to equations (4.58).

<sup>1</sup> On average, Maas used 12 to 14 rays per object point.

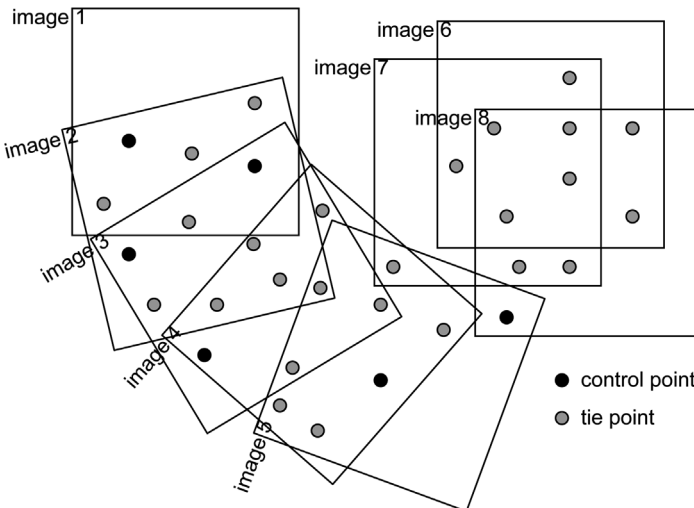


**Figure 4.34** Example of a configuration defect in an arrangement of images:  
images 6,7,8 cannot be oriented with respect to the rest of the images

Translational datum defects can be eliminated if control or reference points with known object coordinates are observed. Options for this are reviewed in the next section.

Rotational datum defects can also be eliminated by reference points, as well as by directly measured directions or angles.

In addition to datum defects, observed networks can exhibit a configuration defect if, due to missing observations, some portions of the network cannot be determined unambiguously. In photogrammetric networks this problem seldom arises. If some images, for example, contain an insufficient number of tie points, they cannot be oriented with respect to the other images (see example in Fig. 4.34).

#### 4.3.3.2 Reference points

##### *Error-free reference points*

Reference points are used for the definition of a global object coordinate system (datum definition). They can be introduced as error-free reference points in the bundle adjustment if their nominal coordinates are known to a high accuracy. Such coordinates could be introduced into the bundle adjustment as constants. Some bundle adjustment programs allow their input as measurements with zero standard deviations. Logically this approach leads to an error-free definition of the datum.

It is assumed, however, that the accuracy of the reference point coordinates is, for example, better by a factor 5–10 than the photogrammetric point determination and that there are no inconsistencies in reference point coordinates. Errors in reference point coordinates are interpreted as errors in observations and are therefore difficult to detect. The definition of the object coordinate system using error-free reference points gives rise to a fixed datum.

In principle, the spatial distribution of reference points should follow the recommendations made for absolute orientation (see section 4.2.5.4). The stereo model discussed there must here be considered a model defined by all images (bundles) i.e. a minimum of three reference points is required for the definition of the object coordinate system. As a minimum, the following coordinate components must be given by these three reference points (the example components in brackets relate to an image plane parallel to XY and viewing direction parallel to Z):

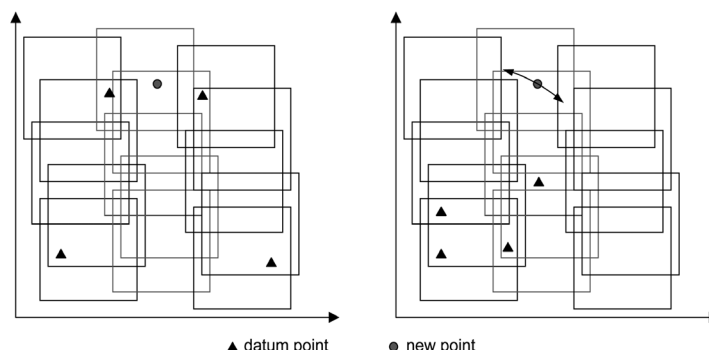


**Figure 4.35** Good (left) and bad (right) distribution of reference points in a multi-image configuration

- a minimum of  $2 \times 2$  coordinates parallel to the primary object plane ( $X_1, Y_1, X_2, Y_2$ )
- a minimum of 3 coordinates perpendicular to the primary object plane ( $Z_1, Z_2, Z_3$ )

The minimum configuration can be established, for example, by 2 full reference points ( $2 \times XYZ$ ) and one additional reference height point ( $1 \times Z$ ) or 2 plane reference points ( $2 \times XY$ ) and 3 reference height points ( $3 \times Z$ ). However, in many applications of close-range photogrammetry there are more than 2 full reference points available.

Reference points should be widely and uniformly distributed over the area covered by the images. Fig. 4.35 (left) shows an image set-up with a suitable distribution of 4 reference points, leading to a stable datum definition and homogeneous accuracies. In Fig. 4.35 (right) the 4 reference points are distributed unfavourably in one corner of the image configuration. As a consequence, the whole system can rotate around this point cloud, which results in discrepancies at more distant points and higher standard deviations.

Reference points used for datum definition must not lie on a common straight line, as the normal system of equations then becomes singular. Unfavourable distributions of reference points which come close to this restriction will result in numerically weak systems of equations.

#### *Coordinates of reference points as observed quantities*

Coordinates of reference points can also be introduced as observed quantities with a weight corresponding to their real point accuracy (e.g. depending on the measuring systems used for coordinate determination; see section 4.3.2.3). Within the adjustment system the coordinates of the reference points are treated as unknowns and receive corrections and accuracy values in the same way as other observations. Standard deviations of weighted reference points can be interpreted as quality measures for the reference points themselves.

Inconsistencies between reference point coordinates can be partially compensated for by an appropriate variation of weights, provided that these inconsistencies are not directly transferred to the photogrammetric observations. A coordinate system defined in this way can be regarded as a weighted datum. Using coordinates of reference points in this way also compensates completely for rank defects in the adjustment system. If the weighted datum also results in a weak definition of the coordinate system, then higher standard deviations for new points are usually obtained.

### *Unconstrained datum definition using reference points*

Using a minimum amount of object information it is possible to define the object coordinate system in order to avoid any possible influence of inconsistencies in the reference points. For this purpose scale is given by a known distance  $S$ . The coordinate axes can be then defined according to the following scheme known as the 3-2-1 method (Fig. 4.36):

1. Fixing the  $X$ ,  $Y$ ,  $Z$  coordinates of point 1 defines an arbitrary 3D reference point in the object coordinate system which can, for example, represent the origin ( $X = Y = Z = 0$ ).
2. Fixing the  $Y$ ,  $Z$  coordinates of point 2 defines the  $X$  axis. At this stage the system can still be rotated about this axis.
3. Fixing the  $Y$  coordinate of point 3 defines the  $XZ$  plane (alternatively define the  $XY$  plane with fixed  $Z$  or  $YZ$  plane with fixed  $X$ .) Hence the coordinate system is uniquely defined without any constraints.

Fig. 4.36 shows an example where the following reference coordinates are available:

point	X	Y	Z
$P_1$	7.0	2.0	2.0
$P_2$	-	4.5	3.5
$P_3$	-	2.0	-

If real reference point coordinates are not available the system can also be defined by fictitious coordinates e.g.

point	X	Y	Z
$P_1$	0	0	0
$P_2$	-	0	0
$P_3$	-	0	-

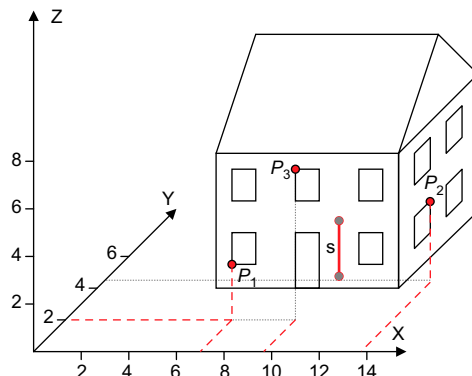


Figure 4.36 Constrained coordinate system definition using reference points (3-2-1 method)

Scaling information can be derived from known distances between reference points, even if their coordinates are not known.

The unconstrained datum definition by reference points does not affect the shape of the photogrammetric network. It is true that the absolute coordinates of object points are related to the arbitrarily selected system origin but the distances between points are independent of the datum. In contrast, the estimated accuracies derived from the covariance matrix are influenced by the datum definition. If datum points are distributed according to Fig. 4.35 (right) then object point accuracy based on datum point accuracy is interpreted too optimistically when they are close to the datum points and too pessimistically in more distant parts of the network.

#### 4.3.3.3 Free net adjustment

If no reference points or equivalent datum definitions are available, the problem of datum definition can be avoided by means of a free net adjustment which fits the network onto the initial coordinates of the unknown points. Initial values for new points are required in any case for the linearisation of the correction equations. They can be generated by the procedures described in section 4.3.4

The initial values of all unknown points (new object points and perspective centres) form a spatial point cloud. This point cloud can be transformed by three translations, three rotations and one scaling factor onto the photogrammetrically determined model of object points, without affecting the shape of the point cloud i.e. without any geometrical constraint. The photogrammetric observations are not influenced by this transformation.

A rank defect of 7 in the normal equation matrix is avoided if exactly 7 observations can be found which are linearly independent with respect to each other and to the other observations. This requirement is exactly fulfilled if the normal system of equations is extended by a matrix  $\mathbf{B}$  with  $d = 7$  rows and  $u$  columns (Zinndorf 1985, Kraus 1997, see also section 2.3.2.3):

$$\mathbf{B}_{d,u} = \left[ \begin{array}{ccccccccc|ccccccccc} 1 & 0 & 0 & 0 & 0 & 0 & \cdots & 1 & 0 & 0 & \cdots & 1 & 0 & 0 \\ 0 & 1 & 0 & 0 & 0 & 0 & \cdots & 0 & 1 & 0 & \cdots & 0 & 1 & 0 \\ 0 & 0 & 1 & 0 & 0 & 0 & \cdots & 0 & 0 & 1 & \cdots & 0 & 0 & 1 \\ 0 & -Z_{01} & Y_{01} & r_{11} & r_{12} & r_{13} & \cdots & 0 & -Z_1^0 & Y_1^0 & \cdots & 0 & -Z_p^0 & Y_p^0 \\ Z_{01} & 0 & -X_{01} & r_{21} & r_{22} & r_{23} & \cdots & Z_1^0 & 0 & -X_1^0 & \cdots & Z_p^0 & 0 & -X_p^0 \\ -Y_{01} & X_{01} & 0 & r_{31} & r_{32} & r_{33} & \cdots & -Y_1^0 & X_1^0 & 0 & \cdots & -Y_p^0 & X_p^0 & 0 \\ X_{01} & Y_{01} & Z_{01} & 0 & 0 & 0 & \cdots & X_1^0 & Y_1^0 & Z_1^0 & \cdots & X_p^0 & Y_p^0 & Z_p^0 \end{array} \right] \quad (4.75)$$

exterior orientations    new points 1 .. p

If scale is defined by a separately measured distance, the potential rank defect decreases to 6 and the last row of matrix  $\mathbf{B}$  can be eliminated.

The first six columns of matrix  $\mathbf{B}$  are related to the unknown parameters of exterior orientation. They are not further discussed as the perspective centres are normally not of interest in the definition of the datum.

The next columns correspond to the unknown object points. Three condition equations are used for the translation of the system, included in the first three rows of matrix  $\mathbf{B}$ :

$$\begin{array}{lclclclclcl} dX_1 & & +dX_2 & & + & \cdots & = & 0 \\ dY_1 & & +dY_2 & & + & \cdots & = & 0 \\ dZ_1 & & +dZ_2 & & + & \cdots & = & 0 \end{array} \quad (4.76)$$

If the sum of coordinate corrections at all object points becomes zero, the centroid of the initial points is identical to the centroid of the adjusted object points.

The next three rows of matrix **B** contain differential rotations of the coordinate system:

$$\begin{aligned} -Z_1^0 dY_1 &+ Y_1^0 dZ_1 & -Z_2^0 dY_2 &+ Y_2^0 dZ_2 & + \dots &= 0 \\ Z_1^0 dX_1 & -X_1^0 dZ_1 & +Z_2^0 dX_2 & -X_2^0 dZ_2 & + \dots &= 0 \\ -Y_1^0 dX_1 & +X_1^0 dY_1 & -Y_2^0 dX_2 & +X_2^0 dY_2 & + \dots &= 0 \end{aligned} \quad (4.77)$$

The final row 7 of matrix **B** defines scale:

$$X_1^0 dX_1 + Y_1^0 dY_1 + Z_1^0 dZ_1 + X_2^0 dX_2 + Y_2^0 dY_2 + Z_2^0 dZ_2 + \dots = 0 \quad (4.78)$$

The extended system of normal equations then becomes:

$$\begin{bmatrix} \mathbf{A}^T \mathbf{A} & \mathbf{B}^T \\ \mathbf{B} & \mathbf{0} \end{bmatrix} \begin{bmatrix} \hat{\mathbf{x}} \\ \mathbf{k} \end{bmatrix} = \begin{bmatrix} \mathbf{A}^T \mathbf{l} \\ \mathbf{0} \end{bmatrix} \quad (4.79)$$

Here **k** consists of seven Lagrange multipliers. The solution of the extended system of normal equations is obtained from the pseudo inverse (Moore-Penrose inverse)  $\mathbf{Q}^+$

$$\begin{aligned} \begin{bmatrix} \hat{\mathbf{x}} \\ \mathbf{k} \end{bmatrix} &= \begin{bmatrix} \mathbf{A}^T \mathbf{A} & \mathbf{B}^T \\ \mathbf{B} & \mathbf{0} \end{bmatrix}^{-1} \begin{bmatrix} \mathbf{A}^T \mathbf{l} \\ \mathbf{0} \end{bmatrix} \\ &= \bar{\mathbf{N}}^{-1} \bar{\mathbf{n}} \\ &= \mathbf{Q}^+ \bar{\mathbf{n}} \end{aligned} \quad (4.80)$$

The pseudo inverse has the property that the resulting covariance matrix has a minimum trace:

$$\text{trace}\{\mathbf{Q}^+\} = \min. \quad (4.81)$$

Hence, the standard deviations of the object points are estimated with minimum quantities. The centroid of object points becomes the origin for the datum which is a fixed point with zero standard deviation. A datum is defined which does not therefore affect the total accuracy of the system.

#### *Full trace minimization*

If all unknown new points are used for datum definition the full trace of the covariance matrix  $\mathbf{Q}^+$  is minimised, as explained above. In this case points used as datum points are not free of error but are introduced without *a priori* standard deviations.

Fig. 4.37 shows an example of a network for which the datum is defined alternatively by three reference points and one distance (left, 3-2-1 method) and by free net adjustment (right, all points used as datum points). The error ellipses of the points illustrate clearly that standard deviations are smaller for object points close to reference points than for those at the edges of the net. In contrast, error ellipses in the free net adjustment are significantly smaller and more homogenous. Their large semi-axes point towards the centroid of the points. The vertical lines in the ellipses indicate the error in Z, which behaves similarly to those in X and Y.

#### *Partial trace minimisation*

There are some applications where not all the object points should be used for datum definition in a free net adjustment. This can occur, for example, when a subset of new points represents an

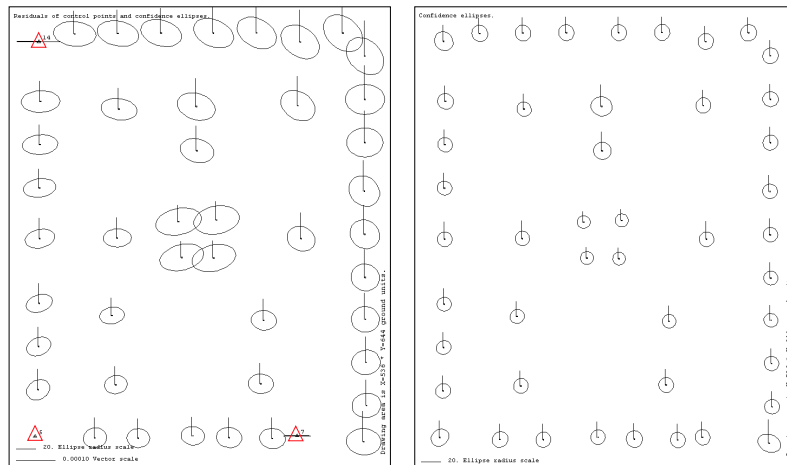


Figure 4.37 Example network based on reference points (left, red points) and by free net adjustment (right)

existing network into which the remaining object points should be optimally fitted. In this case those columns of matrix  $\mathbf{B}$ , which relate to points not used in datum definition, must be set to zero. However, the rank of  $\mathbf{B}$  must not be smaller than  $u - d$ .

$$\mathbf{B} = \underbrace{\begin{bmatrix} 1 & 0 & 0 & 0 & 0 & 0 & \cdots & 1 & 0 & 0 & \cdots & 1 & 0 & 0 \\ 0 & 1 & 0 & 0 & 0 & 0 & \cdots & 0 & 1 & 0 & \cdots & 0 & 1 & 0 \\ 0 & 0 & 1 & 0 & 0 & 0 & \cdots & 0 & 0 & 1 & \cdots & 0 & 0 & 1 \\ 0 & -Z_1^0 & Y_1^0 & 0 & 0 & 0 & \cdots & 0 & -Z_i^0 & Y_i^0 & \cdots & 0 & -Z_p^0 & Y_p^0 \\ Z_1^0 & 0 & -X_1^0 & 0 & 0 & 0 & \cdots & Z_i^0 & 0 & -X_i^0 & \cdots & Z_p^0 & 0 & -X_p^0 \\ -Y_1^0 & X_1^0 & 0 & 0 & 0 & 0 & \cdots & -Y_i^0 & X_i^0 & 0 & \cdots & -Y_p^0 & X_p^0 & 0 \\ X_1^0 & Y_1^0 & Z_1^0 & 0 & 0 & 0 & \cdots & X_i^0 & Y_i^0 & Z_i^0 & \cdots & X_p^0 & Y_p^0 & Z_p^0 \end{bmatrix}}_{\text{new points}} \underbrace{\begin{bmatrix} & & & & & & \\ & & & & & & \\ & & & & & & \\ & & & & & & \\ & & & & & & \\ & & & & & & \\ & & & & & & \\ & & & & & & \end{bmatrix}}_{\text{non-datum points}} \underbrace{\begin{bmatrix} & & & & & & \\ & & & & & & \\ & & & & & & \\ & & & & & & \\ & & & & & & \\ & & & & & & \\ & & & & & & \\ & & & & & & \end{bmatrix}}_{\text{new points}} \quad (4.82)$$

Equation (4.82) shows a modified matrix  $\mathbf{B}$  where all those elements are eliminated which are related to the perspective centres.

#### *Practical aspects of free net adjustment*

With free net adjustment, as with the unconstrained datum definition using reference points, the photogrammetric network is not influenced by possible inconsistencies between reference points. The object coordinate residuals are only affected by the photogrammetric observations and the quality of the model. A free net adjustment therefore provides an optimal precision (inner accuracy) that can be better analysed than standard deviations of unconstrained, or even over-determined, datum definitions.

The free net adjustment is therefore a very flexible tool if

- no reference points are available
- only the relative positions of object points are of interest
- only the quality of the model is to be analysed, for example the model of interior orientation used in simultaneous camera calibration.

However, the standard deviations of object points are not suitable for a direct assessment of accuracy. They only provide information about the internal quality of a photogrammetric network i.e. they express how well the observations fit the selected model. Accuracy can only be properly assessed using comparisons with data of higher accuracy (see also section 4.3.5.3).

#### 4.3.4 Generation of approximate values

The generation of approximate values, to be used as starting values in the iterative solution of a photogrammetric problem, is often a complex task. Approximate values are required for all unknowns to be estimated i.e. all orientation parameters and all new points. Since arbitrary image configurations in arbitrarily oriented object coordinate systems may well occur in close-range applications, the direct calculation of approximate values is virtually impossible (Hinsken 1989).

Fig. 4.38 depicts (within solid lines) that information which is necessary for the generation of approximate values required by the bundle adjustment and (in dotted lines) information which is useful but optional. The key component is a module for the automated calculation of approximate values based on measured image coordinates, camera parameters and, if available, coordinates of reference points. This process is also known as multi-image orientation, whereby bundle triangulation is expressly not implied.

In many cases additional information about the image configuration is available, such as surveyed orientation data, parameters derived from free-hand sketches or CAD models. Manual intervention in the procedures for calculating approximate values can sometimes be necessary and such additional information can support this manual process as well as helping to define the coordinate system. Approximate values can, however, be generated fully automatically.

The following principal methods for the generation of approximate values can be identified. They can also be applied in combination:

- Automatic calculation of approximate values

In order to generate approximate values automatically, three strategies are feasible for complex photogrammetric configurations (see section 4.3.4.1):

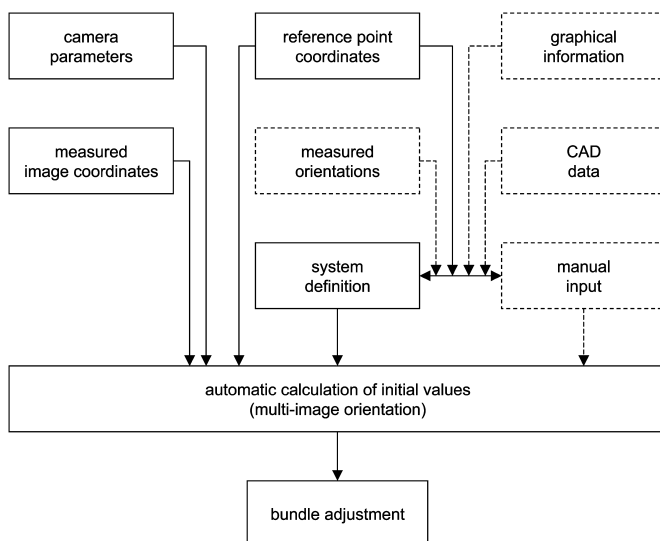


**Figure 4.38** Methods and procedures for the calculation of approximate values

- combined intersection and resection
- successive forming of models
- transformation of independent models

All three strategies are based on a step by step determination of the parameters of exterior orientation, as well as the object coordinates, in a process where all images in the project are added sequentially to a chosen initial model.

- Generation of approximate values by automatic point measurement

Digital photogrammetric systems allow for the automatic identification and measurement of signalised (coded) targets. Reference and tie points can be matched by this method and, by further applying the above orientation strategies, a fully automatic generation of approximate values is possible.

- Integration of graphical information

If a freehand sketch or map of the imaging stations is produced during object recording, this can be used for manual input of approximate values. Available CAD data can be applied in the same way (see section 4.3.4.3).

- Measurement of approximate values

Approximate values of object points, especially of imaging stations and viewing directions, can be measured, for example by survey methods. Fig. 3.50 shows a combination of camera and angle measuring device. It is also possible to use separate measuring equipment for the location of camera stations, such as GPS or inertial navigation units (see also 3.3.5.3).

#### **4.3.4.1 Strategies for the automatic calculation of approximate values**

In order to calculate approximate values automatically the following information must be provided:

- a file containing camera data (interior orientation data which can be approximate)
- a file containing measured image coordinates (see Fig. 4.27)
- a file containing reference point coordinates (if available) or other information for the definition of the object coordinate system
- other known object information (if available) e.g. approximately known exterior orientations

On the basis of this information an iterative process is started which attempts to connect all images via approximate orientations. At the same time all measured tie points can be approximately calculated in object space. The bundle adjustment can then be executed.

The following procedures show sample strategies which employ suitable combinations of various methods for orientation and transformation (resection, relative and absolute orientation, similarity transformation, intersection). In all cases a reasonable starting model formed by two images is defined.

##### *Starting model and order of calculation*

From a multi-image configuration a starting model is provided by one image pair for which relative orientation may be computed. The resulting model coordinate system provides an arbitrary 3D coordinate system for including all subsequent images or models. The choice of starting model, and processing sequence of subsequent images, is not arbitrary and is critical to the success of the automatic calculation of approximate values, especially for complex and irregular image configurations.

Theoretically,  $n$  images of a multi-image configuration lead to  $n(n-1)/2$  possible models. Image pairs with fewer than 5 homologous points would, of course, be eliminated. Quality criteria can be calculated for each possible model and the selected starting model should have the following properties:

- Maximum number of tie points: a large number of tie points leads to a more stable relative orientation where possible gross errors (outliers) can be eliminated more easily.  
starting model: maximum number of tie points
- Minimum accuracy of relative orientation: the standard deviation of unit weight of the relative orientation ( $s_0$ ) should approximate the expected image measuring accuracy.  
starting model: minimum  $s_0$
- Mean intersection angle at model points close to  $90^\circ$ : the mean intersection angle of homologous image rays provides information about the quality of a computed relative orientation. Models with small mean intersection angles (e.g. less than  $10^\circ$ ) have an unfavourable height-to-base ratio and should not be used as starting models.  
starting model: mean intersection angle close to  $90^\circ$
- Mean residuals of model coordinates: the mean intersection offset of homologous image rays which are skew is a quality measure of model coordinate determination.  
starting model: minimum mean intersection offset
- Minimum number of gross errors in relative orientation: models with few or no blunders are preferable for orientation.
- Maximum image area covered by tie points.  
starting model: maximum image area

By giving appropriate weight to these criteria an optimal starting model, as well as a sorted list of further models in order of calculation, can be selected. In general the model with maximum tie points and best mean intersection angle is a suitable starting model. An unfavourable starting model, chosen without regard to these criteria, can cause the iterative orientation procedure to diverge.

#### *Combination of space intersection and resection*

Fig. 4.39 shows the principal steps in generating approximate values by combined space intersections and resections. A starting model is first selected according to the criteria outlined above.

This starting model is used to calculate a relative orientation. Subsequent images are oriented to this model by space resection, provided they have at least 3 spatially distributed tie points with model coordinates known from a previous relative orientation. Model coordinates of new unknown object points are then calculated by intersection. When additional points are calculated by intersection, relevant images can be oriented again by resection in order to improve their exterior orientation in the model system. The image configuration is iteratively stabilised in this process since the number of intersected model points continually increases, thus improving the orientation parameters calculated by space resection.

Once all images have been oriented with respect to the model coordinate system, a final absolute orientation (similarity transformation) can be performed. For this purpose reference points with known coordinates in both model and object coordinate systems are used. The final result delivers approximate exterior orientation values of all images and approximate coordinates for all 3D object points.

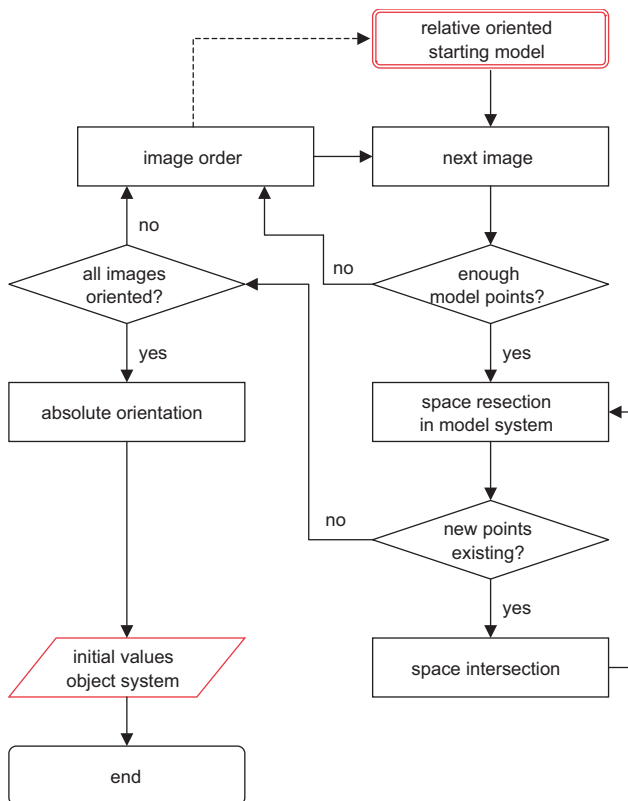


**Figure 4.39** Generation of approximate values with combined space intersection and resection

#### *Successive creation of models*

Fig. 4.40 illustrates the process of initial value generation by successive creation of models. A relative orientation is first calculated for a suitable starting model. If this model contains enough reference points, an absolute orientation can immediately be performed. If not, overlapping photos can be successively oriented into the initial model if they contain a sufficient number of homologous points. Again, if a set of models contains enough reference points it can be absolutely oriented. In this way approximate values of unknown object points in a model or object coordinate system can be computed. At the end of the process the parameters of exterior orientation can be derived from the parameters of relative and absolute orientation.

#### *Transformation of independent models*

The process of initial value generation by transformation of independent models is illustrated in Fig. 4.41. A connection matrix of all image pairs (models) is first established. For each possible model a relative orientation is calculated and stored together with corresponding model coordinates and quality estimators.

The starting model is selected according to the following criteria:

- a maximum number of tie points,
- appropriate intersection angles and
- minimum intersection offsets.

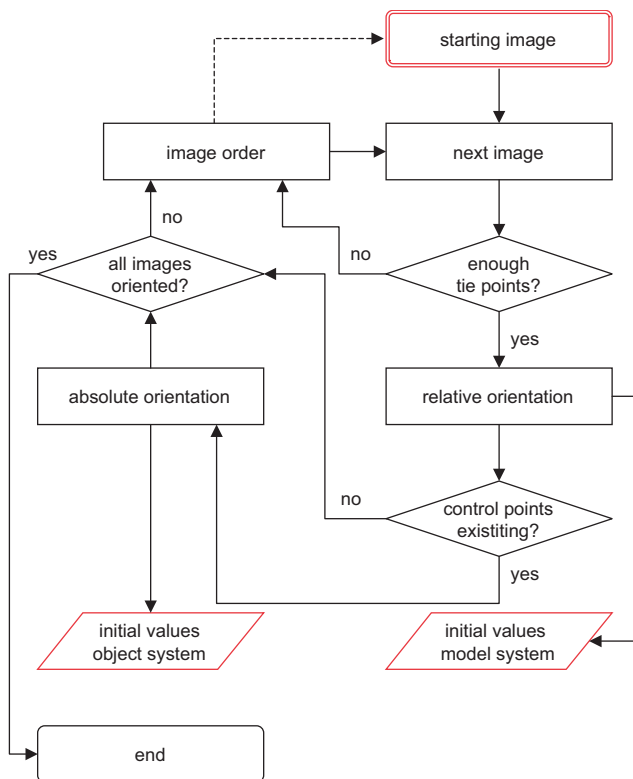


**Figure 4.40** Initial value generation with successive model creation

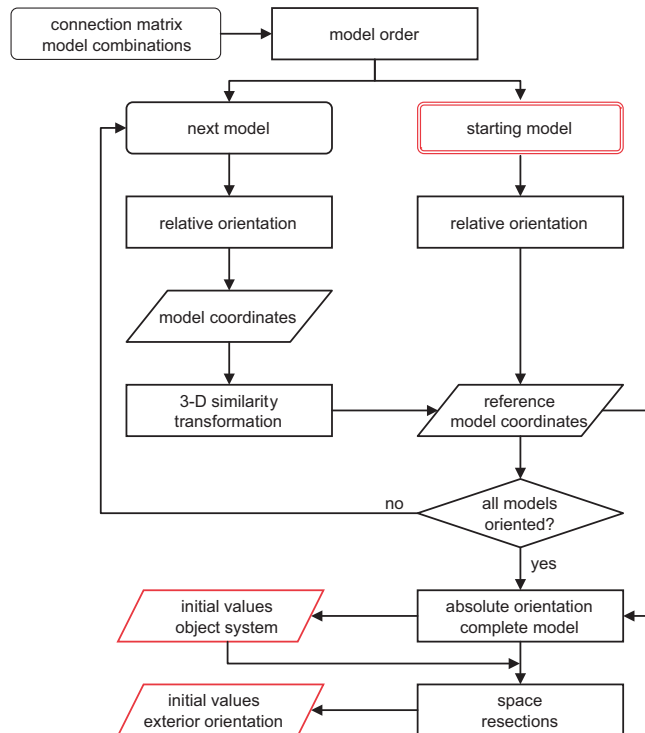
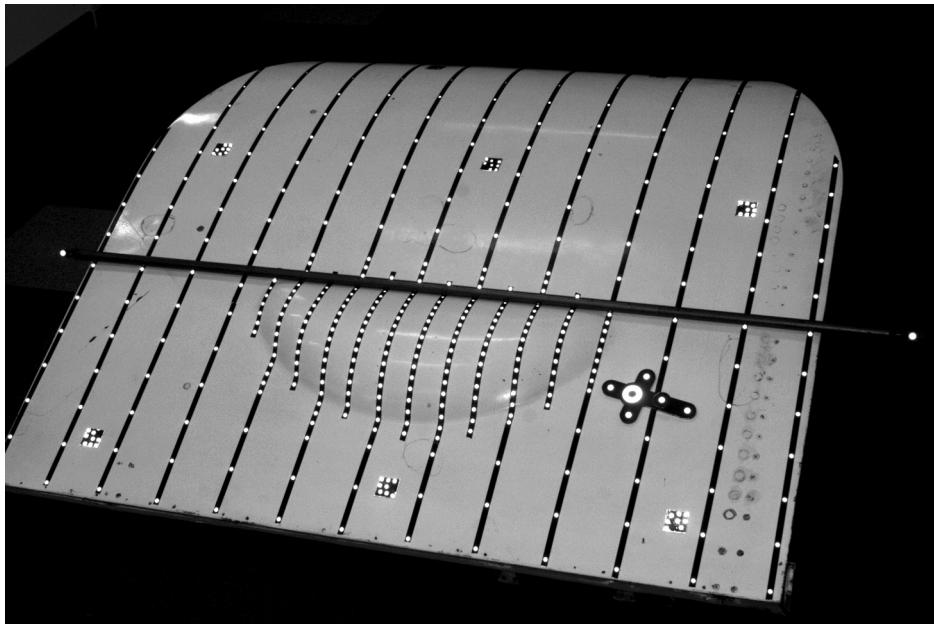
The model coordinates of the relatively oriented starting model are used to define a local coordinate system. All other relatively oriented models are subsequently transformed into this local system using their independent model coordinates as input to a 3D similarity transformation.

When all points in all models are calculated with respect to the local system, a final absolute transformation of the complete model into the object coordinate system is calculated using reference points with known object coordinates. As a result, approximate values of object points in the object coordinate system are generated.

Finally the exterior orientations of all images are calculated by space resection (single image orientation) using the object coordinates computed above. If any object points remain without initial values, these can be provided by space intersection.

#### 4.3.4.2 Initial value generation by automatic point measurement

Fig. 4.42 shows one photo of a multi-image configuration which has been taken to measure a signalised set of points. Targets with coded point numbers have been placed on several points. These can be automatically identified and decoded by the image processing system (see section 3.4.1.1). The majority of points are signalised by standard, non-coded targets. In addition a local reference tool (autobar, front right) is placed in the object space. It consists of a number of coded targets with calibrated local 3D object coordinates. The reference tool need not be imaged in all photos. The example above also shows a reference scale bar which provides absolute scale but is not relevant to initial value generation.

**Figure 4.41** Initial value generation by transformation of independent models**Figure 4.42** Image with signalised targets and local reference system

Approximate values for the freely configured set of images can be generated as depicted in Fig. 4.43. A pattern recognition process detects all coded targets and other potential object points. Those photos in which the reference tool is imaged can be individually oriented by space resection into the tool's coordinate system. Remaining images are oriented by relative orientation using the coded targets and the strategies described above for calculation of approximate values. Object coordinates for coded targets are calculated by intersection. A first bundle adjustment generates improved object coordinates and orientation parameters. Remaining photos which are not at this stage oriented are iteratively integrated by resection and bundle adjustment until all images are oriented.

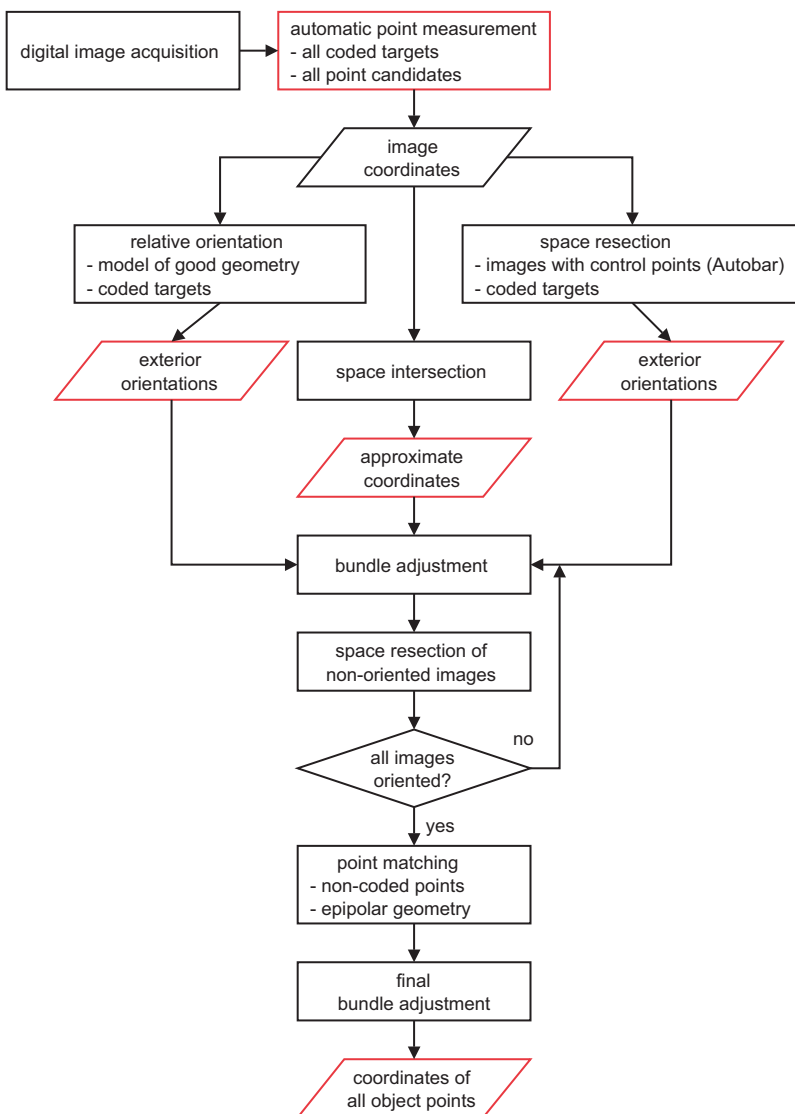


**Figure 4.43** Fully automated generation of initial values and orientation

A subsequent processing stage identifies and consecutively numbers all non-coded targets using a matching process based on epipolar geometry (see section 5.5.3). A final bundle adjustment provides the coordinates of all object points. This and similar methods form part of digital on-line and off-line measuring systems (see section 6.4.2). Initial value generation and precise coordinate determination are integrated in one common procedure (Dold 1999).

#### 4.3.4.3 Other methods of finding initial values

##### *Digitising a free-hand sketch*

A free-hand sketch created during work on site can provide approximate information about the object, location of object coordinate system, camera stations and viewing directions. This sketch can be used to support the generation of approximate values.

Site sketches are normally drawn as plan or side views. It is therefore possible that not all imaging or object parameters can be determined from the sketch. An explicit representation of the camera's angles of rotation is particularly difficult as, for example, a roll angle around the optical axis is difficult to present graphically.

The site sketch is transferred into the processing system by vector-oriented digitising using a graphics tablet or by manual digitising on a computer monitor. Positions of object points and camera stations are determined as point coordinates while viewing directions are modelled as vectors. Point and image numbers are assigned at this stage.

Usually the approximate values derived from sketches or other sources are not sufficient to start the bundle adjustment. It is likely that the computational techniques outlined above will be needed to complement the method which, of course, will provide good starting values for some parameters and help to avoid problems such as the mirror image effect associated with plane surfaces (see section 4.2.3.1).

##### *Graphical construction*

Some off-the-shelf processing systems have a CAD-based environment in which the manually digitised information described above can be directly input graphically. Simple 2D construction tools enable the positioning of camera stations with respect to a roughly defined object e.g. designed in plan view using graphical primitives such as rectangles, triangles and circles (Fig. 4.44).

In contrast, full 3D CAD programs permit a complete spatial construction of the image configuration. The object itself can be included as a 3D model if CAD data is available. In this way critical parameters of the photogrammetric network can be determined prior to measurement during the planning process (see section 7.1) and used as initial values for the subsequent bundle adjustment.

#### 4.3.4.4 Practical aspects of approximate values generation

The automatic calculation of approximate values (multi-image orientation) is often a time-consuming process for the complex image configurations associated with close-range photogrammetry. The stability of a multi-image project depends mainly on the distribution of object points and on the configuration of bundles of rays. If there are no, or only coarse, approximate values of orientation parameters, then even a very few gross data errors can lead to divergent solutions for initial values. Since the imaging configuration is then poorly defined, the detection of gross errors is more difficult.

As a result, effective systems for generating initial values should incorporate the following features which increase the level of automation and the scope for error detection.

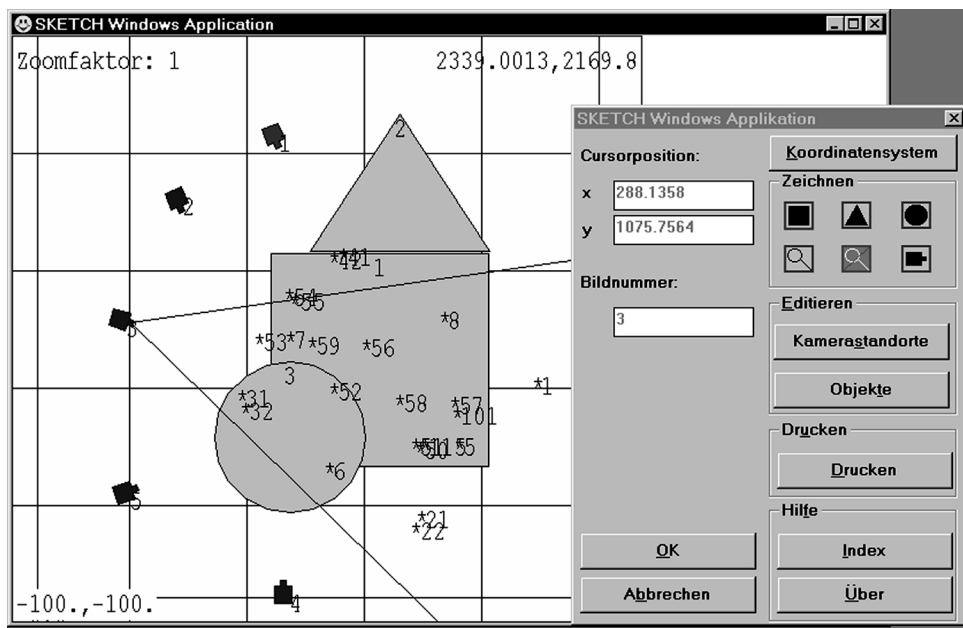


**Figure 4.44** Graphical construction of image configuration (Rollei CDW)

- Use of algebraic rotation matrices

Modules for relative orientation, spatial similarity transformation (absolute orientation) and space resection should use rotation matrices based on algebraic functions instead of trigonometric functions. The use of trigonometric functions in the rotation matrices can lead to singularities or ambiguities. In addition they improve the convergence of solutions (see section 2.2.2.1).

- Robust blunder detection

The detection of gross data errors should be sufficiently robust that more than one blunder can be detected and eliminated more or less automatically. Estimation methods based on the L1 norm are particularly suitable for this purpose (see section 2.3.4).

- Detailed reporting of results

To analyse the results of initial value generation effectively, statistical data (e.g. standard deviations) and graphical information (position and orientation of object and cameras) should be output.

- Automatic and interactive definition of the order of images

With a suitable starting model the order of image orientation can be determined automatically. However, situations occur where the suggested order does not lead to convergence, for example due to images which cannot be controlled by other images. In these cases an interactive definition of image order should be possible.

- Manual activation and deactivation of points and images

During the process of initial value generation it can be necessary to deactivate faulty points or images with weak geometry in order to provide an initial image set which can be oriented.

Once a sufficient number of images have been oriented, images not yet oriented can be successively added.

- Manual input of approximate values

It is efficient to use any additional information about the object or the image configuration which may be available e.g. from additional or previous measurements. In particular, the principal distance should be known in advance, for example approximated by the focal length.

In principle, photogrammetric measuring systems capable of automatic measurement and identification of image points generate significantly fewer gross errors than interactive systems. With appropriate image configurations these systems therefore provide a fully automatic procedure, from the calculation of initial values through to the final result of the bundle adjustment.

### 4.3.5 Quality measures and analysis of results

#### 4.3.5.1 Output report

Typical bundle adjustment programs report on the current status of processing including parameters such as number of iterations, corrections to unknowns, error messages. When the program is complete an output report is generated which summarises all results. It should contain the following information:

- list of input files and control parameters, date, project description
- number of iterations and standard deviation of unit weight  $s_0$
- list of observations (image measurements) including corrections, reliability numbers and test values, sorted by images
- mean standard deviations of image coordinates, sorted by image and divided into x' and y' values
- list of blunders detected and eliminated
- list of reference points
- list of adjusted object points (new points) with standard deviations
- mean standard deviations of new points, divided into X, Y and Z values
- maximum corrections with (numeric) identifiers of the corresponding points
- parameters of interior orientation with standard deviations
- correlations between the parameters of interior orientation
- parameters of exterior orientation with standard deviations
- correlations between the parameters of interior and exterior orientation
- list of additional (survey) observations with standard deviations

#### 4.3.5.2 Precision of image coordinates

The precision of image coordinates is calculated from the cofactor matrix:

$$\hat{s}_i = \hat{s}_0 \sqrt{q_{ii}} \quad (4.83)$$

where  $q_{ii}$  are the principal diagonal elements of matrix  $\mathbf{Q}_{\hat{H}}$  (see equation 2.68).

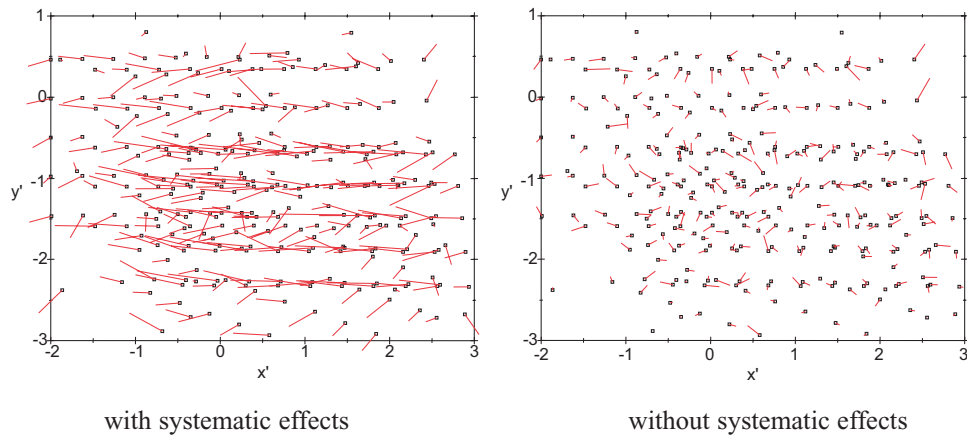


Figure 4.45 Residuals of image coordinates

If the bundle adjustment is calculated using only equally weighted photogrammetric image coordinates as observations,  $\hat{s}_0$  should represent the accuracy of the instrumental combination of camera and image measuring device (see Fig. 7.1).

The standard deviations of the measured image coordinates should be similar in both x and y directions. Different values imply that the measuring device or the camera generates systematic errors. This may occur, for example, with digital images generated by an image scanner whose mechanical construction is different in x and y. Bundle adjustment programs with integrated estimation of variance components (see section 2.3.4.3) allow different weighting for separate groups of observations in order to process observations according to their importance or precision.

A graphical analysis of the distribution of residuals should, in the end, show no systematic errors (Fig. 4.45). However, a rigorous analysis of point accuracy in object space is not possible with this information.

#### 4.3.5.3 Precision of object coordinates

Usually the precision of adjusted object points is of major importance for the quality analysis of a bundle adjustment. The analysis, an example of which is given in Fig. 4.46, should consider two criteria:

- Root mean square error (RMS)

The root mean square error is a measure of the general precision level of the adjustment. Taking the mean image measuring accuracy  $d_{x'}$  and the mean image scale number  $m$  into account, the equation for accuracy estimation can be checked (see section 3.2.1.2):

$$dX = qmdx' \quad (4.84)$$

The design factor  $q$  reflects the accuracy of the imaging configuration with typical values between 0.7 and 1.5 (Fraser 1996).

- Maximum standard deviation of single points

In contrast to the mean standard deviation, maximum residuals indicate the loss of precision which can be expected at problem points or unfavourable areas within the image configuration.

POINT NO.	ADJUSTED OBJECT COORDINATES X	STANDARD DEVIATION				
		Y	Z	SIGX	SIGY	SIGZ
NP 1	-550.0000	550.0000	0.0000	0.0000	0.0000	0.0000
NP 2	-548.8025	76.6273	0.0256	0.0185	0.0216	0.0215
NP 3	-550.0000	-401.0688	0.0000	0.0000	0.0262	0.0000
NP 4	-24.2578	-401.1035	0.0791	0.0226	0.0287	0.0237
NP 5	498.7059	-402.0520	0.0756	0.0279	0.0336	0.0272
NP 6	500.3934	72.0957	0.0000	0.0256	0.0306	0.0000
NP 7	502.2132	547.5473	0.2088	0.0281	0.0302	0.0280
NP 8	-23.2051	549.0098	-0.0653	0.0223	0.0244	0.0244
NP 9	-43.1530	97.4204	30.7236	0.0203	0.0245	0.0192
NP 10	294.5810	-544.1801	30.9239	0.0250	0.0284	0.0268
NP 11	-369.2470	716.9463	30.9868	0.0210	0.0185	0.0246
NP 12	-355.2835	-119.2167	499.6979	0.0236	0.0275	0.0267
NP 13	322.5481	256.7477	500.5552	0.0235	0.0340	0.0273
NP 14	-367.8961	-96.4070	500.5341	0.0233	0.0275	0.0251
NP 15	309.9189	279.5831	500.7111	0.0238	0.0331	0.0285
NP 16	107.0291	-218.9378	550.2870	0.0254	0.0313	0.0257
NP 17	-186.2447	333.0639	550.1281	0.0247	0.0287	0.0247
NP 18	130.0717	-206.7312	550.6317	0.0262	0.0323	0.0280
NP 19	-163.1959	345.2691	550.4474	0.0252	0.0292	0.0251
NP 20	-46.6227	95.7521	805.8236	0.0288	0.0354	0.0227
NP 21	-26.8039	106.0982	12.3571	0.0330	0.0356	0.0256
NP 22	-30.1330	104.4621	762.3889	0.0334	0.0381	0.0259
NP 23	-59.3026	88.9372	12.1583	0.0326	0.0348	0.0250
NP 24	-62.7803	87.2304	762.2332	0.0312	0.0365	0.0250
NP 25	296.2902	427.7684	48.8427	0.0257	0.0384	0.0426
NP 26	-507.1044	1.5373	71.8683	0.0219	0.0266	0.0273
NP 27	-258.4435	574.2591	62.1512	0.0347	0.0294	0.0437
NP 28	134.0411	-171.4542	405.3036	0.0362	0.0348	0.0439
		RMS:	0.0258	0.0302	0.0267	
X-MAX.:	0.0362	AT POINT NO.:	28			
Y-MAX.:	0.0384	AT POINT NO.:	25			
Z-MAX.:	0.0439	AT POINT NO.:	28			

Figure 4.46 Report file showing adjusted object coordinates (CAP)

If object coordinates are to be used for further calculation or analysis, then the maximum standard deviation should stay within specified precision limits.

Both the above quality criteria can be used only to analyse the statistical precision of the photogrammetric procedure. It is necessary here to take into account whether the object coordinate datum was defined without constraints (by minimum number of reference points or by free net adjustment), or if inconsistencies in reference points could be influencing the accuracy of object points.

If image observation accuracy is homogeneous, accuracy differences in object points are mainly caused by:

- different image scales or camera/object distances
- different numbers of image rays per object point
- different intersection angles of image rays
- different image quality of object points
- variations across the image format e.g. lower quality imaging near the edges where distortion is often less well determined
- inconsistencies in reference points

The true accuracy of a photogrammetric project can be estimated only by comparing photogrammatically determined points or distances with reference values measured independently to a higher accuracy. However, a rigorous evaluation is possible only with independent reference points which have not already been used as reference points or for reference distances in the bundle adjustment. Only through independent control will all properties of a photogrammetric

system become visible and a rigorous accuracy assessment become possible. Suggestions for the verification of photogrammetric systems are further discussed in section 6.6.

#### 4.3.5.4 Quality of self-calibration

The adjusted interior orientation parameters, and their correlations, should be carefully examined if the image acquisition system has been calibrated simultaneously in the bundle adjustment.

Fig. 4.47 is a part of a calculation report showing the adjusted interior orientation data, associated standard deviations and a matrix of correlations between the parameters. The following comments can be made about individual parameters:

- principal distance  $c$

The value of  $c$  normally corresponds approximately to the focal length. When plane surfaces are imaged without oblique views, the principal distance cannot be uniquely determined and either the value of  $c$  is unreasonable or its corresponding standard deviation is higher than expected. However, this does not mean that the object points are determined to lower accuracy. If the results of the bundle adjustment are intended to calibrate a camera which is subsequently used on other projects, then the principal distance must be calculated accurately and with a standard deviation of the order of the image measuring accuracy.

- principal point  $x'_0, y'_0$

The principal point normally lies very close to the foot of the perpendicular from the projection centre to the focal plane. When plane surfaces are imaged without oblique views, the position of the principal point cannot be uniquely determined; in this case, however, this does not mean that the object points are determined to a lower accuracy. The importance attached to an accurate knowledge of the principal point will depend on the configuration of the network. If the results of the self calibration are intended to be subsequently used on other projects, then the position of the principal point must be calculated accurately and with a standard deviation of the order of the image measuring accuracy.

It should be remembered that the definition of radial distortion depends on the location of the principal point. A large shift of the principal point may result in irregular parameters for radial distortion. An iterative pre-correction of measured image coordinates is recommended in those cases.

- radial (symmetric) distortion  $A_1, A_2, A_3$

The parameters of radial distortion are normally the most effective additional parameters. Their related standard deviations should be much smaller than the parameters themselves.

CAMERA NO.	10	R0:	20.0000	FOCAL LENGTH (MM)	S.D. (MM)
C :				-59.2616	0.0065
PRINCIPAL POINT		S.D. (MM)		RAD.SYM.DIST.	S.D.
X0:	0.0636	0.0035		A1:	-0.193D-04 0.476D-06
Y0:	0.1284	0.0040		A2:	0.556D-08 0.763D-09
CORRELATION BETWEEN PARAMETERS OF INTERIOR ORIENTATION					
C	1.00				
X0	0.03	1.00			
Y0	0.21	0.03	1.00		
A1	0.04	0.00	0.00	1.00	
A2	0.05	0.00	0.10	-0.97	1.00

Figure 4.47 Result of a self-calibration with correlation between the parameters

Parameter  $A_2$  is often significantly correlated with  $A_1$  (as shown in Fig. 4.47). However, this does not necessarily affect the overall result, especially for the object coordinates. Parameter  $A_3$  can normally be determined to a significant value only in special cases, for example when fish-eye lenses are employed.

- Tangential (asymmetric) distortion  $B_1, B_2$ , affinity and shear  $C_1, C_2$

The statements concerning  $A_1$  and  $A_2$  can also be applied to the optional additional parameters  $B_1, B_2, C_1, C_2$ . For many metric film and plate cameras these parameters cannot be determined with significant accuracy and they often exhibit high correlation with other values of interior orientation. In contrast, digital or video cameras should normally be calibrated using these parameters.

Correlations between the parameters of interior orientation and exterior orientation should be avoided by an appropriate imaging configuration (see section 7.2). They do not need to be considered for point determination if the calculation is performed in a single stage mathematical process. However, if single parameters are extracted for use in further external calculations (e.g. orientation parameters are applied in separate space intersections), correlations, or more accurately the variance-covariance matrix, cannot be further taken into account, which leads to errors in the functional model.

### 4.3.6 Strategies for bundle adjustment

In many practical applications either the generation of initial values or the complete bundle adjustment may not run successfully at the first attempt or the final result might not meet the specification. To avoid these problems a number of practical tips and suggestions for strategies and procedures in bundle adjustments is given below.

#### 4.3.6.1 Simulation

Simulation of the imaging configuration is one method of project planning (see section 7.1.4). Simulation provides *a priori* accuracy estimation for optimising an imaging configuration without real measurements. For this purpose the measured object must be represented by simulated object points similar to the actual measurement in terms of number and distribution. The required 3D coordinates can be provided by manual input if the object is not too complex. Alternatively, the coordinates can be obtained from a CAD model or previous measurements (Fig. 4.48).

The *a priori* definition of camera stations and viewing directions (exterior orientations) is much more complicated. While orientation data can easily be generated for regular image configuration patterns (example in Fig. 4.24), the measurement of complex object structures can often be configured only directly on-site. On the one hand selection of image configurations is more flexible but on the other hand unforeseen problems can often occur in the form of occlusions or restricted camera stations.

Camera data and *a priori* accuracies must also be defined. Image coordinates can then be calculated using collinearity equations and the simulated object coordinates and orientation data. Using these simulated data as input, a bundle adjustment can be calculated. Here it is only necessary to compute the covariance matrix of the unknowns and the standard deviations of interest, instead of a complete parameter estimation. Now object points, imaging configurations, selection of cameras and accuracies can be varied until a satisfactory adjustment is achieved (see section 7.1.4). By applying the Monte-Carlo method, the input data can be altered within specific noise ranges based on normal distribution. The computed output values will vary as a function of the noisy input data (Hastedt 2004).

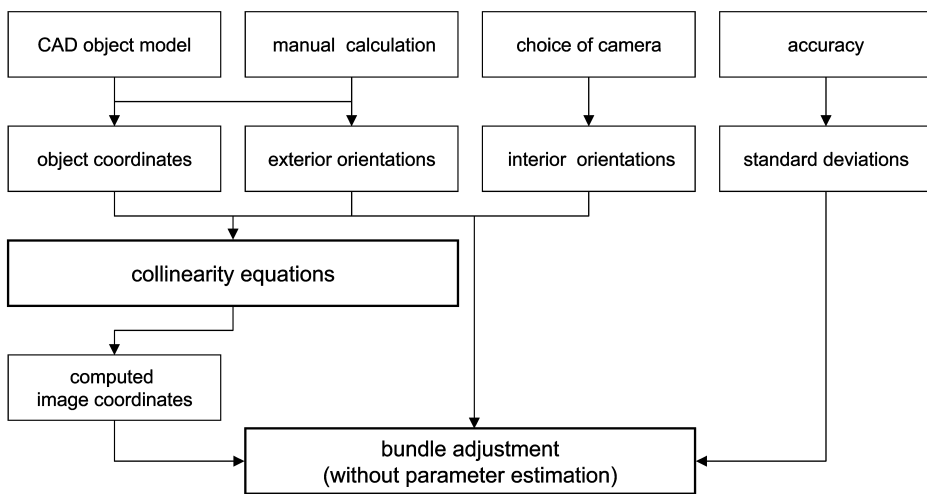


**Figure 4.48** Simulation by bundle adjustment

#### 4.3.6.2 Divergence

Bundle adjustments which do not converge are often a serious problem in practical applications. A major reason for this is that standard statistical methods of error detection only work well if at least one iteration has been successfully calculated. Divergence in adjustments can be caused by:

- Faulty input data: error in data formats, units of measurement, typing errors etc. should be detected by the program but often are not.
- Poor initial values: low quality starting values of the unknowns lead to an inadequate linearisation of the functional model.
- Gross errors in the input data: errors in identifying point or image numbers and measuring errors larger than the significance level of the total measurement. They can be detected in part by statistical tests if robust estimation methods are applied (see section 2.3.4).
- Weak imaging geometry: small intersection angles, a small number of rays per object point and/or poor interior orientation data lead to poorly conditioned normal equations and a lower reliability in the adjustment.

The following steps should therefore be applied to handle divergent bundle adjustments:

- 1) check of the input data
- 2) controlled program abortion after iteration 0, with checking of differences between initial values and adjusted unknowns (see section 2.3.4.1)—high deviations indicate problematic input data
- 3) pre-correction of image coordinates by known distortion values
- 4) adjustment without camera calibration in the first run; subsequent adding of additional parameters (distortion) when blunders have been eliminated from the input data
- 5) check of the geometric configuration of images where gross errors have been detected—the smearing effect of least-squares solutions can lead to misidentification of blunders.

### 4.3.6.3 Elimination of gross errors

Generally speaking the bundle adjustment is very sensitive to gross errors (blunders) in the measured data. In complex imaging configurations gross errors arise easily due to false identification of object points or mistakes in image or point numbering. In contrast, pure measuring errors occur relatively infrequently. The detection of gross errors can fail, especially in geometrically weak configurations where statistical tests based on redundancy numbers are not significant (see section 2.3.3.4). This is of major importance if gross errors in observations occur at *leverage points* which have a strong influence on overall geometry but which cannot be controlled by other (adjacent) observations.

Most professional bundle adjustment programs permit both manual and automatic elimination of blunders. In both cases only one blunder should be eliminated per program run, usually the one with the largest normalised correction. The adjustment program should allow the corresponding observation to be set as inactive, not deleted, in order that it can be reactivated later in case it is discovered to be correct.

If observations are eliminated the corresponding object area and image should be analysed. Uncontrolled elimination of observations can lead to weak imaging geometries if the object is recorded by a small number of images, or represented by only a few object points. A system that is based on the few remaining observations cannot be controlled by a rigorous blunder test and may produce a plausible result even if gross errors are still present.

## 4.4 Object reconstruction

### 4.4.1 Single image processing

Photogrammetric procedures for single image processing are designed either for the determination of object coordinates or for the optical or computational rectification of the image into a different geometric projection (Fig. 4.49). In both cases, image orientation data and additional object geometry (reference points, geometric elements, DSM) are required. In general we must distinguish between the case of plane objects and that of arbitrary three-dimensional surfaces.

#### 4.4.1.1 Projective transformation

##### *Mathematical model*

A special case is the reconstruction of plane object surfaces. The central perspective projection of an object plane onto the image plane is described by the projective transformation (see section 2.2.1.5).

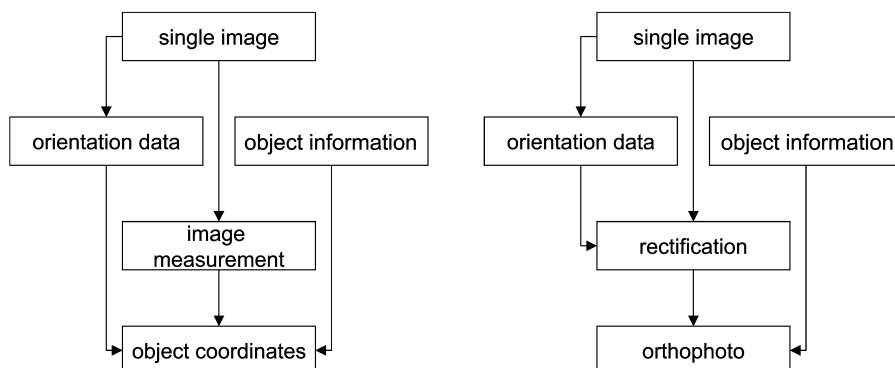


Figure 4.49 Methods for single image processing

Ignoring distortion components, inversion of the collinearity equations (4.8) gives:

$$\begin{aligned} X &= X_0 + (Z - Z_0) \frac{r_{11}(x' - x'_0) + r_{12}(y' - y'_0) + r_{13}z'}{r_{31}(x' - x'_0) + r_{32}(y' - y'_0) + r_{33}z'} \\ Y &= Y_0 + (Z - Z_0) \frac{r_{21}(x' - x'_0) + r_{22}(y' - y'_0) + r_{23}z'}{r_{31}(x' - x'_0) + r_{32}(y' - y'_0) + r_{33}z'} \end{aligned} \quad (4.85)$$

Assuming parameters of interior and exterior orientation are known, object coordinates  $X$  and  $Y$  can be calculated from (4.85) if  $Z$  is known (e.g.  $Z = 0$  for the  $XY$  plane). Collecting terms representing constant orientation parameters and re-arranging, equations representing the central projection of a plane are obtained:

$$\begin{aligned} X &= \frac{a_0 + a_1x' + a_2y'}{c_1x' + c_2y' + 1} \\ Y &= \frac{b_0 + b_1x' + b_2y'}{c_1x' + c_2y' + 1} \end{aligned} \quad (4.86)$$

In order to determine the eight parameters of equation (4.86) at least four reference points are required on the plane, no three of which may lie on a common straight line.

Equations (4.86) are non-linear in the  $a$ ,  $b$ ,  $c$  coefficients. A direct, non-iterative calculation of the unknown parameters is possible if linear equations (2.13) are used. This results in the following equations:

$$\begin{aligned} a_0 + a_1x_i + a_2y_i - c_1x_iX_i - c_2y_iX_i &= X_i \\ b_0 + b_1x_i + b_2y_i - c_1x_iY_i - c_2y_iY_i &= Y_i \end{aligned} \quad (4.87)$$

which can be solved directly according to the scheme

$$\mathbf{A}\hat{\mathbf{x}} = \mathbf{l} \quad (4.88)$$

Using the transformation parameters of (4.86) further image coordinates can be transformed into object coordinates.

Fig. 4.50 shows the position of five plane object points and the corresponding image coordinates with their related transformation parameters. For the special case where  $c_1 = 0$  and  $c_2 = 0$ , the projective transformation (4.86) reduces to an affine transformation (equation 2.6). For the further case of parallel object and image planes (Fig. 4.50 top right), equation (4.86) can be replaced by the plane similarity transformation (2.2).

#### *Influence of interior orientation*

The model of central projection described above assumes straight line rays through the perspective centre. Although the spatial position of the perspective centre (principal distance  $c$ , principal point  $x'_0, y'_0$ ) is modelled by the parameters of the projective transformation, no effects of lens distortion can be compensated for here.

The image coordinates must therefore be corrected for lens distortion before applying the projective transformation. For optimal accuracy, when applying distortion parameters derived from a separate process, care should be taken to prevent the possibility they become correlated with the interior and exterior orientation parameters. Further usage of these parameters might

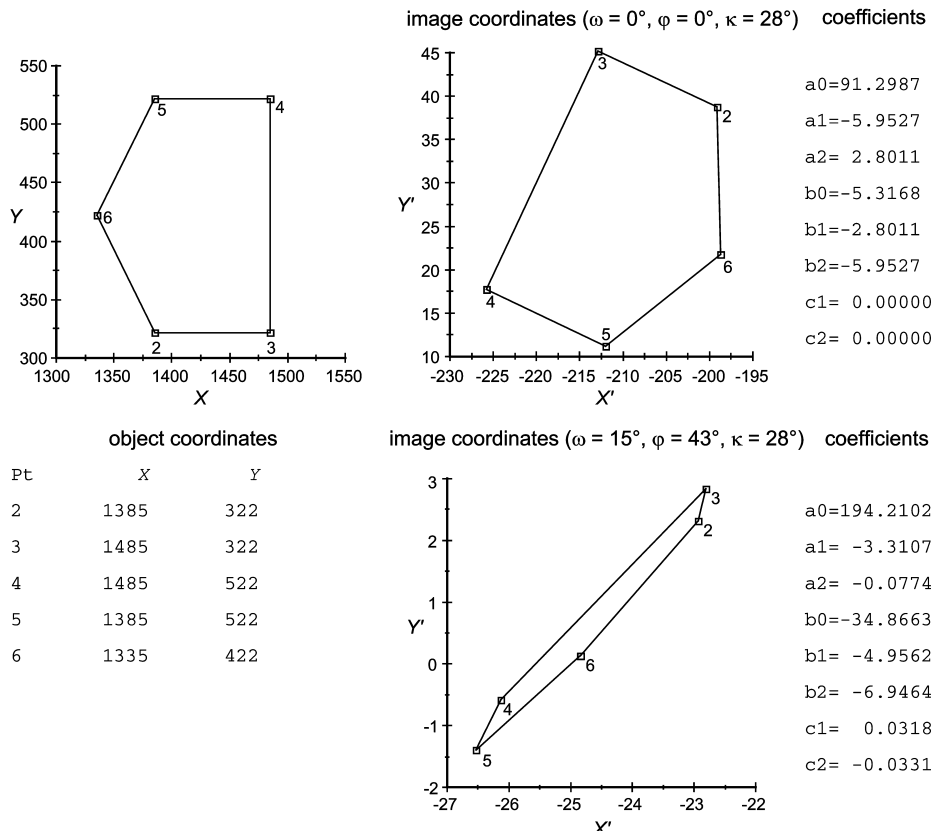


Figure 4.50 Projective transformation of a plane pentagon

involve a different mathematical model where, strictly speaking, the distortion parameters should be applied with their full variance-covariance matrix from the bundle adjustment. However, this transfer of correlation information is rarely done.

#### Influence of non-coplanar object points

Object points which do not lie in the plane of the reference points have a positional error in image space after projective transformation. This shift depends on the height above the reference plane and on the position of the point in the image. The image plane is here assumed to be parallel to the reference plane. Since Fig. 4.51 represents a vertical plane containing the projection centre the shift is radial with respect to the principal point. The image space shift  $\Delta r'$  is shown in Fig. 4.51 and is given by the following expression:

$$\Delta r' = \frac{r'}{h} \Delta h \quad (4.89)$$

Multiplying by the image scale gives the corresponding shift in the reference plane:

$$\Delta r = \frac{h}{c} \Delta r' = m \Delta r' \quad (4.90)$$

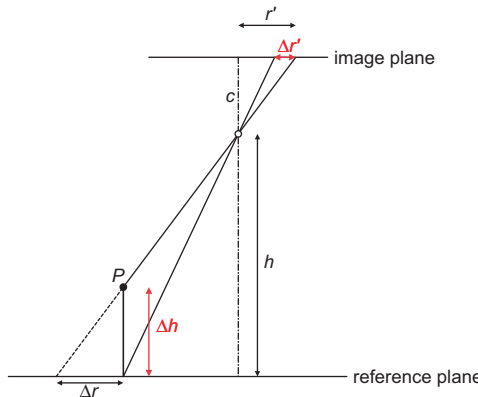


**Figure 4.51** Shift in image space caused by height differences

The equations above can also be used to determine the maximum height of a point above the reference plane which will not exceed a specified shift in image space.

#### Example 4.1:

For the measurement of a flat plate (see section 6.4.3.1), a digital video camera is used with the following specifications:  $c = 8\text{mm}$ ,  $h = 2.5\text{m}$ ,  $r'_{\max} = 5\text{mm}$ . The maximum offset above the object plane must be calculated which ensures that the resulting shift in object space  $\Delta r$  is less than 1mm.

$$\text{Solution: } \Delta h = \Delta r \frac{c}{r'_{\max}} = 1.0\text{mm} \frac{8\text{mm}}{5\text{mm}} = 1.6\text{mm}$$

From equations (4.89) and (4.90)

#### Plane rectification

In addition to coordinate determination, the projective transformation is also used as the mathematical basis for optical or digital image rectification. The aim is the transformation of an analogue or digital image into a new geometric (graphical) projection.

For rectification of a plane, the complete image format, or a defined area of interest, is transformed into the reference system (target system) by the parameters of a single projective transformation i.e. the same transformation coefficients are applied to every point in the source image area. In contrast, for non-planar objects every image point must be rectified as a function of its corresponding XYZ coordinates (differential rectification or orthophoto production, see section 4.4.1.2).

In close-range photogrammetry analogue rectification, using optical rectifiers is no longer of interest. In contrast, digital rectification has gained in importance e.g. for the production of rectified image mosaics of building façades, or for the superposition of natural textures onto CAD elements (see section 5.3). Fig. 4.52 shows an example of the plane rectification of a facade. Object areas outside the reference plane are distorted.

#### 4.4.1.2 Single image evaluation of three-dimensional object models

The spatial ray defined by an image point can be intersected with the object surface, if interior and exterior orientation of the image are known and a geometric model of the surface exists. The object model can be defined by a dense grid of points (digital surface or elevation model), or by a known mathematical element (e.g. straight line, plane, cylinder). The intersection point of the ray and the object model is the desired 3D object coordinate.

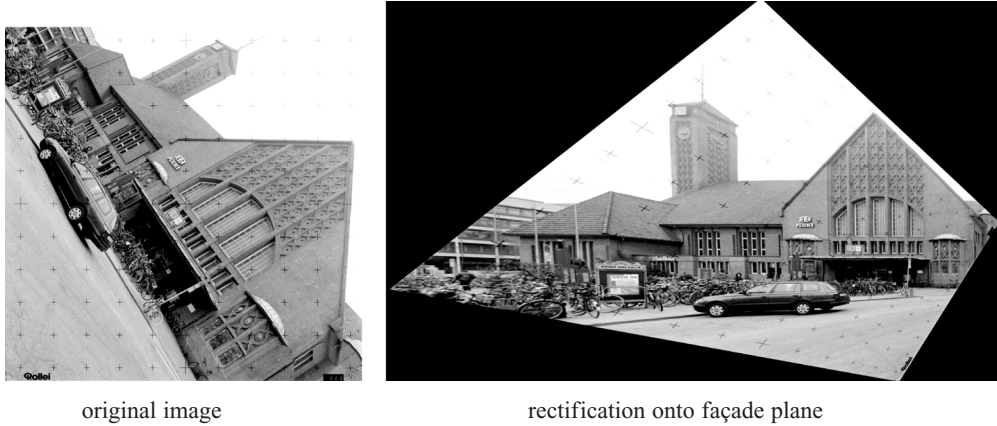


**Figure 4.52** Example of plane rectification

### Object planes

The principle of photogrammetric point determination within an object plane is illustrated in Fig. 4.53. The 3D coordinates of the object point  $P$  result from the intersection of the object surface and the ray defined by the image point  $P'$  and the perspective centre  $O'$ . The reference plane can be defined for example by three photogrammetrically measured points. The parameters of the plane can be calculated from a least-squares best-fit adjustment (see section 2.4.2.2).

### Digital surface models

An arbitrary or free-form object surface can be approximated by a suitably dense grid of 3D points (digital surface model, DSM, see section 2.4.3.1). The point grid can be regular (raster form e.g.  $\Delta X = \Delta Y = \text{const.}$ ) or non-regular. Object edges (breaklines) can be modelled by special point codes or by additional vector data (polygons). Inside the object model further points can be interpolated (Kraus 2000).

Fig. 4.54 shows the principle of spatial point determination from a single image using a digital surface model (DSM). The spatial direction defined by the measured image coordinates  $x'$ ,  $y'$  and  $c$  in the image coordinate system (image vector  $\mathbf{x}'$ ) is transformed into the spatial vector  $\mathbf{X}^*$  using

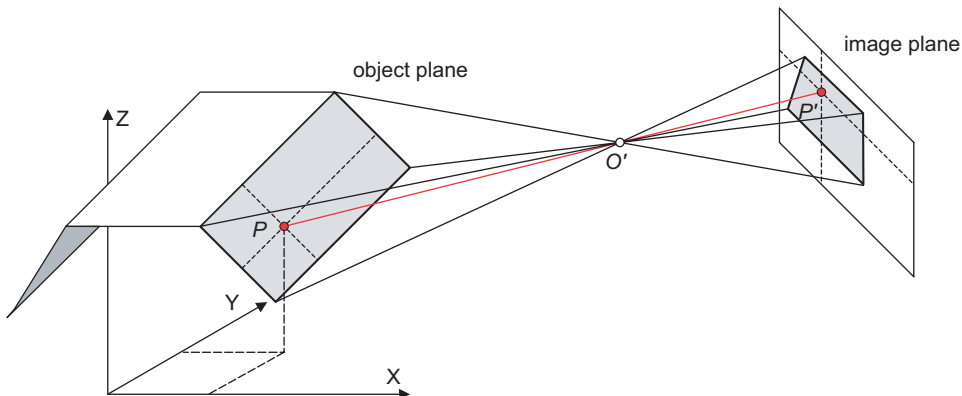


**Figure 4.53** Single image evaluation within an object plane

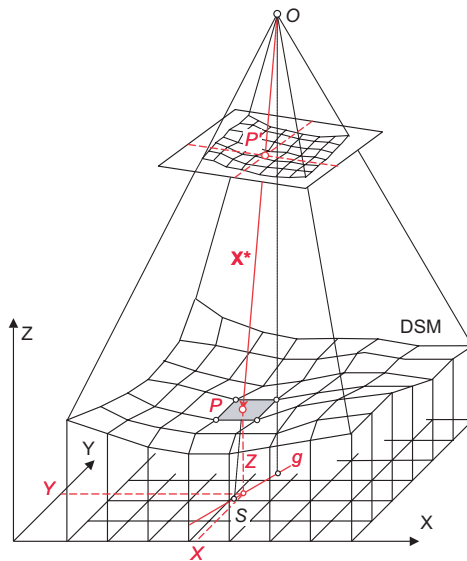


**Figure 4.54** Point determination in a digital surface model (DSM)

the exterior orientation parameters (similarity transform with arbitrary scale e.g.  $m = 1$ ). This ray intersects the DSM at point  $P$  using a local surface plane defined by the four adjacent points.

In order to calculate the point of intersection, the straight line  $g$  is constructed between the intersection point  $S$  of  $X^*$  and the XY plane, and the foot of the perpendicular  $O_{XY}$  from the perspective centre to the XY plane (Fig. 4.55). A search for point  $P$  starts along this line at  $O_{XY}$  until its interpolated height  $Z$  lie within two  $Z$  values of adjacent profile points.

This procedure is known as monoplotting. It is not very popular in close-range photogrammetry, but is gaining importance in the field of CAD technology and 3D Laser technology. As an example Fig. 4.56 shows the determination of the water line of a moving ship model using one oriented image. The object surface model is built up from a dense series of CAD profiles that are intersected with the water line derived from the image.

#### Differential rectification

For the production of an orthophoto by differential rectification, each point (infinitesimally small object patch) is projected individually according to its XYZ coordinates. As a result the

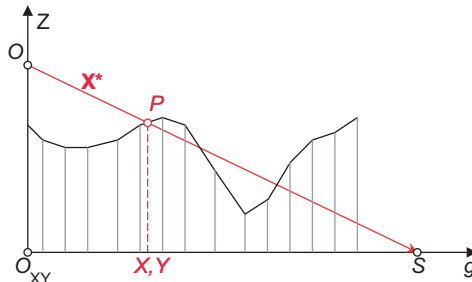


**Figure 4.55** Search and interpolation of object point  $P(XYZ)$  within the height profile above  $g$

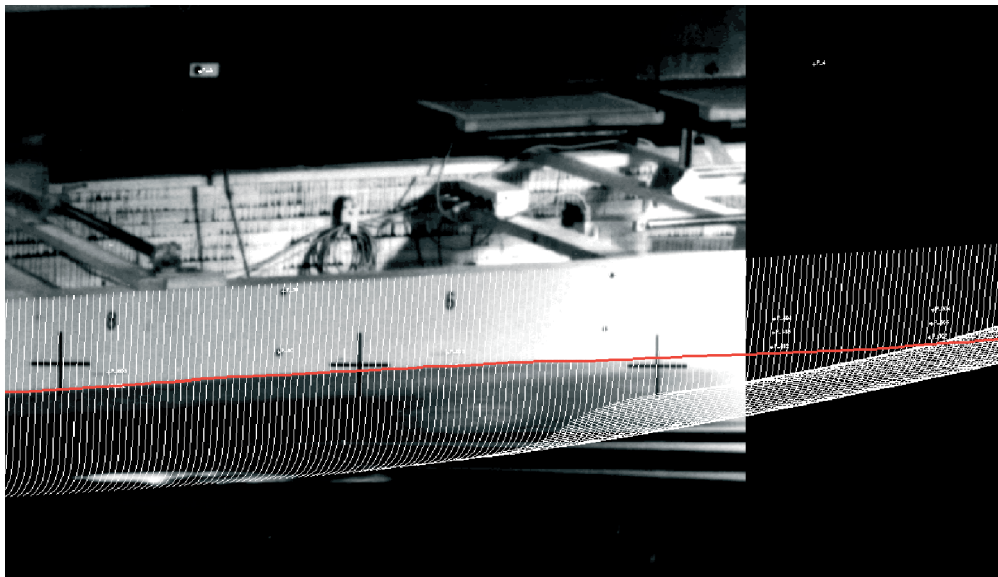


**Figure 4.56** Monoplotted for the determination of a water line by intersection with the CAD surface of the ship model

new image is a parallel projection of the object surface. A digital orthophoto displaying a rectangular area of the ground plane XY is calculated in the following steps (Fig. 4.57):

1. Definition of the rectangular area of interest on the object:

$$\text{lower left corner: } X_1, Y_1$$

$$\text{upper right corner: } X_2, Y_2$$

2. Definition of output scale and print resolution of the orthophoto:

The output scale (map scale)  $m_k$  of the orthophoto and the required resolution  $\Delta x_k, \Delta y_k$  for printing (output) define the grid width (point distance) in object space.

3. Definition of grid width  $\Delta X, \Delta Y$ , used to scan the object:

$$\Delta X = m_k \Delta x_k$$

$$\Delta Y = m_k \Delta y_k$$

4. For each grid point  $(X, Y)_i$  the corresponding  $Z_i$  value is interpolated in the given surface model:

$$X_i = X_1 + j\Delta X \quad Z_i = Z(X_i, Y_i)$$

$$Y_i = Y_1 + k\Delta Y$$

5. Using the collinearity equations (4.8) and the given parameters of interior and exterior orientation, the image coordinate  $(x', y')_i$  corresponding to  $(X, Y, Z)_i$  is calculated:

$$x'_i = F(X_0, Y_0, Z_0, \omega, \phi, \kappa, x'_0, c, dx', X_i, Y_i, Z_i)$$

$$y'_i = F(X_0, Y_0, Z_0, \omega, \phi, \kappa, y'_0, c, dy', X_i, Y_i, Z_i)$$

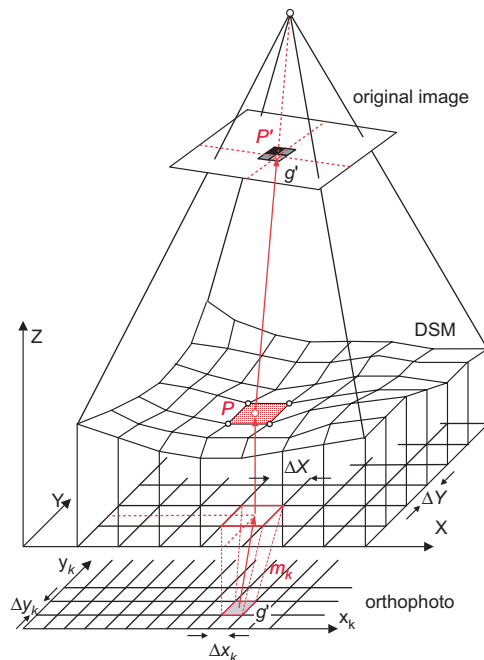


Figure 4.57 Principle of orthophoto production

- At position  $(x', y')_i$  the stored grey value is extracted from the (digital) image. The grey value is usually interpolated, since  $(x', y')_i$  are floating point numbers which do not match the integer pixel raster of the image (see section 5.3.2):

$$g'_i = g(x', y')_i$$

- The interpolated grey value  $g'_i$  is transferred into the output image at position  $(x, y)_i$ :

$$x_i = x_1 + j\Delta x_k$$

$$y_i = y_1 + k\Delta y_k$$

The method described above transforms each point of the orthophoto into the original image. In order to reduce the computational effort, a coarse grid can be predefined from which local grey values can be linearly interpolated (Kraus 2000).



Figure 4.58 Original image and cylindrical projection (monastery church Gernrode, west apse, Fokus Leipzig)



**Figure 4.59** 3D model with rectified image areas and superimposed textures  
(University of Aalborg, FH Bielefeld)

Object areas which are not described by the surface model are again shifted and distorted in image space. Occluded object areas lead to empty (black) spaces in the orthophoto, and can only be projected by additional images from different stations. The latter method however requires either extensive ray tracing or simultaneous multi-image processing, for example using object-based multi-image matching (see section 5.5.5).

Differential rectification is a general approach which, in principle, can be applied to arbitrary projections and object surfaces. In such cases it is necessary only to replace the transformations of steps 3 and 4 with functions relating the 2D coordinates of the original image to the 3D object coordinates. This method can handle, for example, cylindrical or spherical projections as well as the plane projective transformation described above.

An orthophoto can also be generated by combining a number of partial views or original images into a common image mosaic. This procedure, used in the production of aerial image maps, can be employed in close-range photogrammetry for the rectification of façades, or for texture mapping of CAD models (Fig. 5.53, section 5.3.3, Höhle 1997, Hemmleb and Wiedemann 1997).

#### 4.4.2 Stereoscopic processing

##### 4.4.2.1 Principle of stereo image processing

Stereo processing covers all visual or computational methods for the processing of a stereo image pair. It is applied in the case of aerial photogrammetry.

In close-range work, stereo photogrammetry is used mainly in the following applications:

- Visual processing of natural features

The reconstructed object is measured in a stereo plotting instrument using binocular, stereoscopic optical viewing systems. The operator observes an optically or digitally generated ‘floating mark’, the apparent spatial position of which is under his control. A measurement is taken when the floating mark appears to lie on the virtual surface of the object; the point measured corresponds to the pair of homologous image points simultaneously viewed stereoscopically. The movement of the floating mark on to the surface is controlled interactively by the operator. Single points may be measured; continuous lines may also be measured as the operator moves the floating mark over the virtual surface.

- Visual or digital reconstruction of free-form surfaces

Object surfaces of arbitrary shape can be evaluated by stereophotogrammetry if the surface structure permits the identification (matching) of homologous points. Surfaces with insufficient visual pattern or structure must therefore be prepared with a suitable texture e.g. by pattern projection or other method. Image processing is performed either by the visual method above, or by image processing algorithms which implement stereo image matching of corresponding points (see section 5.5). The final goal is the complete 3D reconstruction of the free-form surface, for example as a digital surface model.

- Image acquisition with stereometric cameras

Stereometric cameras (see section 3.3.1.3) are usually configured to correspond to the normal case of stereo photogrammetry. They provide a simple method of imaging and of photogrammetric object reconstruction which, to a large extent, avoids complicated orientation procedures.

- Point-by-point (tactile) object measurement with on-line dual camera systems

On-line photogrammetry systems comprising two digital metric cameras can be treated as stereo systems, although they can easily be extended to incorporate more than two cameras. The object is measured by spatial intersection of targeted points (targets, probes) which can be detected and identified automatically. If the exposure of both cameras is synchronised, the object can be measured by hand-held contact probes (see section 6.4.2.2).

- Control of vision-based machines (e.g. autonomous robots)

There are a number of applications in computer vision (stereo vision, shape from stereo) where a scene is analysed by stereo-based algorithms which reflect the mechanisms of natural human vision. Examples are the control of autonomous robots in unknown environments (avoidance of collisions) and the control of production tools (see example in Fig. 6.17).

The principle of stereo processing is based on the correspondence of homologous points lying in an epipolar plane. The epipolar plane intersects the image planes in epipolar lines (see section 4.2.5.2). For the normal case of stereo photogrammetry (Fig. 4.60) the epipolar lines are parallel and depth information can be determined by measuring the x-parallax  $px'$ .

#### **4.4.2.2 Point determination using image coordinates**

##### *Coordinate calculation in normal case*

The ‘normal’ case of stereophotogrammetry is, in fact, the special case in which two identical cameras have parallel axes pointing in the same direction at right angles to the stereo base. With

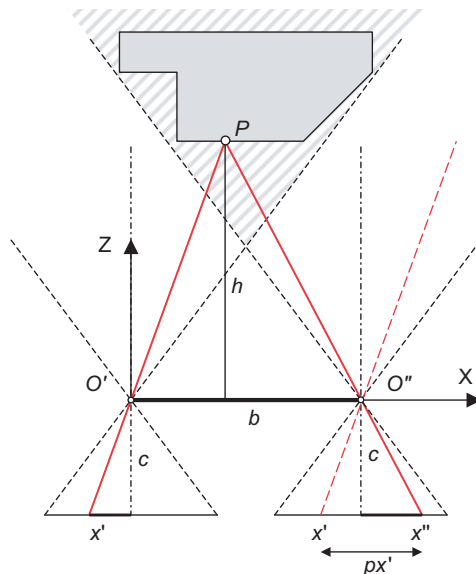


**Figure 4.60** Normal case of stereo photogrammetry

respect to an XYZ coordinate system located in the left perspective centre, object coordinates can be derived from the ratios indicated in Fig. 4.60:

Parallel to the image plane:

$$X = \frac{h}{c} x' = mx' \quad Y = \frac{h}{c} y' = my' \quad = my'' \quad (4.91)$$

In the viewing direction:

$$\frac{h}{c} = \frac{b}{x' - x''} = m$$

and it follows that:

$$Z = h = \frac{bc}{x' - x''} = \frac{bc}{px'} \quad (4.92)$$

Equations (4.91) and (4.92) can also be derived from the collinearity equations (4.8). The rotation angles of both images are zero. The right image is shifted in the X direction by the base length  $b$  with respect to the left image. Hence it follows that:

$$X_{01} = Y_{01} = Z_{01} = Y_{02} = Z_{02} = 0$$

$$X_{02} = b \quad : \text{exterior orientation values}$$

$$\omega_1 = \varphi_1 = \kappa_1 = \omega_2 = \varphi_2 = \kappa_2 = 0$$

$$\mathbf{R}_1 = \mathbf{R}_2 = \mathbf{I}$$

$$x'_{01} = y'_{01} = x'_{02} = y'_{02} = 0 \quad : \text{principal points}$$

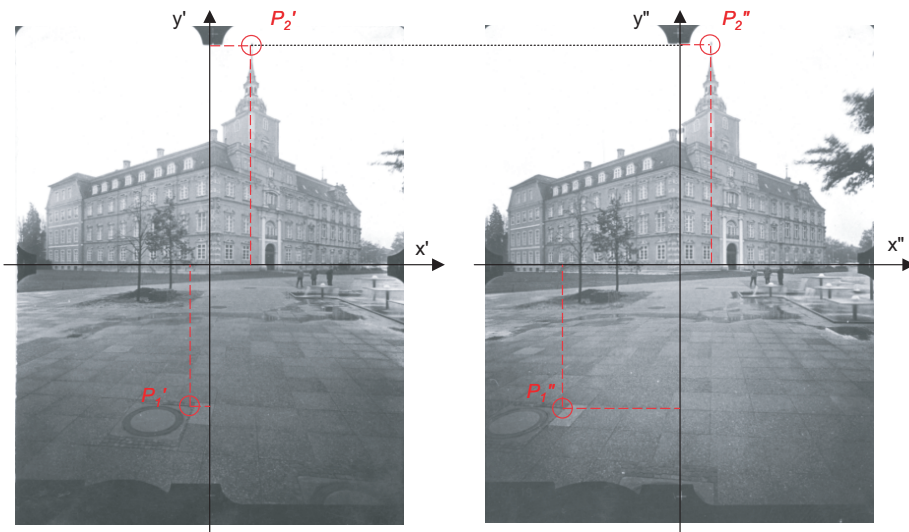


**Figure 4.61** Measurement of two object points in a stereo image pair

The x-parallax (disparity)  $px'$  is measured either by visual examination and coordinate measurement, or by methods of digital image matching. As an example Fig. 4.61 shows the measurement of two object points. Point  $P_1$  on the manhole cover closest to the cameras has a much larger x-parallax than the more distant point  $P_2$  at the top of the tower. The  $y'$  image coordinates are almost equal, i.e. y-parallax is negligibly small.

#### Example 4.2:

The following image coordinates have been measured for the example image pair above (SMK 120,  $b = 1.2$  m,  $c = 64$  mm). The object coordinates of the two points are to be calculated.

Solution:

1. point $P_1$	$x' = -3.924$ mm	$x'' = -23.704$ mm
	$y' = -29.586$ mm	$y'' = -29.590$ mm
	$px' = x' - x'' = 19.780$ mm	
2. point $P_2$	$x' = 7.955$ mm	$x'' = 6.642$ mm
	$y' = 45.782$ mm	$y'' = 45.780$ mm
	$px' = x' - x'' = 1.313$ mm	
3. Z coordinate (distance)	$Z = \frac{bc}{px'}$	$Z_1 = 3.88$ m $Z_2 = 58.49$ m
4. XY coordinates	$X_1 = -0.24$ m $Y_1 = -1.79$ m $m = 61$	$X_2 = 7.27$ m $Y_2 = 41.84$ m $m = 914$

The result shows that point  $P_1$  lies beneath the left-hand camera at a distance of 3.88 m. Point  $P_2$  is located to the right and above the left camera at a distance of 58.49 m and with a smaller image scale.

*Accuracy*

Differentiation of equation (4.92) and application of error propagation gives the following accuracy estimation of the object coordinate in the viewing direction  $Z$  ( $c$  and  $b$  are assumed to be error-free).

$$s_Z = \frac{Z^2}{bc} s_{px'} = \frac{h}{b} \frac{h}{c} s_{px'} = qms_{px'} \quad (4.93)$$

The equation shows that the accuracy in the viewing direction is a function of the accuracies of parallax measurement, image scale  $h/c$  and base-to-height ratio  $h/b$ , which corresponds to the design factor  $q$  introduced in section 3.2.1.2. The equation also shows that, since  $b$  and  $c$  are constant for any particular case, the accuracy falls off in proportion to the square of the distance,  $Z$ . The base-to-height ratio, or more correctly base-to-distance ratio, describes the intersection geometry. If the base is small compared with the distance, ray intersection is weak and accuracy in the viewing direction is poor.

In general parallax measurement accuracy can be estimated as

$$s_{px'} = \frac{s_{x'}}{\sqrt{2}} \quad (4.94)$$

i.e. it is slightly more accurate than a single measured image coordinate.

The accuracy of the X and Y coordinates can be similarly derived from equation (4.91).

$$\begin{aligned} s_X &= \sqrt{\left(\frac{x'}{c} s_Z\right)^2 + \left(\frac{Z}{c} s_{x'}\right)^2} = \sqrt{\left(\frac{x'}{c} qms_{px'}\right)^2 + (ms_{x'})^2} \\ s_Y &= \sqrt{\left(\frac{y'}{c} s_Z\right)^2 + \left(\frac{Z}{c} s_{y'}\right)^2} = \sqrt{\left(\frac{y'}{c} qms_{px'}\right)^2 + (ms_{y'})^2} \end{aligned} \quad (4.95)$$

In equation (4.95) the dominant term is the second term of the square root. Object accuracy can therefore usually be estimated as

$$s_X = s_Y = ms_{x'y'} \quad (4.96)$$

The following object accuracies result in example 4.2 above:

**Example 4.3:**

Assume image coordinates are measured to an accuracy of 10  $\mu\text{m}$ , resulting in a parallax accuracy of 7  $\mu\text{m}$ . Principal distance and base length are assumed to be error-free.

Object accuracies:

$$1. \text{ point } P_1: \quad s_X = 0.6 \text{ mm} \quad s_Y = 0.6 \text{ mm} \quad s_Z = 1.4 \text{ mm} \quad q = h/b = 3.2$$

$$2. \text{ point } P_2: \quad s_X = 9.1 \text{ mm} \quad s_Y = 9.1 \text{ mm} \quad s_Z = 315 \text{ mm} \quad q = h/b = 48$$

It is clear that the accuracy of point  $P_2$  is significantly decreased in  $Z$  and coordinate determination of this point is not practicable.

Fig. 4.62 shows the object accuracies for additional point distances taken from example 4.2. For object distances less than about 1.7 m ( $q = 1.4 = 1:0.7$ ) the accuracy  $s_Z$  in the viewing direction is higher than in the other directions. At longer distances the increase in uncertainty  $s_Z$  is quadratic while the increase in  $s_X$  remains linear.

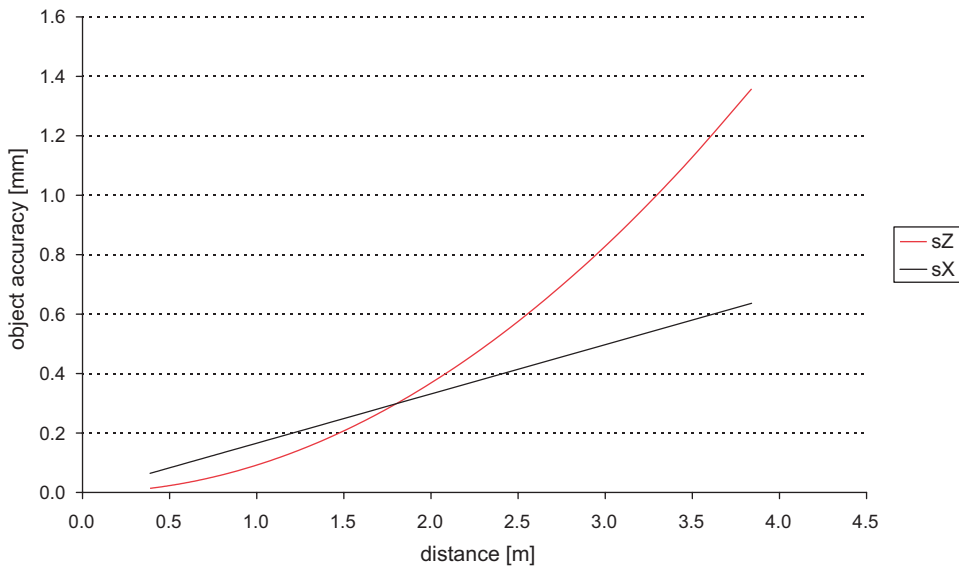


Figure 4.62 Object accuracy for the normal case of stereo photogrammetry (from example 4.2)

#### Intersection in the general stereo case

A stereo pair which is not configured according to the strictly normal case has orientation parameter values which are not equal to zero. In addition the images can have arbitrary parameters of interior orientation.

Object coordinates  $XYZ$  can be calculated by spatial intersection of the rays  $\mathbf{r}'$  and  $\mathbf{r}''$  if the parameters of interior and exterior orientation of both images are known (Fig. 4.63). Both spatial rays are defined by the measured image coordinates, transformed by the orientation parameters. For the special case of a stereo pair, the spatial intersection can be calculated as follows (Albertz and Kreiling 1989, and see also the calculation of model coordinates, section 4.2.5.3):

- Transformation of image coordinates

$$\begin{bmatrix} X' \\ Y' \\ Z' \end{bmatrix} = \begin{bmatrix} X_{01} \\ Y_{01} \\ Z_{01} \end{bmatrix} + \mathbf{R}_1 \begin{bmatrix} x' \\ y' \\ z' \end{bmatrix} \quad \begin{bmatrix} X'' \\ Y'' \\ Z'' \end{bmatrix} = \begin{bmatrix} X_{02} \\ Y_{02} \\ Z_{02} \end{bmatrix} + \mathbf{R}_2 \begin{bmatrix} x'' \\ y'' \\ z'' \end{bmatrix} \quad (4.97)$$

- Stereo base components

$$\begin{aligned} bx &= X_{02} - X_{01} \\ by &= Y_{02} - Y_{01} \\ bz &= Z_{02} - Z_{01} \end{aligned} \quad (4.98)$$

For the simple version of the intersection the skew rays intersect the XY plane at elevation  $Z$  of object point  $P$  i.e.

$$\begin{aligned} X &= X_1 = X_2 \\ Z &= Z_1 = Z_2 \\ Y &= \frac{Y_1 + Y_2}{2} \end{aligned} \quad (4.99)$$

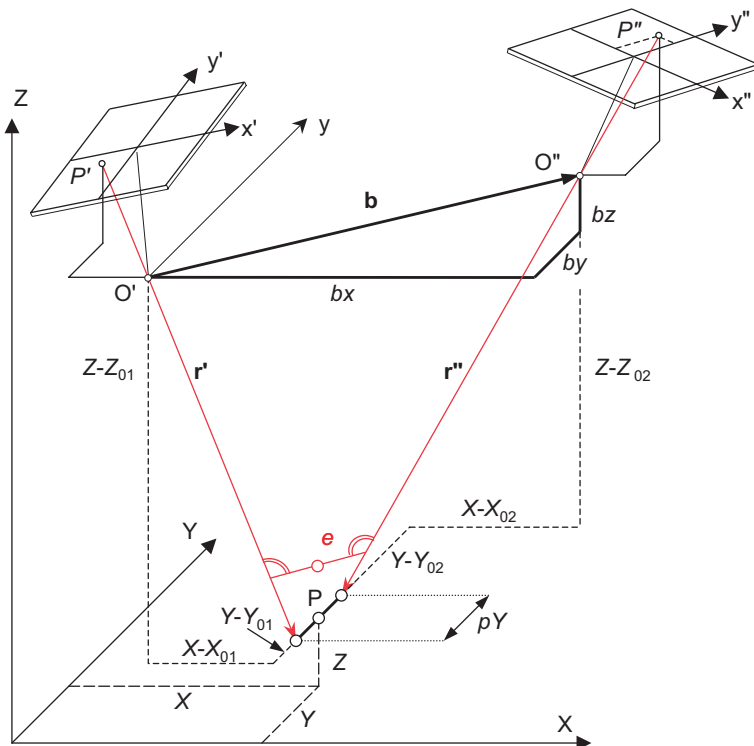


Figure 4.63 Spatial intersection for the general stereo case

### 3. Scale factors:

The scale factors for the transformation of image coordinates are:

$$\lambda = \frac{bx(Z'' - Z_{02}) - bz(X'' - X_{02})}{(X' - X_{01})(Z'' - Z_{02}) - (X'' - X_{02})(Z' - Z_{01})} \quad (4.100)$$

$$\mu = \frac{bx(Z' - Z_{01}) - bz(X' - X_{01})}{(X' - X_{01})(Z'' - Z_{02}) - (X'' - X_{02})(Z' - Z_{01})}$$

### 4. Object coordinates:

$$\begin{aligned} X &= X_{01} + \lambda(X' - X_{01}) & Y_1 &= Y_{01} + \lambda(Y' - Y_{01}) \\ Z &= Z_{01} + \lambda(Z' - Z_{01}) & Y_2 &= Y_{02} + \mu(Y'' - Y_{02}) \\ Y &= \frac{Y_1 + Y_2}{2} & pY &= Y_2 - Y_1 \end{aligned} \quad (4.101)$$

Here the Y-parallax in object space  $pY$  is a quality measure for coordinate determination. It is zero when the two rays exactly intersect.

The solution is not completely rigorous but suffices in most cases where the base is approximately aligned to the X direction and where  $bx$  is large in comparison with  $by$  and  $bz$ .

In the general case of two images with arbitrary orientations, point  $P$  is calculated as the mid point of the shortest distance  $e$  between both rays (Fig. 4.63; for calculation see section 2.4.2.1). The spatial intersection can also be expressed as an over-determined adjustment problem based on the collinearity equations. In this form it can be extended to more than two images (see section 4.4.3.1).

#### 4.4.2.3 Point determination with floating mark

##### *Setting a floating mark on the surface*

The term floating mark is used for an optical, mechanical or digitally generated stereoscopic mark that can be moved through the virtual 3D space of the stereo model. The floating mark is set on the object surface in order to measure a surface point. Although the floating mark primarily serves the interactive and visual analysis of the stereo image, its principle is also useful for automatic, digital stereo measurement.

In analogue stereo photogrammetry, three principal methods can be distinguished (see older textbooks on photogrammetry, such as Slama 1980, Schwidetsky and Ackermann 1976 and Wolf 1974):

- Optical projection

The images are projected on a mapping table using projectors which can be mechanically oriented. The floating mark is a spot of light on a small plate which can be moved on the table and altered in height. If the spatial position of the floating light spot is correct, the projections of both images coincide at that point. To the operator the floating mark appears to coincide with the surface of the virtual model. In most cases, the anaglyph method (red-green glasses) is used to separate the images for stereoscopic viewing. This principle has been implemented in simple analogue plotters (e.g. Multiplex (many versions – Zeiss, Williamson, Bausch and Lomb, Nistri), Balplex ER55, Zeiss DP1).

- Opto-mechanical projection

An opto-mechanical stereo plotter has two separate optical paths, each containing a floating mark (half marks). The spatial position of the measuring mark is determined by the (virtual) intersection of the two corresponding rays which can be mechanically adjusted and visually controlled. The principle has been used in high-end analogue stereo plotters (e.g. Zeiss C8). A subcategory consists of the photogoniometer instruments (e.g. Poivilliers, Nistri, Thompson-Watts).

- Mechanical projection

Here the homologous rays of light are represented by two mechanical space rods which intersect at a point on a carriage movable in three dimensions and so define the spatial measuring position. Image separation is implemented as in the opto-mechanical case with two integrated marks; this method of construction is less expensive than that of opto-mechanical projection (there is a multiplicity of designs e.g. Wild A-series, Kern PG-2, Zeiss Planimat, Santoni, Drobyshev, etc.).

In contrast, the numerical reconstruction of homologous rays, as performed in analytical or digital stereo plotters (see section 6.3.1), is simpler and therefore cheaper and potentially more accurate. Using separate optical paths the operator observes two floating marks which fuse into one common mark if set correctly on the object surface. When the floating mark appears to touch the surface the corresponding XYZ coordinates are recorded.

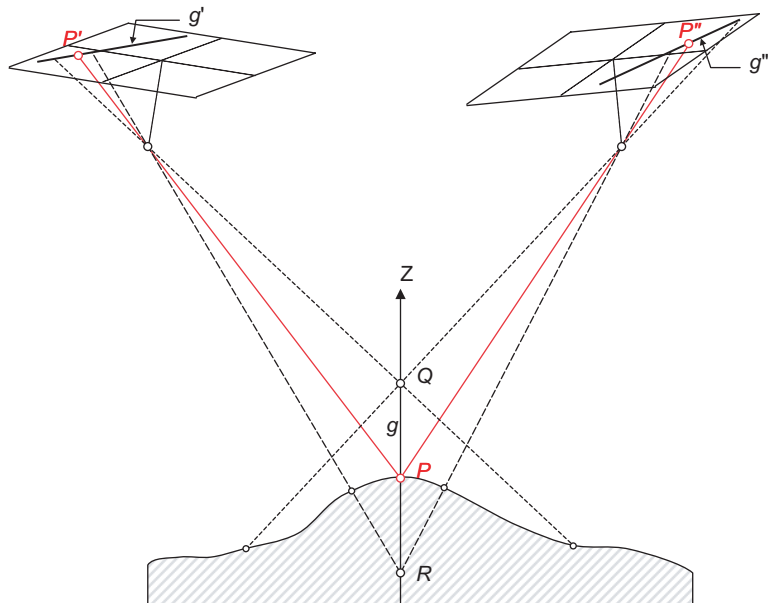


**Figure 4.64** Projections of a vertically shifted spatial floating mark

The XYZ coordinates which correspond to a spatially controlled floating mark can be transformed into image coordinates using equations (4.8). Fig. 4.64 shows how the transformed marks only identify corresponding image patches (homologous points) if the XYZ coordinates represent a point  $P$  on the object surface. A measuring position below  $P$  at point  $R$ , as well as position above  $P$  at point  $Q$ , result in image points which do not correspond, namely the projections of the intersecting points of the non-homologous rays and the object surface. The correct position of the floating mark is controlled either by a visual check or by a digital correspondence algorithm applied to the two calculated image positions. The mechanical effort is reduced to a separate real-time shift of both image planes. Starting from an approximate position, the XYZ coordinates of the floating mark are iteratively corrected until correspondence of both images is achieved.

#### *Vertical line locus*

The image lines  $g'$  and  $g''$  correspond to the projection of the vertical line  $g$  which passes through  $P$  (Fig. 4.64). These straight lines are epipolar lines only if  $g$  is located in the epipolar plane of  $P$ . The image lines  $g'$  and  $g''$  are known as vertical line loci (VLL), in allusion to aerial photogrammetry ( $Z \approx$  viewing direction). With given orientation parameters they can be easily calculated by a variation of the  $Z$  coordinate of  $P$ .

In order to measure a surface point it is possible to calculate all points  $P_i$  at small intervals  $\Delta Z$  between two points (e.g.  $Q$  and  $R$ ), re-project them into the images and search for the best correspondence on the straight lines  $g'$  and  $g''$ .

#### *Surface normal locus*

Very complex surfaces are frequently measured in close range work and the  $Z$  direction is likely to depart significantly from the surface normal at any point. It will frequently be possible, using *a priori* knowledge of the surface, to make a reasonable estimate of the direction of the surface

normal at that point. In this case the direction of the ‘vertical line’  $g$  should be that of the estimated surface normal. The method is not restricted to the stereo case but can be extended to an unlimited number of images per point.

#### 4.4.3 Multi-image processing

This section deals with analytical methods for object reconstruction based on measured image coordinates from an unlimited number of photos. Digital, multi-image methods which additionally process grey values at image points are discussed in chapter 5.

The following methods require known parameters of interior and exterior orientation which usually are calculated by a bundle triangulation (see section 4.3). On this basis object points, surfaces and basic geometric elements can be determined.

##### 4.4.3.1 General space intersection

The general space intersection takes measured image coordinates from multiple images, together with their known orientation parameters, and calculates the spatial point coordinates  $X$ ,  $Y$ ,  $Z$ . The calculation is based on the collinearity equations (4.8) used as observation equations in a least-squares adjustment:

$$\begin{aligned} x'_i + vx'_i &= F(X_{0j}, Y_{0j}, Z_{0j}, \omega_j, \varphi_j, \kappa_j, x'_{0k}, y'_{0k}, c_k, \Delta x'_{ik}, X_i, Y_i, Z_i) \\ y'_i + vy'_i &= F(X_{0j}, Y_{0j}, Z_{0j}, \omega_j, \varphi_j, \kappa_j, x'_{0k}, y'_{0k}, c_k, \Delta y'_{ik}, X_i, Y_i, Z_i) \end{aligned} \quad (4.102)$$

where  $i$ : point index

$j$ : image index

$k$ : camera index

In order to calculate the three unknowns  $X_i$ ,  $Y_i$ ,  $Z_i$  at least three observations (image coordinates) are required. Two images already provide a redundancy of 1 and with each additional observation the redundancy increases by 2.

To set up the normal equations the differential coefficients of the unknown object coordinates are calculated according to equation (4.52).

A global measure of the quality of point determination is given by the shortest distance between the two skew rays (see section 2.4.2.1). If the point accuracy is to be analysed separately for each axis, the covariance matrix must be evaluated. Given the cofactor matrix of unknowns

$$\mathbf{Q}_{\hat{x}\hat{x}} = \begin{bmatrix} q_{XX} & q_{XY} & q_{XZ} \\ q_{YX} & q_{YY} & q_{YZ} \\ q_{ZX} & q_{ZY} & q_{ZZ} \end{bmatrix} \quad (4.103)$$

the standard deviations of adjusted point coordinates are as follows:

$$\begin{aligned} \hat{s}_X &= \hat{s}_0 \sqrt{q_{XX}} \\ \hat{s}_Y &= \hat{s}_0 \sqrt{q_{YY}} \\ \hat{s}_Z &= \hat{s}_0 \sqrt{q_{ZZ}} \end{aligned} \quad (4.104)$$

Hence the mean point error is given by

$$\hat{s}_P = \sqrt{\hat{s}_X^2 + \hat{s}_Y^2 + \hat{s}_Z^2} \quad (4.105)$$

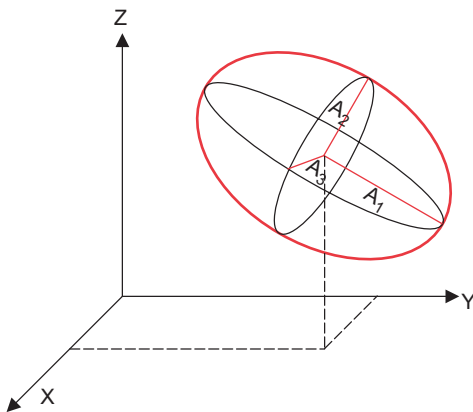


Figure 4.65 Confidence ellipsoid

Spectral decomposition of the corresponding variance-covariance matrix leads to eigenvalues  $\lambda_i$  and eigenvectors  $s_i$ . It is then possible to calculate the error or confidence ellipsoid which contains the ‘true’ point with a confidence level of  $1-\alpha$  (Pelzer 1995).

$$\mathbf{K}_{\hat{x}\hat{x}} = [\mathbf{s}_1 \ \mathbf{s}_2 \ \mathbf{s}_3] \begin{bmatrix} \lambda_1 & 0 & 0 \\ 0 & \lambda_2 & 0 \\ 0 & 0 & \lambda_3 \end{bmatrix} \begin{bmatrix} \mathbf{s}_1^T \\ \mathbf{s}_2^T \\ \mathbf{s}_3^T \end{bmatrix} \quad : \text{spectral decomposition} \quad (4.106)$$

The directions of the semi-axes of the ellipsoid are defined by the eigenvectors and their length is given by the eigenvalues (Fig. 4.65):

$$A_i = \sqrt{\lambda_i \cdot \chi_{3,1-\alpha}^2} \quad : \text{length of semi-axis } A_i, i = 1,2,3 \quad (4.107)$$

where  $\chi_{3,1-\alpha}^2$  : quantile of  $\chi^2$ -distribution

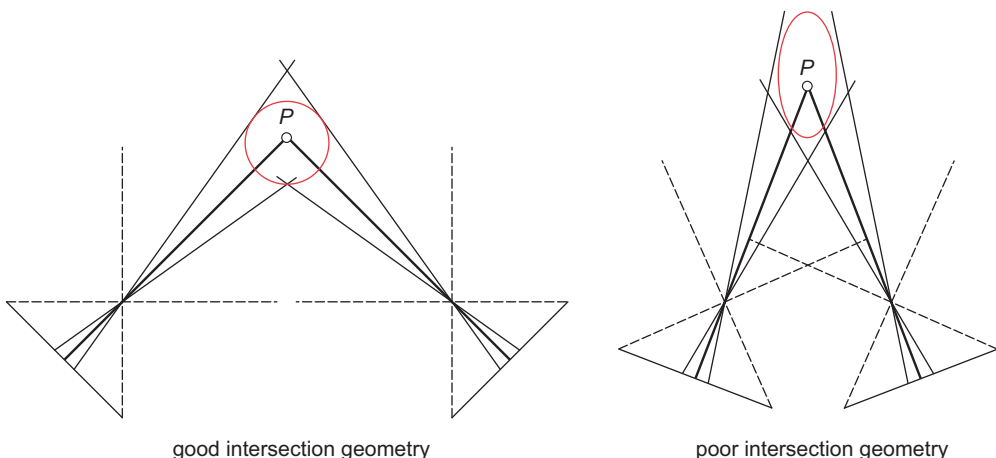


Figure 4.66 On the geometry of spatial intersection

In contrast to the standard bundle adjustment, possible correlations between adjusted point coordinates and orientation parameters are not taken into account in the spatial intersection. Assuming image coordinates of equal accuracy in all images, a stretched error ellipsoid indicates a weak intersection of homologous rays (Fig. 4.66).

#### 4.4.3.2 Direct determination of geometric elements

Geometric 3D elements (straight line, circle, sphere, cylinder etc.) can be determined in two ways:

- calculation of best-fit elements from measured 3D coordinates
- best-fit adjustment of elements to measured 2D outlines (edges, contours) in multiple images

The first method is preferred in conventional coordinate metrology (e.g. Pfeifer 1998, Neumann 1990). The required 3D coordinates are delivered by coordinate measuring machines (CMM) from direct probing of the object surface. The calculation of best-fit elements, and the intersection of these elements, is of major importance as most industrial objects offered for inspection are composed of regular geometric elements. The most important algorithms are discussed in section 2.4.

The second method, contour measurement, was presented by Andresen (1991). It is based on the idea that the imaged edges of geometric elements generate unique grey level contours which can be extracted by suitable edge operators or manual measurements (see sections 5.2.3, 5.4.3). Normally individual 3D points on the object surface cannot be measured, for example by intersection, because there are no discrete or identifiable points along the imaged edge. However, if sufficient edge image points belonging to a common object surface can be detected in a well-configured set of images, an adjustment can be formulated for estimating the parameters of the unknown element. Assuming known parameters of interior and exterior orientation, each image point defines a light ray in space which, in principle, touches or is tangent to the surface of the element. For this purpose a distance offset is defined between the light ray and the spatial element which is minimised by adjustment of the element's parameters.

The method can be used to calculate, for instance, straight lines, 3D circles, cylinders or other elements which generate an appropriate outline in the image. The number of images is unlimited. However, for a reliable determination usually more than two images are required. Applications in the automotive industry provide practical experience (Loser and Luhmann 1992).

##### *Straight line in space*

Straight lines often occur in real objects, for example the intersection lines of walls, rectangular patches defined by windows and the linear textures defined by bricks and tiles. In a central perspective projection, straight lines are projected as straight lines<sup>1</sup>.

For example, according to section 2.4.2.1 a straight line in space is defined by

$$\mathbf{x}_G = \mathbf{a} + \lambda \mathbf{b} \quad (4.108)$$

If the distance vector  $\mathbf{a}$  is perpendicular to the direction vector  $\mathbf{b}$ , which has unit length, then the additional conditions

$$\begin{aligned} |\mathbf{b}| &= 1 \\ \mathbf{a} \cdot \mathbf{b} &= 0 \end{aligned} \quad (4.109)$$

ensure that four independent parameters remain for the definition of a straight line in space.

---

<sup>1</sup> In the following it is assumed that the image coordinates have been corrected for distortion.

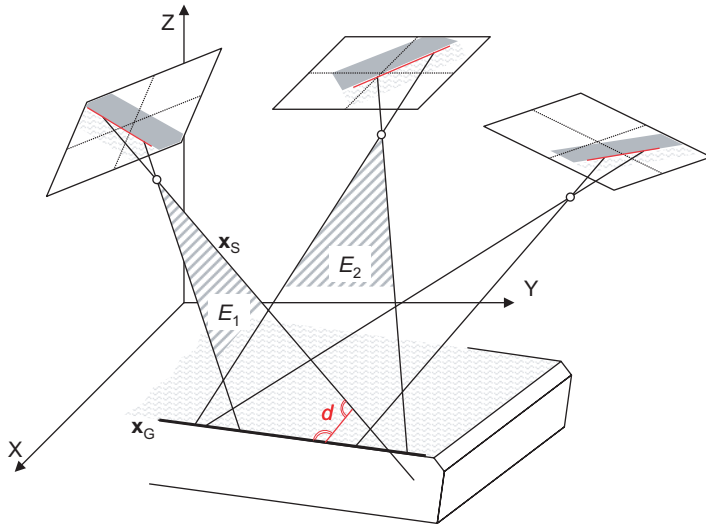


**Figure 4.67** Edge method for the determination of a spatial straight line

With known interior and exterior orientation, each image point  $\mathbf{x}' = (x', y', -c)$  corresponds to a point in the object coordinate system XYZ:

$$\mathbf{X}_B = \mathbf{X}_0 + \mathbf{R}^{-1}\mathbf{x}' \quad (4.110)$$

The image point's spatial ray through the perspective centre then gives a line in parametric form

$$\mathbf{x}_S = \mathbf{X}_0 + \lambda(\mathbf{X}_B - \mathbf{X}_0) = \mathbf{X}_0 + \lambda\mathbf{c} \quad (4.111)$$

The shortest distance  $d_{i,k}$  according to (2.2) between the image rays  $\mathbf{x}_S$  and the desired spatial straight line  $\mathbf{x}_G$  is minimised for all image points  $i$  of image  $k$ :

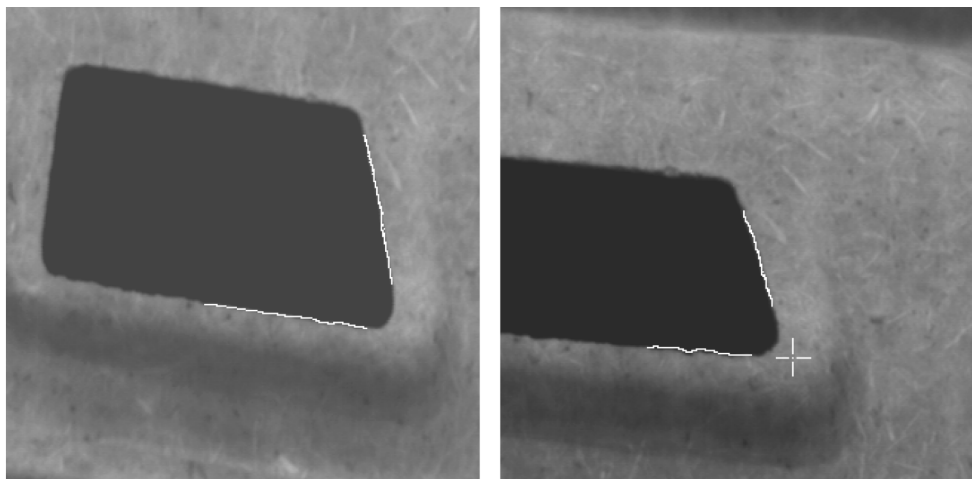
$$\sum_k \sum_i d_{i,k}^2 = \min. \quad (4.112)$$

The linearised correction equations

$$\frac{\partial d_{i,k}}{\partial a_x} \Delta a_x + \frac{\partial d_{i,k}}{\partial a_y} \Delta a_y + \frac{\partial d_{i,k}}{\partial a_z} \Delta a_z + \frac{\partial d_{i,k}}{\partial b_x} \Delta b_x + \frac{\partial d_{i,k}}{\partial b_y} \Delta b_y + \frac{\partial d_{i,k}}{\partial b_z} \Delta b_z = -d_{i,k} \quad (4.113)$$

and the conditions (4.109) build an extended normal system of equations according to equation (2.85). For each program run the approximate parameters of the straight line are iteratively corrected by the adjusted increments  $\Delta$  until there is no significant change.

Approximate values of the straight line can be derived from the intersection of the two planes  $E_1$  and  $E_2$ , derived from the edge points in the image (Fig. 4.67). It is obvious that the calculation of approximate values, as well as the solution of the normal system of equations, will fail in the case of a dual image configuration where the baseline and required straight line are parallel. The addition of at least one image with a perspective centre outside their plane will provide the data for a unique solution.



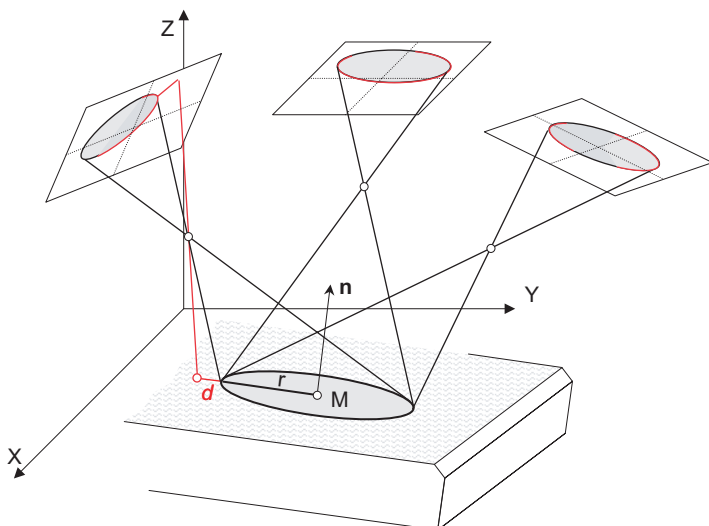
**Figure 4.68** Edge measurements on car door trim

Fig. 4.68 shows an application where edges are determined on the interior trim of a car door. The irregular line is caused by the rough surface texture. The computed lines can be used to calculate additional elements such as intersecting points or quantities such as distance.

### 3D circle

Circles occur on industrial objects mainly as drill holes, end sections of cylindrical features or disks. In general the circles are imaged as ellipses.

According to section 2.4.2.3, a 3D circle is defined by the centre  $\mathbf{X}_M = (X_M, Y_M, Z_M)$ , the vector normal to the plane of the circle  $\mathbf{n} = (a, b, c)$  and the radius  $r$ . Taking into account  $|\mathbf{n}| = 1$ , the circle has 6 independent parameters.



**Figure 4.69** Edge method for determining a 3D circle

The radial distance  $d$  between the circumference and the point of intersection of an image ray with the plane of the circle is taken as the quantity to be minimised (Fig. 4.69). It corresponds to the distance  $e$  in Fig. 2.35. The solution follows the adjustment principle explained above for the straight line in space.

Andresen (1991) describes the following procedure for determining approximate values of the circle parameters:

1. Pseudo orientation parameters are calculated for two images such that the perspective centres of each image are preserved, but the principal points of the cameras are shifted into the centre of the imaged ellipse. The centre of the 3D circle in space is computed by spatial intersection of the rays corresponding to the ellipse centres after transformation into the new pseudo image planes.
2. In each of the two pseudo images the major axis of the ellipse is now approximately parallel to a diameter of the circle. The approximate normal vector to the circle plane can therefore be derived by the cross product of these two major ellipse axes after transforming them from image to object space.
3. The circle radius is approximately given by multiplying either major axis by the corresponding image scale number.

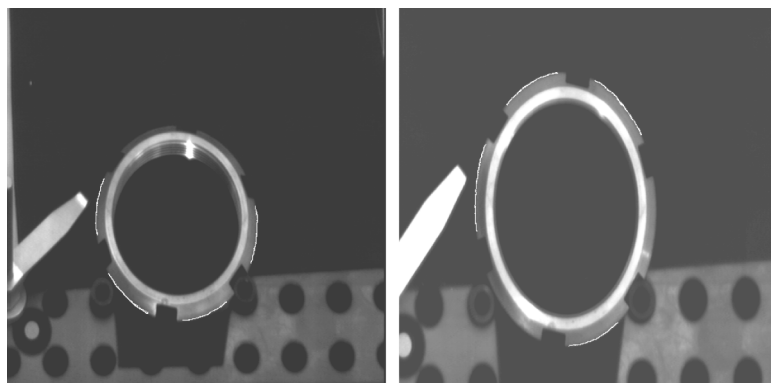
For reasonable parameter estimation more than half of the circle should be visible in at least one image. The procedure fails if the projection centres are located in or close to the plane of the circle, in which case the imaged ellipse becomes a straight line.

Fig. 4.70 shows an application where the position and radius of a coupling ring is determined from measurements of two partial contours in two images.

#### *Right-circular cylinder in space*

Cylindrical objects often occur as pipes, tubes or columns. A cylinder appears in an image as straight line edges of the cylinder surface which result from the intersection of the image plane with the plane through the perspective centre and tangential to the cylinder surface (Fig. 4.71).

A right-circular cylinder is defined by its axis  $g$  and radius  $r$ , hence by five independent parameters. The distance value defined in section 2.4.2.3 between an arbitrary point in 3D space and the cylinder surface cannot be used in this case, since no unique point can be defined on



**Figure 4.70** Edge measurement of a 3D circle created by a coupling ring

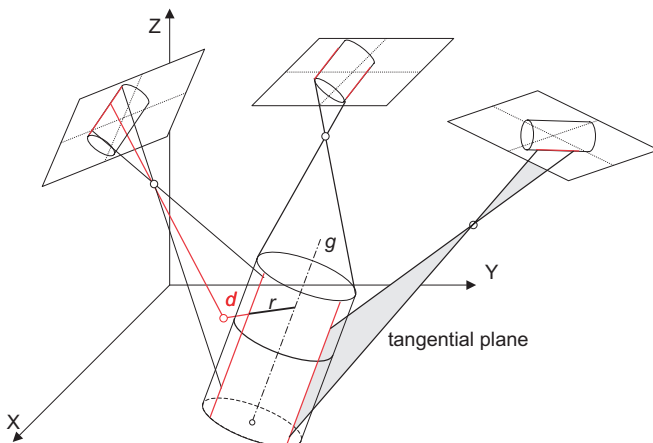


**Figure 4.71** Edge method for determining a right-circular cylinder

the image ray. Instead Andresen (1991) uses the distance  $d$  between the cylinder surface and the intersection point of image ray and radius vector (vector perpendicular to the axis of the cylinder).

Alternatively the shortest distance between cylinder axis and image ray, reduced by the radius  $r$ , can be used as a distance measure.

In a similar way to the straight line in space, approximate parameters of the cylinder axis can be generated using two imaged lines, each of which are the average of opposite cylinder edges. The approximate radius can be calculated as for the 3D circle above, if a cylinder end is visible. If not, many applications use standardised pipe diameters which are the cylinders under evaluation. Alternatively, a radius can be calculated as the shortest distance between cylinder axis and tangential plane. The adjustment process operates in a similar way to the edge methods explained above.

In some simple applications only the cylinder axis is in fact required. The best-fit procedure is an optimised intersection of planes on which the axis lies. This assumes that each image sees both sides of the cylinder.

There is no solution for the cylinder calculation if the cylinder axis is parallel to the baseline between the images (Fig. 4.72). As indicated above, a unique solution can then be found if at

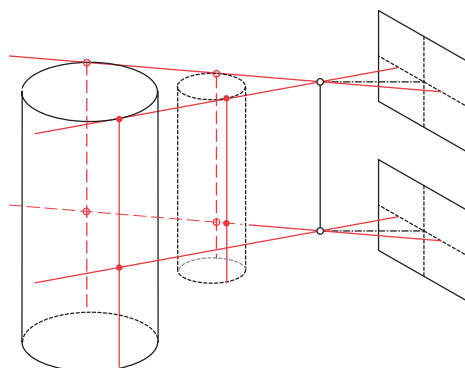


**Figure 4.72** Ambiguity of cylinder determination

least one additional image is used whose perspective centre is not located on the baseline between the first two images.

#### *Accuracy of the edge method*

The accuracy of the edge method depends on the following factors:

- Consistency of optical and physical object edge

The main problem for the edge method is correct illumination which must ensure that the physical edge of the object corresponds to the optical edge in the image, regardless of viewing direction, surface orientation and material characteristics. This requirement applies to all images involved in the measurement.

Simpler objects such as plane components, which are imaged by multiple photos, can usually be made visible by a uniform diffuse illumination. More complex objects whose surfaces have varying spatial orientations, and possibly different materials, must in principle be individually illuminated for each camera position and object component (see section 3.4.2.4).

- Roughness and sharpness of the object edge

The physical properties of the object edge have a major influence on the quality of edge measurement.

A rough object edge leads to higher standard deviations in the image measurements. The least-squares approach calculates an average geometric element. In principle the adjustment model could incorporate circumscribed or inscribed elements as used to determine form deviations in industrial metrology (see section 2.4.4). Fig. 4.68 shows automatic measurement of rough edges.

The sharpness of an object edge is also significant i.e. the shape of the interface between one object surface and another. The contour method can only measure the optically generated edge whilst the element to be measured, or other derived quantities, are related to features defined by design and construction. While sharp edges can normally be uniquely

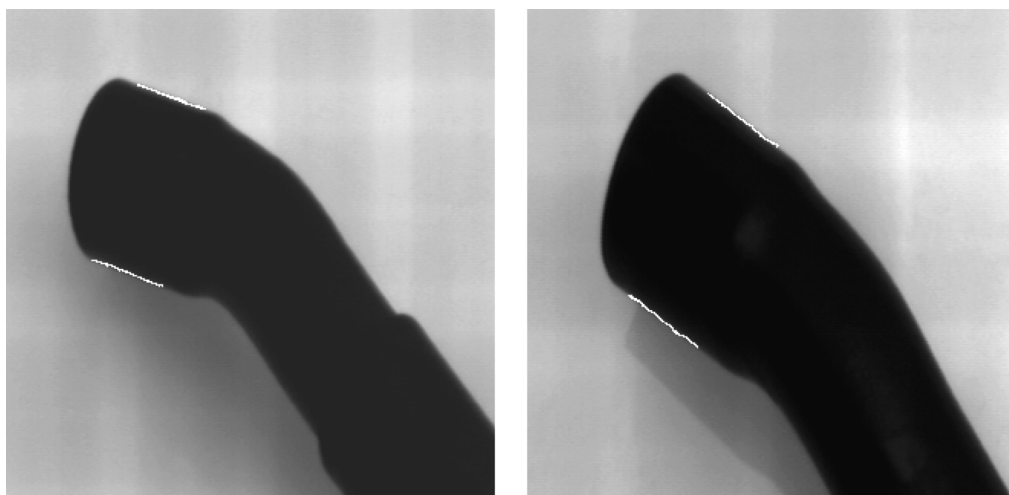


**Figure 4.73** Edge measurement of a cylinder defined by a cooling tube

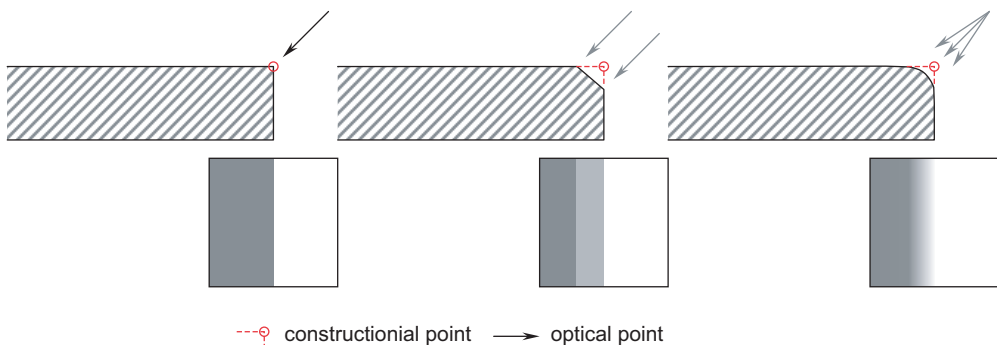


**Figure 4.74** Contour points for different types of edge

measured, round or chamfered edges are much more difficult to define, even with sophisticated illumination techniques. Fig. 4.70 shows an object with sharp edges; Fig. 4.74 illustrates different type of edges.

- Blunder elimination

False measurements along the contour can be eliminated by robust error detection methods (see section 2.3.4).

- Number of measured edge points

Each edge point delivers one observation for the adjustment, which leads to usually high redundancies. As an example, the measurement of a straight line with an average length of 30 pixels measured in three images leads to 90 observations (1 pixel per edge point) which are then used to solve for only four unknowns.

- Accuracy of edge points in the image

Aside from the camera quality, the accuracy of measured image coordinates depends on the quality of the measuring instrument or method. Using digital image edge extraction, an accuracy of about 1/10 to 1/20 of a pixel can be expected, depending on the image operator and the edge sharpness.

- Distribution of edge points

Since the method does not require homologous points, any parts of the contour can be used for calculation. The reliability of calculation increases if edge points are uniformly distributed over the complete element. Straight lines from straight edges and cylinders should be defined by edge points which include both ends of the element in all images. For circular objects more than half of the circle edge should be measured in at least one image.

- Image configuration

As for other photogrammetric point measurements, the quality of the result strongly depends on the configuration of camera stations and viewing directions. At least three images with good intersection angles should be included in the calculation of the element.

#### 4.4.3.3 Determination of spatial curves (snakes)

Arbitrary curves in space can be approximated by suitable polynomial functions, in particular spatial Bezier or B-spline functions (see section 2.4.3.2). These functions provide smoothing effects which can be adjusted by an appropriate choice of parameters (degree of polynomial,

curvature constraints). The final interpolation curve is defined by a set of coefficients which are determined by a system of equations.

The curve approximations discussed in section 2.4.3.2 are based on specific 3D points on the object surface. However, in a similar way to the edge method for direct measurement of elements (section 4.4.3.2), if no discrete 3D points are available on the object contour, the parameters of the curve must be calculated by a multi-image process based on 2D image points. Starting with approximate values of the curve, the related coefficients are computed iteratively by least-squares adjustment. If the adjustment converges the calculated curve gradually conforms to the spatial object curve. If B-spline functions are used, snakes are computed which iteratively wind around the real object curve.

The extension of the plane form of equation (2.166) to three-dimensional B-splines gives:

$$P(t) = \begin{cases} x(t) = \sum_{i=0}^k x_i B_{i,n}(t) \\ y(t) = \sum_{i=0}^k y_i B_{i,n}(t) & 0 \leq t \leq k-n+1 \\ z(t) = \sum_{i=0}^k z_i B_{i,n}(t) \end{cases} \quad (4.114)$$

In the adjustment process the unknown B-spline functions  $B$  are calculated as functions of the unknown object coordinates  $x, y, z$ , which are themselves functions of the measured image coordinates  $x', y'$ .

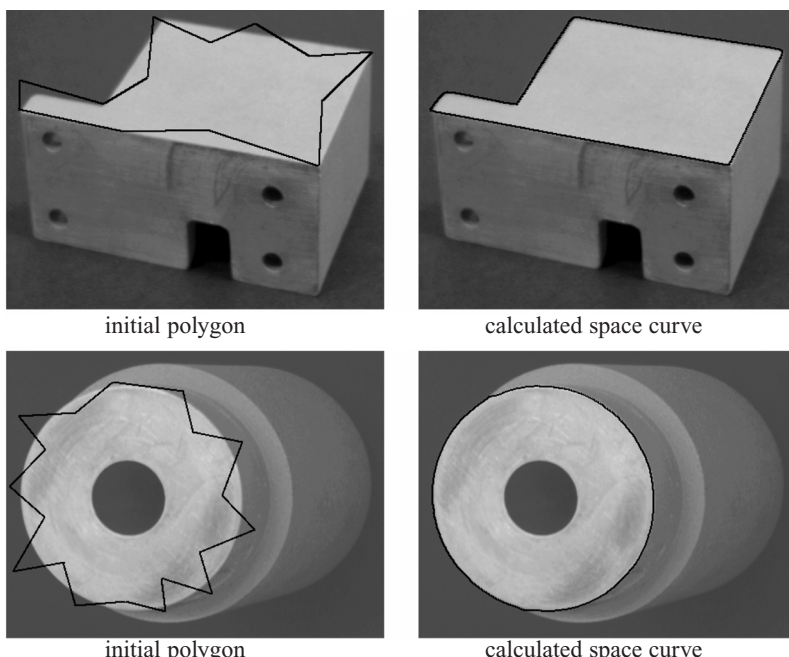


**Figure 4.75** Edge measurement by LSB-snakes (after Li and Gruen 1997)

The method can be extended by a photometric model which uses the grey values of imaged edge points as observations, in a similar way to least-squares matching (see section 5.5.4). For known parameters of interior and exterior orientation, additional geometric constraints (epipolar geometry) can be defined. The approach has been published as LSB-snakes (Li and Gruen 1997). Fig. 4.75 shows the spatial contours of a component calculated by this method.

## 4.5 Line photogrammetry

The standard photogrammetric principle of discrete point measurement is not applicable if discrete object points are not available, point targeting is not possible, or if the final result is based on the analysis of higher-order geometric elements. Since man-made objects are frequently characterised by straight line features (e.g. buildings, industrial components and structures) it is reasonable to use these properties for image orientation and object reconstruction. In this context line photogrammetry specifically deals with linear features in object and image space.

One major characteristic of the central projection is the transformation of straight lines in object space into straight lines in image space, and intersections of straight lines are therefore invariant. In contrast, angles, distances and areas are changed (see section 2.2.1.5). Using the images of suitable object lines it is possible to orient one or more images, as well as performing three-dimensional object reconstruction.

The practical significance of line photogrammetry is enhanced by the use of digital imagery which enables the partially or fully automated extraction of linear features (edges). For discrete point methods the subsequent step of image matching is relatively simple as points can be readily identified. Matching procedures based on linear features are more complex since every imaged object line has a different length and orientation in a different image.

### 4.5.1 Space resection using parallel object lines

The following method determines the exterior orientation of a single picture using an image of a parallelogram; such images arise frequently with objects such as buildings. The process is similar to the minimum solution for the space resection explained in section 4.2.3.1. It is based on the calculation of distance ratios between the perspective centre and the object points of the parallelogram. For the following calculation method published by van den Heuvel (1997) it is assumed that the corner points of the parallelogram can be measured directly or are determined as intersections of the sides.

The tetrahedron illustrated in Fig. 4.76 is defined by the perspective centre  $O'$  and three points  $P_i, P_j, P_k$  of the parallelogram. The volume of this element is then given by

$$V_{ijk} = \frac{d_i d_j d_k |\det[\mathbf{i}, \mathbf{j}, \mathbf{k}]|}{6|\mathbf{i}||\mathbf{j}||\mathbf{k}|} \quad (4.115)$$

where

$$\mathbf{i} = \mathbf{x}'_i = (x'_i, y'_i, -c) \quad : \text{measured image coordinates}$$

and correspondingly for  $\mathbf{j}$  and  $\mathbf{k}$

Alternatively the volume is given by ground area and the height:

$$V_{ijk} = A_{ijk} \frac{h}{3} \quad (4.116)$$

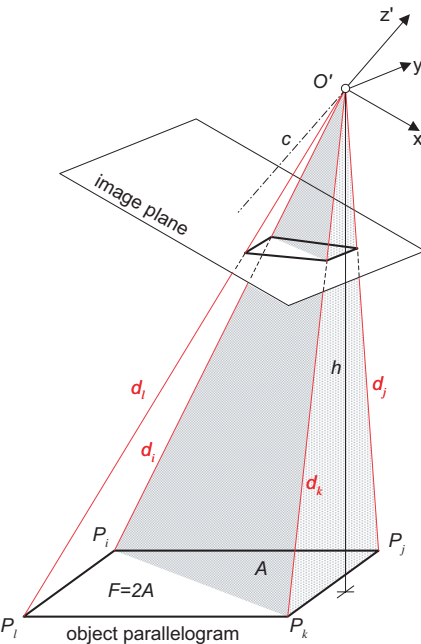


**Figure 4.76** Space resection with object parallelogram

Since the triangular areas  $A$  are the same for all point combinations  $P_i, P_j, P_k, P_l$ , equations (4.115) and (4.116) lead to:

$$\begin{aligned} 2Ah &= \frac{d_i d_j d_k |\det[\mathbf{i}, \mathbf{j}, \mathbf{k}]|}{|\mathbf{i}| |\mathbf{j}| |\mathbf{k}|} = \frac{d_j d_k d_l |\det[\mathbf{j}, \mathbf{k}, \mathbf{l}]|}{|\mathbf{j}| |\mathbf{k}| |\mathbf{l}|} \\ &= \frac{d_k d_l d_i |\det[\mathbf{k}, \mathbf{l}, \mathbf{i}]|}{|\mathbf{k}| |\mathbf{l}| |\mathbf{i}|} = \frac{d_l d_i d_j |\det[\mathbf{l}, \mathbf{i}, \mathbf{j}]|}{|\mathbf{l}| |\mathbf{i}| |\mathbf{j}|} \end{aligned} \quad (4.117)$$

Consequently, three equations in four unknown distances  $d$  are available. From these equations distance ratios  $C_{ij}$  between two arbitrary points  $i$  and  $j$  can be derived:

$$C_{ij} = \frac{d_j |\mathbf{i}|}{d_i |\mathbf{j}|} = \frac{\det[\mathbf{k}, \mathbf{l}, \mathbf{i}]}{\det[\mathbf{j}, \mathbf{k}, \mathbf{l}]} \quad (4.118)$$

Equation (4.118) shows that the distance ratios  $C_{ij}$  can be calculated from the image vectors  $\mathbf{i}, \mathbf{j}, \mathbf{k}, \mathbf{l}$  without knowledge of the absolute distances  $d$ . They do not depend on the principal distance  $c$  which is eliminated in the calculation of the determinant. The determinant of three vectors becomes (close to) zero if the corresponding object points are located on (or close to) a common straight line. As expected no (stable) solution then exists.

If a model coordinate system  $xyz$  is defined with its origin in the image coordinate system  $x'y'z'$ , model coordinates  $\mathbf{x}_i$  can be obtained from image coordinates scaled by a factor  $\lambda_i$ , which is derived from a known distance  $d_i$ :

$$\begin{aligned} \mathbf{x}_i &= \frac{d_i}{|\mathbf{x}'_i|} \mathbf{x}'_i = \lambda_i \mathbf{x}'_i \\ \mathbf{x}_j &= \lambda_i C_{ij} \mathbf{x}'_j \end{aligned} \quad (4.119)$$

The calculation of the parameters of exterior orientation with respect to the object coordinate system XYZ is based on the spatial similarity transformation (see section 2.2.2.2):

$$\lambda \mathbf{R} \mathbf{x}'_i = \mathbf{X}_i - \mathbf{X}_0 \quad : \text{transformation of image point } i \quad (4.120)$$

$$\lambda \mathbf{R} C_{ij} \mathbf{x}'_j = \mathbf{X}_j - \mathbf{X}_0 \quad : \text{transformation of image point } j$$

where

$\mathbf{R}$ : rotation matrix of exterior orientation

$\mathbf{X}_i$ : object coordinates of  $i$

$\mathbf{X}_0$ : position of perspective centre in object coordinate system

The scale factor  $\lambda$  can be determined from a known distance in object space between points  $i$  and  $j$ :

$$\lambda = \lambda_i = \frac{|\mathbf{X}_i - \mathbf{X}_j|}{|\mathbf{x}'_i - C_{ij} \mathbf{x}'_j|} \quad (4.121)$$

Using (4.119), equation (4.120) can be written as

$$(\mathbf{I} + \mathbf{S}) \mathbf{x}_i = (\mathbf{I} - \mathbf{S})(\mathbf{X}_i - \mathbf{X}_0) \quad (4.122)$$

using Cayley's form of the rotation matrix (Cayley 1843):

$$\mathbf{R} = (\mathbf{I} - \mathbf{S})^{-1}(\mathbf{I} + \mathbf{S})$$

$\mathbf{I}$  is the unit matrix and  $\mathbf{S}$  is a skew symmetric matrix with elements  $q$  related to the Euler rotation angles:

$$\mathbf{S} = \begin{bmatrix} 0 & -q_3 & q_2 \\ q_3 & 0 & -q_1 \\ -q_2 & q_1 & 0 \end{bmatrix} \quad (4.123)$$

Equation (4.122) can then be written as

$$\mathbf{x}_i - \mathbf{X}_i = \mathbf{M}_i \mathbf{q} - \mathbf{w} \quad (4.124)$$

where

$$\mathbf{M}_i = \begin{bmatrix} 0 & -z_i - Z_i & y_i + Y_i \\ z_i + Z_i & 0 & -x_i - X_i \\ -y_i - Y_i & x_i + X_i & 0 \end{bmatrix}$$

$$\mathbf{q} = \begin{bmatrix} q_1 \\ q_2 \\ q_3 \end{bmatrix}$$

$$\mathbf{w} = (\mathbf{I} - \mathbf{S}) \mathbf{X}_0$$

This system is linear in  $\mathbf{q}$  and  $\mathbf{w}$ , hence can be solved directly for the parameters of exterior orientation without the need for initial approximate values. The rotation matrix  $\mathbf{R}$  can be calculated using  $\mathbf{q}$  and the position of the perspective centre  $\mathbf{X}_0$  calculated using  $\mathbf{w}$ . Six suitable object coordinates and one reference distance are required for a solution. For redundant object information the solution can be found by iterative least-squares adjustment.

## 4.5.2 Collinearity equations for straight lines

The collinearity equations (4.8) are used as the mathematical model for space resection and bundle triangulation. They can also be derived for straight lines in image and object. For this purpose the equations of image line  $g'$  and the corresponding object line  $G$  are defined as:

$$g': \quad y' = ax' + b \quad (4.125)$$

$$G: \quad X = \alpha Z + \gamma \quad Y = \beta Z + \delta \quad (4.126)$$

The planar image line  $g'$  is defined by two parameters, while the spatial line  $G$  is defined by four parameters (see section 2.4.2.1). The following derivation due to Schwermann (1995) is applicable only to straight lines with small slope values  $a$ ,  $\alpha$  and  $\beta$ . Equations for arbitrary straight lines must be formulated with respect to the appropriate axes ( $X = f(Y)$ ,  $Y = f(X)$ ,  $Z = f(X)$  etc.). However, the structure of the solution corresponds to the following example.

Substituting for  $X$  and  $Y$  from equation (4.126) in (4.8) gives<sup>1</sup>:

$$\begin{aligned} x' &= x'_0 - c \frac{(\alpha r_{11} + \beta r_{21} + r_{31})Z + r_{11}(\gamma - X_0) + r_{21}(\delta - Y_0) - r_{31}Z_0}{(\alpha r_{13} + \beta r_{23} + r_{33})Z + r_{13}(\gamma - X_0) + r_{23}(\delta - Y_0) - r_{33}Z_0} \\ &= x'_0 - c \frac{A_1 Z + A_2}{C_1 Z + C_2} \\ y' &= y'_0 - c \frac{(\alpha r_{12} + \beta r_{22} + r_{32})Z + r_{12}(\gamma - X_0) + r_{22}(\delta - Y_0) - r_{32}Z_0}{(\alpha r_{13} + \beta r_{23} + r_{33})Z + r_{13}(\gamma - X_0) + r_{23}(\delta - Y_0) - r_{33}Z_0} \\ &= y'_0 - c \frac{B_1 Z + B_2}{C_1 Z + C_2} \end{aligned} \quad (4.127)$$

A system of equations is therefore obtained which relates the image coordinates  $x', y'$  of a line and the parameters of the line in object space. Inserting equations (4.127) into (4.125) results in the relationship between the straight line parameters in image and object space:

$$\begin{aligned} (y'_0 C_1 - cB_1 - ax'_0 C_1 + acA_1 - bC_1)Z \\ +(y'_0 C_2 - cB_2 - ax'_0 C_2 + acA_2 - bC_2) = 0 \end{aligned} \quad (4.128)$$

This equation is true for all  $Z$  if both terms in the brackets are zero. There are therefore two equations for parameters  $a, b$  of the image line:

$$\begin{aligned} y'_0 C_1 - cB_1 - ax'_0 C_1 + acA_1 - bC_1 = 0 \\ y'_0 C_2 - cB_2 - ax'_0 C_2 + acA_2 - bC_2 = 0 \end{aligned} \quad (4.129)$$

Replacing the substitutions  $A_1$  etc of equation (4.127) and re-arranging gives:

$$a = \frac{-(\beta Z_0 + \delta - Y_0)r_{11} + (\alpha Z_0 + \gamma - X_0)r_{21} + [\alpha(\delta - Y_0) - \beta(\gamma - X_0)]r_{31}}{(\beta Z_0 + \delta - Y_0)r_{12} - (\alpha Z_0 + \gamma - X_0)r_{22} - [\alpha(\delta - Y_0) - \beta(\gamma - X_0)]r_{32}} \quad (4.130a)$$

<sup>1</sup> Here corrections for distortion effects are neglected.

$$b = x'_0 \frac{(\beta Z_0 + \delta - Y_0)r_{11} - (\alpha Z_0 + \gamma - X_0)r_{21} - [\alpha(\delta - Y_0) - \beta(\gamma - X_0)]r_{31}}{(\beta Z_0 + \delta - Y_0)r_{12} - (\alpha Z_0 + \gamma - X_0)r_{22} - [\alpha(\delta - Y_0) - \beta(\gamma - X_0)]r_{32}} \quad (4.130b)$$

$$+ y'_0 \\ + c \frac{(\beta Z_0 + \delta - Y_0)r_{13} - (\alpha Z_0 + \gamma - X_0)r_{23} - [\alpha(\delta - Y_0) - \beta(\gamma - X_0)]r_{33}}{(\beta Z_0 + \delta - Y_0)r_{12} - (\alpha Z_0 + \gamma - X_0)r_{22} - [\alpha(\delta - Y_0) - \beta(\gamma - X_0)]r_{32}}$$

The relations (4.130) can be directly used as observation equations for a space resection. Approximate values for the unknown parameters of exterior orientation are required for linearisation. Three non-parallel image lines are sufficient for solving the equations.

#### 4.5.3 Relative orientation with straight lines

Relative orientation based on straight lines must fulfil the condition that the projection planes of the images, each defined by the image of a line and the perspective centre, intersect in a common object line. This condition is always fulfilled for two non-parallel image planes; a unique solution for relative orientation with straight lines requires three images covering the same part of the object.

The solution is divided into two steps (Schwermann 1995). In the first step the rotation parameters of the images with respect to each other are determined. The second step generates the remaining translations. By analogy with the relative orientation solution (see section 4.2.4.3) one image can define the reference system. Each of the other two images requires, in principle, three rotations and three translations, making a total of 12 parameters. However, one translation can be arbitrarily fixed in order to define scale and a total of 11 independent parameters must therefore be calculated.

The three homologous projection planes  $E_1, E_2, E_3$  strictly intersect in a common straight line if their normal vectors  $\mathbf{n}_1, \mathbf{n}_2, \mathbf{n}_3$  are coplanar (Fig. 4.77). The projection plane of any one

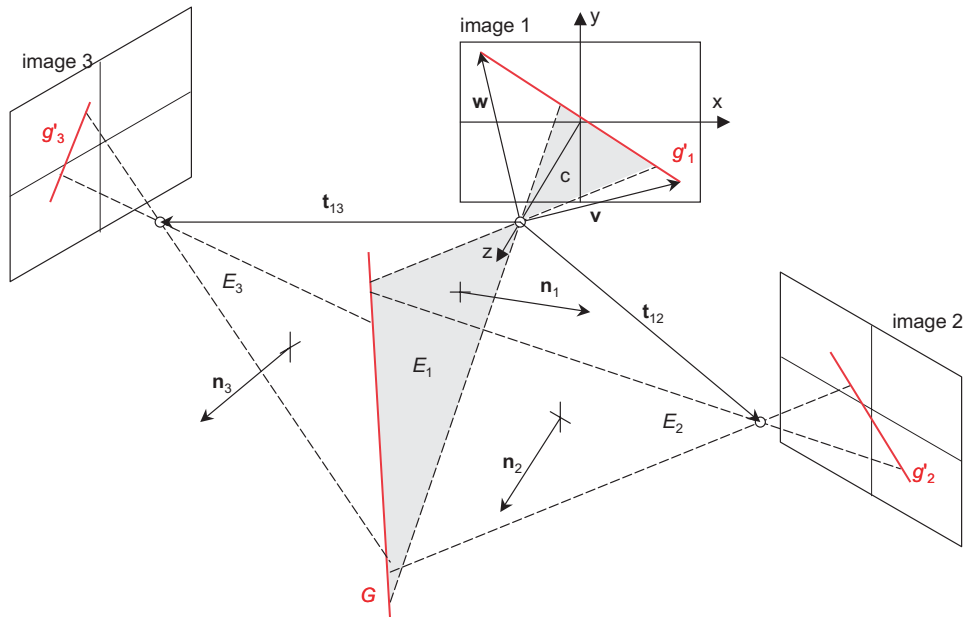


Figure 4.77 Relative orientation based on straight lines

image is defined by two arbitrary points on the imaged line and the corresponding perspective centre. The normal vector to the plane is obtained from the cross product of two direction vectors  $\mathbf{v}$  and  $\mathbf{w}$ , defined as follows using image line parameters  $a$  and  $b$  from equation (4.125) and principal distance  $c$  as a convenient arbitrary value for the  $x_w$  and  $(-x_w)$  image coordinates:

$$\mathbf{v} = \begin{bmatrix} x_v \\ y_v \\ z_v \end{bmatrix} = \begin{bmatrix} c \\ ca+b \\ -c \end{bmatrix} \quad \mathbf{w} = \begin{bmatrix} x_w \\ y_w \\ z_w \end{bmatrix} = \begin{bmatrix} -c \\ -ca+b \\ -c \end{bmatrix} \quad (4.131)$$

$$\mathbf{n} = \mathbf{v} \times \mathbf{w}$$

The values  $x_v$  and  $x_w$  are coordinates of arbitrarily chosen line points which are assigned the values  $c$  and  $-c$  respectively. Coplanarity of the three normal vectors is defined as follows (see equation (4.32)):

$$\mathbf{n}_1(\bar{\mathbf{n}}_2 \times \bar{\mathbf{n}}_3) = 0 \quad (4.132)$$

where the normal vectors of images 2 and 3 are transformed into the model coordinate system xyz of image 1 by the (unknown) rotation parameters:

$$\mathbf{n}_1(\mathbf{R}_2 \mathbf{n}_2 \times \mathbf{R}_3 \mathbf{n}_3) = 0 \quad (4.133)$$

Equations (4.133) are used as observation equations for a least-squares estimation. At least six independent line observations are required for the calculation of the six unknown rotation parameters.

The translations between the images can be calculated by determining the spatial intersection line  $G$ . The equations of the projection planes are given by:

$$\begin{aligned} E_1 : A_1x + B_1y + C_1z &= 0 \\ E_2 : A_2x + B_2y + C_2z + D_2 &= 0 \\ E_3 : A_3x + B_3y + C_3z + D_3 &= 0 \end{aligned} \quad (4.134)$$

or written in the form:

$$\begin{bmatrix} A_i \\ B_i \\ C_i \end{bmatrix} = \mathbf{n}_{0i} \quad i = 1, 2, 3 \quad D_i = -\mathbf{n}_{0i} \mathbf{t}_{1i} \quad i = 2, 3 \quad (4.135)$$

The desired translation vectors  $\mathbf{t}_{12}$  and  $\mathbf{t}_{13}$  are expressed by the coefficients  $D_i$ , hence they are rotation-invariant. The coefficients  $A_i$ ,  $B_i$ ,  $C_i$  can be calculated from the image lines using equations (4.131) and (4.135), and taking account of the relative rotations.

The line of intersection of projected planes  $E_1$  and  $E_2$  can be written in the form<sup>1</sup>

$$\begin{aligned} y &= \alpha_{12}x + \gamma_{12} \\ z &= \beta_{12}x + \delta_{12} \end{aligned} \quad (4.136)$$

<sup>1</sup> The choice of symbols representing coordinates may have to be changed according to section 4.5.2.

From equations (4.136) and (4.134), the following equation to a straight line can be derived (see also equation (2.15)):

$$\begin{aligned} y &= -\frac{A_1 C_2 - A_2 C_1}{B_1 C_2 - B_2 C_1} x + \frac{C_1}{B_1 C_2 - B_2 C_1} D_2 \\ z &= -\frac{A_1 B_2 - A_2 B_1}{B_2 C_1 - B_1 C_2} x + \frac{B_1}{B_2 C_1 - B_1 C_2} D_2 \end{aligned} \quad (4.137)$$

The parameters  $\alpha_{12}$ ,  $\gamma_{12}$ ,  $\beta_{12}$ ,  $\delta_{12}$  can be determined by a comparison of coefficients. The relations between image 1 and image 3 are found in an analogous way. Since only one common intersection line exists for homologous image lines, the conditions

$$\begin{aligned} \gamma_{12} - \gamma_{13} &= 0 \\ \delta_{12} - \delta_{13} &= 0 \end{aligned} \quad (4.138)$$

and equation (4.135) lead to the following functions for the required translations:

$$\begin{aligned} \frac{C_1}{B_1 C_3 - B_3 C_1} (\mathbf{n}_{03} \mathbf{t}_{13}) - \frac{C_1}{B_1 C_2 - B_2 C_1} (\mathbf{n}_{02} \mathbf{t}_{12}) &= 0 \\ \frac{B_1}{B_3 C_1 - B_1 C_3} (\mathbf{n}_{03} \mathbf{t}_{13}) - \frac{B_1}{B_2 C_1 - B_1 C_2} (\mathbf{n}_{02} \mathbf{t}_{12}) &= 0 \end{aligned} \quad (4.139)$$

One of the six translation parameters can be set to a constant value, leaving five unknowns to be determined.

This solution for relative orientation, using lines recorded in three images, requires appropriately configured images. If one object line is (approximately) parallel to the base of images 2 and 3, where image 1 is the reference image, it does not provide information about the rotation parameters. In particular, the determination of rotation and translation parameters fails if all three images are located on a common base line. The optimum configuration is given by an image triple whose centres of projection form an equilateral triangle.

#### 4.5.4 3D similarity transformation with straight lines

The spatial similarity transformation described in section 2.2.2.2 can also be extended to the transformation of lines in space e.g. for the absolute orientation of straight lines which have been determined in a process of relative orientation. The following comprehensive derivation due to Schwermann (1995) is again based on the straight line equations (4.126) (see also footnote 1 on previous page).

Let  $g$  be a straight line in the xyz coordinate system which is to be transformed into straight line  $G$  in the XYZ system:

$$\begin{aligned} g: \quad x &= \alpha z + \gamma \\ y &= \beta z + \delta \end{aligned} \qquad \begin{aligned} G: \quad X &= \bar{\alpha} Z + \bar{\gamma} \\ Y &= \bar{\beta} Z + \bar{\delta} \end{aligned} \quad (4.140)$$

Equations (2.31) of the spatial similarity transformation are given by:

$$\begin{aligned} X &= X_0 + m(r_{11}x + r_{12}y + r_{13}z) \\ Y &= Y_0 + m(r_{21}x + r_{22}y + r_{23}z) \\ Z &= Z_0 + m(r_{31}x + r_{32}y + r_{33}z) \end{aligned} \quad (4.141)$$

Insertion of equation (4.140) into (4.141) and subsequent elimination of  $Z$  leads to the following system:

$$\begin{aligned} m[\bar{\alpha}(\alpha r_{31} + \beta r_{32} + r_{33}) - (\alpha r_{11} + \beta r_{12} + r_{13})]z \\ + [\bar{\alpha}(m\gamma r_{31} + m\delta r_{32} + Z_0) - (m\gamma r_{11} + m\delta r_{12} + X_0 - \bar{\gamma})] = 0 \\ m[\bar{\beta}(\alpha r_{31} + \beta r_{32} + r_{33}) - (\alpha r_{21} + \beta r_{22} + r_{23})]z \\ + [\bar{\beta}(m\gamma r_{31} + m\delta r_{32} + Z_0) - (m\gamma r_{21} + m\delta r_{22} + Y_0 - \bar{\delta})] = 0 \end{aligned} \quad (4.142)$$

These equations are true for each point on a straight line if the terms in square brackets vanish. After some re-arrangement, the parameters of the straight line reduce to:

$$\begin{aligned} \bar{\alpha} &= \frac{\alpha r_{11} + \beta r_{12} + r_{13}}{\alpha r_{31} + \beta r_{32} + r_{33}} \\ \bar{\beta} &= \frac{\alpha r_{21} + \beta r_{22} + r_{23}}{\alpha r_{31} + \beta r_{32} + r_{33}} \end{aligned} \quad (4.143)$$

$$\begin{aligned} \bar{\gamma} &= X_0 - \bar{\alpha}Z_0 + m \frac{-\delta r_{21} + \gamma r_{22} + (\alpha\delta - \beta\gamma)r_{23}}{\alpha r_{31} + \beta r_{32} + r_{33}} \\ \bar{\delta} &= Y_0 - \bar{\beta}Z_0 + m \frac{\delta r_{11} - \gamma r_{12} - (\alpha\delta - \beta\gamma)r_{13}}{\alpha r_{31} + \beta r_{32} + r_{33}} \end{aligned} \quad (4.144)$$

This system of equations can be used to derive the straight line  $G$  from  $g$  if the transformation parameters are known. Alternatively, observation equations for a least-squares estimation of unknown transformation parameters can be derived for given  $g$  and  $G$ . In an analogous way to relative orientation, the slope parameters are independent of the translations and can be calculated separately. In order to determine the seven unknowns, a minimum of seven straight line observations are required.

#### 4.5.5 Bundle adjustment with straight lines

The method of bundle adjustment introduced in section 4.3 can be extended by observation equations (4.130) for straight lines. As a result, points and straight lines can be handled simultaneously in one adjustment process.

In this context, additional constraints or weighted observations based on straight lines can be introduced to eliminate datum defects or stabilise the adjustment system as follows (Schwermann 1995):

- Definition of datum

In one approach the general datum defect of 7 (3 translations, 3 rotations, 1 scale factor) can be eliminated by including suitable reference lines. Horizontal or vertical straight lines, with

fixed slope parameters, will serve this purpose. For arbitrarily oriented lines all four line parameters must be fixed.

In another approach, the line-based bundle adjustment can be configured as a free net adjustment. In a similar way to the procedures in section 4.3.3.3, the required seven additional constraints are introduced by a matrix  $\mathbf{B}$ . For this purpose the effect of differential changes in the line parameters on the 7 datum parameters is formulated. For example, straight lines in the form of equation (4.126) have the following differential effects on the datum parameters:

$X_0$	$Y_0$	$Z_0$	$w_1$	$w_2$	$w_3$	$m$	
0	0	0	$-\alpha\beta$	$1+\alpha^2$	$-\beta$	0	
0	0	0	$-1-\beta^2$	$\alpha\beta$	$\alpha$	0	
1	0	$-\alpha$	$-\alpha\delta$	$\alpha\gamma$	$-\delta$	$\gamma$	
0	1	$-\beta$	$-\beta\delta$	$\beta\gamma$	$\gamma$	$\delta$	

(4.145)

Here  $w_i$  represents the respective parameters of rotation around the coordinate axes used for the current definition of the line.

- Line constraints

In a similar way to section 4.3.2.3, geometric constraints between object lines are introduced as additional weighted constraint equations. They can be used to provide the following properties:

- parallelism of lines
- rectangularity of lines
- angle between lines
- distance between lines

#### 4.5.6 Bundle adjustment with geometric elements

The approaches described above for line photogrammetry can only work with uniquely defined straight lines observed as lines in image space. Alternative geometric elements such as cylinders or spatial curves cannot be used for orientation in the manner described.

In order to use arbitrary image contours (grey level edges) for orientation in a bundle adjustment, it is necessary to assign them a shape in object space. Theoretically, any geometric shape is usable if it can be mathematically projected into the image and if its parameters can be differentiated. However, the geometric shape should be of relatively simple form and represented by a small set of parameters in order to minimise the adjustment effort in terms of orientation and geometry data.

Image edge data is provided as a list of discrete image points. The relevant spatial object is projected back into the image and the distances between measured edge points and back-projected object shape are used as corrections in a least-squares adjustment.

The straight line is the simplest form of linear object. It serves as the basis of all other geometric shapes which might be used for orientation. In the following approach straight lines are processed in a way which, as far as possible, avoids singularities and ambiguities.

The spatial straight line is initially defined as

$$\mathbf{P} = \mathbf{p} + \lambda \mathbf{q} \quad (4.146)$$

for an arbitrary point  $\mathbf{P}$  on the line. Together with the perspective centre, the straight line defines a plane; the intersection of this plane with the image plane defines the corresponding image line. The projection plane can be described by its normal vector as

$$\mathbf{n} = \mathbf{R}^T (\mathbf{q} \times (\mathbf{p} - \mathbf{X}_0)) \quad (4.147)$$

where the normal vector is transformed into the image coordinate system by means of the exterior orientation parameters  $\mathbf{R}$  and  $\mathbf{X}_0$ . In order to calculate the perpendicular distance of an image point to the back-projected line, the length of the normal vector in image space is normalised to 1. The distance corresponds to the correction of a virtual observation, calculated from the product of normal vector  $\mathbf{n}$  and the three-dimensional image vector  $\mathbf{x}'$  (Hemken and Luhmann 2002).

$$v = \frac{\mathbf{n} \cdot \mathbf{x}'}{\sqrt{x_n^2 + y_n^2}} \quad (4.148)$$

$$\text{where } \mathbf{n} = \begin{bmatrix} x_n \\ y_n \\ z_n \end{bmatrix} \quad \text{and} \quad \mathbf{x}' = \begin{bmatrix} x' \\ y' \\ z' \end{bmatrix}$$

In principle, the approach can be extended to a circle in space (Kager 1981), cylinder, sphere and general curved elements (Forkert 1994) in an analogous way to the spatial contour adjustment according to Andresen 1991 (section 4.4.3.2).

As observations show, the adjustment uses lists of measured contour points in which individual points need not be matched to other discrete points. Preprocessing through filters or regression line adjustment is not required. As a result, the observations measured in a distorted image are not only used for the determination of exterior orientation and geometric element parameters, but also for the estimation of distortion parameters in the sense of plumb-line calibration (see section 7.2.1.3).

## 4.6 Multi-media photogrammetry

### 4.6.1 Light refraction at media interfaces

#### 4.6.1.1 Media interfaces

The standard photogrammetric imaging model (see sections 3.2.2, 4.2.1) assumes collinearity of object point, perspective centre and image point. Deviations caused by the lens or sensor are modelled by image-based correction functions. This approach is useful for most image configurations and applications.

If light rays in image or object space pass through optical media with differing refractive indices, they no longer follow a straight line. Using extended functional models for multi-media photogrammetry, it is possible to calculate the optical path of the rays through additional media interfaces and take this into account in object reconstruction. For example, interfaces exist if the optical path intersects:

- walls made of glass in object space (glass container, window panes)
- water (under, through)
- inhomogeneous atmosphere (refraction)

- filter glasses in front of the lens
- lens glasses
- glass covers on CCD sensors
- réseau plates.

For a rigorous model of the optical path, a geometric description of the media interface must be available, for example:

- plane in space
- second order surface (sphere, ellipsoid)
- wave-shaped surfaces.

Usually the transmission media are assumed to be homogenous and isotropic i.e. light rays propagate uniformly in all directions inside the media.

#### 4.6.1.2 Plane parallel media interfaces

The simplest multi-media case occurs if there is only one planar interface located parallel to the image plane (Fig. 4.78). An object point  $P_1$  is then projected onto point  $P'_0$ , passing through intermediate point  $P_0$  which lies on the interface. As a result, a radial shift  $\Delta r'$  occurs with respect to the image point  $P'_1$ , which corresponds to a straight line projection without refraction.

According to Fig. 4.78 the radial shift  $\Delta r'$ , taking account of equation (3.15), is given by:

$$\Delta r' = r'_0 Z_{rel} \left( 1 - \frac{1}{\sqrt{n^2 + (n^2 - 1) \tan^2 \epsilon_1}} \right) \quad (4.149)$$

$$\text{where } Z_{rel} = \frac{Z_i - Z_0}{Z_i} \quad \text{and} \quad r'_0 = c \tan \epsilon_1$$

according to Kotowski (1988).

Equation (4.149) shows that the effect of refraction is a function of distance. The radial shift is zero when:

1.  $\epsilon_1 = 0$ : the light ray is perpendicular to the interface and is therefore not refracted
2.  $n = 1$ : both media have equal refractive indices
3.  $Z_i = Z_0$ : the object point is located on the interface ( $Z_{rel} = 0$ ).

The radial shift  $\Delta r'$  can become significantly large:

##### Example 4.4:

A submerged underwater camera with air-filled lens,  $r'_0 = 21$  mm (small-format 35 mm camera, see also equation 3.36),  $Z_{rel} = 1$  (media interface located in perspective centre) and  $c = 28$  mm (wide angle lens) has a maximum radial shift of  $\Delta r' = 6.9$  mm.

##### Example 4.5:

A medium-format camera used for airborne measurement of the seabed, where  $r'_0 = 38$  mm,  $Z_i = 4$  m,  $Z_0 = 3$  m ( $Z_{rel} = 0.25$ ) (media interface is the water surface) and  $c = 80$  mm (standard angle lens) leads to a maximum radial shift of  $\Delta r' = 2.8$  mm.

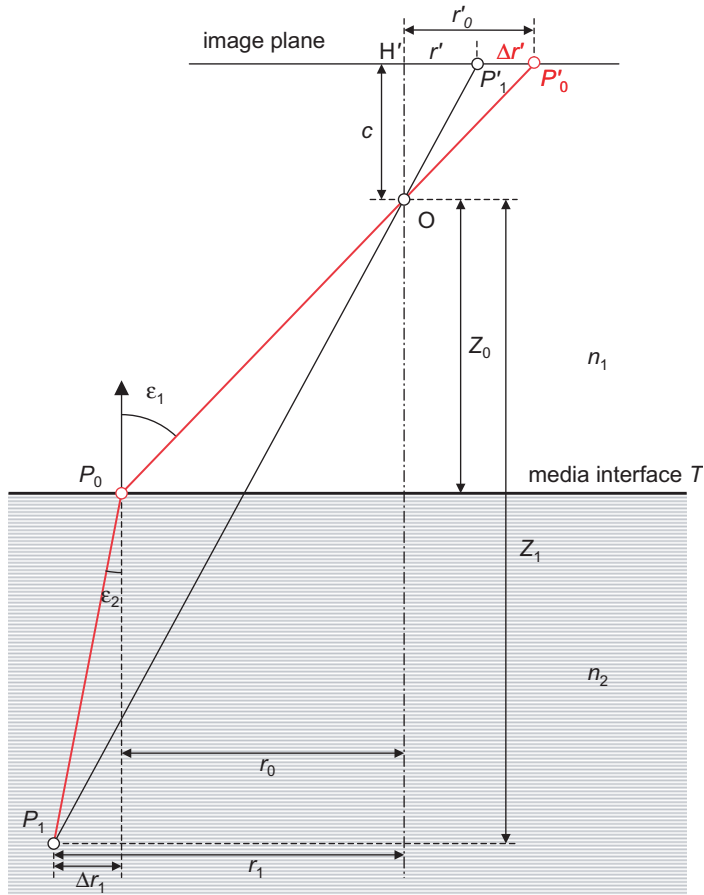


**Figure 4.78** Planar media interface parallel to the image plane

It can be shown that equation (4.149) can be expressed as the following power series:

$$\Delta r' = Z_{rel} (A_0 r'_0 + A_1 r'^3_0 + A_2 r'^5_0 + \dots) \quad (4.150)$$

This power series expansion is similar to the standard functions for correction of simple radial symmetric distortion in equations (3.35) and (3.36), and also to the correction of distance-dependent distortion equation (3.48). For applications where \$Z\_{rel}\$ is close to 1, the effect of a planar parallel media interface can be compensated for completely by the correction function for distance-dependent radial symmetric distortion.

The model of (4.149) can be extended to an unlimited number of parallel planar media interfaces, for instance for the modelling of plane parallel plates inside the camera (filter, reseau), or glass panes in object space (Fig. 4.79). For \$p\$ interfaces the radial shift becomes:

$$\Delta r' = \frac{r'_0}{Z_i} \left[ (Z_i - Z_{01}) - \sum_{l=1}^p \frac{d_l}{\sqrt{N_l^2 + (N_l^2 - 1) \tan^2 \epsilon_l}} \right] \quad (4.151)$$

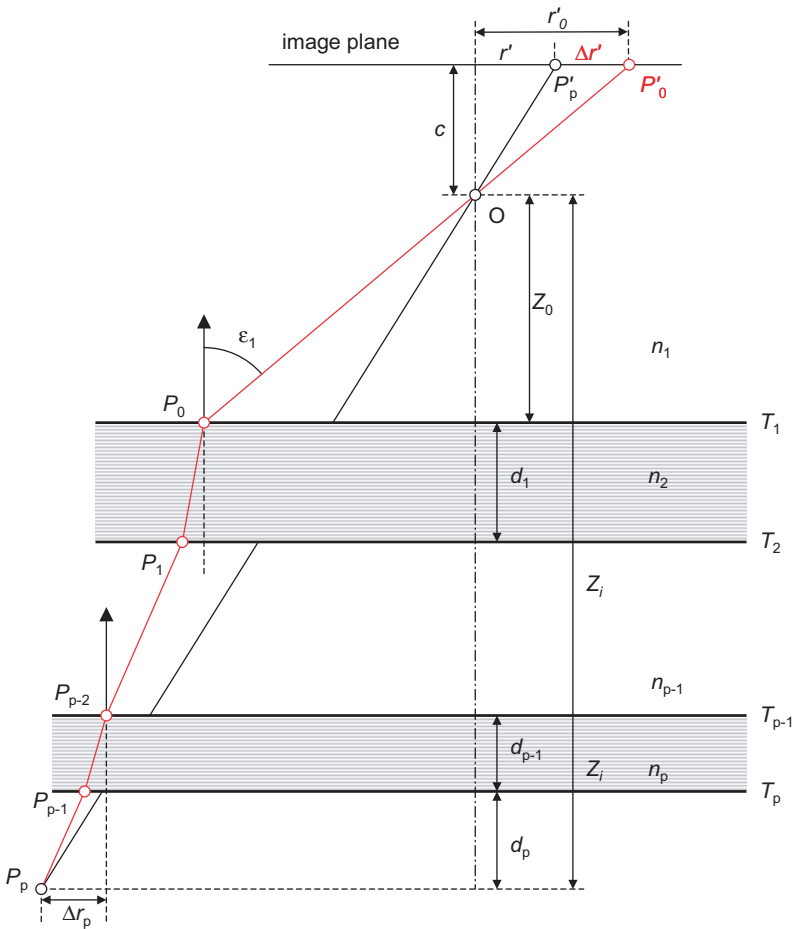


**Figure 4.79** Multiple parallel planar interfaces

where

$$d_l = Z_{l+1} - Z_l \quad : \text{distance between two adjacent interfaces}$$

$$N_l = \frac{n_{l+1}}{n_l} \quad : \text{relative refractive index}$$

If infinitesimal distances between interfaces are used in equation (4.151), multi-layered media can be modelled. For example, this approach can be used to set up model for the description of atmospheric refraction.

#### 4.6.1.3 Ray tracing through refracting interfaces

If arbitrary interfaces must be taken into account in the imaging model, each light ray must be traced through all contributing media by the successive application of the law of refraction (ray tracing, see section 5.3.3.1). For this purpose a set of three constraint equations is set up for each

refracting point of a media interface. These provide the 3D coordinates of the point of refraction and the path of the ray between the point  $P_0$ , the interface point  $P_1$  and the point  $P_2$  (Fig. 4.80):

1.  $P_1$  is located on surface  $F_1$ :  
This condition is fulfilled by

$$F_1(X_1, Y_1, Z_1) = 0$$

where for a general second order surface:

$$\begin{aligned} F_1 &= \mathbf{X}^T \mathbf{A} \mathbf{X} + 2\mathbf{a}^T \mathbf{X} + a = 0 \\ &= f_S(\mathbf{X}, \mathbf{A}, \mathbf{a}, a) \end{aligned} \quad (4.152)$$

where  $\mathbf{X} = \begin{bmatrix} X \\ Y \\ Z \end{bmatrix}$ ,  $\mathbf{a} = \begin{bmatrix} a_1 \\ a_2 \\ a_3 \end{bmatrix}$  and  $\mathbf{A} = \begin{bmatrix} a_{11} & a_{12} & a_{13} \\ a_{21} & a_{22} & a_{23} \\ a_{31} & a_{32} & a_{33} \end{bmatrix}$ ,  $a_{ij} = a_{ji}$  for  $i \neq j$

The surface can be parameterised with respect to the temporary coordinate system  $\bar{X}, \bar{Y}, \bar{Z}$  according to section 4.3.2.3 e.g. as rotationally symmetric surfaces.

2. Fulfilling the law of refraction:

$$F_2 = n_1 \sin \varepsilon_1 - n_2 \sin \varepsilon_2 = 0$$

The angles of incidence and refraction are introduced as a function of the object coordinates and the normal vector  $\mathbf{N}_1$  e.g. for  $\varepsilon_1$ :

$$\cos \varepsilon_1 = \frac{\mathbf{N}_1^T (\mathbf{X}_0 - \mathbf{X}_1)}{|\mathbf{N}_1^T| |\mathbf{X}_0 - \mathbf{X}_1|}$$

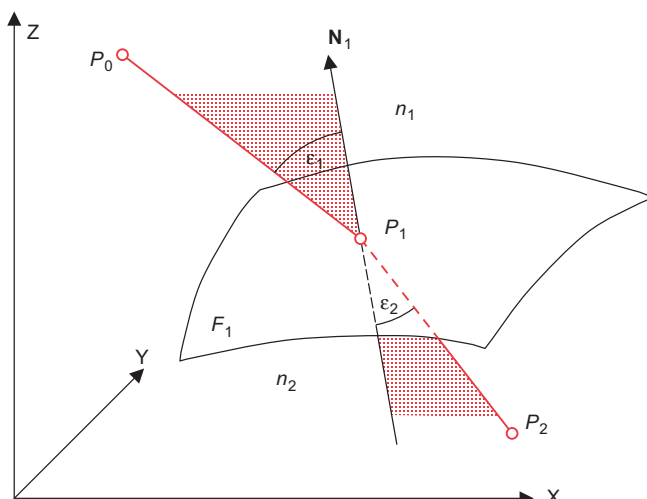


Figure 4.80 Ray tracing through an optical interface

3. Surface normal at  $P_1$ , and the projection rays lie in a common plane:

This is implemented by applying the coplanarity constraint to the three vectors:

$$F_3 = \begin{vmatrix} X_0 - X_1 & Y_0 - Y_1 & Z_0 - Z_1 \\ X_1 - X_2 & Y_1 - Y_2 & Z_1 - Z_2 \\ N_X & N_Y & N_Z \end{vmatrix} = 0$$

The three constraint equations are linearised at approximate values. Solving the system of equations results in the object coordinates  $X_1, Y_1, Z_1$  of the refraction point.

For an imaging system of  $p$  media interfaces, the system of equations is set up for each refraction point  $P_l, l = 1 \dots p$ . This principle is used in optics for the calculation of lens systems. This could be used in photogrammetry for a rigorous determination of distortion which takes account of all optical elements. To date this approach has not, however, been used.

#### 4.6.2 Extended model of bundle triangulation

Using the fundamentals of optical interfaces and ray tracing discussed above, the functional model for bundle adjustment can be extended. For this purpose the ray tracing algorithm with arbitrary interfaces is integrated into the imaging model of the collinearity equations (4.8).

Two major imaging configurations present themselves:

- constant (object invariant) position of interfaces relative to the measured object
- constant (bundle invariant) location of interfaces relative to the camera system

##### 4.6.2.1 Object-invariant interfaces

Object-invariant interfaces occur, for instance, if an object is imaged through a window pane or through water (Fig. 4.81).

The extended observation equations can be derived in three steps:

1. Ray tracing according to equation (4.152) with  $p$  interfaces:

$$\bar{\mathbf{X}}_i^l = f_S(\mathbf{X}_i, \mathbf{X}_{0j}, \mathbf{A}^l, \mathbf{a}^l, d^l, n^l) \quad (4.153)$$

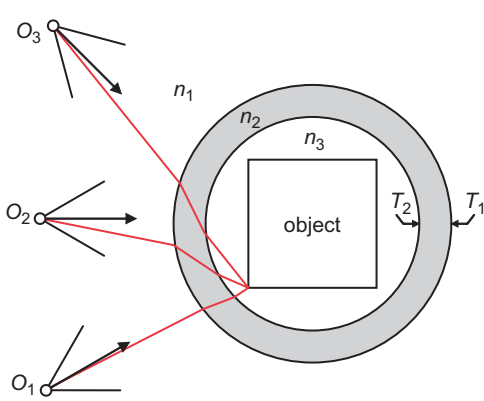


**Figure 4.81** Object-invariant interfaces

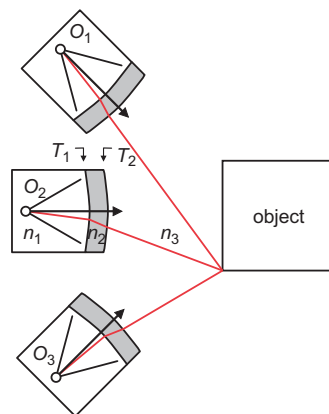


**Figure 4.82:** Bundle-invariant interfaces

308

where

- $\mathbf{A}^l, \mathbf{a}^l, a^l$ : parameters of interface  
 $n^l$ : relative refractive indices  
 $l = 1 \dots p$ : index of interface  
 $i$ : point index  
 $j$ : image index  
 $k$ : camera index

2. Spatial rotation and translation:

$$\begin{aligned} \mathbf{X}_{ij}^* &= \mathbf{R}_j(\bar{\mathbf{X}}_i^1 - \mathbf{X}_{0j}) \\ \begin{bmatrix} X_{ij}^* \\ Y_{ij}^* \\ Z_{ij}^* \end{bmatrix} &= \mathbf{R}_j \begin{bmatrix} \bar{X}_i^1 - X_{0j} \\ \bar{Y}_i^1 - Y_{0j} \\ \bar{Z}_i^1 - Z_{0j} \end{bmatrix} \end{aligned} \quad (4.154)$$

3. Extended collinearity equations:

$$\begin{bmatrix} x'_{ij} \\ y'_{ij} \end{bmatrix} = -\frac{c}{Z_{ij}^*} \begin{bmatrix} X_{ij}^* \\ Y_{ij}^* \end{bmatrix} + \begin{bmatrix} x'_{0k} \\ y'_{0k} \end{bmatrix} + \begin{bmatrix} \Delta x'_{ik} \\ \Delta y'_{ik} \end{bmatrix} \quad (4.155)$$

#### 4.6.2.2 Bundle-invariant interfaces

Bundle-invariant interfaces are given by optical refracting interfaces inside the image acquisition system e.g. underwater housing, add-on front filter, lenses, parallel plate cover on sensor or reseau plate (Fig. 4.82).

In contrast to the object-invariant approach, the calculation is performed in reverse order:

1. Spatial translation and rotation:

$$\mathbf{X}_{ij}^* = \mathbf{R}_j(\mathbf{X}_i^1 - \mathbf{X}_{0j}) \quad (4.156)$$

2. Ray tracing:

$$\bar{\mathbf{X}}_{ij}^l = f_S(\mathbf{X}_{ij}^*, \mathbf{A}^l, \mathbf{a}^l, a^l, n^l) \quad (4.157)$$

3. Extended collinearity equations:

$$\begin{bmatrix} x'_{ij} \\ y'_{ij} \end{bmatrix} = -\frac{c}{\bar{Z}_{ij}^l} \begin{bmatrix} \bar{X}_{ij}^l \\ \bar{Y}_{ij}^l \end{bmatrix} + \begin{bmatrix} x'_{0k} \\ y'_{0k} \end{bmatrix} + \begin{bmatrix} \Delta x'_{ik} \\ \Delta y'_{ik} \end{bmatrix} \quad (4.158)$$

The image point shifts caused by bundle-invariant interfaces are usually independent of the distance (see example 4.2). For rotationally symmetric elements (lenses) or plane parallel plates set parallel to the image plane, these shifts are radially symmetric. With suitable image configurations they can be compensated for by camera calibration which employs standard functions for distortion.

Additional applications and algorithms for multi-media photogrammetry can be found in Maas 1995 (particle tracking, determination of refraction), Fryer and Fraser 1986 (calibration of underwater cameras) and Höhle 1971 (underwater photogrammetry).

## 4.7 Panoramic photogrammetry

Panoramic photogrammetry is a special branch of close-range photogrammetry that uses panoramic images instead of common perspective imagery. Panoramic images can be acquired by specialised cameras or by digital stitching processes with normal images (see section 3.3.2.6). The section gives an overview on the basic imaging model, orientation methods and algorithms for 3D reconstruction. Further information can be extracted from, for example, Luhmann and Tecklenburg (2004), Schneider and Maas (2004), Heikkilä (2002), Chapman and Kotowski (2000).

### 4.7.1 Cylindrical panoramic imaging model

The most common method of panoramic photogrammetry is based on a cylindrical imaging model, as generated by numerous analogue and digital panoramic cameras or by a computational fusion of single central perspective images. Assuming a horizontal scan, the resulting panoramic image has central perspective imaging properties in the vertical direction only.

An image point  $P'$  can be defined either by the cylindrical coordinates  $r, \xi, \eta$  or by the Cartesian panoramic coordinates  $x, y, z$  (Fig. 4.83). The panorama is assumed to be created by a clockwise rotation when viewed from above. The metric image coordinates  $x', y'$  and the pixel coordinates  $u, v$  are defined within the cylindrical surface of the panorama, which is a plane when the cylinder is unrolled.

$$\begin{bmatrix} x \\ y \\ z \end{bmatrix} = \begin{bmatrix} r \cos \xi \\ -r \sin \xi \\ \eta \end{bmatrix} \quad (4.159)$$

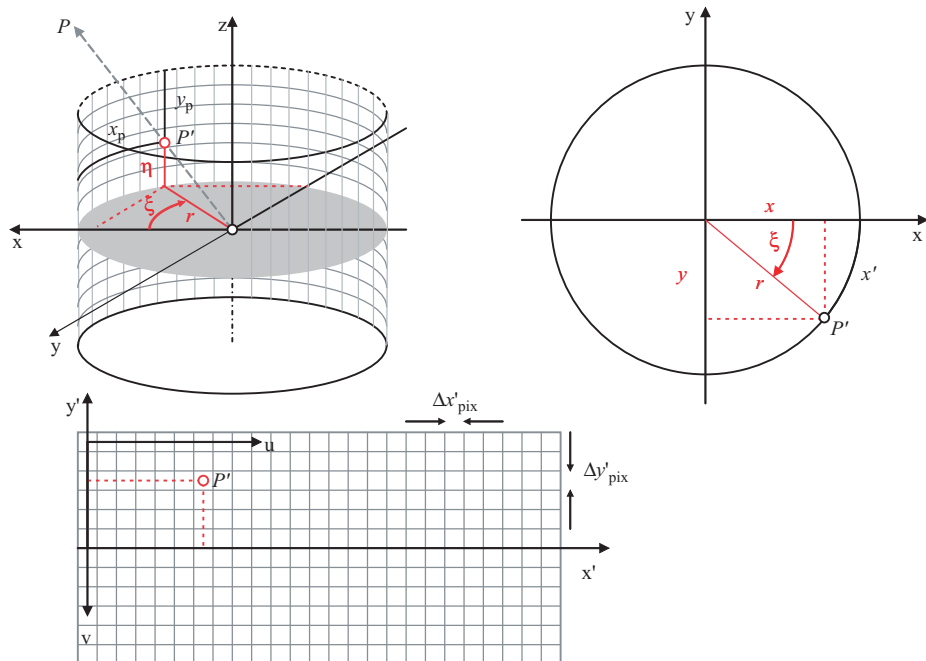


Figure 4.83 Coordinate systems defining a cylindrical panorama

310

$$\begin{bmatrix} x' \\ y' \end{bmatrix} = \begin{bmatrix} r\xi \\ z \end{bmatrix} \quad (4.160)$$

The digital plane panoramic image has  $n_C$  columns and  $n_R$  rows with a pixel resolution  $\Delta x'_p$  and  $\Delta y'_p$ . The circumference of the panorama is therefore  $n_C \Delta x'_p$  and its height is  $n_R \Delta y'_p$ . The radius of the digital image is, in the ideal case, equal to the principal distance of the camera. It can be calculated from the circumference or the horizontal angular resolution  $\Delta\xi$ :

$$r = \frac{n_C \Delta x'_p}{2\pi} = \frac{\Delta x'_p}{\Delta\xi} \quad (4.161)$$

By introducing the parameters of exterior orientation, the transformation between object coordinate system XYZ and panoramic coordinate system xyz (Fig. 4.84) is given by:

$$\mathbf{x} = \mathbf{X}_0 + \frac{1}{\lambda} \mathbf{R} \mathbf{x} \quad (4.162)$$

Rearrangement gives

$$\begin{aligned} \mathbf{x} &= \lambda \mathbf{R}^{-1} (\mathbf{X} - \mathbf{X}_0) \\ x &= \lambda [r_{11}(X - X_0) + r_{21}(Y - Y_0) + r_{31}(Z - Z_0)] = \lambda \bar{X} \\ y &= \lambda [r_{12}(X - X_0) + r_{22}(Y - Y_0) + r_{32}(Z - Z_0)] = \lambda \bar{Y} \\ z &= \lambda [r_{13}(X - X_0) + r_{23}(Y - Y_0) + r_{33}(Z - Z_0)] = \lambda \bar{Z} \end{aligned} \quad (4.163)$$

where  $\bar{X}, \bar{Y}, \bar{Z}$  define a temporary coordinate system that is parallel to the panoramic system. With the scale factor

$$\lambda = \frac{r}{\sqrt{\bar{X}^2 + \bar{Y}^2}} \quad (4.164)$$

the image coordinates in the unrolled (plane) panorama are given by

$$\begin{aligned} x' &= r \arctan \left( \frac{\bar{Y}}{\bar{X}} \right) - \Delta x' \\ y' &= y'_0 + \lambda \bar{Z} - \Delta y' \end{aligned} \quad (4.165)$$

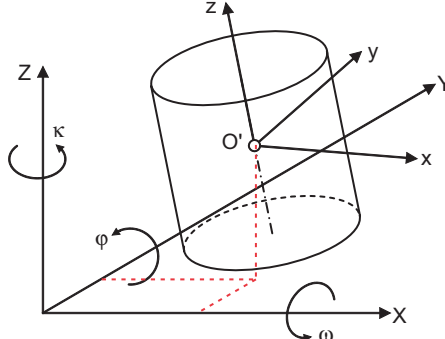


Figure 4.84 Exterior orientation of cylindrical panorama

or directly as collinearity equations between object coordinates and image coordinates:

$$\begin{aligned} x' &= r \arctan \left( \frac{r_{12}(X - X_0) + r_{22}(Y - Y_0) + r_{32}(Z - Z_0)}{r_{11}(X - X_0) + r_{21}(Y - Y_0) + r_{31}(Z - Z_0)} \right) - \Delta x' \\ y' &= y'_0 + \lambda [r_{13}(X - X_0) + r_{23}(Y - Y_0) + r_{33}(Z - Z_0)] - \Delta y' \end{aligned} \quad (4.166)$$

Here  $y'_0$  denotes a shift of the principal point in the y direction and  $\Delta x'$ ,  $\Delta y'$  are correction parameters for potential imaging errors in the camera.

The pixel coordinates  $u$ ,  $v$  of a digital panoramic image can be derived as:

$$\begin{aligned} u &= \frac{x'}{\Delta x'_{\text{pix}}} \\ v &= \frac{n_R}{2} - \frac{y'}{\Delta y'_{\text{pix}}} \end{aligned} \quad (4.167)$$

## 4.7.2 Orientation of panoramic imagery

The method of determining the exterior orientations of one or more panoramic images is analogous to that for central perspective imagery; that is, by application of the panoramic collinearity equations to space resection and/or bundle adjustment. Both methods require suitable approximate values.

### 4.7.2.1 Approximate values

For the usual case of panoramas with an approximate vertical rotation axis, initial values for exterior orientation can easily be derived from reference points. The centre coordinates of the panorama  $X_0$ ,  $Y_0$  can be calculated by plane resection using three control points  $P_1$ ,  $P_2$ ,  $P_3$  and the angles  $\Delta\xi_{12}$ ,  $\Delta\xi_{23}$ , which can be derived from the corresponding image points  $P'_1$ ,  $P'_2$  and  $P'_3$ .

The  $Z_0$  coordinate can, for example, be calculated from reference point  $P_1$ :

$$Z_0 = Z_1 - d_1 \frac{z_1}{r} \quad (4.168)$$

where  $d_1 = \sqrt{(X_1 - X_0)^2 + (Y_1 - Y_0)^2}$

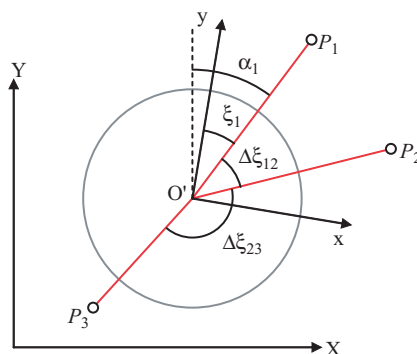


**Figure 4.85** Plane resection

The approximate rotation, angles of exterior orientation can be given to sufficient accuracy by  
 $\omega = 0$   
 $\varphi = 0$   
 $\kappa = \xi_1 - \alpha_1$

(4.169)

#### 4.7.2.2 Space resection

Space resection for a panoramic image can be formulated as an over-determined adjustment problem. For this purpose, the panoramic imaging equations (4.166) can be linearised at the approximate values given above. However, the use of Cartesian panoramic coordinates from (4.159) is much more convenient since they can be directly used as virtual three-dimensional image coordinates for the observation equations of a standard space resection (see section 4.2.3.1). Each image point provides three individual coordinates  $x$ ,  $y$ ,  $z$ , while for central perspective images the principal distance  $z' = -c$  is constant for all image points.

As for the standard space resection, a minimum of three reference points is required, although this can generate up to four possible solutions. Alternatively, using four reference points means a unique solution for the six parameters of exterior orientation is always obtained. If the reference points are distributed over the whole horizon, then even with a small number of points (greater than 4) a very reliable solution is achieved.

#### 4.7.2.3 Bundle adjustment

For a bundle adjustment of panoramic images, the mathematical model is based on space resection extended with unknown object points and additional parameters for self-calibration of the camera. Some programs permit the simultaneous processing of both panoramic and central perspective images.

One advantage of panoramic images is that a stably oriented set of images can be obtained using a comparatively small number of object points. The example in Fig. 4.86 shows a set of

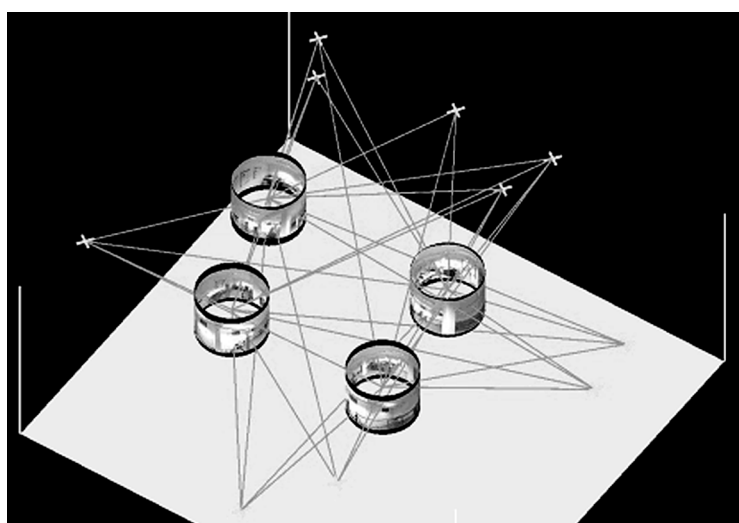


Figure 4.86 Distribution of 4 panoramas in 3D space

four panoramas taken for the interior survey of a room. In this example with four unknown object points, the following number of unknowns must be calculated:

parameter group	unknowns	number	total
exterior orientations	6	4	24
object points	3	4	12
datum definition	-7	1	-7
<b>sum</b>			<b>29</b>

The 29 unknowns can be determined by measuring the object points in all four images, so providing  $4 \times 4 \times 2 = 32$  observations. Since this minimum solution is very sensitive to noise and outliers, the number of object points should be increased to at least 8 in this case. Nevertheless, compared to standard image blocks the number of required object points is much smaller. This is mainly due to the stable geometry of a cylindrical image which can be oriented in 3D space with very little object information.

The bundle adjustment can be extended with parameters for the correction of imaging errors. When a panoramic image results from stitching together single images calibrated using the original camera parameters, no additional corrections are necessary. In contrast, if panoramic images from a rotating line scanner are to be adjusted, parameters specific to the scanner must be introduced (see section 3.3.2.6).

#### 4.7.3 Epipolar geometry

Given two oriented panoramas, epipolar plane and epipolar lines can be constructed for an imaged object point analogously to a stereo image pair. The epipolar plane  $K$  is defined by the object point  $P$  and either both image points  $P'$  and  $P''$  or the projection centres  $O'$  and  $O''$ . The epipolar plane intersects the two arbitrarily oriented panoramic cylinders in the elliptical epipolar lines  $k'$  and  $k''$ .

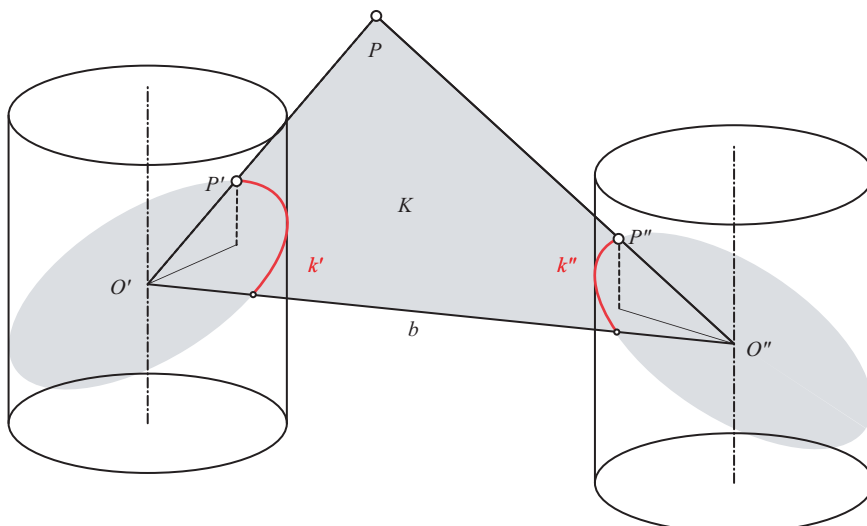
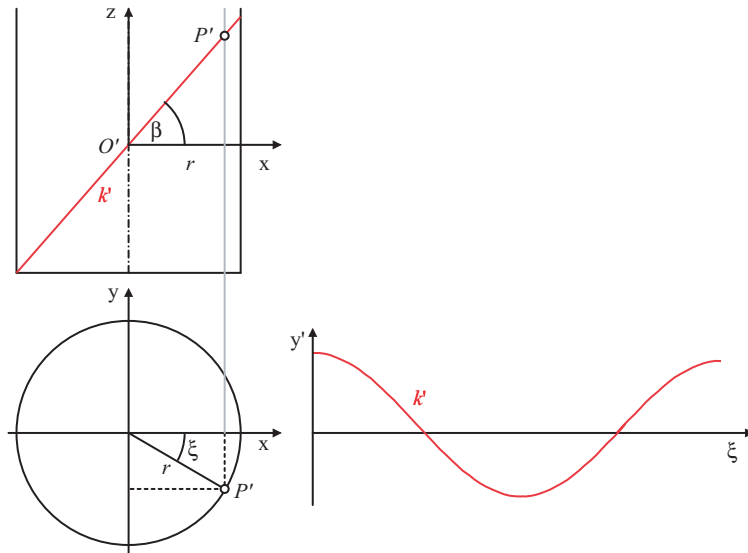


Figure 4.87 Epipolar geometry for panoramic images



**Figure 4.88** Sine form of panoramic epipolar lines

On the unrolled panoramic plane the epipolar lines are sinusoidal. For an image point  $P'$  measured in the left-hand image, an arbitrary object point  $P$  can be defined. The corresponding image point  $P''$  in the right-hand panorama can be calculated according to equation (4.166). If the epipolar plane intersects the panoramic cylinder at angle  $\beta$  corresponding to slope  $m = \tan \beta$ , the intersection straight line

$$z = mx \quad (4.170)$$

corresponding to Fig. 4.88 is obtained. With  $y' = z$  and  $x = r \cos \xi$  the equation for the epipolar line is given by

$$y' = mr \cos \xi \quad (4.171)$$

Fig. 4.89 shows an example of a panoramic image with the epipolar line superimposed.



**Figure 4.89** Measured point (upper) and sine form of corresponding panoramic epipolar line (lower)

#### 4.7.4 Spatial intersection

As for space resection and bundle adjustment for panoramic images, a general spatial intersection using three-dimensional panoramic coordinates can also be calculated. Spatial intersection fails if the object point lies on the baseline  $b$  (see Fig. 4.87).

If intersection is formulated on the basis of equations (4.166), the differential coefficients of the observation equations with respect to the unknown object coordinates are required. Using (4.163) they are given by

$$\begin{aligned}\frac{\partial x'}{\partial X} &= \frac{r}{x^2 + y^2} (r_{12}x - r_{11}y) \\ \frac{\partial x'}{\partial Y} &= \frac{r}{x^2 + y^2} (r_{22}x - r_{21}y) \\ \frac{\partial x'}{\partial Z} &= \frac{r}{x^2 + y^2} (r_{32}x - r_{31}y) \\ \frac{\partial y'}{\partial X} &= \frac{\lambda}{z} \left( \frac{r_{11}x - r_{12}y}{x^2 + y^2} + \frac{r_{13}}{z} \right) \\ \frac{\partial y'}{\partial Y} &= \frac{\lambda}{z} \left( \frac{r_{21}x - r_{22}y}{x^2 + y^2} + \frac{r_{23}}{z} \right) \\ \frac{\partial y'}{\partial Z} &= \frac{\lambda}{z} \left( \frac{r_{31}x - r_{32}y}{x^2 + y^2} + \frac{r_{33}}{z} \right)\end{aligned}\quad (4.172)$$

As usual, the unknown object coordinates  $X, Y, Z$  are calculated by iterative adjustment until corrections to the unknowns become insignificant.

## References

- Abdel-Aziz, Y. and Karara, H. M. (1971) *Direct linear transformation from comparator coordinates into object space coordinates in close range photogrammetry*. ASP Symposium on Close-Range Photogrammetry.
- Ackermann, F., Ebner, H. and Klein, H. (1970) Ein Rechenprogramm für die Streifentriangulation mit unabhängigen Modellen. *Bildmessung und Luftbildwesen*, Heft 4/1970, pp. 206–217.
- Albertz, J. and Kreiling, W. (1989) *Photogrammetric guide*. 4th edition, Wichmann Verlag, Karlsruhe, Germany.
- Andresen, K. (1991) Ermittlung von Raumelementen aus Kanten im Bild. *Zeitschrift für Photogrammetrie und Fernerkundung*, Nr. 6/1991, pp. 212–220.
- Benning, W. and Schwermann, R. (1997) PHIDIAS-MS – Eine digitale Photogrammetrie-applikation unter MicroStation für Nahbereichsanwendungen. Allgemeine Vermessungsnachrichten, 1/1997, pp. 16–25.
- Brown, D. C. (1976) The bundle adjustment – progress and prospects. *International Archives of Photogrammetry*, 21(3), ISP Congress, Helsinki, pp. 1–33.
- Cayley, A. (1843) *Cambridge Mathematical Journal*, III and reprinted in his *Collected Papers*, I, 1889, p. 28.
- Chapman, D. and Kotowski, R. (2000) *Methodology for the Construction of Large Image Archives of Complex Industrial Structures*. Publikationen der DGPF, Band 8, Essen 1999.

- Dold, J. (1999) *Stand der Technik in der Industriephotogrammetrie*. Photogrammetrie-Fernerkundung-Geoinformation, Heft 2, pp. 113–126.
- Forkert, G. (1994) *Die Lösung photogrammetrischer Orientierungs- und Rekonstruktions-aufgaben mittels allgemeiner kurvenförmiger Elemente*. Dissertation, TU Wien, Geowissenschaftliche Mitteilungen der Studienrichtung Vermessungswesen, Heft 41, pp. 147.
- Förstner, W. and Wrobel, B. (2004) Mathematical concepts in photogrammetry. In McGlone et al. (ed.) *Manual of Photogrammetry*, pp. 15–181.
- Fraser, C. S. (1996) Network design. In Atkinson (ed.) *Close Range Photogrammetry and Machine Vision*. Whittles Publishing, Caithness, UK, pp. 256–281.
- Fraser, C. S. and Brown, D. C. (1986) Industrial photogrammetry – new developments and recent applications. *The Photogrammetric Record* **12**(68).
- Fryer, J. G. and Fraser, C. S. (1986) On the calibration of underwater cameras. *The Photogrammetric Record*, **12**(67), pp. 73–85.
- Haralick, R. M. and Shapiro, L. G. (1992) *Computer and robot vision*. Vol. I+II, Addison-Wesley, Reading, Ma., USA.
- Haralick, R. M., Lee, C., Ottenberg, K. and Nolle, M. (1994) Review and analysis of solutions of the three point perspective pose estimation problem. *International Journal of Computer Vision*, **13**(3), pp. 331–356.
- Hartley, R. and Zisserman, A. (2000) *Multiple View Geometry*. Cambridge University Press, Cambridge, UK.
- Hastedt, H. (2004) Monte-Carlo simulation in close-range photogrammetry. *International Archives of Photogrammetry, Remote Sensing and Spatial Information Science*, **35**(B5), pp. 18–23.
- Heikkilä, J. (2002) Performance of circular image blocks in close-range photogrammetry. *ISPRS Symposium Comm. V*, Korfu, 2002.
- Hemken, H. and Luhmann, T. (2002) Photogrammetrische Objekterfassung mit Linienphotogrammetrie. In Luhmann (ed.) *Photogrammetrie und Laserscanning*, Wichmann Verlag, Heidelberg.
- Hemmleb, M. and Wiedemann, A. (1997) *Digital Rectification and Generation of Orthoimages in Architectural Photogrammetry*. Proc. of the CIPA Int. Symposium ‘97, Int. Archives for Photogrammetry and Remote Sensing, Vol. XXXII, Part 5C1B, Göteborg, pp. 261–267.
- Hinsken, L. (1989) CAP: Ein Programm zur kombinierten Bündelausgleichung auf Personalcomputern. *Zeitschrift für Photogrammetrie und Fernerkundung*, Heft 3/1989, pp. 92–95.
- Höhle, J. (1971) *Zur Theorie und Praxis der Unterwasser-Photogrammetrie*. Dissertation, Deutsche Geodätische Kommission, Reihe C, Heft 163.
- Höhle, J. (1997) Photorealistische und dynamische 3D-Bauwerksmodelle. *The Photogrammetric Journal of Finland*, **15**(2), pp. 48–61.
- Hunt, R. A. (1984). Estimation of initial values before bundle adjustment of close range data. *International Archives of Photogrammetry and Remote Sensing*, **25**(5) 419–428.
- Jacobsen, K. (1982) *Selection of additional parameters by program*. ISPRS Comm. III, Helsinki, Int. Archives of Photogrammetry and Remote Sensing, Vol. 24–3, pp. 266–275.
- Kager, H. (1981) Bündeltriangulation mit indirekt beobachteten Kreiszentren. *Geowissenschaftliche Mitteilungen der Studienrichtung Vermessungswesen der TU Wien*, Heft 19, pp. 37.
- Kager, H. (1989) Orient: a universal photogrammetric adjustment system. In Gruen/Kahmen (ed.) *Optical 3-D Measurement Techniques*, Wichmann Verlag, Karlsruhe, pp. 447–455.
- Klette, R., Koschan, A. and Schlüns, K. (1996) Computer Vision – Räumliche Information aus digitalen Bildern. Verlag Vieweg Technik, Braunschweig/Wiesbaden
- Kotowski, R. (1988) *Phototriangulation in Multi-Media Photogrammetry*. 16th ISPRS Congress, Commission V, Vol. XXVII, Kyoto.
- Kraus, K. (2000) *Photogrammetry, Volume 1, Fundamentals and Standard Processes*. With contributions by Peter Waldhäusl, translated by Peter Stewardson, Verlag H. Stam GmbH, Köln.
- Kraus, K. (1997) *Photogrammetry, Volume 2, Advanced Methods and Applications*. With contributions by J. Jansa and H. Kager. Dümmler Verlag, Bonn.
- Kruck, E. (1983) *Lösung großer Gleichungssysteme für photogrammetrische Blockausgleichungen mit erweitertem funktionalen Modell*. Dissertation, Universität Hannover.

- Kyle, S. A. (1990) *A modification to the space resection*. Allgemeine Vermessungs-nachrichten, International Edition, 7/1990, pp. 17–25.
- Li, H. and Gruen, A. (1997) LSB-snakes for industrial measurement applications. In Gruen/Kahmen (ed.) *Optical 3-D Measurement Techniques IV*, Wichmann Verlag, Heidelberg, pp. 169–178.
- Loser, R. and Luhmann, T. (1992) The programmable optical 3-D measuring system POM – applications and performance. *International Archives of Photogrammetry and Remote Sensing*, **29**(B5), Comm. V, Washington, pp. 533–540.
- Luhmann, T. and Tecklenburg, W. (2004) *3-D object reconstruction from multiple-station panorama imagery*. ISPRS workshop on Panorama Photogrammetry, Dresden.
- McGlone, J. C., Mikhail, E. M. and Paderes, F. C. (1989) Analytic data-reduction schemes in non-topographic photogrammetry. In Karara (ed.) *Non-Topographic Photogrammetry*, pp. 37–57.
- Maas, H.-G. (1995) New developments in multimedia photogrammetry. In Gruen/Kahmen (ed.) *Optical 3-D Measurement Techniques III*, Wichmann Verlag, Heidelberg, pp. 91–97.
- Maas, H.-G. (1999) *Ein Ansatz zur Selbstkalibrierung von Kameras mit instabiler innerer Orientierung*. Publikationen der DGPF, Band 7, München 1998.
- Mikhail, E. M., Bethel, J. S. and McGlone, J. C. (2001) *Introduction to Modern Photogrammetry*. John Wiley & Sons, New York.
- Mugnier, C. J., Förstner, W., Wrobel, B., Paderes, F. and Munji, R. (2004) The mathematics of photogrammetry. In McGlone et al. (ed.) *Manual of Photogrammetry*, pp. 181–316.
- Neumann, H. J. (1990) *Koordinatenmeßtechnik – Technologie und Anwendung*. Verlag moderne Industrie, Landsberg/Lech.
- Pelzer, H. (1995) Geodätische Auswertemethodik. In Schwarz (ed.) *Vermessungs-verfahren im Maschinen- und Anlagenbau*, Wittwer Verlag, Stuttgart, pp. 255–280.
- Pfeifer, T. (1998) *Fertigungsmeßtechnik*. R. Oldenbourg Verlag, München.
- Schmid, H. H. (1955) Analytical Photogrammetry as Applied to Flight Testing. *Photogrammetric Engineering*, December 1955, XXI (5), p. 680.
- Schmid, H. H. (1958) Eine allgemeine analytische Lösung für die Aufgabe der Photogrammetrie. *Bildmessung und Luftbildwesen*. 1958 Nr. 4 (103–113) and 1959 Nr. 1 (1–12).
- Schmid, H. H. (1959) *A General Analytical Solution to the Problem of Photogrammetry*. Ballistic Research Laboratories, Report No. 1065, July 1959.
- Schneider, D. and Maas, H.-G. (2004) Development and application of an extended geometrical model for high resolution panoramic cameras. *International Archives of Photogrammetry, Remote Sensing and Spatial Information Sciences*. Vol. XXXV, Part B.
- Schwermann, R. (1995) *Geraedengestützte Bildorientierung in der Nahbereichs-photogrammetrie*. Dissertation, Veröffentlichung des Geodätischen Instituts der Rheinisch-Westfälischen Technischen Hochschule Aachen, Nr. 52.
- Schwidesky, K. and Ackerman, F. E. (1976) *Photogrammetrie*. B. G. Teubner, Stuttgart.
- Shewell, H. A. L. (1953) *The Use of the Cambridge Stereocomparator for Air Triangulation*. Photogrammetric Record, III (16).
- Slama, C. C. (ed.) (1980) *Manual of Photogrammetry*, 4th Edition. American Society for Photogrammetry and Remote Sensing.
- Smith, A. D. N. (1965) The explicit solution of the single picture resection problem, with a least squares adjustment to redundant control. *Photogrammetric Record*, V(26), pp. 113–122.
- Tewinkel, G. C. (1958) Panel - Future of Analytical Aerial Triangulation. *Photogrammetric Engineering*, March 1958.
- Thompson, E. H. (1959) A rational algebraic formulation of the problem of relative orientation. *Photogrammetric Record*, III(14), pp. 152–159.
- Thompson, E. H. (1966) Space resection: failure cases. *Photogrammetric Record*, V(27), pp. 201–204.
- van den Heuvel, F. A. (1997) *Exterior orientation using coplanar parallel lines*. Proceedings, 10th Scandinavian Conference on Image Analysis, Lappeenranta, pp. 71–78.
- Wester-Ebbinghaus, W. (1985) Bündeltriangulation mit gemeinsamer Ausgleichung photogrammetrischer und geodätischer Beobachtungen. *Zeitschrift für Vermessungswesen*, **110**(3), pp. 101–111.

- Wolf, P. R. (1974) *Elements of Photogrammetry*. McGraw-Hill.
- Wrobel, B. (1999) Minimum solutions for orientation. In Huang/Gruen (ed.) *Calibration and Orientation of Cameras in Computer Vision*, Washington D.C., Springer Verlag, Heidelberg.
- Zinndorf, S. (1985) Freies Netz – Anwendungen in der Nahbereichsphotogrammetrie. *Bildmessung und Luftbildwesen*, Heft 4/1985, pp. 109–114.

# 5 Digital image processing

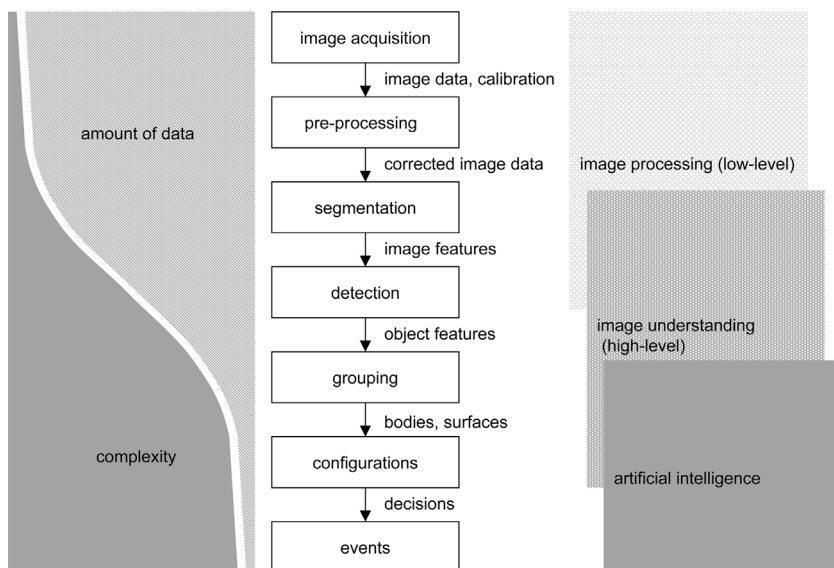
## 5.1 Fundamentals

### 5.1.1 Image processing procedure

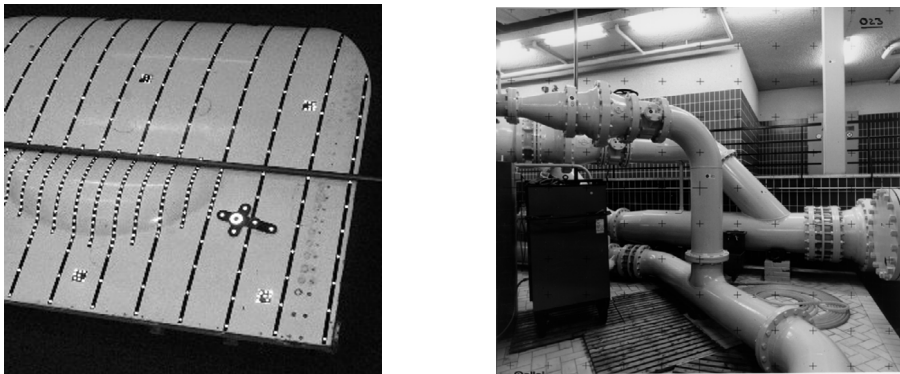
The availability of digital image processing techniques have significantly enhanced the possibilities for photogrammetric image measurement and analysis. As in other fields, digital images not only enable new methods for the acquisition, storage, archiving and output of images, but most importantly for the automated processing of the images themselves.

Fig. 5.1 illustrates a typical image processing work flow, starting with image acquisition and ending with some intelligent initiation of events. As the sequence proceeds from top to bottom, the volume of data is reduced while the complexity of processing increases.

Photogrammetric image processing methods are primarily developed and applied in the fields of image acquisition (sensor technology, calibration), pre-processing and segmentation



**Figure 5.1** Image processing sequence



**Figure 5.2** Signalised and non-signalised object scenes

(image measuring, line following, image matching). Major considerations for these methods are the automation of relatively simple repetitive measuring tasks and the achievement of appropriate measurement accuracy. Everyday methods which apply standard tasks such as digital point measurement (fiducial marks, reseau arrays, targets) or stereo-photogrammetry (automated orientation, surface reconstruction) are well developed. In contrast, methods appropriate to high-level image processing (object recognition) and image understanding are still under development.

In close-range photogrammetry, two characteristic features can be identified which clearly illustrate the possibilities and limitations of automatic image processing:

- The consistent use of object targeting composed of retro-reflective marks which are in part coded, combined with suitable illumination and exposure techniques, results in quasi-binary images that can be processed fully automatically (Fig. 5.2 left).
- Arbitrary image configurations result in large variations in image scale, occlusions and incomplete object imaging (Fig. 5.2 right). In contrast to simple stereo configurations such as those found in aerial photogrammetry, close-range applications are often characterised by complex object surfaces and convergent multi-image network configurations which require a large amount of interactive processing.

This chapter concentrates on those image processing methods which have been successfully used in practical digital close-range photogrammetry. The emphasis is on methods for geometric image processing and image measurement. Extensions to basic principles and specialised algorithms can be found in digital image processing literature (e.g. Gonzales and Wintz 1987, Gonzales and Woods 2003, Graham 2005, Jähne *et al.* 1999, Parker 1996, Seul 2000) and in computer vision (e.g. Hartley and Zisserman 2000, Klette *et al.* 1996, Haralick and Shapiro 1992, Snyder and Qi 2004).

### 5.1.2 Pixel coordinate system

The definition of the pixel coordinate system is fundamental to image processing methods used for image measurement<sup>1</sup>. For an image

$$S = s(x, y) \quad (5.1)$$

<sup>1</sup> Here the expression pixel coordinate system is used to define the coordinate system of a digital image. In contrast, the image coordinate system defines the reference system physically defined in the camera. The systems can be identical in digital cameras if the pixels themselves are physically square.

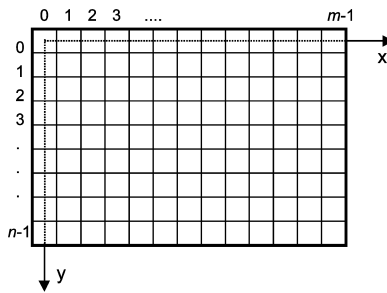


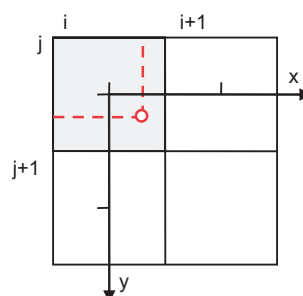
**Figure 5.3** Definition of the pixel coordinate system

where conventional processing usually adopts a left handed  $xy$  system of rows and columns related to the display of the image on the computer monitor;  $x$  denotes the row and  $y$  the column direction.

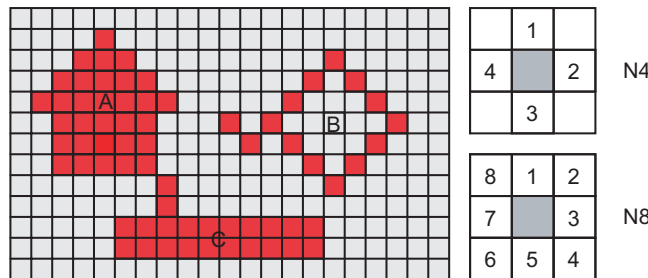
The origin of this system is located in the upper left hand corner and the first image element has the row and column numbers  $(0, 0)$ .  $m$  is the number of columns,  $n$  the number of rows. The last image element has the coordinates  $(m-1, n-1)$ . Width and height of a pixel are equal to 1 (Fig. 5.3).

In this discrete grid each pixel has whole integer coordinate values. When an object is imaged by a sensor characterized by such a grid, each pixel acquires a pixel value corresponding to the local image brightness across its area. In a grey scale image, pixel values are usually quantised with an 8 bit depth to provide 256 grey levels ranging from 0 (black) and 255 (white). Since human vision can only distinguish about 60 shades of grey, this pixel level depth is sufficient for a visual representation of images. However, machine systems can handle a much higher information content and quantisations of 10 bits (1024 grey levels), 12 bits or 16 bits can be used. True colour images are usually stored with 24 bits per pixel, 8 bits for each red, green and blue (RGB) colour channel.

Due to the pixel dimensions and optical transfer characteristics (MTF, PSF) of the image acquisition system (see section 3.2.4.2), an imaged object can cover more than one pixel. This leads to a possible subpixel position for the coordinates of the imaged object. Measurement to subpixel level is only possible if the position of an imaged object can be interpolated over several pixels. Here it is assumed that a small shift of an object edge leads to a corresponding subpixel change in the imaged pixel values. When subpixel coordinates are employed it is conventional to assign the integer  $xy$ -coordinate  $(i, j)$  to the centre of a pixel (Fig. 5.4).



**Figure 5.4** Position of a pixel in the  $xy$  coordinate system

**Figure 5.5** Objects and connectivity

Imaged objects must usually cover more than one pixel in order to be detected or processed. Adjacent pixels belonging to one object are characterised by pixel values that have uniform properties within a limited region (connectivity). Within a discrete image raster each pixel possesses a fixed number of neighbours, with the exception of the image border. In defining connectivity, neighbouring pixels are classified according to the N4 or the N8 scheme (Fig. 5.5). In the following example, three objects A, B and C are imaged. If N4 connectivity is assumed then object B decomposes into individual pixels and objects A and C are separated. In contrast, N8 connectivity leads to a single integral object B. However, A and C merge together due to their corner connection. Extended algorithms for connectivity must therefore consider the distribution of pixel values within certain regions by using, for example, appropriate filters (see section 5.2.2).

### 5.1.3 Handling image data

#### 5.1.3.1 Image pyramids

Image or resolution pyramids describe sequences where successive images are reductions of the previous image, usually by a factor of 2 (Fig. 5.6). Prior to image reduction the image can be smoothed, for example using Gaussian filters (see section 5.2.2). As resolution is reduced smaller image structures disappear i.e. the information content decreases (Fig. 5.7). The total amount of data required to store the pyramid is approximately only 30% more than in the original image. Image pyramids are typically used in hierarchical pattern recognition problems which start with a search of coarse features in the lowest resolution image (pyramid top). The search is refined with increasing resolution, working progressively down through the pyramid layers, each time making use of the results of the previous resolution stage.

#### 5.1.3.2 Data formats

There are many ways to organise digital image data. Numerous data formats have been developed for digital image processing and raster graphics that, in addition to the actual image data, allow the storage of additional information such as image descriptions, colour tables and overview images etc. For photogrammetric purposes the unique reproducibility of the original image is of major importance. Loss of information can occur not only in certain data compression methods but also by using an insufficient depth of pixel values (bits per pixel).

From the large number of different image formats the following are in common use:

- Direct storage of raw data

Here the original pixel values of the image are stored in a binary file without compression. Using one byte per pixel the resulting file size in bytes is exactly equal to the total number

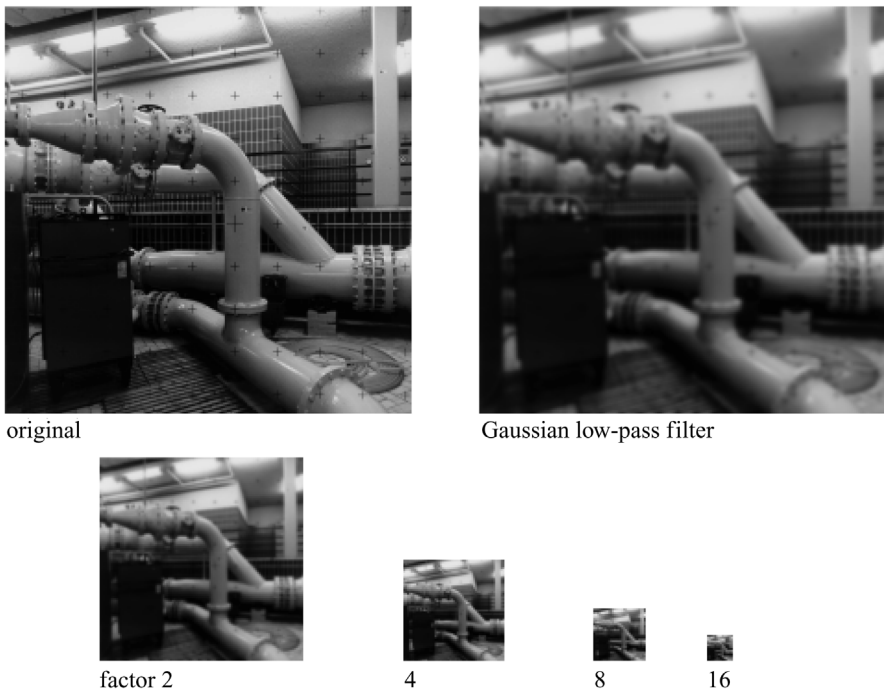


**Figure 5.6** Image pyramids with 5 steps

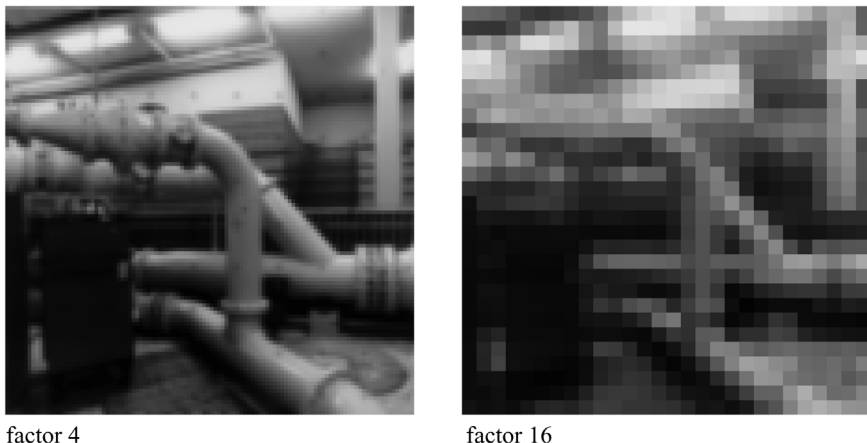


**Figure 5.7** Information content at reduction factors 4 and 16

of pixels in the image. The original image format in rows and columns must be separately recorded since the raw image data cannot otherwise be read correctly. Multi-channel images can be usually stored in the order of their spectral bands, either pixel by pixel (pixel interleaved), line by line (line interleaved) or channel by channel (band interleaved).

- TIFF: Tagged Image File Format

The TIFF format is widely used due to its universal applicability. It is based on a directory of pointers to critical image information such as image size, colour depth, palettes, resolution

etc. which must be interpreted by the import program. Numerous variants of TIFF exist and this can sometimes lead to problems with image transfer. The format permits different methods of image compression (LZW, Huffman, JPEG) (Welch 1984).

- **BMP:** Windows Bitmaps

The BMP format is the standard format for images within the Microsoft Windows environment. It enables the storage of arbitrary halftone and colour images (up to 24 bit) with varying numbers of grey levels or colours.

- **GIF:** Graphic Interchange Format

Images stored in GIF format are compressed without loss of information. Grey level and colour images are limited to 8 bits per pixel.

- **PNG:** Portable Network Graphics

A development of GIF which provides a higher compression level.

- **JPEG:** Joint Photographic Expert Group

JPEG is a format which allows compression levels up to a factor of 100 and in which a certain loss of information is accepted (see below). The baseline JPEG format utilises discrete cosine representation and a table of coefficients to store a tiled version of the image, while an updated version (JPEG2000) utilises wavelet compression (see section 5.1.3.3)

Additional data formats such as PCX (Paintbrush), PCD (Kodak Photo CD), EPS (PostScript) or RAS (Sun Raster Graphic) can also be used. However, they tend not to be very popular in digital photogrammetry.

Table 5.1 provides a comparison between different image storage formats applied to two images with different structures. The column headed ‘pipes’ provides data on the pipe

**Table 5.1:** File size in bytes for different image data formats  
(see also Fig. 5.8 and Fig. 5.9)

data format	zero-loss	image1 ‘pipes’	compression level	image2 ‘testfield’	compression level
image size [pixel]		440 × 440		1000 × 1000	
raw data	×	193600	100%	1000000	100%
BMP	×	194678	101%	874698	87%
PCX	×	191025	98%	668874	67%
TIFF	×	194762	101%	1001722	100%
TIFF LZW-compression	×	141088	73%	305022	31%
GIF	×	174266	90%	284770	28%
PNG	×	111492	58%	268528	27%
JPG comp.factor 1	×	111002	57%	266667	27%
JPG comp.factor 10		49463	25%	54507	5%
JPG comp.factor 20		34164	18%	32066	3%
JPG comp.factor 99		1899	1%	5102	0.5%
Wavelet, factor 1	×	109604	57%	281432	28%
Wavelet, factor 10		19360	10%	100000	10%
Wavelet, factor 100		1936	1%	10000	1%
EPS	×	388065	200%	2001436	200%

measurement image shown in Fig. 5.6. The second image ‘testfield’ is taken from a set of images which have been acquired for camera calibration purposes (see Fig. 7.8). The resulting file sizes show that the ‘pipes’ image with its inhomogeneous structures can be compressed up to only 80% of the original size without loss of information. In contrast, the more homogeneous ‘testfield’ image can be reduced to less than 30% of its original size. However, compression methods with information loss, such as JPEG or wavelet compression, permit much higher levels of data reduction. Note that the EPS format doubles the file size because it transforms pixel values into ASCII characters.

### 5.1.3.3 Image compression

Image compression is of major practical importance to digital photogrammetry due to the large amounts of data which are handled. For example, a monochromatic set of 50 images each of  $3000 \times 2000$  pixels represents some 300 MB of raw data. The same number of digitised aerial images (pixel size 15  $\mu\text{m}$ ) requires more than 11 GB of disk space.

Run-length encoded compression methods count the number of identical pixel values within a line or a region and code the corresponding image area by its pixel value and a repetition factor. This method is useful for images with extensive homogeneous regions, but for images of natural scenes this often leads to an increased amount of data.

Frequency-based compression methods apply a spectral analysis to the image (Fourier, cosine or wavelet transformations, see section 5.2.2.1) and store the coefficients of the related functions. Eliminating coefficients of low significance results in data compression with loss of information, often called lossy compression. Particular attention is drawn to wavelet compression which permits higher compression levels than the original JPEG method (see below)

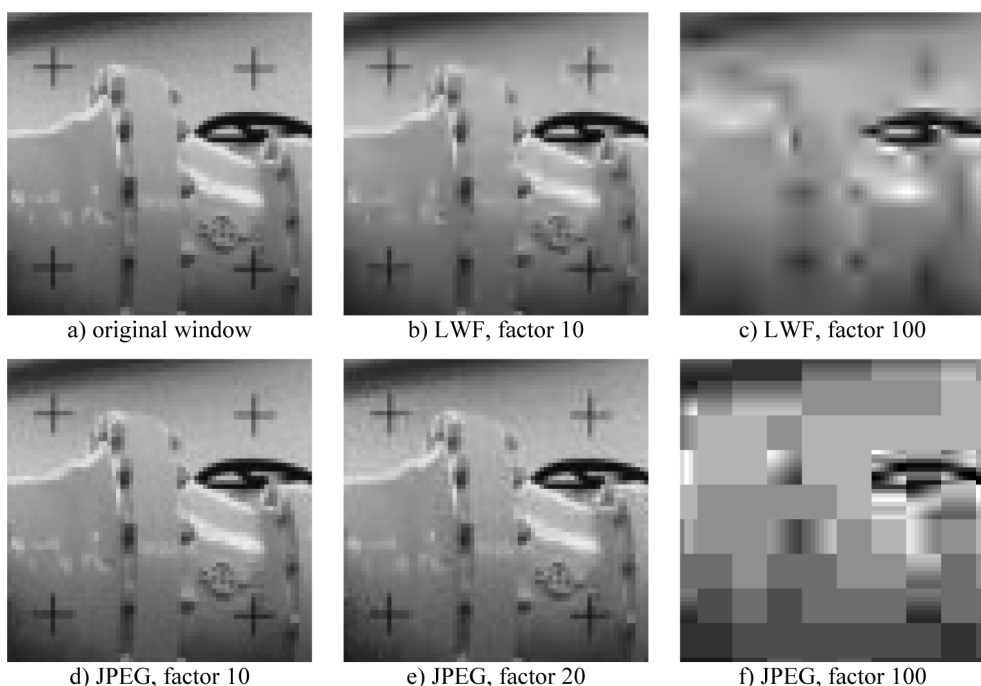


**Figure 5.8** Effect on visual quality of compression losses in image ‘pipes’ (see Table 5.1)

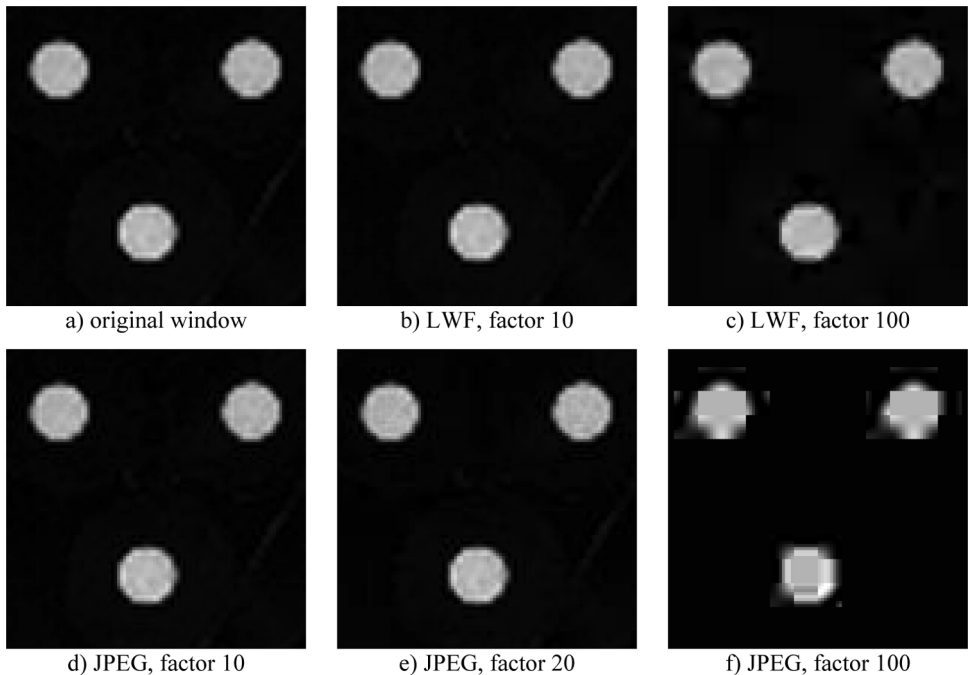


**Figure 5.9** Effect on visual quality of compression losses in image ‘testfield’ (see Table 5.1)

while maintaining equal visual image appearance (see Fig. 5.8 and Fig. 5.9). For natural image scenes an increasing smoothing effect can be observed at high compression levels (Fig. 5.8c).

The base line JPEG image format is also based on a compression method with loss of information. The goal is to preserve the essential image content without a significant lack of visual quality, even at high compression levels. Due to the high compression performance, JPEG is widely used in many graphical and technical fields and the procedure is standardised to ensure consistent and appropriate image quality for the given application (Pennebaker and Mitchell 1992).

The compression algorithm is based on the 3-stage Baseline Sequential method (Fig. 5.10). A discrete cosine transformation (DCT) is calculated in disjunctive  $8 \times 8$  pixel patches. The resulting coefficients are weighted using a selectable quantisation table and finally run-length coded. Data decompression is performed in the reverse order. For colour images an additional IHS (intensity, hue, saturation) colour transformation is performed.

The actual loss of information is controlled by the choice of intervals in the quantisation table. Usually the table is designed such that no significant loss of image quality can be visually observed (Fig. 5.8 and Fig. 5.9).

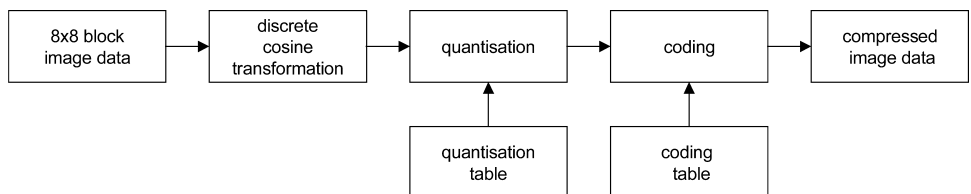


**Figure 5.10** JPEG image compression

The effect of JPEG compression on photogrammetric measurement mainly depends on the image content. In general, JPEG compression can give rise to localised image displacements of the order of 0.1 to 1 pixel. This significantly exceeds the accuracy potential of automatic point measurement which lies around 0.02–0.05 pixel (see section 5.4.2.6). In addition the use of  $8 \times 8$  pixel tiles within the JPEG process can cause undesirable edge effects (Pennebaker and Mitchell 1992, Düppe and Weisensee 1996, Weisensee 1997, Santa-Cruz and Ebrahimi 2000).

## 5.2 Image preprocessing

### 5.2.1 Point operations

#### 5.2.1.1 Histogram

The histogram provides the frequency distribution of the pixel values in the image. It displays the absolute or relative frequency of each pixel value either in tabular or graphical form (Fig. 5.11).

The most important parameters of a histogram are:

$$p_S(g) = \frac{a_S(g)}{M} \quad : \text{relative frequency } p_S(g) \text{ and} \\ \text{absolute frequency } a_S(g) \text{ where} \\ M = mn \text{ and } 0 \leq p_S(g) \leq 1 \quad (5.2)$$

$$g_{\min}, g_{\max} \quad : \text{minimum and maximum pixel} \\ \text{value of the image}$$

$$C = \frac{g_{\max} - g_{\min}}{g_{\max} + g_{\min}} \quad : \text{contrast} \quad (5.3)$$

$$m_S = \frac{1}{M} \sum_{u=0}^{m-1} \sum_{v=0}^{n-1} s(u, v) \quad : \text{mean of pixel values} \\ = \sum_{g=0}^{255} g p_S(g) \quad (5.4)$$

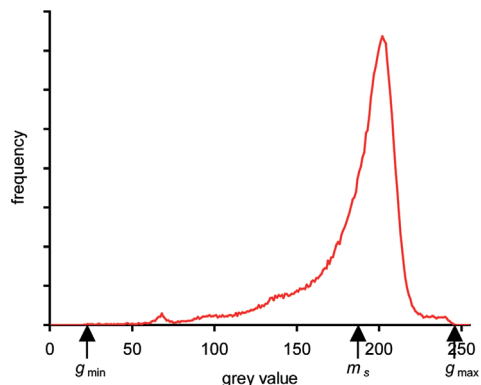


**Figure 5.11** Grey scale image with corresponding histogram and parameters

328

$$\begin{aligned} q_S &= \frac{1}{M} \sum_{u=0}^{m-1} \sum_{v=0}^{n-1} [s(u, v) - m_S]^2 \\ &= \sum_{g=0}^{255} (g - m_S)^2 p_S(g) \end{aligned} \quad : \text{variance of pixel values} \quad (5.5)$$

$$H = \sum_{g=0}^{255} [p_S(g) \log_2 p_S(g)] \quad : \text{entropy} \quad (5.6)$$

$$\alpha = \frac{-\sum_{g=0}^k [p_S(g) \log_2 p_S(g)]}{H} \quad : \text{symmetry (anisotropic coefficient)} \quad (5.7)$$

*k*: minimum pixel value where:

$$\sum_{g=0}^k p_S(g) \geq 0.5$$

While minimum and maximum pixel values define the image contrast, the mean is a measure of the average intensity (brightness) of the image. For statistical image processing, variance or standard deviation is also calculated, but both are of minor interest in metrology applications.

The information content in an image can be measured by its entropy. This corresponds to the average number of bits necessary to quantise the pixel values. Entropy can also be used to calculate an appropriate factor for image compression (see section 5.1.3.3).

The degree of symmetry of a histogram is determined by the anisotropic coefficient. Symmetrical histograms have a coefficient  $\alpha = 0.5$ . This coefficient can also be used to determine a threshold for bimodal histograms (see section 5.2.1.4).

### 5.2.1.2 Lookup tables

Lookup tables (LUT, colour tables, palettes) are simple tools for the global manipulation of pixel values. Each pixel value of an input image is assigned a unique pixel value in an output image. This method of processing pixel values is simple to implement and can be found in almost all graphics or image processing programs. LUTs are easily displayed in diagrammatic form (Fig. 5.12). LUT operations are unique but usually non-reversible.

Given the lookup table

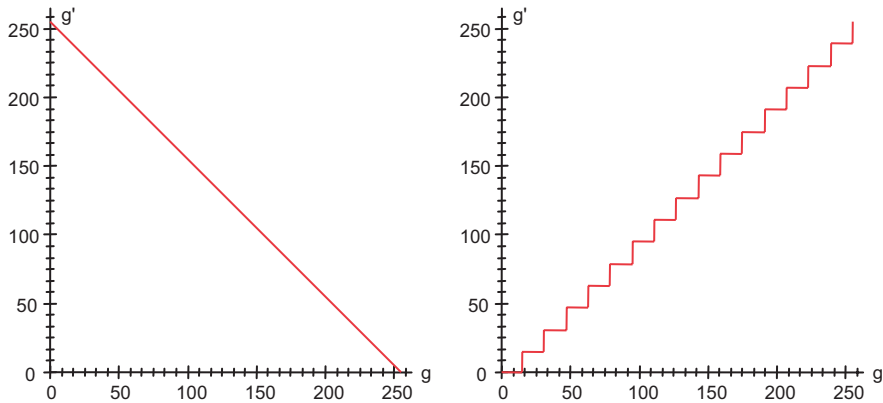
$$LUT(g) \quad g = 0, 1, 2, \dots, 255 \quad (5.8)$$

the pixel values of the output image are calculated:

$$g' = LUT(g) \quad (5.9)$$

### 5.2.1.3 Contrast enhancement

Manipulating the brightness and contrast of an original image results in a change of the pixel value distribution within certain regions, for example along an image edge. Variations of pixel value are not only a function of object intensity but are also influenced by the relative position of camera and object. In general a non-linear manipulation of pixel values can affect the geometry

**Figure 5.12** Examples of lookup tables

of an object's image and should therefore be avoided if possible. However, contrast enhancement can provide a better visual interpretation for interactive image processing<sup>1</sup>.

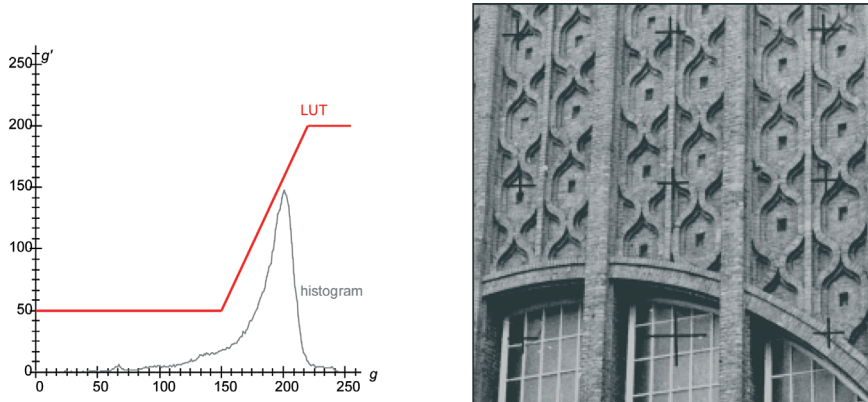
Image contrast changes are easily applied by a lookup table. Table values can be defined interactively, pre-calculated or derived from the image content itself. Common methods for adjusting brightness and contrast are:

- Linear contrast stretching:

The LUT is a linear interpolation between  $g_{\min}$  and  $g_{\max}$  (Fig. 5.13). Minimum and maximum pixel values can be derived from the histogram, or defined interactively.

- Histogram equalization:

The cumulative frequency function is calculated from the histogram of the original image:

**Figure 5.13** Linear contrast enhancement (original image in Fig. 5.11)

<sup>1</sup> Various digital image measuring methods are independent of contrast and calculate radiometric correction parameters (see section 5.4.2.4).

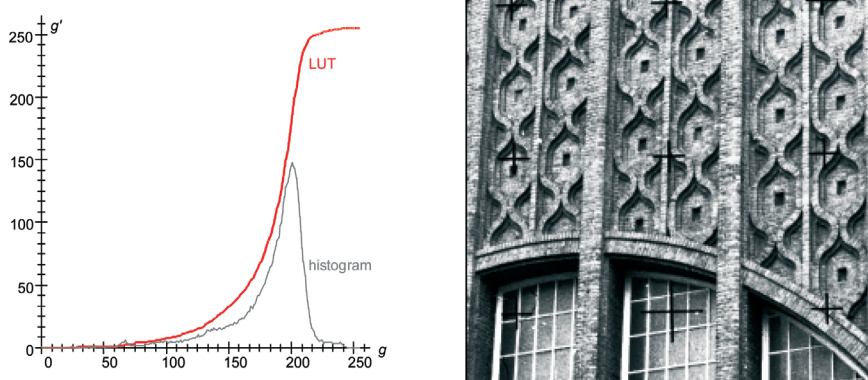


**Figure 5.14** Contrast stretching by histogram equalisation (original image in Fig. 5.11)

$$h_S(g) = \sum_{k=0}^g p_S(k) \quad g = 0, 1, 2, \dots, 255 \quad (5.10)$$

with  $0 \leq h_S(g) \leq 1$

The LUT values are given by:

$$\text{LUT}(g) = 255h_s(g)$$

The function is dependent on the histogram since the slope of the LUT is proportional to the frequency of the corresponding pixel value (Fig. 5.14). Image contrast is consequently strongly enhanced in areas where pixel values have high frequencies. The output image  $S'$  therefore has a histogram  $p_{S'}(g')$  with relative cumulative frequencies which are constant for each pixel value according to the definition  $h_{s'}(g') = 1/255g'$ .

- Gamma correction:

Many interactive image processing programs permit a Gamma correction where, in analogy with the gamma characteristic in the photographic process (see section 3.3.1.1), the slope of the LUT is adjusted logarithmically.

#### 5.2.1.4 Thresholding

In general, thresholding is used to clearly differentiate pixel values which belong to different object classes e.g. to separate objects and background. Thresholding is often a pre-processing stage prior to segmentation.

Consider a simple case where the image consists only of two classes i.e.

- class  $K_1$ : background (e.g. dark)
- class  $K_2$ : objects (e.g. bright)

The corresponding histogram can be expected to be bimodal having two significant groupings of data each represented by a maxima (hill) which are separated by a minimum (valley). Clearly both classes can be separated by a single threshold  $t$  (bimodal thresholding) located within the minimum region between the class maxima e.g. by defining

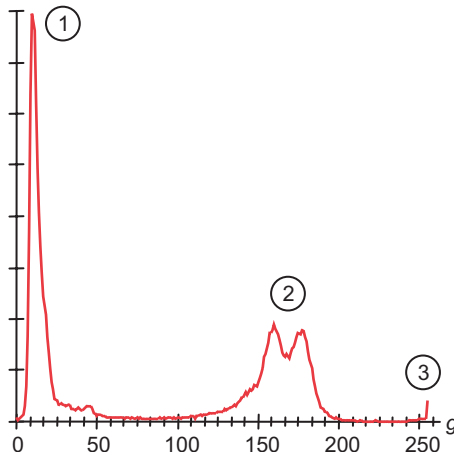


**Figure 5.15** Histogram of Fig. 5.16 with two primary maxima (1, 2) and one secondary maximum (3)

$$T = \frac{m_2 - m_1}{2} \quad (5.11)$$

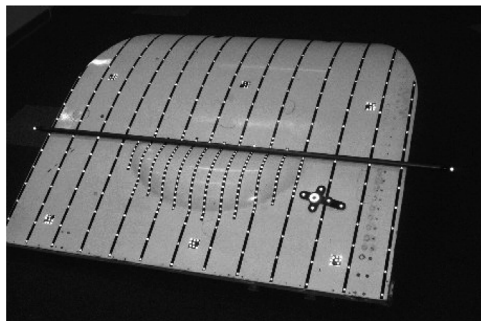
where  $m_1, m_2$  are the mean pixel values of classes  $K_1, K_2$

Applying the lookup table

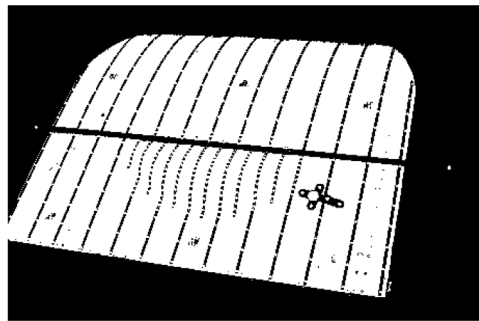
$$LUT(g) = \begin{cases} g_1 & \text{for } g \leq T \\ g_2 & \text{for } g > T \end{cases} \quad (5.12)$$

where  $g_1, g_2$  are the new pixel values for classes  $K_1, K_2$ , results in a binary (two-level) image consisting only of pixel values  $g_1$  (e.g. 0) and  $g_2$  (e.g. 1 or 255). Fig. 5.15 shows the histogram of the image in Fig. 5.16 with two significant primary maxima ( $m_1 \approx 18$ ,  $m_2 \approx 163$ ), representing background and object. The secondary maximum ( $m_3 \approx 254$ ) is caused by the imaged retro-reflective targets. The binary image of Fig. 5.17 is the result of thresholding with  $T = 90$  (between the primary maxima).

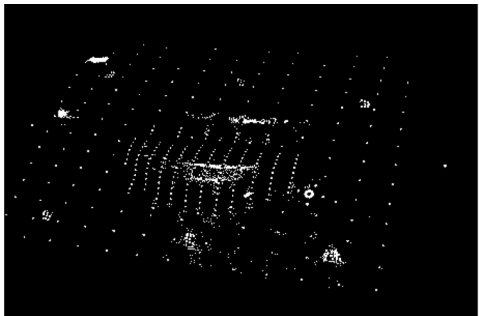
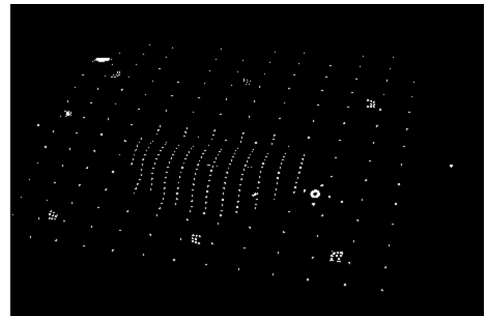
Fig. 5.18 shows the result with threshold value  $T = 192$ , located near maximum 2. This preserves some image information in addition to the targets. With  $T = 230$  (Fig. 5.19) almost all targets are separated or segmented out from the background (but see also Fig. 5.27).



**Figure 5.16** Metric image with retro-reflective targets



**Figure 5.17** Result after thresholding with  $T = 90$

Figure 5.18 Result after thresholding with  $T = 192$ Figure 5.19 Result after thresholding with  $T = 230$ 

For more complex images the problem of thresholding lies in both the calculation of representative class averages and with the subsequent definition of the threshold value itself. Natural image scenes usually have more than two pixel value classes and this requires a much more complex thresholding procedure (multi-modal or dynamic thresholding).

Overviews of suitable thresholding methods are given by El-Hakim 1996 and Haberäcker 1991.

### 5.2.1.5 Image combinations

Two or more images or image subsets can be combined numerically:

- arithmetic: addition, subtraction, division, multiplication

The pixel values of the images are combined arithmetically e.g. subtracted:

$$s'(x, y) = s_2(x, y) - s_1(x, y) \quad (5.13)$$

The result of this image operation (difference image) shows the differences between the input images. If necessary, the pixel values of the output image, where negative values are possible, must be transformed into the positive range [0...255], or alternatively stored as 16 bit signed integers.

- logical:  $=, <, >, \leq, \geq, \neq$

The pixel values of both images are compared logically, resulting in Boolean values 1 (true) or 0 (false).

- bitwise: AND, OR, NOT, XOR

The pixel values of both input images are combined bit by bit. The XOR operation is used in practice for the temporary superimposition of a moving cursor on the image. The original pixel value can be recovered without the use of temporary storage by executing two sequential XOR operations with the value 255.

decimal value	binary value	action
38	0010 0110	original pixel value
255	1111 1111	XOR
217	1101 1001	pixel value of cursor
255	1111 1111	XOR
38	0010 0110	original pixel value

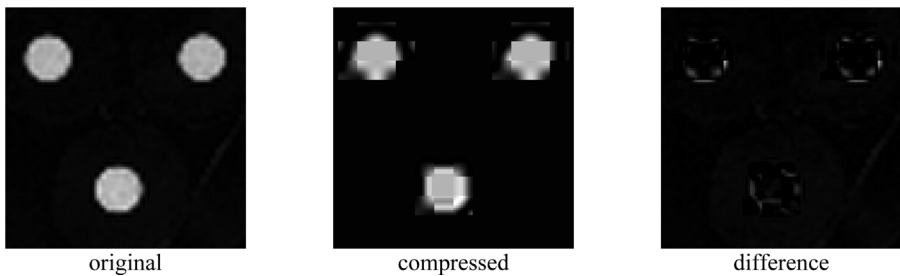


**Figure 5.20** Example of a difference image to illustrate information loss after JPEG image compression

## 5.2.2 Filter operations

### 5.2.2.1 Spatial domain and frequency domain

The theory of digital filtering is based on the fundamentals of digital signal processing (communication engineering, electronics). Its fundamental method is the Fourier transform which represents arbitrary signals (series of discrete values, waves) as linear combinations of trigonometric functions. The discrete one-dimensional Fourier transformation for  $n$  samples of an input signal  $s(x)$  is given by:

$$\begin{aligned} F(u) &= \frac{1}{n} \sum_{x=0}^{n-1} s(x) \exp\left(-i \frac{2\pi}{n} ux\right) \\ &= \operatorname{Re}(F(u)) + i \operatorname{Im}(F(u)) \end{aligned} \quad (5.14)$$

Here  $u$  denotes the spatial frequency and  $i = \sqrt{-1}$ . The inverse Fourier transformation is given by:

$$s(x) = \frac{1}{n} \sum_{u=0}^{n-1} F(u) \exp\left(+i \frac{2\pi}{n} ux\right) \quad (5.15)$$

i.e. the original signal can be exactly reconstructed from its Fourier transform.

The Euler formulae show the connection with the underlying trigonometric functions:

$$\begin{aligned} \exp(-i2\pi ux) &= \cos(2\pi ux) - i \sin(2\pi ux) \\ \exp(i2\pi ux) &= \cos(2\pi ux) + i \sin(2\pi ux) \end{aligned} \quad (5.16)$$

The power spectrum of  $s(x)$  is defined by

$$P(u) = |F(u)|^2 = \operatorname{Re}^2(u) + \operatorname{Im}^2(u) \quad (5.17)$$

The 1D Fourier transformation can easily be extended to the discrete 2D Fourier transformation.

When applied to an image, the discrete Fourier transformation transforms it from the spatial domain  $S = s(x, y)$  into the frequency domain  $F(u, v)$ . A visual evaluation of the spatial frequencies (wave numbers) in the image can be made through the power spectrum. For example, edges generate high frequencies. A power spectrum example is illustrated in Fig. 5.21, where bright points in the spectrum correspond to large amplitudes. This example shows high amplitudes which are perpendicular to the significant edges in the original image (spatial domain). The two horizontal and vertical lines in the spectrum are caused by the image borders.

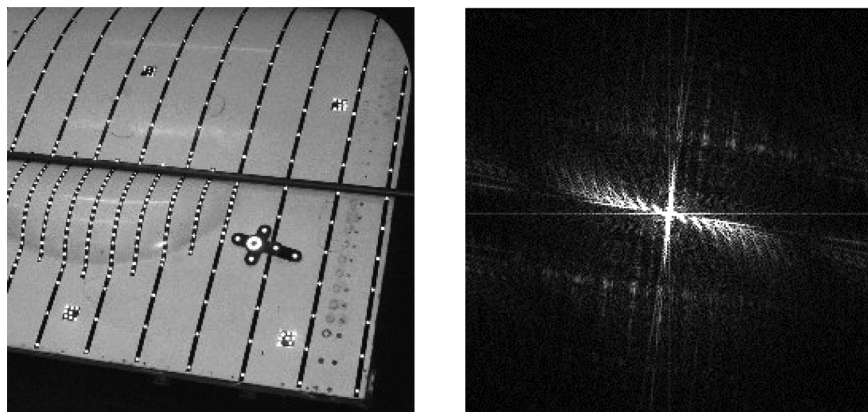


**Figure 5.21** Grey scale image and corresponding power spectrum

Different basic functions result in alternative image transformations that can be performed different from the Fourier transform. For example the discrete cosine transformation (DCT) uses only cosine terms. The wavelet transformation uses various basic functions such as the Haar function to transform the original signal not only into the frequency domain but also into a scale domain of different resolutions. Wavelets are especially useful for image operations which must simultaneously account for coarse (smoothed) structures and detailed features having high information content (see Graps 1995 for an overview). One application of the wavelet transformation is in image compression with information loss (see section 5.1.3.3).

Filters can be used to select or suppress certain spatial frequencies in the original image (high-pass filter, band-pass filter, low-pass filter). In the frequency domain, the desired frequencies are multiplied by a filter function which defines the filter characteristics. Fig. 5.22 shows a circular filter in the frequency spectrum. In this example the spectrum within the inner circle and beyond the outer circle is multiplied by 0 and within the ring zone it is multiplied by 1. After transformation back into the spatial domain this band-pass filter produces edge enhancement.

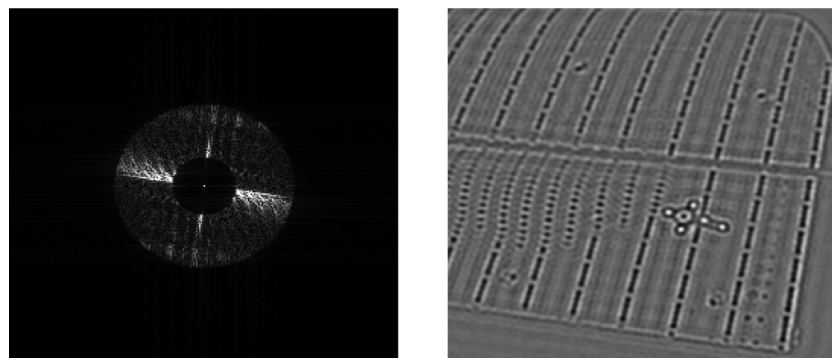


**Figure 5.22** Band-pass filter in power spectrum and resulting image

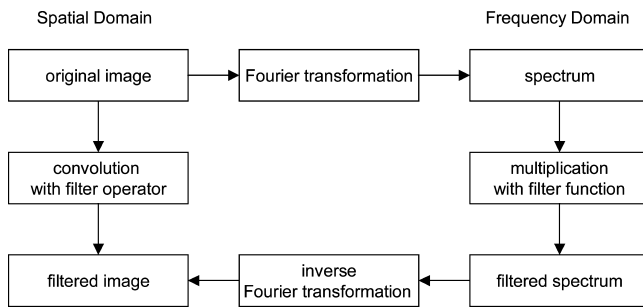


**Figure 5.23** Filtering in the spatial and frequency domains

In the spatial domain, filters are applied by convolution with a filter operator, equation (5.18). It can be shown that both approaches have identical results.

Filter methods based on a one or two-dimensional convolution calculate a weighted sum of pixel values in a given pixel region of the input image  $S$ . The result is assigned to the output image  $S'$  at the position of the region's central pixel.

$$s'(x, y) = \frac{1}{f} \sum_{u=-k}^{+k} \sum_{v=-l}^{+l} s(x-u, y-v) h(u, v) \quad (5.18)$$

$$S' = S \otimes H$$

Here  $H = h(u, v)$  denotes the filter matrix (filter operator) with  $p \times q$  elements, where  $k = (p-1)/2$  and  $l = (q-1)/2$ . Usually  $p$  and  $q$  are odd numbers and often  $p = q$ . The factor  $f$  is used for normalisation to the range [0...255]. The operator  $\otimes$  symbolises the convolution operation.

In order to filter the complete image, the filter operator is shifted over the image in rows and columns as shown in Fig. 5.24. At each  $x, y$  position the convolution is calculated and the resulting pixel value stored in the output image. The number of computational instructions amounts to  $(2k + 1)^2$  multiplications and  $(2k + 1) - 1$  additions. For example an image with  $1024 \times 1024$  pixels,  $p = 5$ ,  $k = 2$  requires around  $26 \times 10^6$  multiplications and  $25 \times 10^6$  additions. Some filter masks can be split into one-dimensional convolutions which can be separately computed in the x and y directions. In this case only  $(4k + 2)$  multiplications and  $4k$  additions are required. In the example this results in around  $10 \times 10^6$  multiplications and  $8 \times 10^6$  additions.

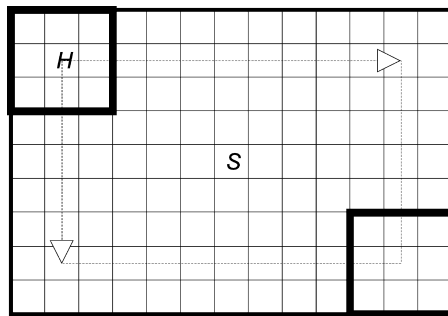


**Figure 5.24** Scheme for image filtering with  $p = q = 3$

### 5.2.2.2 Smoothing filters

Smoothing filters (low-pass filters) are mainly used for the suppression of pixel level noise, such as the quantisation noise associated with digitisation. This type of filter principally divides into linear smoothing filters based on convolution and non-linear smoothing filters based on rank orders (median filter). Table 5.2 shows one- and two-dimensional examples of typical filter operators.

**Table 5.2:** Filter operators for image smoothing (selection)

filter method	1D	2D
smoothing filter (moving average)	$H_{3,1} = \frac{1}{3}[1 \ 1 \ 1] = [1/3 \ 1/3 \ 1/3]$	$H_{3,3} = \frac{1}{9}\begin{bmatrix} 1 & 1 & 1 \\ 1 & 1 & 1 \\ 1 & 1 & 1 \end{bmatrix} = \begin{bmatrix} 1/9 & 1/9 & 1/9 \\ 1/9 & 1/9 & 1/9 \\ 1/9 & 1/9 & 1/9 \end{bmatrix}$
smoothing filter (binomial filter)	$H_{3,1} = \frac{1}{4}[1 \ 2 \ 1] = [1/4 \ 1/2 \ 1/4]$	$H_{3,3} = \frac{1}{4}(1 \ 2 \ 1)\frac{1}{4}\begin{pmatrix} 1 \\ 2 \\ 1 \end{pmatrix} = \frac{1}{16}\begin{pmatrix} 1 & 2 & 1 \\ 2 & 4 & 2 \\ 1 & 2 & 1 \end{pmatrix}$
	$H_{5,1} = \frac{1}{16}[1 \ 4 \ 6 \ 4 \ 1]$	$H_{5,5} = \frac{1}{256}\begin{pmatrix} 1 & 4 & 6 & 4 & 1 \\ 4 & 16 & 24 & 16 & 4 \\ 6 & 24 & 36 & 24 & 6 \\ 4 & 16 & 24 & 16 & 4 \\ 1 & 4 & 6 & 4 & 1 \end{pmatrix}$

Linear low-pass filters smooth the image but, depending on choice of filter coefficients, also smear image edges. The smoothing effect increases with larger filter sizes.

Gaussian filters possess optimal mathematical smoothing properties. The coefficients of the filter are derived from the two-dimensional Gaussian function:

$$f(x, y) = \frac{1}{2\pi\sigma^2} \exp\left(-\frac{x^2 + y^2}{2\sigma^2}\right) \quad (5.19)$$

A suitable filter matrix of size  $p$  is usually chosen empirically. As an example, given  $\sigma = 1$  a filter size of  $p = 7$  is appropriate. The Gaussian filter coefficients can be well approximated by the binomial coefficients of Pascal's triangle (see Table 5.2).

The non-linear median filter performs good smoothing while retaining sharp edges. The median filter is not based on convolution. Instead the median value (as opposed to the mean) of a sorted list of pixel values in the filter matrix is computed and used as the output pixel value. The output image therefore consists only of pixel values which exist in the input image. This property is essential for the filtering of images which consist of attributes or special palettes instead of intensities. The median filter is a member of the group of rank-order filters.

### 5.2.2.3 Morphological operations

Morphological operations form their own class of image processing methods. The basic idea is the application of non-linear filters (see median filter, section 5.2.2.2) for the enhancement or suppression of black and white image regions with (known) shape properties e.g. for the segmentation of point or circular features. Filtering is performed with special structuring

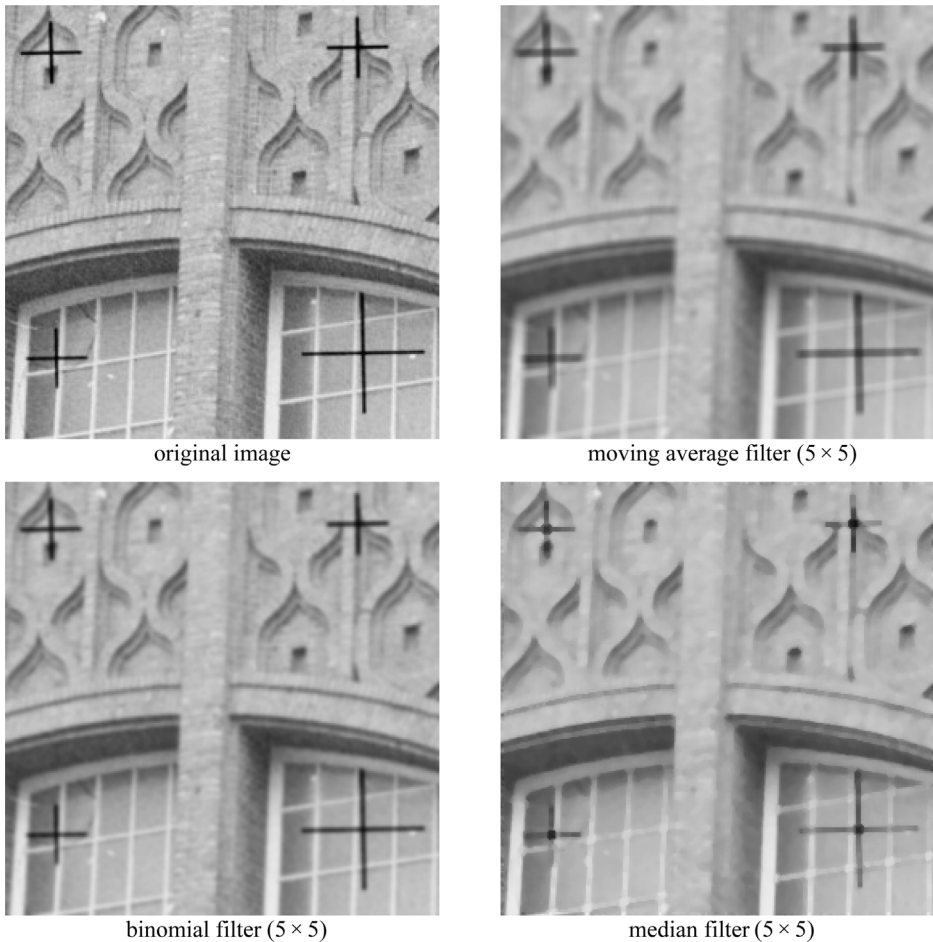


**Figure 5.25** Effect of different smoothing filters

elements which are tuned to the feature type to be detected and are successively stepped across the whole image (see Parker 1996 and Soille 1998 for an overview). It is necessary to ensure that the focus or active point for the structuring element is carefully defined in order to avoid offsets in the identified locations of the features being detected.

Two fundamental functions based on Boolean operations for binary images are defined for morphological image processing:

- Erosion, which leads to the shrinking of regions. The value 1 is set in the output image if all pixels in the filter region (e.g.  $3 \times 3$  elements) correspond to the structure element, i.e. the structure element is in complete agreement with the image region. Otherwise the value 0 is set.
- Dilation, which yields to the extension of connected regions. The number 1 is set if the structure element includes at least one matching pixel within the image filter region.

Sequential application of dilation and erosion can be used to close gaps or to separate connected regions in the image. The following combinations of basic operations are useful:

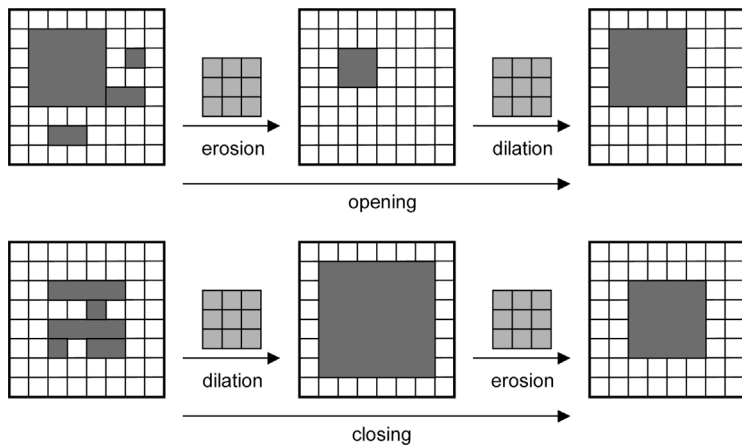


**Figure 5.26** Morphological operations with  $3 \times 3$  structure element  
(after Bässmann and Kreyss 1998)

- Opening, achieved by an erosion followed by dilation (Fig. 5.26, upper). Small objects are removed.
- Closing, the reverse of opening. Dilation is followed by erosion in order to close gaps between objects (Fig. 5.26, lower).

An application of opening is the segmentation of bright signalised targets in a photogrammetric image. Fig. 5.27 shows the problematic situation for an image region with a number of targets lying close together. After simple thresholding the intermediate result shows several small circular features which do not correspond to target points, as well as connected regions which actually represent separate targets. Segmentation, based on the procedure of section 5.2.1.4 with a minimum point size of 15 pixel, results in nine objects of which two have joined together features from adjacent objects.

Fig. 5.28 shows the same image region processed using opening. Starting with the same binary image, erosion eliminates objects smaller than the applied  $3 \times 3$  structure element. In addition the targets shrink. Subsequent application of dilation enlarges the remaining objects to their original size. This type of segmentation correctly extracts all 11 objects.

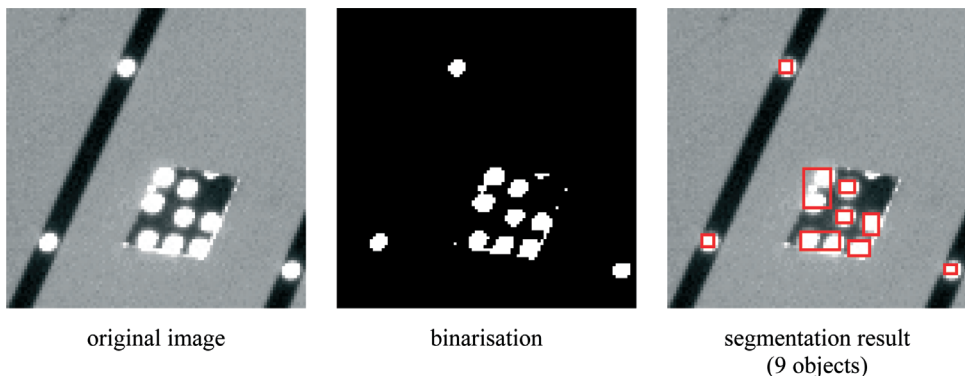


**Figure 5.27** Simple segmentation after binarisation

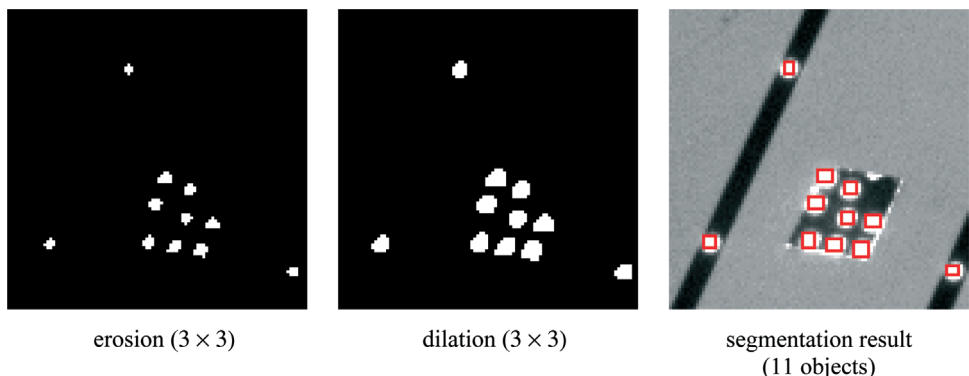


**Figure 5.28** Segmentation after binarisation and opening

Morphological operators must be extended for grey scale images. Instead of the Boolean decision for each pixel of the structure element, the minimum grey value difference (grey value erosion) or the maximum grey value sum (grey value dilation) between structure element and original image is used as the result.

### 5.2.3 Edge extraction

Edges are the primary image structures used by the human visual system for object recognition. They are therefore of fundamental interest for digital image measurement and pattern recognition. Every object stands out from the background on the basis of a characteristic change in the relevant image structures (Fig. 5.29).

This change in image structure can be due to:

- significant change in pixel values (grey scale image) along the physical object edge  
→ edge extraction
- change in pixel colour values (colour edge)  
→ multi-spectral edge extraction
- change in surface texture (e.g. hatched vs. point pattern)  
→ texture analysis

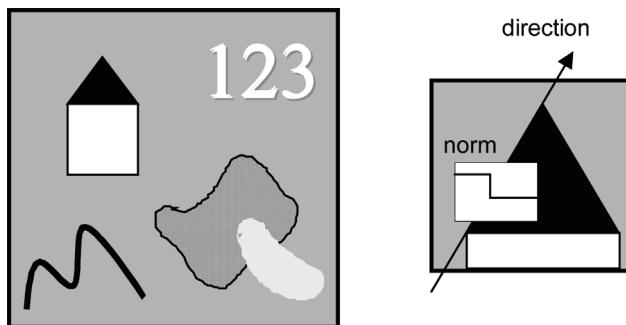


**Figure 5.29** Objects and edges

The following discussion concerns only the extraction of edges in grey scale images which can be characterised by the following properties:

- a significant change in adjacent pixel values perpendicular to the edge direction
- edges have a direction and magnitude
- edges are formed by small image structures i.e. the region of pixel value change may not be too large
- small image structures are equivalent to high frequencies (wave numbers) in the frequency domain

If edges are to be extracted by means of filters then, in contrast to smoothing filters, high frequencies must be enhanced and low frequencies suppressed (= high-pass filter or band-pass filter).

An edge, or more precisely ramp, is a significant change of intensity between two pixel value areas of a particular size. In contrast, a line is a thin pixel value image area which cannot be resolved into two opposite edges. Extensive summaries of edge detection methods are given, for example, by Parker 1996, Seul 2000, Bässmann and Kreyss (1997), Gonzales and Woods (2003) and other standard textbooks on digital image processing.

### 5.2.3.1 First order differential filters

The first derivative of a continuous function  $s(x)$  is given by

$$s'(x) = \frac{ds}{dx} = \lim_{\Delta x \rightarrow 0} \frac{s(x + \Delta x) - s(x)}{\Delta x} \quad (5.20)$$

and for a discrete function by:

$$s'(x) = \frac{s(x+1) - s(x)}{1} = s(x+1) - s(x) \quad (5.21)$$

A filter mask known as a Roberts gradient,  $H_2 = [-1 \ 1]$  can be derived from equation (5.21). Larger filter masks which also offer low-pass filtering are often used, for example:

$$H_3 = [-1 \ 0 \ 1]$$

$$H_5 = [-1 \ 0 \ 0 \ 0 \ 1] \text{ or } [-2 \ -1 \ 0 \ 1 \ 2]$$

These filters approximate the discrete first derivative of the image function by (weighted) differences. They evaluate local extremes in pixel value distribution from gradients calculated separately in the x and y directions. The zero crossing of the first derivative is assumed to give the position of a pixel value line and its maximum gives the position of an edge (ramp), see Fig. 5.30.

From the gradient

$$\text{grad}(s) = \left( \frac{ds(x, y)}{dx}, \frac{ds(x, y)}{dy} \right)^T \quad (5.22)$$

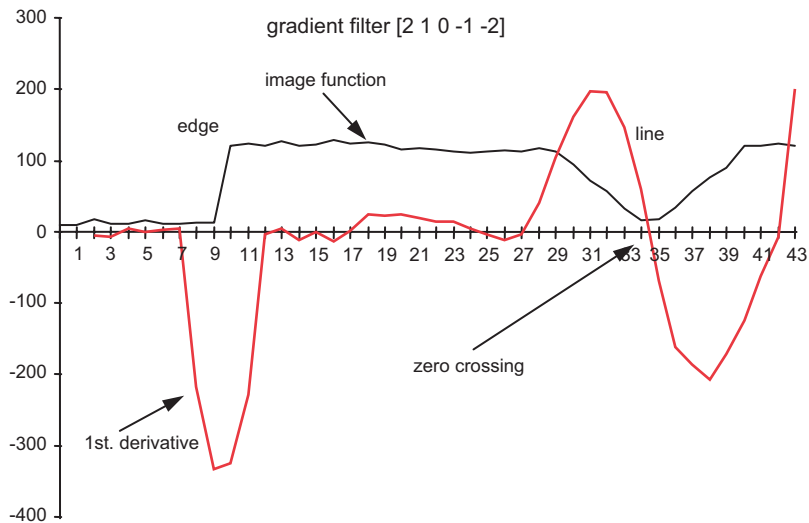


**Figure 5.30** Convolution of an image row with gradient filter  $H = [2 \ 1 \ 0 \ -1 \ -2]$

magnitude and direction of an edge can be derived:

$$\sqrt{\left(\frac{ds(x,y)}{dx}\right)^2 + \left(\frac{ds(x,y)}{dy}\right)^2} \quad : \text{magnitude of gradient} \quad (5.23)$$

$$\begin{pmatrix} \frac{ds(x,y)}{dy} \\ \frac{ds(x,y)}{dx} \end{pmatrix} \quad : \text{direction of gradient} \quad (5.24)$$

A well-known two-dimensional gradient filter is given by the Sobel operator. It approximates the first derivatives in x and y by separated convolution of the filter masks

$$H_x = \begin{bmatrix} 1 & 0 & -1 \\ 2 & 0 & -2 \\ 1 & 0 & -1 \end{bmatrix} \quad H_y = \begin{bmatrix} 1 & 2 & 1 \\ 0 & 0 & 0 \\ -1 & -2 & -1 \end{bmatrix}$$

The operator can be extended to larger filter masks. The magnitude of the gradient is calculated from the intermediate convolution results and stored as a pixel value. The direction of the gradient can also be stored as a coded pixel value image. Magnitude and direction image can be used for further line and edge extraction e.g. for line thinning and chaining. Fig. 5.31 shows the application of a  $5 \times 5$  gradient operator followed by line thinning.

### 5.2.3.2 Second order differential filters

For a continuous function  $s(x)$  the second derivative is given by

$$s''(x) = \frac{d^2s}{dx^2} = \lim_{\Delta x \rightarrow 0} \frac{s(x + \Delta x) - s(x) - [s(x) - s(x - \Delta x)]}{(\Delta x)^2} \quad (5.25)$$

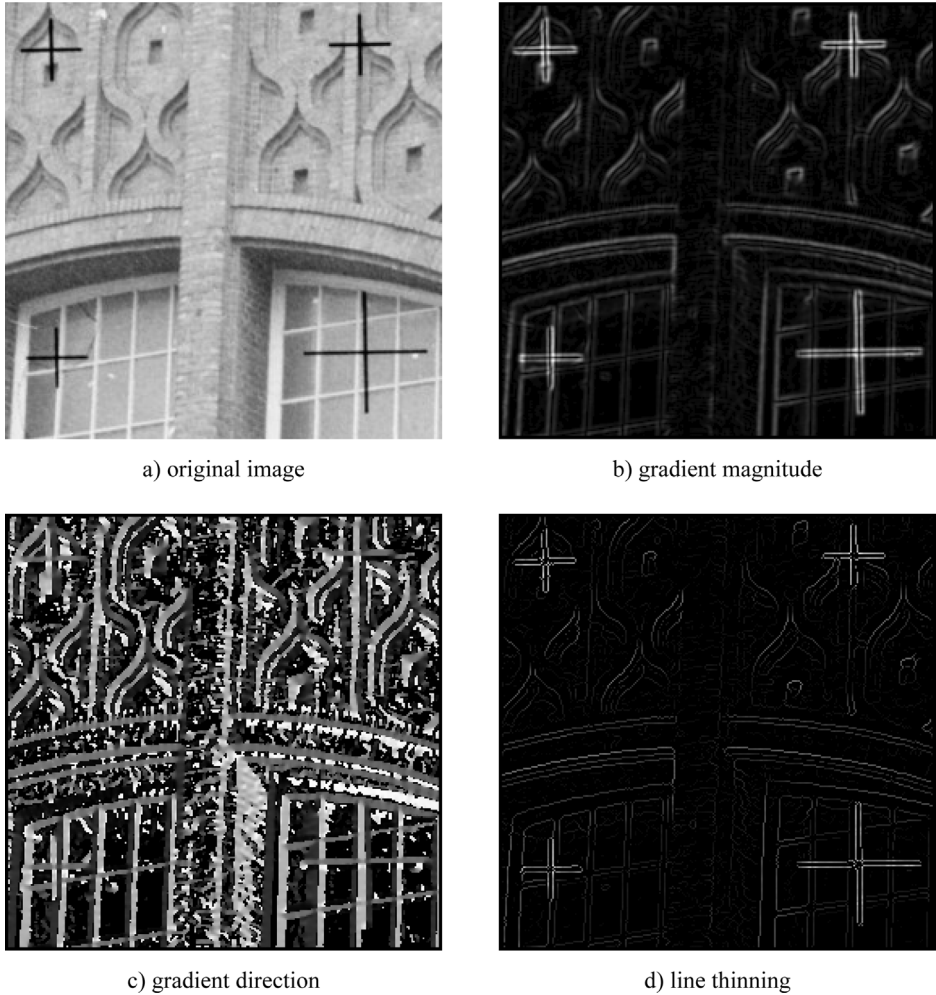


**Figure 5.31** Application of a  $5 \times 5$  gradient operator

and for a discrete function:

$$s''(x) = \frac{s(x+1) - s(x) - [s(x) - s(x-1)]}{(1)^2} = s(x+1) - 2s(x) + s(x-1) \quad (5.26)$$

Here a filter mask  $H_3 = [+1 -2 +1]$  can be derived. The second derivative can also be generated by double application of the first derivative.

A pixel value edge is formed by a ramp change in pixel values. The position of the edge is given by the zero crossing of the second derivative (Fig. 5.32).

The second derivative of a two-dimensional function is given by the total second order differential:

$$s''(x, y) = \nabla^2 s = \frac{d^2 s}{dx^2} + \frac{d^2 s}{dy^2} \quad (5.27)$$

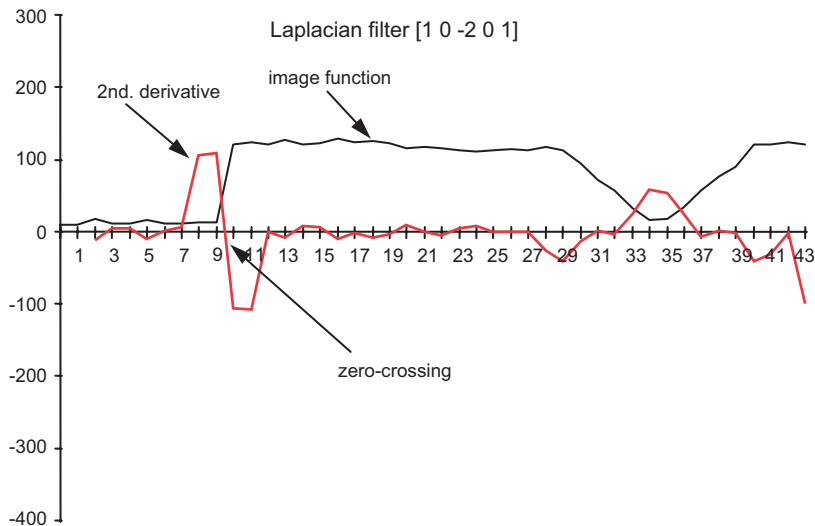


**Figure 5.32** Convolution of an image row by a Laplacian filter  $H = [1 \ 0 \ -2 \ 0 \ 1]$

For a discrete function  $s''(x, y)$  the second derivative can therefore be formed by addition of the partial second derivatives in the x and y directions.

$$\begin{bmatrix} 0 & 1 & 0 \\ 0 & -2 & 0 \\ 0 & 1 & 0 \end{bmatrix} + \begin{bmatrix} 0 & 0 & 0 \\ 1 & -2 & 1 \\ 0 & 0 & 0 \end{bmatrix} = \begin{bmatrix} 0 & 1 & 0 \\ 1 & -4 & 1 \\ 0 & 1 & 0 \end{bmatrix}$$

The resulting convolution mask is called a Laplacian operator. Its main properties are:

- edges are detected in all directions and so it is invariant to rotations
- light-dark changes produce an opposite sign to dark-light changes

### 5.2.3.3 Laplacian of Gaussian filter

Fig. 5.33 illustrates the sensitivity to noise of the Laplacian filter, hence minor intensity changes are interpreted as edges. A better result would be expected if the image were smoothed in advance. As the Gaussian filter is an optimal smoothing filter (see section 5.2.2.2), the second derivative of the Gaussian function is regarded as an optimal edge filter which combines smoothing properties with edge extraction capabilities.

The second derivative of the Gaussian function (5.19) is given by:

$$f''(r, \sigma) = \nabla^2 \text{GAUSS} = -\left(1 - \frac{r}{\sigma^2}\right) \exp\left(-\frac{r^2}{2\sigma^2}\right) \quad (5.28)$$

where  $r^2 = x^2 + y^2$

The filter based on this function is known as Laplacian of Gaussian or LoG filter. Due to its shape it is also called a mexican hat (Fig. 5.34). Empirical analysis shows that a filter size of 11–13 corresponds to a  $\pm 3\sigma$  interval. Fig. 5.33 shows the result of LoG filtering with  $\sigma = 3.0$ .



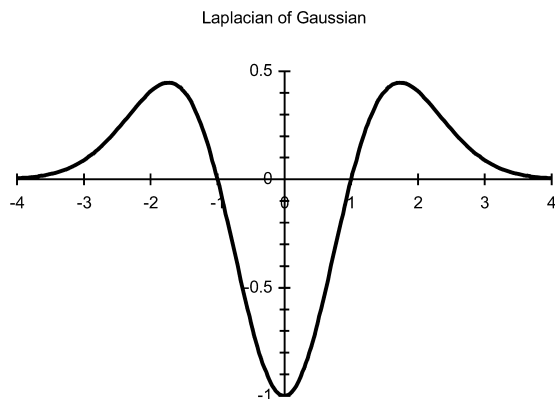
Figure 5.33 Edge extraction with differential operators

#### 5.2.3.4 Hough transform

The Hough transform is based on the condition that all points on an analytical curve can be defined by one common set of parameters. While a Hough transform can be applied to the detection of a wide variety of imaged shapes, one of the simplest solutions is the case of imaged straight lines where all points must fulfil the line equation in Hesse's normal form

$$r = x\cos\varphi + y\sin\varphi \quad (5.29)$$

In order to determine the parameters  $r$  and  $\varphi$  a discrete two-dimensional parameter space (Hough space) is spanned with elements initialised to zero. For each edge point at position  $x, y$  in the image, the direction of the gradient  $\varphi + 90^\circ$  is known and  $r$  can therefore be determined. At position  $r, \varphi$  the corresponding value in Hough space is increased by 1 i.e. each point on the line accumulates at the same position in Hough space (due to rounding errors and noise it is actually a small local area). Hence, straight lines can be detected by searching the Hough accumulator for local maxima.

Figure 5.34 Laplacian of Gaussian (LoG) with  $\sigma = 1$

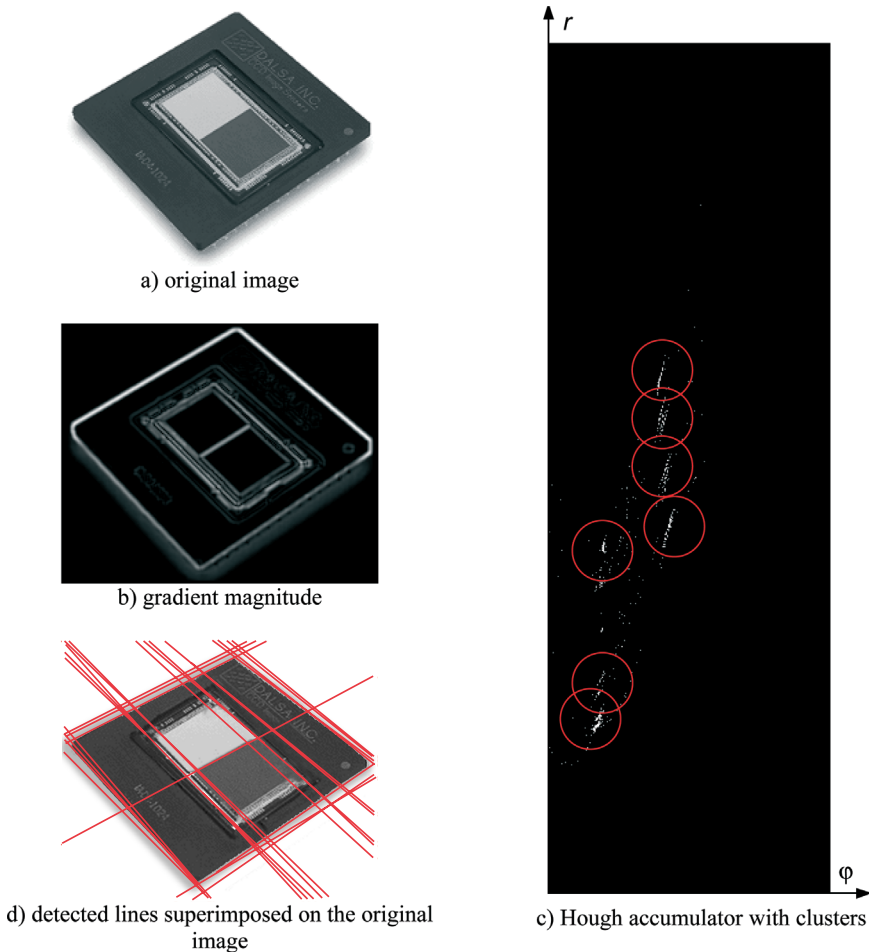


**Figure 5.35** Hough transform

Fig 5.35 illustrates the application of the Hough transform to an image with several well-structured edges (a). Edge extraction is performed by a  $5 \times 5$  gradient filter (in analogy to Fig. 5.31), which delivers a magnitude and direction image (b). Several maxima (clusters) can be recognised in Hough space (c). Clusters which are arranged in one column of the Hough accumulator represent parallel edges in the original image. The value pairs in Hough space can be transformed back into the spatial domain  $x, y$ . Analytical lines are determined as a result, although their start and end points cannot be reconstructed (d).

Such a Hough transform is most relevant for the detection of objects predominantly formed by straight lines. The method can be expanded to curves of higher order (e.g. circles of unknown radius) although the dimension of the Hough accumulator is then no longer two-dimensional.

### 5.2.3.5 Enhanced edge operators

The simple methods of edge extraction discussed in the previous sections often do not deliver satisfactory results. An edge filter suitable for measurement tasks should have the following properties:

Figure 5.36 Canny operator with  $\sigma = 1.5$ Figure 5.37 Deriche operator with  $\sigma = 1.5$ 

- complete extraction of all relevant edges (robustness)
- simple parameterisation (possibly without interactive input)
- high subpixel accuracy
- minimum computational effort

Numerous methods for edge extraction are given in the literature such as the following well-established methods. In contrast to simple convolution operators they are extended by pre- and post-processing as well as adaptive parameter adjustment. They are capable of providing good results even for complex images.

- Canny operator and Deriche operator:

The Canny operator (Canny 1986) belongs to the class of operators based on LoG. It optimises the following quality criteria in edge measurement:

- sensitivity to true edges (uniqueness of edge)
- robustness to noise (maximum signal-to-noise ratio)
- accuracy of edge position

A function is defined for each criterion whose parameters are used to build a non-recursive linear filter. The Canny operator delivers a list of connected contour points with subpixel resolution (see section 5.4.3). In contrast, the Deriche operator which achieves the quality criteria above by recursive filtering. Fig. 5.36 and Fig. 5.37 show the application of both filters, where almost identical results are obtained by appropriate parameter settings (see Deriche 1987 and Lanser and Eckstein 1991 for an overview).

- Edge extraction in image pyramids:

Image pyramids (see section 5.1.3.1) represent the image content at different spatial resolutions. Since the ability to detect edges in natural images varies with image resolution (image scale), an approach is sought which determines the optimal scale for each edge pixel.

LoG filters or morphological operators can be used as edge operators (see Köthe 1997 for an overview).

- Least-squares edge operators:

A model describing the geometric and radiometric properties of the edge can be determined by least-squares parameter estimation. By adjusting their initial parameter values, a priori edge models (templates) can be fitted to the actual region defining an edge (see section 5.4.2.4, least squares template matching). An optimal fit could be the least squares estimate with which the differentials have the least entropy.

A global approach to edge extraction is possible if the energy function

$$E = E_{\text{int}} + E_{\text{pixel}} + E_{\text{ext}} \quad (5.30)$$

where  $E_{\text{int}}$  : curve energy function

$E_{\text{pixel}}$ : pixel value conditions

$E_{\text{ext}}$  : geometric constraints

is minimised in a least-squares solution. The curve energy function  $E_{\text{int}}$  describes the behaviour of the curvature along the edge or the sensitivity with respect to possible changes in direction. Pixel value conditions  $E_{\text{pixel}}$  along the edge can be defined by requiring, for example, maximum gradients. Additional geometric constraints such as straight lines or epipolar geometries are specified by  $E_{\text{ext}}$  (see El-Hakim 1996 for an overview).

### 5.2.3.6 Subpixel interpolation

#### Subpixel resolution

In digital photogrammetry, line and edge filters are used for the measurement of geometric elements (points, lines) which are described by their contours (see section 5.4.2.5). The objective is to locate these patterns to the highest accuracy. As discussed in section 5.1.2, object structures covering several pixels can be measured by interpolation to the subpixel level.

The theoretical resolution of the position of a digitised pixel value edge is, in the first instance, a function of the slope of the pixel values along the edge and quantisation depth (number of bits per pixel value). It is defined by a parameter  $d$ , sometimes called the slack value, where the position of the imaged edge can be varied without changing the related pixel values (Fig. 5.38). For a step change ( $\beta = 0$  in Fig. 5.38) the slack is maximized and amounts to 1.

Förstner (1985) shows that, for  $N$  quantisation steps, the uncertainty of edge positioning is at least  $1/(N-1)$  (see also Clarke *et al.* 1993). This corresponds to 0.004 pixels for  $N = 256$  pixel levels. In this case the average deviation of a single edge point can be estimated, independently of the slope of the edge, as

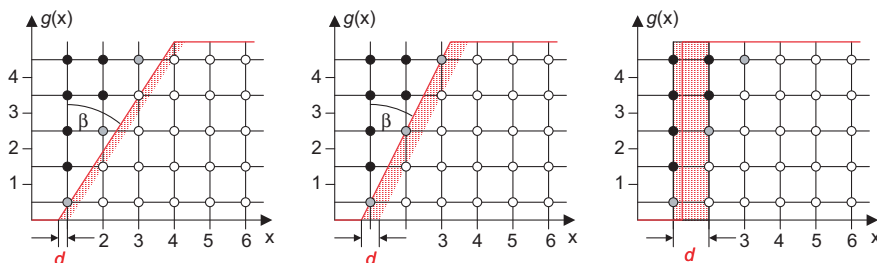


Figure 5.38 Slack in a digitised edge (after Förstner 1985)

$$\bar{\sigma}_d = 0.015 \text{ pixels} \quad (5.31)$$

This theoretical quantity will be higher in practice due to optical limitations and noise but it defines a lower limit for the estimation of positional accuracy of image measurements. Hence, the accuracy of an edge of length  $n$  pixels can be estimated as

$$\bar{\sigma}_K = \frac{\bar{\sigma}_d}{\sqrt{n}} \text{ pixels} \quad (5.32)$$

This is also approximately true for the centre of a circle measured by  $n$  edge points. For a circular target of diameter 6 pixels there are approximately  $n = 19$  edge points. Hence, in the ideal case, the centre of such a target can be determined to an accuracy of about 0.004 pixel (4/1000 pixel). Further investigations are discussed in section 5.4.2.6.

A selection of edge extraction methods providing subpixel interpolation, together with their principal parameters, are summarised in Table 5.3.

**Table 5.3:** Methods for subpixel interpolation of edge points

method	model	intermediate result	subpixel interpolation
differential filter	deflection point	gradient image	linear interpolation
moment preservation	pixel value plateaux	1 <sup>st</sup> , 2 <sup>nd</sup> and 3 <sup>rd</sup> moments	solution of 3 equations
feature correlation ( <i>template matching</i> )	edge template, cross-correlation	correlation coefficients	2nd order interpolation
least-squares matching	edge template, geometric and radiometric transformation	up to 8 transformation parameters	shift parameters

#### Zero-crossing interpolation

As shown in Fig. 5.30 and Fig. 5.32 the derivative functions do not pass zero at an integer pixel coordinate. The subpixel position of an edge can be determined by first or second order interpolation in the neighbourhood of the zero crossing (Fig. 5.39a). This method is used, for example, for the edge measurement of patterns based on points (see section 5.4.2.5). Interpolation of zero crossings provides edge location with a precision of up to 1/100 pixel.

#### Moment preservation

The moment preservation method is based on the assumption that an edge within a one-dimensional image function (e.g. an image row) of window size  $n$  can be described by three parameters. These define the left pixel value plateau  $h_1$ , the right pixel value plateau  $h_2$  and the coordinate of the pixel value step  $x_E$  (Fig. 5.39b). The three required equations are formed by the 1<sup>st</sup>, 2<sup>nd</sup> and 3<sup>rd</sup> moments (Tabatabai and Mitchell 1984):

$$m_i = \frac{1}{n} \sum_{j=1}^n g_j^i \quad i = 1, 2, 3 \quad (5.33)$$

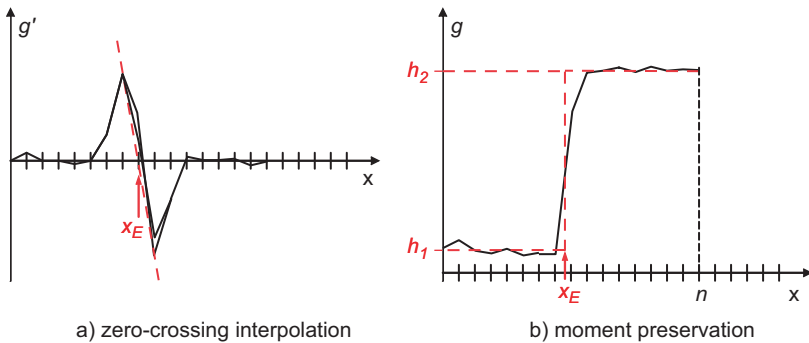


Fig. 5.39 Edge interpolation methods

The following parameters are determined (without derivation):

$$\begin{aligned} h_1 &= m_1 - \bar{\sigma} \sqrt{\frac{p_2}{p_1}} \\ h_2 &= m_1 + \bar{\sigma} \sqrt{\frac{p_1}{p_2}} \\ p_1 &= \frac{1}{2} \left[ 1 + \bar{s} \sqrt{\frac{1}{4 + \bar{s}^2}} \right] \end{aligned} \quad (5.34)$$

where

$$\begin{aligned} \bar{s} &= \frac{m_3 + 2m_1^3 - 3m_1m_2}{\bar{\sigma}^3} \\ \bar{\sigma}^2 &= m_2 - m_1^2 \end{aligned} \quad (5.35)$$

The desired edge position is given by:

$$x_E = np_1 \quad (5.36)$$

The moment preservation method is easy to implement and it delivers the subpixel edge location without any further interpolation. It is used, for example, with the Zhou operator for the edge extraction of elliptically shaped target images (see section 5.4.2.5).

#### Correlation methods

Correlation methods determine the position in a search image which has the highest similarity with a reference pattern (template). The reference pattern can be a subset of a natural image, or a synthetically created image. For example, when searching for a vertical edge which switches from dark to light, a reference pattern similar to Fig. 5.40 can be used.

The similarity between two patterns can be measured by the normalised cross-correlation coefficient  $r$  (see section 5.4.2.3). If  $r$  is plotted as a function of  $x$ , the position of maximum correlation is most likely to be the true position of the reference pattern. If the curve around the maximum is approximated by a quadratic function (parabola), the desired position can be determined to subpixel precision (Fig. 5.40).

Least-squares matching (see section 5.4.2.4) determines a transformation which describes both the change of contrast and the geometric projection between reference pattern and search

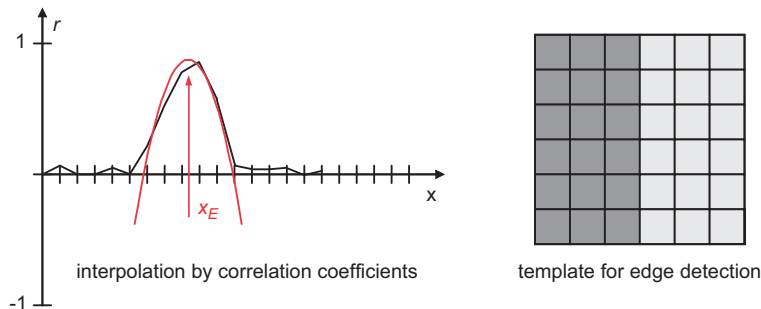
**Figure 5.40** Interpolation by correlation coefficients

image. The approach requires reasonably good initial values of the unknown parameters, in particular the required shift parameters. The adjustment process directly delivers the subpixel positions of the pattern (edge).

### 5.3 Geometric image transformation

The process of modifying the geometric projection of a digital image is here referred to as a geometric image transformation. Related methods are required in photogrammetry for photo rectification and orthophoto production, for combining images with CAD models and for template matching procedures. Rendering and morphing methods also belong to this category. Fig. 5.41 shows an example of the projective rectification of a façade (see also Fig. 4.52).

The term rectification denotes a general modification of pixel coordinates e.g. for

- translation and rotation
- change of scale or size (magnification, reduction)
- correction of distortion effects
- projective rectification (from central perspective to parallel projection)
- orthophoto production (differential rectification)
- rectification of one image with respect to another
- superimposition of natural structures onto a surface e.g. a CAD model (texture mapping)

**Figure 5.41** Geometric rectification of a façade

Geometric image transformations are generally performed in two stages:

- transformation of pixel coordinates (image coordinates) into the target system (rectification) – this transformation is the reverse of the imaging process
- calculation (interpolation) of output pixel values

### 5.3.1 Fundamentals of rectification

Rectification is founded on the geometric transformation of pixel coordinates from an original image to an output image:

$$s'(x', y') = G(s(x, y)) = g'$$

where

(5.37)

$$x' = f_1(x, y)$$

$$y' = f_2(x, y)$$

Here the pixel value  $g$ , at position  $(x, y)$  in the original image, appears in the output image, after pixel value interpolation  $G$ , as pixel value  $g'$  at position  $(x', y')$ .

The geometric transformations  $f_1$  and  $f_2$  are typically selected from a range of possible coordinate transformations. The affine transformation (2.6) is often used for standard modifications such as translation, scaling, rotation or shearing. The projective transformation (8 parameters, see equation 2.12) is suited to the rectification of images of planar objects. Where a digital surface model is available, arbitrary free-form surfaces can be transformed into orthophotos by use of the collinearity equations (4.8) (see section 4.4.1.2).

In all cases there is a transformation between the pixel coordinates  $(x, y)$  of the input image and the pixel coordinates  $(x', y')$  of the output image. The pixel values of the input image in the region of  $(x, y)$  must be stored in the output image at position  $(x', y')$ . For this purpose an indirect rectification method is usually applied in which the output image is processed pixel by pixel. By reversing the geometric transformation, the pixel value of the input image is interpolated at the reverse-transformed position  $(x, y)$  and then stored in the output image. This algorithm is easy to implement and avoids gaps or overlapping regions in the output image (Fig. 5.42).

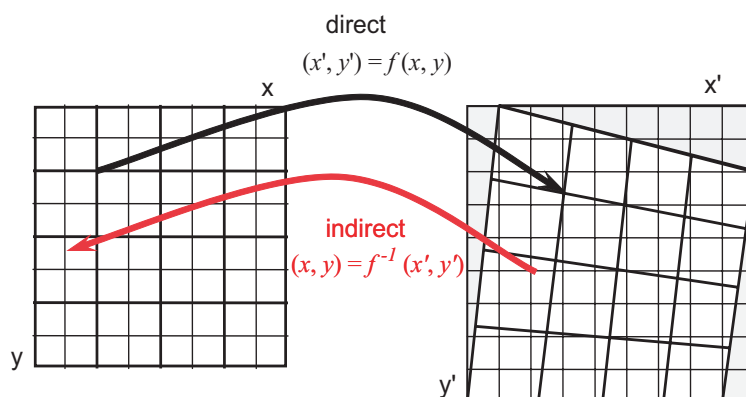


**Figure 5.42** Direct and indirect rectification methods

### 5.3.2 Pixel value interpolation

The second step in rectification consists of the interpolation of a suitable pixel value from the local neighbourhood using an arbitrary non-integer pixel position, and then storing this quantity in the output image (resampling). The following methods are normally used for pixel value interpolation (Rosenfeld and Kak 1982, Bähr and Vögtle 1998):

- zero order interpolation (nearest neighbour)
- first order interpolation (bilinear interpolation)
- second order interpolation (bicubic convolution, Lagrange polynomials)

For the method of nearest neighbour, the pixel value at the rounded or truncated real pixel coordinate is used in the output image. The interpolation rule is given by:

$$g' = s(\text{round}(x), \text{round}(y)) \quad (5.38)$$

pixel value for the example of Fig. 5.4:  $g' = 32 = g_4$

This approach leads to the visually worst rectification result. However, the computational effort is small and the output image consists only of pixel values which also exist in the input image.

The bilinear or biquadratic interpolation takes into account the  $2 \times 2$  adjacent pixel values of the computed pixel position. The interpolated pixel value is the result of the weighted average of adjacent pixel values in which the weight is given by the relative coverage of the current pixel. The interpolation rule is given by:

$$g' = F_1 s(i, j) + F_2 s(i+1, j) + F_3 s(i, j+1) + F_4 s(i+1, j+1) \quad (5.39)$$

where  $F_1 + F_2 + F_3 + F_4 = 1$

or analogously to equation (2.10):

$$\begin{aligned} g' = & s(i, j) + dx[s(i+1, j) - s(i, j)] + dy[s(i, j+1) - s(i, j)] \\ & + dxdy[s(i+1, j+1) - s(i+1, j) - s(i, j+1) + s(i, j)] \end{aligned} \quad (5.40)$$

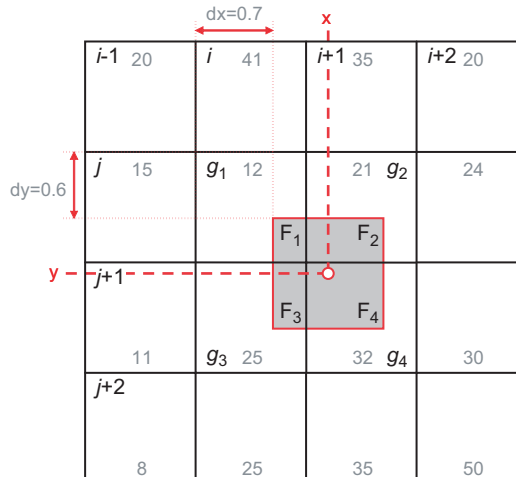


Figure 5.43 Pixel value interpolation in  $2 \times 2$  and  $4 \times 4$  neighbourhoods

pixel value for the example of Fig. 5.4:  $g' = 25.3 \approx 25$

With modest computational effort, bilinear interpolation generates slightly smoothed rectifications of good quality.

Bicubic convolution and Lagrange interpolation are usually applied only in output rectifications where the highest image quality is required. These methods use a  $4 \times 4$  environment for interpolation which results in computation times up to 10 times longer than that of the nearest neighbour method. The algorithm for bicubic convolution is as follows:

$$\begin{aligned} df(x) &= |x|^3 - 2|x|^2 + 1 && \text{for } |x| < 1 \\ df(x) &= -|x|^3 + 5|x|^2 - 8|x| + 4 && \text{for } 1 \leq |x| < 2 \\ df(x) &= 0 && \text{other cases} \end{aligned}$$

$$\begin{aligned} a(n) &= s(i-1, j+n-2)df(dx+1) \\ &\quad + s(i, j+n-2)df(dx) \\ &\quad + s(i+1, j+n-2)df(dx-1) \\ &\quad + s(i+2, j+n-2)df(dx-2) \end{aligned} \tag{5.41}$$

for  $n = 1, 2, 3, 4$

$$\begin{aligned} g' &= a(1)df(dy+1) + a(2)df(dy) + a(3)df(dy-1) \\ &\quad + a(4)df(dy-2) \end{aligned}$$

pixel value for the example of Fig. 5.4:  $g' = 23.7 \approx 24$

The arbitrarily chosen example of Fig. 5.4 shows clearly that the three different interpolation methods generate quite different values for the interpolated pixel level. Fig. 5.44 shows an enlarged image region after rotation, generated by the three methods. The nearest neighbour approach gives rise to clearly visible steps along sloping edges. The other two interpolation methods yield results which are visually very similar.

The problem of pixel value interpolation at real positions also occurs in least-squares matching (see section 5.4.2.4). Bilinear interpolation is normally used as an efficient

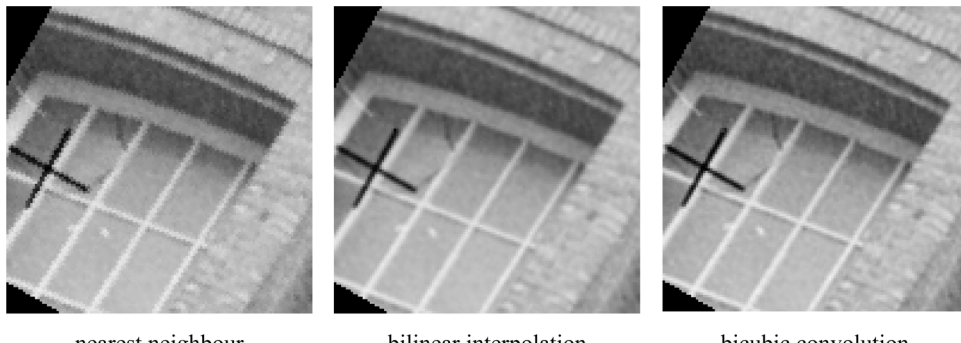


**Figure 5.44** Rectification results with different pixel value interpolations

compromise between computation time and image quality. If edge detection is to be carried out on the output rectified image, it is better to carry out edge detection prior to rectification not only to avoid interpolation biases but also since rectification of edges rather than large arrays of pixel data is more economical in terms of processing power.

### 5.3.3 3D visualisation

#### 5.3.3.1 Overview

The field of computer graphics offers a number of methods for visualizing three-dimensional objects in the form of a photo-realistic image. Visualisation of 3D objects is increasingly important e.g. for the following applications:

- analysis of manufactured CAD models
- design studies
- quality analysis of manufactured components
- illustration of volume models e.g. computer tomograms
- animation of movies, TV scenes and advertisements
- design of virtual-reality scenes
- visualisation of dynamic processes e.g. simulated movements
- combination of natural and artificial objects e.g. for the planning of new buildings in existing residential districts

In close-range photogrammetry the main focus of 3D visualisation is the representation of photogrammetrically reconstructed, real objects. In general, 3D graphics or CAD programs are used here to provide additional elements and graphical editing of the 3D data.

The mathematical and, in particular, physical imaging models central to many visualisation methods also help in understanding object-based image processing methods (see section 5.5.5). These algorithms model the object surface with geometric and radiometric parameters determined from a least-squares adjustment to observed image coordinates and pixel values.

Fig. 5.45 illustrates the typical stages in the graphical visualisation of a 3D scene which include:

- 3D model

The object to be visualised is defined by a discrete 3D object surface model (e.g. by triangulation) and/or as a set of geometric elements (lines, planes, cylinders etc.). A 3D wire model is not in itself sufficient because the single surface points must be linked topologically and combined to form (opaque) surface patches.

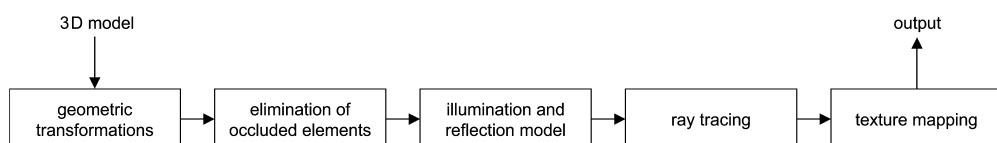


**Figure 5.45** Visualisation chain

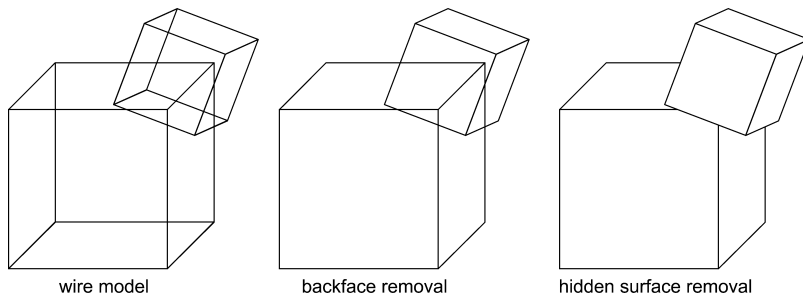


**Figure 5.46** Elimination of occluded elements

- Geometric transformations

After selecting the spatial observation position, object points can be projected onto a (virtual) display or projection plane using the graphical transformations described in section 2.2.2.3. Object areas outside the visible volume can be excluded from further processing.

- Elimination of occluded elements

Reverse facing object regions, which are not visible from the chosen viewpoint, can be eliminated by simple comparison of the observation direction with the surface normal vector (backface removal). Subsequently any remaining object elements must be checked for partial or complete occlusion by other objects (hidden surface removal) (Fig. 5.46). Traditionally this is carried out using a Z buffer which stores the range to each object in the scene.

- Illumination and reflection model

In 3D space light sources with various characteristics (illumination power, direction, colour) can be positioned as required. In addition, individual reflection parameters dependent on the properties of the surface materials can be assigned to each partial surface element.

- Texture mapping

In texture mapping an artificial or natural structure is assigned to the visualised surface element. Structure or texture can be generated in different ways:

- by assignment of a colour value (if no spectral reflection model is available)
- by superimposition of an artificial texture (pattern)
- by superimposition of a natural texture derived from existing photos of the object.

- Ray tracing

A virtual camera position (observer's position) and the required geometric projection is defined. The light ray associated with a new output image pixel is traced back into object space (ray tracing). If the ray strikes a surface element the corresponding pixel value is modified according to the local reflection function. If appropriate, the pixel's output intensity or colour value takes into account multiple reflections and the effects of shadowing. Inverse ray tracing can also be used, having the benefit in some circumstances of reducing CPU time and allowing the elimination of occluded elements.

### 5.3.3.2 Reflection and illumination

Illumination and reflection models describe the light paths which start from one or more light sources and strike one or more object surfaces before registration in the (virtual) camera.

An intensity or colour value is then registered at the corresponding position in the camera image. The visualised intensity value is therefore a function of:

- spectral characteristics of light sources
- spatial position of light sources
- properties of the atmosphere (media)
- spectral characteristics of surface materials (reflection, absorption, transmission)
- surface structure (roughness)
- location and orientation of surfaces
- optical and radiometric characteristics of the camera (sensor)
- location and orientation of the camera (observer)

The extent to which these properties are applied depends on the complexity of the model. Most cases are restricted to simple models which use only one light source, do not permit multiple reflections off surfaces and impose only limited properties of materials. Here it is more important for the observer to visualise a three-dimensional situation rather than view a photo-realistic image.

#### *Reflection types*

The ambient reflection model is based on the idea that a certain proportion  $k_a$  of the incident light  $I_i$  reflects uniformly in all directions. The reflected radiation  $I_r$  is given by:

$$I_r(\lambda) = k_a I_i(\lambda) \quad (5.42)$$

where  $0 \leq k_a \leq 1$

This model does not consider the spatial orientation of the surface. The factor  $k_a$  results in a uniform intensity variation of the whole scene.

Diffuse reflection (Fig. 5.47) is based on Lambert's law. The intensity of the reflected light reduces as a function of the cosine of the angle  $\alpha$  between the surface normal  $\mathbf{n}$  and the direction to the light source  $\mathbf{l}$  and is expressed by the scalar triple product of the two vectors:

$$I_r(\lambda) = k_d(\lambda) \max((\mathbf{n} \cdot \mathbf{l}), 0) I_i(\lambda) \quad (5.43)$$

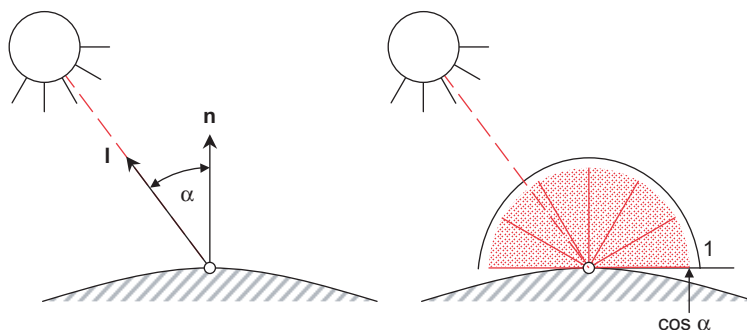
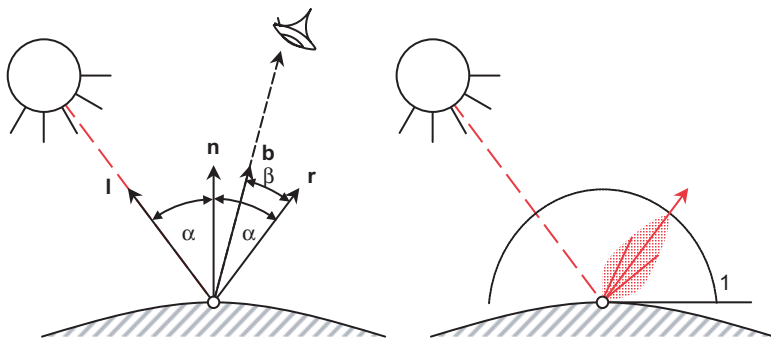


Figure 5.47 Diffuse reflection



**Figure 5.48** Mirrored reflection

The material-dependent term  $k_d(\lambda)$  is a function of the wavelength and results in the perception of colour. The reflected component is independent of the observer's position.

The basic idea of mirrored reflection (Fig. 5.48) is the principle that angle of incidence = angle of reflection. For a perfect mirror the light is reflected in direction  $\mathbf{r}$ . Consequently, in viewing direction  $\mathbf{b}$  the intensity is given by:

$$I_r(\lambda) = \begin{cases} I_i(\lambda) & \text{if } \mathbf{b} \cdot \mathbf{r} = 0 \\ 0 & \text{otherwise} \end{cases} \quad (5.44)$$

Since perfect mirrors rarely exist in reality, and as they would generate a signal only in one direction  $\mathbf{b} = \mathbf{r}$  ( $\beta = 0$ ), some spread around this direction is permitted:

$$I_r(\lambda) = k_s(\lambda) \max((\mathbf{b} \cdot \mathbf{r}), 0)^m I_i(\lambda) \quad (5.45)$$

Here the exponent  $m$  defines the material-dependent characteristic of the variation and the term  $k_s(\lambda)$  specifies the spectral reflective properties. Large values of  $m$  describe polished surfaces (metals, mirror), small values specify matte, non-metallic surfaces.

#### *Phong illumination model*

The Phong illumination model (Phong 1975) assumes parallel rays of light between light source, surface and observer for each point on the surface. With the highlight vector  $\mathbf{h}$  defined as:

$$\mathbf{h} = \frac{\mathbf{b} + \mathbf{l}}{|\mathbf{b} + \mathbf{l}|} \quad (5.46)$$

a complete model which includes all reflection types above can be defined:

$$I_r(\lambda) = I_i(\lambda)[k_a + k_d(\lambda) \max(0, (\mathbf{n} \cdot \mathbf{l})) + k_s(\alpha, \lambda) \max(0, (\mathbf{n} \cdot \mathbf{h}))^m] \quad (5.47)$$

In the special case where light source and observer have the same position then  $\mathbf{l} = \mathbf{b} = \mathbf{h}$ . If this position is in the negative z direction<sup>1</sup>, it follows that

<sup>1</sup> In computer graphics the position of the viewer is often the point  $(0, 0, -z)$ .

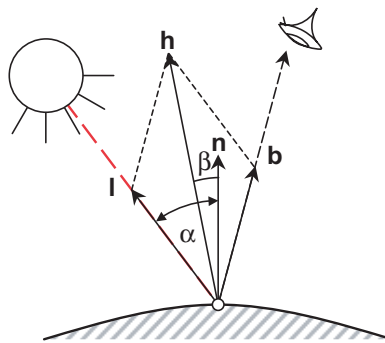


Figure 5.49 Phong's illumination model

$$(\mathbf{n} \cdot \mathbf{l}) = \begin{bmatrix} n_x \\ n_y \\ n_z \end{bmatrix} \cdot [0 \quad 0 \quad -1] = -n_z \quad (5.48)$$

and therefore

$$I_r(\lambda) = I_i(\lambda)[k_a + k_d(\lambda) \max(0, -n_z) + k_s(\alpha, \lambda) \max(0, -n_z)^m] \quad (5.49)$$

Phong's illumination model generates acceptable results with moderate computational effort as can be seen in Fig. 5.50.

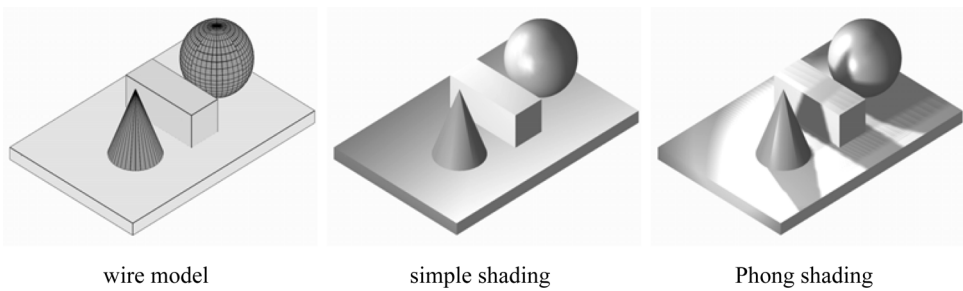


Figure 5.50 Visualisation of illuminated 3D scene

### *Complex illumination models*

In order to generate realistic scenes, the Phong model must be extended. The various approaches cannot be discussed in sufficient detail here, but they are founded on the following features:

- linearly approximate the input and output light directions from the vertices of each triangle in the triangulation
- introduction of surface roughness by means of micro-facets
- introduction of absorption which varies with material and incident angle as a function of the refractive index  $n$  at the interface between different media (e.g. air/metal)
- introduction of a visual colour perception model (CIE model)

- introduction of a bi-directional reflection distribution function (BRDF) which is a function of the specified material for each individual wavelength  $\lambda$  of the spectrum
- introduction of stochastic models defining the probability of a certain reflection.

These functions are firstly used to model the physical reflection at the surface. In addition, a global illumination model requires a description, using ray tracing, of the complete path taken by all light rays (emitted by light sources and/or surfaces) including transmission, multiple reflection and shadowing. Since this procedure would require an unreasonable computational effort, the process is instigated in a similar way to indirect rectification (see section 5.3.1), the algorithm starts at the output pixel position and computes the corresponding intensity by tracing backwards into object space.

The principle of calculation is as follows. The light ray defined by the image coordinates and the perspective centre strikes the first surface. This ray is divided into a transmitted and a reflected ray and both are recursively traced until:

- the corresponding intensity is less than a threshold,
- a certain recursion depth (e.g. 5) is reached or
- a light source (which can also include a window) is intersected.

This procedure defines a tree structure which is processed from the leaves down to the root. At each division the registered intensity values are accumulated and stored in the output image.

An extended model is provided by the radiosity approach in which every surface point acts as an emitter, either as a light source itself or by reflected radiation. The unknown emission is determined in a system of equations which must be solved for every surface point and for wavelength. The approach requires high computational power and leads to realistic visualisations. Additional information on illumination models are given by Foley *et al.* (1995), Janser *et al.* (1996) and Tönnies and Lemke (1994).

### 5.3.3.3 Texture mapping

The pattern or structure on a surface is referred to as texture. It results from a variation of small surface elements within a limited neighbourhood. Textures are physically generated by the different reflection properties and geometric characteristics of surface particles which, in the limit, can be as small as molecules. With the aid of textures, visualised objects can achieve a realistic appearance.

The generation of texture in a visualised scene can be generated most simply by projection of a texture image onto the surface (texture mapping). A texture image is a digital image whose pattern is superimposed on the object in the manner of a slide projection. The texture image can be a real photograph or it can consist of artificial patterns (examples in Fig. 5.51).

Texture mapping includes the following principle techniques:

- 2D texture mapping onto plane object surfaces
- 3D texture mapping onto plane object surfaces
- 3D texture mapping onto arbitrarily shaped object surfaces
- 3D texture mapping onto arbitrarily shaped object surfaces in combination with an illumination model

For 2D texture mapping, a plane transformation between a region in the visualised image and the texture image is calculated. According to the principle of plane rectification (see section

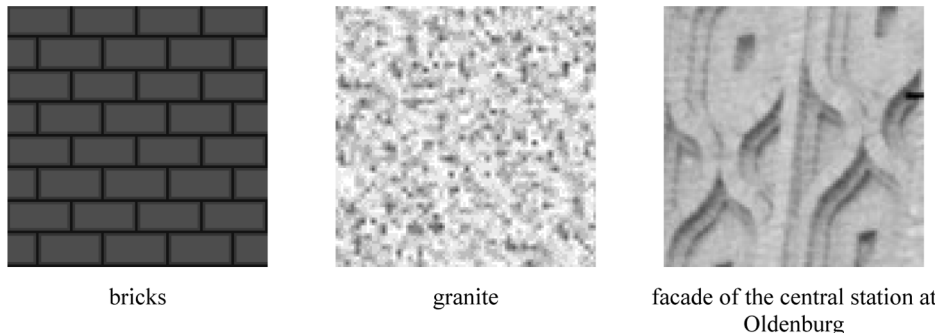


**Figure 5.51** Artificial and natural textures

4.4.1.1), corresponding image patches are defined in both images and their corner points are mapped by affine, bilinear or projective transformation. There is no direct relationship to the 3D object model i.e. for each new visualisation the texture regions must be redefined, if necessary by manual interaction.

Texture mapping is more flexible if the known geometric relationship between visualisation and 3D model is utilised. Assuming an object composed of plane surface elements defined by polygons (e.g. triangles or quadrangles), each polygon can be mapped onto a corresponding area of the texture image by projective transformation (2.12). If a spatially oriented metric image provides the natural surface textures, the photogrammetric projection equations can map the individual surface elements onto the metric image texture to define a texture patch (Fig. 5.52). These texture patches can then be transferred into the output image by interpolation within the transformed polygon.

Fig. 5.53 shows the example of texture mapping for a combination of artificial patterns (bricks) and natural structures derived from the photogrammetric images of the project.

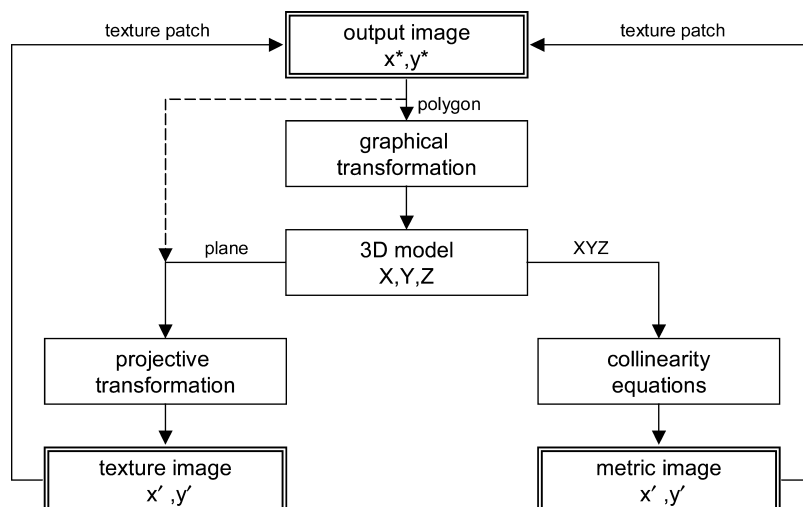


**Figure 5.52** Texture mapping



**Figure 5.53** Texture mapping with artificial and natural patterns (detail from Fig. 1.6)

For texture mapping of curved surfaces the workflow of Fig. 5.52 must be implemented pixel by pixel in the output image. By incorporating a (global) illumination model it is possible to generate a photo-realistic scene consisting of lights, shadows and natural surface structures.

## 5.4 Digital processing of single images

This section deals with methods for locating objects in single digital images. It distinguishes between algorithms for the determination of single point features (pattern centres) and those for the detection of lines and edges. The common aim of these methods is the accurate and reliable measurement, to subpixel resolution, of image coordinates for use in analytical object reconstruction. Three-dimensional image processing methods are discussed in section 5.5.

### 5.4.1 Approximate values

#### 5.4.1.1 Possibilities

The image processing methods discussed here require initial approximations for the image position which is to be accurately determined. These approximate values can be found in different ways:

- by pre-determined (calculated) image coordinates e.g. from (approximately) known object coordinates and known image orientation parameters
- by manually setting an on-screen cursor
- by pattern recognition (segmentation) during image pre-processing e.g. by searching for appropriate patterns in the image

- using interest operators which detect regions of significant image structure (see section 5.5.2.1)

In close-range photogrammetry, and especially in the industrial field, simple image structures can often be engineered through specific targeting and illumination techniques so that, for example, only (bright) object points on a homogeneous (dark) background exist in the image (examples in Fig. 5.2, Fig. 7.8). In this case the generation of approximate values reduces to the location of simple image patterns and can, in many cases, be fully automated (see section 5.4.1.2).

The use of coded targets in industrial applications has been particularly successful. These encode a point identification which can be detected and decoded automatically (see section 3.4.1.2).

#### 5.4.1.2 Segmentation of point features

The measurement (segmentation) of bright targets is an important special case in practical photogrammetric image acquisition. If no information about the position of target points is available, potential candidates must be searched for. Since practical measurement tasks involve different image scales, perspective distortion, extraneous lighting, occlusions etc., the following hierarchical process of point segmentation has proven effective:

1. adaptive binarisation by thresholding (see section 5.2.1.4)
2. detection of connected image regions exceeding a threshold
3. analysis of detected regions with respect to size (number of pixels) and shape
4. storing image positions which meet appropriate conditions of size and shape

Thresholding is relatively simple for signalised targets. If retro-reflective targets with flash illumination or LED targets are used, these generate significant peaks in the upper region of the pixel value histogram (see Fig. 5.15). For non-reflective targets (e.g. with a paper surface) the contrast against the image background is often weaker. In some circumstances thresholding cannot then be performed globally but must be adapted to different parts of the image.

Connected regions are detected by a neighbourhood or connectivity analysis. Using the sequential process outlined in Fig. 5.54, the left and the upper three neighbouring pixels are analysed. If the pixel value of one of these neighbours exceeds the threshold, the neighbour belongs to a region already detected; otherwise a new region is created. Pixels in connected

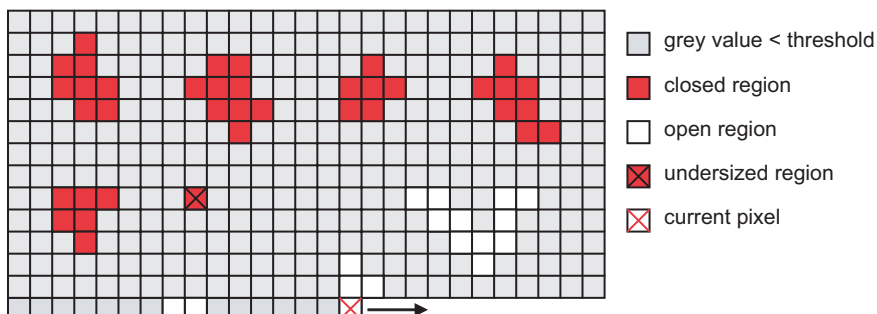
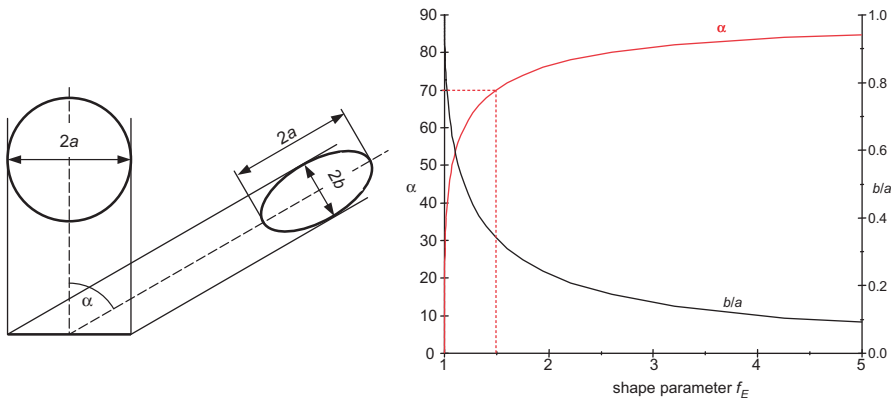


Figure 5.54 Sequential connectivity analysis (after Maas *et al.* 1993)



**Figure 5.55** Shape parameter of ellipse (after Ahn and Kotowski 1997)

regions are marked in either list structures or label images. V-shaped objects which are temporarily assigned to different regions are recombined by a contact analysis.

In a non-sequential connectivity analysis, adjacent pixels are traced recursively in all directions until one or more of the following termination criteria are met:

- the corresponding pixel value is less than the threshold
- the maximum number of pixels permitted in a region is exceeded
- the pixel already belongs to a known region

The resulting connected regions can now be analysed with respect to their shape and size. Here the number of pixels is only a coarse indicator of suitable feature size, which is possibly known *a priori*. In the case of circular targets, shape parameters describing the expected elliptical shape of the feature can be derived from the region's pixel distribution. A possible test criterion is given by the following shape parameter  $f_E$  (Ahn and Kotowski 1997):

$$f_E = \frac{U^2}{4\pi A} \quad (5.50)$$

where

$U$ : periphery

$A$ : area

The value of the shape parameter is 1 for a circle and greater than 1 for all other shapes. For an ellipse, a suitable threshold for  $f_E$  can be estimated by the ratio of semi-axes  $b/a$  which depends on the imaging angle  $\alpha$  between image plane and circle plane in object space (Fig. 5.55). As imaging angles of more than  $70^\circ$  result in highly elongated ellipses, a threshold of 1.5 is highly suitable.

The regions which remain after binarisation and shape analysis are indexed and stored sequentially.

Fully-automated segmentation is particularly successful if the following criteria are met:

- good image contrast between target and background through suitable targeting and illumination techniques (retro-targets, flash)

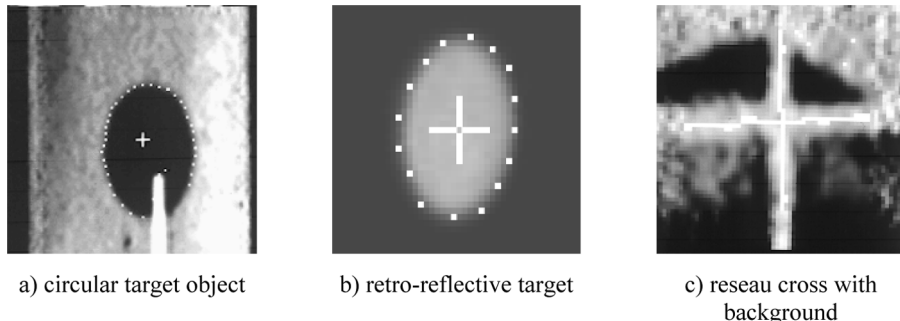


**Figure 5.56** Examples of single point features with detected contour points

- no extraneous reflections from the object surface (avoidance of secondary light sources)
- no occlusions due to other object parts
- good separation of individual targets in image space
- minimum target size in image space (5 pixel diameter)
- no excessive differences in image point size

The problems of point imperfections and false detections are illustrated in the examples of Fig. 5.16, Fig. 5.27, Fig. 5.28 and Fig. 5.56a. In some cases the segmentation steps above must be extended by additional pre-processing (e.g. morphological operations) and further analysis.

#### 5.4.2 Measurement of single point features

Here single point features are taken to mean image patterns where the centre of the pattern is the reference point. Examples are shown in Fig. 5.56.

##### 5.4.2.1 On-screen measurement

Arbitrary image features can be measured manually by positioning a digital floating mark (cursor) on the computer screen. For this purpose the cursor should be displayed as a cross or circle. The minimum movement of the floating mark is 1 pixel. The average measurement accuracy of non-signalised points (e.g. building corners) is around 0.3-0.5 pixel. If the image is zoomed the measurement accuracy can be improved to approximately 0.2 pixel with clearly defined image content.

##### 5.4.2.2 Centroid methods

If the feature to be measured consists of a symmetrical distribution of pixel values, the local centroid can be used to determine the centre. The centroid is effectively a weighted mean of the pixel coordinates in the processing window:

$$x_M = \frac{\sum_{i=1}^n (x_i Tg_i)}{\sum_{i=1}^n (Tg_i)} \quad y_M = \frac{\sum_{i=1}^n (y_i Tg_i)}{\sum_{i=1}^n (Tg_i)} \quad (5.51)$$

Here  $n$  is the number of processed pixels in the window,  $g_i$  is the pixel value at the pixel position  $(x_i, y_i)$ . The decision function  $T$  is used to decide whether a pixel is used for calculation.  $T$  can be defined by an (adaptive) pixel value threshold  $t$ , for example:

$$T = \begin{cases} 0 & \text{for } g < t \\ 1 & \text{for } g \geq t \end{cases}$$

For features whose structure is defined by pixel value edges, such as the circumference of a circle, it is reasonable to include edge information in the centroid calculation. For this purpose a weighting function based on gradients is employed:

$$x_M = \frac{\sum_{i=1}^n x_i \text{grad}^2(g_{x,i})}{\sum_{i=1}^n \text{grad}^2(g_{x,i})} \quad \text{or} \quad y_M = \frac{\sum_{i=1}^n y_i \text{grad}^2(g_{y,i})}{\sum_{i=1}^n \text{grad}^2(g_{y,i})} \quad (5.52)$$

Centroid operators are computationally fast and easy to implement. In general they also work for very small features ( $\emptyset < 5$  pixel) as well as slightly defocused points. However, the result depends directly on the pixel value distribution of the target feature such that they are only suitable for symmetrical homogenous patterns as shown in Fig. 5.56b. Defective pixels within the processing window will negatively affect the calculation of centre coordinates.

The theoretical accuracy of the centroid can be estimated by applying error propagation to equation (5.51) (Maas *et al.* 1993):

$$\sigma_{x_M} = \frac{1}{\sum g_i} \sqrt{\sum (x_i - x_M)^2} \sigma_g$$

$$\sigma_{y_M} = \frac{1}{\sum g_i} \sqrt{\sum (y_i - y_M)^2} \sigma_g \quad (5.53)$$

The standard deviation of the centroid is clearly a linear function of the pixel value noise  $\sigma_g$  and the distance of a pixel from the centre and is therefore dependent on the size of the feature.

### Example 5.1:

A signalised point has the parameters

point diameter: 6 pixel

window size:  $13 \times 13$  pixel

target pixel value: 200

background pixel value: 20

pixel value noise: 0.5 pixel level

The theoretical standard deviation of the centroid is therefore  $\sigma_{x_M} = \sigma_{y_M} = 0.003$  pixel.

In practice, centroid operators can reach an accuracy 0.03–0.05 pixel if circular or elliptical white targets on dark backgrounds are used (see section 5.4.2.6).

### 5.4.2.3 Correlation methods

In image processing, correlation methods are procedures which calculate a similarity measure between a reference pattern (reference image)  $f(x, y)$  and a target image patch extracted from a larger search area within the acquired image  $g(x, y)$ . The position of best agreement is assumed to be the location of the reference pattern in the image.

A common similarity value is the normalised cross-correlation coefficient. It is based on the following covariance and standard deviations (see section 2.3.3.3):

$$\rho_{fg} = \frac{\sigma_{fg}}{\sigma_f \sigma_g} \quad : \text{correlation coefficient} \quad (5.54)$$

where

$$\begin{aligned}\sigma_{fg} &= \sqrt{\frac{\sum[(f_i - \bar{f})(g_i - \bar{g})]}{n}} \\ \sigma_f &= \sqrt{\frac{\sum(f_i - \bar{f})^2}{n}} \quad \sigma_g = \sqrt{\frac{\sum(g_i - \bar{g})^2}{n}}\end{aligned}$$

and

$\bar{f}, \bar{g}$ : arithmetic mean of pixel values

$n$ : number of pixels in the reference pattern

For pattern recognition the reference pattern is successively shifted across a window of the search image according to Fig. 5.24, with the correlation coefficient calculated at each position.

Fig. 5.57 shows the reference image and correlation result for the search for circular targets in Fig. 5.2. Dark spots in the correlation image indicate high correlation results. As expected, correlation maxima occur at bright targets, but medium correlation values are also caused by background noise and edges.

To identify pattern positions in the search image, all  $x, y$  positions with correlation coefficient  $\rho$  greater than a threshold  $t$  are stored. The choice of a suitable threshold  $t$  depends on the image content. For correlating stereo images of similar appearance, the threshold  $t$  can be derived from the auto-correlation function. A suitable threshold lies in the range  $t = 0.5$  to  $0.7$ .

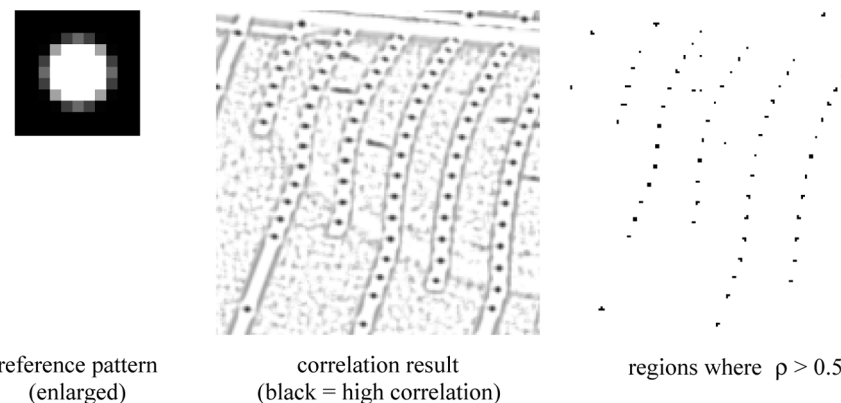


Figure 5.57 Cross correlation (example search image from Fig. 5.2)

Where synthetic patterns (templates) are used for image correlation, optimal correlation values may be lower if the corresponding patch in the search image deviates from the reference image in terms of background or other disturbances.

In the regions where correlation maxima are detected, a further interpolating function applied to the neighbouring correlation values can determine the feature position to subpixel coordinates (see section 5.2.3.6).

The calculation process can be accelerated by prior calculation of the values which are constant in the reference image ( $\sigma_f$  in equation 5.54) and by reducing the image resolution. The pattern matrix can then be shifted across the image in larger steps but this effectively leads to a loss of information. However, a hierarchical calculation based on image pyramids (see section 5.1.3.1) can be performed in which the search results of one stage are used as prior knowledge for the next higher resolution stage.

Cross correlation is a robust method, independent of contrast but requiring a high computational effort. Target patterns can have an almost arbitrary structure. However, differences in scale and rotation, or any other distortions between reference and target image, are not readily modelled and lead directly to a reduction in similarity value (Duda and Hart 1973, Göpfert 1991, Piechel 1991). An image measuring accuracy of about 0.1 pixel can be achieved.

#### 5.4.2.4 Least-squares matching

##### *Principle*

The method of least-squares matching (LSM) employs an iterative geometric and radiometric transformation between reference image and search image in order to minimise the least-squares sum of pixel value differences between the images. The reference image can be a window in a real image which must be matched in a corresponding image (e.g. stereo partner). For a known pixel value structure, the reference image can be generated synthetically and used as a template for all similar points in the search image (least squares template matching).

The geometric fit assumes that both image patches correspond to a plane area of the object. The mapping between two central perspective images can then be described by the projective transformation (2.12). For sufficiently small image patches where the 3D surface giving rise to the imaged area can be assumed to be planar, the 8-parameter projective transformation can be replaced by a 6-parameter affine transformation (2.6). The six parameters are estimated by least-squares adjustment using the pixel values of both image patches as observations. The radiometric fit is performed by a linear pixel value transformation with two parameters. Fig. 5.58 shows the iterative geometric and radiometric transformation of a reference pattern to a target pattern which has been extracted from a larger search area.

The formulation as a least-squares problem has the following implications:

- An optimal solution is obtained if the mathematical model is a reasonably good description of the optical imaging process.
- The mathematical model can be extended if additional information or conditions are available e.g. geometric constraints between images or on the object.
- The approach can be adapted to simultaneous point matching in an unlimited number of images.
- The observation equations are non-linear and must therefore be linearised at given initial values.
- The adjustment is normally highly redundant because all pixel values in the image patch are used as observations to solve for only eight unknowns.

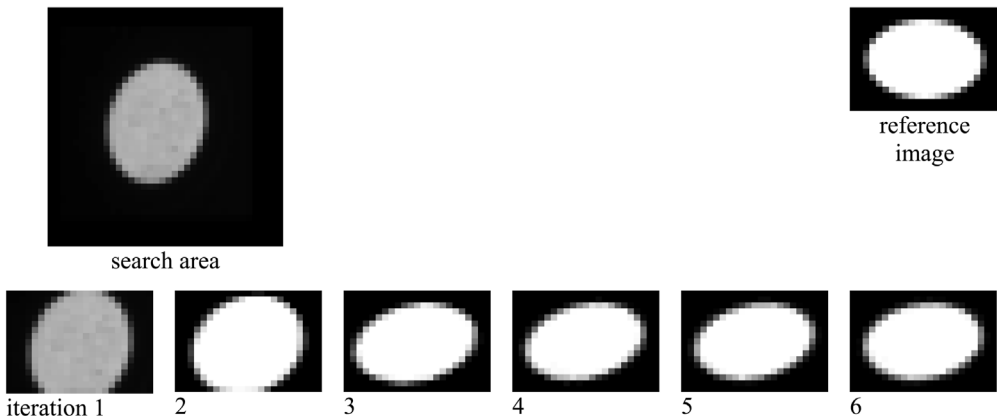


**Figure 5.58** Iterative transformation of an image patch

- Accuracy estimates of the unknowns can be derived from the covariance matrix. Internal quality measures are therefore available which can be used for blunder (gross error) detection (see section 2.3.4), quality analysis and post-processing.

Least-squares matching was developed in the mid eighties for digital stereo image analysis and is now established as a universal method of image analysis (Förstner 1982, Ackermann 1983, Gruen 1985). In two-dimensional image processing it can, in addition to single point measurement, be applied to edge extraction and line following. For three-dimensional object reconstruction it can be configured as a spatial intersection or bundle triangulation and also integrated into the determination of object surface models and geometric elements.

#### Mathematical model

Given two image patches  $f(x, y)$  and  $g(x, y)$ , identical apart from a noise component  $e(x, y)$ <sup>1</sup>:

$$f(x, y) - e(x, y) = g(x, y) \quad (5.55)$$

For a radiometric and geometric fit, every pixel value at position  $(x, y)$  in the reference image  $f_i$  is expressed as the corresponding radiometrically and geometrically transformed pixel value  $g_i$  at position  $(x, y)$  in the search image as follows:

$$\begin{aligned} f_i(x, y) - e_i(x, y) &= r_0 + r_1 g_i(x', y') & i = 1, \dots, n \\ x' &= a_0 + a_1 x + a_2 y & n = pq \quad (\text{window size}) \\ y' &= b_0 + b_1 x + b_2 y & n \geq 8 \end{aligned} \quad (5.56)$$

Both translation parameters  $a_0$  and  $b_0$  are of major importance as they define the relative shift between reference image and search image. Coordinates  $x', y'$  are non-integer values and so the corresponding pixel values must be appropriately interpolated e.g. using bilinear interpolation (see section 5.3.2).

The observation equation (5.56) must be linearised since the image function  $g(x', y')$  is non-linear. In summary the linearised correction equations are given by (ignoring the index  $i$ ):

<sup>1</sup> The notation is adapted from Gruen (1996).

$$\begin{aligned} f(x, y) - e(x, y) = & g^0(x, y) + g_x da_0 + g_x x da_1 + g_x y da_2 + \\ & + g_y db_0 + g_y x db_1 + g_y y db_2 + r_0 + r_1 g^0(x, y) \end{aligned} \quad (5.57) \quad 369$$

The partial differentials are given by the pixel value gradients (see section 5.2.3.1):

$$g_x = \frac{\partial g^0(x, y)}{\partial x} \quad g_y = \frac{\partial g^0(x, y)}{\partial y} \quad (5.58)$$

It is convenient and sufficient for most purposes to set initial parameter values as follows:

$$\begin{aligned} a_0^0 = a_2^0 = b_0^0 = b_1^0 = r_0^0 = 0 \\ a_1^0 = b_2^0 = r_1^0 = 1 \end{aligned} \quad (5.59)$$

If the transformation parameters are written as the vector of unknowns  $\hat{\mathbf{x}}$ , the partial derivatives as the design matrix  $\mathbf{A}$  and the pixel value differences between reference image and search image as the vector of observations  $\mathbf{l}$ , then the linearised correction equations are given by:

$$\underset{n,1}{\mathbf{l}} + \underset{n,1}{\mathbf{v}} = \underset{n,u}{\mathbf{A}} \underset{u,1}{\hat{\mathbf{x}}} \quad (5.60)$$

where

$$\underset{u,1}{\hat{\mathbf{x}}}^T = [da_0, da_1, da_2, db_0, db_1, db_2, r_0, r_1]$$

$$\hat{\mathbf{x}} = (\mathbf{A}^T \mathbf{P} \mathbf{A})^{-1} (\mathbf{A}^T \mathbf{P} \mathbf{l})$$

$$\hat{s}_0 = \sqrt{\frac{\mathbf{v}^T \mathbf{P} \mathbf{v}}{n-u}}$$

$n$ : number of observations = number of pixels in window

$u$ : number of unknowns (8)

It is usual to give all observations equal weight by setting  $\mathbf{P} = \mathbf{I}$ . The adjustment equations must be solved iteratively. In every iteration the unknowns are corrected. This leads to new pixel value differences between search image and transformed (rectified) reference image, until the least-squares sum of the corrections is less than a predefined threshold.

During computation the estimated parameters should be tested for significance. Depending on image content i.e. the similarity between reference and search image and the accuracy of initial values, the chosen transformation model (5.56) may have to be simplified or extended in successive iterations. This effect can be demonstrated by the least-squares matching of an elliptical pattern to a circular target in the search image. For this purpose the affine transformation is over-parameterised because rotation and scaling can either be modelled by a shear angle  $\beta$  and different scales in  $x$  and  $y$ , or equivalently by a global rotation  $\alpha$  and a scale factor (Fig. 5.59). In this case a 5-parameter transformation without a parameter for shear should be used. In addition it is useful to compute the geometric parameters first, with radiometric coefficients included in the final iterations.

#### *Quality of least-squares matching*

The adjustment equations for least-squares matching are usually highly redundant. For example, a window size of  $21 \times 21$  pixels generates  $n = 441$  observations for only  $u = 8$  unknowns.

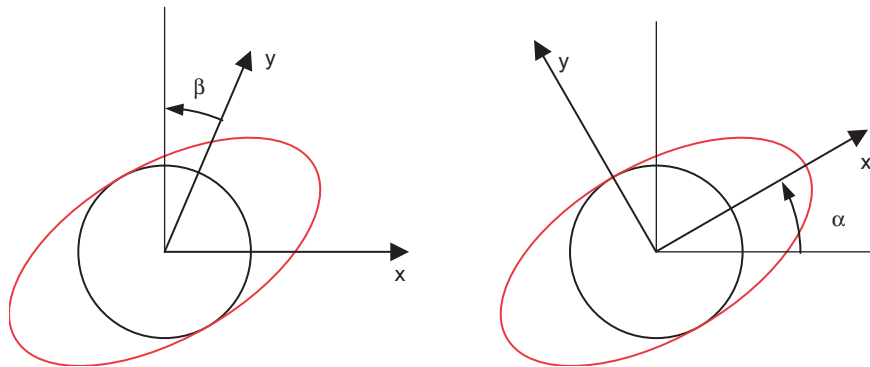


**Figure 5.59** Transformation of a circle into a rotated ellipse

Pixel level (commonly grey level) gradients are used in the linearised correction equations (5.57), and a solution exists only if enough image structures (edges) are available in the matched windows. For homogeneous image patches the normal system of equations is singular.

The approach requires approximate initial values, especially for the shift coefficients  $a_0$  and  $b_0$ . As a rule of thumb, the approximate window position should not be displaced more than half the window size from the desired point. Approximate values can be derived from a previous segmentation process or from known object geometry and orientation data.

After solving the system of adjustment equations (5.60), any residuals describe the remaining pixel value differences between reference image and adjusted search image which are not described by the mathematical model.

$$v_i = f_i(x, y) - \hat{g}_i(x, y) \quad (5.61)$$

They are a measure of the noise level in the image as well as the quality of the mathematical model.

The calculated cofactor matrix  $\mathbf{Q}_{ll}$  can be used to judge the quality of parameter estimation. Similarly to (2.89), the *a posteriori* standard deviation of estimated parameter  $j$  is given by:

$$\hat{s}_j = \hat{s}_0 \sqrt{q_{jj}} \quad (5.62)$$

where

$$q_{jj} : \text{diagonal element of } \mathbf{Q}_{ll}$$

The standard deviations of parameters  $a_0$  and  $b_0$  can reach high accuracies of the order of 0.01–0.04 pixel if there is good similarity between reference and search image. However, the standard deviation is only an analytical error estimate. The example in Fig. 5.60 shows the result of a least-squares matching with 5 geometric and 2 radiometric parameters. Standard deviations of shift parameters for the good-quality search image are less than 0.02 pixel. For low quality images standard deviations can still be of the order of 0.08 pixel, although the centre coordinates are displaced by 0.29 pixel and –0.11 pixel with respect to the non defective optimum point.

Using blunder detection as explained in section 2.3.4 it is possible to eliminate a limited number of gross errors in the observations. Here, blunders refer to pixels whose pixel values are caused, for example, by occlusions or other artefacts, and are not described by the functional model. If the adjustment additionally tests for the significance of parameters, and if non-significant

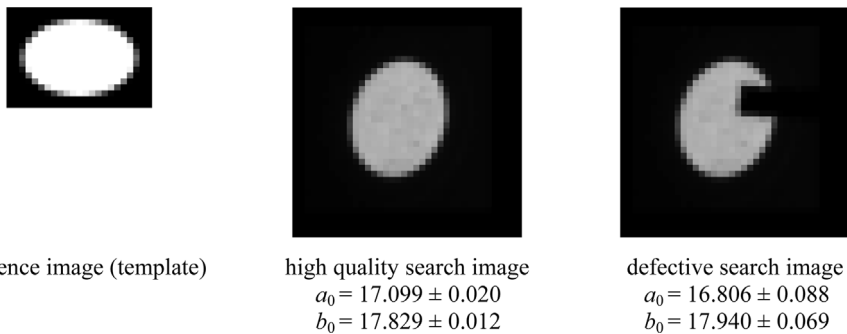


**Figure 5.60** Least-squares matching (5+2 parameters): shift parameters with standard deviations

parameters are eliminated automatically, then least-squares matching becomes an adaptive, self-controlled method of point measurement.

The least-squares matching algorithm described above can be extended by the integration of simultaneous processing of multiple images (multi-image matching) and by the introduction of geometric constraints (epipolar geometry), as described in section 5.5.4.2. For further references see Baltsavias (1991) and Maas *et al.* (1993).

#### 5.4.2.5 Structural measuring methods

Structural measuring methods extract edges in the image which are relevant to the object and reconstruct its geometry with the aid of mathematically defined shapes.

##### *Circular and elliptical features*

In general, circular objects are imaged as ellipses. To a first approximation the ellipse centre corresponds to the projected circle centre (see section 3.4.1.1). For this purpose the star operator (Luhmann 1986a) or the Zhou operator (Zhou 1986) have been proven to be effective. The centre of the ellipse is determined in several steps:

1. Definition of a search window based on a given approximate position
2. Extraction of edge points (ellipse boundary)
3. Calculation of ellipse parameters

The star operator determines points on the ellipse by edge detection (e.g. according to section 5.2.3) along search lines radiating from an approximation position inside the ellipse (Fig. 5.61, Fig. 5.62). These search lines intersect the ellipse at favourable angles and pixel values must be appropriately interpolated along the lines.

The coordinates of the extracted edge points are subsequently used as observations for calculating the parameters of a best-fit ellipse (see section 2.4.1.3). Individual false edge points can be eliminated by blunder detection. Of the five ellipse parameters the centre coordinates can be directly used. However, they depend on the initial approximate centre position and should therefore be used as improved starting values for a further iteration until changes in the centre coordinates are below a threshold value.

The Zhou operator makes use of conjugate ellipse diameters (see section 2.4.1.3). Ellipse diameters are straight lines connecting mid points of parallel chords. The intersection point of conjugate diameters corresponds to the ellipse centre. In the image the ellipse edge points are determined within rows and columns and the corresponding middle point is calculated. Two

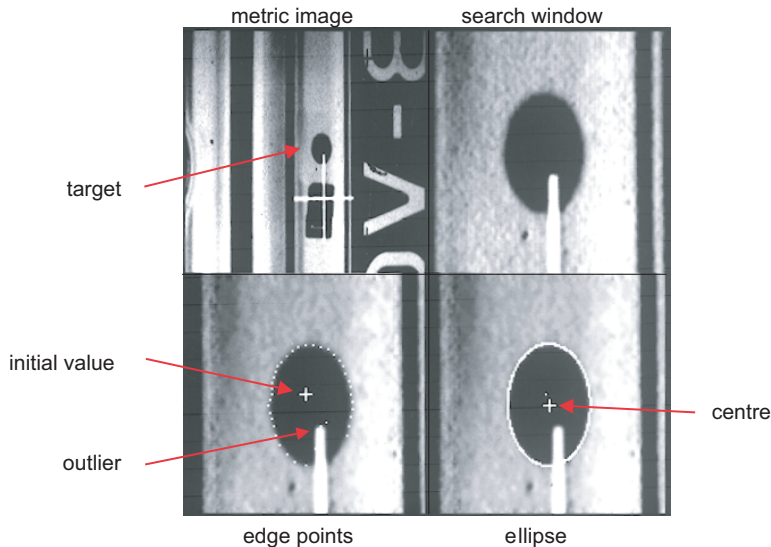


**Figure 5.61** Procedure for ellipse measurement

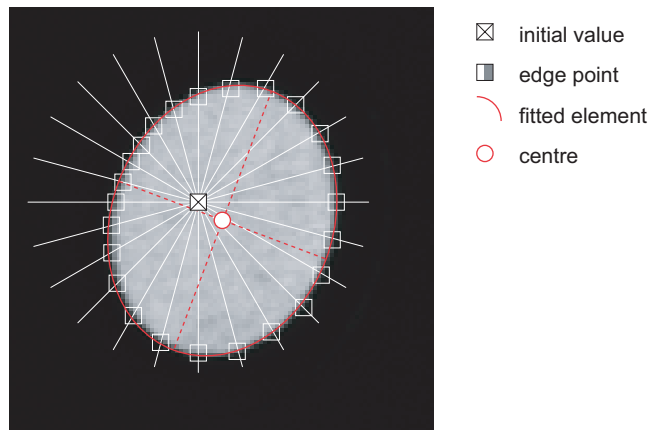


**Figure. 5.62** Principle of the star operator

regression lines are determined for the middle points belonging to the diameters with intersection point corresponding to the desired ellipse centre (Fig. 5.63).

This method of ellipse measurement requires good quality targets. A small number of defective edge points can be handled by robust blunder detection within the ellipse or line adjustment. There are limits to the measurement of damaged or occluded targets (e.g. Fig. 3.119) as the number of false edge points increases. Circular targets cannot be correctly measured by ellipse approximation if they are located on non-planar surfaces (Fig. 5.64).

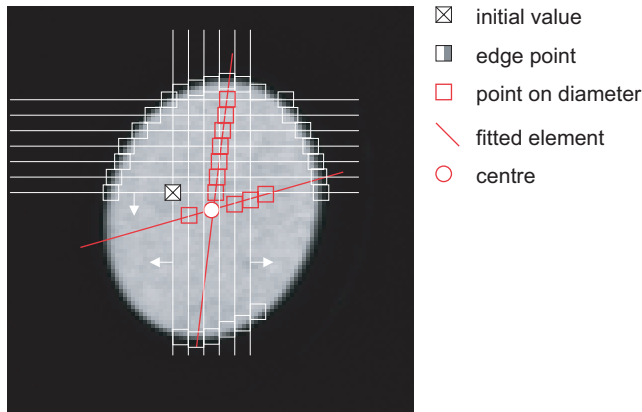


**Figure 5.63** Principle of Zhou ellipse operator

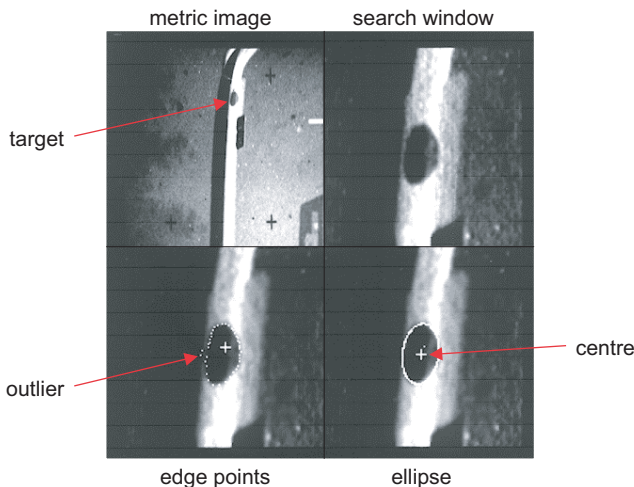


**Figure 5.64** Example of ellipse measurement on curved surface

### Cross-shaped features

Cross-shaped features (e.g. reseau crosses, object corners) can be measured in a similar way to ellipse measurement by edge detection. Here the objective is also to extract the relevant pixel value edges which define the cross.

For upright crosses (see example in Fig. 5.56c) the centre points of the bars are extracted along rows and columns, with the central region ignored. As with the Zhou operator, a regression line is fitted to the centre points of each bar. The intersection point of both lines defines the centre of the cross.

Arbitrary rotated crosses can only be reliably measured by the above algorithm if the extracted line points are analysed in order to correctly assign them to the appropriate cross bar. A rotation-invariant method is provided by the ring operator (Luhmann 1986) which extracts edge points within concentric rings around the approximate initial centre point (Fig. 5.65).

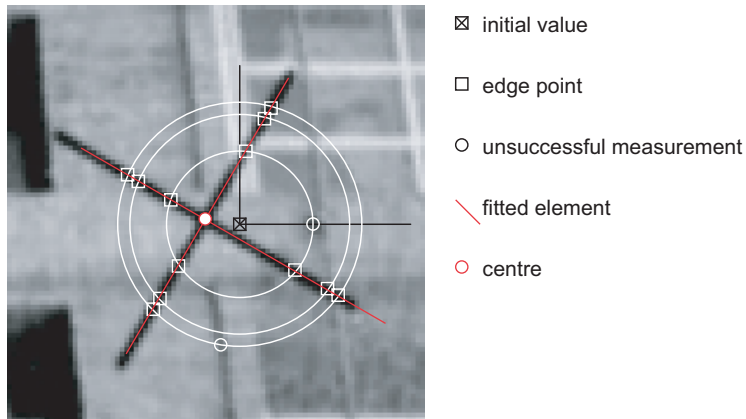


**Figure 5.65** Principle of the ring operator

Extracted edge points within a ring are initially defined by polar coordinates (radius and arc length). These are easily transformed into Cartesian coordinates to which regression lines can be fitted.

Measurements based on edge detection have the advantage that feature and background can be separated relatively easily and the only image points used are those which describe the actual shape of the feature. As an example, imaged reseau crosses are often disturbed by background structures. False edge points can be detected and eliminated *a priori* by a classification of image gradients (sign and magnitude). Any remaining blunders can be identified as outliers on the regression line.

#### 5.4.2.6 Accuracy issues

The location accuracy of single point features can be assessed as follows:

- Comparison with nominal coordinates of synthetic reference features

Single point features with a regular geometric structure, variable centre coordinates, shape parameters and contrast, can be generated synthetically (Fig. 5.66). These can be analysed

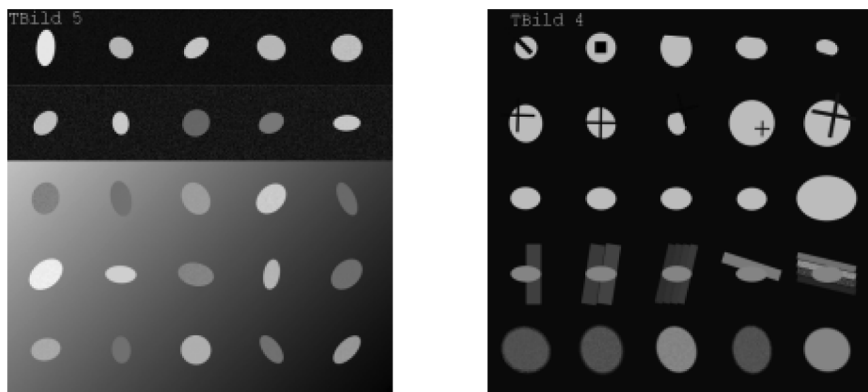


**Figure 5.66** Synthetic patterns for testing single point measurement

after known arbitrary subpixel displacements are applied, for example, by geometric transformations and appropriate pixel value interpolations. Accuracy analysis using synthetic features is particularly useful for testing the capabilities of an algorithm.

- Analytical error analysis of adjustment

If the centre of a feature is calculated by adjustment (e.g. by least-squares matching or a best-fit ellipse) standard deviations and reliability figures can be computed for the centre coordinates (Trinder 1989, Shortis *et al.* 1995). However, these only indicate the precision to which the chosen mathematical model fits the observations supplied, such as pixel values or edge points (see section 5.4.2.4), and they effectively measure the quality of the model.

- Analysis of bundle adjustment

Multi-image bundle adjustment can offer the possibility of a more rigorous accuracy assessment which takes into account all influences in the measurement process (image acquisition system, digitisation, point detection operator, mathematical model). This can be achieved, for example, by calibration against a test field of high-accuracy reference points. The image residuals remaining after the adjustment can be interpreted as a quality measure for the target point accuracy. Note though the residuals are also potentially influenced by systematic effects that are not accounted for in the functional model. Ultimately however, only independently measured reference points, distances or surface shape provide a strictly rigorous method of analysing point measurement accuracy (see sections 4.3.5, 6.6).

Many comparative investigations of different measuring algorithms applied to synthetic and real test images have shown the potential of digital point measurement.

Measurement resolution is limited to about 1/1000–1/500 pixel if adjustment methods (least-squares matching, ellipse operators) are applied to the localisation of appropriately sized and undamaged synthetic features. This result corresponds to the theoretical positioning accuracy of edge-based operators (see section 5.2.3.6).

For real imagery with well exposed and bright elliptical targets, accuracies of 1/50–1/20 pixel can be achieved if least-squares operators or adaptive centroid operators are applied to multi-image configurations. Ellipse measurement based on edge detection tends to be slightly more accurate than least-squares matching and centroid methods if image noise increases or distinct target image quality related blunders occur.

A significant factor in determining point accuracy is the size (diameter) of imaged points. The optimum target size ranges between about 5 and 15 pixels in diameter. Smaller points do not provide enough information, which limits the localisation accuracy of matching procedures or edge-oriented operators. Larger point diameters result in larger numbers of observations but the number of significant edge points increases only linearly while the number of pixels in the window increases quadratically. In addition, disturbances in the image are more likely and the centre of the ellipse is displaced with respect to the actual centre of the target circle as it increases in size (see section 3.4.1.1).

Fig. 5.67 shows the empirical relationship between target size and achievable point accuracy (illustration not scaled), together with typical application areas for different operators. As target size increases, the function converges to an accuracy of about 0.005 pixel.

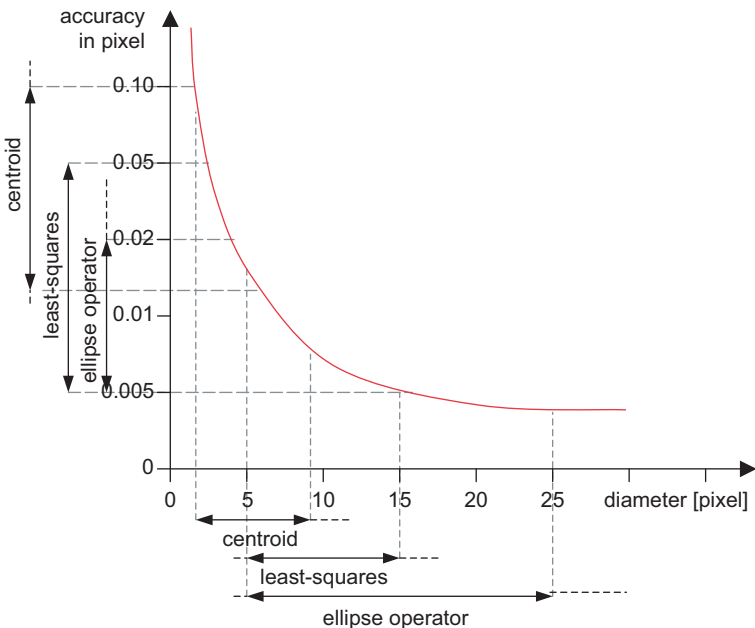


**Figure 5.67** Practical use and accuracy potential of different point measurement operators as a function of target diameter (y axis not to scale)

### 5.4.3 Contour following

Raster-to-vector conversion not only leads to a significant reduction in data but also enables the description of symbolic and topological information. One method of conversion is contour following where the objective is to create vector data structures by combining connected edge or line points.

The initial result of contour following is a series of point coordinates. Integer contour coordinates can be stored, for example, using N8 connectivity (section 5.1.2) in which the direction code of subsequent pixels is recorded. Floating point coordinates with subpixel resolution can be stored as point lists. Start and end points, crossing and divisions can be described by additional attributes within the point list.

There are different approaches to contour following which differ mainly in terms of the required *a priori* knowledge about the contour. If information is available about start and end points, or the approximate contour path, the extraction of contour points by edge detection can be simplified and accelerated. Contour following without any *a priori* knowledge requires processing of the complete image, the analysis of connected pixels and the elimination of false image contours, caused by noise for example.

Two algorithms selected from a large variety of published methods are presented here for illustration.

#### 5.4.3.1 Profile-driven contour following

Assume the starting point and direction of a single contour are known e.g. by interactive input or by calculated image coordinates. Contour points are extracted within pixel value profiles perpendicular to the current contour direction. Within these cross profiles line or edge points are extracted to subpixel resolution according to the methods described in section 5.2.3 (Fig. 5.68).

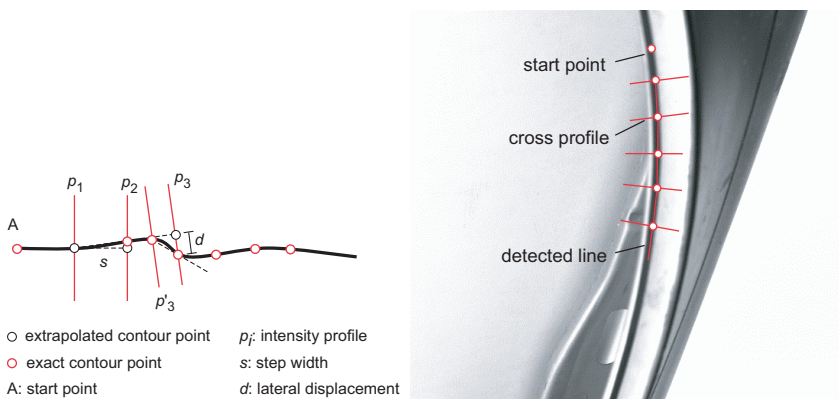


**Figure 5.68** Principle and application of profile-driven contour following

From a minimum of two contour points extracted in this way, the approximate position of the next cross profile  $p_i$  is estimated. The sampling width  $s$  along the contour can be adjusted by evaluating the lateral displacement  $d$  of the next edge point. If the displacement exceeds a certain threshold, the width is reduced and a new cross profile  $p'$  is measured. This approach leads automatically to a denser point distribution along contours with higher curvatures.

Geometric and radiometric variations along the contour e.g. contrast changes due to background differences, can be determined by analysing and comparing a profile's pixel values with previously measured profiles. Profile-driven contour following can therefore adaptively determine the current contour path. Fig. 5.68 illustrates the principle using the example of a form line on a car body component.

#### 5.4.3.2 Contour following by gradient analysis

Given a gradient image (e.g. Sobel operator, section 5.2.3.1) the window at an arbitrary approximate position is analysed. If the magnitude of the gradient exceeds a threshold, the next window position along the current contour path is searched. This process is repeated until a termination criterion determines that there is no suitable further window to be analysed. Of the numerous possible strategies for contour following, the following two methods are outlined:

##### *Analysis of gradient direction*

Edge detection generates a pixel value image of gradient magnitudes and a corresponding image of gradient directions (see example in Fig. 5.31). The following strategy can be used for contour following:

1. if  $\text{grad}(x, y) > t$ , then gradient magnitude > threshold
2. mark the contour point  $P(x, y)$   $P(x, y)$  is permitted only once as a contour point
3. proceed with sample width  $s$  in gradient direction  $\phi + 90^\circ$  to  $x + \Delta x, y + \Delta y$  contour must be perpendicular to the gradient direction
4. if  $\text{grad}(x, y)$  is similar to  $\text{grad}(x + \Delta x, y + \Delta y)$ , then set  $x = x + \Delta x$  and  $y = y + \Delta y$  and proceed with step 2; otherwise: reduce step width  $s$  or terminate contour similarity measure controls integrity of contour

This algorithm follows the contour depending on the gradient direction. Its sensitivity can be controlled by the selection of a suitable similarity measure in step 4 and by geometric constraints e.g. a minimum contour length or a maximum permitted change in direction. In step 4 topological termination criteria can also be introduced, for instance the detection of contours already measured or closed contour lines.

#### *Analysis of gradient environment*

If no information is available about gradient direction, the contour path can be followed by analysing the centroid of the gradients according to (5.52). Within the processed window all gradients above a threshold are used for a centroid calculation. If the contour is characterised by a suitable number of high gradients inside the window, the centroid is shifted in the direction of the contour.

The steps in the procedure are:

1. calculate centroid  $x_s, y_s$  at current position  $x, y$  using (5.52) for all pixels exceeding the threshold
2. set gradient to 0 at contour point  $P(x, y)$   $P(x, y)$  is permitted only once as a contour point and therefore does not participate in any further centroid calculation
3. if  $\text{grad}(x_s, y_s) > t$ , then set  $x = x_s$  and  $y = y_s$  and proceed with step 2, otherwise terminate contour the next contour point must again exceed the threshold

This algorithm is very simple and fast. It does not require any additional parameters except the gradient threshold  $t$  (see further references in Bässmann and Kreyss 1997).

## 5.5 Image matching and 3D object reconstruction

### 5.5.1 Overview

Image matching methods are used to identify and uniquely match identical object features (points, patterns, edges) in two or more images of the object. Matching methods are also required for:

- identification of discrete (signalised) image points for 3D point measurement
- identification of homologous images features for 3D surface reconstruction
- identification and tracking of objects in image sequences

One of the earliest problems in computer vision, which is still a popular research topic today, is automatic matching of corresponding image features. Correspondence analysis is a fundamental requirement in understanding images of spatial scenes and is closely related to human visual perception. While digital image matching of suitably structured object scenes (e.g. using targets or projected patterns) can surpass human performance in some areas (measuring accuracy, processing speed), the analysis of arbitrary object scenes is still an issue of intensive research.

Correspondence analysis can be classified as an ill-posed problem i.e. it is uncertain if any solution exists which is unique and robust with respect to variations in the input data. In principle the following problems may occur when matching arbitrary scenes:

- due to occlusion, an image point  $P_{ij}$  (point  $i$  in image  $j$ ) does not have a homologous partner point  $P_{ik}$

- due to ambiguous object structures or transparent surfaces there are several candidates  $P_{ik}$  for image point  $P_{ij}$
- for regions with poor texture the solution becomes unstable or sensitive with respect to minor disturbances in the image (noise)

Practical solutions assume the following preconditions for object and image acquisition:

- intensities in all images cover the same spectral regions
- constant illumination, atmospheric effects and media interfaces for the period of image acquisition
- stable object surface over the period of image acquisition
- macroscopically smooth object surface
- opaque object surface
- largely diffuse reflection off the surface
- known approximate values for orientation data (image overlap) and object data (geometric and radiometric parameters)

From the wide range of matching techniques, a selection of successful methods is discussed below. These are directly related to geometric surface reconstruction.

Image matching methods are based on a hierarchical strategy (Fig. 5.1). The necessary calibration and orientation data for the input images are usually calculated in advance. Preprocessing includes image enhancement (smoothing, noise reduction, contrast adjustment) and the reduction of resolution (image pyramids).

In the feature extraction step, image features such as distinct points or edges are extracted from the images independently of one another and a large percentage are assumed to be common to all images. For this purpose not only interest operators (section 5.5.2.1) and edge operators (section 5.2.3) are used, but also segmentation methods for the coarse detection of object points (e.g. coded targets, section 3.4.1.2). In addition to the geometric parameters the

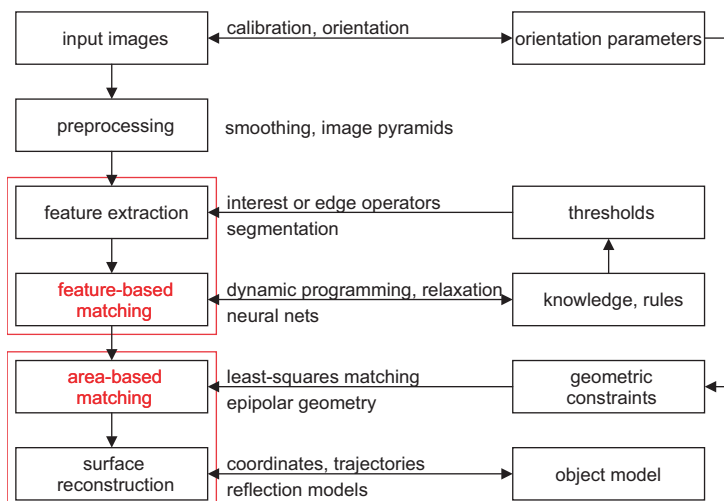


**Figure 5.69** Strategy for image matching

extracted features are characterised by additional attributes (e.g. topological relationships, point numbers).

The subsequent step of feature-based matching attempts to identify as many corresponding features as possible in all images. Additional information in the form of knowledge or rules can be used here to limit the search space and to minimise mismatches. In general the matching of features is the most problematical step in correspondence analysis because the type and extent of additional knowledge may vary widely and success in matching depends directly on the shape and form of the object scene. A successful matching process results in approximate values for homologous image structures.

Area-based precise matching of original pixel values can then be applied to determine corresponding object elements to high accuracy. Correlation and least-squares methods are classified as area-based matching methods. In this step additional geometric information (e.g. epipolar geometry (see section 4.2.5.2), object constraints) can be used to improve accuracy and reliability. 3D object data can be derived from the calculated homologous image elements. Extended object-based matching methods use a geometric and a radiometric object model where the corresponding image regions are determined iteratively. The final result is a structured spatial object description in the form of coordinates, geometric elements or vector fields.

Overviews of image matching can be found in Helava (1998), Maas (1996), Gruen (1996), Klette *et al.* (1996), Heipke (1995), Förstner and Ruwiedel (1992), Haralick and Shapiro (1992), Baltsavias (1991), Marr (1982).

## 5.5.2 Feature-based matching procedures

### 5.5.2.1 Interest operators

Interest operators are algorithms for the extraction of distinctive image points which are potentially suitable candidates for image-to-image matching. Suitable candidates for homologous points are pixel value image patterns (features) which, as far as possible are unique within a limited region and are likely to have a similar appearance in the corresponding image. For each pixel interest operators determine one or more parameters to compute an interest value which can be used for subsequent feature matching. They are typically applied to the matching of digitised aerial images, but are also useful for determining approximate points for surface reconstruction in close-range imagery. However, they are rarely applied when searching for signalised target points.

Criteria for such distinctive candidate features, and the requirements for an optimal interest operator, can be summarised as follows:

- individuality (locally unique, distinct from background)
- invariance in terms of geometric and radiometric distortions
- robustness (insensitivity to noise)
- rarity (globally unique, distinct from other candidates)
- applicability (interest values are suitable for further image analysis)

Within a local window the following is a selection of possible criteria for determining the presence of readily identifiable structures:

- local variance

The pixel value variance in a window can be calculated by equation (5.5). Highly structured image patterns have high variances, homogeneous regions have zero variance. The variance

does not have any geometric meaning, high numbers can also result from edges and therefore it is not suitable as an interest value.

- auto-correlation function

The auto-correlation function results from calculation of the normalised cross-correlation (section 5.4.2.3) of an image patch with itself. If the function shows a sharp maximum it indicates a distinctive image structure which is not repeated locally.

- pixel value surface curvature

If the pixel values in a local region are regarded as a spatial surface (pixel value is analogous to height), distinctive points have a high local curvature in all directions, declining rapidly in the near neighbourhood. Curvature can be calculated by differential operators (section 5.2.3.2) which approximate the second derivative.

- gradient sums (Moravec operator)

This operator (see the following section) computes the squared gradient sums in the four principal directions of a window. If the smallest of the four sums exceeds a threshold a distinct feature is indicated. This approach eliminates single edges which show little structural variation along the edge. The remaining image regions are those which have significant intensity changes in all directions.

- Förstner operator

The Förstner operator calculates the covariance matrix of the displacement of an image window. The corresponding error ellipse becomes small and circular for image features which are distinctive in all directions.

#### *Moravec operator*

The Moravec operator computes the mean square sums of gradients within the four principal directions of a window of size  $p \times q$ . If the interest value  $V$  exceeds a threshold, a distinctive image feature is present which has significant intensity variations in all four directions. Edges with a linear extent do not therefore represent distinctive features in this sense.

$$\begin{aligned}
 V_1 &= \frac{1}{p(q-1)} \sum_{i=-k}^{+k} \sum_{j=-l}^{+l-1} [g(i, j) - g(i, j+1)]^2 \\
 V_2 &= \frac{1}{(p-1)q} \sum_{i=-k}^{+k-1} \sum_{j=-l}^{+l} [g(i, j) - g(i+1, j)]^2 \\
 V_3 &= \frac{1}{(p-1)(q-1)} \sum_{i=-k}^{+k-1} \sum_{j=-l}^{+l-1} [g(i, j) - g(i+1, j+1)]^2 \\
 V_4 &= \frac{1}{(p-1)(q-1)} \sum_{i=-k}^{+k-1} \sum_{j=-l}^{+l-1} [g(i, j+1) - g(i+1, j)]^2
 \end{aligned} \tag{5.63}$$

$$V = \min(V_1, V_2, V_3, V_4)$$

where

$$p = 2k + 1 \quad \text{and} \quad q = 2l + 1$$

The Moravec operator is easy to implement and relatively fast in terms of computation time. However, it is not rotation invariant and its positioning accuracy is limited to 1 pixel.

Fig. 5.70a shows the points in a façade image which have been extracted by the Moravec operator. The reseau crosses, also visible, cannot be used for image matching but they clearly show the characteristics of the operator. Distinct corners are detected and the resulting point coordinates are displaced by around 1–2 pixels with respect to the actual point of interest. Quite a number of significant points are not detected in the brickwork, presumably because they fall just under the chosen global threshold. A more homogeneous point distribution across the image can be achieved if a local threshold is introduced.

#### *Förstner operator*

The Förstner operator (Förstner and Gülch 1987) is based on the assumption that the region around a point  $f(x, y)$  is a shifted and noisy copy of the original image signal  $g(x, y)$  (see equation (5.55)):

$$f(x, y) = g(x + x_0, y + y_0) + e(x, y) \quad (5.64)$$

Linearisation at initial values  $x_0 = 0, y_0 = 0$  gives

$$\mathrm{dg}(x, y) - e(x, y) = \frac{\partial g}{\partial x} x_0 + \frac{\partial g}{\partial y} y_0 = g_x x_0 + g_y y_0$$

where

$$\mathrm{dg}(x, y) = f(x, y) - g(x, y)$$

Using the unknown shift parameters  $x_0, y_0$  and the uncorrelated, equally weighted observations (pixel value differences)  $\mathrm{dg}(x, y)$ , the following normal system of equations for a least-squares estimation is obtained:

$$\mathbf{N}\mathbf{x} = \mathbf{A}^T \mathbf{A}\mathbf{x} = \mathbf{A}^T \mathrm{dg}$$

or

$$\begin{bmatrix} \sum g_x^2 & \sum g_x g_y \\ \sum g_y g_x & \sum g_y^2 \end{bmatrix} \begin{bmatrix} x_0 \\ y_0 \end{bmatrix} = \begin{bmatrix} g_x \mathrm{dg} \\ g_y \mathrm{dg} \end{bmatrix}$$

The normal equation matrix  $\mathbf{N}$  contains the functional model of a displacement of the image window in  $x$  and  $y$ . Its inverse can be interpreted as a variance-covariance matrix whose eigenvalues  $\lambda_1, \lambda_2$  indicate the semi-axes of an error ellipse. Features forming well-defined points are characterised by small circular error ellipses. In contrast, elongated ellipses are obtained for edge points. Unstructured or noisy image features result in large error ellipses.

Based on the parameters

$$w = \frac{\det(\mathbf{N})}{\text{trace}(\mathbf{N})} = \frac{1}{\lambda_1 + \lambda_2} \quad : \text{measure of ellipse size}$$

$$w > 0$$

$$q = \frac{4 \det(\mathbf{N})}{\text{trace}(\mathbf{N})^2} = 1 - \left( \frac{\lambda_1 - \lambda_2}{\lambda_1 + \lambda_2} \right)^2 \quad : \text{measure of roundness of ellipse} \quad (5.67)$$

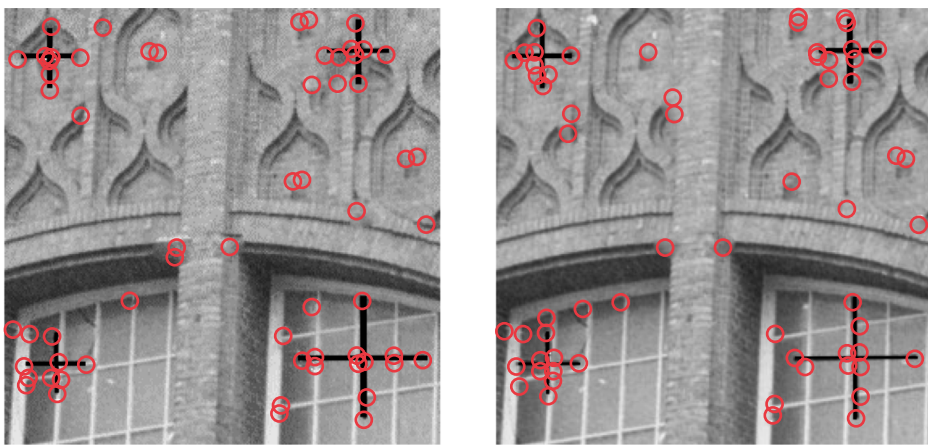
$$0 \leq q \leq 1$$

a distinct point is observed if thresholds  $w_{\min}$  and  $q_{\min}$  are exceeded. Suitable windows are 5 to 7 pixels in size, appropriate thresholds are in the ranges

$$w_{\min} = (0.5 \dots 1.5) \times w_{\text{mean}}, \quad w_{\text{mean}} = \text{mean of } w \text{ for the complete image}$$

$$q_{\min} = 0.5 \dots 0.75$$

Fig. 5.70b shows the result of the Förstner operator after a thinning procedure. As with the Moravec operator, distinct corners are detected but a slight displacement can also be observed here. A more precise point location can be obtained if the unknowns  $x_0, y_0$  in (5.65) are calculated. As expected, several points on the brickwork are detected, whilst other similar features fall below the threshold.



a) Moravec operator (filter size  $5 \times 5$ ,  $v_{\min} = 100$ )

b) Förstner operator (filter size  $7 \times 7$ ,  
 $w_{\min} = 1.0 \times w_{\text{mean}}$ ,  $q_{\min} = 0.5$ )

**Figure 5.70** Point detection with interest operators

### 5.5.2.2 Correspondence analysis

As a result of applying an interest operator, an unstructured list of image points (coordinates and interest values) is generated for each image. Correspondence analysis then has the task of extracting a set of corresponding points based on the stored interest values and coordinates in both lists. The complexity of this process mainly depends on:

- configuration of images (stereo images, convergent multi-image configuration)
- available geometric information (initial values, orientation parameters)
- object's surface structure (projected patterns, variety of edges, occlusions)

The simplest case is given by normal stereo imaging of an object with a simply structured surface and no occlusions (example in Fig. 6.16). The interest value is a suitable matching criterion due to the high similarity between the content of both images. In addition, the search space in the partner image can be considerably reduced if the relative overlap between the images is known.

The matching process becomes much more complicated for convergent multiple images of complex objects with no artificial pattern projection. Point features are not then normally

appropriate for image matching as numerous distinctive image locations are detected at non corresponding image features. In these cases edge extraction and matching is more useful.

A list of potential matches with associated attributes is derived from the extracted point or edge features. Either primitive image features (pixel values, interest values, edge parameters) or derived parameters (e.g. relations) can be used as attributes. The list of candidates, and consequently the possible search space, can be significantly reduced by employing *a priori* knowledge e.g. maximum permitted distances in image space (parallaxes, disparities). The subsequent correspondence analysis solves the matching of homologous features and the elimination of non-corresponding objects, as far as possible by generating a quality measure for each match.

The following four basic procedures are derived from the numerous feature-based matching methods available (overviews given in Förstner 1986, Klette *et al.* 1996, Haralick and Shapiro 1992, Baltsavias 1991):

- Relaxation

The imaged objects to be matched (e.g. points resulting from interest operators applied to two images) are associated with properties (e.g. their interest values from the Förstner operator) which, after appropriate normalisation, can be interpreted as probabilities. In an initialisation stage the probability of a match is computed for every possible pair of candidates. During an internal process these probabilities are altered step by step, taking the properties of adjacent objects into account using a compatibility function in order to arrive at the most probable set of matches. In this way, the relationship between clusters of interest points can be taken into account during the matching process.

- Dynamic programming

This process is most commonly used where the number of possible combinations of candidate features to be matched exceed the ability of the system to make all comparisons. Instead of commencing with the first possible pair of matching features and testing them, dynamic programming starts by considering the properties of the final outcome and defining it with a cost function. The method then minimises the cost function to determine the best set of matches.

Dynamic programming can be used, for example, in a one-dimensional search for corresponding points in epipolar images where image features are directly given by the grey value profile.

- Relational matching

Correspondence analysis by relational matching uses relationships between image objects (e.g. "to left of", "above" etc.) in addition to the features themselves. A matching function is required which takes into account the extracted features and also applies the relationships in the left image to those in the right. An error value for matching is provided by an assessment of the number of left-to-right matches, together with right-to-left matches made with the inverse application of the relationships.

Relational matching is of major importance in high-level object recognition and scene description.

- Matching in image pyramids

Features are extracted at different resolutions in an image pyramid. At the lowest resolution few distinctive features are visible which, for instance, can be matched by one of the above methods. The matching result from a coarser resolution is used as approximate information

for the next higher resolution where additional features are extracted and matched. The approach combines robustness (coarse feature extraction) with precision (precise matching at the highest resolution).

### 5.5.3 Correspondence analysis based on epipolar geometry

The correspondence problem can be greatly simplified if the relative orientation of the images is known. This is the case for fixed stereo vision systems and in close-range applications where image orientation is solved in a separate process, e.g. by application of coded targets. The search space for a corresponding point in the neighbouring image can then be reduced to an epipolar line (see section 4.2.5.2 and Fig. 5.71).

#### 5.5.3.1 Matching in image pairs

Consider first the matching process in an image pair  $B_1, B_2$  (Fig. 5.71). Point  $P''$  corresponding to  $P'$  is located within a small band either side of epipolar line  $k''$ . The band width  $\epsilon$  depends on the uncertainty of the orientation parameters and the image measurement quality of  $P'$ . The search space is strictly reduced to the straight line  $k''$  only for perfect input data. The length of the search space  $l_{12}$  is a function of the maximum depth  $\Delta Z$  in object space (Maas *et al.* 1993).

With increasing number of image points  $n$ , and area  $f$  of the search space, the probability  $P_a$  of ambiguous point matches also increases:

$$P_a = 1 - e^{-\frac{nf}{F}} \quad (5.68)$$

where

- $n$ : number of image points
- $F$ : image area
- $f$ : area of epipolar search space

The total number of ambiguities  $N_a$  for an image pair is given by:

$$N_a = (n^2 - n) \frac{2c\epsilon b_{12}(Z_{\max} - Z_{\min})}{F Z_{\max} Z_{\min}} \quad (5.69)$$

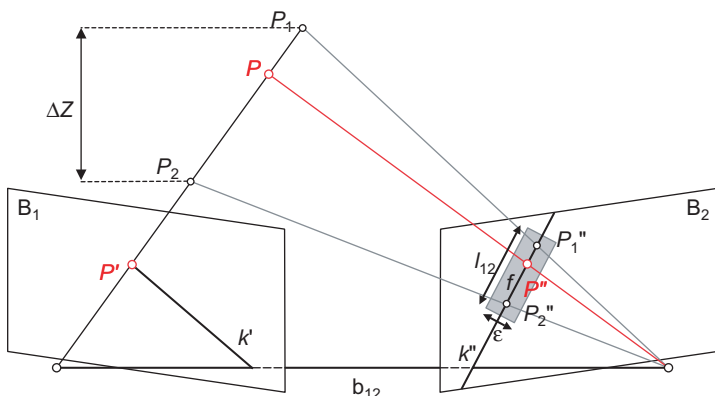


**Figure 5.71** Matching in an image pair based on epipolar lines (after Maas *et al.* 1993)

where

386

- $c$ : principal distance
- $b_{12}$ : base length between image  $B_1$  and image  $B_2$
- $\epsilon$ : width (tolerance) of search space
- $Z_{\min} < Z < Z_{\max}$ : depth of object

It therefore increases

- quadratically with the number of image points
- linearly with the length of the epipolar lines and with the base length and approximately linearly with object depth
- linearly with the width of the search space

### Example 5.2:

Consider an image pair (Kodak DCS 420) with parameters  $c = 18$  mm,  $F = 18 \times 28$  mm<sup>2</sup>,  $b_{12} = 1$  m,  $Z_{\max} = 3$  m,  $Z_{\min} = 1$  m and  $\epsilon = 0.02$  mm. Depending on the number of image points  $n$  the following ambiguities result:

$n = 50$ :	$N_a = 2$
$n = 100$ :	$N_a = 10$
$n = 250$ :	$N_a = 60$
$n = 1000$ :	$N_a = 950$

The example above shows that epipolar geometry leads to a match if the number of image points is relatively small. It depends mainly on the application as to whether ambiguities can be reduced by an analysis of interest values, a reduction of object depth using available approximations or by a reduced search width.

#### 5.5.3.2 Matching in image triples

Ambiguities can be considerably reduced if the number of images is increased. Fig. 5.72 illustrates the matching principle for a configuration of three images. Starting with an image

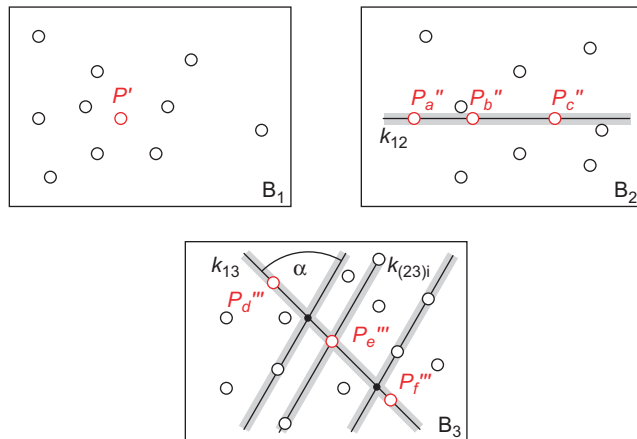


Figure 5.72 Matching in image triples based on epipolar lines (after Maas *et al.* 1993)

point  $P'$  in image  $B_1$ , the corresponding epipolar lines  $k_{12}$  and  $k_{13}$  can be calculated for the other images. For both partner images ambiguities are represented as candidates  $P_a''$ ,  $P_b''$ ,  $P_c''$  in image  $B_2$  and  $P_d''$ ,  $P_e''$ ,  $P_f''$  in image  $B_3$ . The homologous points of  $P'$  cannot therefore be uniquely determined.

If, in addition, the epipolar lines  $k_{(23)i}$  are calculated in image  $B_3$  for all candidates  $P_i$  in image  $B_2$ , it is most likely that only one intersection point with  $k_{13}$  is located close to a candidate in image  $B_3$ , in this case  $P_e'''$ . The search space is therefore restricted to the tolerance region of the intersection points. The number of possible ambiguities for three images is given by:

$$N_a = \frac{4(n^2 - n)\epsilon^2}{F \sin \alpha} \left( 1 + \frac{b_{12}}{b_{23}} + \frac{b_{12}}{b_{13}} \right) \quad (5.70)$$

where

- $n$ : number of image points
- $F$ : image area
- $\epsilon$ : width (tolerance) of the search space
- $\alpha$ : angle between epipolar lines in image  $B_3$
- $b_{jk}$ : base length between image  $B_j$  and image  $B_k$

Ambiguities are minimised if the three cameras are arranged in a equilateral triangle such that  $b_{12} = b_{13} = b_{23}$  and  $\alpha = 60^\circ$ . In the numerical example above ( $n = 1000$ ) the number of ambiguities is then reduced to  $N_a = 10$ .

### 5.5.3.3 Matching in an unlimited number of images

The method can be extended to a virtually unlimited number of images. In order to search for homologous points of  $P'$  in all other images, a combinatory approach must be applied which investigates all likely combinations of epipolar line intersections. The following matching strategy represents a practical solution for limiting the required computational effort (Maas 1996):

1. selection of an image point in image  $B_i$
2. search for candidates on epipolar lines in images  $B_{i+j}$ , until at least 1 candidate is found
3. verification of all candidates by calculating their object coordinates using spatial intersection followed by back projection into all images  $B_{i+j+1} \dots B_n$
4. counting all successful verifications i.e. the calculated (back projected) image position must contain an image point
5. acceptance of the candidate possessing the significantly largest number of successful verifications.

This approach offers some major advantages:

- an arbitrary number of images can be processed
- an object point need not be visible in every image e.g. due to occlusions or limited image format
- interest values can optionally be used in order to reduce the number of candidates
- approximate values of image points are not required i.e. there are no pre-conditions for the continuity (smoothness) of the object surface nor the spatial distribution of object points.

### 5.5.4 Area-based multi-image matching

The least-squares matching approach introduced in section 5.4.2.4 for two image patches (reference and search image) can be extended by the following features:

- simultaneous matching of one point in multiple images (multi-image matching)
- simultaneous matching of multiple points in multiple images (multi-point matching)
- introduction of geometric conditions in image space and object space (multi-image geometrically constrained matching)
- introduction of object models (object-space matching)

#### 5.5.4.1 Multi-image matching

Consider a reference image  $f(x, y)$  and  $m$  search images  $g_i(x, y)$  which are to be matched to the reference image. Equation (5.55) can be extended to multiple images:

$$f(x, y) - e_i(x, y) = g_i(x, y) \quad i = 1, \dots, m \quad (5.71)$$

Here  $e_i(x, y)$  indicates random noise in image  $i$ . In a similar way to least-squares matching, the following adjustment system results:

$$\underset{n,1}{\mathbf{v}} = \underset{n,u}{\mathbf{A}} \underset{u,1}{\mathbf{x}} - \underset{n,1}{\mathbf{1}} \quad (5.72)$$

where

$$\underset{i}{\mathbf{x}}^T = [da_0, da_1, da_2, db_0, db_1, db_2, r_0, r_1]_i \quad i = 1, \dots, m$$

$m$ : number of search images

$n$ : total number of observations

$n = n_1 + n_2 + \dots + n_m$ ;  $n_i$  = number of observations (pixel) in image  $g_i(x, y)$

$u$ : total number of unknowns,  $u = 8m$

The  $m$  parameter vectors  $\underset{i}{\mathbf{x}}^T$  can be determined independently within the system of equations (5.72) because they have no cross connections within the design matrix  $\mathbf{A}$ .

#### 5.5.4.2 Geometric constraints

##### Functional model

The multi-image approach of equation (5.71) enables the simultaneous determination of all matches of a point. However, it does not consider the constraint that all homologous points must correspond to one common object point. This constraint can be formulated by the condition that all homologous image rays, taking account of image orientation parameters, must intersect optimally at the object point (Gruen and Baltsavias 1988).

This constraint is also the basis for the bundle adjustment model (section 4.3.2) where the collinearity equations (4.8) are used. The three-dimensional coordinates of point  $p$  in image  $k$  are given by<sup>1</sup>:

---

<sup>1</sup> Image coordinates have their origin at the principal point and are corrected for distortion.

$$\mathbf{x}'_{pk} = \frac{1}{m_{pk}} \mathbf{R}_k^{-1} (\mathbf{X}_p - \mathbf{X}_{0k})$$

$$\begin{bmatrix} x' \\ y' \\ -c \end{bmatrix}_k = \frac{1}{m_{pk}} \begin{bmatrix} r_{11} & r_{21} & r_{31} \\ r_{12} & r_{22} & r_{32} \\ r_{13} & r_{23} & r_{33} \end{bmatrix}_k \begin{bmatrix} X_p - X_{0k} \\ Y_p - Y_{0k} \\ Z_p - Z_{0k} \end{bmatrix}$$
(5.73)

In simplified notation, the image coordinates  $x'_p, y'_p$  are given by

$$\Delta x'_{pk} = \Delta c_k \left( \frac{k_x}{N} \right)_{pk} = \Delta F_{pk}^x$$

$$\Delta y'_{pk} = \Delta c_k \left( \frac{k_y}{N} \right)_{pk} = \Delta F_{pk}^y$$
(5.74)

Using initial values  $(x'_p, y'_p)^0$  the following non-linear observation equations for the required shifts  $\Delta x'_p, \Delta y'_p$  are derived:

$$\Delta x'_{pk} + F_{pk}^x + x'^0_{pk} = 0$$

$$\Delta y'_{pk} + F_{pk}^y + y'^0_{pk} = 0$$
(5.75)

Here  $\Delta x'_p, \Delta y'_p$  correspond to the shift coefficients  $da_0, db_0$  in equation (5.71). The equations (5.75) establish the relationship between image space and object space. In contrast to the collinearity equations, which only establish the functional relationship between observed image coordinates and unknown point and orientation data, this approach uses as observations the original grey values, in combination with least-squares matching. Additional observation equations can be set up using the parameters in terms  $F_{pk}$  e.g. for the simultaneous calculation of object coordinates  $XYZ$  or for the formulation of geometric constraints (e.g.  $Z = \text{const.}$ ).

#### *Object restrictions*

It is first assumed that the interior and exterior orientation parameters of all images are known e.g. by a prior bundle triangulation. The system of equations (5.75) must be linearised at initial values of the remaining unknowns  $X, Y, Z$ :

$$\Delta x'_{pk} + \frac{\partial F_{pk}^x}{\partial X_p} dX_p + \frac{\partial F_{pk}^x}{\partial Y_p} dY_p + \frac{\partial F_{pk}^x}{\partial Z_p} dZ_p + F_{pk}^{x^0} + x'^0_{pk} = 0$$

$$\Delta y'_{pk} + \frac{\partial F_{pk}^y}{\partial X_p} dX_p + \frac{\partial F_{pk}^y}{\partial Y_p} dY_p + \frac{\partial F_{pk}^y}{\partial Z_p} dZ_p + F_{pk}^{y^0} + y'^0_{pk} = 0$$
(5.76)

In summary, the system of additional observation equations is as follows:

$$\mathbf{w}_{m',1} = \mathbf{B}_{m',3} \hat{\mathbf{y}}_{3,1} - \mathbf{t}_{m',1}$$
(5.77)

where

$$\hat{\mathbf{y}}^T = [dX, dY, dZ]$$

$m'$ : number of images:

$m' = m$ , if no transformation of the reference image is permitted

$m' = m+1$ , if the reference image is also to be transformed e.g. with respect to an artificial template

For the extended system of (5.75) and (5.77) the complete vector of unknowns is given by

$$\bar{\mathbf{x}} = (\mathbf{A}^T \mathbf{P} \mathbf{A} + \mathbf{B}^T \mathbf{P}_t \mathbf{B})^{-1} (\mathbf{A}^T \mathbf{P} \mathbf{l} + \mathbf{B}^T \mathbf{P}_t \mathbf{t}) \quad (5.78)$$

The parameter vector  $\bar{\mathbf{x}}$  consists of the simultaneously calculated displacements of the image patches in  $g_i(x, y)$  as well as the adjusted corrections of the object coordinates. Because of their relationship to the XYZ object coordinates, the image shifts cannot take arbitrary values but are constrained to follow an epipolar line (Fig. 5.73). The influence of this geometric condition can be controlled by the weight matrix  $\mathbf{P}_t$ .

The model in equations (5.76) is appropriate for determining arbitrary 3D object points. In order to measure surface models, some of the coordinate components of the surface points can be fixed.

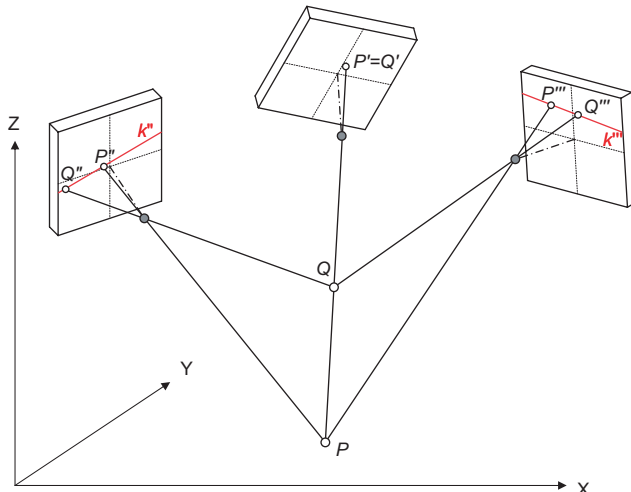


Figure 5.73 Geometric condition of ray intersection

- constant  $X, Y$ :

If the surface points are located on a particular grid of  $XY$  coordinates (e.g. where  $\Delta X = \Delta Y = \text{constant}$ ), corresponding terms can be eliminated from equations (5.76) and only  $Z$ -value adjustments remain:

$$\begin{aligned} \Delta x'_{pk} + \frac{\partial F_{pk}^X}{\partial Z_p} dZ_p + F_{pk}^{X^0} + x'^0_{pk} &= 0 \\ \Delta y'_{pk} + \frac{\partial F_{pk}^Y}{\partial Z_p} dZ_p + F_{pk}^{Y^0} + y'^0_{pk} &= 0 \end{aligned} \quad (5.79)$$

In consequence the normal system of equations becomes simpler. The approach corresponds to the manual measurement of terrain models in stereoscopic plotters. In this case the image shifts do not take place within epipolar lines but on the so-called vertical line locus instead (see section 4.4.2.3).

- constant  $Z$ :

In order to measure contour lines at a given height  $Z = \text{constant}$  only coordinate displacements in the  $X$  and  $Y$  directions are permitted and equations (5.76) reduce to:

$$\begin{aligned} \Delta x'_{pk} + \frac{\partial F_{pk}^X}{\partial X_p} dX_p + \frac{\partial F_{pk}^X}{\partial Y_p} dY_p + F_{pk}^{X^0} + x'_{pk}^0 &= 0 \\ \Delta y'_{pk} + \frac{\partial F_{pk}^Y}{\partial X_p} dX_p + \frac{\partial F_{pk}^Y}{\partial Y_p} dY_p + F_{pk}^{Y^0} + y'_{pk}^0 &= 0 \end{aligned} \quad (5.80)$$

The possibility of restricting particular coordinate components enables surface models to be recorded with respect to specific reference planes or along specified sections through the surface. The (topological) structure of the surface model is therefore defined directly during measurement and not by a later analysis of an unstructured point cloud which could be the result, for instance, of an active projection method (see sections 6.5.1 and 5.5.5.1).

#### *Additional extensions*

The concept of additional observation equations, described above, permits the introduction of further constraints on the adjustment system. The influence of additional observations can be controlled by appropriate weighting from  $p_i = 0$  where the constraint has no effect through to  $p_i = \infty$  where the constraint is strictly enforced.

As examples, additional constraints can be formulated for the following tasks:

- Edge extraction by least-squares matching:

Single edge points can be determined by a suitable edge template (see example in Fig. 5.40). As edges are linear features, an additional constraint can be introduced which forces the template to move in the direction of the gradient i.e. perpendicular to the edge.

- Determination of spatial object contours:

Spatial object contours can be described by geometric elements (straight line, circle etc.) or spline functions. The corresponding analytical parameters can be included as unknowns in a least-squares fit. An example of this approach is the method of LSB snakes (section 4.4.3.3) which combines edge extraction and determination of a B-spline spatial curve (snake) in a single analysis.

- Measurement of point grids:

The least-squares matching concept for a single object point can easily be extended to an unlimited number of points. However, if no geometric relationship between the points exists, then the result is identical to single point matching. Geometric relations can be formulated either by associating points with a common geometric element (e.g. all points belong to a plane or a cylinder), or by defining neighbourhood relationships.

The latter approach can be compared to the interpolation of digital surface models where points on a grid are connected by additional constraints such as minimum surface curvature

(section 3.2.3.5). The approach of multi-patch matching utilises this idea by defining constraints between adjacent grid elements (patches).

- **Bundle concept:**

If the interior and exterior orientation parameters of images are known only approximately, they can be included as unknowns in the least-squares matching. Equation (5.76) is then extended by corresponding differential coefficients of the additional orientation parameters.

### 5.5.5 Matching methods with object models

The matching methods described in the previous sections are mainly based on geometric relationships between images, or between images and object. Although contrast differences are modelled in the least-squares matching by two radiometric parameters they are completely independent of the reflection characteristics of the surface.

In order to create a complete object model it is necessary to combine the geometric object properties (position and shape) with the reflection properties of the surface. This idea is used in various 3D visualisation methods (see section 5.3.3) and can also be used for object reconstruction. The features of such a complete reconstruction method are:

- introduction of a surface reflection model (material characteristics, illumination)
- ray tracing through different media (as a minimum through the atmosphere)
- multi-image adjustment based on least-squares matching
- topological structuring of the surface by surface grid and shape lines

The global objective is the 3D surface reconstruction by simultaneous calculation of all orientation parameters, object point coordinates, geometric element parameters as well as illumination and reflection parameters. Pixel values in multiple images are available as observations, as are initial values of unknowns. The number of parameters is extremely high and the resulting system of equations is correspondingly complex.

#### 5.5.5.1 Object-based multi-image matching

Object-based multi-image matching is based on a relationship between the intensity (colour) value of a surface element  $G_i$  and the pixel values  $g_{ij}$  of the associated images (Fig. 5.74). The pixel values are a function of the orientation parameters  $\mathbf{O}_j$  of an image  $j$  and the surface parameters  $\mathbf{Z}_i$  of an element  $i$ :

$$G_i = g_{ij}(\mathbf{Z}_i, \mathbf{O}_j) \quad i = 1, \dots, m \\ j = 1, \dots, n \quad (5.81)$$

where

$m$ : number of surface elements

$n$ : number of images

In order to solve this system of equations, initial values for the unknown surface and the orientation parameters are required. The difference between the pixel values calculated from the initial values can be regarded as a stochastic value which gives

$$\Delta g_{ij} = G_i^0 - g_{ij}(\mathbf{Z}_i^0, \mathbf{O}_j^0) \quad (5.82)$$

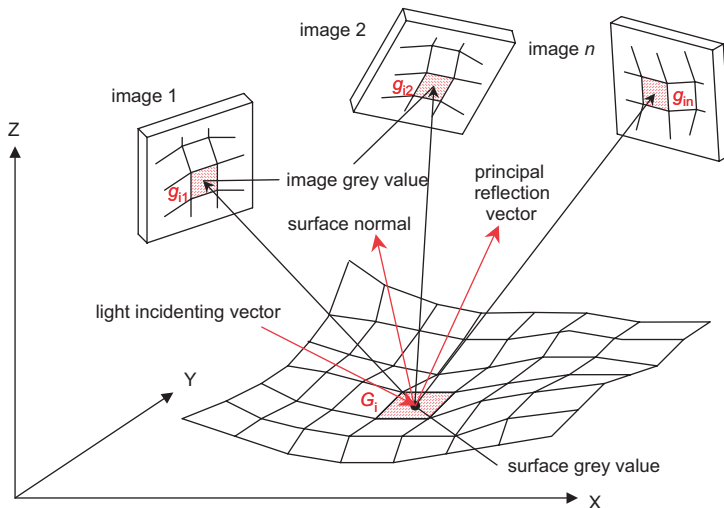


**Figure 5.74** Relationship between intensity value of surface and pixel value of image  
(after Schneider 1991)

The imaged light intensity depends on the properties of the surface material and of the geometric orientation of surface element, light source and imaging sensor (Fig. 5.74) as, for example, described by the Phong illumination model (section 5.3.3.2). Similarly to least-squares matching, the pixel values in the individual images are matched using two radiometric parameters which are dependent on material:

$$\Delta g_{ij} = G_i^0 - \left( r_{1,j}^0 + r_{2,j}^0 g'_{ij}(\mathbf{Z}_i^0, \mathbf{O}_j^0) \right) \quad (5.83)$$

where

$r_{1,j}^0, r_{2,j}^0$ : approximate radiometric correction parameters

$g'_{ij}$ : observed image pixel value:  $g'_{ij} = r_{1,j}^0 + r_{2,j}^0 g_{ij}$

Equation (5.83) can form the observation equation for each pixel value in all images where a specific surface element is visible. Using the substitution

$$r_{2,j} = 1 + r'_{2,j}$$

and re-arranging the linearised correction equations, the following is obtained:

$$\begin{aligned} v_{ij} &= G_i^0 - dG_i - (r_{1,j}^0 + dr_{1,j}) - (r_{2,j}^0 + dr'_{2,j}) g'_{ij}(\mathbf{Z}_i^0, \mathbf{O}_j^0) \\ &\quad - \frac{\partial g'}{\partial \mathbf{Z}} d\mathbf{Z} - \frac{\partial g'}{\partial \mathbf{O}} d\mathbf{O} - g'_{ij}(\mathbf{Z}_i^0, \mathbf{O}_j^0) \end{aligned} \quad (5.84)$$

## The differential coefficients

$$\begin{aligned}\frac{\partial g'}{\partial \mathbf{Z}} &= \frac{\partial g'}{\partial x'} \frac{\partial x'}{\partial \mathbf{Z}} + \frac{\partial g'}{\partial y'} \frac{\partial y'}{\partial \mathbf{Z}} \\ \frac{\partial g'}{\partial \mathbf{O}} &= \frac{\partial g'}{\partial x'} \frac{\partial x'}{\partial \mathbf{O}} + \frac{\partial g'}{\partial y'} \frac{\partial y'}{\partial \mathbf{O}}\end{aligned}\quad (5.85)$$

contain the pixel value gradients  $\partial g'/\partial x'$  and  $\partial g'/\partial y'$ . This approach can therefore only be applied when an appropriate number of edges or structures exists in the images. The remaining differential coefficients  $\partial x'/\partial \mathbf{Z}$  etc. correspond to the derivatives from the space resection and bundle triangulation models (see equation (4.14)).

Now all the relevant parameters are available for an iterative adjustment

$$\mathbf{v} = \mathbf{A}\hat{\mathbf{x}} - \mathbf{l}$$

with observations

$$\mathbf{l} = \mathbf{g}'(\mathbf{Z}^0, \mathbf{O}^0)$$

which leads to a vector of unknowns

$$\hat{\mathbf{x}}^T = (d\mathbf{Z}^T, d\mathbf{O}^T, dr_1^T, dr_2^T, d\mathbf{G}^T) \quad (5.86)$$

The importance of object-based multi-image matching has two aspects. One is the simultaneous determination of all parameters influencing the formation of the image, including the object itself. The other is that the method can be extensively modified by altering object parameters relevant to the application. In this way the following tasks can be solved by use of appropriate functions:

- Measurement of signalised points

Circular targets can be defined as a circle in space (see section 2.4.2.3) whose centre must be determined. An additional transformation converts the coordinates of the plane of the circle into the object coordinate system. The target's pixel values have a radiometric model which is a function of the radius and consists, for example, of a white circle on a black background (Fig. 5.75).

The surface element size should approximately correspond to the size of a pixel in image space. The circle centre in object space is determined ignoring any eccentricities (see section 3.4.1.1).

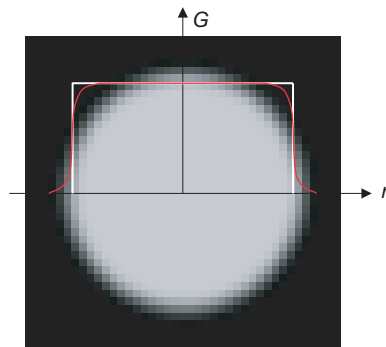


**Figure 5.75** Distribution of smoothed object pixel values for a circular target

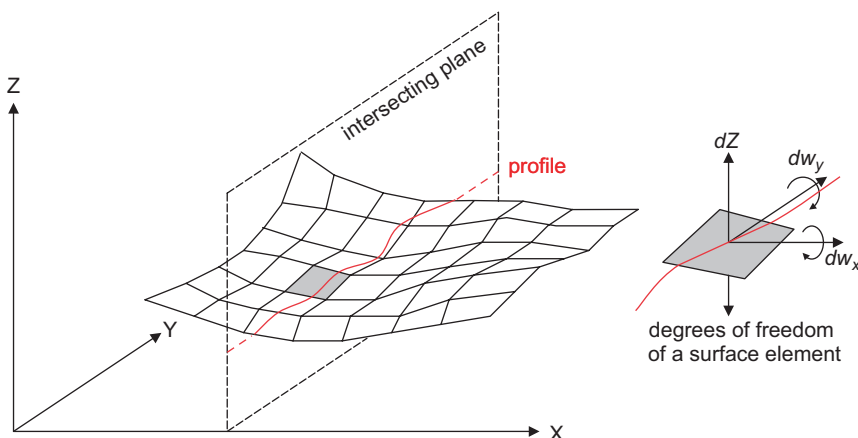


**Figure 5.76** Resulting profile from intersection of section plane and surface

- Measurement of surfaces

Surfaces are recorded as profiles, surface models or free-form surfaces. If the measurement is based on profiles, an arbitrarily oriented section is defined in which the profile is represented by a two-dimensional curve (Fig. 5.76). Within the section a surface element is defined by a tangential plane whose degrees-of-freedom are reduced to two rotations and a shift within the section plane.

- Bundle triangulation

The system of equations (5.83), extended to determine 3D circles and additional parameters of interior orientation (simultaneous calibration), leads logically to an object-based bundle triangulation for photogrammetric images with circular targets.

- Orthophoto production

Object-based multi-image matching can also be applied to the production of ortho-photos where the calculated pixel values of the object are used in this case for image generation. The required 3D object model can be estimated within the multi-image matching process itself, or it can be generated from other sources. In principle this approach enables orthophotos to be generated from an arbitrary number of images, with occlusions and radiometric variations no longer affecting the result.

Object-based multi-image matching, briefly described here, has considerable potential for wide application and makes use only of the original image pixel values. Feasibility in principle and some test applications have been demonstrated but so far practical use has been limited by the high computational effort needed to solve the large systems of normal equations. The generation of appropriate initial values for the unknown parameters is, in addition, a non trivial problem.

### 5.5.5.2 Multi-image matching with surface grids

Surface elements calculated by object-based multi-image matching (section 5.5.5.1) are independent of their adjacent elements in terms of geometry and radiometry. However, this assumption is invalid for piecewise smooth surfaces. With the exception of discontinuities

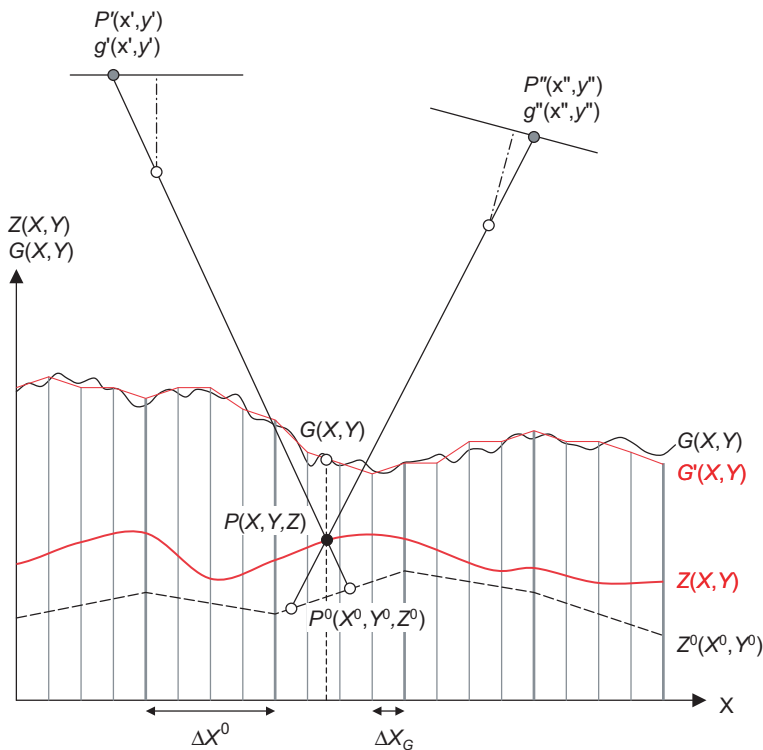


**Figure 5.77** Interpolation and projection of surface and reflection model (after Wrobel 1987)

(breaklines), adjacent object elements can be connected by radiometric and geometric interpolation functions. The above approach can therefore be extended by coefficients of piecewise linear functions for both the radiometric model and the geometric model (terrain model). For this purpose the surface is represented by triangular or quadrilateral patches (facets) within which linear or bilinear interpolation can be applied.

Fig. 5.77 illustrates the principle. The required surface  $Z(X, Y)$  consists of pixel values  $G(X, Y)$ . Photographic recording of surface points  $P(X, Y, Z)$  results in image points  $P'(x', y')$  with pixel values  $g'(x', y')$ . Based on an approximately known height model  $Z^0(X^0, Y^0)$ , surface points are interpolated e.g. on a fixed grid with separations  $\Delta X^0 = \Delta Y^0 = \text{constant}$ . The surface reflection model  $G'(X, Y)$  is calculated on a dense grid width  $\Delta X_G, \Delta Y_G$  (Fig. 5.78).

The grid width of the reflection model should be adjusted to the maximum spatial frequency in object space. If this information is missing the grid width should be chosen with respect to the mean pixel size  $\Delta x', \Delta y'$  in the images:

$$\begin{aligned} \Delta X_G &\geq m\Delta x' \\ \Delta Y_G &\geq m\Delta y' \end{aligned} \tag{5.87}$$

where  $m$  is the image scale number.

For the height model the grid width should adapt to the local object shape in order to achieve an reasonable result. For example, grid width can be reduced on object breaklines. Usually a square grid is chosen where

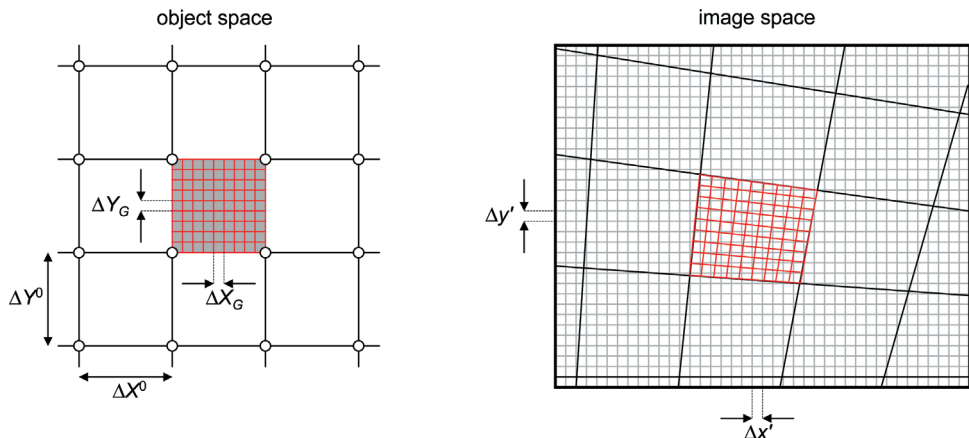


**Figure 5.78** Projection of object facets into image space

$$\Delta X^0 = \Delta Y^0 > \Delta X_G = \Delta Y_G \quad (5.88)$$

The introduction of radiometric facets with corner point grey values  $G(X_k, Y_l)$  leads to

$$G(X, Y) = \sum_{kl} a_{kl}(X, Y) G(X_k, Y_l) \quad (5.89)$$

where  $\sum_{kl} a_{kl} = 1$ .

Correspondingly, coefficients for the height model's geometric facets  $Z(X_r, Y_s)$  are introduced to give:

$$Z(X, Y) = \sum_{rs} b_{rs}(X, Y) Z(X_r, Y_s) \quad (5.90)$$

where  $\sum_{rs} b_{rs} = 1$ .

The system of equations (5.83) is extended by equations (5.89) and (5.90). Coefficients  $a_{kl}$  and  $b_{rs}$  are determined by the nodal point values of each object grid or triangle facet.

Object-based multi-image matching based on object facets offers additional benefits:

- By choosing suitable weights for the coefficients, the smoothness of a surface can be controlled so that image matching can bridge critical areas containing intensity distributions where texture is not present.
- Occlusions and discontinuities can be handled by correspondingly detailed object surfaces or 3D models.

Further references for object-based multi-image matching and surface include: Bösemann 1994, Schlüter (1999), Kempa (1995), Wrobel and Weisensee (1987), Heipke (1992), Schneider (1991), Ebner and Heipke (1988), Wrobel (1987).

## References

- Ackermann, F. (1983) *High precision digital image correlation*. 39. Photogrammetrische Woche, Stuttgart.  
 Ahn, Sung J. and Kotowski, R. (1997) Geometric Image Measurement Errors of Circular Object

- Targets. In Gruen/Kahmen (ed.) *Optical 3-D Measurement Techniques IV*, Wichmann, Heidelberg, pp. 463–471.
- Baltsavias, E. (1991) *Multiphoto geometrically constrained matching*. Dissertation, ETH Zürich, Institut für Geodäsie und Photogrammetrie, Nr. 49.
- Bähr, H.-P. and Vögtle, T. (1998) *Digitale Bildverarbeitung – Anwendung in Photogrammetrie, Kartographie und Fernerkundung*. 3. Aufl., Wichmann Verlag, Heidelberg.
- Bässmann, H. and Kreyss, J. (1998) *Bildverarbeitung Ad Oculos*. 3. Aufl., Springer Verlag, Berlin.
- Bösemann, W. (1994) Geometric models in object based multi-image matching. Proceedings of SPIE, **2249**, 192–199.
- Canny, J. (1986) A computational approach to edge detection. *IEEE Transactions on Pattern Analysis and Machine Intelligence; PAMI-8*, Vol. 6; pp. 679–698.
- Clarke, T. A., Cooper, M. A. R. and Fryer, J. G. (1993) An estimator for the random error in subpixel target location and its use in the bundle adjustment. *Optical 3D Measurement Techniques II*. Wichmann Karlsruhe, pp. 161–168.
- Deriche, R. (1987) Using canny's criteria to derive a recursively implemented optimal edge detector. *International Journal on Computer Vision*, **1**, 167–187.
- Duda, R. O. and Hart, P. E. (1973) *Pattern Classification and Scene Analysis*. John Wiley & Sons, New York, 482 pages.
- Düppé, R. D. and Weisensee, M. (1996) Auswirkungen der verlustbehafteten Bildkompression auf die Qualität photogrammetrischer Produkte. *Allgemeine Vermessungs-nachrichten*, Heft 1, pp. 18–30.
- Ebner H. and Heipke C. (1988) Integration of digital image matching and object surface reconstruction, *Int. Archives for Photogrammetry and Remote Sensing* (**27**) B11, III, pp. 534–545.
- El-Hakim, S. F. (1996) Vision-based automated measurement techniques. In Atkinson (ed.) *Close Range Photogrammetry and Machine Vision*. Whittles Publishing, Caithness, UK, pp. 180–216.
- Foley, J. D., van Dam, A., Feiner, S. K. and Hughes, J. F. (1995) *Computer Graphics: Principles and Practice in C* (2nd Edition). Addison Wesley, 1200 pages.
- Förstner, W. (1982) On the geometric precision of digital correlation. *International Archives of Photogrammetry and Remote Sensing*, Vol. 26/3, pp. 150–166.
- Förstner, W. (1985) *Prinzip und Leistungsfähigkeit der Korrelation und Zuordnung digitaler Bilder*. 40. Photogrammetrische Woche, Stuttgart.
- Förstner, W. (1986) A feature based correspondence algorithm for image matching. Proceedings of ISPRS Commission III Symposium, Rovaniemi, Finland. Volume XXVI-3/3 of International Archives of Photogrammetry and Remote Sensing, 150–166.
- Förstner, W. and Gülich, E. (1987) *A fast operator for detection and precise location of distinct points, corners and centres of circular features*. Proceedings, ISPRS Intercommission Workshop on *Fast Processing of Photogrammetric Data*, Interlaken, pp. 281–305.
- Förstner, W. and Ruwiedel, S. (ed.) (1992) *Robust Computer Vision*. Wichmann Verlag, Heidelberg.
- Gonzales, R. C. and Wintz, P. (1987) *Digital Image Processing*. 2<sup>nd</sup> edition, Addison Wesley, p. 503.
- Gonzales, R. C. and Woods, R. E. (2003) *Digital Image Processing*. Prentice Hall, p. 813.
- Göpfert, W. (1991) *Raumbezogene Informationssysteme*. Wichmann Verlag, Karlsruhe.
- Graham, R. (1998) *Digital Imaging*. Whittles Publishing, Caithness, Scotland, UK.
- Graps, A. (1995) An introduction to wavelets. *IEEE Computational Science and Engineering*, **2**(2), Los Alamitos, USA.
- Gruen, A. (1985) Adaptive least squares correlation – a powerful image matching technique. *South African Journal of Photogrammetry, Remote Sensing and Cartography*, **14** (3), pp. 175–187.
- Gruen, A. (1996) Least squares matching: a fundamental measurement algorithm. In Atkinson (ed.) *Close Range Photogrammetry and Machine Vision*. Whittles Publishing, Caithness, UK, pp. 217–255.
- Gruen, A. and Baltsavias, E. (1988) Geometrically constrained multiphoto matching. *Photogrammetric Engineering and Remote Sensing*, **54**(5) pp. 633–641.
- Haberäcker, P. (1991) *Digitale Bildverarbeitung*. Hanser Verlag, München.
- Haralick, R. M. and Shapiro, L. G. (1992) *Computer and Robot Vision*. Vol. I+II, Addison-Wesley, Reading, Ma., USA.

- Hartley, R. and Zisserman, A. (2000) *Multiple View Geometry*. Cambridge University Press, Cambridge, UK.
- Heipke, C. (1992) A global approach for least squares image matching and surface reconstruction in object space. *Photogrammetric Engineering & Remote Sensing* **58**(3), pp. 317–323.
- Heipke, C. (1995) State-of-the-art of digital photogrammetric workstations for topographic applications. *Photogrammetric Engineering & Remote Sensing* **61**(1), pp. 49–56.
- Helava, U. V. (1988) Object-space least-squares correlation. *Photogrammetric Engineering and Remote Sensing*, **54**(6), 711–714.
- Janser, A., Luther, W. and Otten, W. (1996) *Computergrafik und Bildverarbeitung*. Vieweg Verlag, Braunschweig.
- Jähne, B., Haußecker, H. and Geißler, P. (1999) *Handbook of computer vision and applications; Vol. 1 Sensors and imaging; Vol. 2 Signal processing and pattern recognition; Vol. 3 Systems and applications*. Academic Press.
- Kempa, M. (1995) *Hochauflöste Oberflächenbestimmung von Natursteinen und Orientierung von Bildern mit Facetten-Stereosehen*. Dissertation, Technische Universität Darmstadt.
- Klette, R., Koschan, A. and Schlüns, K. (1996) *Computer Vision – Räumliche Information aus digitalen Bildern*. Verlag Vieweg Technik, Braunschweig/Wiesbaden.
- Köthe, U. (1997) *Parameterfreie Merkmalsextraktion durch automatische Skalenselektion*. Publikation der DGPF, Band 5, Oldenburg, 1996, pp. 29–36.
- Kraus, K. (1997) *Photogrammetry, Volume 2, Advanced Methods and Applications*. With contributions by J Jansa and H Kager. Dümmler Verlag, Bonn.
- Lanser, S. and Eckstein, W. (1991) *Eine Modifikation des Deriche-Verfahrens zur Kantendetektion*. 13. DAGM-Symposium, München; Informatik Fachberichte 290, Springer Verlag, pp. 151–158.
- Luhmann, T. (1986) *Automatic point determination in a réseau scanning system*. Symposium ISPRS Commission V, Ottawa.
- Maas, H.-G. (1996) Automatic DEM generation by multi-image feature based matching. *Int. Archives for Photogrammetry and Remote Sensing*, **31**(B3), pp. 484–489.
- Maas, H.-G., Grün, A. and Papantoniou, D. (1993) Particle tracking in three dimensional turbulent flows - Part I: Photogrammetric determination of particle coordinates. *Experiments in Fluids* **15**, pp. 133–146.
- Marr, D. (1982) *Vision*. Freeman, San Francisco.
- Parker, J. R. (1996) *Algorithms for Image Processing and Computer Vision*. John Wiley & Sons Inc, p. 432.
- Pennebaker, W. B. and Mitchell, J. L. (1992) *JPEG Still Image Data Compression Standard*. Van Nostrand Reinhold, New York, Springer, 650p.
- Phong, B. T. (1975) *Illumination for computer generated pictures*. Comm. ACM **18** (8), pp. 311–317.
- Piechel, J. (1991) Stereobild-Korrelation. In Bähr/Vögtle (ed.) *Digitale Bildverarbeitung – Anwendung in Photogrammetrie, Kartographie und Fernerkundung*. Wichmann Verlag, Heidelberg, pp. 96–132.
- Rosenfeld, A. and Kak, A. C. (1982) *Digital Picture Processing*, 2nd edition, Academic Press.
- Santa-Cruz, D. and Ebrahimi, T. (2000) An analytical study of JPEG 2000 functionalities. Proceedings of the *International Conference on Image Processing*, **2**, 49–52.
- Schlüter, M. (1999) *Von der 2D/2D- zur 3D-Flächenmodellierung für die photogrammetrische Rekonstruktion im Objektraum*. Dissertation, TU Darmstadt. Deutsche Geodätische Kommission, Reihe C, Nr. 506.
- Schneider, C.-T. (1991) *Objektgestützte Mehrbildzuordnung*. Dissertation, Deutsche Geodätische Kommission, Reihe C, Nr. 375.
- Seul, M. (2000) *Practical Algorithms for Image Analysis: Descriptions, Examples and Code*. Cambridge University Press, 295 pages.
- Shortis, M. R., Clarke, T. A. and Robson, S. (1995) Practical testing of the precision and accuracy of target image centering algorithms. *Videometrics IV*. SPIE **2598**, 65–76.
- Snyder, W. E. and Qi, H. (2004) *Machine Vision*. Cambridge University Press, 452 pages.
- Soille, P. (1998) *Morphologische Bildverarbeitung. Grundlagen, Methoden, Anwendung*. Springer Verlag, Berlin.

- Tabatabai, A. J. and Mitchell, O. R. (1984) Edge location to subpixel values in digital imagery. *IEEE Transactions on Pattern Analysis and Machine Intelligence*, PAMI-6, No. 2.
- Tönnies, K. D. and Lemke, H. U. (1994) *3D-computergrafische Darstellungen*. R. Oldenbourg Verlag, München.
- Trinder, J. C. (1989) Precision of digital target location. *Photogrammetric Engineering and Remote Sensing*, **55**(6), 883–886.
- Welch, T. A. (1984) A technique for high-performance data compression. *Computer*, 8–19.
- Weisensee, M. (1997) *Wechselwirkungen zwischen Bildanalyse und Bildkompression*. Publikation der DGPF, Band 5, Oldenburg 1996, pp. 37–45.
- Wrobel, B. (1987) Facets Stereo Vision (FAST Vision) – A new approach to computer stereo vision and to digital photogrammetry. *Fast Processing of Photogrammetric Data*, Interlaken, pp. 231–258.
- Wrobel, B. and Weisensee, M. (1987) Implementation aspects of Facets Stereo Vision with some applications. *Fast Processing of Photogrammetric Data*, Interlaken, pp. 259–272.
- Zhou, G. (1986) Accurate determination of ellipse centers in digital imagery. ASPRS Annual Convention, Vol. 4, March 1986, pp. 256–264.

# 6 Photogrammetric measuring systems

This chapter deals with practical systems for the acquisition and processing of images from metric cameras. As opposed to consideration of standard systems developed especially for aerial imagery, the main emphasis lies on digital systems for industrial metrology which are intended for use in production engineering.

In contrast to traditional (mechanical or optical/mechanical) instruments, digital processing systems consist of hardware and software components which are subject to rapid technical change. Hence, the solutions and products presented here represent only the current stage of technical development. Plans and possibilities for development, as well as systems of the future, should become clear.

## 6.1 Comparators

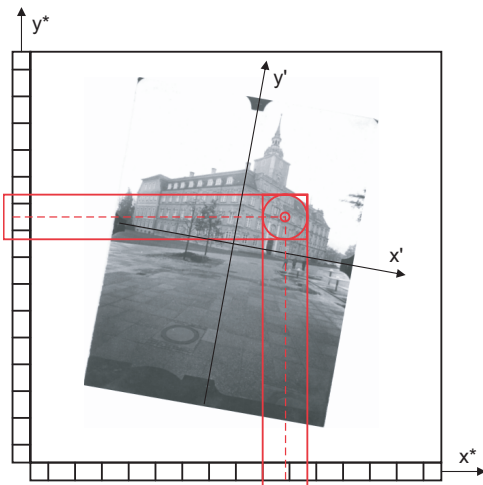
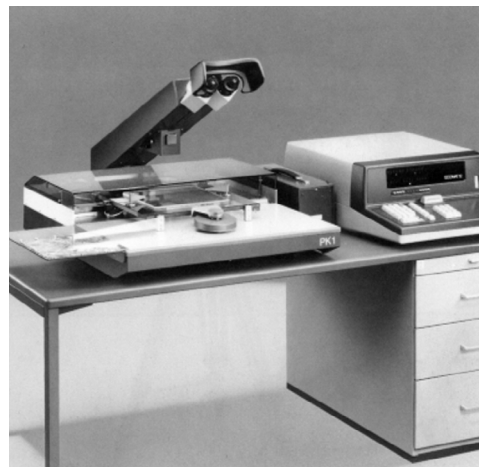
### 6.1.1 Design principles

Measurement of discrete (for example signalised) object points in single analogue images is performed with precision comparators; some such instruments allow automatic image measurement (see section 6.1.3).

In a comparator two precise length measuring devices are fixed at right angles to each other. A measuring mark, which will sometimes be a cross produced digitally on a computer screen and sometimes a component of an optical system, is set on the image point to be measured. Comparator or machine coordinates are registered and are afterwards transformed into the actual image coordinate system. (see sections 2.1.2 and 2.2.1).

High-precision photogrammetric comparators incorporate Abbe's comparator principle: if the measuring scale and the point to be measured are always collinear, errors arising from a misalignment of the components will be avoided. The coordinate measuring device represented in Fig. 6.1 is not based on Abbe's comparator principle.

The accuracy of a comparator is set in the first place by the unit of subdivision of the measuring system. For mechanical systems accuracies of less than 1 µm can be achieved over a field of 230 mm × 230 mm. The image measuring accuracy for photogrammetric purposes is also a function of the definition and reproducibility of the image coordinate system (by means, for example, of fiducial marks or réseau), of the stability of the camera and always of the detectability of the image point. Consequently, the high accuracy of particular comparators can only be used successfully if object targeting and camera are appropriately matched.

**Figure 6.1** Comparator principle**Figure 6.2** Mono-comparator Zeiss PK-1

### 6.1.2 Analogue image comparators

Analogue image comparators are among the earliest photogrammetric image measuring instruments (for example, Pulfrich's stereocomparator of 1901, Fig. 1.25). They were used most extensively during the period between about 1960 and 1980 when high accuracy image coordinates were required for the newly developed methods of analytical computation.

Photogrammetric mono-comparators are usually designed according to the principles described in section 6.1.1. The measuring mark is incorporated in a fixed optical-mechanical viewing system. The images are moved by hand or with motor-driven image carriers with respect to the measuring mark, while the registration of length measurements is performed by electro-optical read-out of precision glass scales. The achievable accuracy ranges between about 0.5  $\mu\text{m}$  and 2  $\mu\text{m}$ . Examples of photogrammetric mono-comparators are the Zeiss PK-1, Kern MK-1 or Komess 3000 instruments.

Stereocomparators consist of two image carriers each working in the same way as a mono-comparator. Stereoscopic viewing allows non-signalled object points to be identified more reliably. Stereocomparators are, however, no longer used in normal practice.

### 6.1.3 Digital image comparators

Using a CCD camera with high optical magnification, digital image comparators scan a patch of the analogue photograph; the point is set by means of digital image processing. In order to measure comparator coordinates, a geometric relationship between the pixel system of the digitised image and the comparator coordinate system has to be determined, a procedure sometimes known as sensor orientation. For this purpose two different solutions have been successful:

- mechanical measurement of the sensor position
- optical-numerical determination of sensor position.

### 6.1.3.1 Comparators using mechanical sensor positioning

The principle is illustrated in exemplary fashion by the precision comparator GSI AutoSet-1/2. The CCD camera (sensor format: 8.8 mm × 6.6 mm) of the comparator (Fig. 6.3) images a measuring window of the photograph with an approximate magnification of 5. A single pixel of the resulting digital image corresponds to an area of about  $4 \mu\text{m} \times 2.5 \mu\text{m}$  on the original image. Because the CCD image covers an area on the photograph of only about  $1.6 \text{ mm} \times 1.2 \text{ mm}$ , coarse positioning is assisted by an additional overview camera. The photographic image is moved by an xy slide system that fulfills Abbe's principle, its position being measured by encoded glass scales. Mechanical components and measuring devices are manufactured and calibrated with high accuracy.

The system is able to detect signalised (retro-reflective) targets automatically, and to measure their positions with an average accuracy of about  $0.5 \mu\text{m}$ . The mean measuring time is about 1 s per point. The comparator is mainly used in combination with a large format camera of type GSI CRC-1 or CRC-2 (see section 3.3.1.4, Fraser and Brown 1986).

### 6.1.3.2 Comparators using optical-numerical sensor positioning

Likewise, a comparator employing optical-numerical sensor positioning also uses a CCD video camera for the acquisition of small image patches. In this case the position of the camera with respect to the comparator system is determined by means of a réseau on a removable plate which is placed on top of the photograph. A transformation between the CCD pixel system and the comparator system can be calculated based on the measurement, each time, of four réseau points made visible using a special technique of illumination (see réseau scanning, Fig. 6.4, and also section 3.3.2.5).

The réseau-scanner Rollei RS1-C (Fig. 6.5) is an example of a digital image comparator based on réseau scanning. The integrated CCD camera produces a pixel size of about  $7 \mu\text{m} \times 10 \mu\text{m}$ . The system software allows the measurement of cross shaped and ellipse shaped targets. Based on a mean accuracy of  $<0.1$  pixel, a measuring accuracy of  $1 \mu\text{m}$  with respect to the original photograph is achieved (Luhmann and Wester-Ebbinghaus 1986).

When pictures from a camera equipped with a dense réseau are to be measured, the comparator réseau plate can be dispensed with. Then the transformation of the digital image



**Figure 6.3** High-precision comparator GSI AutoSet-1

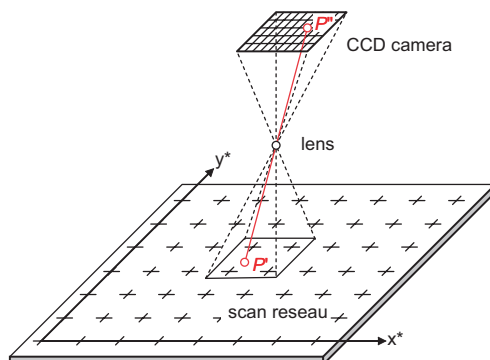


**Figure 6.4** Principle of réseau scanning

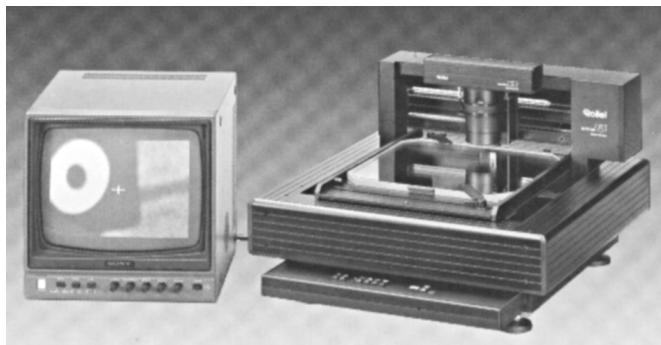


**Figure 6.5** Réseau-scanner Rollei RS1-C

patch into the original photo can be determined directly by the measurement of the camera réseaux points visible in the photograph. The réseaux scanner is, therefore, typically used in combination with the Rollei LFC (Fig. 3.56) or Rollei 6008 metric (Fig. 3.128) which both possess a 2 mm réseaux grid (Dold 1997).

## 6.2 Single camera systems

### 6.2.1 Camera with hand-held probing device

Based on the idea of inverse space resection (see section 4.2.4.1), it is possible to design a single camera system which observes a probing device. Fig. 6.6 shows an example where the operator uses a hand-held probing device which incorporates a number of calibrated control targets. If the probe is visible to a calibrated camera, the relative position and orientation of the probe can be determined in 3D space.



**Figure 6.6** Example of a single camera system with 3D probe (Metronor Solo)

Usually the centre of a spherical probing tip is used as the measuring point. Its position has to be calibrated with respect to the local reference points of the probing device. The reference points are typically either passive reflective targets, or active LEDs. The measurement is started by a switch on the probing device that initiates a signal for the image acquisition and processing.

### 6.2.2 Probing system with integrated camera

In this case both camera and probe are mounted in a single unit in a known geometrical relationship with each other. The camera orientation is computed by resection with respect to an object reference field. In the AICON ProCam system the probe consists of a CCD camera and one or more probing tips which are calibrated with respect to each other in a local xyz system (Fig. 6.7, Fig. 6.8). A system of reference points with known positions in a superior XYZ coordinate system are arranged on the borders of the desired measuring volume. If the measuring probe is positioned in such a way that the camera images a minimum of three reference points, the exterior orientation of the probe can be calculated by space resection. Coded targets provide automatic identification of the reference points.

The measuring probe is connected to the control computer by wire in such a way that a synchronised image is acquired at the moment when the tip of the probe touches the object. The images of the reference points are found and measured automatically. A measuring accuracy of about 0.1 mm can be achieved in a variable measuring volume that is limited only by the dimensions and accuracy of the control point or reference field. The reference field can be mounted in a fixed position, or it can be mobile. By adapting the size of the control points, the distance to the reference field can be configured freely (Sinnreich and Bösemann 1999).

Compared to the usual on-line systems the principle of the self-orienting measuring probe has the advantage that the measuring accuracy is independent of the intersection angles of image rays.

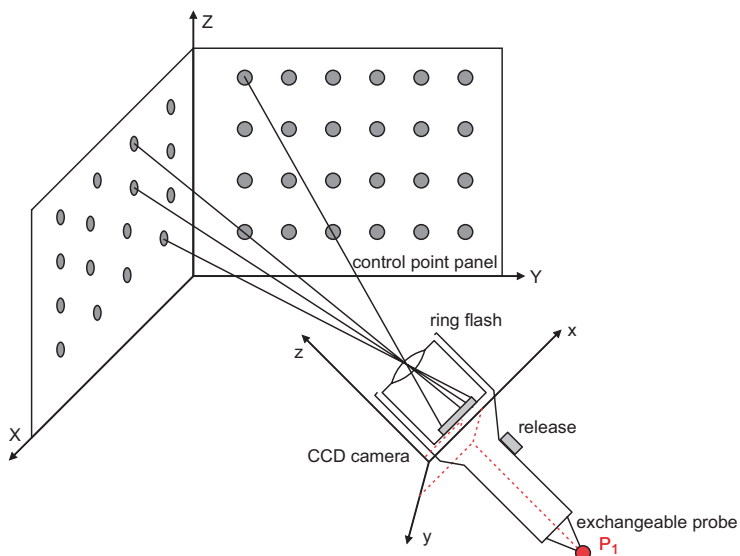


**Figure 6.7** Principle of a probing device with integrated camera



**Figure 6.8** Probe with integrated camera (AICON ProCam)

the work space of the robot. The robot arm is fitted with a calibrated reference object which is moved to various positions in space. By space resection the position and orientation of the calibrated reference object with respect to the cameras and the robot arm are determined.

The CAROS<sup>+</sup> system is a photogrammetric on-line system which uses one (or optionally two) Rollei RSC réseau-scanning cameras (section 3.3.2.5). The one-camera version is used for adjustment of industrial robots (Fig. 6.9), the measured poses (robot position and orientation) being determined by space resection with respect to the test field plate which is tracked and measured within the workspace automatically. The two-camera version for robot calibration is a normal on-line system. The workspace (measuring volume) is about  $3 \times 3 \times 2$  m<sup>3</sup> within which an object accuracy of 0.1 mm can be achieved (Godding *et al.* 1997).

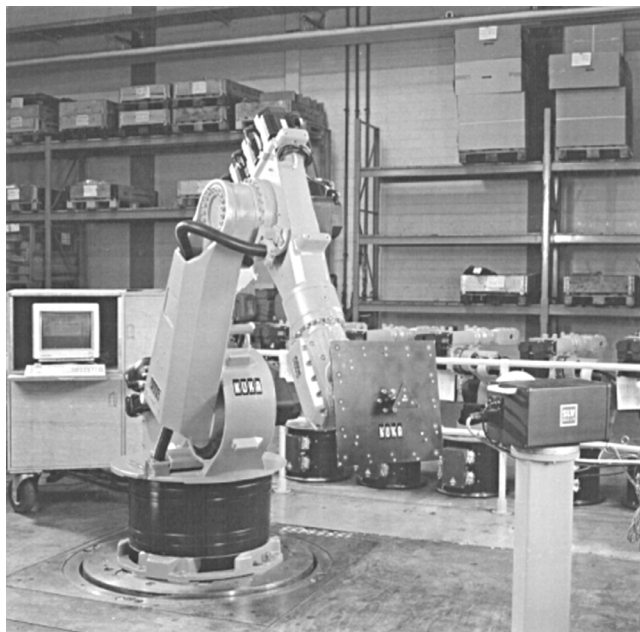


**Figure 6.9** Measuring system CAROS<sup>+</sup> for robot calibration and adjustment

In addition, arbitrary object points can be measured without re-arranging the camera configuration, if a sufficient number of reference points are visible.

### 6.2.3 Camera system for robot calibration

In general, robot calibration is used to check the robot arm position with respect to its nominal position, and to derive correction data for angle and distance adjustments. This task can be solved by on-line or by off-line photogrammetry (Maas 1997).

One possible solution is to have digital cameras fixed in such a way that they observe

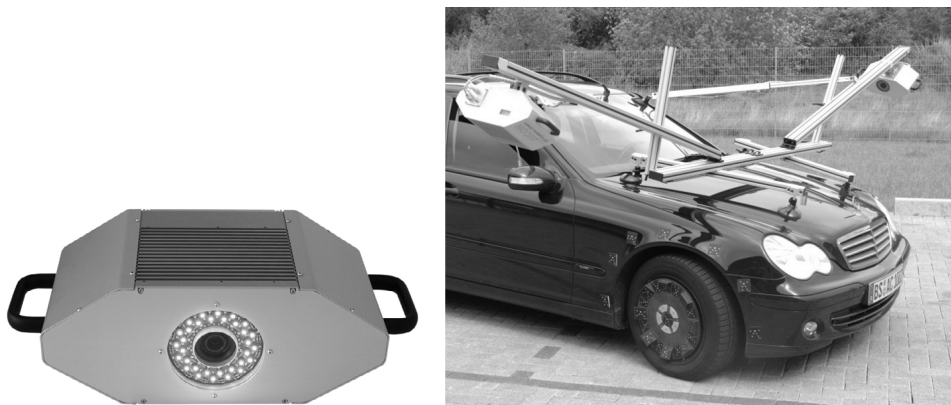


**Figure 6.10** High-speed 6 DOF system used for wheel measurements (AICON)

## 6.2.4 High-speed 6 DOF system

Fig. 6.10 shows a high-speed camera system (AICON WheelWatch) which is used to measure the spatial position and orientation of a moving object with respect to a stable reference system. The mathematical model is based on space resections as described in section 4.2.4.2. Since this particular system has a camera-integrated processing unit for real-time target detection, unlimited timed measurement sequences of dynamic processes can be observed.

## 6.3 Stereoscopic processing systems

### 6.3.1 Analytical stereo-instruments

#### 6.3.1.1 Principle of the analytical plotter

Overwhelmingly today, analytical plotters or digital stereoworkstations are used for stereophotogrammetry. The systems are based on the same principles (Fig. 6.11).

Using suitable input devices (hand and foot wheels, 3D cursor/mouse), a floating mark is moved in 3D model space in coordinate increments  $\Delta X$ ,  $\Delta Y$ ,  $\Delta Z$ . Using the collinearity equations (4.8) and the parameters of interior and exterior orientation the incrementally changed  $XYZ$  position is transformed into corresponding image positions  $x'$ ,  $y'$  and  $x''$ ,  $y''$ . The two images are moved to these positions in real-time by means of servo-motors or digital panning. Under stereoscopic vision, the operator continuously controls the 3D position of the floating mark in model space. The position of the floating mark is adjusted interactively by appropriate corrections to its  $XYZ$  coordinates so that it appears to touch the model surface (“setting the floating mark”). Only when the two measuring marks lie on homologous image points does the operator have a convincing visual impression that the floating mark lies on the model surface; at that stage the computed  $XYZ$  values may be stored. Hence, the analytical plotter is based not on direct measurement of image coordinates but on the computation of coordinates in 3D space.

As an example, Fig. 6.12 shows an off-the-shelf system. Typically, the image coordinate measuring accuracy of an analytical plotter lies in the range of about 2–5  $\mu\text{m}$  for precision instruments or about 5–10  $\mu\text{m}$  for standard instruments.

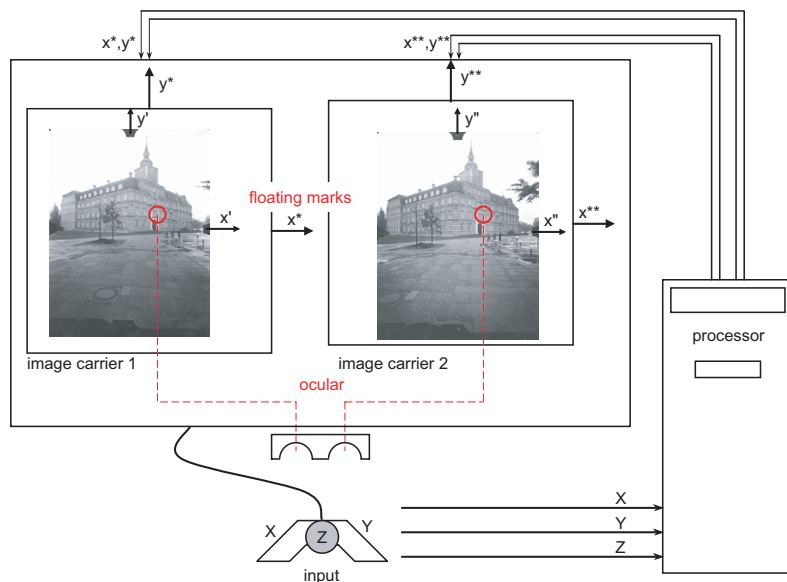


**Figure 6.11** Principle of the analytical plotter

Visual stereoscopic compilation is restricted to the so-called normal case in which the camera axes are approximately parallel and normal to the base. Large differences in image scale or in the rotation angles  $\varphi, \omega$  between the two images cannot be accommodated by a human operator. On the other hand, rotations  $\kappa$  about the optical axis can be compensated for by optical image rotation (dove prism).

Instrumental control (control of image carriers, illumination, input devices) and transformation of introduced  $XYZ$  values is performed by a processor which delivers continuous 3D object coordinates. Hence the analytical plotter can be regarded as a 3D digitiser. Using a suitable interface these 3D coordinates can be transferred to any post-processing system, for example a 3D CAD system or a geographic information system which can be located on a separate computer system.



**Figure 6.12** Analytical plotter Leica SD 2000

Analytical plotters can be equipped with CCD video cameras integrated in the optical path of the eyepiece. The digitised image areas around the measuring mark positions are processed using a correlation or image matching algorithm in order to enable automated parallax measurement and in effect automated setting of the floating mark (an example is described in section 6.5.2.3). In addition, the superimposition of images and graphics is made possible by the projection into the optical train of the image of a graphical computer monitor.

### 6.3.1.2 Orientation procedures

The orientation parameters required for stereoscopic measurement are determined according to the orientation procedures explained in section 4.2. In the first instance, the interior orientation has to be established. Machine coordinates of fiducial marks or réseau crosses, defining the camera reference system, are measured monocularly, their calibrated values being known. Parameters are computed for a plane transformation which will bring the machine coordinates into their calibrated values.

Typically, the parameters of exterior orientation are determined by one of the following procedures:

- Two step orientation

In the traditionally established way, the parameters are determined in two separate steps of relative orientation and absolute orientation. After successful relative orientation the model can be correctly established in any desired three-dimensional model coordinate system.

- Transfer of known orientation parameters

If the parameters of exterior orientation are known from previous calculations they can be loaded either for single images or for stereomodels. Consequently the system will be ready for use as soon as the interior orientation has been established. Usually the exterior orientation will have been determined by bundle triangulation. In such cases care must be taken to ensure the correct order in which rotation angles are to be computed; it may be necessary to transform the previously computed values.

The special requirements of close-range applications can be met by specialised programs with which computation of the orientation of arbitrarily tilted images is possible and which allow the simultaneous use of several small-format photographs, the processing of réseau images and transformation into arbitrarily located object coordinate systems (Hinsken and Meid 1994).

### 6.3.1.3 Object reconstruction

In the first instance, analytical stereo-instruments allow the 3D measurement only of object points. Polygons are recorded as lines and areas are represented by dense point grids (digital surface models).

In order to measure linear object structures an analytical plotter can be switched into a continuous measuring mode. In this mode, object point coordinates are registered continuously after fixed increments of time or of position of the floating mark which is moved along the linear feature by the operator.

To a large extent, the measurement of digital surface models can be automated. For this purpose the control program calculates a fixed point grid for the reference plane (for example  $\Delta X = \Delta Y = \text{constant}$ ). The analytical plotter automatically moves to these points, at each of

which the operator (or a correlation algorithm) only has to set the floating point on the surface in order to determine its Z coordinate.

### 6.3.2 Digital stereoprocessing systems

Digital stereo-workstations have no mechanical image carrier system. Instead, digitised images are displayed and moved digitally on a suitable stereo-monitor. Each image may be moved relative to a superimposed measuring mark. The measuring marks, the images, or both simultaneously, can thereby be moved.

Stereoscopic viewing is achieved through either optical or electronic image separation. Essentially, the following techniques are used:

- Split screen

Both images are displayed side by side on a standard monitor and are viewed stereoscopically using a simple optical system similar to that of a mirror stereoscope. A fixed floating mark is required, since the images are moving. The operator is forced to sit in a fixed position in front of the monitor.

- Anaglyphs (chromatic separation)

Usually images are coloured in red and green, and are viewed through glasses that consist of red and green colour filters. This principle is only useful for grey level images. Stereoscopic viewing is possible over large viewing distances and angles, and for a number of people simultaneously.

- Alternating image display

Left and right images are alternately displayed in a fast switching mode (frequency >100 Hz). The operator wears glasses which have synchronised shutters so that only the currently displayed image is visible for the corresponding eye. Stereoscopic viewing is possible within a large workspace in front of the monitor.

- Polarised image display

In front of the monitor an LCD filter is mounted which polarises the images differently within each image switching phase. The operator wears glasses with corresponding polarising filters in order to separate both images. Electronic control of these glasses is not required (Fig. 6.13a).

- Auto-stereoscopic display (micro-prisms)

In this case the stereoscopic image is displayed in separated image columns (even columns for the left image and odd columns for the right image). On top of the monitor surface a vertical micro-prism system is mounted which deflects the column images in the desired spatial viewing direction. The stereoscopic effect may be observed without any additional aids; the resolution of the stereoscopic image corresponds to half of the monitor resolution. Movements of the operator can be compensated for by an automatic image and prism adjustment (eye finder) thus creating a large workspace in front of the monitor (Fig. 6.13b).

- LCD monitor glasses

The operator wears glasses with two separated LCD mini-monitors. This kind of stereo-viewer is used mostly for virtual reality applications.

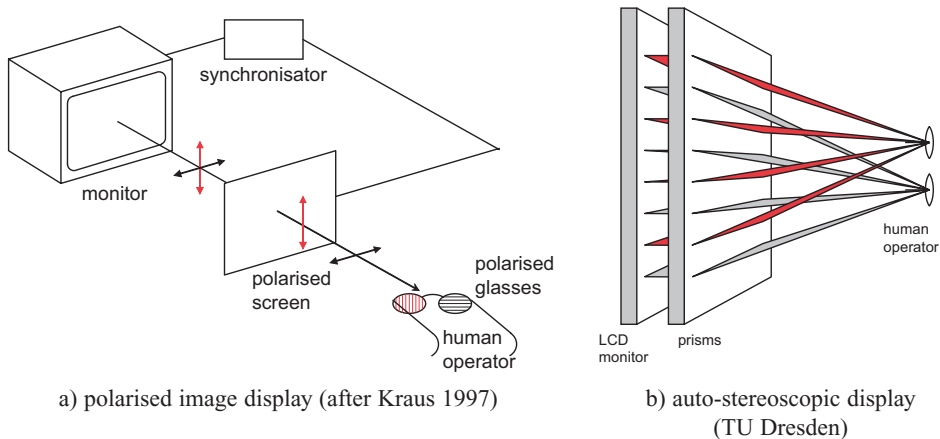


**Figure 6.13** Possible designs of stereo monitors

Compared to analogue systems, digital stereo-workstations (see, for example, Fig. 6.14) offer a variety of benefits:

- simultaneous display of image (raster) and graphic (vector) information is possible
- several workstations can be connected by networks in order to have parallel access to the same image material
- one common integrated system may perform as comparator, analytical plotter, rectifier or graphical workstation
- orientation procedures and measurement of points, lines and surfaces can be automated.

Digital stereoplotters can in principle be used for the processing of any stereopairs. There are no technical restrictions on the imaging sensors used. However, the integrated standard software is frequently adapted to aerial imagery (Heipke 1995). As an example of a close-range application, Fig. 6.15 shows a digital stereo-image and the result of automatic height model



**Figure 6.14** Digital stereo workstation Leica/Helava DPW 770

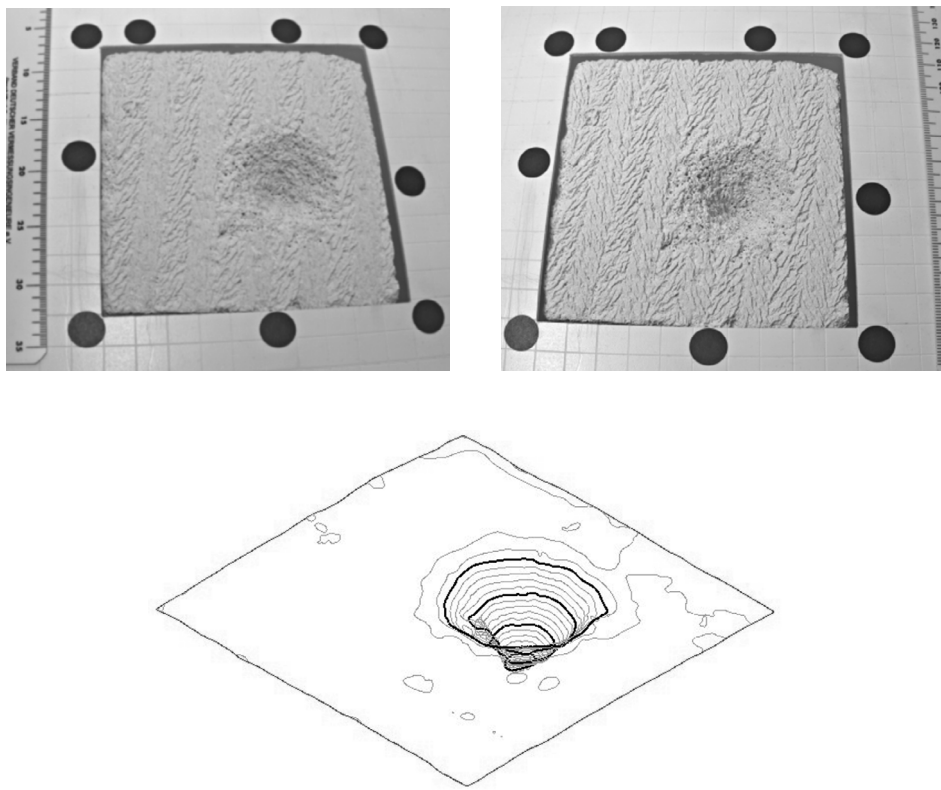


**Figure 6.15** Digital stereo-image pair and height measurement using Leica/Helava DPW  
(camera: Kodak DCS420,  $f = 15$  mm,  $m = 15$ )

measurement of a crater in a cellular concrete block, demonstrating the properties of high-pressure injection nozzles.

### 6.3.3 Stereovision systems

The term stereovision systems is used for two-camera systems that enable the 3D recognition of an object scene on-line, for example in the following applications:

- navigation of autonomous vehicles (detection of obstacles)
- control of workfloor robots (location of workpieces)
- 3D recording of the interior of pipes
- examination using stereo-endoscopy (medicine, material testing)

In general these systems consist of two identical CCD video cameras, mounted with their axes parallel. Their images are processed on-line by computer, or they are transmitted for visual observation. Fig. 6.16 shows a robot with stereocameras; Fig. 6.17 illustrates the design of the stereocamera of the Mars Pathfinder (Dorrer 1998).

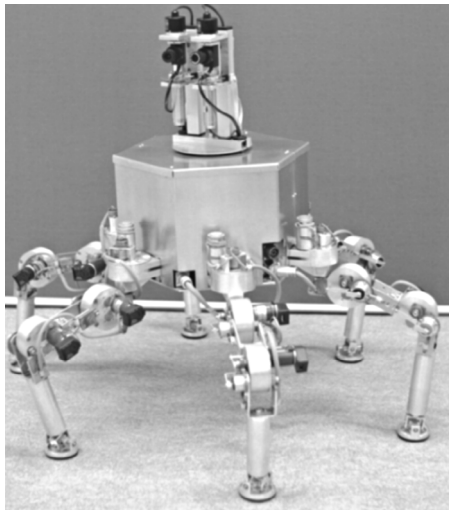


**Figure 6.16** Autonomously navigated robot with a stereovision system (Katharina, IFF Magdeburg)

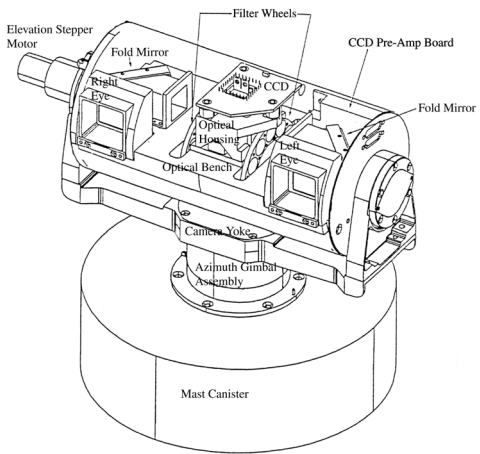


**Figure 6.17** Design of the IMP stereocamera of the Mars Pathfinder (NASA)

## 6.4 Multi-image measuring systems

### 6.4.1 Interactive processing systems

Interactive multi-image processing systems permit the measurement of image points in more than two images. Checking of point identification and correspondence is performed by the operator. As well as pure coordinate measurement, these systems are used above all for the reconstruction of graphical features, such as lines. The data acquired are usually transferred to a CAD program for further processing.

#### 6.4.1.1 Image measurement systems based on a digitising tablet

Since the mid-1980s multi-image processing systems have been available which allow the measurement of paper prints (enlargements) of analogue photographs using a graphics tablet (digitiser). Just as with analytical instruments the orientation of the images with respect to the digitiser tablet must first be determined (interior orientation). If photographs from réseau cameras are used, the measurement of réseau points compensates for possible image deformations or digitiser errors.

Usually the orientation parameters are determined by bundle triangulation while additional object points for point or line measurements are calculated by intersection. There is no limit on the number of images which can be used.

The principal fields of application of these systems are architecture and monument preservation as well as forensic measurement (accident recording, scene-of-crime surveying). Example systems are Rollei MR2 (Fig. 6.18) or Elcovision 10. Today their functionality has been broadened to allow the use of multiple digital images.

#### 6.4.1.2 Digital processing systems

If the images are provided in digital form, they can be analysed and evaluated directly in a graphical user interface. In exactly the same way as with digital stereo-workstations, the use of



**Figure 6.18:** Interactive analytical multi-image system Rollei MR2

digital images leads to clearly identifiable increases in efficiency and improvements in quality of interactive image evaluation:

- Once-only interior orientation

In contrast to analogue systems, the transformation from the digital pixel system to the camera-based image coordinate system need be established once only as parameters can then be stored within the image file.

- Image processing

The contrast, sharpness<sup>1</sup> and brightness of the images can be enhanced for ease of use. Image rectification or orthophoto production can be integrated into the processing system.

- Automation

Functions for the detection and measurement of point features not only allow automated interior orientation but they also expand interactive systems to photogrammetric on-line or off-line systems.

- Superimposition of graphical information

Digital images and graphical information (vector data) can easily be superimposed permitting improved interactive control of the measurement.

- Integration into CAD environment

Display and measurement of images and 3D CAD processing of the resulting object data can take place within one closed system.

The interactive photogrammetric system PHIDIAS-MS (Fig. 6.19) demonstrates the integration of digital photogrammetry and the 3D CAD environment (Benning and Schwermann 1997). The system is embedded in the CAD program Microstation which offers all standard CAD functions directly for the photogrammetrically reconstructed object. The system is well suited for the graphical representation of (complex) objects such as occur in architectural applications or in the as-built documentation of industrial plants. Further interactive multi-image systems are offered, for example, by PhotoModeler (EOS Systems), ImageModeler (RealViz) or PHAUST (INVERS, Woytowicz 2002).

---

<sup>1</sup> Manipulated images can exhibit changed geometry (see section 5.2.1.3).

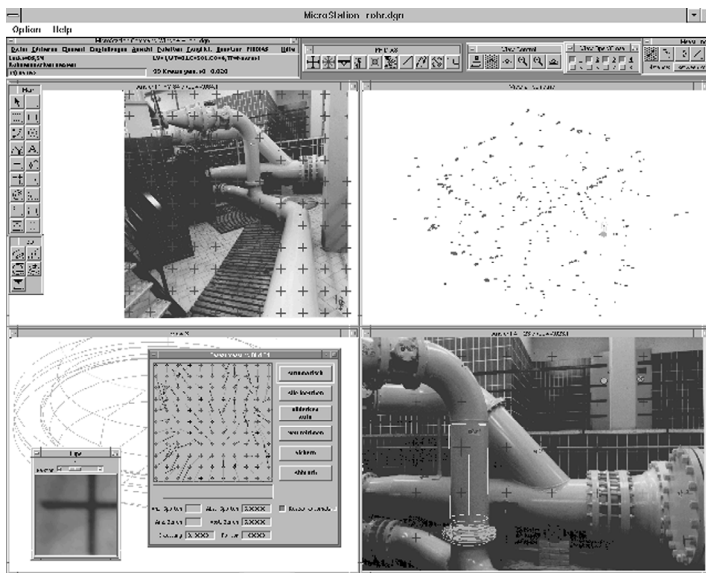


**Figure 6.19** Interactive digital multi-image system PHIDIAS-MS

#### 6.4.2 Mobile industrial point measuring systems

With the introduction and use of digital cameras and digital image processing, the customarily separate procedures of image acquisition on-site followed by image processing in the office may be combined. The complete measurement of an object can be performed on-site.

For point-wise photogrammetric measurement of objects, a distinction is made between on-line and off-line systems. In both cases discrete object points are measured, in some cases by optical setting on distinctive points or targets and in other cases by use of a mechanical probe. In the latter case the point of the probe is set on the object point while targets on the probe are imaged; from the computed positions of these targets and a knowledge of the geometry of the probe the coordinates of the probed point are found.

Some different systems, on the other hand, incorporate a projector which provides a suitable pattern of fringes, grids or random dots on the surface. The projector itself may be either an active, oriented measuring device or simply a passive projection tool, providing points that define the surface.

##### 6.4.2.1 Photogrammetric off-line systems

A photogrammetric off-line system is characterised by:

- photography of the object with at least two images from one or more cameras
- subsequent orientation of the set of images, simultaneous calibration and 3D point determination by bundle triangulation.

The above two steps are separated in time and, possibly, in space. As in much of photogrammetry, there are no restrictions in terms of imaging sensors, object targeting and image configuration (number and position of images).



**Figure 6.20** Object recording using a photogrammetric off-line system (Imetric)

Off-line photogrammetry is common, above all, in industrial applications. The use of digital cameras (still-video cameras) and signalised and/or coded targets (retro targets) is implicit. As a result automatic orientation and image measurement are possible.

Fig. 6.20 shows the recording of an object which is fitted with a number of simple targets (tie points) and special adapters for the measurement of hidden parts of the object. Fig. 6.21 shows the user-interface of a typical multi-image system. Object measurement with industrial off-line systems has the following characteristics:

- sequential image acquisition with high-resolution still-video cameras (image storage and processing within the camera) and ring flash
- object signalisation using retro-reflective targets
- coded targets for automated generation of approximate values and image orientation
- calibrated reference tools which establish a local 3D object coordinate system
- bundle triangulation with self-calibration

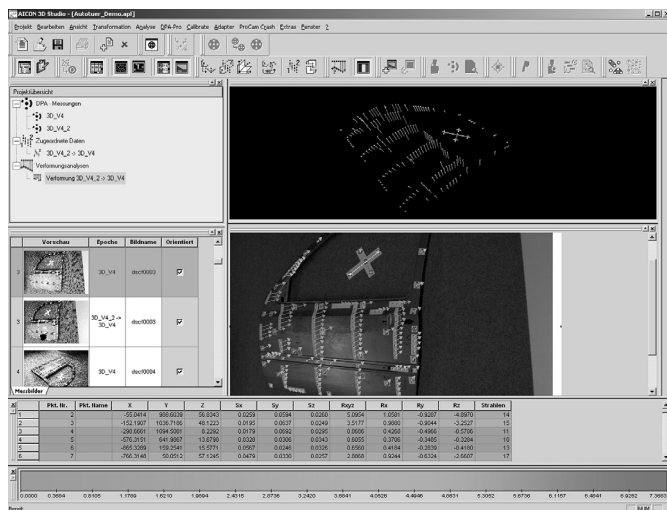


**Figure 6.21** User-interface of the system AICON 3D Studio

- digital point measurement with sub-pixel accuracy (0.02–0.05 pixel)
- typical number of images between 10 and 50 (in principle, without limit)
- typical number of images per object point between 6 and 20 (in principle, without limit)
- typical object dimensions between 1 m and 15 m (in principle, without limit)
- typical duration for object recording and processing between about 10 min and 60 min
- achievable relative accuracy about 1:50,000 to 1:100,000.

The achievable accuracy in object space is strongly dependent on the imaging configuration and on the stability of the camera during image acquisition. The values quoted above can be achieved when adequate ray intersection angles and uniform distribution of points over the available image format are ensured.

#### 6.4.2.2 Photogrammetric on-line systems

Photogrammetric on-line systems enable the direct measurement of 3D object coordinates much in the manner of a coordinate measuring machine. In the majority of systems, at least two synchronised digital cameras are used for image acquisition, each with known calibration values and pre-determined orientation with respect to an established coordinate system<sup>1</sup>. Usually a tactile probe or adapter (see section 3.4.1.3) is used; its spatial position and orientation within the measuring volume are determined photogrammetrically at the moment the operator activates the cameras, the positions of the reference points on the probe being calculated by intersection with respect to the established coordinate system. The positions of the probing tip  $P$  and of the reference points on the probe are known with respect to the probe's own local coordinate system; it is, therefore, possible to transform the coordinates of  $P$  into the established coordinate system.

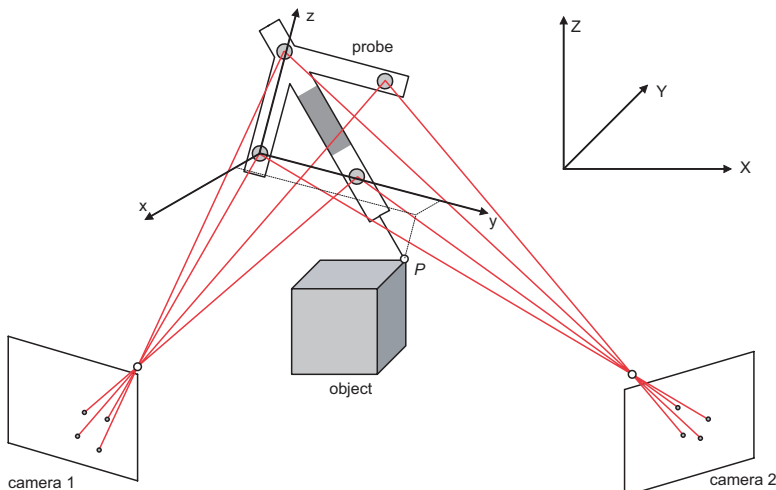


**Figure 6.22** Measurement principle of an on-line system with tactile probing

<sup>1</sup> See section 6.2 for tactile systems with a single camera.

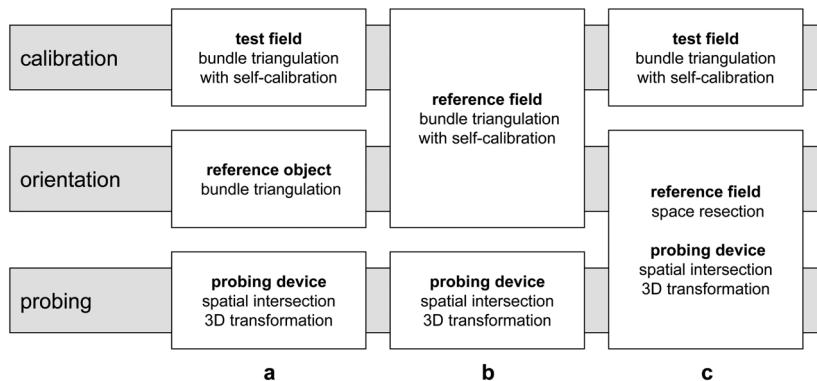


**Figure 6.23** Strategies for calibration, orientation and point measurement for on-line systems

With one type of probe, the operator must press a button to trigger the cameras when he has placed the tip on the point to be measured. A second type of probe, which might be described as self-triggering, causes the cameras to fire as soon as its tip comes into contact with the surface.

Camera operation, illumination (flash) and image transfer are controlled by a networked computer which also provides image processing and coordinate calculations. The computer can be located externally (laptop, computer trolley) or within the camera. In the latter case image processing (point measurement) is performed directly within the camera, so that only a small number of image coordinates have to be transferred to the post-processing computer (examples in Fig. 3.83 to Fig. 3.85).

Calibration and orientation of on-line systems can be performed in various ways according to the following schemes (Fig. 6.23):

(a) Separate pre-calibration, orientation and point measurement

The parameters of interior orientation of the cameras are determined separately from the process of object measurement, for example by test field calibration. All cameras are oriented by simultaneous imaging of a reference field that defines a local 3D coordinate system. Subsequently, the object is measured point by point by intersection and 3D transformation of the target points and the probing tip.

This approach requires stable interior orientation of the cameras for the complete period between calibration and completion of the measurement. In addition the exterior orientation of the cameras must be kept constant, for example by the use of fixed mechanical camera mountings or stable tripods.

(b) Calibration and orientation using a reference object connected to the measuring object

A calibrated reference field is positioned on the object to be measured providing local 3D control points. After setting up of the cameras their positions and orientations can be calculated by space resection (separately for each camera) or by bundle triangulation. Under some circumstances the interior orientation can be determined simultaneously if the reference field provides a sufficient number and distribution of control points, or if it is moved and photographed in a number of different spatial positions. Point measurement follows as in (a).

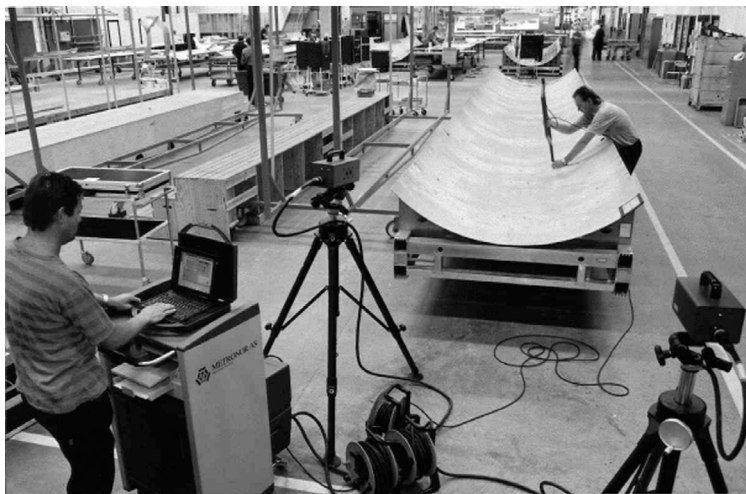


**Figure 6.24** On-line system with manually guided tactile probing (Metronor)

### (c) Integrated orientation during point measurement

The orientation of the cameras can be combined with the point measurement process itself. For each new measurement of the probe position the cameras also record a reference field which is used to check or recalculate the exterior orientations. Such a method is essential if stability of the cameras cannot be ensured.

Various different configurations and applications for on-line systems exist, such as:

- two-camera system with manually guided tactile probing (as described above, see Fig. 6.24)
- two-camera system for tracking of dynamic processes, for example the spatial movement of a robot
- multi-camera system for the observation of deformations by continuously repeated measurements of check points

If one assumes that the system components are the same in each case, the measuring accuracy of on-line systems will be less than that of off-line systems, mainly for the following reasons:

- small number of images for each point measurement
- possible different measuring accuracies in X, Y and Z (see section 4.4.2.2)
- the strict stability requirements for interior and, especially, exterior orientation are difficult to meet
- contact of the probe with the surface and the triggering of the cameras must occur simultaneously; unless a self-triggering type of probe is being used, this is dependent on the operator's skill.

Under the above circumstances off-the-shelf on-line systems offer an accuracy in the object space of about 0.1–0.2 mm for a measuring distance up to 2 m (assumptions: image scale  $m = 100$ , base length  $b = 2$  m). This corresponds to a relative accuracy of about 1:10,000 to 1:20,000, or an image measuring accuracy of 1  $\mu\text{m}$ .

Available systems differ mainly in terms of the operating procedure and the strategies for orientation and error detection. Operational on-line and off-line systems in different configurations are offered by, for example: AICON (DPA Win, Peipe *et al.* 1994), GSI/Leica (VSTARS, Brown and Dold 1995), Imetric (TPxx, Beyer *et al.* 1995), Metronor (Pettersen 1992), Rollei (CDW, Fellbaum and Godding 1995) or GOM (Winter and Reich 1997). An overview is given by Dold (1999).

### 6.4.3 Stationary industrial on-line measuring systems

In contrast to mobile systems, stationary systems can be designed in which the photogrammetric measuring components (such as cameras, projectors, devices for rotating the object) can remain calibrated for a long period; the cameras can be oriented automatically using a fixed and known reference point field. This provides a system which is in a permanent state of readiness for repetition of the same measurements or similar measurements within a fixed, limited volume and which can employ a considerable degree of automation.

#### 6.4.3.1 Multi-image systems for production control

Integrated multi-image photogrammetric systems can be used for quality control on a production line. The measuring problem usually concerns a limited variety of parts, so that a fixed arrangement of cameras, light sources and control points is possible. The function of such a system is real-time measurement of the objects followed by quality analysis and the transfer of results to the manufacturing control system.

##### *System for measurement of hydraulic brake lines*

The measuring system AICON TubeInspect offers a solution for the automatic 3D measurement of variously shaped objects in the form of pipes, rods or wires (an example occurs in the automobile industry where the—often unusual—form of hydraulic brake lines must be monitored). This non-contact approach has replaced the previous use of gauges.

The system consists of several vertically arranged planes (Fig. 6.25). The upper two planes contain up to 16 CCD video-cameras. The lower two planes consist of an illuminating surface and a transparent plate with spatially distributed reference points which are used for camera orientation. The brake pipe is mounted on the plate in an arbitrary position.

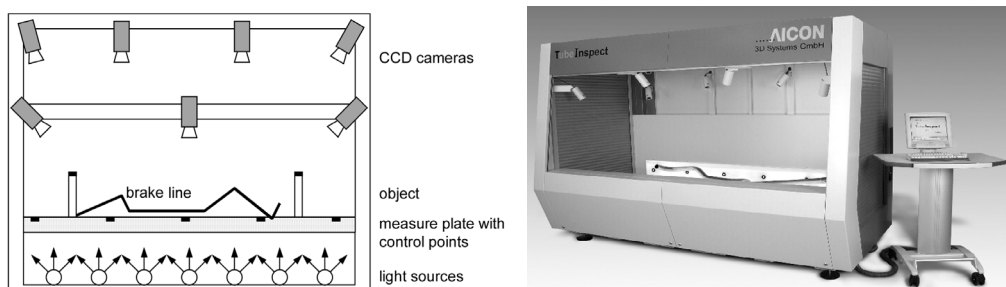


**Figure 6.25** On-line system for check measurement of hydraulic brake lines (AICON)

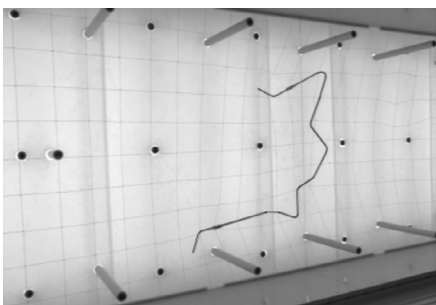


**Figure 6.26** Metric video image for hydraulic brake line recording (AICON)

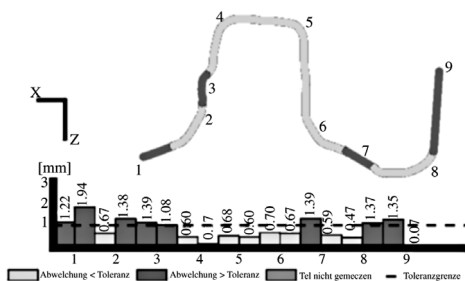


**Figure 6.27** Comparison with nominal values in hydraulic brake line measurement (AICON)

In each image the hydraulic line appears as an easily identified black contour against a bright background (Fig. 6.26). Bending points, bending angles, straight lines and arcs can be determined fully automatically by digital multi-image processing. The system also calculates correction data with respect to given nominal values that are directly transferred to the bending machine for adjustment of the manufacturing process (Fig. 6.27). The measuring accuracy has been reported as 0.3–0.5 mm within a measuring volume of about  $2.5 \times 1.0 \times 0.7 \text{ m}^3$  (Bösemann 1996).

#### *System for the control of tooling machines and robots*

The system Imetric TI<sup>2</sup>-PCS is used for the high-precision control of large manufacturing devices. The tool (for example a drill) is fitted with targets which are calibrated in three dimensions with respect to the tip (tool centre point). Since the object being worked on is also signalised, the spatial relationship between object and tool can be determined automatically, allowing continuous, on-line correction of positioning errors, geometric deviations of the tool and of deformations caused by temperature changes.

For image acquisition a high-resolution digital camera Imetric ICam 6 (see Fig. 3.85) is used, designed and optimised for industrial environments. Image processing and system control are fully automated, so that unskilled personnel are able to operate the system.

The object shown in Fig. 6.28 (behind the pressure bulkhead, Boeing), with a diameter of about 5 m, consists of 10 layers of aluminium and steel sheet connected by about 4000 rivets.

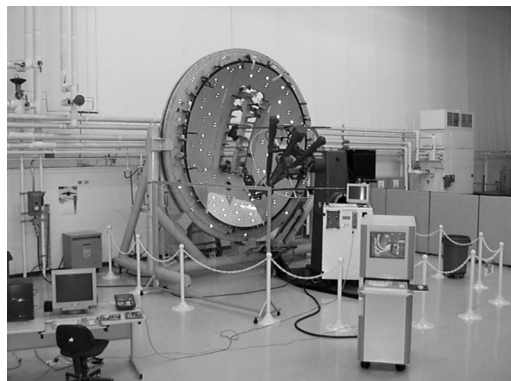


**Figure 6.28** System for the control of manufacturing machines at Boeing (Imetric)

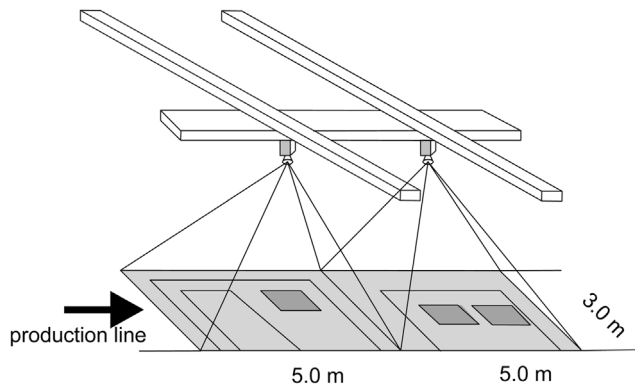


**Figure 6.29** On-line system for the measurement of plane precast concrete parts

Previously, all the holes required were drilled manually using special jigs or templates. In the photogrammetric solution, the positions of targets and reference adapters on the object are determined with respect to the object coordinate system. The drilling robot is approximately positioned manually using a coarse monitor display. Fine positioning is performed during machining by on-line measurement and comparison against nominal values, with a reported accuracy of about 0.05 mm.

#### *System to measure outline shape of plane objects*

Measurement of the outline shape of a plane object is a special case of photogrammetric processing. Using the projective transformation equations (2.12), image coordinates can be transformed uniquely into object space. The transformation parameters are usually determined by at least four co-planar control points.

Fig. 6.29 illustrates the principle of a measuring system for pre-cast concrete parts (Luhmann and Broers 1998). Using a suitable diffuse illumination, the edges of the object are portrayed such that an automatic outline-following procedure can be applied (section 5.4.3). The cameras are calibrated using a test field which is moved into the measuring volume from time

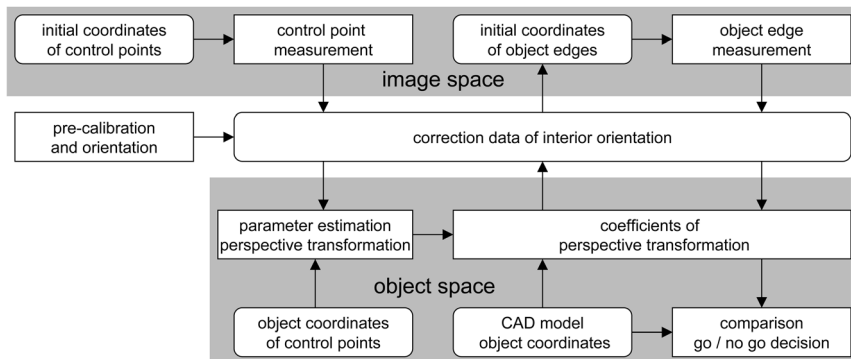


**Figure 6.30** Process for measurement of edges in a plane

to time. CAD design data is used for a coarse segmentation of object edges, and for the final comparison between the design shape and the constructed shape. Calculated and measured image coordinates must be corrected for the effects of interior orientation (radial and tangential distortion, affinity and shear) in order to apply the projective transformation (Fig. 6.30). Deviations from planarity lead directly to positioning errors in the edge measurement according to equation (2.89).

For the checking of precast concrete parts the system works with up to four (independent) CCD video-cameras integrated in an automated production environment. The measuring accuracy amounts to about 1 mm within a measuring volume of about  $10 \times 3 \text{ m}^2$ . The same measurement principle can also be applied to any other plane objects.

#### 6.4.3.2 Multi-image system with rotary table

The POM system (Leica/Rollei) was developed in the late 1980s as a prototype for flexible 3D on-line measurements of automobile parts. It consists of three réseau-scanning cameras, Rollei RSC (see section 3.3.2.5), fixed in a mounting frame. An integrated digital rotary table enables all-round observations of the workpieces to be made (Fig. 6.31).

The system is able to measure signalised targets, and 3D geometric elements by the outline or edge method (see section 4.4.3.2). In order to generate variable illumination, up to 64 computer-controlled light sources are used.

The rotary table is equipped with an angle measuring unit; a multi-stage bundle adjustment determines the orientation and calibration of both camera and rotary table. For rotations  $\alpha$  of the rotary table virtual camera positions  $K'$  are calculated that correspond to new orientation values such as would result from a rotation of the camera around the stationary object (Fig. 6.32). For a non-rotated position  $K$  an object point  $P$  appears at image position  $x$ , and after rotation at position  $x'$ . With only one camera but several rotations of the table, the spatial point coordinates may be calculated (Godding and Luhmann 1992).

The measurement system provided an object accuracy of 0.1 mm within a measuring volume of about  $2.0 \text{ m} \times 2.0 \text{ m} \times 0.6 \text{ m}$  but it was not developed further (Loser and Luhmann 1992).

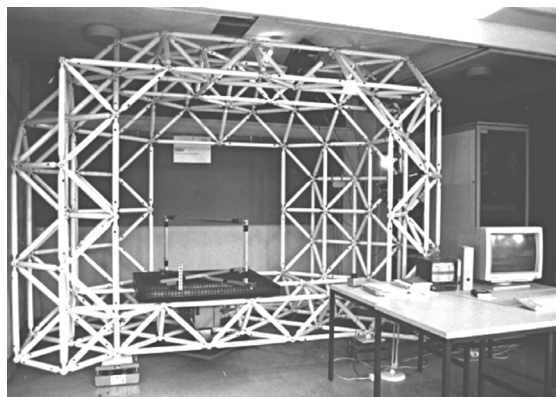


**Figure 6.31** On-line system with digital rotary table (POM)

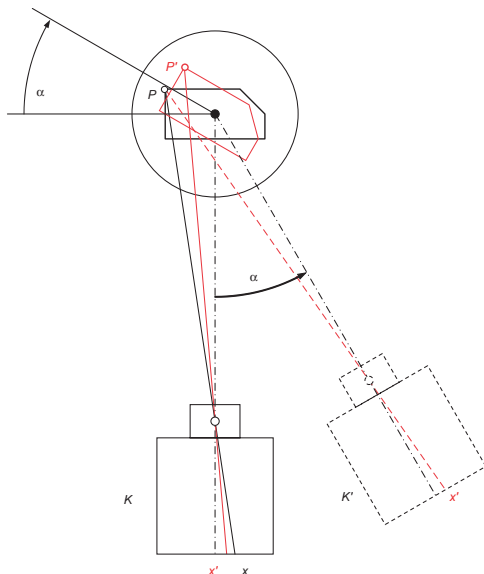


**Figure 6.32** Virtual camera orientation using a rotary table

## 6.5 Systems for surface measurement

In general, area-based probing systems are used when measuring the 3D shape of arbitrary free-form surfaces. A pattern which is projected on the surface is measured and this defines the surface model. Two major approaches can be distinguished:

- Active pattern projection:

The geometry of the projected pattern is known and is used in the calculation. This known geometry includes interior and exterior orientation of the projector and information about the pattern, for example spacing and wavelength of projected fringes. The projector can be regarded as an inverse camera.

At least one oriented camera is used to register the reflected signal from the object surface. The shape of the surface can be reconstructed by phase or parallax measurement.

- Passive pattern projection:

No knowledge of calibration and orientation of the projector or of the pattern geometry is required. The pattern simply provides a visible structure defining the surface. Object reconstruction is performed photogrammetrically by image matching with at least two cameras which record the reflected pattern.

The two approaches can be combined. For example, a fast active projection method can be applied for coarse surface measurement which is then refined using a number of cameras and passive illumination. In the same way these approaches can be combined with usual point-wise photogrammetric measuring methods.

## 6.5.1 Active pattern projection

### 6.5.1.1 Stationary fringe projection

Methods of stationary fringe projection are based on a fixed grid of fringes generated by a projector and observed by one camera (overview in Breuckmann 1993). The grid has a periodical structure, normally with a square or sine-wave intensity distribution with constant wavelength  $\lambda$ .

Fig. 6.33 shows the principle of phase measurement for parallel fringe projection and parallel (telecentric) image acquisition at an angle  $\alpha$ . The wave length  $\lambda$  corresponds to a height difference  $\Delta Z_0$ :

$$\Delta Z_0 = \frac{\lambda}{\sin \alpha} \quad (6.1)$$

The height difference  $\Delta Z$  with respect to a reference plane corresponds to the phase difference  $\Delta\varphi$ :

$$\Delta Z = \frac{\Delta\varphi}{\tan \alpha} \quad (6.2)$$

The phase difference  $\Delta\varphi$  can be measured by counting the fringe number and detecting the grid line in the image. It is unique only in the range  $-\pi \dots +\pi$ . Hence the measuring method is useful only for continuous surfaces which enable a unique matching of fringes. A resolution in height measurement of about  $\lambda/20$  can be obtained.

The method can be extended by using cross grids whose line intersections are measured in the image. The telecentric configuration illustrated in Fig. 6.33 is restricted to the measurement of objects not larger than the lens diameter; if larger objects are to be measured the method has to be extended to perspective lenses. Stationary fringe projection can also be applied to dynamic scenes, for example moving objects.

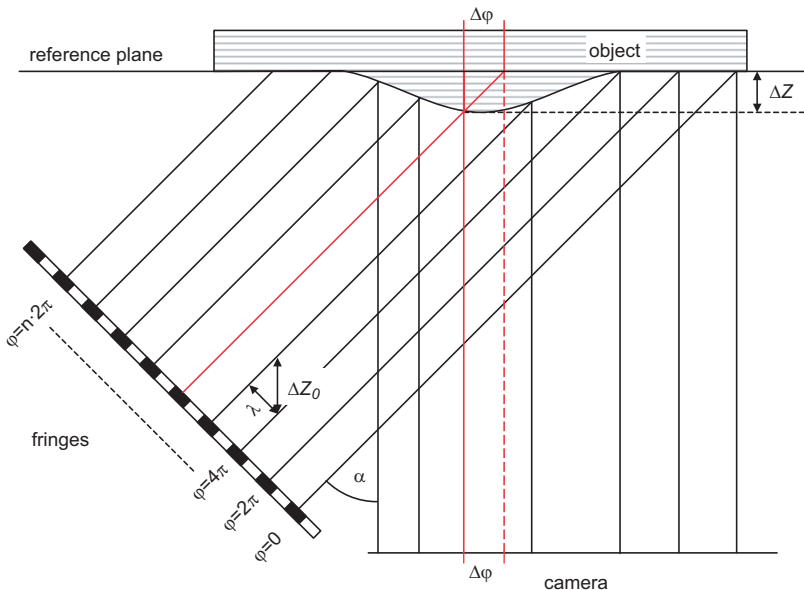


**Figure 6.33** Fringe projection with phase measurement in telecentric configuration

### 6.5.1.2 Dynamic fringe projection (phase-shift method)

Phase measurement can be performed directly using intensity values in the image. For this purpose the projected fringes are regarded as an interferogram. For the intensities of an interferogram at a fringe position  $n$  equation 6.3 applies:

$$I_n(x,y) = I_0(1 + \gamma(x,y) \cos(\delta(x,y) + \varphi_m)) \quad (6.3)$$

where

$I_0$ : constant or background intensity

$\gamma(x,y)$ : fringe modulation

$\delta(x,y)$ : phase

$\varphi_m$ : phase difference

The equation above contains the three unknowns  $I_0$ ,  $\gamma(x,y)$  and  $\delta(x,y)$ . Hence at least three equations of this type have to be set up for a solution. They can be obtained by  $m$  sequential shifts of the fringes by the difference  $\varphi_n$ .

$$\varphi_n = (n-1)\varphi_0 \quad (6.4)$$

where

$m$ : number of shifts

$n = 1 \dots m$ , where  $m \geq 3$

$\varphi_0 = 2\pi/n$

The measuring principle is known as the phase-shift method. For the case of  $m = 4$ , the phase of interest  $\delta(x,y)$  reduces to:

$$\delta = \arctan \frac{I_2 - I_4}{I_3 - I_1} \quad \delta = \delta(x,y) \quad I_n = I_n(x,y) \quad (6.5)$$

Just as with stationary fringe projection the result is unique only in the interval  $-\pi \dots +\pi$ , so that integer multiples of  $2\pi$  have to be added. This process is described as demodulation or unwrapping (Fig. 6.34). Discontinuities of the object surface lead to problems in the unique identification of the fringe number.

Finally, the height profile is given by

$$Z(x,y) = \frac{\lambda}{2 \times 2\pi} \delta(x,y) \quad (6.6)$$

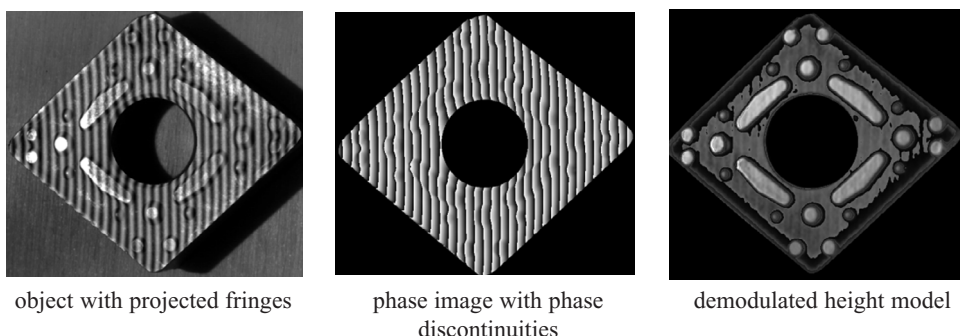


Figure 6.34 Phase-shift method (after Breuckmann 1993)

The accuracy of height measurement is about  $\lambda/100$ . The interior and exterior orientation of projector and camera must be found by calibration. Equation (6.5) is processed for each pixel  $(x, y)$ . The computations can be solved using fast look-up table operations, with the result that height measurements can be processed for all pixels of a camera (for example  $780 \times 570$  pixels) in less than one second.

The performance of this method is determined mainly by the reflective properties of the surface. Usually, homogeneous, diffuse-reflecting surfaces are required. Specular reflections and hot spots must be avoided by means of preparation of the surface (for example by dusting with white powder) and provision of suitable ambient lighting conditions.

Dynamic fringe projection can be applied only for stable, non-moving objects. Occluded surface areas are not visible with the basic configuration, that is, just one camera. The most important advantage of the phase-shift method is the fast measurement of a few hundreds of thousands of surface points. At the same time, however, the problem of thinning and structuring of the measured point cloud arises, necessary for further processing of the 3D data.

A measuring volume between  $0.1 \times 0.1 \times 0.1 \text{ m}^3$  and  $1 \times 1 \times 1 \text{ m}^3$  is typical for fringe projection systems. In order to measure larger objects mobile fringe projection system are combined with photogrammetric methods for spatial orientation. Relative accuracies of 1:8000 can be achieved (see section 6.5.1.4).

### 6.5.1.3 Coded light approach

Solving ambiguities is a major problem for fringe projection methods, especially for discontinuous surfaces. In contrast the coded light approach or Gray code provides an absolute method of fringe projection measurement (Wahl 1986, Stahs and Wahl 1990).

The projector generates  $m$  coded fringes sequentially, so that perpendicular to the fringe direction  $x_p$ , a total of  $2^m$  different projection directions can be identified by an  $m$ -digit code word (the bit order 0011001 for  $m = 7$  in the example of Fig. 6.35). A synchronised CCD camera observes the fringe pattern reflected and deformed by the object surface. The  $m$  images acquired

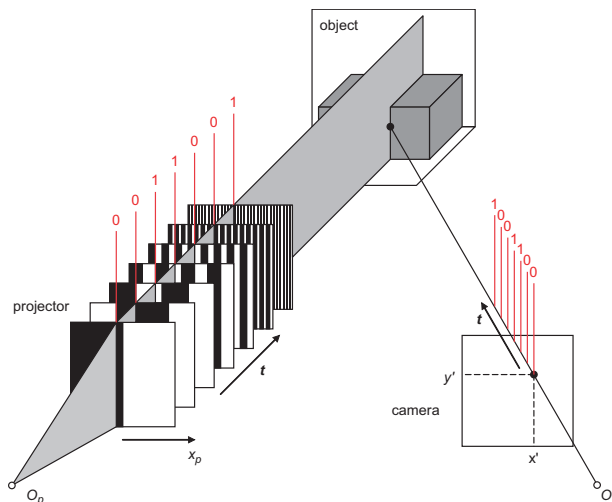


**Figure 6.35** Coded light approach (after Stahs and Wahl 1990)

are binarised and stored as bit values 0 or 1 in an  $m$ -bit-deep bit plane memory. Hence, each grey value at position  $(x', y')$  denotes a specific projection direction  $x_p$  from  $O_p$ .

This procedure requires known orientation parameters of camera and projector but otherwise requires no initial values related to the object. It is relatively insensitive with respect to changing illumination and reflection properties of the object; continuity of the surface is not a requirement. The accuracy of the method is limited to about 1:500. Thus it is mostly useful for fast surface measurements of lower accuracy, for example as a preliminary to subsequent measurement by phase-shift.

#### 6.5.1.4 Multi-camera systems with fringe projection

In their basic configuration the methods of fringe projection mentioned above use one projector and one CCD camera. Because the projector serves as a component of the measurement system, uncertainties in its geometry affect the results adversely. In addition, for objects with large surface variations, occluded and shadowed areas readily occur; these areas cannot be observed by a single camera. Furthermore, smooth surfaces are often subject to excessive illumination or highlights visible in the direction of the single camera.

Consequently, a number of advantages are offered by multi-camera systems with active fringe projection:

- reduced measuring uncertainty as a result of greater redundancy (number of cameras)
- more robust methods in the case of occlusions or highlights
- no requirement for the inclusion of the geometric parameters of the projector in object reconstruction
- possibility of measuring moving objects using synchronised multi-imaging
- higher flexibility with respect to different measuring tasks through variation of the projected pattern and the relative arrangement of projector and cameras.

Calibration and orientation of multi-camera systems with active illumination follow the principles of test field calibration (section 7.2.1.2). The orientation parameters of the projector can also be determined in this process since the projector can be regarded as an inverse camera.

Fig. 6.36 shows a mobile two-camera system with a pattern projector. Two convergent CCD video cameras are arranged on a fixed base and an LCD pattern projector is mounted between them. The measuring volume of a single recording lies between  $12 \times 7 \times 8 \text{ mm}^3$  and  $750 \times 500 \times 500 \text{ mm}^3$  depending on the system configuration. A relative accuracy between 1:2000 and 1:8000 can be achieved.

Using several spatially distributed camera stations, larger more complex objects can be measured. For this purpose the object is prepared with suitable targets that can be measured photogrammetrically, serving as reference or tie points. Then the 3D point clouds generated by each single view can be transformed to a complete object model (Scharsich and Pfeifer 1998, Michaelis 1997, Riechmann and Thielbeer 1997, Winter and Reich 1997). Fig. 6.36 shows a design model measured by this procedure.

#### 6.5.1.5 Phasogrammetry

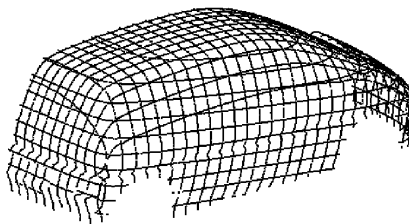
Phasogrammetry, also combines photogrammetric procedures with active pattern projection (Kirschner *et al.* 1997). The basic principle is that two series of pattern sequences (for example Gray-code sequences in combination with phase-shifted fringes) are projected on the measured object from at least two different positions. The second sequence is rotated by  $90^\circ$  with respect



two-camera system with pattern projector



3D point cloud



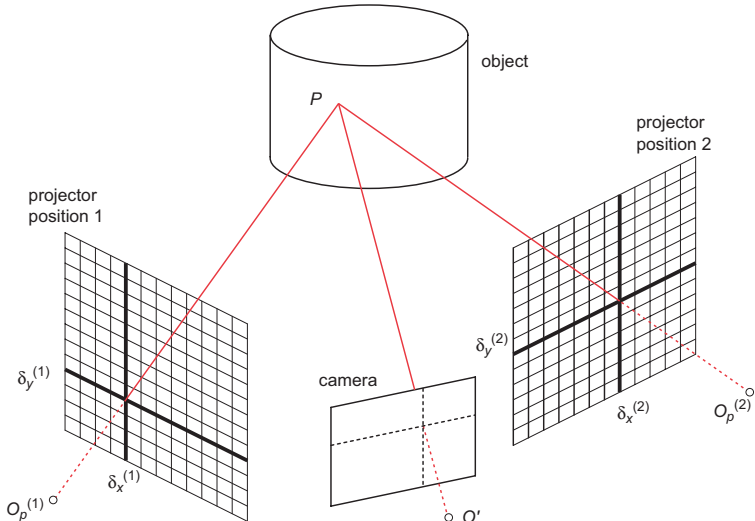
profile lines



shadowing

**Figure 6.36** Measurement of a design model by a photogrammetric fringe projection system (GOM)

to the first sequence while the imaging camera stays fixed in relation to the object. Hence each object point is associated with at least 4 phase values. The phase values  $\delta_x^{(i)}$  and  $\delta_y^{(i)}$  measured at the object point  $P$ , and the related perspective centres, define bundles of rays that can be used for coordinate determination in the same way as photogrammetric bundles (see Fig. 6.37).

**Figure 6.37** Geometric imaging model of phasogrammetry

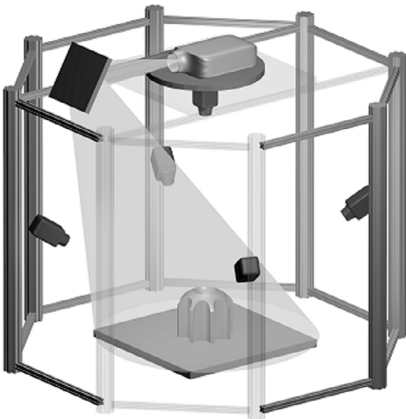


**Figure 6.38** Phasogrammetric multi-camera measuring system Kolibri (FhI IOF)

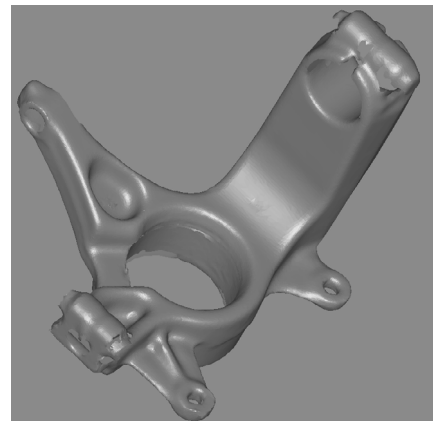


**Figure 6.39** Phasogrammetrically measured workpiece (FhI IOF)

Phasogrammetric systems can be represented in a closed mathematical form based on the collinearity equations (4.8). The normal image coordinates  $x'$ ,  $y'$  are replaced by the projector related phase values  $\delta_x^{(i)}$ ,  $\delta_y^{(i)}$  of object point  $P$  and, in the same manner, the principal point coordinates  $x'_0$ ,  $y'_0$  are replaced by the phase values  $\delta_{x0}^{(i)}$ ,  $\delta_{y0}^{(i)}$ . To convert them into units of length measurement, the phase values are multiplied by  $\lambda/2\pi$  ( $\lambda$  corresponds to the grid constant of the projector according to Fig. 6.33). Consequently, the collinearity equations become:

$$\begin{aligned}\delta_x^{(i)} &= \delta_{x0}^{(i)} - \left( c^{(i)} \frac{2\pi}{\lambda} \right) \cdot \frac{r_{11i} (x - x_0^{(i)}) + r_{21i} (y - y_0^{(i)}) + r_{31i} (z - z_0^{(i)})}{r_{13i} (x - x_0^{(i)}) + r_{23i} (y - y_0^{(i)}) + r_{33i} (z - z_0^{(i)})} + d\delta_x^{(i)} \\ \delta_y^{(i)} &= \delta_{y0}^{(i)} - \left( c^{(i)} \frac{2\pi}{\lambda} \right) \cdot \frac{r_{11i} (x - x_0^{(i)}) + r_{21i} (y - y_0^{(i)}) + r_{31i} (z - z_0^{(i)})}{r_{13i} (x - x_0^{(i)}) + r_{23i} (y - y_0^{(i)}) + r_{33i} (z - z_0^{(i)})} + d\delta_y^{(i)}\end{aligned}\quad (6.7)$$

where

$i$ : index of projector position

A distinctive feature of the phasogrammetric approach is that the system is completely defined by the parameters of the projector. As a consequence, using only the recorded phase values without the inclusion of the camera parameters, it succeeds in simultaneously computing the 3D coordinates and all the orientation parameters of the projectors.

Phasogrammetric measuring systems can be extended to a network for all-round measurements where the object is sequentially illuminated by one or more projectors from different positions, while being sequentially observed by a single camera, or by multiple cameras in parallel (Schreiber and Notni 2000). Various task-specific systems can be implemented. Fig. 6.38 shows an example of a stationary arrangement for all-round measurements.

In the example of Fig. 6.38, cameras are arranged in such a way that they observe the object from different directions. In order to establish different directions of illumination, the projector is mounted on a rotary table. After deflection by a mirror, the pattern sequences are projected from various directions, which may be chosen at will, on the surface of the object to be measured. For each pattern sequence projected in a certain direction, the essential pattern

sequence at  $90^\circ$  is brought about by way of different angular positions of the rotation unit. All cameras acquire their images simultaneously. These steps, changing projection direction and simultaneously imaging the object, are repeated until each object point has been illuminated from at least two different directions. In this way even geometrically complex objects can be measured (an example is shown in Fig. 6.39).

The above-mentioned procedure means that phasogrammetric measuring systems show little sensitivity with respect to temperature deviations, vibrations and so on. Compared with other fringe projection systems higher measuring accuracies can be achieved of the order of 1:50,000 to 1:100,000 of the object size. Since no control points, matching procedures or mechanical or optical guidance systems are involved, minimum mismatches occur for individual patches of multi-station measurements.

## 6.5.2 Passive pattern projection

### 6.5.2.1 Multi-camera system with point projection

A non-targeted free-form surface can be measured point by point; each point is projected onto the surface (section 3.4.2.3) by a laser-scanner and is imaged by a number of CCD video-cameras synchronised with the laser-scanner. Coordinates of each point are calculated by intersection. It is not necessary to know the orientation of the laser-scanner.

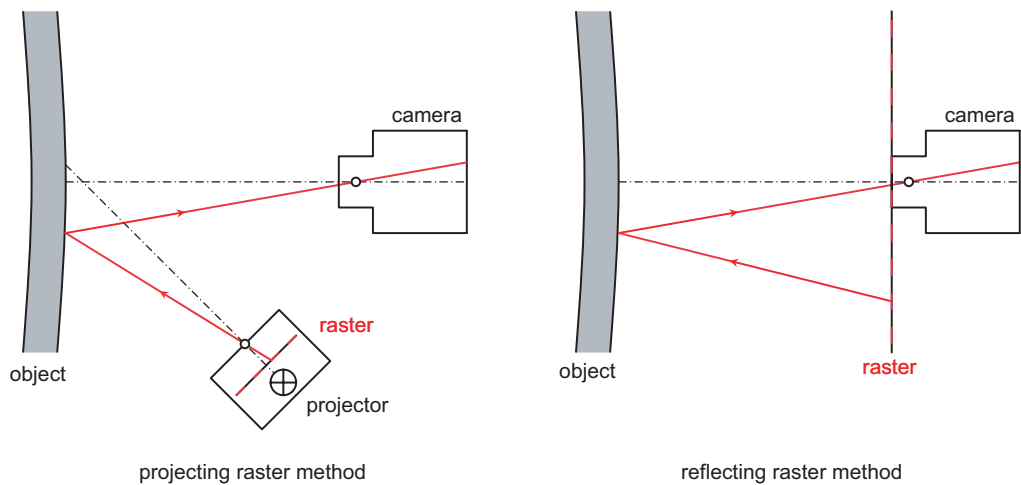
Fig. 6.40 shows the form of a multi-camera measuring system with point projection for surface measurement of curved windshields in the automobile industry (Mapvision). The scanner emits ultraviolet light rays which cause fluorescence when they penetrate the glass, the light spot at the surface being imaged on CCD arrays sensitive to the relevant wavelength. The measuring accuracy of the system has been reported as 0.2 mm.

### 6.5.2.2 Multi-camera systems with raster projection

Raster projection methods are used mainly in materials-testing where displacement or extension fields are to be mapped (Ritter 1995). The surface shape can be reconstructed by analysing the deformation of the raster with respect to a reference position. The reference raster can be generated in different ways:



**Figure 6.40** Multi-image measuring system with laser point projection for the 3D measurement of wind shield surfaces (Mapvision)

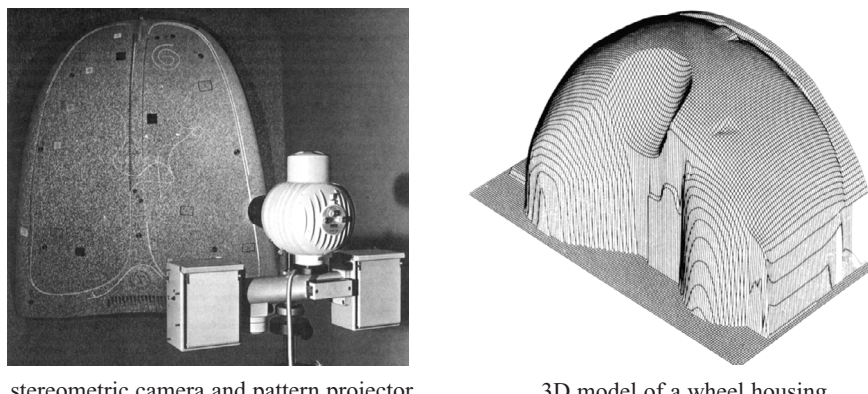
**Figure 6.41** Raster measuring methods (after Ritter 1995)

- by a raster that is physically created at the object surface
- by projection of a raster from the side (Fig. 6.41 left)
- by reflection of a raster (Fig. 6.41 right)

The arrangement of the raster projection method corresponds to that of stationary fringe projection (section 6.5.1.1) and, therefore, can be extended to multiple cameras. The raster reflection method presupposes virtually specular surfaces and allows the measurement only of the inclination of a surface.

### 6.5.2.3 Multi-camera systems with projection of a random dot pattern

The Zeiss Indusurf system was developed as early as the 1980s for the off-line measurement of car body surfaces (Schewe 1988). It consists of an analogue stereometric camera system Zeiss SMK 120 (Fig. 1.26) and a slide projector for the projection of a random dot pattern (Fig. 6.42). The analysis is carried out using an analytical plotter which is equipped with CCD cameras for

**Figure 6.42** Zeiss Indusurf for the measurement of car body surfaces (Schewe 1988)

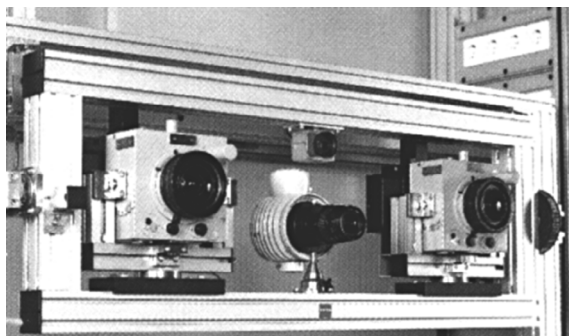


**Figure 6.43** Zeiss Indusurf Digital

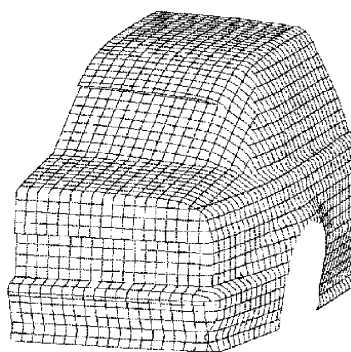
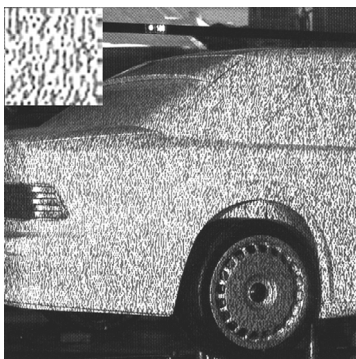


**Figure 6.44** Metric image with random dot pattern and reconstructed CAD model (Zeiss)

digital image acquisition. Parallax measurement is performed using least-squares matching. A measuring accuracy of 0.1 mm can be achieved.

The system developed out of the earlier design uses on-line imaging by two digital cameras (for example, two Zeiss UMK HighScan with pattern projector, Fig. 6.43). Again, the analysis is carried out using least-squares adjustment (Fig. 6.44). The system is used, for example, for on-line shape measurement of containers for molten steel (Kludas 1995).

## 6.6 Acceptance and re-verification of measuring systems

The checking of achievable accuracy is of fundamental importance in industrial metrology. In the field of mechanical coordinate measuring machines (CMM), long-established and standardised methods (VDI/VDE 2617, ISO 10360-2, GUM 1993) define parameters and procedures for acceptance, re-verification and monitoring of measuring accuracy which are generally accepted and implemented in practice. In addition to tactile probing CMMs, additional optical sensors are also considered.

### 6.6.1 Definition of terms

- Acceptance test

An acceptance test is the procedure for acceptance and approval of a measuring system after installation on the customer's site. The acceptance procedure selected is usually

incorporated in the delivery contract. The goal of the test is the first and final proof of the specified measuring accuracy under defined environmental conditions. The acceptance test is usually performed jointly by system supplier and customer.

- Re-verification or monitoring

Re-verification or monitoring is the periodical checking of the measuring system after commissioning. As compared to the acceptance test, the re-verification can be simpler. As a rule it is carried out by the user, who also defines the time interval between such checks.

- Traceability

By traceability is understood the establishment of a link between the measured quantities and a standardised norm, for example the standardised length of a metre. The reference length used must be calibrated and certified by a recognised calibration service.

- Acceptance tolerance

By acceptance tolerance is understood a measured or calculated value (threshold, maximum permitted value) which is permitted under a report on the performance of a system or of single components (for example probing uncertainty, see below).

- Probing deviation

Probing deviation is the value that describes the precision of probing of a single measured point. This parameter is used mainly with respect to CMMs in which the active probe, as distinct from the length measuring system, contributes to the total system accuracy. For example, the probing deviation can be determined by repeated measurement of geometrically known reference objects (for example a sphere). Deviations (residuals) of single measurements with respect to the surface of the reference object indicate the probing deviation.

- Length measurement error

The three-dimensional length measurement error  $\Delta l$  is defined as the difference between a measured (displayed) length  $l_a$  and the calibrated reference length  $l_r$ :

$$\Delta l = l_a - l_r \quad (6.8)$$

The length measurement error is usually derived from the measurement of two single probings (for example on a gauge block). Alternatively it can be determined from the distance measurement of two balls if the probing error can be eliminated.

The characteristic parameter, length measurement error, is used to analyse the accuracy of length measurement. Calibrated reference lengths can easily be established (for exceptions see below), and they can be traced back to a standard. Uncertainty of length measurement implicitly includes the probing uncertainty. The maximum permitted positive and negative limit of length measurement error  $E$  is in the first place defined as a length-dependent value that may not be exceeded in the checking of any deviation of length measurement (see Fig. 6.48):

$$E = A + K L \leq B \quad (6.9)$$

$E$ : limit of error of length measurement

$A, K$ : machine-specific constant

$L$ : measured length

$B$ : maximum permitted deviation of length measurement

Since the error of photogrammetric length measurement does not necessarily depend on the length itself, the constant  $K$  may be zero.

- Reference object

A reference object is a physically defined object with known geometric parameters. It should be manufactured at reasonable cost, and it should be easy to use. Examples of reference objects are step gauges, ball plates or reference scale bars. The calibration accuracy for a reference object should be approximately five times higher than that of the measuring system to be checked. Acceptance and re-verification procedures usually require a calibration certificate for the reference object.

## 6.6.2 Differentiation from coordinate measuring machines

For a long time standardised guidelines were not available for acceptance and re-verification tests for photogrammetric metrology systems. In Germany the guideline VDI/VDE 2634 for optical 3D measuring systems was published in 2000. It proposes procedures for optical systems which differ from CCM methods especially on the following points:

- Image-based measurement of a large number of points

Optical 3D measuring systems, being image-based, enable the simultaneous registration of large numbers of object points (in the limit, each pixel). By contrast, CMMs usually measure only one point per probe.

- Triangulation principle

Photogrammetric and fringe projection systems are based on triangulation, which leads to accuracies of object points which are dependent on scale and configuration. A homogeneous accuracy cannot, therefore, be expected within a specified measuring volume.

- Mobility

Mobile optical 3D measuring systems can be moved to the object. Consequently, their calibration data may change from time to time, they can operate under changing environmental conditions, or their imaging configuration may vary.

- Flexible configurations

Non-stationary photogrammetric systems allow free choice of camera stations. Thus the user himself determines the number and distribution of the images, the selection of cameras and lenses and the type of object targeting or probing.

- Unlimited measuring volume

In principle, the measuring volume of photogrammetric systems is unlimited in so far as depth of focus and field of view allow. If scale-dependent resolution of object details is taken into account, arbitrary object dimensions can be measured. Conversely, the measuring volume of mechanical CMMs is always limited.

- Reference objects

Supplying reference objects for acceptance and re-verification tests for photogrammetric systems can be problematic. It is difficult to find scale bars suitable for simulation of large measuring volumes (dimensions  $> 3 \text{ m}$ ). For smaller measuring volumes ( $< 1 \text{ m}^3$ ) optical 3D systems achieve measuring accuracies of the order of  $10 \mu\text{m}$  (1:100,000)

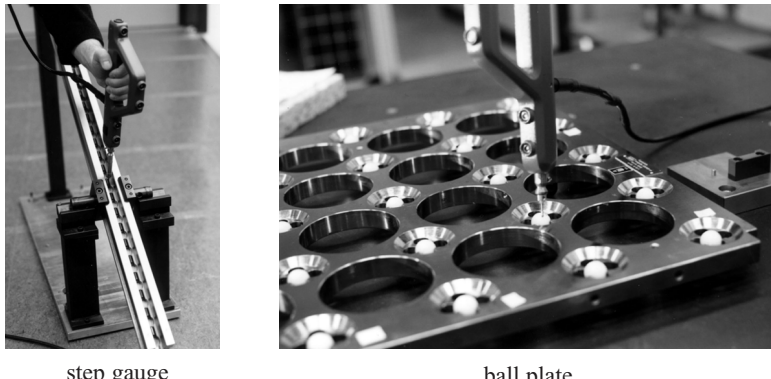


**Figure 6.45** Standard reference objects for 3D coordinate measuring machines

requiring high-precision reference objects with suitable targets. Because of their optical characteristics, standard reference objects such as step gauges or ball plates, which may be successfully used in CCM metrology, are useful only for photogrammetric on-line systems with tactile probing (Fig. 6.45).

For larger measuring volumes, such as in the measurement of parabolic antennae or ships, measuring accuracy is often checked using industrial theodolite systems or laser trackers. Differences in coordinates or in computed distances allow comparison of accuracies. It should be observed that high accuracy photogrammetric systems almost match the performance of theodolites. It should also be noted that theodolite measurements are costly in time and personnel and that they require geometric stability over the period of the observations. Laser trackers provide high accuracy in length measurement owing to their interferometric range finders, but they are quite expensive.

### 6.6.3 Uncertainty of length measurement

In the industrial field, checking of selected distances in object space is a proven method for assessment of system accuracy. In contrast to control point coordinates, reference distances can be supplied relatively easily and, above all, accuracy in length measurement is easy to interpret (Dold 1997, Schwenke *et al.* 1997).



a) reference scale bars with retro-targets

b) ball scale bar

**Figure 6.46** Reference scale bars

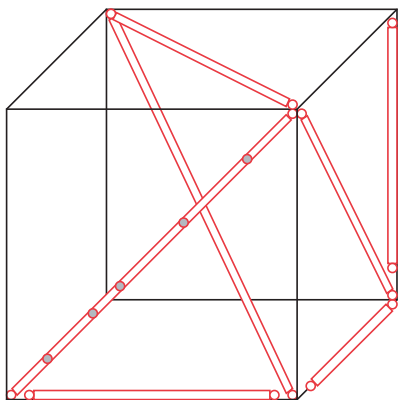


**Figure 6.47** Arrangement of reference distances within the measuring volume

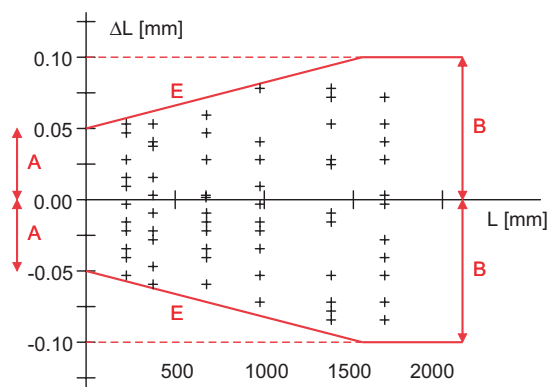


**Figure 6.48** Diagram of length measurement deviations

To serve as reference lengths, scale bars can be produced in appropriate lengths. They should use the same type of targets as are used for the actual object measurement. The length can be calibrated, for example, by optical CMMs (for shorter lengths), photogrammetrically (using large format cameras), by field survey (using theodolites) or by laser interferometry.

In order to guarantee a sound analysis of the system, the arrangement of reference scale bars in object space should suit the measuring task. If equal measuring accuracies are required for all coordinate axes, the scale bars must be arranged in such a way that direction-dependent length measurement deviations can be determined. A possible set-up is illustrated in Fig. 6.47. Of seven scale bars, three are arranged parallel to the coordinate axes and four along diagonals of a cuboid measuring volume. In order to extend the number of reference lengths, individual reference bars may be sub-divided. For example, the scale bar, displayed in the foreground of Fig. 6.47 carries five targets which can be used in various combinations to provide 21 different lengths.

In order to provide a practical tool for the analysis and illustration of length measurement deviations, a diagram can be generated which displays the measured differences with respect to the nominal distances (Fig. 6.48). The maximum permitted limits are determined according to equation (6.9). A measuring system can be accepted as successful if all measured deviations lie within the maximum permitted interval.

Area-based systems can be tested according to VDI 2634/2. The guideline recommends the measurement of the following parameters:

- Probing error: indicates the local noise of surface measurement on a calibrated reference sphere. The probing error depends on different factors such as digitising errors, phase measuring errors, pixel and image coordinate measuring errors and lateral structural resolution.
- Flatness measurement error: indicates the ability of a system to measure a reference plane.
- Sphere spacing error: signifies the ability of the system to measure the distance between two spheres, hence approximately conforming to the ISO-conform length measurement error.

In addition, VDI 2634/3 will deal with those systems that provide area-based measurements and sensor orientations in order to measure objects that are larger than the initial measuring volume of a surface measuring sensor.

## References

- Benning, W. and Schwermann, R. (1997) PHIDIAS-MS – Eine digitale Photogrammetrie-applikation unter MicroStation für Nahbereichsanwendungen. *Allgemeine Vermessungsnachrichten*, 1/1997, pp. 16–25.
- Beyer, H. A., Uffenkamp, V. and van der Vlugt, G. (1995) Quality control in industry with digital photogrammetry. In Gruen/Kahmen (ed.) *Optical 3-D Measurement Techniques III*. Wichmann, Heidelberg, pp. 29–38.
- Bösemann, W. (1996) The optical tube measurement system OLM – photogrammetric methods used for industrial automation and process control. *International Archives of Photogrammetry and Remote Sensing*, 31(B5), pp. 55–58.
- Breuckmann, B. (1993) *Bildverarbeitung und optische Meßtechnik in der industriellen Praxis*. Franzis Verlag, München.
- Brown, J. and Dold, J. (1995) V-STARS – a system for digital industrial photogrammetry. In Gruen/Kahmen (ed.) *Optical 3-D Measurement Techniques III*. Wichmann Verlag, Heidelberg, pp. 12–21.
- Dold, J. (1997) *Ein hybrides photogrammetrisches Industriemeßsystem höchster Genauigkeit und seine Überprüfung*. Dissertation, Heft 54, Schriftenreihe Studiengang Vermessungswesen, Universität der Bundeswehr, München.
- Dold, J. (1999) Stand der Technik in der Industriephotogrammetrie. *Photogrammetrie-Fernerkundung-Geoinformation*, Heft 2, pp. 113–126.
- Dorrer, E. (1998) *Einsatz der IMP-Stereokamera beim Mars Pathfinder*. Publikation der DGPF, Band 6, Frankfurt 1997, pp. 259–270.
- Fellbaum, M and Godding, R. (1995) Economic Solutions in Photogrammetry through a Combination of Digital Systems and Modern Estimation Techniques. In Gruen/Kahmen (ed.) *Optical 3D Measurement Techniques III*, Wichmann Verlag, Karlsruhe, pp. 362–372.
- Fraser, C. S. and Brown, D. C. (1986) Industrial photogrammetry – new developments and recent applications. *The Photogrammetric Record* 12(68).
- Godding, R., Lehmann, M. and Rawiel, G. (1997) Robot adjustment and 3-D calibration – photogrammetric quality control in daily use. In Gruen/Kahmen (ed.) *Optical 3-D Measurement Techniques IV*, Wichmann Verlag, Heidelberg, pp. 158–165.
- Godding, R. and Luhmann, T. (1992) Calibration and accuracy assessment of a multi-sensor online-photogrammetric system. *International Archives of Photogrammetry and Remote Sensing*, 29(5), Washington, pp. 24–29.
- GUM (1993) *ISO guide to the expression of uncertainty in measurement (GUM)*.
- Heipke C. (1995) State-of-the-art of digital photogrammetric workstations for topographic applications, *Photogrammetric Engineering & Remote Sensing* 61(1), pp. 49–56.
- Hinsken, L. and Meid, A. (1994) *Eine hochgenaue, analytische, photogrammetrische Arbeitsstation als 3D-Eingabeinstrument eines CAD-Paketes für Nahbereichs-anwendungen*. Publikation der DGPF, Band 2, Augsburg 1993, pp. 121–128.
- ISO 10360: *Geometrical Product Specifications (GPS) – Acceptance and reverification tests for coordinate measuring machines (CMM)*. Beuth, Berlin.
- Kirschner V., Schreiber W., Kowarschik R. and Notni G. (1997) *Selfcalibrating shape-measuring system based on fringe projection*. Proc. SPIE 3102, pp. 5–13.
- Kludas, T. (1995) Three-dimensional surface reconstruction with the Zeiss photogrammetric industrial measurement system InduSURF Digital. ISPRS Intercommission Workshop, *From Pixels to Sequences*, Zürich, pp. 285–291.
- Kraus, K. (1997) *Photogrammetry, Volume 2, Advanced Methods and Applications*. With contributions by J. Jansa and H. Kagar. Dümmler Verlag, Bonn.
- Loser, R. and Luhmann, T. (1992) The programmable optical 3-D measuring system POM – applications and performance. *International Archives of Photogrammetry and Remote Sensing*, 29(B5), Comm. V, Washington, pp. 533–540.

- Luhmann, T. and Broers, H. (1998) *An automatic system for the measurement of flat workpieces*. ISPRS Conference, Commission V, Hakodate, Japan.
- Luhmann, T. and Wester-Ebbinghaus, W. (1986) *Rolleimetric RS – A New System for Digital Image Processing*. Symposium ISPRS Commission II, Baltimore.
- Maas, H.-G. (1997) *Dynamic photogrammetric calibration of industrial robots*. Videometrics V, SPIE Proceedings Series Vol. 3174.
- Michaelis, M. (1997) *3D-Objekterfassung mit Photogrammetrie und Streifenprojektion*. Publikation der DGPF, Band 5, Oldenburg 1996, pp. 167–173.
- Peipe, J., Schneider, C.T. and Sinnreich, K. (1994) Performance of a PC based digital photogrammetric station. *International Archives of Photogrammetry and Remote Sensing*, **30**(5), pp. 304–309.
- Pettersen, H. (1992) Metrology Norway System – an on-line industrial photogrammetry system. *International Archives of Photogrammetry and Remote Sensing*, **24**(B5), pp. 43–49.
- Riechmann, W. and Thielbeer, B. (1997) Hochaufgelöste Oberflächenerfassung durch Photogrammetrie und Streifenprojektion. *Photogrammetrie-Fernerkundung-Geoinformation*, Heft 3, pp. 155–164.
- Ritter, R. (1995) Optische Feldmeßmethoden. In Schwarz (ed.) *Vermessungsverfahren im Maschinen- und Anlagenbau*, Verlag Konrad Wittwer, Stuttgart, pp. 217–234.
- Scharsich, P. and Pfeifer, T. (1998) *Aktive Mehrbildphotogrammetrie für die flächenhafte dreidimensionale Form erfassung*. Publikation der DGPF, Band 6, Frankfurt 1997, pp. 279–286.
- Schewe, H. (1988) Automatische photogrammetrische Karosserievermessung. *Bildmessung und Luftbildwesen*, Heft 1/1988, pp. 16–24.
- Schreiber W. and Notni G. (2000) Theory and arrangements of self-calibrating whole-body three-dimensional measurement systems using fringe projection technique. *Optical Engineering* **39**, pp. 159–169.
- Schwenke, H., Wäldele, F. and Wendt, K. (1997) Überwachung und Meßunsicherheit von optischen 3D-Meßsystemen. GMA-Bericht 30, *Optische Form erfassung*, Langen, pp. 271–280.
- Sinnreich, K. and Bösemann, W. (1999) *Der mobile 3D-Meßtaster von AICON - ein neues System für die digitale Industrie-Photogrammetrie*. Publikation der DGPF, Band 7, München 1998.
- Stahs, T., and Wahl F. M. (1990) Oberflächenmessung mit einem 3D-Robotersensor. *Zeitschrift für Photogrammetrie und Fernerkundung*, Heft 6/1990, pp. 190–202.
- VDI/VDE 2617: *Accuracy of coordinate measuring machines; characteristics and their checking*. VDI/VDE guide line, Part 1–6, Beuth, Berlin
- VDI/VDE 2634: *Optical 3D measuring systems*. VDI/VDE guide line, Beuth, Berlin.
- Wahl, F. M. (1986) A coded light approach for depth map acquisition. In Hartmann (ed.) *Mustererkennung 1986*, Springer Verlag, Berlin, pp. 12–17.
- Winter, D. and Reich, C. (1997) Video-3D-Digitalisierung komplexer Objekte mit frei beweglichen, topometrischen Sensoren. GMA-Bericht 30, *Optische Form-erfassung*, Langen, pp. 119–127.
- Woytowicz, D. (2002) 3D-Geometrieerfassung von Anlagen und Gebäuden mit Hilfe der digitalen Nahbereichsphotogrammetrie. In Luhmann (ed.) *Photogrammetrie und Laserscanning*, Wichmann Verlag, Heidelberg, pp. 29–31.



# 7 Measurement concepts and solutions in practice

This chapter summarises basic imaging configurations and practical solutions which can be applied to a wide variety of measurement problems. Criteria and methods for planning a photogrammetric project are first discussed. This is followed by a discussion on configurations for the self-calibration of cameras. The special requirements for the recording of dynamic phenomena are then presented. The final section deals with aerial image acquisition from low altitudes.

## 7.1 Project planning

### 7.1.1 Planning criteria

The planning of a photogrammetric project includes the description of the actual measuring task, the concept for a solution and the presentation of results. It should be carried out in close co-operation with the client in order to ensure that requirements are clearly understood. Close association with the client is vital as misunderstandings of requirements are otherwise only detectable at a late stage when they are difficult to correct. Planning the imaging configuration is one aspect of the complete project plan which should include, in addition to metrology issues, economic aspects such as staff and time management, use of instruments, cost management etc.

The initial project plan should specify the following features of the measuring task:

- number and type of object areas to be measured including a description of the object, its situation and the measuring task requirements
- smallest object feature (resolution of fine detail)
- type of data that will be produced (coordinated points, line strings, surfaces, textured model, etc.)
- environmental conditions (variations in temperature, humidity, pressure and the presence of any vibration)
- options for object targeting
- definition and implementation of the object coordinate system
- determination of scale and reference points (geodetic measurements)
- alternative or supplementary measuring methods

- on-line or off-line measurement
- acceptance test procedure or verification of accuracy
- available times for on-site work
- maximum permitted time for analysis and evaluation
- output of results (numerical and graphical, interfaces)

In the subsequent detailed planning stages an appropriate concept for the solution can be developed. In particular the image acquisition system and imaging configuration, as well as the type of image and data processing, must be defined. Apart from purely technical considerations (e.g. accuracy), the choice of components used also depends on the availability of instruments and personnel.

The following criteria should be defined in detail:

- estimation of average image scale
- camera stations (number of images, network design, ray intersection design)
- required image measuring accuracy
- selected imaging system (analogue, digital, image format, focal lengths)
- optical parameters (depth of field, resolution)
- selected processing system (analogue/digital, monoscopic, stereoscopic, multi-image)
- amount of memory for image data (type and cost of archiving)

### 7.1.2 Accuracy issues

Besides economic aspects, meeting accuracy requirements is generally of highest priority in practical project planning. Approximate accuracy estimates can be based on the relationships given in section 3.2.1 which depend on three primary parameters:

- image measurement accuracy
- image scale
- design factor of the imaging configuration

Image measurement accuracy depends on the performance of the camera (stability and calibration), the accuracy of the image processing system (image quality, measurement algorithm, instrumental precision) and the positioning capability (identification of features). These criteria must be balanced with respect to each other and given appropriate weight in the planning process. The camera and lens selected for any given project is particularly important as it not only defines the quality of image acquisition and processing but, through choice of lens, also defines image scale and configuration.

Fig. 7.1 illustrates schematically the accuracy potential of typical imaging and processing systems as well as common and optimal system combinations. For analogue cameras image measurement accuracies between 1 µm and 20 µm can be achieved, depending on how image coordinate system (reseau, image flattening) and camera calibration have been implemented. The accuracy potential of generally available analytical image measuring instruments is within a similar range.

Digital imaging systems can reach image measurement accuracies of 0.2–1 µm (1/50–1/10 pixel) depending on the mechanical stability and signal transfer type (A/D conversation). Digital processing systems providing subpixel operators for signalised targets can yield image accuracies between 1/100–5/100 pixels.

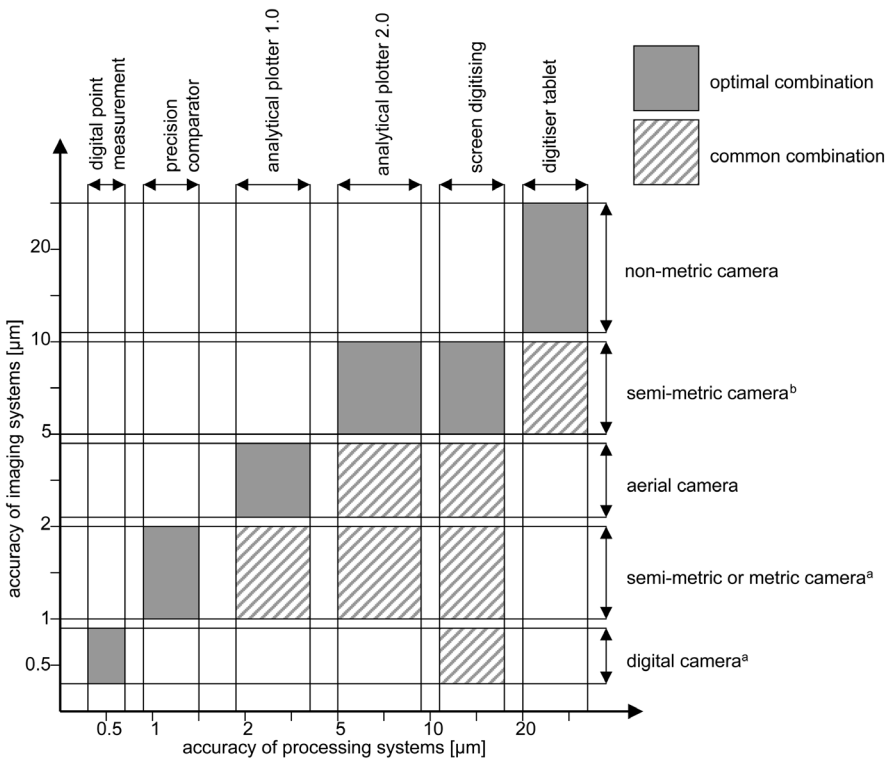


**Figure 7.1** Accuracy potential of imaging and analysis systems<sup>1</sup>  
a) with self-calibration and b) without self-calibration

### 7.1.3 Restrictions on imaging configuration

A generally applicable geometric configuration for photogrammetric measurement cannot be defined because it always depends on circumstances specific to the object. A compromise must normally be found between different and partly incompatible restrictions (Fraser 1996):

- Image scale

The image scale is influenced by object distance, lens focal length (principal distance) and usable image format (see Fig. 3.4). A larger image format enables shorter object distances for the same imaged object area. It not only leads to a larger scale (and higher accuracy) but also to a smaller number of images (economic benefits in reduced data processing and storage). It must be remembered that for complex object structures and highly convergent images, image scale can vary significantly within an image or from image to image and that this situation will be compounded by short camera to object distances.

- Image quality

The ability to detect and measure object details is again a function of image scale. The size of imaged object structures should lie between certain limits.

<sup>1</sup> The displayed accuracy ranges are typical values with variable borders.

- visual analogue processing: one to three times the diameter of the floating mark
- visual digital processing: 2–10 pixels
- automatic digital point measurement: 6–10 pixels
- automatic digital surface measurement: 11–25 pixel window size

- Object environment

The selection of suitable camera stations is often restricted by inaccessible object areas. It is therefore often necessary to use either additional lenses (allowing a variety of object distances), to increase the number of images or to dispense with optimal ray intersections.

- Depth of field

The available depth of field (section 3.2.2.5) is a function of image scale and f-stop. Given an object with significant 3D shape, depth of field can restrict the choice of camera stations, especially for large image scales and under difficult lighting conditions. If signalised targets are measured automatically, a slightly defocused image can be accepted if image contrast and point diameter are sufficiently large.

- Imaging angle

The imaging angle  $\beta$  at which an object is photographed should not be less than  $20^\circ$  for critical object features and not less than  $30^\circ$  for retro-reflective targets in order to achieve suitable image sizes and contrasts (Fig. 7.2). Furthermore, extremely oblique views have an eccentricity effect on the centre of circular targets as explained in section 3.4.1.1. Spherical targets, in contrast, can be observed at arbitrary imaging angles.

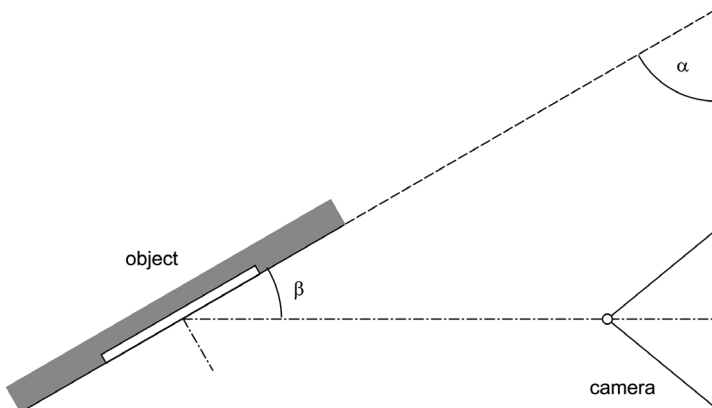


**Figure 7.2** Imaging angle

- Number and distribution of image points

Given a strong network the total number of object points has little effect on the overall redundancy of the bundle adjustment. The quality of bundle triangulation depends more on the number and configuration of camera stations which, in addition to creating a reasonable intersection geometry, should ideally utilise the full image format (see Fig. 7.3).

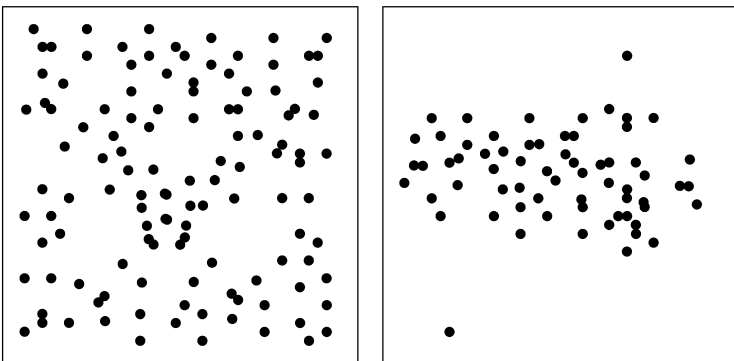


**Figure 7.3** Optimal (left) and poor (right) distribution of image points

- Intersection angle

Good intersection angles are critical to the accuracy of point measurement (see Fig. 4.66). For the graphical reconstruction of approximately flat object surfaces (building facades) a reduced accuracy in the viewing direction can often be tolerated and in these cases it is possible to work with poor intersection angles (or insufficient base-to-height ratios).

Engineering or industrial projects often require an object accuracy which is equal in all directions. Optimal intersections exist if image rays intersect at angles of around  $90^\circ$ – $100^\circ$ . In practice intersection angles between  $45^\circ$  and  $120^\circ$  are sufficient if at least 4 to 6 images contribute to the measurement.

- Viewing angle and visibility

The viewing angle defines the field of view of a camera (section 3.2.2.7). If all object points can be imaged in all photos then the imaging configuration is simplified and the number of images required is reduced. At the same time, the total redundancy of the bundle triangulation increases. Since this assumption is only valid for simple structured objects (e.g. test fields for calibration purposes, see section 7.2.1.2) occluded object areas must be recorded with additional photos which only include a small portion of all object points. To ensure network stability, these additional images should contain a reasonable number of well distributed tie points.

#### 7.1.4 Computer-aided design of the imaging network

The restrictions mentioned above limit the choice of camera stations and viewing directions. In practice a well configured network which surrounds the object, as indicated in Fig. 3.3, is impossible for many applications because of object restrictions or economic circumstances (e.g. minimum number of images). Image scales and intersection angles can therefore vary widely within a project, so that equation (3.5) is only valid for average accuracy estimations. Weak areas in an imaging network cannot be detected by this approach.

The image configuration can be simulated by bundle adjustment (section 4.3.6.1) if there are sufficient *a priori* object coordinates to represent object geometry. In this process the principal distance and exterior orientation of all cameras are iteratively varied until maximum accuracy (minimum standard deviations of object coordinates) is optimised.

In general, object point accuracy and associated derived quantities (lengths, distances etc.) are of greatest importance in practice. In order to assess the expected accuracy it is helpful to split up the vector of unknowns in the bundle adjustment and express equation (4.55) in the form:

$$\begin{bmatrix} \hat{\mathbf{x}}_1 \\ \hat{\mathbf{x}}_2 \end{bmatrix} = \begin{bmatrix} \mathbf{A}_1^T \mathbf{P} \mathbf{A}_1 & \mathbf{A}_1^T \mathbf{P} \mathbf{A}_2 \\ \mathbf{A}_2^T \mathbf{P} \mathbf{A}_1 & \mathbf{A}_2^T \mathbf{P} \mathbf{A}_2 \end{bmatrix}^{-1} \begin{bmatrix} \mathbf{A}_1^T \mathbf{P} \mathbf{l} \\ \mathbf{A}_2^T \mathbf{P} \mathbf{l} \end{bmatrix} \quad (7.1)$$

and

$$\mathbf{Q} = \begin{bmatrix} \mathbf{Q}_1 & \mathbf{Q}_{12} \\ \mathbf{Q}_{21} & \mathbf{Q}_2 \end{bmatrix}$$

where

- $\hat{\mathbf{x}}_1$  : exterior orientation and additional parameters
- $\hat{\mathbf{x}}_2$  : object point coordinates

In order to optimise the object point accuracy,  $\mathbf{Q}_2$  should be analysed according to the following considerations:

- Maximum reliability (ability to control and detect outliers)

Statistical measures for reliability and robustness of an adjustment can be derived from the cofactor matrix of corrections  $\mathbf{Q}_{vv}$  (section 2.3.3.4, equation (2.103)).

- Maximum economic efficiency

The objective is to achieve the specified accuracy and reliability for minimum instrumental and personal effort.

The optimisation of photogrammetric imaging configurations (network optimisation, network design) can be considered in four stages (Fraser 1996, Mason 1994):

1. Zero order design: definition of datum (object coordinate system)

Standard deviations of object coordinates are directly influenced by the definition of the object coordinate system (section 4.3.3). Potential network deformation can be avoided by a datum definition without constraints. Optimal standard deviations are obtained by a free net adjustment which minimises the trace of the covariance matrix. In most cases the covariances of the object coordinates of a point  $i$  can be estimated by

$$\mathbf{Q}_{2i} \approx s_0^2 (\mathbf{A}_2^T \mathbf{P} \mathbf{A}_2)_i^{-1} \quad (7.2)$$

2. First order design: optimisation of the observation configuration

The purpose of optimising the configuration is to define an observation network whose design matrix  $\mathbf{A}$ , given a predefined weight matrix  $\mathbf{P}$ , results in a covariance matrix  $\mathbf{Q}_2$  corresponding to the specified accuracy. This is primarily a question of achieving good intersection angles at the object points. Assuming an appropriate minimum configuration which does this,  $\mathbf{Q}_2$  can be estimated by:

$$\mathbf{Q}_2 = \frac{s_{x'y'}^2}{k} (\mathbf{A}_{2B}^T \mathbf{P} \mathbf{A}_{2B})^{-1} \quad (7.3)$$

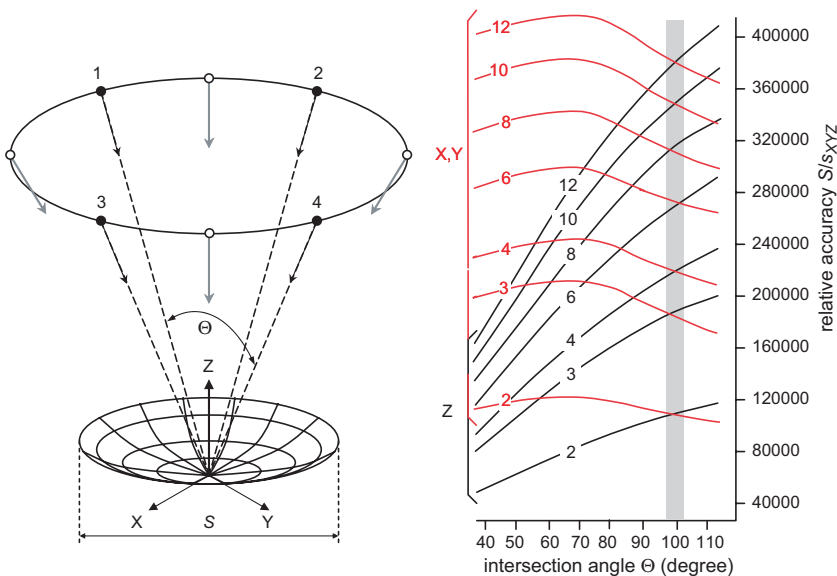


**Figure 7.4** Imaging configuration for antenna measurement and resulting object accuracies after variation of intersecting angles and number of camera stations (after Fraser 1996)

where

$\mathbf{A}_{2B}$ : basic configuration design matrix

$s_{x'y}^2$ : standard deviations of image coordinates

$k$ : number of additional, symmetrically arranged camera stations

The design factor  $q$  and the image scale number of equation (3.5) are reflected here in the matrix product.

Fig. 7.4 illustrates the imaging configuration for an antenna measurement. The basic configuration consists of four camera stations. Additional images are added symmetrically at equal object distances. The intersection angle  $\Theta$  (see Fig. 7.4) is defined between the viewing directions of diametrically opposite camera stations. The diagram shows the resulting relative object accuracies  $S/s_{XYZ}$  as a function of the intersection angle and the number of camera stations. The relative accuracy increases with an increasing number of images. Equal values in all coordinate axes are obtained at  $\Theta \approx 100^\circ$ .

### 3. Second order design: definition of observation weights (image measurement precision)

The normal system of equations can be readily manipulated by appropriate choice of observation weights. Generally the *a priori* standard deviations of image measurements are defined according to the precision of the image measuring device. Normally all image observations are given equal weights. Unequal weights are only justified if different measuring devices or algorithms are employed. In such cases an analysis of variances enables balanced groups of observations to be defined (see section 2.3.4.3).

### 4. Third order design: optimisation of point density (object points)

Where self calibration of the camera is not required, around 20–50 object points are sufficient to achieve a stable network geometry, optimised according to the above criteria. The quality of point measurement does not significantly improve if the number of object

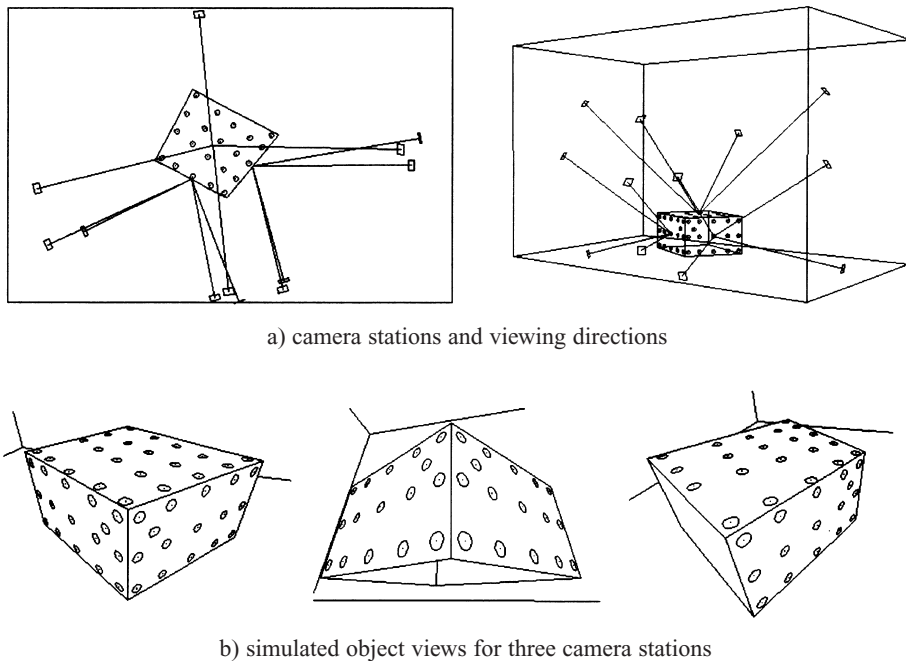


**Figure 7.5** Example of an automated design of an imaging configuration (after Mason 1994)

points is further increased. However, if the camera must be calibrated (self calibration), the imaged targets must have a good distribution and density in order to determine distortion parameters reliably across the entire image format (Fig. 7.3).

Significant effort is required for realistic simulations because in many cases object coordinates are either not available or must be generated. In addition the selection of camera stations and viewing directions is usually performed interactively. Photogrammetric multi-image processing systems connected to 3D CAD systems offer an efficient basis for the simulation of imaging configurations if the object can be represented as a CAD model and if the camera stations can be edited graphically.

Another possibility for the simulation of standard configurations is to describe the object by primitive geometric solids (parallelepiped, hemisphere, plane etc.). In these cases object and reference point coordinates can be calculated automatically (Schlögelhofer 1989). In contrast, the automated definition of camera positions is much more complicated and expert knowledge and decision rules are required. Fig. 7.5 shows an imaging configuration which has been calculated by an expert system (CONSENS) for the measurement of the three faces of a parallelepiped (Mason 1994). Each face is recorded by four images.

## 7.2 Camera calibration

### 7.2.1 Calibration methods

The purpose of camera calibration is to determine the geometric camera model described by the parameters of interior orientation (see section 3.2.3.1):

- principal distance
- image coordinates of principal point
- radial distortion
- tangential (asymmetric or decentring) distortion
- affinity and shear of the image coordinate system
- other additional parameters

In general the interior orientation is assumed to be known and constant for metric cameras. The problem of camera calibration therefore mainly concerns those imaging systems (e.g. semi-metric cameras, CCD cameras) whose geometry is subject to variation over time. However, depending on the actual accuracy specifications, even metric cameras may have to be calibrated for the duration of image acquisition.

Three calibration methods can effectively be distinguished. These are characterised by the reference object used and by the time and location of calibration:

- laboratory calibration (section 7.2.1.1)
- test field calibration (section 7.2.1.2)
- self-calibration (section 7.2.1.5)

Recent state-of-the-art camera calibration techniques involve a computational solution for camera parameters (camera model) which often cannot be separated from the actual object measurement. Consequently, an understanding of the different approaches to calibration requires a detailed knowledge of photogrammetric orientation and object reconstruction, especially bundle adjustment (see chapter 4). Overviews of calibration methods are given by Gruen and Huang (2001), Fryer (1996), Klette *et al.* (1996), Godding (1999), Maas (1988), Kupfer and Wester-Ebbinghaus (1985), Wester-Ebbinghaus (1983), Brown (1971).

### **7.2.1.1 Laboratory calibration**

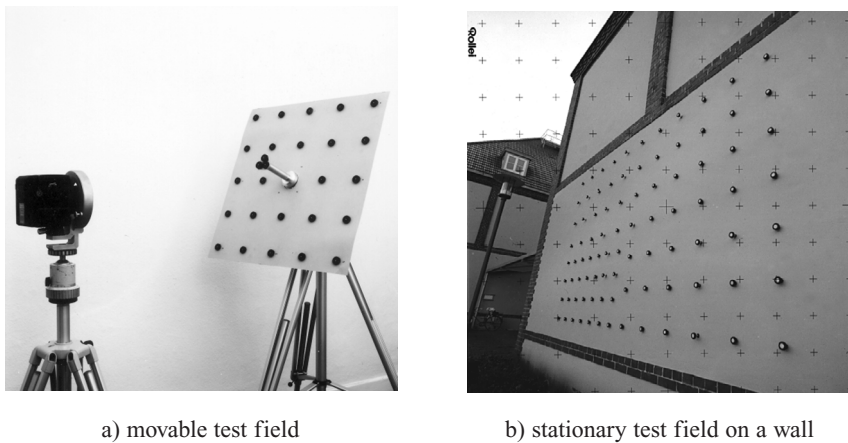
Laboratory calibration is generally only used for metric cameras. Interior orientation parameters are determined by goniometers, collimators or other optical alignment techniques where imaging direction or angles of light rays are measured through the lens of the camera. Laboratory calibrations cannot normally be performed by a user or customer, and these methods have therefore seen little practical application in close-range photogrammetry.

### **7.2.1.2 Test field calibration**

Test field calibration is based on a suitable targeted field of object points with known coordinates or distances. This test field is imaged from several camera stations, ensuring good ray intersections and filling the image format. Test fields can be mobile (Fig. 7.6a), or stationary (e.g. building wall, Fig. 7.6b).

Fig. 7.7 shows a suitable image configuration for a test field calibration. In order to calibrate the camera, eight images are acquired, each imaging as many of the test field targets as possible. They should image the test field perpendicularly and obliquely and each image should have a relative rotation of 90° around the optical axis (see also Fig. 7.12). Fig. 7.8 shows a series of images acquired for test field calibration.

Measured image coordinates and approximately known object data are processed by bundle adjustment to give the parameters of the camera model (interior orientation) as well as the



a) movable test field

b) stationary test field on a wall

Figure 7.6 Examples of photogrammetric test fields

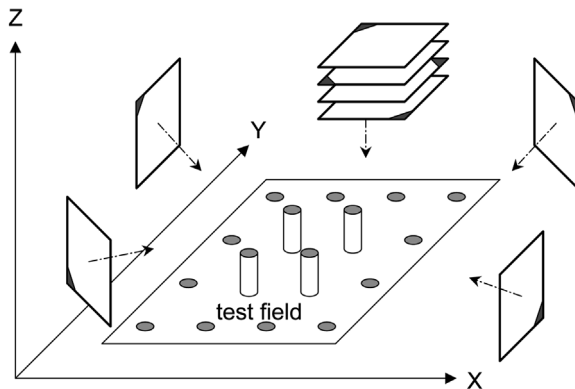
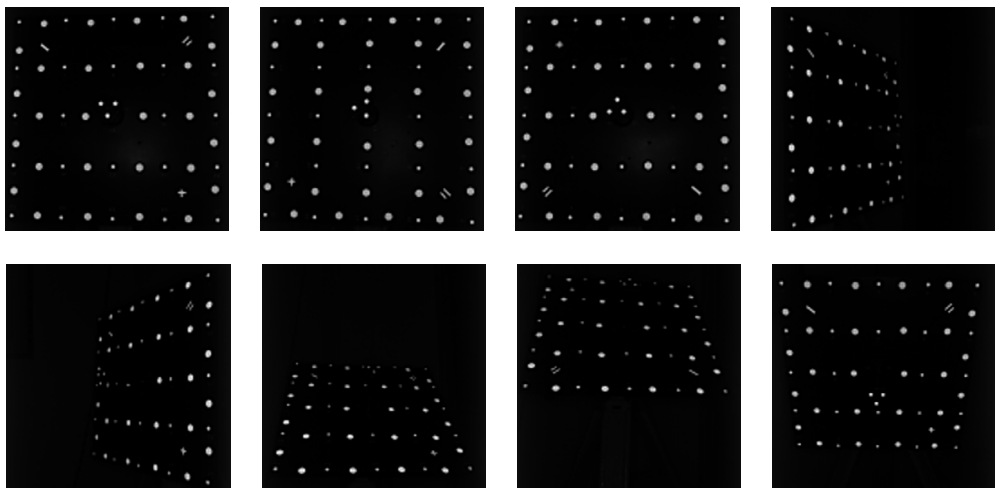


Figure 7.7 Imaging configuration for test field calibration

adjusted test field coordinates and the parameters of exterior orientation. For test field calibration the datum is usually defined by free-net adjustment (see section 4.3.3.3).

Numerical calculations can lead to unwanted correlations between the calculated parameters but these can largely be avoided by suitable imaging configurations. It is most important to provide at least one piece of scale information along the viewing direction in order to reliably compute the principal distance. This can, for example, be achieved by a reference distance, by spatially distributed test field points or by oblique images of a plane test field. Images rotated by 90° around the optical axis are used primarily to determine the principal point coordinates and affinity parameters.

In general, the design of the test field should be representative of the volume of the actual object to be measured. The number and distribution of image points are of major importance for an accurate determination of distortion parameters.



**Figure 7.8** Image series for test field calibration

#### 7.2.1.3 Plumb-line calibration

The plumb-line method uses a test field with several straight lines, created for example by vertically hanging wires (Fig. 7.9). Since in theory the projection of straight lines is invariant for perspective geometry, all departures from this condition must be caused by distortion effects. The deformation of the imaged test field lines can be used to determine distortion parameters with respect to a pre-defined principal distance and point of best symmetry. However, the calculated distortion parameters are not correlated with the further parameters of interior orientation or the exterior orientation parameters.

In a practical implementation of a plumb-line test field, object lines can be created by, for example, thin white plastic cords that have no discernible surface structure which would

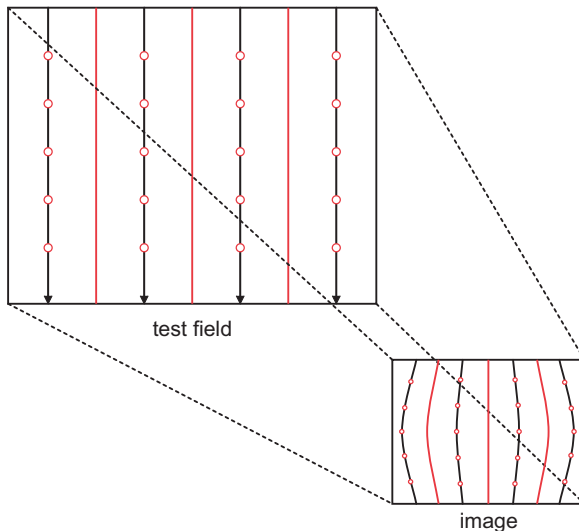


**Figure 7.9** Plumb-line method for test field calibration

influence the measurement algorithms used and enable sufficient contrast for automated processing imaged against a dark background. Such a situation facilitates automatic line following at high point densities (see section 5.4.3). Alternatively, natural straight line object features such as building edges can be used for calibration (Bräuer-Burchardt and Voss 2000).

Plumb-line calibration can be sensibly applied in cases where a pre-calibration of distortion parameters is desired e.g. if lenses with high distortions (up to fish-eye lenses) are used and the measured image coordinates are to be corrected for distortion prior to a system calibration (see section 7.2.1.6).

#### 7.2.1.4 On-the-job calibration

The term on-the-job calibration is often used where a test field calibration (recording of a known point field) is combined with the actual object measurement (example in Fig. 7.10). This approach is reasonable, for example, if the measuring object itself does not provide suitable surface structures or known geometric information which would enable self-calibration. Since the acquired set of images is processed by a self-calibrating bundle adjustment, on-the-job calibration belongs to the class of self-calibration (see section 7.2.1.5).

A simple solution is provided by a portable frame consisting of several spatially distributed scale bars, positioned beside the measuring object and photographed simultaneously. The local coordinate system of the test field can be used as a three-dimensional object coordinate system and further reference points are not required. Fig. 7.10 shows such a test field that is used for the digital off-line measurement of a railroad wagon.



**Figure 7.10** On-the-job calibration using a movable test object (Imetric)

### 7.2.1.5 Self-calibration

An extension to test field or on-the-job calibration is self-calibration which simultaneously uses the images acquired for the actual object measurement. In this case the test field is replaced by the actual object which must be imaged under conditions similar to those required for test field calibration itself (spatial depth, tilted images and suitable ray intersections). The essential advantage of self-calibration is that the parameters of interior orientation are determined simultaneously with measurement of the object, so providing an optimal solution for object reconstruction.

Self-calibration does not require coordinates of known reference points. The parameters of interior orientation can be calculated solely by the photogrammetric determination of the object shape i.e. by incorporating only image information and intersection conditions for unknown object points. If employed, reference points can be used to define a particular global coordinate system for the parameters of exterior orientation. In order to define scale it is sufficient to measure a single reference length in object space (although it is good practice to measure multiple reference lengths).

If the object to be measured does not permit a suitable image configuration, or if a multi-camera on-line system is used, then a test field or on-the-job calibration must normally be performed.

### 7.2.1.6 System calibration

The expression system calibration is generally used for the determination of all geometric parameters of a complete measurement system i.e. the interior and exterior orientation parameters of all the system components. For analogue measuring systems, system calibration may involve the calibration of the measuring device (comparator) in addition to the actual camera calibration. System calibration is more relevant for digital multi-camera systems that are either mobile and can be freely configured (e.g. dual camera on-line systems), or are mounted in a fixed position (e.g. 16-camera system for the inspection of brake pipes, see section 6.4.3.1).

For dual camera on-line systems it is possible to calibrate each camera individually in advance. Alternatively, self-calibration can be applied to a set of images which have been acquired with both cameras simultaneously.

During operation, multi-camera systems on fixed mountings require particular care in monitoring and calibration. Such mechanical restrictions can cause problems, for instance, by not permitting convergent or tilted images. In general exterior orientation parameters can be monitored on a regular basis by the use of reference points and, if necessary, can be recalculated by bundle adjustment or spatial resection. However, the interior orientation parameters can only be determined by object fields with a suitable distribution of object points. Fig. 6.31 shows an example of a multi-camera system which can be oriented and calibrated by a motor-driven rotating test field and where the orientation of the rotary table itself is simultaneously calculated (Godding and Luhmann 1992).

## 7.2.2 Imaging configurations

The following imaging configurations are principally designed for self-calibration by bundle adjustment. The illustrated configurations of point fields and camera stations are a limited selection from many possibilities (Wester-Ebbinghaus 1985, Kraus 1997). Extensions and combinations are possible and often unavoidable. Multi-image configurations and self-calibration are the norm in photogrammetric practice while camera calibration based on single image analysis is common in many areas of robotics and computer vision.

### 7.2.2.1 Calibration using a plane point field

If the photogrammetrist is restricted to a planar test field or flat measurement object, several convergent images are necessary. The minimum number of images depends on the availability and distribution of reference points with known coordinates. If reference points are not provided, known distances in object space can also be used for calibration.

Fig. 7.11a and b illustrate minimal image configurations for a plane test field with known reference points and an invariant camera interior orientation. Fig. 7.11a shows a convergent arrangement of two camera stations while in Fig. 7.11b two images with a relative roll, but the same perspective, are created at only one station. However, these configurations are geometrically weak and should be avoided in practice.

The number of required images increases if reference points are not available. Fig. 7.11c illustrates the minimal configuration of four convergent images. In contrast Fig. 7.11d shows an improved configuration of 8 images which, above all, generates better ray intersections, higher redundancy and improved use of the image format (more reliable determination of distortion).

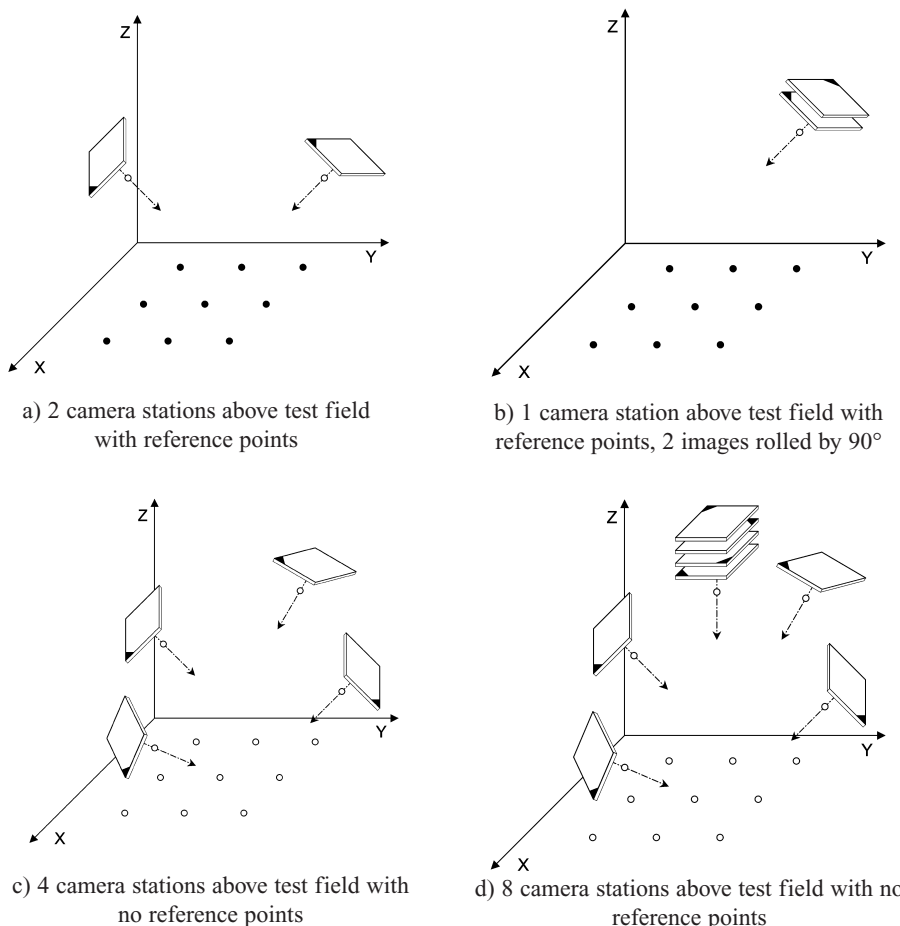


**Figure 7.11** Calibration configurations for plane test fields (after Wester-Ebbinghaus 1983, 1985)

● control point ○ target point

### 7.2.2.2 Calibration using a spatial point field

Self-calibration is more reliable if object points are spatially distributed in three dimensions. Spatial point fields are preferable if the measuring task permits.

Fig. 7.12a shows an example of single image calibration using a known 3D test field (see section 4.2.3.1). As shown in Fig. 7.12b, reference points are not required if additional scale information in the form of known distances is available in object space. The number of distances can be reduced if two rolled images are taken (Fig. 7.12c). Fig. 7.12d illustrates the minimal configuration for a system composed of two different cameras (image-variant interior orientation),

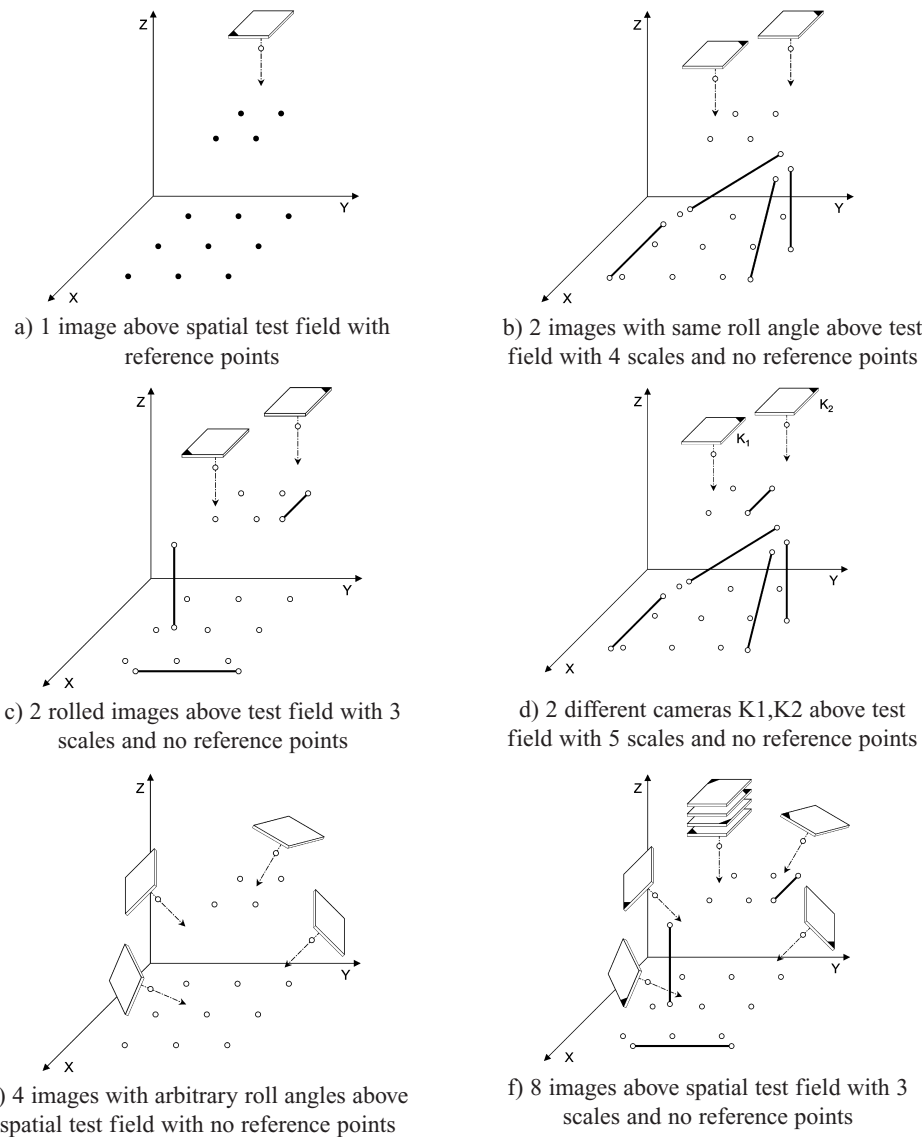


**Figure 7.12** Calibration configurations for spatial test fields (after Wester-Ebbinghaus 1983, 1985)

● reference point   ○ target point   —○— known distance

for example an on-line dual camera system. Explicitly rolled images are not necessary if at least four convergent images of a spatial point field are available (Fig. 7.12e). Finally Fig. 7.12f displays the most expensive but also most reliable imaging configuration comprising eight images tilted with respect to each other and arranged above a spatial point field containing known distances.

In principle, all the imaging configurations shown above can be simulated by placing a portable test field in multiple positions with respect to the camera to be calibrated, such that the same perspective conditions between test field and camera are created. In addition, the number of object points, reference points, distances and images can be increased arbitrarily, e.g. for special camera investigations (e.g. Beyer 1992).

### 7.2.2.3 Single station self-calibration

Single station self-calibration is a special case of camera calibration (Wester-Ebbinghaus 1983). The imaging configurations mentioned above are restricted to only one camera station and the calibration derived from image information only (self-calibration). In this case several images, tilted with respect to one another, are taken from one station. The test field need not be three-dimensional (Fig. 7.13). In this configuration the use of the image format is not optimal and the determination of distortion is correspondingly less certain. The configurations shown here are of more theoretical than practical interest.

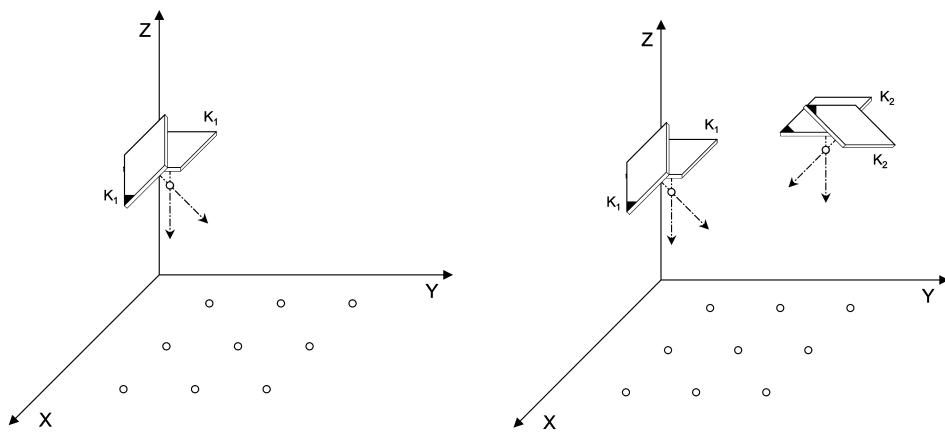
### 7.2.2.4 Calibration with extended single image orientation

The parameters of interior orientation can be derived from only one image if a spatial point field with a suitable number and density of reference points is available. In general, calibration is limited to a camera model comprising principal distance, principal point and radial distortion.

In the literature there are three main approaches to the simultaneous determination of interior and exterior orientation:

- Space resection with extended camera model

The parameters of exterior orientation are determined by solving a non-linear (over-determined) system of equations. The mathematical model is based on the collinearity



a) 1 camera station with 2 tilted images above plane test field without reference points

b) as (a), but for 2 different cameras K1 and K2

**Figure 7.13** Single station self-calibration

equations, extended by terms to correct for the effects of distortion. In this case six unknown parameters of exterior orientation and up to five parameters of interior orientation are calculated. This approach requires a spatial test field with at least six reference points having known XYZ coordinates (see Kraus 1997 and also section 4.2.3.1).

- Direct linear transformation (DLT) with distortion parameters (see Abdel-Aziz and Karara 1971 and also section 4.2.3.2)

The DLT method calculates 11 transformation parameters in a linear system of equations. The method can be extended by additional parameters for radial distortion. At least six spatial reference points are required.

- Camera calibration by projective geometry

In computer vision, camera calibration based on methods of projective geometry is widely used. Here the projection matrix of unknowns contains 6 parameters of exterior orientation and 5 additional parameters for the camera model. There is a linear solution which makes it similar to the DLT method (Mugnier *et al.* 2004).

These single image calibration methods are of major interest in applications where redundant multi-image configurations cannot be achieved or where a check of the imaging geometry of a single camera is required for every image taken. One example is in robotics where a camera, perhaps with variable focus, is moved through the object space on a robot arm and is continually subject to changes in camera geometry.

The simple imaging configuration ensures that camera calibration can be performed in real-time. However, it must be expected that the accuracy and reliability of the estimated parameters will be significantly lower than for self-calibration with multi-image configurations.

### 7.2.2.5 Problems with self-calibration

Practical problems with camera calibration typically arise in the following cases:

- Correlations between parameters

Using a bundle adjustment with self-calibration for the estimation of interior orientation parameters usually results in correlations between adjusted parameters. The presence of any significant correlations can be ascertained from analysis of the covariance matrix. High correlation values indicate linear dependencies between single parameters and should be avoided. Correlations often arise between the following parameters:

- principal distance, principal point and exterior orientation
- $A_1, A_2$  and  $A_3$  (or  $K_1, K_2, K_3$  respectively) will always be correlated to some extent as they are sequential terms in the radial lens polynomial model
- principal point  $x'_0$  and affine parameter  $C_1$  or alternatively  $y'_0$  and  $C_2$

Correlations between parameters can largely be neglected if object reconstruction and camera calibration are calculated in one simultaneous computation, as is the case for bundle adjustment with self-calibration. Nevertheless parameters with no statistical significance can be detected by suitable test procedures and eliminated from the functional model. If individual interior orientation parameters are correlated and then used in subsequent, separate calculations, they no longer completely represent the chosen mathematical camera model. For example, if cameras in a fixed on-line measuring system are pre-calibrated using a different imaging configuration, then the subsequent on-line use of the resulting

parameters can lead to errors in the computation of 3D coordinates. In general, calibration against a spatial test field results in lower correlations and more reliable camera parameters.

- Images without relative roll angles

If the test field does not provide a suitable distribution of reference points, or if sufficient convergent images cannot be acquired, then images with relative roll angles (rotations about the optical axis) are necessary for the determination of principal point coordinates and possible affine transformation parameters. The coordinates of the principal point are highly correlated with the parameters of exterior orientation if rolled images are not available.

- Incomplete use of the image format

The imaging sequence for camera calibration should be arranged in such a way that, within the full set of images, use of the complete image format is achieved. Only then is it possible to determine distortion parameters which are valid across this whole format (Fig. 7.3).

- Use of high distortion lenses

Many wide-angle and super wide-angle lenses cause large distortions in the image corners. For these lenses standard distortion models are often insufficient and result in lower accuracies of points imaged in the corners. The problem becomes even more critical if the image format is incompletely used at the calibration stage. In cases where there is any doubt it is good practice to ignore any image measurements made in the outer 10% of the image format.

- Lack of camera stability

Determination of interior orientation becomes more uncertain if the camera geometry changes from image to image within a sequence, for example due to unstable mounting of the imaging sensor with respect to the lens. Each variation in this case must be handled by defining a separate camera in the adjustment model. However, many imaging configurations only permit the simultaneous calibration of a small number of cameras. In section 4.3.2.4 an approach to the calibration of image-variant parameters is discussed.

- Missing scale information in the viewing direction

If scale information in the viewing direction is missing, as in the case of orthogonal images of plane test fields, principal distance and object distance cannot be uniquely determined. Just one known distance in the viewing direction (e.g. through the use of known reference points) or one known coordinate component (e.g. for convergent imagery of a plane test field) is sufficient for the calculation of principal distance. As a simple alternative, a network of convergent images of a planar target field will allow recovery of principal distance, but the user must be aware that the use of such a solution requires careful assessment. It must be borne in mind that the 3D volume of the object to be measured should be comparable in depth to the target field if extrapolation from a limited set of calibration data is to be avoided.

## 7.3 Dynamic photogrammetry

### 7.3.1 Relative movements between object and imaging system

#### 7.3.1.1 Static object

Relative movements between a static object and camera occur in a number of applications:

- hand-held photography
- photography from an airborne vehicle

- image acquisition from a moving car
- image acquisition on unstable ground (oscillations, vibrations)

Stationary objects can be recorded off-line by sequential imaging with only one camera. Movements of the camera during exposure cause an image blur  $\Delta s'$ , dependent on velocity, exposure time and image scale:

$$\Delta s' = \frac{\Delta t v}{m} \quad (7.4)$$

where

- $\Delta t$ : exposure time
- $v$ : velocity of camera movement
- $m$ : image scale factor

Blurring due to image motion results in a decreased modulation transfer in the direction of movement. The maximum permitted image motion can therefore be expressed as a function of resolving power. Investigations of aerial cameras have shown a maximum tolerable image motion of:

$$\Delta s'_{\max} = 1.5 \cdot RP^{-1} \quad (7.5)$$

where

- $RP$ : resolving power of the sensor [L/mm]

Hence, the maximum permitted exposure time from (7.4):

$$\Delta t_{\max} = \frac{\Delta s'_{\max} m}{v} \quad (7.6)$$

### Example 7.1:

A row of houses is imaged from a moving car ( $v = 30 \text{ km/h} = 8.33 \text{ m/s}$ ) at image scale factor  $m = 2000$ . The resolving power of the CCD camera according to section 3.3.2.3 is approximately  $RP = 100 \text{ L/mm}$ . It is necessary to find the maximum exposure time  $\Delta t$  and the resulting blur in object space:

Solution:

$$1. \text{ permitted image motion: } \Delta s'_{\max} = 1.5 / 100 = 0.015 \text{ mm} = 15 \mu\text{m}$$

$$2. \text{ maximum exposure time: } \Delta t_{\max} = \frac{0.015 \times 10^3 \times 2000}{8.33} = 0.0036 \text{ s} \approx 1/280 \text{ s}$$

$$3. \text{ blurring in object space: } \Delta S = 2000 \times 0.015 = 30 \text{ mm}$$

For practical image acquisition, exposure times must also be selected on the basis of illumination conditions, available lens aperture, required depth of field and the light sensitivity of the film or sensor.

#### 7.3.1.2 Moving object

The relationships discussed above for blurring due to camera motion are also valid for a moving object. However 3D measurement of a moving object requires at least two synchronised cameras.

Depending on object velocity, synchronisation errors lead to positional errors  $\Delta s'$  which are proportional to the corresponding distance moved  $\Delta S$ .

$$\Delta s' = \frac{\Delta t v}{m} = \frac{\Delta S}{m} \quad (7.7)$$

where

- $\Delta t$ : synchronisation error
- $v$ : object velocity
- $\Delta S$ : distance moved
- $m$ : image scale factor

If the object is moving parallel to the baseline between two cameras, the positional error is effectively an x-parallax error  $\Delta p_x'$ . According to the standard case of stereo-photogrammetry shown in Fig. 7.14, it is clear that the movement  $\Delta S$  between times  $t_0$  and  $t_1$  results in a measurement of virtual point  $P^*$ . The corresponding error  $\Delta Z$  in the viewing direction is given by the following expression:

$$\Delta Z = \frac{h}{b} \Delta S = \frac{h}{b} m \Delta p_x' \quad (7.8)$$

where

- $h$ : object distance
- $b$ : stereo base
- $\Delta p_x'$ : x-parallax error
- $m$ : image scale factor

In the direction of movement the lateral error  $\Delta X$  is as follows:

$$\Delta X = \frac{x'}{c} \Delta Z \quad (7.9)$$

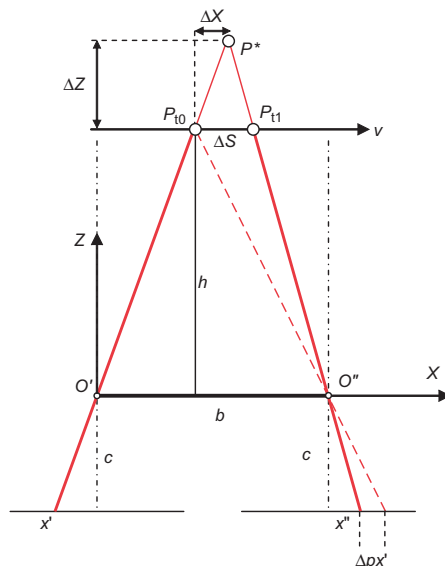


Figure 7.14 Lateral and range errors caused by synchronisation error

where

- $x'$ : image coordinate in left image
- $c$ : principal distance

### Example 7.2:

For the application in example 7.1 ( $v = 30 \text{ km/h} = 8.33 \text{ m/s}$ ;  $m = 2000$ ) stereo images with two CCD video cameras are also to be recorded ( $b = 1.5 \text{ m}$ ,  $c = 8 \text{ mm}$ ,  $h = 16 \text{ m}$ ,  $x' = 4 \text{ mm}$ ). Technical limitations in the installation require a synchronisation error of  $\Delta t = 1/50 \text{ s}$  (single frame duration time) to be taken into account. (In fact, suitable frame grabbers permit exact synchronous image input, see below):

Solution:

$$1. \text{ distance moved: } \Delta S = 1/50 \times 8.33 = 0.166 \text{ m}$$

$$2. \text{ lateral image error: } \Delta p_{x'} = \Delta s' = \frac{0.166}{2000} = 83 \times 10^{-3} \text{ m} = 83 \mu\text{m}$$

$$3. \text{ error in viewing direction: } \Delta Z = \frac{16}{1.5} \times 2000 \times 83 \times 10^{-3} = 1.78 \text{ m}$$

$$4. \text{ error in direction of movement: } \Delta X = \frac{4}{8} \times 1.78 = 0.89 \text{ m}$$

The example demonstrates the serious effect of a synchronisation error on the quality of object coordinates. The lateral image error of  $83 \mu\text{m}$  exceeds the potential image measurement accuracy of  $<10 \mu\text{m}$  by almost an order of magnitude.

Conventional cameras can be synchronised by an electrical pulse linked to the shutter release. Progressive scan cameras (see section 3.3.2.3) work in non-interlaced mode and are therefore particularly suitable for dynamic imaging. For the synchronous image input from multiple video cameras it is possible to use frame grabbers with multiple parallel A/D converters (e.g. RGB inputs), whose common synchronisation signal is used to control the cameras.

### 7.3.2 Recording cinematic sequences

Image sequences can record a timed sequence of spatial object movements (deformations, trajectories, velocity and acceleration curves). In addition to recording time, suitable measures must be taken to identify and image discrete object points. Examples of cinematic applications are:

- recording crash tests in the automotive industry
- investigating turbulent flow in fluids or gases
- surveying structural deformations (buildings, bridges, etc.)
- material testing under mechanical or thermal stress
- vibration analysis
- calibrating and evaluating robot movement
- human motion analysis

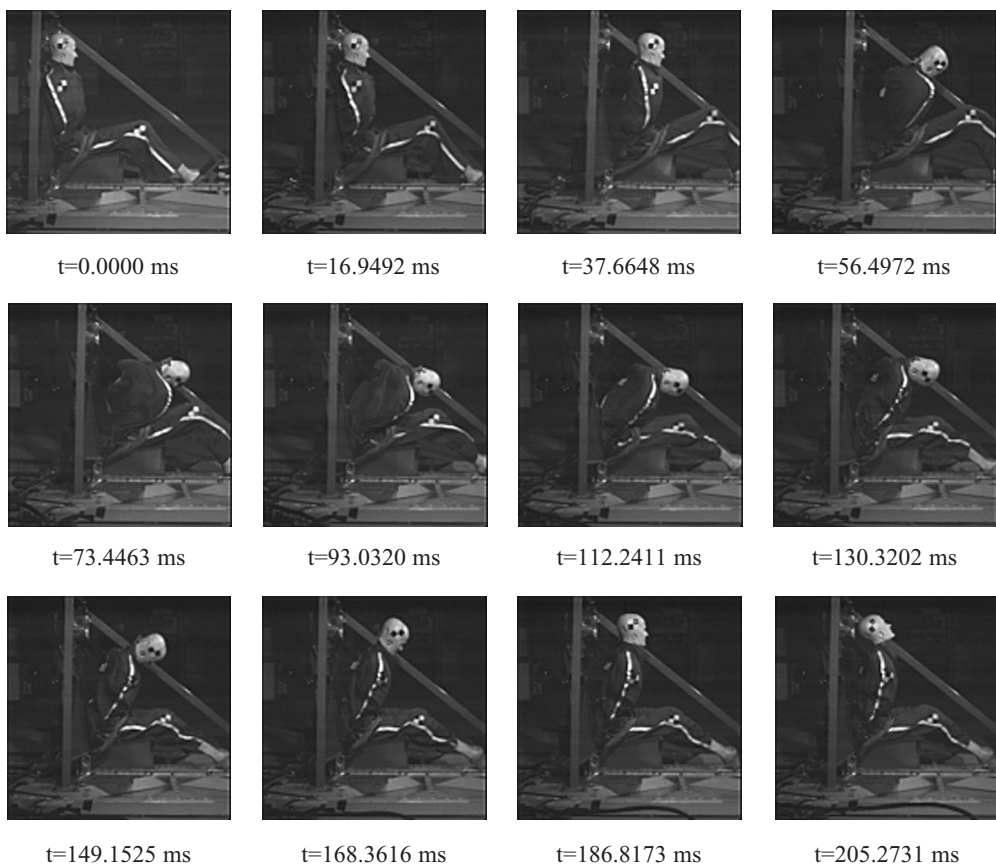
### 7.3.2.1 Image sequences

Image sequences usually imply a sequential series of multiple images which record an object movement at an appropriate frequency. In object space, a stationary set of reference points is required to which the object movements can be related. It can also be used for image orientation e.g. with moving camera stations.

Slow movements, such as the deformation of a cooling tower due to changes in the direction of the sun's illumination, can be recorded sequentially by a single conventional camera followed by a standard photogrammetric object reconstruction.

The recording of high-speed image sequences is also known as cinematography and can be achieved using either analogue or digital high-speed cameras (section 3.3.2.8). Fig. 7.15 shows part of a high-speed image sequence taken to investigate seat belt operation in a car crash. This sequence does not enable a three-dimensional analysis of the movement as only one camera was used. Since object movement is closely parallel to the image plane, good numerical estimates to describe the kinematics can be made.

Fig. 7.16 illustrates the experimental set-up for recording spatial trajectories by a multi-camera image sequence. Three CCD video cameras are used to observe particle flow in a water tank. A light section projector creates an approximate plane of light in which particles are visible. The image



**Figure 7.15** High-speed image sequence (Weinberger)

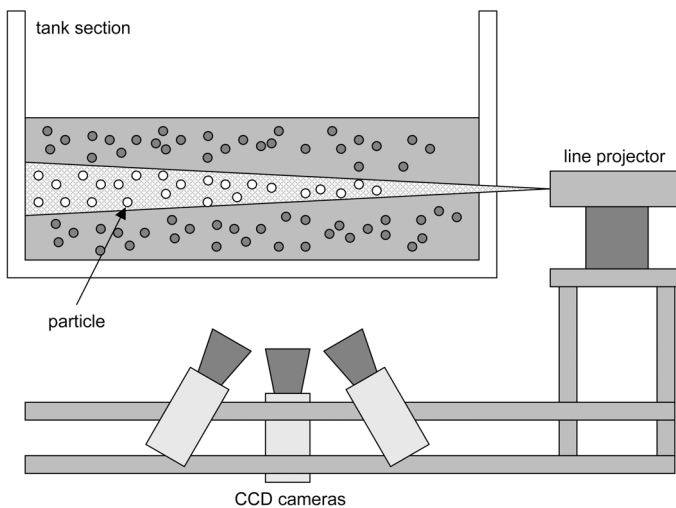


**Figure 7.16** Experimental set-up for multi-image recording of particle flow (after Maas *et al.* 1993)

sequence is stored at video rate on a video recorder. The multi-media path of the imaging rays through the transparent wall of the tank are taken into account by the photogrammetric model (section 4.6). For this application the key problem lies in solving the correspondence, at a given point in time, between the three images of a large number of particles which are recorded as bright points (Fig. 7.17). The correspondence problem is solved by an image matching process based on epipolar geometry as outlined in section 5.5.3 (Maas *et al.* 1993).

As a result of the photogrammetric analysis, the 3D coordinates of all particles throughout the complete image sequence can be determined. Particle trajectories can subsequently be derived, although this requires that the correspondence problem between consecutive images in the sequence be solved.

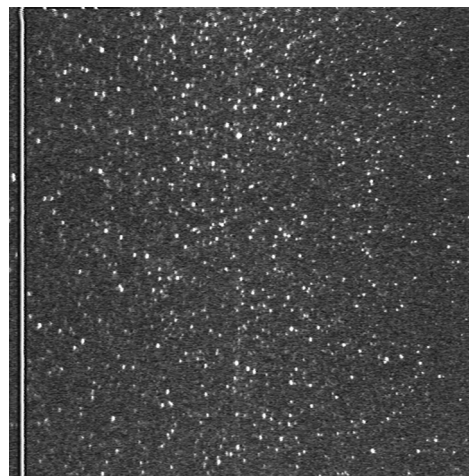


**Figure 7.17** Particle flow (after Maas *et al.* 1993)

### 7.3.2.2 Time series recording and motography

Motography is a technique by which motion is captured using time exposure or multiple exposure images. In contrast to image recording by high-speed cameras, motography permits the use of normal photogrammetric systems with corresponding exposure options for obtaining high resolution images.

For long exposure images, moving objects are recorded by an image trace (Fig. 7.18). If stereo or multi-image recordings are used the object should be signalised by luminous targets which flash at a frequency appropriate to the speed of motion (pulsed light technique, Fig. 7.19). Using this technique, discrete points are visible on the image trace which can be identified and matched. In order to avoid over exposure under daylight conditions, the technique of band absorption is used to darken the object space. A light source emitting a narrow band of frequencies illuminates the scene and the imaging system is equipped with a corresponding narrow band absorption filter which only transmits the light traces to be recorded.

Multiple exposures can create discrete image points, including non-targeted object points, by periodic illumination or shutter opening (stroboscopy). In contrast to single images separated in time, the complete movement is visible on one image.

The following applications are example uses for motography:

- motion studies for investigating ergonomic issues
- motion studies for sports medicine
- motion analysis in biology and bionics
- robot calibration
- vibration analysis
- deformation analysis

Overviews on motography are provided, for example, by Dorrer and Peipe (1987) and Güthner and Peipe (1988).

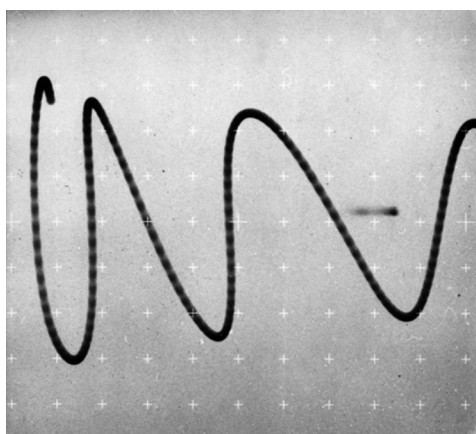


**Figure 7.18** Continuous recording of the vibration of a test object

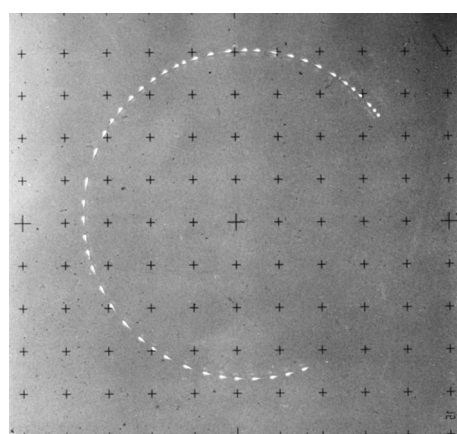


**Figure 7.19** Movement recording by motography using pulsed light targets

## 7.4 Close-range aerial imagery

Images from low flying aerial platforms are used, for example, in the following applications:

- archaeological survey records
- volumetric measurement of spoil heaps and waste disposal sites
- roofscape mapping
- large-scale mapping of inaccessible areas
- test site mapping for geographical investigations
- biotope monitoring
- water pollution control
- reconnaissance

The acquisition of low-altitude aerial images is, in the first instance, a problem of flight technology (choice of sensor platform, navigation, flight authorisation) (Graham 1988). Photogrammetric processing is based on standard methods.

Manned aircraft are suitable for large scale aerial images if their minimum speed gives rise to acceptable image motion. For example, with an exposure time of  $\Delta t = 1/1000$  s, flying speed  $v = 180$  km/h and image scale factor  $m = 1000$ , image motion is approximately  $50 \mu\text{m}$  according to equation (7.4). Specialised aerial cameras use Forward Motion Compensation (FMC) to compensate for image motion (Kraus 2000). Low-speed ultra-light aircraft (microlights) ( $v_{\min} = 40$  km/h) provide advantageous flight properties but lower payloads (<100 kg). Manned helicopters generate large vibrations whose negative influence on image quality must be compensated for by a special camera mounting or hand-held photography.

For large scale mapping of smaller areas, pilotless model aircraft (Remotely Piloted Vehicle RPV), helicopters, balloons, blimps and kites are all usable (Table 7.1).

In addition to the photogrammetric camera, the flying platform must carry additional components such as remote control, navigation devices, video camera or camera housing. Even with skilled operators navigation remains a practical problem. If uniform aerial blocks are to be recorded it is useful to target the required image centres on the ground so that these can be observed by an airborne video camera. Alternatively the platform can be observed by a vertically directed

**Table 7.1** Unmanned platforms for low-altitude aerial imagery

	typical (max.) altitude <sup>1</sup> [m]	payload [kg]	range <sup>2</sup> [m]	number of operators	max. flying time [min]
model aircraft, RPV	50–100 (150)	3–6	1000	2	30–60
model helicopter	10–100 (150)	3–7	500	2	10–15
hot-air balloon, blimp	10–100 (200)	10–50	1000	3–5	60
gas balloon, blimp	10–100 (200)	10	stationary	2–3	unlimited <sup>3</sup>
kite	50–100 (300)	10–50	stationary	2	unlimited <sup>3</sup>

<sup>1)</sup> limited to 100 m in Germany; <sup>2)</sup> usually required to stay in view; <sup>3)</sup> weather dependent

terrestrial camera. Altimeters, or optical aids based on the principle of geodetic range measurement by base length, can be used in order to ensure a constant altitude. Navigation and inertial systems based on DGPS can also be used for microlights (Bäumker *et al.* 1998, Mills *et al.* 2005).

Fig. 7.20 shows a remotely controlled model helicopter carrying a photogrammetric camera. The system was used for mapping a seawater swimming pool (Fig. 7.21). For subsequent stereo measurement a uniform image block was recorded (144 images, flying height ca. 70 m, image scale  $m = 2500$ ). Fig. 7.22 shows the use of a balloon for recording the archaeological site of an oasis. Heckes and Mauelshagen (1987) and Warner *et al.* (1996) report on additional applications.



**Figure 7.20** Model helicopter with photogrammetric camera



**Figure 7.21** Aerial image for mapping a seawater swimming pool



**Figure 7.22** Use of a balloon for photography of Siwa oasis, Egypt

## References

- Abdel-Aziz, Y. and Karara, H. M. (1971) *Direct linear transformation from comparator coordinates into object space coordinates in close range photogrammetry*. ASP Symposium on Close-Range Photogrammetry.
- Bäumker, M., Brechtken, R., Heimes, F.-J. and Richter, T. (1998) Hochgenaue Stabilisierung einer Sensorplattform mit den Daten eines (D)GPS-gestützten Inertialsystems. Zeitschrift für Photogrammetrie und Fernerkundung, Heft 1/1998, pp. 15–22.
- Beyer, H. (1992) *Geometric and radiometric analysis of a CCD-camera based photogrammetric close-range system*. Mitteilungen Nr. 51, Institut für Geodäsie und Photogrammetrie, ETH Zürich.
- Bräuer-Burchardt, C. and Voss, K. (2000) *Automatic lens distortion calibration using single views*. Mustererkennung 2000, Springer, pp. 187–194.
- Brown, D. C. (1971) Close-range camera calibration. *Photogrammetric Engineering*, **37**(8), pp. 855–866.
- Dorrer, E. and Peipe, J. (ed.) (1987) *Motografie*. Schriftenreihe Studiengang Vermessungswesen, Heft 23, Universität der Bundeswehr, München.
- Fraser, C. S. (1996) Network design. In Atkinson (ed.) *Close Range Photogrammetry and Machine Vision*. Whittles Publishing, Caithness, UK, pp. 256–281.
- Fryer, J. G. (1996) Camera calibration. In Atkinson (ed.) *Close Range Photogrammetry and Machine Vision*. Whittles Publishing, Caithness, UK, pp. 156–179.
- Godding, R. (1999) Geometric calibration and orientation of digital imaging systems. In Jähne et al. (ed.) *Handbook of Computer Vision and Applications*, Vol. 1, Academic Press, pp. 441–461.
- Godding, R. and Luhmann, T. (1992) Calibration and accuracy assessment of a multi-sensor online-photogrammetric system. *International Archives of Photogrammetry and Remote Sensing*, **29**(5), Washington, pp. 24–29.
- Graham, R. W. (1998) Small format aerial surveys from light and microlight aircraft. *Photogrammetric Record*, **12**(71), 561–573.
- Grün, A. and Huang, T. S. (ed) (2001) *Calibration and orientation of cameras in computer vision*. Springer series in information sciences. Springer Berlin.
- Güthner, K. and Peipe, J. (1988) Motography and Photogrammetry for the Study of Movements. *Int. Archives of Photogrammetry and Remote Sensing*, **27**(B10), Kyoto, pp. 246–254.
- Heckes, J. and Mauelshagen, L. (ed.) (1987) *Luftaufnahmen aus geringer Flughöhe*. Veröffentlichungen aus dem Deutschen Bergbaumuseum, Nr. 41.
- Klette, R., Koschan, A. and Schlüns, K. (1996) *Computer Vision – Räumliche Information aus digitalen Bildern*. Verlag Vieweg Technik, Braunschweig/Wiesbaden.
- Kraus, K. (1997) *Photogrammetry, Volume 2, Advanced Methods and Applications*. With contributions by J. Jansa and H. Kager. Dümmler Verlag, Bonn.
- Kraus, K. (2000) *Photogrammetry, Volume 1, Fundamentals and Standard Processes*. With contributions by Peter Waldhäusl, translated by Peter Stewardson, Verlag H. Stam GmbH, Köln.
- Kupfer, G. and Wester-Ebbinghaus, W. (ed.) (1985) *Kammerkalibrierung in der photogrammetrischen Praxis*. Deutsche Geodätische Kommission, Reihe B, Heft 275.
- Maas, H.-G. (1988) Image sequence based automatic multi-camera system calibration techniques. *International archives of Photogrammetry and Remote Sensing*, **32**(B5), 763–768.
- Maas, H.-G., Grün, A. and Papantoniou, D. (1993) Particle tracking in three dimensional turbulent flows - Part I: Photogrammetric determination of particle coordinates. *Experiments in Fluids* **15**, pp. 133–146.
- Mason, S. O. (1994) *Expert system-based design of photogrammetric networks*. Dissertation, Mitteilungen Nr. 53, Institut für Geodäsie und Photogrammetrie, ETH Zürich.
- Mills, J. P., Buckley, S. J., Mitchell, H. L., Clarke, P. J. and Edwards, S. J. (2005) A geomatics data integration technique for coastal change monitoring. *Earth Surface Processes and Landforms*, **30**(6), 651–664.
- Mugnier, C. J., Förstner, W., Wrobel, B., Paderes, F. and Munji, R. (2004) The mathematics of photogrammetry. In McGlone et al. (ed.) *Manual of Photogrammetry*, pp. 181–316.

- Schlögelhofer, F. (1989) *Qualitäts- und Wirtschaftlichkeitsmodelle für die Ingenieurphotogrammetrie.* Dissertation, Geowissenschaftliche Mitteilungen, Nr. 32, Technische Universität Wien.
- Warner, W. S., Graham, R. and Read, R. E. (1996) *Small Format Aerial Photography.* Whittles Publishing, Caithness.
- Wester-Ebbinghaus, W. (1983) *Einzelstandpunkt-Selbstkalibrierung – ein Beitrag zur Feldkalibrierung von Aufnahmekammern.* Deutsche Geodätische Kommission, Reihe C, Nr. 289.
- Wester-Ebbinghaus, W. (1985) Verfahren zur Feldkalibrierung von photogrammetrischen Aufnahmekammern im Nahbereich. In Kupfer/Wester-Ebbinghaus (ed.) *Kammerkalibrierung in der photogrammetrischen Praxis,* Deutsche Geodätische Kommission, Reihe B, Heft Nr. 275, pp. 106–114.

# 8 Example applications

The techniques of close-range photogrammetry provide universal methods for the geometric measurement of almost any kind of object. As a result there are a wide range of potential application areas. The following example applications represent only a small selection from the entire spectrum of possibilities. They are restricted to sample images, results and key technical specifications. Although some of the examples were processed using analogue imagery, concepts and solutions are still up to date. Further information can be obtained from selected literature references e.g. Fryer *et al.* 2006, Luhmann 2002.

## 8.1 Architecture and cultural heritage

### 8.1.1 Photogrammetric building records

Photogrammetric building records mostly aim to generate plan and elevation views for the following applications:

- preservation and restoration of the building
- art historical analysis
- documentation

The essential technical requirements for this field of architectural photogrammetry were already developed in the 19th century (see section 1.4). Photogrammetry offers a number of advantages compared with classical manual methods of measured building surveys:

- non-contact measurement avoiding scaffolding on the façade
- reduced risk of accidents
- fast on-site image acquisition
- high accuracy
- three-dimensional coordinate measurement
- measurement of free-form contours and surfaces (ornamental details)
- combination of graphical output with rectified original images (image maps)
- subsequent object measurement from archived metric images or historical photos

Targeted object points are mostly used as reference points and for image orientation. The actual object reconstruction is based on natural object features.



**Figure 8.1** Graphical elevation and rectified image of a terrace of buildings

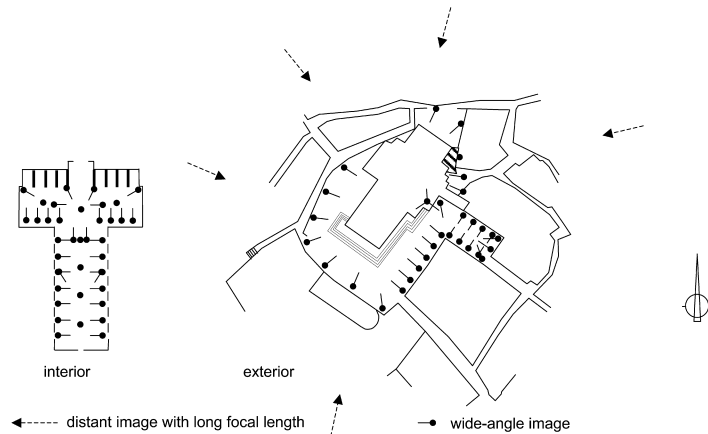
Analytical stereo instruments are still in use but digital multi-image systems are increasingly employed as they provide higher redundancy and direct superimposition of graphical information. In addition, digital processing systems are efficient in generating rectified images e.g. for the production of façade mosaics (Fig. 8.1) or image maps (e.g. Wiedemann 1997).

Overviews of architectural photogrammetry are given by, for example: Streilein 1998, Albertz and Wiedemann 1997, Dallas 1996, Grün 1994, Regensburger 1990, Carbonell 1989, Weimann 1988.

### 8.1.1.1 Siena Cathedral

The photogrammetric reconstruction of Siena Cathedral is a prime example of the measurement of a complex building in an environment with restricted access. The objective is to produce precise plans and detailed illustrations for preservation of both the external façade and the interior.

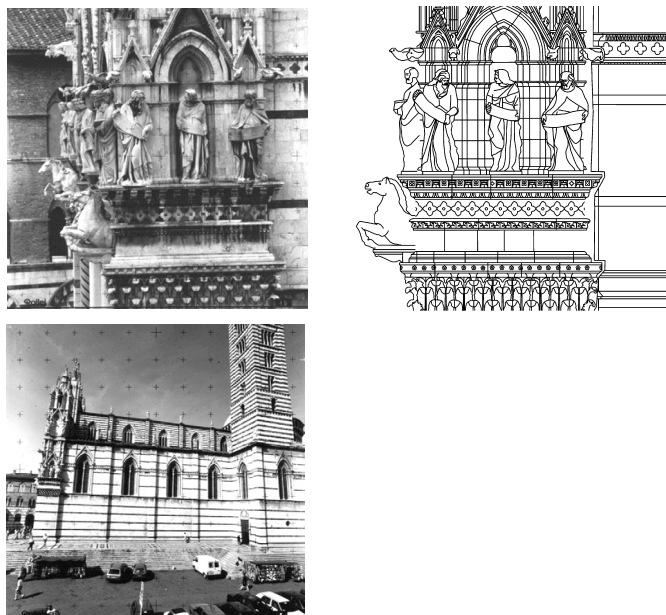
The complexity of the object demands a flexible multi-image configuration with a number of camera/lens combinations which are calibrated and oriented by bundle adjustment. Table 8.1 summarises the project's principal technical data. Fig. 8.2 shows a plan view of the imaging configuration and Fig. 8.3 shows sample metric images and results (Kotowski *et al.* 1989, Fellbaum and Hau 1996).



**Figure 8.2:** Imaging configuration for Siena Cathedral

**Table 8.1** Technical specifications for Siena Cathedral project

Situation on site		Remarks
object dimensions (L × W × H)	ca. 100 m × 30 m × 30 m	
measurement timescale	1989 – 1995	
camera; focal lengths	Rollei 6006; f = 40 – 1000 mm Zeiss UMK; f = 64 mm	exterior façade interior
number of images acquired	ca. 4000	
number of images processed	ca. 2250	
image scales	1:100	
number of control points	ca. 400	
control point accuracy	<13 mm	
Image measurement and bundle triangulation		
measuring instrumentation	Zeiss Planicomp C100, Rollei reseau-scanner	monoscopic
mean image measurement accuracy	12–16 µm	
number of object points	ca. 15 in model images, < 200 in triangulation images total of 7100 tie points	
mean object accuracy	< 13 mm	
Object reconstruction		
processing system	Zeiss Planicomp C100, Zeiss Planicomp P3, Rollei MR2	stereo compilation multi-image compilation
number of object points	unknown	
mean object accuracy	1–2 cm	
output of results	profiles, ground plot, vertical projections	

**Figure 8.3** Metric images and results for Siena Cathedral (after Fellbaum and Hau 1996)

### 8.1.1.2 Gunpowder tower, Oldenburg

The photogrammetric reconstruction of the historic Gunpowder Tower in Oldenburg provides an example of a multi-sided imaging configuration for the exterior and interior areas. The objective is to deliver stone-by-stone measurement data for the preparation of renovation work. Output of results is required, amongst others, as a plane projection of this essentially cylindrical object. Project specifications are summarised in Table 8.2. The principal imaging configuration is shown in Fig. 4.30 although the internal dome is recorded by additional stereo imagery. Fig. 8.4 shows the cylindrical part of the reconstructed 3D CAD model. Superimposition of CAD data on a metric image is illustrated in Fig. 1.12, while Fig. 1.13 shows the cylindrical projection onto a plane (Luhmann and Tecklenburg 1997).

**Table 8.2** Technical specifications for the measurement of Oldenburg's Gunpowder Tower

Situation on site		Remarks
object dimensions (L × W × H)	ca. 12 m × 12 m × 10 m	
measurement timescale	1994	
camera; focal lengths	Rollei 6006; f = 40 mm	
number of images acquired	96	
number of images processed	48	
image scales	1:100–1:300	
number of control points	40	
control point accuracy	1 – 3 mm	
Image measurement and bundle triangulation		
scanning	HP ScanJet IIc	
pixel size	19 µm	
image size	2800 × 2800	
total amount of data	368 MB	
measuring instrumentation	Phidias	screen digitising
mean image measurement accuracy	12 µm	
number of object points	ca. 60	
mean object accuracy	<1.5 mm	
Object reconstruction		
processing system	Zeiss Planicomp P3 Phidias	stereo compilation spatial intersections (2 images)
number of object points	ca. 32,000	
mean object accuracy	3–5 mm	
output of results	CAD model, projections	

### 8.1.2 3D models

#### 8.1.2.1 Building visualisation

If a building's 3D CAD data is available in a topologically structured form (e.g. by a photogrammetric process), 3D visualisation methods (section 5.3.3: illumination models, texture

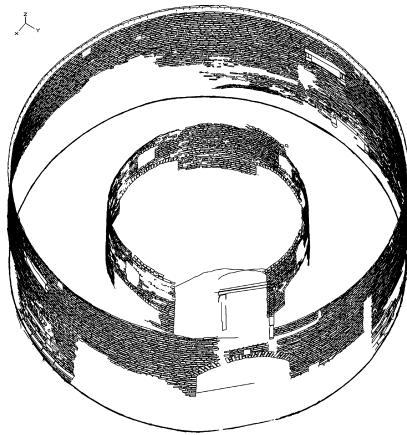


**Figure 8.4** 3D CAD data for Oldenburg's Gunpowder Tower

mapping) can generate a photo-realistic representation. In addition to the purely aesthetic effect, these models also have practical application in building planning or facility management.

In contrast to standard graphical mapping, 3D visualisation requires topological surfaces, i.e. points and lines (polygons) belonging to a closed surface must be grouped together into logical surface patches, usually by interactive editing. For CAD-based multi-image processing systems (see section 6.4.1) this can be implemented during the photogrammetric measurement stage, an approach also known as CAAD (computer aided architectural design).

Data can be stored in standard 3D CAD formats such as DXF and DGN. Attention is increasingly focused on standardised 3D graphics languages such as VRML which enable system-independent visualisations and interaction with the 3D model. Fig. 8.5 and Fig. 8.6 show



**Figure 8.5** Sequence of images of the Otto Wagner Pavilion, Vienna (after Strelein 1998)



Figure 8.6 3D model of the Otto Wagner Pavilion, Vienna (after Streilein 1998)

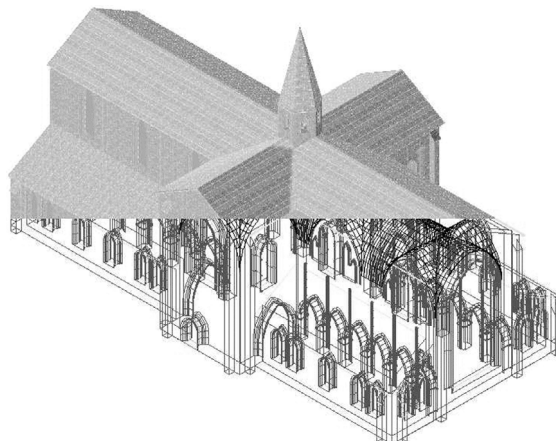


Figure 8.7 3D model of the Monastery at Hude (IAPG Oldenburg)

the Otto Wagner Pavilion in Vienna, used by CIPA as a reference building for testing modern methods of measurement and processing in architectural photogrammetry (Almagro *et al.* 1996, Patias and Streilein 1996). Additional visualisation examples are shown in Figures 1.6, 4.59 and 8.7.

### 8.1.2.2 City models

3D city models are increasingly of interest, for example in:

- urban planning
- emissions analysis (sound, exhaust gases)
- planning mobile telephone networks
- setting up information systems (operational planning for rescue services, transport management)
- tourism (internet presentation)
- three-dimensional city maps



a) using a panoramic camera (Frank Data)



b) using multiple video cameras (Transmap)

**Figure 8.8** Mobile mapping vehicles for city environments**Figure 8.9** Sample view of a 3D city model (IfP Stuttgart)

These applications require the 3D model to be up-to-date and complete, rather than having high accuracy in the geometry and detail. Fast generation of city models can be achieved through:

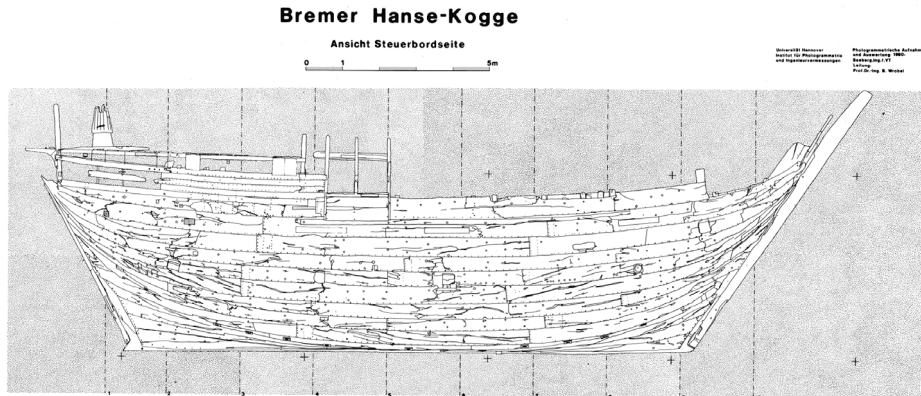
- aerial photogrammetry (automatic extraction of buildings)
- airborne laser scanning (to extract buildings from discontinuities in the height model)
- video acquisition from moving vehicles (Fig. 8.8)

Fig. 8.9 shows sample views from a virtual flight through a 3D city model created by laser scanning and aerial photogrammetry. Close-range images of the building facades are used for texture mapping in order to give a realistic impression of street scenes (Brenner and Haala 1998).

### 8.1.3 Free-form surfaces

#### 8.1.3.1 Historical objects and works of art

The art historical analysis and restoration of sculptures and ornamental building features requires the measurement of free-form surfaces. Classical stereo measurement is suitable for line extraction if the object surface has distinct contours (Fig. 8.10). The surfaces of smaller objects can be measured by active pattern projection methods, as described in section 6.5. The example in Fig. 8.11 shows the digital surface measurement of a sculpture from all sides. Control data for NC milling machines or stereo-lithographic procedures can be derived from the extracted 3D data and used to produce precise copies of the object (e.g. Kludas 1995).



**Fig. 8.10:** Stereoscopic line extraction (Bremen Cog, IPI Hannover)

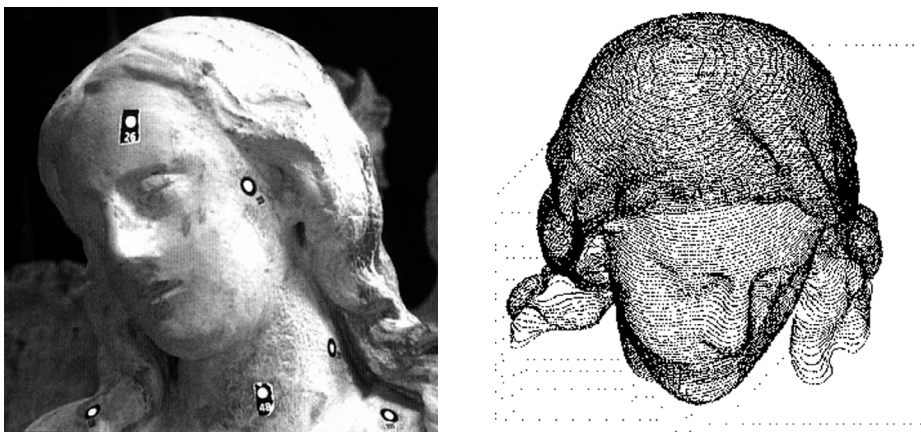


**Figure 8.11** Digital photogrammetric surface measurement of a sculpture (Zeiss)

### 8.1.3.2 Surface measurement of masonry joints

The following application is an example of deformation analysis in building maintenance and is concerned with the measurement of erosion which is affecting the pointing (mortar joints) in brickwork. Over a period of some 10 years, the progress of erosion will be monitored on site every two years. The test sites are located on a church tower at a height of around 40 m (Fig. 8.12). Each test area is approximately 360 mm × 220 mm.

The accuracy is specified to about 1/10 mm. A separate reference frame containing calibrated reference points can be re-attached to a test area in order to deal with repeated measurement. Since the measurements must be made under difficult daylight conditions, a fringe projection system cannot be employed and a Kodak DCS460 digital camera was used instead (see Table 8.3). The natural surface structure provides enough texture for image matching and 3D reconstruction. Results are presented as isolines and differential height models (Fig. 8.13).

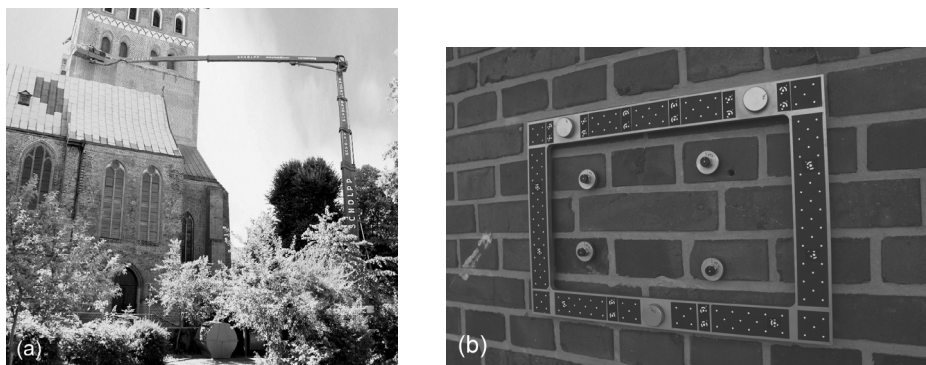


**Figure 8.12** Data acquisition for erosion measurement: (a) on site location and (b) sample image (IAPG Oldenburg)

**Table 8.3** Technical specifications for erosion measurement of masonry joints

Situation on site		Remarks
object dimensions (L × W × H)	360 mm × 220 mm × 10 mm	
measurement timescale	every 2 years for 10 years	
camera; focal lengths	Kodak DCS460, f = 21 mm	
number of images acquired	12	
number of images processed	all	
image scales	1:20	
number of control points	4	in brick wall
control point accuracy	ca. 0.08 mm	
Image measurement and bundle triangulation		
measuring instrumentation	Aicon DPA-Win, AXIOS Ax.Ima, AXIOS Ax.Ori, Leica SocetSet	
mean image measurement accuracy	0.5 µm (1/20 pixel)	( $\sigma_0$ )
number of object points	140	
mean object accuracy	0.06 mm	
number of points of surface model	more than 100,000	in 0.5 mm spacing
output of results	object coordinates, surface model	

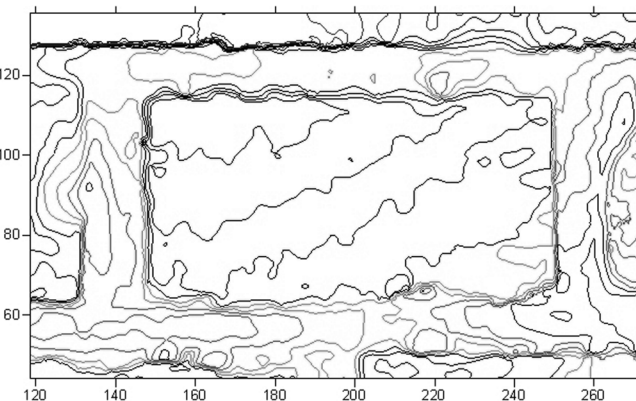


**Figure 8.13** Surface model derived from stereo matching (IAPG Oldenburg)

## 8.2 Engineering surveying and civil engineering

### 8.2.1 Measurement of deformations

A key task in geodetic engineering surveys is to monitor deformations on buildings exposed to some particular mechanical or thermal strain. For these applications, accuracy requirements are typically in the order of millimetres for object dimensions of more than 100 m (e.g. cooling towers, chimneys, dams, sluices, cranes, historical buildings etc.).

Photogrammetric deformation analysis is usually applied in cases where object or environmental conditions do not allow sufficient time on-site for extensive geodetic measurements. Image acquisition additionally provides an objective documentation of the object's state at the time of exposure.

High precision photogrammetric object measurement requires high resolution, large format cameras. These can include large format, analogue metric cameras (e.g. Zeiss UMK 1318, Fig. 3.48), large format reseau cameras (e.g. Rollei LFC, Fig. 3.56) or high-resolution digital cameras (e.g. Kodak DCS645M, Fig. 3.87). If possible, the critical object points are targeted. A stable network of reference points is necessary for detecting possible object deformations or movements (see section 7.3).

The images are measured to an accuracy corresponding to camera quality, usually by precision comparator or first order analytical plotter for analogue images, or by subpixel operators for digital images. 3D object coordinates are calculated by bundle adjustment with simultaneous camera calibration and the inclusion of any additional geodetic measurements. Deformation analysis can also be performed by bundle adjustment, or by separate 3D transformations of the object points in different measurement epochs.

#### 8.2.1.1 Shape measurement of large steel converters

In the steel industry, raw iron is refined into steel in a converter. Converters are pear-shaped vessels of around 10 m in height and 7 m in diameter (Fig. 8.14). After several years of operation, thermal and mechanical stresses lead to deformations which affect the exterior flow of cooling air. By measuring the wall of the vessel, critical areas can be detected and deformation monitored.

Images are acquired using a Rollei 6006 metric camera which, due to the limited time available for photography, is equipped with a 70 mm high-capacity film magazine (see Table 8.4). Camera stations are arranged in nine planes through the longitudinal axis of the converter. Viewing

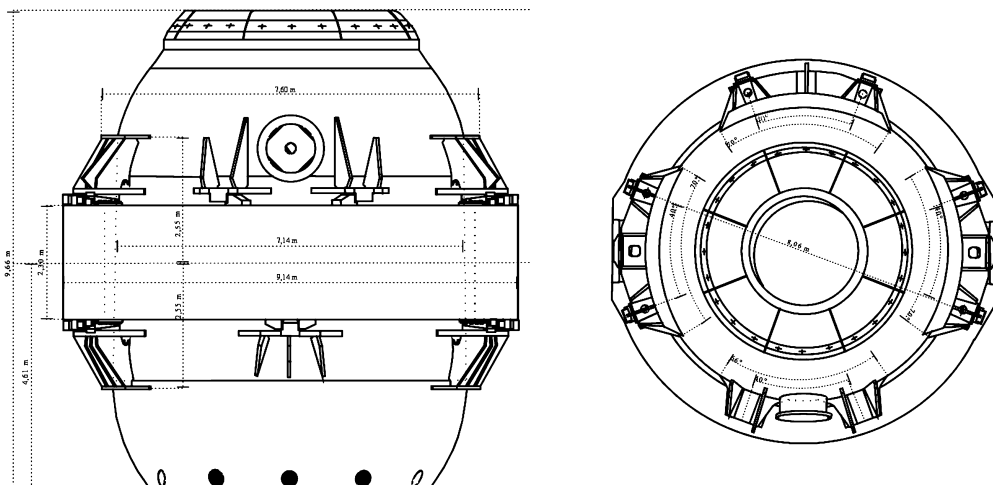
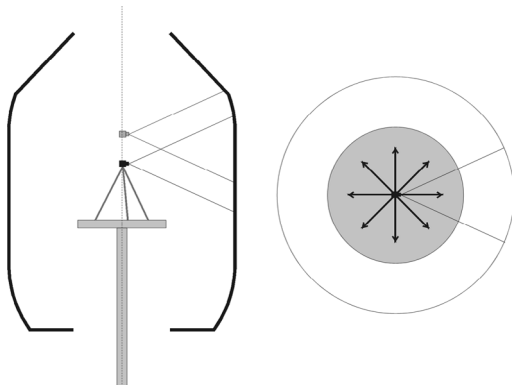


Figure 8.14 Construction drawing of a steel converter (IPI Hannover)

**Table 8.4** Technical specifications for the measurement of a steel converter

Situation on site		Remarks
object dimensions ( $L \times W \times H$ )	ca. 7 m diameter, 10 m height	
measurement timescale	ca. 3 months	
camera; focal lengths	Rollei 6006 metric, $f = 40$ mm	
number of images acquired	72	
number of images processed	all	
image scales	1:50–1:85	
number of control points	19	
control point accuracy	ca. 1.0 mm	
Image measurement and bundle triangulation		
measuring instrumentation	Zeiss Planicomp P1	
mean image measurement accuracy	11 $\mu\text{m}$	$(\sigma_0)$
number of object points	ca. 4000	
mean object accuracy	ca. 5.0 mm	
output of results	object coordinates, CAD model	

**Figure 8.15** Steel converter and internal imaging configuration (IPI Hannover)

directions have a star-shaped form (Fig. 8.15). The required base length is given by the vertical overlap in adjacent images. Tie points, identified by white spots, support image measurement.

Inside the converter a net of reference points is provided by two rings located close to its tilt axis. They are measured by Total Stations with respect to a nearby field of control points.

Tie points and reference features are measured monoscopically (due to the Rollei reseau crosses) and processed in a common bundle adjustment.

### 8.2.1.2 St. Michael's church, Lüneburg

The photogrammetric measurement of the St Michael's church in Lüneburg (Germany) provides an example of the long-term inspection of a building subject to continual movement. The complex object structure and high accuracy specifications again demand large format cameras and a multi-image configuration shown in Fig. 8.16 (see Table 8.5). In order to stabilise the image block geometry, geodetic observations provide improved accuracy, mainly through the addition

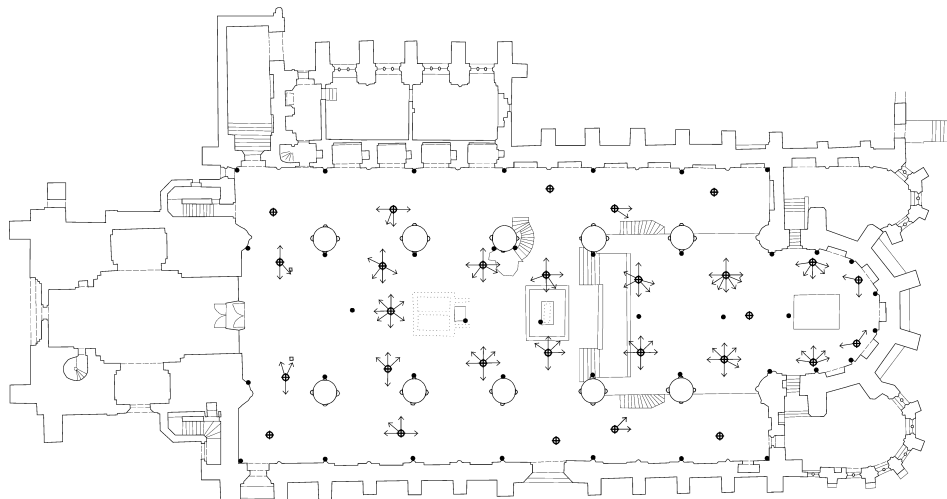


**Figure 8.16** Imaging configuration for the interior of St Michael's church (IPI Hannover)

**Table 8.5** Technical specifications for the measurement of St Michael's church, Lüneburg

Situation on site	Remarks	
object dimensions (L × W × H)	ca. 55 m × 25 m × 13 m	
measurement sequence timescale	annually to 1990, every 2 years to 1996, every 3 years subsequently	
camera; focal lengths	Zeiss UMK 1318; f = 100 mm	
number of images acquired	about 100	
number of images processed	all	
image scales	1:50–1:400	
number of control points	3 partial control points, 14 levelled heights	quasi-free adjustment
control point accuracy	0.1–0.3 mm (in height)	
add. geodetic observations	H/V-directions, (originally also distances), levelling, forced centring and reciprocal measurement between stations	
Image measurement and bundle triangulation		
measuring instrumentation	Zeiss Planicomp C100 and P1	
mean image measurement accuracy	2.8–3.9 µm	$(\sigma_0)$
number of object points	ca. 180	
mean object accuracy	ca. 0.5 mm	
output of results	object coordinates	

of horizontal directions. A forced centring system ensures the use of identical measurement stations for theodolites and cameras and enables reciprocal measurements between both.

In order to compare different epochs, there are no reference points sufficiently accurate and stable throughout the several year's measurement period. Only relative coordinate changes can therefore be determined. These nevertheless indicate clear trends which enable a meaningful assessment of the internal building movements (Fig. 8.17).

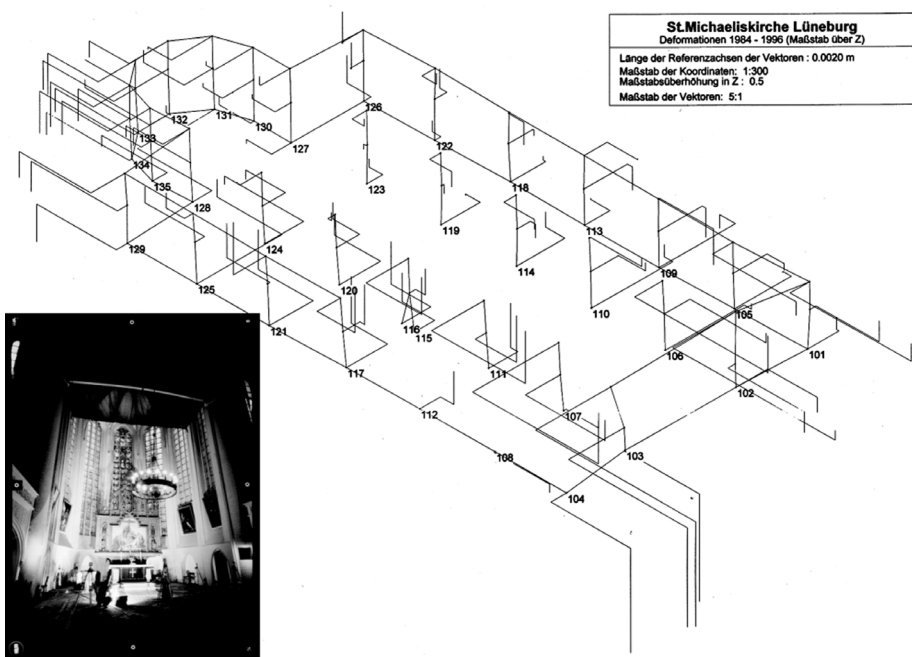


**Figure 8.17** Metric image and coordinate components for displacement vectors of St Michael's church, 1984–96 (IPI Hannover)

### 8.2.2 Tunnel profile measurement

A particular task in engineering surveying is the measurement of tunnel interiors for shape and deformation analysis. Tunnel cross-sections are normally determined. There are severe limitations on the choice of suitable camera stations which are usually located along the longitudinal axis of the tunnel.

There are two main methods of targeting the tunnel wall:

- point-by-point marking with discrete targets
- linear marking using rotating lasers or light sections

Use of discrete targets corresponds to standard photogrammetric practice. If the targets are not located in a common vertical plane, three-dimensional point determination by multi-image processing is required. In contrast, a plane of light can generate a visible intersection profile on the tunnel wall and this can be related to a reference plane. The tunnel cross-section in this plane can therefore be calculated by projective single-image evaluation (see section 4.4.1).

Fig. 8.18 shows the principle of profile measurement by light sectioning. A movable platform carries a rotating laser and a plane reference point field located in the projection plane of the laser. The camera is also mounted on the platform. Geodetic measurements locate the measuring system with respect to the longitudinal axis of the tunnel. Fig. 8.19 illustrates a metric image with a visible laser trace and a measurement sample of a profile section. With a medium format camera, a cross-section of diameter 4–6 m can be measured to an accuracy of 2–10 mm (Wojtowicz 1998).

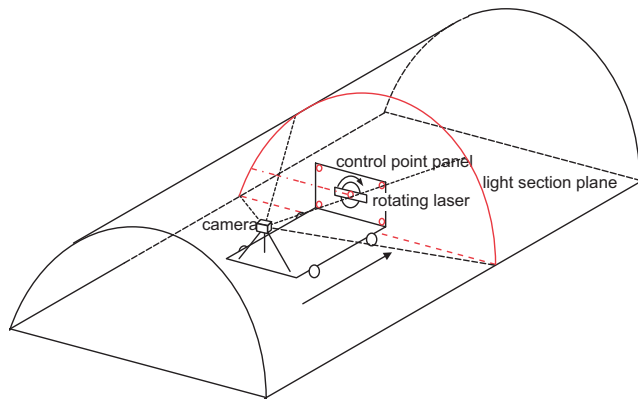


**Figure 8.18** Imaging configuration for tunnel profile measurement

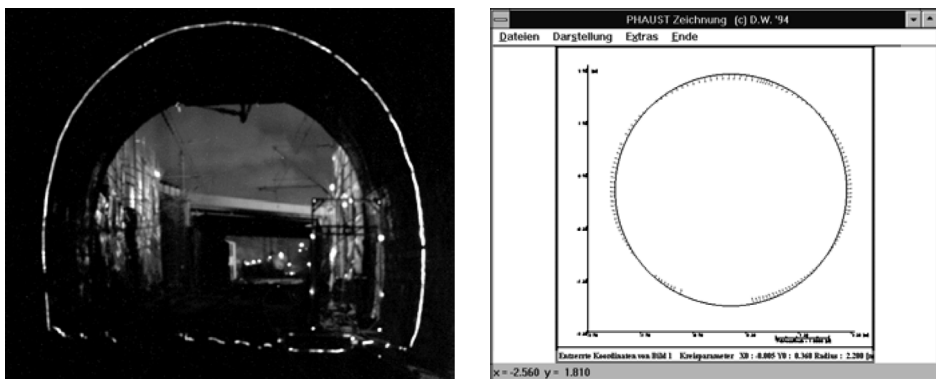


**Figure 8.19** Metric image with laser trace and sample result (INVERS)

Area-based measurement of tunnel walls can be performed by digital stereo images and automated surface reconstruction. The DEBIT system consists of two high-resolution video cameras mounted on an orientation frame whose orientation parameters are determined by a tracking video-theodolite. If the tunnel wall provides a suitable surface texture, a surface model and orthophoto can be derived for each position of the system (Weithe 1999).

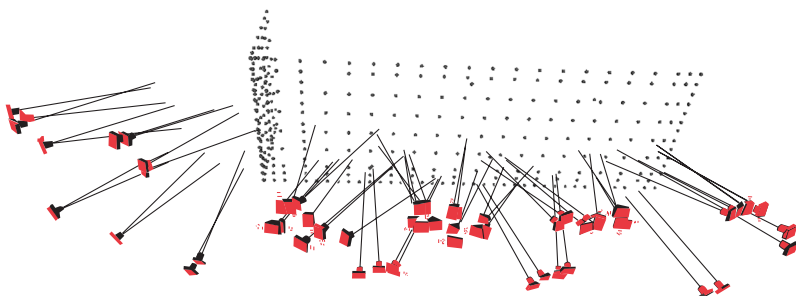
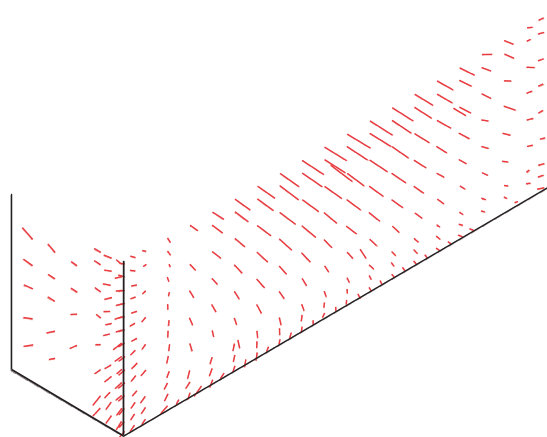
### 8.2.3 Deformation of concrete tanks

In this example, the deformation of concrete tanks used for galvanizing and electroplating had to be measured under working conditions (see Table 8.6). The tanks are constructed from a special concrete and have dimensions of approximately  $4 \text{ m} \times 1 \text{ m} \times 2 \text{ m}$ . In operation they are slowly filled with liquid of total weight 7.5 tons. The tank walls are subject to critical deformations which must be observed photogrammetrically at 10 minute intervals. Around 325 points must be measured to an accuracy of less than 0.1 mm.

Due to the very confined object environment, the shortest focal length available ( $f = 14 \text{ mm}$ ) had to be used. However, points on the smaller object side could not be observed with optimal intersection angles, hence object point accuracy is weaker in those areas.

**Table 8.6** Technical specifications for the measurement of electroplating tanks

Situation on site		Remarks
object dimensions (L × W × H)	ca. 4 m × 1 m × 2 m	
measurement sequence	every 10 minutes	9 epochs
camera; focal lengths	Fuji FinePix S2; $f = 14$ mm	
number of images acquired	about 50-60 per measurement	
number of images processed	all	
image scales	1:70–1:120	
number of control points	2 reference scale bars	free net adjustment
control point accuracy	0.1–0.3 mm (in height)	
add. geodetic observations		
Image measurement and bundle triangulation		
measuring instrumentation	AXIOS Ax.Ima, AICON 3D Studio	
mean image measurement accuracy	0.5 $\mu\text{m}$ (1/15 pixel)	$(\sigma_0)$
number of object points	ca. 325	
mean object accuracy	ca. 0.1 mm	
output of results	object coordinates and deformation vectors	

**Figure 8.20** Imaging configuration**Figure 8.21** Resulting deformation vectors between two sequential measurements

## 8.3 Industrial applications

### 8.3.1 Power stations and industrial plant

As-built documentation encompasses the measurement and inventory recording of an existing production facility. Most commonly, the complex structures and arrangements of pipes and machinery must be measured three-dimensionally for the following purposes:

- generation of up-to-date construction plans and CAD models, to centimetre accuracy, for production planning and control, and plant information systems (facility management)
- provision of precise geometric data (millimetre accuracy or better) to enable the replacement of large components which are manufactured off-site to fit existing mechanical interfaces

For power plants, and especially for nuclear facilities, on-site measurement time must be minimised in order to reduce the danger to personnel and avoid interruption of processes in operation. Components such as pipe sections, heat exchangers and boilers are replaced during regular shutdown periods and the necessary geometric data must be available in advance. Using targets attached to the objects, accuracies are specified to about 0.5 mm for object dimensions of 10–20 m.

The documentation of complex pipework is of considerable importance. Corresponding sites such as chemical plants, oil refineries and water works are characterised by difficult environmental conditions, bad visibility and complex geometries (Fig. 8.22). The objective of documentation is to produce a correct inventory and plans which in practice can only be processed by 3D CAD systems due to the three-dimensional nature of the facility. The data acquired can be used for 2D and 3D views (Fig. 8.23), inventory analysis (e.g. location of pipes, parts list), as well as the simulation of production processes (Przybilla 1999).

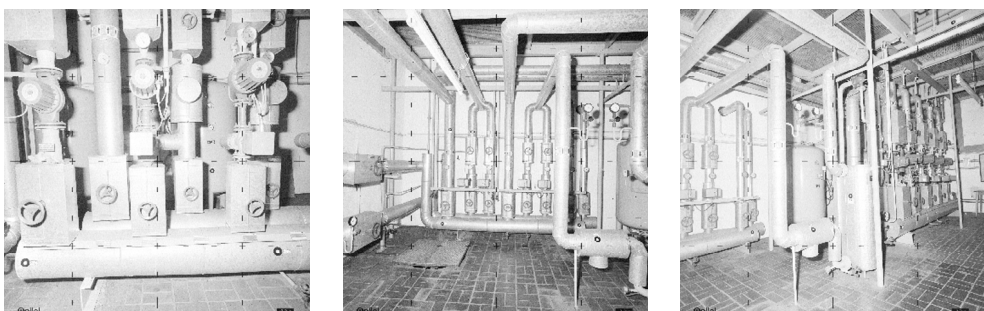


**Figure 8.22:** Metric images of pipework (INVERS)

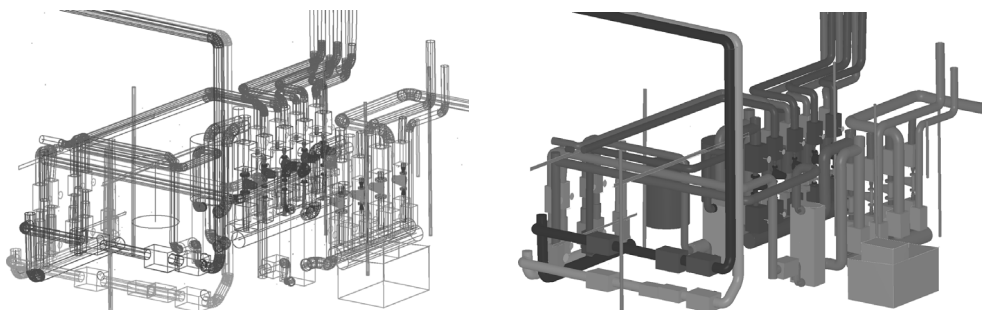


**Figure 8.23** CAD wire model and rendered view of pipework (INVERS)

### 8.3.2 Aircraft and space industries

Photogrammetric applications in the aerospace industry are distinguished by extremely high accuracy specifications for very large objects. Typical specifications for relative accuracies are between 1:100,000 and 1:250,000 or more. By the 1980s, large format analogue cameras, in conjunction with reseau techniques and precise digital comparators, were already in successful use. Since high-resolution digital cameras have become available, a number of applications for (automated) industrial photogrammetry have been developed. Examples of application areas include:

- measurement of parabolic antennas
- measurement of large tooling jigs and mechanical gauges
- production control of large components and assembly interfaces
- space simulations

Parabolic antennas can only be measured from one side of the object. The imaging configuration (Fig. 8.24) is designed to record each object point in a maximum number of convergent images (see Fig. 7.4). A homogeneous accuracy in all axes can then be expected. The surface is marked with circular retro-reflective targets (Fig. 8.25). Fraser (1996), among others, provides further information on the measurement of parabolic antennas.

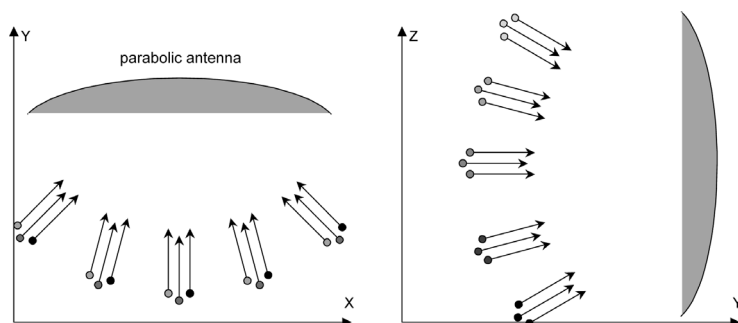


**Figure 8.24** Camera stations and viewing directions for antenna measurement  
(single side, multi-view configuration)

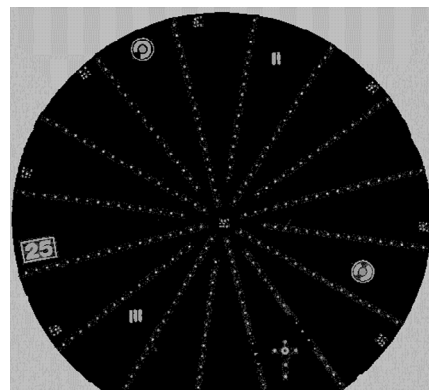


**Figure 8.25** Targeting of a parabolic antenna

For the inspection of large tooling jigs in the aircraft industry (Fig. 8.26), accuracy is again specified to about 0.1 mm for object sizes up to 50 m (length of aircraft) i.e. a relative accuracy of up to 1:500,000 is required. Until recently this task could only be solved by large format cameras (see section 3.3.1.4).

Verifying the achieved accuracy is problematic in measuring tasks of these dimensions. Reference scale bars longer than 3 m are difficult to handle in practice and significant effort is required to provide reference coordinates (see section 6.6). Reference measurement by high precision theodolite or laser tracker systems is not only time-consuming but also requires targets suitable for both systems in order to relate their measurements to one another. Additional information can be found in Fraser (1996) and Dold (1997).

The example in Fig. 8.27 shows a digital photogrammetric system employed for the on-line measurement of corner joints in aircraft wings. Tailored adhesive target sheets are positioned on the interface between wing and aircraft body. Only 17 minutes, including system set-up, are allowed for the complete measurement of the corner connection. Image acquisition is an on-line procedure via a high-resolution video camera (see Fig. 3.76c) which, together with a light source, is mounted in a compact housing.

The imaged targets are measured fully automatically. An initial bundle adjustment provides object coordinates. If the resulting standard deviations exceed a certain threshold, the corresponding points are displayed in a different colour on the computer screen. The user can add more images until the specified accuracy of 0.02–0.1 mm is reached (Bösemann *et al.* 1997).

The application of close-range photogrammetry under conditions experienced in space, places special demands on the image acquisition technology. Fig. 8.28 shows the air-conditioned, protective casing of a digital camera (Rollei ChipPack, Fig. 3.82) which is designed for extreme temperature variations in vacuum (up to  $\pm 100^\circ \text{C}$ ). The camera is used in a space simulator (ESTEC) for the measurement of thermally and mechanically stressed objects (Bouman *et al.* 1995).

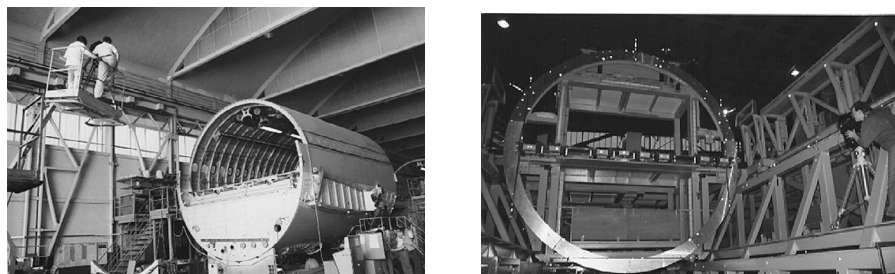


**Figure 8.26** Photogrammetric measurement of aircraft tooling jigs

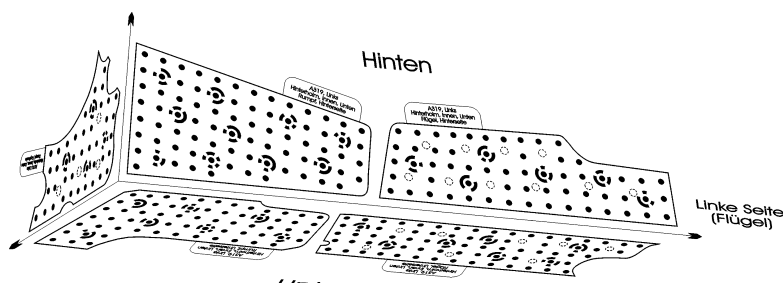


**Figure 8.27** Targeting of corner fittings (AICON)



**Figure 8.28** Digital camera in protective housing (ESTEC, Rollei)

### 8.3.3 Car industry

Three-dimensional measurement technology has, for some time, been one of the most important tools for quality control in the car industry. Mechanically probing coordinate measuring machines (CMMs) are mainly used for the high-precision measurement ( $1\text{--}10 \mu\text{m}$ ) of small components. In contrast, optical 3D measuring methods, with typical accuracies of 0.05 to 0.2 mm, are mostly applied where an object cannot be transported to a stationary measuring system, cannot be probed mechanically or a very large number of object points must be measured within a short time. The following shows a selection of areas where photogrammetry can be applied (see also Riechmann 1993):

- alignment of production cells and assembly facilities
- surface measurement of design models (reverse engineering, Fig. 6.36, 6.38)
- car body measurement in a wind tunnel
- deformation measurement in torsion and car safety tests
- inspection of parts from third party suppliers (see windscreens measuring system, Fig. 6.40)
- control of production machines (e.g. brake pipes, Fig. 6.25)

Measuring systems in production environments today almost exclusively utilise digital cameras, on or off line, in order to handle the necessary high data flows. In addition to the actual optical 3D measurement, these systems generally also provide data interfaces to CAD or CAM systems.

Prototypes are designed and manufactured prior to series production. If the corresponding parts contain free-form contours or surfaces, then the conventional generation of production data e.g. for milling machines, is a costly and normally iterative process. Rapid prototyping methods can lead to much faster manufacturing of prototypes, permitting multiple passes through the production sequence shown in Fig. 8.29. The measuring task is essentially the complete 3D registration of the model in order to derive machine control data (reverse engineering).

Both single point and surface measurement systems are employed. They are portable, flexible and can be taken directly to the object. Since it is costly and time-consuming to place targets, single point systems are often used online with tactile probing (measuring adapters and

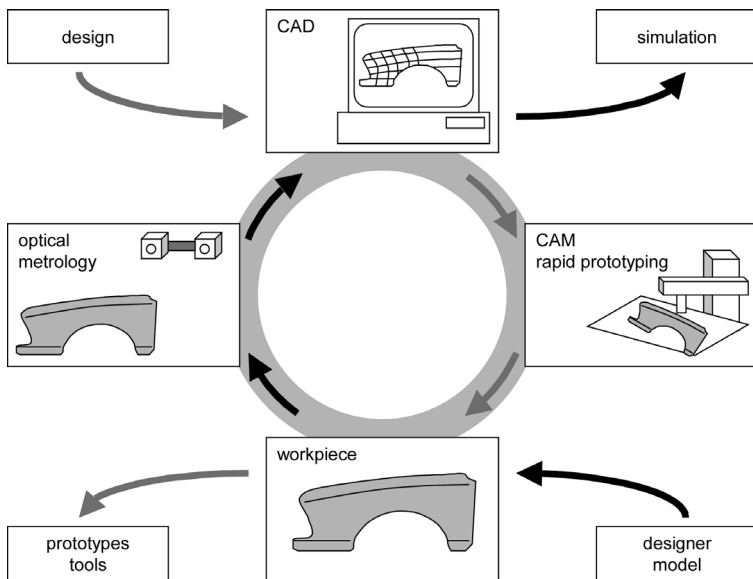


Figure 8.29 Reverse engineering (after Bieder 1997)

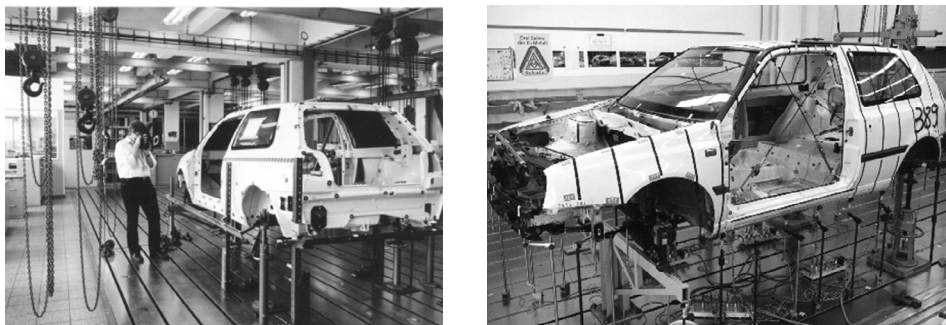


Figure 8.30 Photogrammetric measurement of targets for a torsion experiment (Volkswagen)

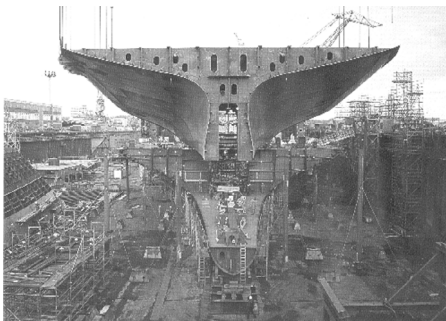
probing sticks, see also section 6.4.2.2). The surface measurement systems are typically oriented using object reference points and photogrammetric orientation methods (see Fig. 6.36).

Fig. 8.30 illustrates a car body torsion test. In this case strips of retro-reflective targets are placed along selected profiles and imaged from all sides. After interactive setting of a starting point, all targets on a strip can be measured automatically. In this example an object accuracy of 0.1 mm has been achieved (Riechmann and Ringel 1995).

### 8.3.4 Ship building industry

Metrology applications in the ship building industry are characterised by:

- measurement of large objects (> 30m)
- restricted access
- vibrations and disadvantageous environmental conditions



**Figure 8.31** Assembly of ship sections  
(HDW Kiel)

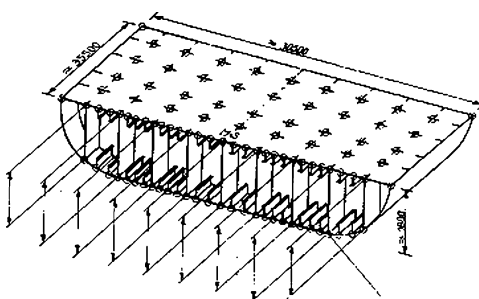


**Fig. 8.32:** Results of a section measurement  
(after Schneider 1994)

An example is the application of photogrammetry for quality control in the assembly of ship sections (Fig. 8.31) in order to minimise subsequent corrective work in dry dock. Part dimensions can be up to  $30\text{ m} \times 40\text{ m}$ . Segment planes and assembly interfaces are marked by targets and adapters. Specified object accuracy is 0.3–0.5 mm which corresponds to a relative accuracy of around 1:30,000 for a section and up to 1:250,000 for a complete ship. Image acquisition is via large and medium format cameras or high-resolution digital cameras. Fig. 8.32 illustrates a typical measurement result.

Other applications include the photogrammetric shape measurement of sheet metal components and hull sections. In addition to photogrammetry, geodetic measuring methods are also applied in the ship industry (Schneider 1994, Miebach 2002).

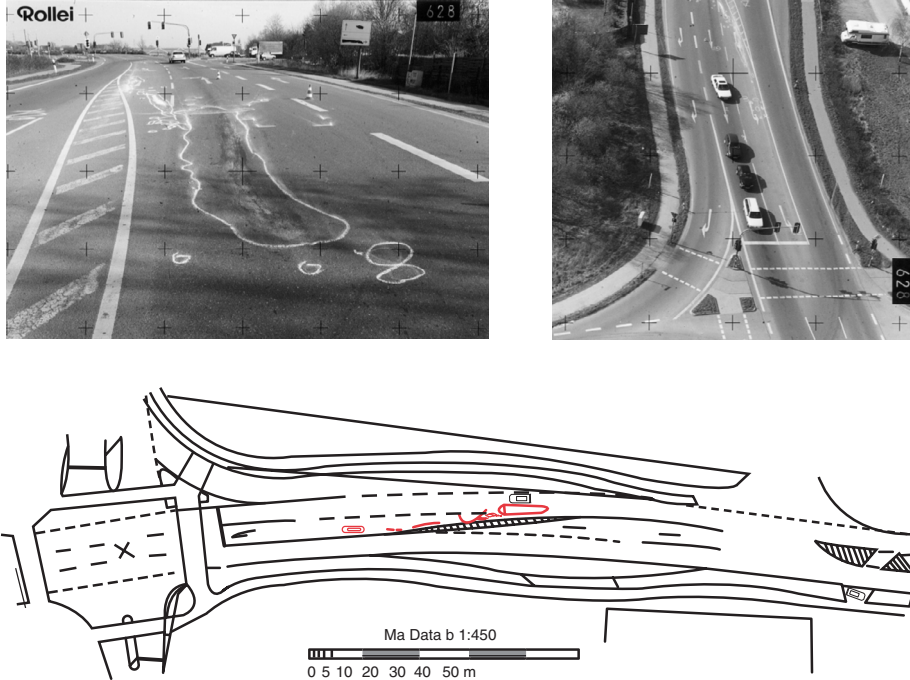
## 8.4 Forensic applications

Photogrammetry is often used in accident and crime applications, including:

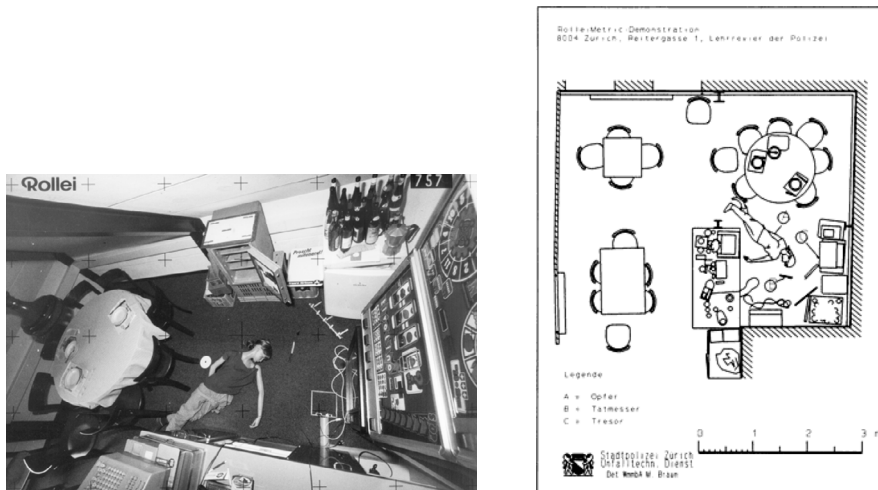
- traffic accident recording
- recording and reconstruction of aircraft crashes
- scene-of-crime measurement
- estimating the height of criminals
- reconstructing bullet trajectories
- object reconstruction from amateur images
- detecting environmental pollution from aerial images

Fig. 8.33 shows metric images from a photogrammetric accident record. Some reference distances are measured in object space because control points cannot usually be provided due to the limited time available. The scene is recorded with a convergent set of images which can optionally include aerial images. Results can be output as scaled plans, CAD drawings or coordinates of the accident site. Photogrammetric measurements are accepted as valid evidence in criminal trials and legal disputes (forensic photogrammetry).

Scenes-of-crime can be measured and documented by photogrammetry without disturbing the local environment or further police activities, such as the collection of evidence. Fig. 8.34 shows a metric image from a multi-image configuration and the scene-of-crime reconstruction which results.



**Figure 8.33** Photogrammetric accident recording by a combination of aerial and terrestrial images



**Figure 8.34** Photogrammetric scene-of-crime measurement

## 8.5 Medicine

In medicine, photogrammetry is mainly used to measure parts of the body, for example:

- to prepare and carry out operations
- to adapt prostheses
- in motion studies
- in the therapy for bone and spinal deformations
- to monitor growth

### 8.5.1 Surface measurement

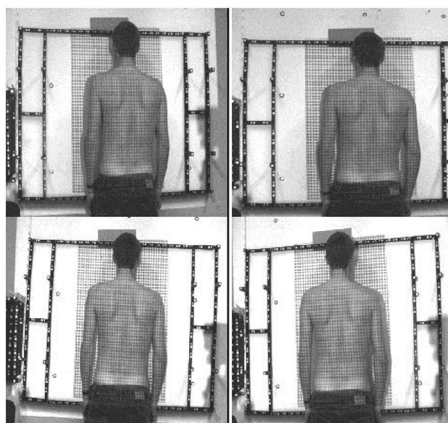
Medical surface measurements are mostly characterised by:

- the measurement of unstructured, soft, free-form surfaces
- the recording of objects showing small or limited movement
- the absence of permanent reference points on the object surface

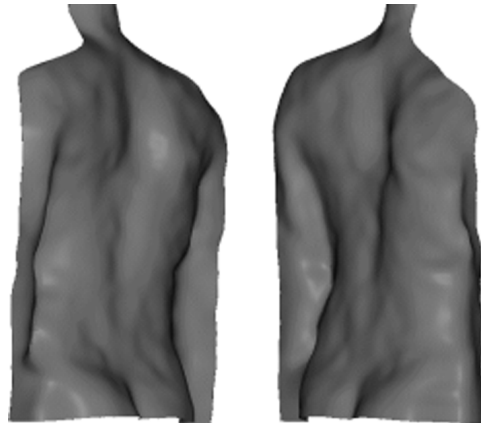
Poorly textured, free-form surfaces must be given an artificial structure e.g. by fringe or raster projection (see section 6.5.2). Stereoscopic configurations are mostly chosen for surface measurement and the term biostereometrics identifies this general procedure. It is, of course, possible to use synchronised multiple images for these applications also.

Fig. 8.35 shows a set of four images for back measurement. The patient is positioned in front of a spatial field of reference points and a target grid is projected onto the surface of the patient's back. This is all imaged by four synchronised cameras. Least-squares matching is used for surface reconstruction. The resulting three-dimensional model can be analysed for asymmetries (Fig. 8.36). Features of the photogrammetric process are:

- non-contact measurement without causing stress to the patient
- short measurement time (tenths of a second)
- no radiation exposure



**Figure 8.35** Multiple image configuration for back measurement (after Gäbel 1993)



**Figure 8.36** 3D visualisation of human back measurement (after Gäbel 1993)

- suitable also for infants and children
- subsequent measurement and diagnostic comparison over time

Overviews of medical applications of photogrammetry can be found, for example, in Gäbel 1993 and Newton and Mitchell 1996.

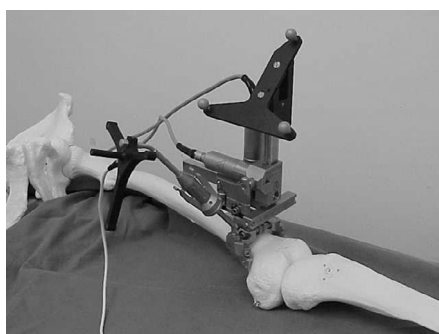
### 8.5.2 On-line measuring systems

Medicine increasingly uses digital, photogrammetric, on-line measuring systems with tactile body probing. They usually consist of two cameras fixed into a mobile housing. Fig. 8.37 shows examples of such dual camera, on-line systems with point-by-point tactile probing. These can not only use target adapters with probing tips (Fig. 8.38, see section 3.4.1.3), but also the actual tools used in operations, if equipped with suitable targets (Fig. 8.37b). They are a critical component in image-based planning and execution of operations (image guided surgery) where a spatial relationship between patient and surgical instrument must be established. In medicine this process is known as navigation.

The key problem in navigated operations is the unstable position of the patient during the intrusion. It cannot be assumed that patient and measuring system have a constant geometric relationship with respect to one another. For this reason, local reference target arrays (locators) are attached to the patient whose potential motion can then be continuously monitored by the



a) point-by-point object measurement  
(AXIOS 3D CamBar)



b) surgical robot with locators (Galileo, Plus Orthopedics)



c) on-line system for use in operating theatres  
(Plus Orthopedics)

**Figure 8.37** Medical, dual camera, on-line systems

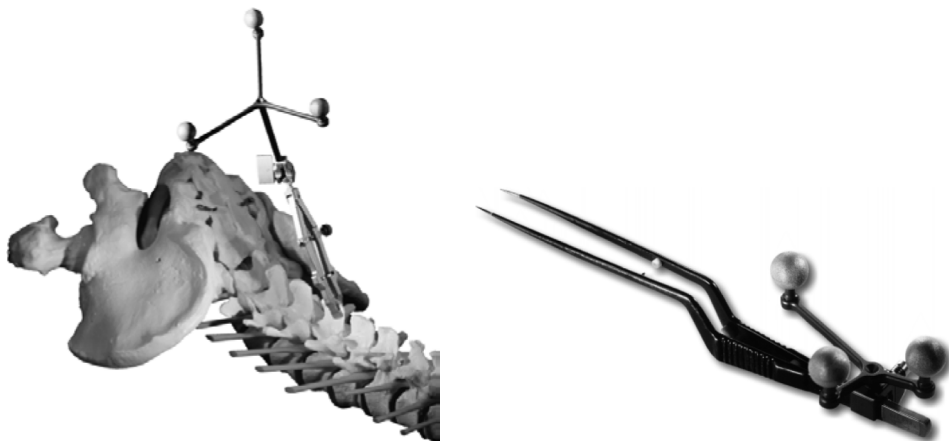


**Figure 8.38** Surgical tools with spatial target arrays (BrainLAB)

navigation system. The spatial position of surgical tools or predefined operation data (e.g. related computer tomograms) can be transformed into the coordinate system of the locator. Fig. 8.37b shows an example where a locator fixed to a bone is measured, together with a moving locator mounted on an surgical robot. In this way it is possible to compensate for any motion of the legs.

Accuracy requirements for navigation systems depend on application and range from around 0.1 mm for spinal surgery, around 0.5 mm for implanting knee and hip joints and up to 1 mm or so in brain surgery. These applications require measurement frequencies of 10 to 50 3D measurements per second, with up to 20 points or more simultaneously measured or tracked in 3D space. Motion analysis requires significantly lower accuracies but much higher measurement frequencies.

Photogrammetric navigation systems are also employed to implement pre-operative planning which is usually derived from computer tomography (CT) imagery. Fig. 8.39 shows an example of the planned insertion of a CAD-designed hip joint in a CT image. Using anatomical navigation points (landmarks), the transformation between CT and real bone can be generated during the operation.



**Figure 8.39** Implementation plan for inserting a hip joint (Plus Orthopedics)

## References

- Albertz, J. and Wiedemann, A. (ed.) (1997) *Architekturphotogrammetrie gestern-heute-morgen*. Technische Universität Berlin.
- Almagro, A., Patias, P. and Waldhäusl, P. (1996) The CIPA “O. Wagner Pavillion” test. *International Archives of Photogrammetry and Remote Sensing*, **31**(B5), pp. 463–470.
- Bieder, H. (1997) *Optische Formerfassung und Reverse Engineering – Anforderungen an die Software*. GMA-Bericht 30, Optische Formerfassung, Langen, pp. 139–146.
- Bouman, J., van Oel, J., Müller-Stute, F., Sarti, B. and Dold, J. (1995) A photogrammetric system for use in thermal vacuum testing. *ESA Bulletin* **81**, 2/1995, pp. 69–76.
- Bösemann, W., Drohne, U. and Schneider, C.-T. (1997) Application of an integrated photogrammetric system for the Airbus A319–A321 wing assembly. In Gruen/Kahmen (ed.) *Optical 3-D Measurement Techniques IV*, Wichmann, Heidelberg, pp. 151–157.
- Brenner, C. and Haala, N. (1998) Fast production of virtual reality city models. *International Archives of Photogrammetry and Remote Sensing*, **32**(B4), pp. 77–84.
- Carbonell, M. (1989) Architectural photogrammetry. In Karara (ed.) *Non-Topographic Photogrammetry*. 2nd Edition, American Society for Photogrammetry and Remote Sensing, pp. 321–347.
- Dallas, R. W. A. (1996) Architectural and archaeological photogrammetry. In Atkinson (ed.) *Close Range Photogrammetry and Machine Vision*. Whittles Publishing, Caithness, UK, pp. 283–302.
- Dold, J. (1997) *Ein hybrides photogrammetrisches Industriemeßsystem höchster Genauigkeit und seine Überprüfung*. Dissertation, Heft 54, Schriftenreihe Studiengang Vermessungswesen, University of Armed Forces, Munich.
- Fellbaum, M. and Hau, T. (1996) Photogrammetrische Aufnahme und Darstellung des Doms von Siena. *Zeitschrift für Photogrammetrie und Fernerkundung*, Heft 2/1996, pp. 61–67.
- Fraser, C. S. (1996) Industrial measurement applications. In Atkinson (ed.) *Close Range Photogrammetry and Machine Vision*. Whittles Publishing, Caithness, UK, pp. 329–361.
- Fryer, J. G., Mitchell, H. L. and Chandler, J. H. (2006) *Applications of 3D measurement from images*. Whittles Publishing, Caithness, Scotland, UK.
- Gäbel, H. (1993) *Photogrammetrische Verfahren zur Erfassung von menschlichen Körperoberflächen*. Dissertation, Deutsche Geodätische Kommission, Reihe C, Nr. 405.
- Grün, A. (1994) Von Meydenbauer zur Megaplus – Die Architekturphotogrammetrie im Spiegel der technischen Entwicklung. *Zeitschrift für Photogrammetrie und Fernerkundung*, Heft 2/1994, pp. 41–56.
- Kludas, T. (1995) *Three-dimensional surface reconstruction with the Zeiss photogrammetric industrial measurement system InduSURF Digital* (in German). Publikationen der DGPF, Band 3, Dresden, pp. 127–133.
- Kotowski, R., Meid, A., Peipe, J. and Wester-Ebbinghaus, W. (1989) Photogrammetrische Bauaufnahme der “Kirchen von Siena” – Entwicklung eines Konzepts zur Vermessung von Großbauwerken. *Allgemeine Vermessungsnachrichten*, 4/1989, pp. 144–154.
- Luhmann, T. (ed.) (2002) *Nahbereichsphotogrammetrie in der Praxis*. Wichmann, Heidelberg, 318 p.
- Luhmann, T. and Tecklenburg, W. (1997) Hybride photogrammetrische Aufnahme großer Ingenieurobjekte. *Photogrammetrie-Fernerkundung-Geoinformation*, Heft 4, pp. 243–252.
- Miebach, R. (2002) Anwendungen im Schiffbau. In Löffler (ed.) *Handbuch Ingenieurgeodäsie – Maschinen und Anlagenbau*, Wichmann Verlag, pp. 355–387.
- Newton, I. and Mitchell, H. L. (1996) Medical photogrammetry. In Atkinson (ed.) *Close Range Photogrammetry and Machine Vision*. Whittles Publishing, Caithness, UK, pp. 303–327.
- Patias, P. and Strelein, A. (1996) Contribution of videogrammetry to the architectural restitution – Results of the CIPA “O. Wagner Pavillion” test. *International Archives of Photogrammetry and Remote Sensing*, **31**(B5), pp. 457–462.
- Przybillia, H.-J. (1999) Sensorvermessung im Industrie- und Anlagenbau. VDI-Berichte Nr. 1454, *Moderne Sensorik für die Bauvermessung*, VDI Verlag, Düsseldorf, pp. 173–183.

- Regensburger, K. (1990) *Photogrammetrie – Anwendungen in Wissenschaft und Technik*. VEB Verlag für Bauwesen, Berlin.
- Riechmann, W. (1993) Photogrammetrie in der Automobilindustrie. *Zeitschrift für Photogrammetrie und Fernerkundung*, Heft 2/1993, pp. 90–97.
- Riechmann, W. and Ringel, H. (1995) Photogrammetrische Verformungsanalysen in der Karosserie-Entwicklung. Tagung *Optische Meßmethoden in der modernen Automobilentwicklung*, Haus der Technik, Essen.
- Schneider, C.-T. (1994) *Einsatz der Industriephotogrammetrie im Schiffbau*. Publikationen der DGPF, Band 2, Augsburg 1993, pp. 117–119.
- Streilein, A. (1998) *Digitale Photogrammetrie und CAAD*. Dissertation, Mitteilungen Nr. 68, Institut für Geodäsie und Photogrammetrie, ETH Zürich, 160 p.
- Weimann, G. (1988) *Architekturphotogrammetrie*. Wichmann Verlag, Karlsruhe.
- Weithe, G. (1999) Tunnelprofilmessung mit dem Digitalmeßsystem DIBIT am Beispiel von Projekten der Deutschen Bahn AG. VDI-Berichte 1454, *Moderne Sensorik für die Bauvermessung*, VDI Verlag, Düsseldorf, pp. 155–171.
- Wiedemann, A. (1997) Orthophototechnik in der Architekturphotogrammetrie – Möglichkeiten und Grenzen. In Albertz/Wiedemann (ed.) *Architektur-photogrammetrie gestern-heute-morgen*. Technische Universität Berlin, pp. 79–94.
- Woytowicz, D. (1998) *Profilmessungen auf der Basis eines Lichtschnittverfahrens*. Publikationen der DGPF, Band 6, Frankfurt 1997, pp. 295–300.



**Blackwell**  
Publishing

Blackwell Publishing  
9600 Garsington Road  
Oxford  
OX4 2DQ  
UK

Tel: +44 (0) 1865 776868  
Fax: +44 (0) 1865 714591



# The Photogrammetric Record

An International Journal of Photogrammetry

*Published on behalf of the Remote Sensing and Photogrammetry Society*

Edited by: Paul Newby

*The Photogrammetric Record* contains original, independently and rapidly refereed articles which reflect current photogrammetric practice and research throughout the world. The journal provides a record of new research which will contribute both to the advancement of photogrammetric knowledge and to the application of photogrammetric techniques in traditional and novel ways. It also seeks to stimulate debate in its correspondence and shorter contributions sections, and carries reviews of recent photogrammetric literature.

For more information visit

**[www.blackwellpublishing.com/photrec](http://www.blackwellpublishing.com/photrec)**

**Blackwell**  
**Synergy**

Register FREE at [www.blackwell-synergy.com](http://www.blackwell-synergy.com) and you can:

- Receive tables of contents e-mail alerts directly to your desktop with links to article abstracts
- Search across all full text articles for key words or phrases
- Access free sample issues from every online journal
- Browse all tables of contents and abstracts, and save favourites on your own custom page.

*When your inspection requires  
“Picture Perfect Measurements”*

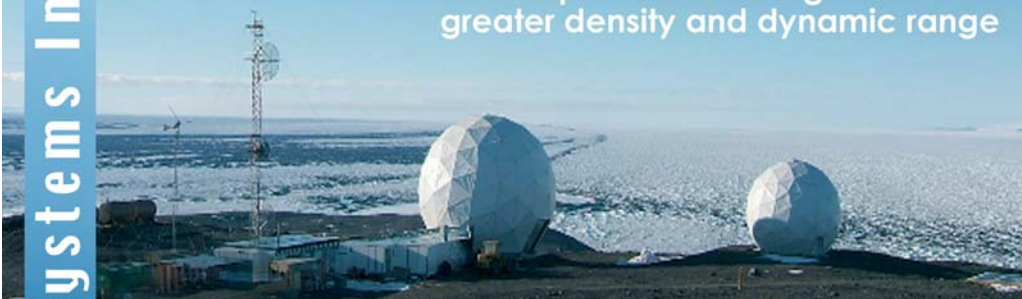
# V-STARS



**We boldly go where others fear to tread**

If you need to make fast, accurate, non-contact, in-place 3-D measurements in difficult conditions where other metrology systems just can't cut it, give V-STARS a try.

- \* New rugged light-weight probes
- \* New improved scanning with greater density and dynamic range



Visit [www.geodetic.com](http://www.geodetic.com) to request a copy of our video



**“Picture Perfect Measurements”**

See V-STARS in action in aerospace, automotive, shipbuilding, and other industries.

[www.geodetic.com](http://www.geodetic.com)

Ph +1 321 724 6831



**Geodetic Systems Inc.**

# ACCESSIBLE AFFORDABLE PHOTOGRAMMETRY PHOTOMODELER®

PhotoModeler, easy-to-use close-range-photogrammetry software, since 1992.

- extensive modeling set: points, lines, edges, NURBS curves, NURBS and triangulated surfaces, cylinders and surface draw
- manual marking or high precision automated target detection
- extracts photographic textures
- efficient error-propagating bundle adjustment
- video and target tracking add-on
- coded target add-on for full automation
- camera calibration methods
- self / field calibration & inverse camera
- support for control points and constraints
- single photo solutions based on resections or vanishing point methods
- highly precise and accurate
- exports to popular CAD formats
- supports any digital or film camera
- extensive tutorials and videos
- easy-to-reach technical support

The best value in photogrammetry software. High quality for a low price!

engineering

archaeology

accident reconstruction

photograph

photomodeler

measure & export

architecture

Eos Systems Inc. [www.photomodeler.com](http://www.photomodeler.com) +1.604.732.6658



**GOM**

## Optical measuring solutions for 3D coordinate measurement and deformation measurement



**gom**  
Optical Measuring Techniques  
[www.gom.com](http://www.gom.com)





# iWitness™

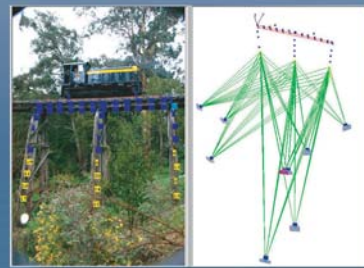
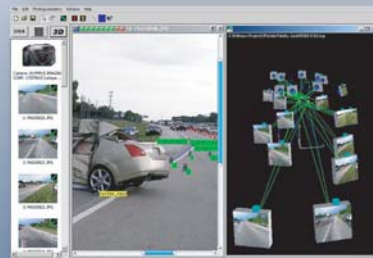
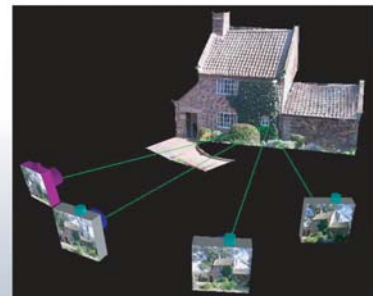
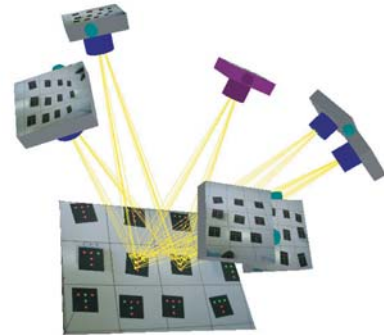
Close Range Photogrammetry

An affordable and exceptionally easy-to-use close-range photogrammetric system that provides fast and accurate 3D measurements from images recorded with both consumer-grade and professional cameras.

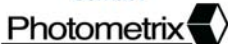
- Exceptionally intuitive and simple to operate
- Automatic recognition of the camera
- Fully automatic camera calibration, as well as on-the-job self-calibration
- All photogrammetric orientation processes are initiated automatically
- Robust and reliable error detection through on-line data processing
- Flexible generation of photo-textured 3D models
- Auto-assisted image marking and referencing leading to high-accuracy XYZ coordinates
- Efficient and fast 'stitching' of overlapping networks

**iWitness** is widely used in engineering, architecture, heritage recording, animation and modeling, and especially in accident reconstruction and forensics.

With its ease of use, **iWitness** is an ideal tool for teaching.



Contact



Photometrix Pty Ltd

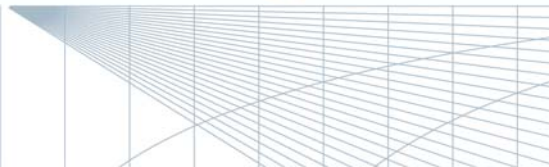
[www.Photometrix.com.au](http://www.Photometrix.com.au)

In North America



DeChant Consulting Services DCS Inc.

[www.iWitnessphoto.com](http://www.iWitnessphoto.com)





→ Whatever your photogrammetry application.

Whether you need to:

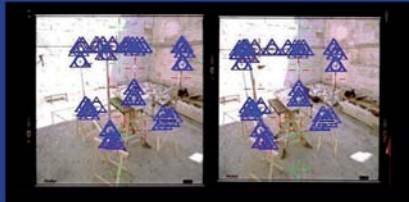
**Solve** a complicated three-dimensional block triangulation using automated point transfer and minimal control...

**Measure**, model and analyse critical dimensions and surfaces...

or simply **Visualise** your results in stereo, wireframe or rendered model...

## Intergraph ImageStation™ is the solution.

Measure > Analyse > Model > Visualise



ImageStation™ Photogrammetric System; the world's most productive stereo workstation and software suite.

For more information contact:  
[info-uk@intergraph.com](mailto:info-uk@intergraph.com)  
or visit [www.intergraph.co.uk](http://www.intergraph.co.uk)

Intergraph and the Intergraph logo are registered trademarks of Intergraph Corporation. ZI Imaging and ImageStation are registered trademarks of ZI Imaging Corporation. Other brands and product names are trademarks of their respective owners. © 2006 Intergraph Corporation, Huntsville, AL 35824

Industrial-measurement

Medical-engineering



More than state-of-the-art

- » Photogrammetry
- » Bundle block adjustment
- » Digital image processing
- » Industrial measuring techniques
- » Optical 3D-measurement
- » Contour measurement
- » Camera calibration

w w w . a x i o s 3 d . d e

# The ultimate 3D surveying tool...

**“...the ADAM Technology software is more accurate, faster, more flexible, easier to use, more robust and more rapidly developing, provides better quality models, has better software support and requires less training...”**

— BMA Coal, "Report on Field Test of New Safe Highwall Mapping Technologies for BMA"

## 3DM Analyst

*Focussing on the Future*

### Mining Analysis Software



Advanced Design and Manufacturing Pty. Ltd.

Suite 3, 41 Belmont Avenue, Belmont, Western Australia 6104

Phone: +61 8 9479 5575 [www.adamtech.com.au](http://www.adamtech.com.au)

**3DM Analyst** is a ground-breaking digital photogrammetric package that brings unprecedented levels of power and flexibility to surveying and geological applications.



### Digital Close Range Photogrammetry



- 3D-Modeling and Measurement
- Bundle Block Adjustment
- Rectification
- Digital Orthophoto
- Camera Calibration



technet GmbH  
Maassenstr. 14  
10777 Berlin  
Germany

tel +49 30 2154020  
fax +49 30 2154027  
[mail@technet-gmbh.com](mailto:mail@technet-gmbh.com)  
[www.technet-gmbh.com](http://www.technet-gmbh.com)



## Mobile 3D Metrology for Testing & Inspection

[www.aicon3d.com](http://www.aicon3d.com)

AICON 3D Systems GmbH

Biberweg 30 C  
D-38114 Braunschweig  
Germany

tel. +49 (0)531-58 000 58  
fax +49 (0)531-58 000 60

info@aicon.de  
[www.aicon3d.com](http://www.aicon3d.com)

MEASURE THE ADVANTAGE

# Index

- 2½ D surface 90
- 3-2-1 method 247, 249
- 35 mm camera 143, 165
- 360° scanner 176
- 3-chip method 172
- 3D
  - circle 86, 88, 89
  - digitiser 408
  - Helmut transformation 45
  - surface 90
- 4-parameter transformation 34
- 6-parameter transformation 35
- 6 DOF 214
- Abbe's comparator principle 401
- absolute orientation 227–29
  - datum definition 228–29
  - model 227–28
  - spatial point distribution 245
- absorption 155
- acceptance
  - test 433–34, 442
  - tolerance 434
- accident record 489
- accuracy
  - contour method 290–91
  - image measurement 442
  - inner 250
  - instruments 442
  - length measurement 434, 436
  - object point 99
  - on-line systems 417
  - normal stereo case 104
  - self-calibration 263–64
  - stereo image processing 275
- acquisition
  - multi-image 98, 99–100
  - single image 98, 102
- adapter 417, 489, 492
- additional
  - parameter functions 242
  - parameters 120
- adjustment
  - conditional least squares 58–59
  - Gauss-Markov method 55
  - least squares 34, 46, 55, 79
  - of direct observations 55–56
  - procedure 38
  - reliability 64–66
  - systems 43
  - techniques 52–72
- aerial
  - image 465–66, 475, 489
  - photogrammetry 5, 202
  - triangulation 230
- aerospace industry 13, 485
- affine transformations
  - matrix notation 36
  - plane 35–36
  - spatial similarity 44
- affinity 114, 119, 120, 162, 243, 264
- airborne laser scanning 475
- aliasing 133, 154, 159
- all-round measurements 430
- altimeter 466
- amateur camera 127, 163, 165
- anaglyph 281, 410
- analogue photogrammetry 5, 8
- analogue-to-digital converter 161
- analysis procedures 10–11

- analytical  
photogrammetry 5, 20  
plotter 20, 407–09
- angle of convergence 98
- angular resolution 310
- antenna measurement 447
- anti-aliasing filter 133
- aperture  
depth of field 110–12  
lens 106, 107  
linear 106  
relative 112–13  
size 134, 153  
telecentric lenses 114
- approximate values 46–48  
3D transformation 46–48  
bundle adjustment 230, 234, 251–60  
functional model 54  
panorama orientation 311–12  
relative orientation 221, 226  
rotation parameters 211  
space resection 209
- approximation 11, 83  
B-spline 80–81  
Bezier 81–82  
point 79  
surface 92
- archaeology 6, 13, 466
- architectural photogrammetry 6, 469–77
- archiving 11
- artificial cooling 156
- as-built documentation 414, 484
- autobar 255
- auto-focus 165
- auto-stereoscopic display 410
- auxiliary coordinate system 241–42
- B-spline 292  
approximation 80–81  
surface 81, 93
- background  
intensity 426  
noise 156
- balanced  
observations 447  
radial distortion 117
- ball plate 435, 436
- band  
absorption technique 464  
interleaved 323
- band-pass filter 133
- barcode 188
- basal plane 217
- base *see* stereobase
- base components 219, 220, 229
- basic configuration 447
- Bayer pattern 173
- beamer 192
- Bernstein polynomial 81
- best-fit element 285
- Bezier  
approximation 81–82  
surface 93
- bilinear transformation 37–39, 126
- bistereometrics 6, 491
- black-and-white film 130, 135
- blooming 153, 156
- blunder 217  
robust detection 259
- BMP 324
- Brown's parameters 116
- bucket brigade device 150
- building  
planning 473  
records 469–70
- bundle adjustment 11, 21  
additional observations 242  
approximate values 251–52  
collinearity equations 234  
data flow 202, 232–33  
datum defect 244–45  
development 230  
divergence 265  
error-free reference points 245–46  
extended model 239–40, 307–08  
geometric elements 301–02  
initial values, other methods 258  
method 229  
model 234–35  
multi-image 229  
number of unknowns 70  
packages 231  
panorama orientation 311–13  
process 232–33  
quality measure 260–64  
report 260  
strategies 264–66  
with straight lines 300–01
- bundle of rays 226, 229, 258  
limitation of 114
- bundle triangulation *see* bundle adjustment

- C-mount 160  
 CAAD 473  
 CAD  
     data 252, 258  
     model 251, 264, 274, 472, 479, 484  
     system 48, 72, 408, 448  
 calibration 118, 119, 448–58  
     correction values 118  
 image variant camera 127  
 laboratory 126, 128, 449  
 matrix 121  
 on-the-job 452  
 plumb-line 302, 451–52  
 quality 263–64  
 robot 464  
 self- 122, 128, 141, 144, 145, 165, 188, 238,  
     242–43, 263–64, 453  
 simultaneous 100  
 single station self- 456  
 system 453  
 test field 128, 144, 236, 238, 449–51  
     with plane point field 454  
     with variable test field orientation 243  
 camera  
     35 mm 143, 165  
     amateur 127, 163, 165  
     colour 151, 163, 172–74  
     consumer 174  
     digital 143, 147, 163–67, 180  
     GPS 182  
     high speed 174–75, 465  
     integrated in probing device 404–05  
     interior orientation 128–29, 144  
     inverse 424, 428  
     large format 122, 140, 145, 146  
     line scanning 169  
     medium format 138, 143, 144, 145, 166  
     metric 124, 126–27, 128, 140–41  
     micro-head 159  
     non-metric 127, 146  
     panorama 171  
     réseau 143, 144  
     réseau-scanning 169, 170  
     robot 170  
     scanning 147, 168–71, 176  
     semi-metric 127, 129  
     single lens reflex 138–39, 165  
     stereometric 19, 99, 142  
     still-video 163, 165, 166  
     studio 139  
     video 147, 157–63, 178  
         view finder 138, 139, 144  
 CameraLink 163  
 camera-view scanner 176  
 car  
     industry 487–88  
     safety testing 462, 487  
 CCD  
     CMOS, comparison to 152–53  
     digital camera 164  
     geometric accuracy 154–55  
     line sensor 169–71  
     parallel method 172  
     resolving power 153–54  
     sensor principals 148–52  
     signal-to-noise ratio 157  
     spectral sensitivity 156  
     still-video 163, 165, 166  
     technology 147–48  
     video camera 157–63  
 CCIR 157, 158, 162  
 central  
     perspective 107–09, 115  
     projection 37, 45, 48, 50, 204, 267, 293  
 centroid 48, 75, 84  
     optical 111, 193  
 charge 148  
 Cholesky factorisation 70  
 cinematography 462  
 circle of confusion 109, 110  
 circuit noise 157  
 circumscribed element 290  
 city model 474–75  
 closed loop image configuration 236  
 CMOS 125, 152–53, 164, 173, 174  
 coded light approach 427–28  
 coefficient matrix *see* Jacobian matrix 53  
 cofactor matrix 54, 60, 64  
 collimator 449  
 collinearity equations 45, 204–06  
     bundle adjustment 234  
     epipolar geometry 218, 222  
     exterior orientation 206  
     floating mark 407  
     panorama image 311  
     space intersection 283  
     space resection 206  
     straight lines 296–97  
     with phase values 430

- colour
  - camera 151, 163, 172–74
  - coupler 136
  - film 130, 135
  - reversal film 136
  - transformation 326
- comparator 401–04
  - coordinate system 32
  - coordinates 402
- compression *see* image compression
- computer aided architectural design 473
- confidence
  - ellipsoid 284
  - interval 61–63
  - level 62
- configuration defect 245
- conjugate diameter 78
- connection matrix 236, 254
- connectivity 322, 362, 376
- constraint
  - density 69
  - equations 58
- constraints
  - between unknowns 58
  - non-linear 58
- consumer camera 174
- contour measurement 285
- contrast 131–32, 135, 137, 143, 194
  - transfer function 131
- control points 10 *see also* reference points
- convergent imagery 111, 458
- coordinate metrology 285
- coordinate system
  - auxiliary 241–42
  - comparator 32
  - image 31, 115, 119, 123–25, 126–27, 146, 203, 211
  - intermediate 46
  - machine 125
  - model 32, 218–20, 227, 252, 294
  - national geodetic 33
  - object 33, 227, 446, 452
  - pixel 320–22
  - sensor 125
  - temporary 306, 310
  - world 33, 45
- coplanarity 298
  - constraint 219–20, 307
- correction
  - equations 53, 58
  - functions 115, 117
- correlation
  - between adjusted parameters 63, 233, 243, 260, 263, 264, 457–58
  - coefficient 54, 63
  - image 366
- $\cos^4$  law 111
- covariance matrix 54, 60, 63, 67, 70, 235, 249, 283, 446, 457
- cross ratios 39
- curves 78–82
  - B-spline 93
  - second order 75
- cycles per pixel 154
- cylinder 87–88, 288–90, 309, 313–14
- cylindrical projection 472
- danger
  - cylinder 225
  - surface 212, 225
- dark current noise 156, 157
- data snooping 67
- datum 228–29, 236, 244–51, 301
  - defect 57, 244–45, 300
  - definition 232, 235, 245, 246, 247, 446
  - point 248, 249
- decentring distortion 113, 118
- defocusing 107, 110, 111, 134
- deformation analysis 476, 478, 481
- degrees of freedom 59, 62, 214
- Delaunay triangulation 91
- demodulation 426
- density 47
  - high point 178
  - neutral density filter 111
  - optical 136, 137
  - refraction 105
  - target 185
- depth
  - information 275
  - of field 110–12, 138, 444
- design *see also* network design
  - factor 103, 104, 261, 278
  - matrix *see* Jacobian matrix
- detectability 401
- detector
  - signal 134
  - size 153, 154
  - spacing 134, 153
- development, chemical 136
- diffraction 106–107
  - disk 106

- digital  
 camera 143, 147, 163–67, 180  
 image comparator 402–04  
 imaging system 147–76  
 photogrammetry 5, 22  
 surface model 270–71, 275, 409  
 digitising 11  
 tablet 413  
 Dirac pulse 134  
 Direct Linear Transformation 146, 206, 212–14, 457  
 direction cosine 43, 82–85, 88  
 discrete cosine transformation 326, 334  
 disparity 277  
 dispersion 106  
 distance ratios 293, 294  
 distortion  
   asymmetric 243, 264  
   curve 116, 117, 121  
   decentring 113, 118  
   distance-dependent 304  
   iterative correction 122–23  
   lens 267  
   parameters 205, 235, 263, 268  
   parameters, correlation 116  
   radial 108, 115–20, 121, 208, 213, 243, 263, 304  
   tangential and asymmetric 109, 118, 243, 264  
 distribution of image points 444–50, 450  
 dove prism 408  
 drill holes 94, 189, 190  
 dynamic range 134, 153, 156, 157  
 eccentric targeting 189–90  
 eccentricity  
   circle centre 186, 444  
   degree of 186  
   effect of 187  
   targeting 189–90  
   vector 171  
 edge  
   adapter 190  
   algorithm 188  
   detection 147, 185, 194  
   enhancement 194  
   profiles 134  
 eigenvalue 284  
 eigenvector 284  
 electron holes 148  
 electronic flash 190–91  
 element  
 maximum inscribed 94  
 minimum circumscribed 94  
 minimum zone 94  
 ellipse 76–78, 183, 186  
 emulsion 130, 135, 137, 140, 147, 154  
 engineering  
   civil 14  
   photogrammetry 6  
 entrance pupil 107, 112  
 environmental conditions 441  
 epipolar geometry 217–18, 463  
   line 217–18  
   panorama images 313–14  
   plane 217–18, 275, 313  
 error ellipse 249  
 estimated parameters 54, 55  
 exit pupil 107  
 expected value 58, 59, 61, 65  
 expert system 448  
 exposure time 137, 138, 147, 174, 459  
   long 464  
 exterior orientation 202–04, 240–41  
   approximate values 209  
   bundle adjustment 232  
   collinearity equations 206  
   correlations 264, 267  
   digital surface model 269–70  
   inverse resection 214–15  
   model 234, 254, 269  
   multi-image processing 283–93  
   panoramic imagery 311–13  
   parameters 205, 212, 213, 248, 252, 260, 267, 279  
   single image 206  
   space resection 206–08, 253, 255, 293, 312  
   spatial similarity transformation 295  
   stereo pair 215–29  
 f-number 112, 138, 191  
 facility management 473, 484  
 fiducial marks 31, 124  
 field of view 112, 178  
 film  
   black-and-white 130, 135  
   deformations 125, 126, 143, 146  
   flattening 141, 146  
   panchromatic 138  
   sensitivity 136, 137, 138  
   unflatness 120  
 final computing test 57  
 finite elements 155

- Firewire 163  
fish-eye lens 264  
fixed datum 245  
fixing 136  
flatness measurement error 437  
floating mark 99, 183, 186, 275, 281–83, 407, 409  
fluorescence 431  
focal length 107  
  extension of 165  
  image 101  
  internal 104  
  lens 100, 101, 112–15, 144, 146  
focal plane shutter 139  
focusing 109–11, 113, 116, 138, 144  
  methods 4  
forensic photogrammetry 6, 489–90  
format angle 112–13, 165  
forward motion compensation 465  
frame  
  grabber 119, 161–63, 465  
  transfer 150  
free-form surfaces 72, 93, 275, 475–76, 487, 491  
free net adjustment 248–51, 262, 301, 446, 450  
frequency  
  limiting 153  
  modulation 180  
Nyquist 133, 153, 154  
pixel 162  
sampling 132  
scanning 161–62  
spatial 129, 131, 133  
fringe modulation 426  
fringe projection  
  coded light approach 427–28  
  dynamic 426–27  
  multi-camera 428  
  phasogrammetry 428–31  
  stationary 425  
full-frame transfer 150  
functional model 52–54
- galvanometer 176, 194  
Gaussian  
  algorithm 70  
  distribution 61–62  
  filter 322, 336, 343  
geodetic engineering surveys 478  
geometric elements 72–94  
GIF 324  
goniometer 128, 449  
GPS 182–83, 242, 252
- grain noise 135  
graphical  
  plotting 11  
  transformation 48–52  
Gray code 427  
gross error  
  detection 67–69  
  divergence 265  
  elimination of 266  
  reliability 64–66  
  standard deviation 60  
Grüber points 224  
guide number 190  
gyroscope 242
- HDTV 161  
height-to-base ratio 99, 104  
high-speed camera 174–75, 465  
homologous points 216, 219, 225, 226, 234  
horizontal  
  parallax 217  
  synchronisation 157, 161  
hyperfocal distance 111
- identification capability 103  
IHS transformation 326  
illuminance 137  
image  
  compression 324, 325–27, 328, 334  
  coordinate system 31, 115, 119, 123–25,  
    126–27, 146, 203, 211  
  display 410  
  distance 104, 107, 121  
  format 100, 101, 113, 117, 141, 143, 458  
  guided surgery 492  
  line 282, 296–97, 298, 302  
  map 470  
  mosaic 269, 274, 470  
  plane 108, 114, 115, 121, 124, 126, 141, 162  
  pyramid 322, 346–47, 367, 379, 384  
  quality 326, 353, 354, 375  
  radius 108, 115, 116, 117, 186, 187  
  rectification 223, 269  
  scale 100–04, 111, 114, 121, 130, 443  
  scale factor 459, 460, 465  
  sequence 163, 175, 461–64  
  space shift 268  
  storage 324  
image matching  
  digital stereo 216  
  with lines 293

- 
- imaging
    - angle 444
    - errors 115, 120, 122
    - optical 104, 114
    - scale 105, 110
    - sequential 462–63
    - synchronous 461
    - vector 115
  - imaging configuration 103, 128, 183, 443–45
    - camera calibration 453
    - planning 444
  - indoor GPS 4
  - industrial
    - metrology 93, 433
    - photogrammetry 6, 485
  - inertial
    - navigation units 242, 252
    - system 182, 183, 466
  - information
    - content 129, 321, 322, 328, 334
    - systems 14, 24
  - infra-red
    - absorbing filter 156
    - remote control 144
  - initial values by bundle adjustments 251–60
    - graphical 258
    - independent model transformation 254–56
    - space intersections and resections 253–54
    - spatial successive model creation 254
      - with automated point measurement 252, 255–58
  - inscribed element 290
  - integration time 147, 156, 175, 194
  - intensity
    - changes 134
    - diffraction 106–07
    - film layers 136
    - laser scanning 178
    - luminous 111
    - radiometric properties 156
  - interchangeable lens 140
  - interference 106, 193
  - interferogram 426
  - interferometry 4, 437
    - speckle 4
  - interior orientation
    - calibration 128–29
    - image coordinate system 123–25
    - imaging errors 115–22, 112–23
    - metric camera 140–41
    - non-metric 146
    - panoramic cameras 171–72
  - parameters 114–15
    - semi-metric cameras 142–46
    - transformations 125–26
  - interlaced scanning 157
  - interlens shutter 140, 144
  - interline transfer 134, 150–52, 168
  - interpolation 78, 92–93
    - grid 125, 126
    - within triangle 92
  - intersection 279–81
    - angle 224, 225, 253, 254, 447
    - spatial 280, 283
  - inventory recording 484
  - inverse
    - camera 424, 428
    - space resection 214
  - iris diameter 112
  - isometry 50
  - Jacobian matrix 43, 53, 54, 56, 57, 66, 70, 76, 78, 87, 89
  - JPEG 324, 325–26
  - L1 norm 259
  - L2 norm 55, 69
  - laboratory calibration 126, 128, 449
  - Lagrangian multipliers 59
  - large format camera 122, 140, 145, 146
  - laser
    - projector 193–94
    - scanner 176–79, 194, 431
    - scanning 475
    - tracker 436, 486
  - Laussedat 15
  - LCD projector 192
  - least squares
    - best-fit 76, 93
    - conditional adjustment 58–59
    - error detection 67
    - general adjustment 34, 56–58
    - linear model 55–59
    - matching 367
    - method 55–59
    - polynomial coefficients 79
    - robust estimation 69
  - LED 185
  - length measurement
    - accuracy 434, 436
    - error 434–35
    - uncertainty 436

- lens  
    aperture 107  
    distortion 267  
    equation 104  
    design 107–09  
    interchangeable 140  
    zoom 113  
leverage point 69, 266  
light  
    fall-off 111  
    gathering capacity 112  
    section 481  
    -section projector 462  
    sensitivity 134, 135, 137, 159  
limiting  
    bundles 107  
    frequency 153  
line  
    constraints 301  
    extraction 475  
    interleaved 323  
    jitter 161  
    pairs per pixel 154  
    photogrammetry 5, 293–302  
    projection 193  
    -scanning camera 169  
    section method 193  
    synchronisation 157  
    widths per picture height 154  
linear programming 69  
linearisation 70  
locator 214–15, 492, 493  
lookup table (LUT) 161  
luminous intensity 111
- machine coordinate system 125  
macro  
    photogrammetry 5  
    scanning 168–71  
material testing 412  
matrix sensor 148, 150–52  
    accuracy potential 176  
    coordinate system 125  
    geometric accuracy 154–55  
    macro-scanning 169–71  
    micro-scanning 168  
    signal-to-noise ratio 157  
    space-multiplex method 173  
    still-video cameras 165  
    time-multiplex method 173  
    video camera 157
- mean point error 283  
mechanical projection 281  
media 302–08  
    bundle-invariant 308  
    interfaces 105, 302–03  
    object-invariant 307–08  
medical applications 491–93  
medicine and physiology 14  
medium format camera 138, 143, 144, 145, 166  
metric camera 124, 126–27, 128, 140–41  
Meydenbauer 16  
micro  
    -head camera 159  
    -mirrors 193  
    -prism 184  
    -scanning 168  
    microlens 152, 159  
        array 152  
mobile mapping 183  
mobility 435  
model  
    coordinate system 32, 218–20, 227, 252, 294  
    coordinates 221–22, 253  
    functional 52–54  
    Gauss-Markov linear 55–59  
    helicopter 465, 466  
    matrix *see* Jacobian matrix  
    stochastic 54–55  
modulation  
    frequency 180  
    of detector system 134  
    transfer 459  
    transfer function 107, 131, 133  
mono-comparator 402  
monoplotting 271  
Moore-Penrose inverse 249  
mosaic 269, 274, 470  
motography 6, 464  
MPEG 163  
MTF50 154  
multi-channel image 323  
multi-image  
    acquisition 98, 99–100  
    configuration 99–100, 252–53, 255  
    orientation 229, 251, 258  
    photogrammetry 5, 6  
    processing 274, 283–93  
    triangulation 99  
multi-media photogrammetry 6, 302–08, 463  
navigation 465, 492, 493  
nearest

- neighbour 322  
 sharp point 111  
 net strain 242  
 network design 446  
 non-centrality parameter 55, 61  
 non-metric camera 127, 146  
 normal  
     case of stereophotogrammetry 217, 222, 275–77  
     distribution 65  
     equation matrix 243, 248  
     equations 56, 57, 58  
     vector 85, 86  
 normalised images 222–23  
 Nyquist frequency 133, 153, 154  
 null hypothesis 65
- object  
     accuracy 445  
     coordinate system 33, 227, 446, 452  
     distance 100, 104  
     edge measurement 423  
     environment 444  
     line 293–302  
 observation  
     vector 52  
     weights 447  
 off-line photogrammetry 6, 11, 22, 415–17  
 on-line photogrammetry 6, 11, 417–20, 486,  
     492–93  
 on-the-job calibration 452 *see also* self-calibration  
 optical  
     axis 31  
     centroid 111, 193  
     projection 281  
 optimisation  
     configuration 446  
     point density 447  
 opto-mechical projection 281  
 order  
     of calculation 252–53  
     of images 259  
     of observations 236  
 orientation  
     absolute 227–29  
     exterior 8, 202–04  
     for analytical instruments 413  
     interior 7, 21, 114–29  
     panoramic image 311–13  
     procedures 11  
     relative 218–27
- single image 206–14  
 stereo pairs 215–17  
 orthochromatic 138  
 orthonormal 35  
     matrix 213  
 orthophoto 5, 11, 271–74  
 outlier 11, 64, 67  
 outline shape measurement 422–23  
 output of results 442  
 over  
     -exposure 137  
     -parameterisation 120  
 overflow effect 156
- panchromatic film 138  
 panorama  
     camera 171  
     photogrammetry 5, 309–14  
 panoramic scanner 176  
 parabolic antennas 485  
 paraboloid 86, 89–90  
 parallax  
     horizontal 217  
     image 99  
     measurement 409, 424  
     x- 104, 217, 275, 277  
     y- 219, 223, 277, 280  
 parallel projection 114, 171, 272  
 parallelepiped 85  
 parameter  
     estimation 46, 288  
     vector 52  
 parametric form 73, 82, 86  
 partial metric camera *see* semi-metric camera  
 particle flow 463–64  
 pattern projection 194  
     active 424, 425–31  
     passive 424, 431–33  
 payload 465  
 pentagonal prism 139, 144  
 perspective centre 109–09, 113–15  
 phase  
     angle 106, 107  
     measurement 425, 426  
     shift method 426–27  
 phase difference 425, 426  
     measurement 176  
 phase locked loop 161  
 phasogrammetry 428–31  
 photo coordinates *see* image coordinates  
 photo diode 151, 153

- photogrammetry  
aerial 5, 202  
analogue 5, 8  
analytical 5, 20  
architectural 6, 469–77  
digital 5, 22  
engineering 6  
forensic 6, 489–90  
industrial 6, 485  
line 5, 293–302  
macro 5  
multi-image 5, 6  
multi-media 6, 302–08, 463  
off-line 6, 11, 22, 415–17  
on-line 6, 11, 417–20, 486, 492–93  
panorama 5, 309–14  
plane table 5, 17  
real-time 5, 9, 22  
satellite 5  
single image 5, 266–74  
stereo 5  
terrestrial 5  
underwater 308
- photon 148–49, 155  
shot noise 157
- phototheodolite 16, 181
- picture tube 148
- pixel 320  
clock 162  
coordinate system 320–22  
frequency 162  
interleaved 323  
jitter 162  
level depth 321  
spacing 134  
value 321
- Planck's quantum 156
- plane 84–86  
best-fit 270  
resection 311  
table photogrammetry 5, 17
- PLL synchronisation 161
- plumb-line calibration 302, 451–52
- PNG 324
- point  
density 447  
of autocollimation 108  
of symmetry 108  
projection 193  
spread function 107, 134
- polar mode 182
- polarised image display 410
- polygon 78–81, 91–92
- polynomial 36, 78–79  
Bernstein 81  
transformation 36
- positive image 31
- power of test 65–66
- pre  
-exposure 143  
-processing 10
- precision 59–61, 66, 250  
comparator 401, 403  
of adjusted object coordinates 261–63  
of image coordinates 260–61
- primary rotation 42
- principal  
distance 31, 100–01, 104, 107–08, 113–15, 121, 263, 267, 278  
plane 105, 107, 114  
point 108, 114–16, 127, 141
- probability density 61
- probing  
camera integrated in 404–05  
device 404–05, 415  
error 434, 437  
tools 189
- progressive-scan 154, 158, 174
- projection  
axonometric 50  
central 50  
centre *see* perspective centre  
isometric 50  
matrix 48, 49, 50, 121, 214  
plane 297–98, 302
- projective  
geometry 48  
transformation 37–39, 266–69
- projector  
laser 193–94  
LCD 192–93  
light section 462  
orientation parameter 430  
pattern 428
- propagation of light 106
- pseudo inverse 249
- pulsed light technique 464
- pupil  
entrance 107, 112  
exit 107
- pyramid *see* image pyramid

- 
- quadrilateral 37  
 quantisation 132  
     table 326  
 quantum efficiency 148  
 quaternions 42  
  
 radial distortion 108, 115–20, 121, 208, 213, 243,  
     263, 304  
 random  
     error 52, 61  
     vector 52  
 rank defect 57, 59, 244–45, 246, 248  
 rapid prototyping 487  
 raster  
     projection 431–32  
     reflection 432  
 raw data 322, 324  
 ray tracing 305–07, 307–08  
 read-out register 148, 149, 150, 151  
 real-time photogrammetry 5, 9, 22  
 reconnaissance 465  
 recording 10–11, 15  
 rectification  
     differential 271–74  
     digital 269  
     image 269  
     plane 269  
     projective 266  
 redundancy 46, 55, 64, 66  
     average 69  
     matrix 64  
     number 60, 63, 64, 65, 68, 69  
 reference  
     lines 300  
     object 435–36  
     scale bar 483, 486  
 reference points 44–47, 57, 245–48, 441  
     inconsistencies 245–48, 250, 262  
     minimum configuration 246  
     observed 245, 246  
 reflection 106  
     in a line 49  
 reflex camera  
     single lens 138–39, 165  
 refraction 305–06  
     index 105  
 regression line 74–75  
 relative  
     aperture 112–13  
     orientation 218–27  
 reliability 64–66, 446  
  
     data snooping 67  
     external 66  
     internal 66, 67  
 remote control 465  
 Remotely Piloted Vehicle 465  
 repeated measurements 55  
 réseau 31, 37, 124–25  
     camera 143, 144  
     scanner 403–04  
     scanning camera 169, 170, 403–04, 406, 423  
     transformation 126  
 resection  
     inverse 214  
     plane 311  
     space 206–12  
 residuals  
     error detection 67–69  
     least squares method 55–59  
     quality measure 59  
     reliability 64–66  
     span 61  
 residuum 56, 59, 64  
 resolution 129–32, 441  
     pyramid *see* image pyramid  
 resolving  
     power 129–30, 153–54, 459  
     threshold of application system (RETAS) 131  
 retro target 104, 184–85, 188  
 re-verification 433–37  
 reverse engineering 487  
 RGB 321  
 ring flash 144, 184, 188, 191  
 RMS 60  
 RMSE 60  
 robot  
     calibration 464  
     calibration probe 406  
     camera 170  
     pose estimation 406  
 robust adjustment 68  
 robust estimation  
     L1-norm 69  
     with weighting function 68–69  
 rotary table 423–24, 430  
 rotating  
     laser 481  
     line scanner 171  
 rotation  
     axis 311  
     primary 42  
     secondary 41, 42

- sequence 204
- spatial 39–44, 49
- rotation matrix 35, 39–44, 45, 47, 49, 87
  - for exterior orientation 203
  - for small rotations 44
  - plane 35–36
  - with algebraic functions 42–43
  - with direction cosines 43
- rotationally symmetric shapes 86–90
- RS-170 157, 158
- run-length encoding 325, 326
- sampling
  - device 134
  - frequency 132
  - theorem 132–33
- satellite photogrammetry 5
- saturation 148, 156
- scale factor 98, 205, 211
  - bundle adjustment 300
  - Direct Linear Transform 213
  - model 221, 369
  - panoramic system 310
  - relative orientation 226
  - space resection 295
  - spatial intersection 280
- scanning 98
  - camera 147, 168–71, 176
  - frequency 161–62
  - theorem 153
- scene-of-crime measurement 489
- Scheimpflug's condition 139
- self-calibration 122, 128, 141, 144, 165, 188, 238, 242–43, 263–64, 453
- semi-metric camera 127, 129
- sensitometry 136
- sensor
  - clock 160
  - coordinate system 125
  - deformations 155
  - element 134, 148–51, 153–58
  - unflatness 120, 126, 155
- shading methods 5
- shaft view finder 144
- shape from stereo 6
- sharpness of object edge 290
- shear 119–21, 243, 264
- shifted cameras 98
- shipbuilding industries 13, 488–89
- shutter 139–40
- Siemens star figure 130
- signal-to-noise ratio 157
- significance level 65, 66
- similarity transformation 34–35
  - plane 34–35
  - spatial 38, 44–48
  - with lines 299–300
- simulation 448
- simultaneous calibration *see* self-calibration
- sinc function 134
- single
  - image photogrammetry 5, 266–74
  - lens reflex camera 138–39, 165
  - station self-calibration 456
- slit diaphragm 106
- slow scan 158
- SLR camera 138, 144
- smear 156
- snakes 291–93
- Snell's law 105
- solid state sensor 148
- space intersection 222, 275, 279–81, 283–85, 288, 315
  - combined with resection 253–54
  - for panorama images 315
- space multiplex 173
- space resection 206–12, 293–95, 405, 406 *see also* resection
  - for panorama image 312
  - inverse 404
  - with minimum object information 209–11
  - with parallel object lines 293–95
- sparse technique 71
- spatial
  - frequency 129, 131, 133
  - similarity transformation 38, 44–48, 49, 211, 226, 228, 241, 289, 300
- spectral decomposition 284
- spectral sensitivity
  - film 138
  - imaging sensors 156
- spline 79–82
  - B- 80–81, 93
  - Bezier approximation 81–82
  - cubic 79, 80, 93
- split screen 410
- standard deviation
  - a posteriori* 55, 56, 57, 59, 60, 68
  - a priori* 55, 56, 60, 66, 68
  - average value 56
  - unit weight 55, 56, 60, 66, 68
  - unknowns 60

- starting model 252–55, 259  
 stationary measuring systems 420–24  
 step gauge 435, 436  
 stereo  
     image matching 216, 223, 275  
     -lithography 475  
     vision 275  
     -workstation 407, 410–11  
 stereobase 104, 219, 224, 279  
 stereocamera 412–13  
 stereocomparator 17, 20, 402  
 stereometric camera 19, 99, 142, 432  
 stereophotogrammetry 5  
     normal case 142  
 Stereoplanigraph 18–19  
 stereoplotter 18–20  
 stereoplotting instruments 18  
 stereoscope 17  
 stereoscopic viewing 402, 410  
 stereovision system 412–13  
 still-video camera 163, 165, 166  
 stitching 309, 313  
 stochastic model 52, 54–55, 56, 60  
 storage zone 150  
 straight line  
     best-fit 74, 84  
     in space 82, 86, 285–87  
     regression line 74–75  
 stroboscopy 464  
 structure zone 130  
 structured light 4  
 Student distribution *see* t-distribution  
 studio camera 139  
 subpixel coordinates 321, 367  
 subtractive colour 136  
 surface  
     measurement systems 424–33  
     model 37, 90, 91, 93  
 surfaces 90–94  
 surveyed directions 241  
 synchronisation  
     error 460–61  
     horizontal 157, 161  
     line 157  
     PLL 161  
     vertical 157  
 system  
     calibration 453  
     combinations 442  
     noise 157
- t-distribution 62, 65  
 tactile  
     measuring probe 417, 419  
     probing 487, 492  
 tangential and asymmetric distortion 109, 118, 243, 264  
 target 183–95, 255–58, 275  
     circular 183  
     coded 188–89, 255–58  
     diameter 186–88  
     eccentricity 186–88  
     luminous 185, 464  
     microprism 184  
     retro-reflective 184–85  
 targeting 10, 183–95  
     eccentric 189–90  
     object 441  
 telecentric lens 114  
 telephoto lens 109  
 temporary coordinate system 306, 310  
 terrestrial photogrammetry 5  
 test  
     field calibration 128, 144, 236, 238, 449–51  
     pattern 130  
 tetrahedron 209, 293  
 theodolite 100  
     measuring system 182, 436, 437, 480, 486  
     video 181–82, 482  
 threshold function 131  
 tie points 216–17, 219, 224–26, 245, 252–54  
 TIFF 323–24  
 tilted images 453, 456  
 time  
     -of-flight 4  
     -multiplex method 173  
 topology 472–73  
 total redundancy 64  
 trace 249  
 traceability 434  
 trajectory 461–63  
 transformation  
     3D Helmert 45  
     4-parameter 34  
     6-parameter 35  
     affine 35  
     bilinear 37, 126  
     graphical 48–52  
     interior orientation 125–26  
     plane affine 35  
     polynomial 36

- 
- 510
- projective 37–39
  - réseau 126
  - spatial similarity 38, 44–48, 49, 211, 226, 228, 241, 289, 300
  - translation 34, 45
  - transparency 136
  - triangulation 91–92
    - aerial 230
    - bundle adjustment 5, 8, 15, 99, 172
    - geometric elements 72
    - laser projection 193
    - photogrammetric 20
    - principle 435
    - targeting 184
    - techniques 4
  - true colour
    - image 321
    - sensor 172, 173
  - tunnel profile measurement 481–82
  - ultra-light aircraft 465
  - uncertainty
    - image measurement 102–04
    - length measurement 436
  - under-exposure 137
  - undersampling 133
  - underwater photogrammetry 308
  - unflatness
    - film 120
    - sensor 120, 126, 155
  - unwrapping 426
  - USB 163
  - variance component estimation 67–68, 261
  - vario lens 113
  - vector
    - image coordinates 31
    - inconsistencies 58
  - velocity 459–60
    - of propagation 105–06, 156
  - verification of accuracy 442
  - vertical
    - line focus 282
    - synchronisation 157
  - video
    - beamer 192
    - camera 147, 157–63, 178
      - theodolite 181–82, 482
    - videogrammetry 5, 22
    - view finder camera 138, 139, 144
  - viewing angle 445
  - vignetting 111
  - visual processing 275
  - visualisation
    - 3D 472–74, 491
      - building 472–74
    - VRML 473
  - wavelet compression 324–25
  - weight matrix 54, 56, 68
  - weighted datum 246
  - wire model 91
  - x-parallax 217, 275, 277
  - y-parallax 219, 223, 277, 280
  - zoom lens 113
  - $\chi^2$ -distribution 284